



**GAS TURBINE FUEL FLEXIBILITY: PRESSURIZED SWIRL
FLAME STABILITY, THERMOACOUSTICS, AND EMISSIONS**

BY

JON RUNYON

A thesis submitted in partial fulfilment of the requirements for the degree of:

Doctor of Philosophy

in

Mechanical Engineering

**CARDIFF UNIVERSITY
SCHOOL OF ENGINEERING
GAS TURBINE RESEARCH CENTER**

MAY 2017

SIGNED STATEMENTS

DECLARATION

This work has not been submitted in substance for any other degree or award at this or any other university or place of learning, nor is being submitted concurrently in candidature for any degree or other award.

Signed(candidate) Date

STATEMENT 1

This thesis is being submitted in partial fulfillment of the requirements for the degree of PhD in Mechanical Engineering

Signed(candidate) Date

STATEMENT 2

This thesis is the result of my own independent work/investigation, except where otherwise stated, and the thesis has not been edited by a third party beyond what is permitted by Cardiff University's Policy on the Use of Third Party Editors by Research Degree Students. Other sources are acknowledged by explicit references. The views expressed are my own.

Signed(candidate) Date

STATEMENT 3

I hereby give consent for my thesis, if accepted, to be available online in the University's Open Access repository and for inter-library loan, and for the title and summary to be made available to outside organizations.

Signed(candidate) Date

“Engineering is not just a profession to be learned and practiced as a way of making a living. It is one of the few ways in which human talent can be given the chance to improve, and frequently to transform, the comfort and prosperity of the human community.”

– HRH Prince Philip, Duke of Edinburgh

“Life might be difficult for a while, but I would tough it out because living in a foreign country is one of those things that everyone should try at least once. My understanding was that it completed a person, sanding down the rough provincial edges and transforming you into a citizen of the world.”

– David Sedaris

TABLE OF CONTENTS

FIGURES INDEX	IX
TABLES INDEX	XXI
SYMBOL LIST	XXII
ABBREVIATION LIST	XXV
ACKNOWLEDGEMENTS	XXVII
JOURNAL PUBLICATION AND CONFERENCE PROCEEDINGS LIST	XXVIII
SUMMARY	1
CHAPTER 1 – INTRODUCTION	2
1.1 Motivation	2
1.1.1 Energy Policy – Decarbonization of Electrical Power Generation	2
1.1.1.1 United Kingdom Energy Policy	3
1.1.2 United Kingdom Power Generation – Past, Present, and Future	5
1.1.3 Natural Gas in the UK.....	7
1.1.3.1 Liquefied Natural Gas	8
1.1.3.2 Natural Gas – Hydrogen Blends	9
1.2 Thesis Aims and Objectives.....	11
1.3 Thesis Structure	12
CHAPTER 2 – STATE OF THE ART AND LITERATURE REVIEW	13
2.1 Gas Turbine Fuel Flexibility	13
2.1.1 Gas Turbine OEM Experience	14
2.1.2 Gas Turbine Operator Experience.....	16
2.1.3 Fundamentals of Higher Hydrocarbons in Natural Gas	18
2.1.3.1 Chemical Kinetics	18
2.1.3.2 Ignition Delay	19
2.1.3.3 Burning Velocity.....	20
2.1.4 Fundamentals of Hydrogen Addition to Natural Gas	21
2.1.4.1 Chemical Kinetics, Ignition Delay, and Burning Velocity	21
2.2 Swirl Flame Stability.....	24
2.2.1 Flame Stabilization Mechanisms	24
2.2.2 Flame Instabilities	27
2.2.2.1 Thermoacoustic Instabilities	28
2.2.2.2 Lean Flame Blowoff	30
2.2.2.3 Lean Flame Flashback	32
2.3 Combustion under Elevated Temperature and Pressure Conditions	33

2.3.1 Turbulence Effects	33
2.3.2 Chemical Kinetic Effects	35
2.4 Exhaust Gas Emissions Formation	37
2.4.1 Chemical Kinetics	37
2.4.2 Influence of Fuel Composition	39
2.4.2.1 Influence of Higher Hydrocarbons in Natural Gas	39
2.4.2.2 Influence of Hydrogen in Natural Gas	40
2.5 Chapter Summary	41
CHAPTER 3 – EXPERIMENTAL FACILITIES AND METHODOLOGIES	42
3.1 Cardiff University Gas Turbine Research Centre	42
3.1.1 High Pressure Combustion Rig.....	42
3.1.1.1 Fuel and Air Delivery System	42
3.1.1.2 High Pressure Optical Chamber	44
3.1.1.3 HPCR Data Acquisition	45
3.1.1.4 HPCR Instrumentation Measurement Accuracy	46
3.1.2 Swirl Burners.....	47
3.1.2.1 High Pressure Generic Swirl Burner (Mk. I)	48
3.1.2.2 High Pressure Generic Swirl Burner (Mk. II)	49
3.2 Non-Intrusive Diagnostics.....	52
3.2.1 Optical Diagnostics.....	52
3.2.1.1 Chemiluminescence	53
3.2.1.2 Planar Laser Induced Fluorescence	55
3.2.1.3 Particle Image Velocimetry.....	58
3.2.2 Thermoacoustic Diagnostics	62
3.2.2.1 Dynamic Pressure Measurement.....	63
3.2.3 Emissions Gas Analysis.....	65
3.3 Numerical Techniques	66
3.3.1 Chemical Kinetics Modeling.....	66
3.3.2 Low Order Thermoacoustic System Modeling.....	67
3.4 Experimental Matrix Development	69
3.4.1 Fuel Selection.....	69
3.4.1.1 Natural Gas Blended with Higher Hydrocarbons and Nitrogen.....	69
3.4.1.2 Natural Gas Blended with Hydrogen	72
3.4.2 HPCR Operating Conditions	73
CHAPTER 4 – NEW DIAGNOSTIC SUITE FOR PRESSURIZED COMBUSTION FACILITY ..	77
4.1 Chemiluminescence Measurement Facility.....	77
4.1.1 System Setup and Components.....	78

4.1.2 Image Processing and Data Analysis.....	81
4.1.3 System Commissioning	84
4.2 Planar Laser Induced Fluorescence Measurement Facility	87
4.2.1 System Setup and Components.....	88
4.2.2 Image Processing and Data Analysis.....	90
4.2.3 System Commissioning	93
4.2.3.1 PLIF Commissioning in the HPGSB	93
4.2.3.2 PLIF Commissioning in the HPGSB-2.....	95
4.3 Dynamic Pressure Measurement Facility	98
4.3.1 System Setup and Components.....	99
4.3.2 Data Processing and Analysis.....	100
4.3.3 System Commissioning	101
4.4 Chapter Summary	104
CHAPTER 5 – CHARACTERIZATION OF NEW GENERIC SWIRL BURNERS.....	106
5.1 High Pressure Generic Swirl Burner (Mk. I)	106
5.1.1 Combustion Characterization	107
5.2 High Pressure Generic Swirl Burner (Mk. II)	111
5.2.1 Isothermal Characterization	112
5.2.1.1 Isothermal Acoustic Characterization.....	112
5.2.1.2 Isothermal Flow Characterization Using PIV.....	115
5.2.2 Combustion Characterization	122
5.2.2.1 Elevated Inlet Temperature and Pressure Combustion.....	124
5.2.2.2 Application of LBO Instability Prediction Methods.....	137
5.3 Chapter Summary	142
CHAPTER 6 – FUEL FLEXIBILITY FOR GAS TURBINES – HIGHER HYDROCARBONS	146
6.1 Chemical Kinetics Modeling and Flame Speed Measurements.....	147
6.1.1 Chemical Kinetics Modeling.....	147
6.1.2 Flame Speed Measurements	151
6.2 Flame Stabilization.....	153
6.2.1 Influence of Ethane Addition	154
6.2.2 Investigation of Ternary Natural Gas Mixtures.....	157
6.2.3 Constant Wobbe Index Evaluation	160
6.2.4 Influence of Heat Release and Reaction Zone Thickness.....	163
6.2.4.1 Evaluation of Experimental and Numerical Heat Release Measurements.....	163
6.2.4.2 Evaluation of Experimental and Numerical Reaction Zone Thickness Measurements.....	169
6.3 Thermoacoustics.....	172

6.3.1 Frequency Domain Analysis.....	173
6.3.2 Time Domain Analysis.....	177
6.4 Exhaust Gas Emissions	180
6.5 Chapter Summary	184
CHAPTER 7 – FUEL FLEXIBILITY FOR GAS TURBINES – HYDROGEN ADDITION	186
7.1 Chemical Kinetics Modeling and Flame Speed Measurements.....	187
7.1.1 Chemical Kinetics Modeling.....	187
7.1.2 Flame Speed Measurements	191
7.2 Flame Stabilization.....	193
7.2.1 Influence of Premixed Fuel Composition.....	193
7.2.2 Influence of Burner Confinement Geometry.....	197
7.2.3 Influence of Burner Geometric Swirl Number	202
7.3 Thermoacoustics.....	208
7.3.1 Influence of Burner Confinement Geometry.....	208
7.3.2 Influence of Burner Geometric Swirl Number	211
7.4 Exhaust Gas Emissions	215
7.5 Chapter Summary	220
CHAPTER 8 – REVIEW OF A GAS TURBINE THERMOACOUSTIC MODELING TOOL	222
8.1 Model Initialization	223
8.1.1 Geometry Input.....	223
8.1.2 Flame Model and Boundary Conditions	225
8.1.2.1 Flame Model Selection and Inputs	225
8.1.2.2 Boundary Conditions Selection and Inputs.....	227
8.2 Acoustic Modeling of Selected Experimental Conditions.....	228
8.2.1 CH ₄ Combustion Thermoacoustic Instability (Chapter 5.2.2.2)	228
8.2.2 CH ₄ / CH ₄ -H ₂ Combustion Thermoacoustic Instability (Chapter 7.3.1)	232
8.2.3 CH ₄ / CH ₄ -H ₂ Combustion Noise (Chapter 7.3.1).....	237
8.3 Model Prediction at Gas Turbine Relevant Conditions.....	241
8.4 Chapter Summary	243
CHAPTER 9 – CONCLUSIONS AND FUTURE WORK.....	245
9.1 Facilities	245
9.2 Methodologies.....	246
9.3 Fuel Blends.....	247
9.3.1 Methane-Higher Hydrocarbons	247
9.3.2 Methane-Hydrogen.....	248
9.4 Future Work.....	249
REFERENCES	250

APPENDIX A – UNITED KINGDOM GAS TRANSMISSION NETWORK.....	268
APPENDIX B – BURNER AND RIG CAD DRAWINGS/PHOTOGRAPHS	269
Appendix B.1 – HPGSB-2 CAD Drawings	269
Appendix B.2 – Photographs and Diagrams	275
Appendix B.2.1 – HPCR and HPGSB/HPGSB-2 Photographs and Diagrams.....	275
Appendix B.2.2 – Optical Diagnostics Photographs and Diagrams.....	278
APPENDIX C – COMPUTATIONAL CODES	282
Appendix C.1 – Chemiluminescence Image Temporal Average and Integral Intensity MATLAB code.....	282
Appendix C.2 – Chemiluminescence Abel Deconvolution MATLAB code	284
Appendix C.3 – Planar Laser Induced Fluorescence Image Processing MATLAB codes	286
Appendix C.4 – Dynamic Pressure Measurement Processing MATLAB code.....	291
Appendix C.5 – PIV Image Processing, Length Scale, and Turbulence Characterization MATLAB code.....	297
APPENDIX D – IMAGE PROCESSING STATISTICAL ANALYSIS	305
Appendix D.1 – Chemiluminescence Total Image Number Selection	305
Appendix D.2 – PLIF Total Image Number Selection	306
Appendix D.3 – PIV Total Image Number Selection.....	308
APPENDIX E – GLOBAL EXPERIMENTAL SWIRL BURNERS	310

FIGURES INDEX

Figure 1.1: Fuels used to generate electricity in the UK from 1948-2008. Reproduced from [11].	6
Figure 1.2: Shares of UK electricity generation by fuel type in 2014 and 2015. Reproduced from [3].	6
Figure 1.3: Projected UK electricity generation capacities by source in the UK National Grid “Gone Green” scenario. Reproduced from [13].	7
Figure 1.4: UK natural gas flow chart in TWh for 2015. Reproduced from [3].	8
Figure 2.1: Projected fuel types for Siemens installed GT fleet. Reproduced from [26].	15
Figure 2.2: Photograph of damaged GT combustion chamber due to excessive combustion dynamics. Reproduced from [16].	17
Figure 2.3: Lewis number as a function of H ₂ content in CH ₄ (a) and C ₃ H ₈ (b) at $\varphi = 0.6$ with blending laws (solid line) and experimental values (solid square). Reproduced from [51, 52].	23
Figure 2.4: General representation of industrial can-type GT combustor. Reproduced from [1].	24
Figure 2.5: Schematic of the formation of the CRZ in unconfined swirl flows. Reproduced from [60].	25
Figure 2.6: Typical mean flow streamlines and coherent flow structures for a confined, swirling, reacting flow. Reproduced from [59, 61].	26
Figure 2.7: Closed-loop diagram of combustion thermoacoustic instability formation.	29
Figure 2.8: Premixed turbulent combustion flame regime diagram. Reproduced from [59].	34
Figure 2.9: Influence of turbulence intensity and H ₂ (a) or C ₃ H ₈ (b) addition to CH ₄ on the turbulence burning velocity, S_t . Reproduced from [96].	36
Figure 2.10: Influence of equivalence ratio on measured Markstein length of methane, ethane, propane, and hydrogen-air flames at 293 K and 0.101 MPa. Methane and ethane data from [97], propane data from [98], and hydrogen data from [99].	37
Figure 2.11: Typical NO _x and CO emissions levels from GT combustion as a function of temperature. Reproduced from [100].	38
Figure 3.1: Simplified schematic of the fuel and air delivery systems for premixed, preheated, and pressurized operation at the GTRC HPCR. Note that the HPOC is not shown.	44
Figure 3.2: Photographs of HPOC during maintenance (left) and installed in the HPCR (right).	45

Figure 3.3: Sectioned detail view of the HPGSB/HPOC assembly with (a) instrumentation and pilot lance, (b) inlet plenum, (c) HPOC casing, (d) premixing chamber, (e) radial-tangential swirler, (f) burner exit nozzle, (g) quartz window, and (h) quartz burner confinement tube. Reproduced from [112].	49
Figure 3.4: Sectioned detail view of the HPGSB-2/HPOC assembly with (a) instrumentation and pilot lance, (b) inlet plenum, (c) mixing chamber, (d) radial-tangential swirler, (e) burner exit nozzle, (f) quartz window, (g) quartz burner confinement tube, and (h) HPOC casing.	50
Figure 3.5: Radial-tangential swirler geometries with $S_g = 0.8$ (left) and $S_g = 0.5$ (right). Tangential inlet width dimension in meters.	50
Figure 3.6: Schematic of HPGSB-2 showing the instrumentation and pilot lance (a), inlet plenum (b), HPOC connecting flange (c), mixing chamber (d), burner exit nozzle (e), and quartz confinement (f). Dimensions in meters. Reproduced from [123].	52
Figure 3.7: Typical CL spectra of atmospheric natural gas-air flames at varying ϕ . Reproduced from [165].	54
Figure 3.8: Schematic diagram of the PLIF molecular energy states. Reproduced from [180].	55
Figure 3.9: OH radical A and X states potential curves. Reproduced from [185].	57
Figure 3.10: Simulated combined LIF absorption and emission spectra from LIFBASE [186] for OH radical at 0.1 MPa and 1700 K, including vibrational bands.	58
Figure 3.11: Schematic diagram of the PIV image capture and laser timing control system in the HPCR	60
Figure 3.12: Ideal (black) and practical (red) correlation coefficient relationship for determination of integral length scale. Adapted from [192].	62
Figure 3.13: Representative combustor geometry input to OSCILOS, mathematical domain (left) and example OSCILOS input (right), flow left to right across flame (red line). Reproduced from [205].	68
Figure 3.14: WI of LNG from exporting countries as a function of higher heating value, H_5 . UK maximum WI limit and investigated fuel blends shown for reference.	71
Figure 3.15: WI of LNG from exporting countries as a function of C_{2+} content. UK maximum WI limit and investigated fuel blends shown for reference.	71
Figure 3.16: HPGSB-2 dimensionless turbulence scaling parameter, τ_T / τ_η , as a function of $P2$ for the selected target operating conditions (a) and extended to theoretical $P2 = 1.5$ MPa (b, red).	76
Figure 4.1: CL measurement system timing, image capture, and utility setup at Cardiff University's GTRC as used for measurements with the HPGSB-2.	80

Figure 4.2: Time-averaged OH* chemiluminescence image before (a) and after (b) Abel inversion for 50 kW BOS gas flame at $T_2 = 285$ K, $P_2 = 0.101$ MPa, and $\varphi = 0.98$	82
Figure 4.3: Effect of image intensifier gain and intensifier gate signal pulse width on the integral intensity of OH* and CH* signal in CH ₄ -air and BOS gas flames at $\varphi = 1.0$	83
Figure 4.4: Abel inversion of OH* chemiluminescence images for 50 kW CH ₄ -air flame at atmospheric pressure (a) and 0.2 MPa (b) and $\varphi = 0.8$	85
Figure 4.5: Time-averaged CH* chemiluminescence image (a) and after Abel inversion (b) of a 50 kW atmospheric BOS gas flame at $\varphi = 0.98$	86
Figure 4.6: Effect of φ on the integral intensity of OH* (diamond) and CH* (square) for both CH ₄ and BOS gas flames at $T_2 = 285$ K and $P_2 = 0.101$ MPa.	86
Figure 4.7: Effect of φ on normalized integral intensity (a) and S_L (b) of CH ₄ and BOS flames at atmospheric temperature and pressure.	87
Figure 4.8: Fixed laser sheet PLIF measurement system timing and image capture setup at Cardiff University's GTRC.	90
Figure 4.9: PLIF laser sheet intensity (a) and Gaussian fit to intensity distribution (b) for image correction.	92
Figure 4.10: Average OH PLIF measurement (a) and extracted flame surface (b) for a 42 kW CH ₄ -air flame at $T_2 = 573$ K, $P_2 = 0.11$ MPa, and $\varphi = 0.7$ in the HPGSB-2 with convergent confinement.	93
Figure 4.11: Average OH PLIF measurements for a premixed 55 kW CH ₄ -air flame at $T_2 = 288$ K and $P_2 = 0.101$ MPa, with $\varphi = 0.7$ (a) and $\varphi = 0.8$ (b) in the HPGSB.	94
Figure 4.12: I_{OH^*} measurements as a function of t_{gate} for a premixed 55 kW CH ₄ -air flame at $T_2 = 288$ K, $P_2 = 0.101$ MPa, and $\varphi = 0.7$ (a) and 0.8 (b)	95
Figure 4.13: Averaged images using scanning OH PLIF method (with 2 passes) of a 42 kW CH ₄ -air flame at $T_2 = 288$ K, $P_2 = 0.11$ MPa, and $\varphi = 0.64$ (a), 0.70 (b), and 0.80 (c)	96
Figure 4.14: Defining the reaction zone thickness, δ_r , based on maximum CH and OH mole fraction location in one-dimensional flame model from CHEMKIN PREMIX code. Modeled conditions for CH ₄ -air flame shown in Figure 4.22.c.	97
Figure 4.15: Comparisons between measured δ_{flame} at the maximum OH PLIF intensity location and modeled δ_r (a) and between axial location of maximum OH PLIF intensity and modeled maximum OH mole fraction location (b) for a 42 kW CH ₄ -air flame with varying number of scanning PLIF passes	98

Figure 4.16: Schematic of the DPT measurement system and DPT locations in the HPGSB-2 (green) and HPOC (black), including overall combustor length and dynamic pressure impulse line (purple) length. Note also the cylindrical quartz confinement (blue), piloted instrumentation lance (red), and 10 m semi-infinite copper tubing (brown). For Detail “A”, refer to Figure 4.26.	100
Figure 4.17: Detail “A” from Figure 4.25 of the HPGSB-2 (green), showing locations of the “Pilot” and “Burner Face” DPTs in addition to details of the instrumented pilot lance (red) bluff body location within the burner exit nozzle. Premixed air/fuel flow (yellow) shown for reference.....	100
Figure 4.18: Influence of \bar{u} and S_g on measured Pilot DPT f_{peak} for isothermal air flow study in the HPGSB, with values unscaled (a) and correct (b) to account for swirl.	102
Figure 4.19: FFT of Burner Face DPT measurement for isothermal air flow in the HPGSB-2 with varying swirl number	103
Figure 4.20: Swirl-corrected normalized pressure amplitude as a function of P_2 and S_g for isothermal air flow at 0.11 MPa, 0.22 MPa, and 0.33 MPa	104
Figure 5.1: Chemical kinetics modeling of S_L as a function of AFT for LPM CH ₄ -air and C ₃ H ₈ -air flames.....	108
Figure 5.2: Fixed sheet OH PLIF measurement of LPM CH ₄ -air and C ₃ H ₈ -air flames in the HPGSB at $T_2 = 288$ K, $P_2 = 0.101$ MPa, $S_g = 0.8$, and varying ϕ	109
Figure 5.3: Abel transformed OH* chemiluminescence of LPM CH ₄ -air and C ₃ H ₈ -air flames in the HPGSB at $T_2 = 288$ K, $P_2 = 0.101$ MPa, $S_g = 0.8$, and varying ϕ	110
Figure 5.4: I_{OH^*} as a function of AFT (a) and scaled by the fuel H:C ratio (b) for CH ₄ -air and C ₃ H ₈ -air flames	111
Figure 5.5: Exhaust gas measurements for premixed CH ₄ -air and C ₃ H ₈ -air flames as a function of AFT, showing CO ₂ (closed) / O ₂ (open) (a), and NO _x (closed) / CO (open) (b).....	111
Figure 5.6: Temporal variation of dynamic pressure measurement for all four DPTs during an isothermal loudspeaker 40-1000 Hz linear tone sweep with the BPV in the fully open (a) and fully closed (b) positions	112
Figure 5.7: Spectrograms of the Burner Face DPT measurement during an isothermal loudspeaker 40-1000 Hz linear tone sweep with the BPV in the fully open (a) and fully closed (b) positions	114
Figure 5.8: Isothermal air flow Helmholtz and Strouhal numbers as a function of f_{peak} for $T_2 = 286$ K, 423 K, and 523 K and $P_2 = 0.101$ MPa, 0.2 MPa, and 0.4 MPa with open confinement and $S_g = 0.8$	115
Figure 5.9: Helmholtz number as a function of Re for fixed T_2 and P_2 isothermal air flow tests in the HPGSB-2 with open confinement and $S_g = 0.8$	115

Figure 5.10: Isothermal air flow PIV velocity vector maps with axial velocity contours for the HPGSB-2 (open confinement) at varying P_2 and $T_2 = 573$ K	117
Figure 5.11: Isothermal air flow PIV velocity vector maps with axial velocity contours for the HPGSB-2 (convergent nozzle confinement) at varying P_2 and $T_2 = 573$ K	118
Figure 5.12: Axial velocity profiles of isothermal air flow in the HPGSB-2 open (a) and convergent (b) confinement at $y = 32$ mm with varying P_2	119
Figure 5.13: Isothermal air flow axial relative turbulence intensity (T_{int}) contours for the HPGSB-2 at $T_2 = 573$ K, with varying burner confinement and P_2 . Note change in colormap scaling.	121
Figure 5.14: Integral length scale ($L_{T,e}$ and $L_{T,int}$) variation in the axial direction along the burner centerline (a) and in the radial direction fixed at height $y = 32$ mm above the burner exit nozzle (b). Note varying P_2 (0.11, 0.22, 0.33 MPa) and confinement: open ("O", open symbols) and convergent ("C", closed symbols)	122
Figure 5.15: Color photograph of 55 kW CH_4 -air flame at $P_2 = 0.105$ MPa, $T_2 = 287$ K, and $\varphi = 0.8$	123
Figure 5.16: Stable operating curves for selected ATAP, ETAP, and ETEP combustion cases in the HPGSB-2.....	125
Figure 5.17: Abel transformed OH^* chemiluminescence images for ETAP CH_4 -air flames ($T_2 = 573$ K, $P_2 = 0.101$ MPa, $P_{therm} = 55$ kW) at $\varphi = 0.50$ (a), 0.60 (b), and 0.75 (c).....	127
Figure 5.18: Time-averaged OH PLIF images for ETAP CH_4 -air flames ($T_2 = 573$ K, $P_2 = 0.101$ MPa, $P_{therm} = 55$ kW) at $\varphi = 0.53$ (a) and 0.60 (b).	128
Figure 5.19: Effect of φ on II'_{OH^*} for ETAP CH_4 -air flames ($T_2 = 573$ K, $P_2 = 0.101$ MPa, $P_{therm} = 55$ kW).....	128
Figure 5.20: PSD of Burner Face DPT measurement during LBO instability at $\varphi = 0.50$ (a) and operation at $\varphi = 0.60$ (b) for ETAP CH_4 -air flames ($T_2 = 573$ K and $P_{therm} = 55$ kW)	129
Figure 5.21: Effect of φ on the observed dynamic pressure fluctuation of the Burner Face DPT for ETAP CH_4 -air flames ($T_2 = 573$ K and $P_{therm} = 55$ kW)	129
Figure 5.22: Bandpass filtered PSD for Burner Face DPT during LBO instability in ETAP CH_4 -air flames at $T_2 = 423$ K and $P_{therm} = 49$ kW (a), $T_2 = 423$ K and $P_{therm} = 55$ kW (b), $T_2 = 560$ K and $P_{therm} = 42$ kW (c), and $T_2 = 573$ K and $P_{therm} = 55$ kW (d).....	130
Figure 5.23: Abel inverted OH^* chemiluminescence images for ETEP CH_4 -air flames at $\varphi = 0.50$ (a), 0.53 (b), and 0.60 (c).....	132
Figure 5.24: Time-averaged OH PLIF image for an 110 kW ETEP CH_4 -air flame at $\varphi = 0.53$	133
Figure 5.25: Effect of φ on II'_{OH^*} for 110 kW ETEP CH_4 -air flames	134

Figure 5.26: OH* chemiluminescence intensity fluctuation (left) with solid markers corresponding to selected instantaneous OH* chemiluminescence images (right) for a 110 kW ETEP CH ₄ -air flame during LBO instability at $\varphi = 0.49$	135
Figure 5.27: PSD of Burner Face DPT measurement for 110 kW ETEP CH ₄ -air flames during LBO instability at $\varphi = 0.49$ (a) and operation at $\varphi = 0.60$ (b)	136
Figure 5.28: Effect of φ on the total dynamic pressure fluctuation of the Burner Face DPT for 110 kW ETEP CH ₄ -air flames	136
Figure 5.29: Bandpass filtered PSD for Burner Face DPT during LBO instability for an 110 kW ETEP CH ₄ -air flame at $\varphi = 0.49$	137
Figure 5.30: Effect of φ on the measured Burner Face DPT kurtosis across 3 operating cases in the HPGSB-2.....	138
Figure 5.31: Effect of bandpass maximum cutoff frequency on the measured Burner Face DPT kurtosis during LBO instability of an 110 kW ETEP CH ₄ -air flame at $\varphi = 0.49$	139
Figure 5.32: Time series of measured Burner Face DPT kurtosis (a) and p'_{RMS} (b) at the approach to LBO instability in the 55 kW ATAP and $T_2 = 573$ K, 55 kW ETAP operating cases	140
Figure 5.33: Strouhal number as a function of LBO dominant frequency in the HPGSB-2	140
Figure 5.34: Effect of τ_{chem} on the LBO f_{peak} in the HPGSB-2	141
Figure 5.35: Comparison of Da relationship applied by Cavaliere et al. [89] with the observed LBO instability (a) and with swirl-corrected exit velocity (b).....	142
Figure 6.1: Modeled S_L of all experimental conditions as a function of AFT with varying P_2 , 0.11 MPa (open), 0.22 MPa (closed), 0.33 MPa (hashed)	148
Figure 6.2: Normalized modeled S_L of selected experimental conditions as a function of P_2 at varying φ , 0.55 (a) and 0.60 (b).	149
Figure 6.3: Modeled S_L of selected experimental conditions as a function of fuel molar H:C ratio at varying φ , 0.55 (a) and 0.60 (b), and P_2 , 0.11 MPa (open), 0.22 MPa (closed), 0.33 MPa (hashed)	150
Figure 6.4: Pressure influence on modeled S_L of selected experimental conditions at $\varphi = 0.55$ (open symbols) and 0.60 (closed symbols).....	150
Figure 6.5: S_L measurements for BASE and EMIX1 flames at 298 K and 0.101 MPa	151
Figure 6.6: Measured stretched flame speed (at $\varphi = 0.60$, a) and Markstein length (at varying φ , b) for BASE and EMIX1 flames at $T_2 = 298$ K and $P_2 = 0.101$ MPa.....	152
Figure 6.7: Abel-transformed OH* chemiluminescence images for BASE and FARNG flames at $\varphi = 0.55$ with varying P_2	155

Figure 6.8: Scanning OH PLIF measurements of BASE and FARNG flames at $T_2 = 573$ K, $P_2 = 0.33$ MPa, and varying φ	157
Figure 6.9: Abel-transformed OH* chemiluminescence images for MIDNG and EMIX1 flames at $\varphi = 0.55$ with varying P_2	159
Figure 6.10: Scanning OH PLIF measurements of MIDNG and EMIX1 flames at $T_2 = 573$ K, $P_2 = 0.33$ MPa, and varying φ	160
Figure 6.11: Abel-transformed OH* chemiluminescence images for FARNG and EMIX1 flames at $\varphi = 0.60$ with varying P_2	162
Figure 6.12: Lean operating curves for FARNG and EMIX1 flames as a function of φ and P_2 , 0.11 MPa (open), 0.22 MPa (closed), and 0.33 MPa (hashed).	163
Figure 6.13: OH* chemiluminescence intensity centroid locations and flame angles at $T_2 = 573$ K, $\varphi = 0.55$, and varying P_2 , 0.11 MPa (open), 0.22 MPa (closed), 0.33 MPa (hashed). Arrows indicate the transition from $P_2 = 0.11$ MPa to 0.22 MPa.	164
Figure 6.14: Measured I_{OH^*} as a function of AFT (a), Q' (b), and Q (c) for all experimental conditions with varying P_2 , 0.11 MPa (open), 0.22 MPa (closed), 0.33 MPa (hashed).....	165
Figure 6.15: Measured I_{OH^*} as a function of fuel molar H:C ratio at $\varphi = 0.55$ with varying P_2 , 0.11 MPa (open), 0.22 MPa (closed), and 0.33 MPa (hashed).	167
Figure 6.16: Measured I_{OH^*} as a function of P_2 for varying fuel composition at $\varphi = 0.55$	167
Figure 6.17: Measured I_{OH^*} as a function of AFT and P_2 , 0.11 MPa (open), 0.22 MPa (closed), 0.33 MPa (hashed), for all experimental conditions, scaled by fuel molar H:C ratio (a) and then additionally by the exponential pressure influence (b)	169
Figure 6.18: Projected I_{OH^*} levels in the HPGSB-2 as a function of AFT and fuel molar H:C ratio at $P_2 = 1.5$ MPa (573 kW).	169
Figure 6.19: Modeled maximum CH mole fraction, X_{CH} , as a function of P_2 at $\varphi = 0.55$	170
Figure 6.20: Modeled reaction zone thickness, δ_t , as a function of P_2 at $\varphi = 0.55$ (open) and 0.60 (closed).....	170
Figure 6.21: Measured mean flame brush thickness, δ_{flame} , as a function of P_2 at $\varphi = 0.55$ (open) and 0.60 (closed)	171
Figure 6.22: Measured mean flame brush area, A_{flame} , as a function of P_2 at $\varphi = 0.55$ (open) and 0.60 (closed).....	172
Figure 6.23: FFT of Burner Face DPT measurement for varying fuel composition and P_2 at $\varphi = 0.55$. Note the change in y-axis scaling for each plot.	174
Figure 6.24: FFT of Burner Face DPT measurement for varying fuel composition and P_2 at $\varphi = 0.60$. Note the change in y-axis scaling for each plot.	175

Figure 6.25: Dominant Burner Face DPT frequency, f_{peak} , plotted against Q	177
Figure 6.26: Normalized Burner Face DPT amplitude as a function of Q'_{max}	178
Figure 6.27: Influence of fuel molar H:C ratio on normalized Burner Face DPT amplitudes at $\varphi = 0.55$ and varying $P2$, 0.11 MPa (open), 0.22 MPa (closed), and 0.33 MPa (hashed).....	178
Figure 6.28: Normalized Burner Face DPT amplitude as a function of normalized $P2$ at $\varphi = 0.55$, unscaled (a) and scaled by fuel (H:C) ³ (b)	179
Figure 6.29: Projected combustion noise levels in the HPGSB-2 as a function of $P2$ and fuel molar H:C ratio up to $P2 = 1.5$ MPa (573 kW).....	179
Figure 6.30: NO _x emissions versus AFT at varying $P2$ for all experimental conditions at $T2 = 573$ K	181
Figure 6.31: NO _x emissions versus fuel molar H:C ratio at $\varphi = 0.55$ and varying $P2$, 0.11 MPa (open), 0.22 MPa (closed), 0.33 MPa (hashed)	182
Figure 6.32: NO _x emissions plotted versus $P2$ at varying φ , 0.55 (a) and 0.60 (b). Note difference in y-axis scaling.	183
Figure 6.33: Normalized NO _x emissions plotted against normalized maximum CH mole fraction (a) and normalized modeled reaction zone thickness (b) at $\varphi = 0.55$ and varying $P2$, 0.11 MPa (open), 0.22 MPa (closed), 0.33 MPa (hashed)	184
Figure 7.1: Modeled S_L of experimental BASE flames as a function of AFT at $P2 = 0.11$ MPa with varying $T2$, burner confinement, and S_g	188
Figure 7.2: Modeled S_L of experimental BASE (a) and FARH2 (b) flames as a function of AFT at $T2 = 573$ K with varying $P2$, burner confinement, and S_g	189
Figure 7.3: Pressure influence on modeled S_L of experimental BASE and FARH2 flames at $\varphi = 0.55$ (open symbols) and $\varphi = 0.60$ (closed symbols) with $T2 = 573$ K, convergent confinement, and $S_g = 0.8$	189
Figure 7.4: Modeled κ_{ext} plots for experimental BASE and FARH2 flames at $T2 = 573$ K, convergent confinement, and $S_g = 0.8$ with varying φ and $P2$	191
Figure 7.5: S_L measurements for BASE and FARH2 flames at 298 K and 0.101 MPa.....	192
Figure 7.6: Measured stretched flame speed (at $\varphi = 0.60$, a) and Markstein length (at varying φ , b) for BASE and FARH2 flames at $T2 = 298$ K and $P2 = 0.101$ MPa	192
Figure 7.7: Abel-transformed OH* chemiluminescence images for BASE and FARH2 flames in the HPGSB-2 with convergent confinement at $T2 = 573$ K, $\varphi = 0.55$, and $S_g = 0.8$ with varying $P2$	195

Figure 7.8: Abel-transformed OH* chemiluminescence images for BASE and FARH2 flames in the HPGSB-2 with convergent confinement at $T_2 = 573$ K, $\varphi = 0.60$, and $S_g = 0.8$ with varying P_2	197
Figure 7.9: Abel-transformed OH* chemiluminescence for BASE flames at $T_2 = 290$ K and $P_2 = 0.11$ MPa with varying φ and burner confinement: open, (a) and (b), convergent, (c) and (d)	199
Figure 7.10: Combined PLIF (left) and Abel-transformed OH* chemiluminescence (right) images for BASE flames at $T_2 = 573$ K and $\varphi = 0.55$ with varying P_2 and burner confinement: open, (a) and (b), convergent, (c) and (d)	201
Figure 7.11: Combined OH PLIF (left) and Abel-transformed OH* chemiluminescence (right) images for FARH2 flames at $T_2 = 573$ K, $\varphi = 0.55$ with varying P_2 and burner confinement: open, (a) and (b), convergent, (c) and (d)	202
Figure 7.12: Abel-transformed OH* chemiluminescence images for BASE flames in the HPGSB-2 with open confinement at $T_2 = 573$ K and $\varphi = 0.55$ with varying P_2 and S_g	203
Figure 7.13: Combined OH PLIF (left) and Abel-transformed OH* chemiluminescence (right) images for BASE flames at $T_2 = 573$ K, $P_2 = 0.11$ MPa, and $\varphi = 0.6$ with convergent confinement and varying S_g : 0.8 (a) and 0.5 (b)	205
Figure 7.14: Combined OH PLIF (left) and Abel-transformed OH* chemiluminescence (right) images for FARH2 flames at $T_2 = 573$ K and $\varphi = 0.6$ with varying P_2 and S_g : 0.8, (a) and (b), 0.5, (c) and (d)	206
Figure 7.15: Combined OH PLIF (left) and Abel-transformed OH* chemiluminescence (right) images for FARH2 flames at $T_2 = 573$ K, $P_2 = 0.33$ MPa, and $\varphi = 0.55$ with varying S_g : 0.8 (a) and 0.5 (b)	207
Figure 7.16: OH* chemiluminescence intensity centroid locations and flame angles for BASE and FARH2 flames at $T_2 = 573$ K, $\varphi = 0.55$, and varying P_2	208
Figure 7.17: FFT of Burner Face DPT measurements for isothermal air flow, BASE, and FARH2 flames at $T_2 = 573$ K, $\varphi = 0.55$, and $S_g = 0.8$ with varying P_2 and confinement: open, (a) and (b), convergent, (c) and (d)	209
Figure 7.18: Confinement and φ effects on normalized Burner Face DPT pressure fluctuation for BASE and FARH2 flames at $T_2 = 573$ K, with varying P_2 : 0.11 MPa (a) and 0.22 MPa (b) ..	211
Figure 7.19: FFT of Burner Face DPT measurement for isothermal air flow, BASE, and FARH2 flames at $T_2 = 573$ K, $P_2 = 0.11$ MPa, $\varphi = 0.55$, $S_g = 0.5$, and convergent confinement	211
Figure 7.20: P_2 and S_g effect on Burner Face DPT amplitudes for BASE and FARH2 flames with open confinement at $T_2 = 573$ K and $\varphi = 0.55$	212
Figure 7.21: P_2 and S_g effect on Burner Face DPT amplitude for FARH2 flames with convergent confinement at $T_2 = 573$ K and $\varphi = 0.55$ with values unscaled (a) and scaled (b) by S_g	213

Figure 7.22: P_2 and S_g effect on Burner Face DPT amplitude for BASE and FARH2 flames with convergent confinement at $T_2 = 573$ K and $\varphi = 0.55$ with values unscaled (a) and scaled (b) by $(\text{H:C})^3$	214
Figure 7.23: Predicted combustion noise amplitudes in the HPGSB-2 for BASE and FARH2 flames up to $P_2 = 1.5$ MPa at $T_2 = 573$ K and $\varphi = 0.55$ with varying S_g	214
Figure 7.24: Measured and predicted combustion noise amplitudes for BASE and FARH2 flames with convergent confinement at $T_2 = 573$ K and $\varphi = 0.55$ with predicted values using Equation 7.2 (a) and after S_L scaling (b).	215
Figure 7.25: NO_x emissions versus AFT for BASE flames with convergent confinement, $P_2 = 0.11$ MPa, $S_g = 0.5$, and varying T_2	216
Figure 7.26: NO_x emissions versus AFT at varying P_2 for all experimental conditions at $T_2 = 573$ K	218
Figure 7.27: NO_x emissions versus AFT for BASE (a) and FARH2 (b) flames with convergent confinement and varying S_g at $P_2 = 0.11$ MPa	219
Figure 7.28: P_2 effect on NO_x emissions for BASE and FARH2 flames at $\varphi = 0.55$ (AFT = $1788 \text{ K} \pm 6 \text{ K}$)	220
Figure 8.1: OSCILOS geometry input for the HPGSB-2 with open cylindrical confinement including inlet plenum and water-cooled exhaust piping (a) and highlighting the mixing plenum, swirler, and confinement tube (b). Flame location marked in red.	224
Figure 8.2: OSCILOS geometry input for the HPGSB-2 with convergent nozzle confinement including inlet plenum and water-cooled exhaust piping (a) and highlighting the mixing plenum, swirler, and confinement tube (b). Flame location marked in red.	224
Figure 8.3: Raw residual plots of OSCILOS predicted eigenvalues with closed (a) and open (b) burner inlet boundary conditions	228
Figure 8.4: FFT of Burner Face DPT measurement for ISO-O-8-0.2 (a) and BASE-O-8-0.2 (b). Note the difference in y-axis scaling	230
Figure 8.5: Contour plots of eigenvalues and growth rates predicted by OSCILOS for ISO-O-8-0.2 (a) and BASE-O-8-0.2 (b). The main modes of the system are indicated by white circles.	230
Figure 8.6: Contour plots of eigenvalues and growth rates predicted by OSCILOS for BASE-O-8-0.2 with different velocity perturbations: $\hat{u}_u / \bar{u}_u = 0.50$ (a) and $\hat{u}_u / \bar{u}_u = 0.75$ (b). The main modes of the system are indicated by white circles	231
Figure 8.7: Predicted eigenvalues (circles) and growth rate (triangles) plotted against normalized velocity perturbation. Red lines mark the predicted limit cycle frequency and velocity perturbation.	232
Figure 8.8: FFT of Burner Face DPT measurement for ISO-O-8-0.22 (a), BASE-O-8-0.22 (b), and FARH2-O-8-0.22 Note the difference in y-axis scaling.	234

Figure 8.9: Contour plots of eigenvalues and growth rates predicted by OSCILOS for ISO-O-8-0.22 (a), BASE-O-8-0.22 (b), and FARH2-O-8-0.22 (c). The main modes of the system are indicated by white circles.	235
Figure 8.10: Predicted eigenvalues (circles) and growth rate (triangles) plotted against normalized velocity perturbation for BASE-O-8-0.22 (a) and FARH2-O-8-0.22 (b). Red lines mark the predicted limit cycle frequency and velocity perturbation.....	237
Figure 8.11: FFT of Burner Face DPT measurement for ISO-CQ-8-0.22 (a), BASE-CQ-8-0.22 (b), and FARH2-CQ-8-0.22 (c). Note the difference in y-axis scaling.....	239
Figure 8.12: Contour plots of eigenvalues and growth rates predicted by OSCILOS for ISO-CQ-8-0.22 (a), BASE-CQ-8-0.22 (b), and FARH2-CQ-8-0.22 (c). The main modes of the system are indicated by white circles.	240
Figure 8.13: Contour plots of eigenvalues and growth rates predicted by OSCILOS at $T_2 = 900$ K, $P_2 = 1.5$ MPa, and $\hat{u}_u / \bar{u}_u = 0.0$ with open (a) and convergent nozzle (b) confinement. The main modes of the system are indicated by white circles.....	242
Figure 8.14: Predicted eigenvalues (circles) and growth rate (triangles) plotted against normalized velocity perturbation for HPGSB-2 at $T_2 = 900$ K, $P_2 = 1.5$ MPa with open (a) and convergent nozzle (b) confinement. Red lines mark the predicted limit cycle frequency and velocity perturbation.	242
Figure A. 1: UK gas transmission network including LNG import facilities and interconnectors. Reproduced from [19].	268
Figure B.1: HPGSB-2 Fuel and Air Inlet Pipe (see Figure 3.4.b).....	269
Figure B.2: HPGSB-2 Fuel/Air Inlet Pipe and HPOC Connection Flange Assembly (see Figure 3.4.b & c).....	270
Figure B.3: HPGSB-2 Main Fuel/Air Mixing Chamber (see Figure 3.4.c).....	271
Figure B.4: HPGSB-2 Radial Tangential Swirler Insert Back Plate (Figure 3.4.d).....	272
Figure B.5: HPGSB-2 Radial Tangential Swirler Insert and Exit Nozzle, $S_g = 0.8$ (see Figure 3.4.d)	273
Figure B.6: HPGSB-2 Radial Tangential Swirler Insert and Exit Nozzle Detail, $S_g = 0.8$ (see Figure 3.4.d).....	274
Figure B.7: Photographs of HPCR setup prior to installation of the air and fuel preheating systems with the HPGSB (top) and after installation of these systems with the HPGSB-2 (bottom).....	275
Figure B.8: Photograph of assembled HPGSB prior to installation in the HPOC. Reproduced from [115].	276

Figure B.9: Photographs of HPGSB-2 during construction (a) and complete, fully instrumented (b).....	276
Figure B.10: Photographs of HPGSB-2 burner components with an end-on view of the burner face, exit nozzle, and instrumentation/pilot lance prior to installation in the HPOC (a) and after installation in the HPOC with the spark igniter installed (b).	277
Figure B.11: Photograph of the instrumentation at the front end of the HPGSB-2 as installed in the HPOC, including DPTs for the “Pilot” (left semi-infinite line) and “Burner Face” (right semi-infinite line). The exhaust DPT semi-infinite line can be seen in the background (back left).	277
Figure B.12: Photograph of the ICCD camera system as installed in the IP-67 enclosure. Refer to Figure 3.2 for installed location in the HPCR.....	278
Figure B.13: Photograph of PLIF laser system as installed at Cardiff University’s GTRC.	278
Figure B.14: PLIF measurement system utility setup at Cardiff University’s GTRC.	279
Figure B.15: Images of scaled calibration targets installed in the HPGSB (a) and HPGSB-2 (b)	279
Figure B.16: Photograph of the Nd:YAG laser mounted for PIV measurements in the HPCR as shown in Figure 3.15.....	280
Figure B.17: Images of scaled calibration targets installed in the HPGSB-2 for PIV measurements with the open cylindrical confinement (a) and convergent nozzle confinement (b).....	280
Figure B.18: Schematic of scanning laser sheet PLIF measurement system timing and image capture setup at Cardiff University’s GTRC (top) and photograph of servo installation in the TDL-90 dye laser (bottom).	281

TABLES INDEX

Table 1.1: UK annual LNG imports by exporting country from 2005-2015. Compiled from [3].	9
Table 2.1: Gas quality limits for entry into the UK natural gas system. WI values referenced at $p_2 = 0.101$ MPa and $t_1, t_2 = 288$ K. Compiled from data in [20].	14
Table 3.1: Selected methane and methane- C_2+ fuel characteristics for HPGSB-2 study	72
Table 3.2: Selected methane and methane-hydrogen fuel characteristics for HPGSB-2 study	73
Table 3.3: Selected target HPGSB-2 burner operating conditions and dimensionless scaling parameters with theoretical $P_2 = 1.5$ MPa values	76
Table 4.1: Dye laser excitation wavelengths for OH PLIF with varying P_2 and fuel type	89
Table 5.1: Selected methane and propane fuel characteristics for HPGSB commissioning	107
Table 5.2: HPCR conditions for methane and propane commissioning of the HPGSB	107
Table 5.3: HPCR conditions for ATAP, ETAP, and ETEP combustion experiments in the HPGSB-2	124
Table 6.1: HPCR operating ranges for C_2+ combustion experiments	147
Table 7.1: HPCR operating ranges for isothermal, CH_4 , and CH_4-H_2 combustion study	187
Table 8.1: HPGSB-2 OSCILOS isothermal and CH_4 combustion input conditions at $P_2 = 0.20$ MPa with open cylindrical confinement	229
Table 8.2: HPGSB-2 OSCILOS isothermal and CH_4/CH_4-H_2 combustion input conditions at $P_2 = 0.22$ MPa with open cylindrical confinement	233
Table 8.3: HPGSB-2 OSCILOS isothermal and CH_4/CH_4-H_2 combustion input conditions at $P_2 = 0.22$ MPa with convergent nozzle confinement	238
Table E.1: Global experimental confined swirl burners and their operating pressures	310

SYMBOL LIST

- α – Thermal Diffusivity (m^2/s)
 α_1 – Nonlinear FDF coefficient
 β – Nonlinear FDF coefficient
 γ – Ratio of Specific Heats
 δ_{flame} – Flame Brush Thickness (mm)
 δ_t – Reaction Zone Thickness (cm)
 ϵ – Turbulence Dissipation Rate (m^2/s^3)
 η – Kolmogorov Length Scale (mm)
 η_{eff} – Transmission Efficiency of Collection Optics
 ϑ – Phase Angle (rad)
 Θ – Flame Angle (deg)
 κ – Flame Stretch Rate (s^{-1})
 κ_{ext} – Flame Stretch Rate (s^{-1})
 λ – Wavelength (nm or cm^{-1})
 λ_{therm} – Thermal Conductivity (W/m-K)
 μ – Dynamic Viscosity (Pa-s)
 ν – Kinematic Viscosity (m^2/s)
 ρ – Density (kg/m^3)
 σ – Standard Deviation
 τ – Time Delay (ms)
 τ_{chem} – Chemical Time Scale (s)
 τ_{flow} – Flow Time Scale (s)
 τ_η – Kolmogorov Time Scale (s)
 τ_T – Integral Time Scale (s)
 φ – Equivalence ratio
 X_m – Mole Fraction of the Absorbing State
 Ω – Solid Angle of Collection (rad)
 Ω_1 – Rayleigh Criterion Flow Domain
 α – Linear (n- τ) Flame Model Gain
 A_k – Acoustic Wave Propagation Direction
 A_{flame} – Flame Area (mm^2)
 A_{noz} – Area of Burner Exit Nozzle (m^2)
 A_{tan} – Area of Radial-Tangential Swirler Inlet (m^2)
 A_{21} – Rate Constant for Spontaneous Emission (s^{-1})
 AFR_{mass} – Stoichiometric Air-Fuel Ratio (Mass-Basis)
 B_{12} – Einstein coefficient for stimulated absorption ($\text{cm}^2\text{-Hz}/\text{J}$)
 c – Speed of Sound (m/s)
 $\langle c \rangle$ – Reaction Progress Variable
 C_p – Specific Heat Capacity at Constant Pressure (J/kg-K)
 d – Relative Density of Fuel Mixture with respect to Air for Wobbe Index Calculation
 D – Diameter (m)
 D_{ij} – Mass Diffusivity (m^2/s)
 $D_{confine}$ – Burner Confinement Diameter (mm)
 $D_{dump/noz}$ – Burner Dump Plane/Nozzle Diameter (mm)
 D_{exit} – Burner Confinement Exit Diameter (mm)
 D_{lance} – Diameter of Instrumentation/Pilot Lance Bluff Body in HPGSB/HPGSB-2 (m)
 Da – Damköhler Number
 E_v – Spectral Fluence of Laser System (J($\text{cm}^2\text{-Hz}$))
 f – Frequency (Hz)

- f_{peak} – Dominant Frequency (Hz)
 $f_1(T)$ – Fractional Population of the Lower-Coupled State
 Δh_f – Heat of Formation (J)
 He – Helmholtz Number
 H_s – Real Higher (Gross) Calorific Value, Volumetric (MJ/m³)
 I_{OH} – OH PLIF Intensity
 $\bar{I}_{OH^*_{i,j}}$ – Temporally-Averaged OH* Chemiluminescence Image Pixel Intensity (a.u.)
 II_{CH^*} – Mean CH* Chemiluminescence Integral Intensity (a.u.)
 II_{OH^*} – Mean OH* Chemiluminescence Integral Intensity (a.u.)
 II'_{OH^*} – Instantaneous Integrated OH* Chemiluminescence Intensity (a.u.)
 K – Kurtosis
 K' – Time-Varying Kurtosis
 L – Length (mm)
 Lb – Markstein Length (mm)
 Le – Lewis Number
 LHV – Lower Heating Value, Mass (MJ/kg)
 $L_{r,u}$ – Radial Longitudinal Integral Length Scale (mm)
 $L_{r,v}$ – Radial Transverse Integral Length Scale (mm)
 $L_{y,u}$ – Axial Transverse Integral Length Scale (mm)
 $L_{y,v}$ – Axial Longitudinal Integral Length Scale (mm)
 L_r – Radial Integral Length Scale (mm)
 L_y – Axial Integral Length Scale (mm)
 L_T – Integral Length Scale (mm)
 $L_{T,e}$ – Integral Length Scale Calculated by $R(y)$ or $R(r) = 1/e = \sim 0.37$
 $L_{T,int}$ – Integral Length Scale Calculated by Integration of $R(r)$ or $R(y)$ to First Zero Crossing
 \dot{m}_{air} – Air Mass Flow Rate (g/s)
 \dot{m}_{fuel} – Fuel Mass Flow Rate (g/s)
 M – Mach Number
 n_{tot} – Total Gas Number Density (m⁻³)
 N – Number of Images/Measurements
 N_p – Number of Photons Detected by a Photo-Detector
 $NO_{x, dry}$ – NO_x Corrected for Exhaust H₂O Concentration (ppmV)
 $NO_{x, dry, 15\% O_2}$ – NO_x Corrected for Exhaust H₂O Concentration and 15% Excess O₂ (ppmV)
 $NO_{x, meas}$ – Uncorrected (Hot, Wet) Measured NO_x (ppmV)
 $O_{2, meas}$ – Measured Exhaust O₂ Concentration (% vol)
 $O_{2, ref}$ – Reference Exhaust O₂ Concentration for Emissions Correction (% vol)
 \bar{p} – Centrifugal Pressure Distribution
 p' – Dynamic Pressure Measurement (kPa)
 p'_{RMS} – Dynamic Pressure RMS Measurement (kPa)
 P_{atm} – Atmospheric Pressure (MPa)
 $P2$ – Burner Inlet Pressure (MPa)
 $P3$ – Burner Outlet Pressure (MPa)
 p_2 – Combustion/Metering Reference Pressure for Wobbe Index Calculation (MPa)
 p_4 – Fourth Moment about the Mean for Kurtosis Calculation
 P_{therm} – Thermal Power Based on Fuel Lower Heating Value (kW)
 ΔP – Swirler Pressure Drop (kPa)
 Q – Area-Based Heat Release Rate (W/cm²)
 Q_{tan} – Tangential Volumetric Flow Rate Through Swirler Insert (m³/s)
 Q_{tot} – Total Volumetric Flow Rate Through Swirler Insert (m³/s)
 Q'_{max} – Maximum Volumetric Heat Release Rate (W/cm³)

- Q_{21} – Rate Constant for Collisional Quenching (s^{-1})
 r – Radial Distance from Burner Exit Nozzle Centerline (mm)
 r_{tan} – Effective Radius of Tangential Inlet of Swirler (mm)
 r_{noz} – Burner Exit Nozzle Radius (mm)
 R – Acoustic Reflection Coefficient
 R_{ij} – Spatial Correlation Coefficient
 $R_{specific}$ – Specific Gas Constant (J/kg-K)
 Re – Reynolds Number
 S_g – Geometric Swirl Number
 S_L – Laminar Flame Speed (m/s)
 S_t – Turbulent Flame Speed (m/s)
 St – Strouhal Number
 T_2 – Burner Inlet Temperature (K)
 T_3 – Combustor Outlet Temperature (K)
 T_{Line1} – 5 Gas Mixing Line 1 Temperature (K)
 T_{Line2} – 5 Gas Mixing Line 2 Temperature (K)
 T_{Line3} – 5 Gas Mixing Line 3 Temperature (K)
 T_{Line4} – 5 Gas Mixing Line 4 Temperature (K)
 T_{Line5} – 5 Gas Mixing Line 5 Temperature (K)
 T_{BF} – Burner Face Temperature (K)
 T_{pilot} – Pilot Bluff Body Tip Temperature (K)
 T_{quartz} – Quartz Tube OD Temperature (K)
 T_{TBC} – HPOC TBC Temperature (K)
 T_{int} – Relative Turbulence Intensity
 t_{gate} – Image Intensifier Gate Time (μs)
 t_1 – Combustion Reference Temperature for Wobbe Index (K)
 t_2 – Metering Reference Temperature for Wobbe Index (K)
 u – Radial Velocity Component for Integral Length Scale Calculation (m/s)
 \bar{u} – Mean Burner Exit Nozzle Velocity (m/s)
 \bar{u}_y – Mean Axial Velocity Component of \bar{u} (m/s)
 u' – Fluctuating Velocity Component
 u'_{RMS} – RMS Velocity Fluctuation / Turbulence Intensity (m/s)
 u_i – Instantaneous Velocity (m/s)
 U – Mean Velocity (m/s)
 v – Axial Velocity Component for Integral Length Scale Calculation (m/s)
 v'_{RMS} – RMS Velocity Fluctuation / Turbulence Intensity (m/s)
 v'/v'' – Atomic Vibrational Level
 V – Collection Volume (m^3)
 \bar{w} – Tangential (or Azimuthal) Velocity Distribution
 WI – Wobbe Index (MJ/m^3)
 X_{CH} – Mole Fraction of CH radical
 X_{H_2O} – Mole Fraction of Water
 X_{OH} – Mole Fraction of OH radical
 $x_{CH,peak}$ – 1-D location of peak CH radical mole fraction (mm)
 $x_{OH,peak}$ – 1-D location of peak OH radical mole fraction (mm)
 y – Axial Distance from Burner Exit Nozzle (mm)
 Z – Compression Factor

ABBREVIATION LIST

AGSB – Atmospheric Generic Swirl Burner
AFT – Adiabatic Flame Temperature (K)
ATAP – Ambient Temperature, Atmospheric Pressure Rig Conditions
BASE – 100% CH₄ Fuel
BO - Blowoff
BOS – Basic Oxygen Steelmaking
BPV – Backpressure Valve
BSI – British Standards Institution
CBP – Common Business Practice
CCC – Committee on Climate Change (UK)
CCD – Charge-Coupled Device
CCGT – Combined Cycle Gas Turbine
CCS – Carbon Capture and Storage
CFD – Computational Fluid Dynamics
CHP – Combined Heat and Power
CL – Chemiluminescence
CMF – Coriolis Mass Flowmeter
CRZ – Central Recirculation Zone
CVCB – Constant Volume Combustion Bomb
DLE – Dry Low Emissions
DLN – Dry Low NO_x
DPT – Dynamic Pressure Transducer
DUKES – Digest of United Kingdom Energy Statistics
EASEE-gas – European Association for the Streamlining of Energy Exchange - gas
EGR – Exhaust Gas Recirculation
EMIX1 – 85-12.6-2.4%vol CH₄-C₃H₈-N₂ Fuel Blend
ETAP – Elevated Temperature, Atmospheric Pressure Rig Conditions
ETEP – Elevated Temperature, Elevated Pressure Rig Conditions
EU – European Union
FARH2 – 85-15% vol CH₄-H₂ Fuel Blend
FARNG – 85-15%vol CH₄-C₂H₆ Fuel Blend
FC – Fully Closed
FCV – Flow Control Valve
FDF – Flame Describing Function
FFT – Fast Fourier Transform
FO – Fully Open
FTF – Flame Transfer Function
GA – Gas Analysis
GS(M)R – Gas Safety (Management) Regulations (UK)
GT – Gas Turbine
GTRC – Gas Turbine Research Center at Cardiff University
HFD – High Frequency Dynamics
HPCR – High Pressure Combustion Rig
HPGSB – High Pressure Generic Swirl Burner (Mk. I)
HPGSB-2 – High Pressure Generic Swirl Burner (Mk. II)
HPOC – High Pressure Optical Chamber
HRR – Heat Release Rate
H:C – Fuel Molar Hydrogen to Carbon Ratio

ICCD – Intensified Charge-Coupled Device
ID – Inner Diameter
IED – Industrial Emissions Directive
IFD – Intermediate Frequency Dynamics
LBO – Lean Blowoff
LDA – Laser Doppler Anemometry
LFD – Low Frequency Dynamics
LIF – Laser Induced Fluorescence
LNG – Liquefied Natural Gas
LCPD – Large Combustion Plant Directive
LPG – Liquefied Petroleum Gas
LPM – Lean Premixed
LSL – Lean Stability Limit
MFC – Mass Flow Controller
MIDNG – 90-6-4%vol CH₄-C₂H₆-C₃H₈ Fuel Blend
NG – Natural Gas
NO_x – Nitrogen Oxides
OCGT – Open Cycle Gas Turbine
OD – Outer Diameter
OEM – Original Equipment Manufacturer
ORZ – Outer Recirculation Zone
OSCILOS – Open Source Combustion Instability Low Order Simulator
PC – Partially Closed
PIV – Particle Image Velocimetry
PLIF – Planar Laser Induced Fluorescence
PM – Particulate Matter
PSD – Power Spectral Density
PVC – Precessing Vortex Core
P2G – Power-to-Gas
RSL – Rich Stability Limit
SNR – Signal to Noise Ratio
SPT – Static Pressure Transducer
SO_x – Sulfur Oxides
TBC – Thermal Barrier Coating
TC – Thermocouple
TFB – Technical Flashback
THC – Total Hydrocarbon
UK – United Kingdom
UKCS – United Kingdom Continental Shelf
UV – Ultraviolet
VSD – Variable Speed Drive

ACKNOWLEDGEMENTS

My sincerest thanks begin with my PhD supervisors, Dr. Richard Marsh and Prof. Phil Bowen, without whom my journey from the United States to Cardiff would have remained simply a dream. To Dr. Marsh, my confidence as a researcher and engineer has flourished with your guidance and trust, even when life's obstacles tried to get in the way. To Prof. Bowen, thank you for welcoming me to Cardiff almost 5 years ago, and for your thoughtful input, feedback, and reassurance throughout my PhD. To Mr. Steve Morris, for your leadership and keen eye for detail, and for allowing a bicycle shed to be installed as a laser enclosure at the GTRC.

To Dr. Dan Pugh and Dr. Tony Giles, for your help on all those test days. I owe a great deal of the work contained within this thesis to your support. There's some fig rolls, cups of tea, and a whole lot of petrol in it for you both. To Dr. Yura Sevcenco, Mr. Paul Malpas, Mr. Terry Treherne, and Mr. Jack Thomas, my thanks for your roles in designing, building, fitting, re-designing and re-fitting the equipment that sits at the heart of this work. My thanks also to Gina for all your help throughout my time in Cardiff. This thesis also would not have been possible without the support of the academic and industrial partners in the Flex-E-Plant Consortium, in particular Cath Goy and Dave Abbott from Uniper Technologies and Suresh Sadasivuni and Jonathan May from Siemens, as well as funding provided by the UK Engineering and Physical Sciences Research Council.

I am forever grateful for the support of my parents, family, and friends. To Mom and Dad, for becoming masters of Skype, always encouraging me to explore the world, and for your unending and limitless love and care. We are truly never further apart than our hearts will allow. To my brother Tim, for the constant encouragement, belief, and grounding. Our travels around Europe inspired this journey and you have supported me every step of the way. To my best friends Mike, Joel, and Annie, your encouragement has lifted me up not only in the toughest times, but always. We have grown up but never apart. Like many things in life, I could not have done this without you all.

And finally, to my grandmother. I did it, Grandma Runyon, and wish I could tell you all about it. I will miss you until the day we meet again.

JOURNAL PUBLICATION AND CONFERENCE PROCEEDINGS LIST

Journal Publications

Daniel Pugh, Philip Bowen, Richard Marsh, Andrew Crayford, **Jon Runyon**, Steven Morris, Agustin Valera-Medina, Anthony Giles: *Dissociative influence of H₂O vapour/spray on lean blowoff and NO_x reduction for heavily carbonaceous syngas swirling flames*. Combustion and Flame, 2017, Vol. 177, pp. 37-48. DOI: [10.1016/j.combustflame.2016.11.010](https://doi.org/10.1016/j.combustflame.2016.11.010)

Richard Marsh, **Jon Runyon**, Anthony Giles, Steven Morris, Daniel Pugh, Agustin Valera-Medina, Philip Bowen: *Premixed methane oxycombustion in nitrogen and carbon dioxide atmospheres: measurement of operating limits, flame location and emissions*. Proceedings of the Combustion Institute, 2017, Vol. 36(3), pp. 3949-3958. DOI: [10.1016/j.proci.2016.06.057](https://doi.org/10.1016/j.proci.2016.06.057)

Agustin Valera-Medina, Richard Marsh, **Jon Runyon**, Daniel Pugh, Paul Beasley, Timothy Hughes, Phil Bowen: *Ammonia–methane combustion in tangential swirl burners for gas turbine power generation*. Applied Energy, 2017, Vol. 185(2), pp. 1362-1371. DOI: [10.1016/j.apenergy.2016.02.073](https://doi.org/10.1016/j.apenergy.2016.02.073)

Hayder Kurji, Agustin Valera-Medina, **Jon Runyon**, Anthony Giles, Daniel Pugh, Richard Marsh, Nadia Cerone, Francesco Zimbardi, Vitorio Valerio: *Combustion characteristics of biodiesel saturated with pyrolysis oil for power generation in gas turbines*. Renewable Energy, 2016, Vol. 99, pp. 443-451. DOI: [10.1016/j.renene.2016.07.036](https://doi.org/10.1016/j.renene.2016.07.036)

Agustin Valera-Medina, Steven Morris, **Jon Runyon**, Daniel Pugh, Richard Marsh, Paul Beasley, Timothy Hughes: *Ammonia, Methane and Hydrogen for Gas Turbines*. Energy Procedia, 2015, Vol. 75, pp.118-123. DOI: [10.1016/j.egypro.2015.07.205](https://doi.org/10.1016/j.egypro.2015.07.205)

Jon Runyon, Richard Marsh, Philip Bowen, Daniel Pugh, Anthony Giles, Steven Morris: *Lean methane flame stability in a premixed generic swirl burner, Part I: Isothermal flow and atmospheric combustion characterization*. Experimental Thermal and Fluid Science.

- Currently under editorial review

Jon Runyon, Richard Marsh, Philip Bowen, Daniel Pugh, Anthony Giles, Steven Morris: *Lean methane flame stability in a premixed generic swirl burner, Part II: Detailed analysis at elevated temperature and pressure combustion conditions*. Experimental Thermal and Fluid Science.

- Currently under editorial review

Marco Buffi, Agustin Valera-Medina, Richard Marsh, Daniel Pugh, Anthony Giles, **Jon Runyon**, David Chiaramonti: *Experimental Combustion Tests for Hydrotreated Renewable Jet Fuel from Used Cooking Oil and its Blends*. Applied Energy.

- Currently under editorial review

Conference Proceedings

Jon Runyon, Richard Marsh, Daniel Pugh, Philip Bowen, Anthony Giles, Steven Morris, Agustin Valera-Medina: *Experimental Analysis of Confinement and Swirl Effects on Premixed CH₄-H₂ Flame Behavior in a Pressurized Generic Swirl Burner*. ASME Turbo Expo 2017: Turbomachinery Technical Conference and Exposition, Charlotte, North Carolina, USA, 2017. Paper Number GT2017-64794.

Jon Runyon, Richard Marsh, Agustin Valera-Medina, Anthony Giles, Steven Morris, Daniel Pugh, Yura Sevcenco, Phil Bowen: *Methane-Oxygen Flame Stability in a Generic Premixed Gas Turbine Swirl Combustor at Varying Thermal Power and Pressure*. ASME Turbo Expo 2015: Turbine Technical Conference and Exposition, Montreal, Quebec, Canada, 2015. DOI: [10.1115/GT2015-43588](https://doi.org/10.1115/GT2015-43588)

Jon Runyon, Richard Marsh, Philip Bowen, Daniel Pugh, Anthony Giles, Steven Morris: *Influence of higher hydrocarbons in LNG on natural gas flame stability under elevated conditions*. Topic Oriented Technical Meeting (TOTeM) 44, International Flame Research Foundation, Essen, Germany, 2017.

Jon Runyon, Richard Marsh, Philip Bowen, Daniel Pugh, Anthony Giles, Steven Morris: *Premixed CH₄-H₂ flame behavior in pressurized generic swirl burner for power-to-gas applications*. Topic Oriented Technical Meeting (TOTeM) 44, International Flame Research Foundation, Essen, Germany, 2017.

Jon Runyon, Richard Marsh, Steven Morris, Anthony Giles, Daniel Pugh, Philip Bowen: *Fuel Flexibility for Industrial Gas Turbine Generation: Effects of Higher-Hydrocarbon Variation in Natural Gas on Swirling Flame Stability*. 9th International Charles Parsons Turbine and Generator Conference, Loughborough, United Kingdom, 2015.

Jon Runyon, Richard Marsh, Yura Sevcenco, Daniel Pugh, Steven Morris: *Development and Commissioning of a Chemiluminescence Imaging System for an Optically-Accessible High-Pressure Generic Swirl Burner*. 7th European Combustion Meeting, Budapest, Hungary, 2015.

Daniel Pugh, Philip Bowen, Andrew Crayford, Richard Marsh, **Jon Runyon**, Steven Morris, Anthony Giles: *Catalytic Influence of Water Vapour on Lean Blowoff and NO_x Reduction for Pressurised Swirling Syngas Flames*. ASME Turbo Expo 2017: Turbomachinery Technical Conference and Exposition, Charlotte, North Carolina, USA, 2017. Paper Number GT2017-64609.

Richard Marsh, Anthony Giles, **Jon Runyon**, Daniel Pugh, Philip Bowen, Agustin Valera-Medina, Steven Morris, Karen Finney, Mohamed Pourkashanian: *Selective exhaust gas recycling for carbon capture applications: combustion and operability measurement*. 8th International Gas Turbine Conference, European Turbine Network, Brussels, Belgium, 2016.

Marco Buffi, Agustin Valera-Medina, **Jon Runyon**, Daniel Pugh, Anthony Giles, Richard Marsh, David Chiaramonti: *Evaluation of Combustion Behavior of Renewable Jet Fuel in a Combustor Rig: Influence of HEFA and its Blends on Flame Stability and Emissions Compared to Aviation Kerosene*. 24th European Biomass Conference & Exhibition, Amsterdam, Netherlands, 2016.

Agustin Valera-Medina, Steven Morris, **Jon Runyon**, Daniel Pugh, Richard Marsh, Paul Beasley: *Ammonia, Methane and Hydrogen for Gas Turbines*. Clean, Efficient and Affordable Energy for a Sustainable Future: The 7th International Conference on Applied Energy (ICAE2015), Abu Dhabi, United Arab Emirates, 2015.

SUMMARY

Power generation gas turbine manufacturers and operators are tasked increasingly with expanding operational flexibility due to volatility in global gaseous fuel supplies and increased renewable power generation capacity. Natural gas containing high levels of higher hydrocarbons (e.g. ethane and propane) is typical of liquefied natural gas and shale gas, two natural gas sources impacting gas turbine operations, particularly looking forward in the United Kingdom. In addition, hydrogen-blending into existing natural gas infrastructure represents a potential energy storage opportunity from excess renewable power generation, with associated combustion impacts not fully appreciated. This thesis aims to address the specific operational problems associated with the use of variable gaseous fuel compositions in gas turbine combustion through a combination of experimental and numerical techniques, with a focus on natural gas blends containing increased levels of higher hydrocarbons and hydrogen.

Parametric experimental combustion studies of the selected fuel blends are conducted in a new fully premixed generic swirl burner at elevated ambient conditions of temperature and pressure to provide representative geometry and flow characteristics typical of a can-type industrial gas turbine combustor. New non-intrusive diagnostic facilities have been designed and installed at Cardiff University's Gas Turbine Research Centre specifically for the characterization of the influence of fuel composition, burner geometry, and operating parameters on flame stability, flame structure, thermoacoustic response, and environmental emissions. Experimental measurements are supported through the use of numerical chemical kinetics and acoustic modelling. Results from this thesis provide an experimental validation database for chemical kinetic reactor network and CFD modelling efforts. In addition, it informs gas turbine manufacturers on potential burner design modifications for future fuel flexibility and provide enhanced empirical tools to power generation gas turbine operators for increased operational stability, reduced environmental impact, and increased utilization.

CHAPTER 1 – INTRODUCTION

1.1 Motivation

Global gas turbine (GT) original equipment manufacturers (OEM) and electrical power generation GT operators are increasingly required to meet changing demands for increased operating and fuel flexibility with reduced environmental impacts [1]. In the United Kingdom (UK) specifically, GT electrical power generators and OEMs will be expected to meet increased flexibility demands resulting from increased renewable energy production and declining domestic gas production while maintaining their economic viability and meeting strict environmental targets [2]. Volatility in available gaseous fuel supplies resulting from declining conventional gas reserves [3], increased global gas mobility [4], and economic factors have therefore motivated GT combustion research to focus on a wide range of alternative gaseous fuel sources. This thesis is therefore focused on fuel variability, flame behavior, and combustion sensitivity to fuel composition, considering natural gas blends that are currently utilized by UK industrial power generators and may be used in GT power generation in the future due to changes in supply, operating conditions, or regulations. This will aid in the development of fuel-flexible GT engines and improved operational control of GT power generation. The following sections provide the motivational background for this study with a brief introduction to the current state of energy policies affecting GT power generation, the outlook for GT power generation in the UK, and the future fuel sources expected to influence the operational flexibility of GTs in years to come.

1.1.1 Energy Policy – Decarbonization of Electrical Power Generation

Global energy policies, such as the recent United Nations Paris Agreement, aim to set broad limits on average global temperature increases ($< 2^{\circ}\text{C}$ above pre-industrial levels) through reductions in greenhouse gas (GHG) emissions, which are widely accepted to contribute to adverse global climate change [5]. In order for a broad energy policy such as the Paris Agreement to take shape when involving almost 200 independent countries, detailed policies and regulations are required at regional and local levels to influence the decarbonization of the electrical power generation sector. The European Union (EU) committed to reducing GHG emissions to 80-95% below 1990 levels by 2050 [6]. It is acknowledged, however, that Europe will become increasingly dependent on gas imports, with liquefied natural gas (LNG) playing an increasing role in the diversification of supply [6]. As proven domestic gas reserves decline and a great deal of uncertainty surrounds domestic shale gas production, LNG has the potential to

provide long-term gas security of supply. In line with this, increased use of LNG has been markedly apparent in the UK over the past decade, and it is a key focus given its wide variation in physical and chemical properties from different sources around the world. Furthermore, with increases in renewable energy sources expected, energy storage technologies such as power-to-gas (P2G), which utilizes excess electricity from renewable resources to produce hydrogen for storage in the natural gas grid, are already being operated at pilot scale and developed for industrial scale in the UK and Europe [7].

GT OEMs and operators in Europe must adhere to the European Parliament's Industrial Emissions Directive (IED), which provides the specific legal framework for current and future GHG emission limits from industrial combustion plants, including power generation stations utilizing GTs [8]. However, the EU has largely left implementation of its broader climate change ambitions to the Member States.

1.1.1.1 United Kingdom Energy Policy

The 2008 United Kingdom Climate Change Act and 2011 UK Carbon Plan put into place the legal framework addressing climate change and GHG emissions in the UK. As the world's first legally binding national legislation addressing climate change, the UK Climate Change Act defines the GHG emissions reduction target for the year 2050, set at 80% lower than baseline levels from the year 1990, an aggregate of net UK emissions of CO₂, CH₄, nitrous oxide (N₂O), hydrofluorocarbons, perfluorocarbons, and sulfur hexafluoride [9]. Thus, total emissions in 2050 must be 156.2 MtCO₂e, roughly equal to the total emissions of the entire UK power sector in 2010 [10]. The first clear target set is for 2020, when carbon-based emissions must be at least 26% lower than the 1990 baseline [9].

Despite the fact that the UK Climate Change Act provides little by way of specific actions to be taken to meet the emission reduction targets, it does provide the legal foundation for the reduction in carbon-based and GHG emissions in the UK. It broadly paints a picture for the UK gas-fired power generation sector that current operation methods for the last few decades cannot be maintained in order to reduce carbon emissions 80% lower than 1990 levels. There are a number of proposed scenarios which lead to that particular goal, all with varying amounts of renewable, nuclear, and conventional power generation coupled with energy efficiency measures and CCS. It is clear that the UK is taking an "all of the above" approach to meeting the carbon budgets, which means that gas-fired generation will continue to have a

role in the UK energy portfolio. However, it cannot be understated that gas-fired generation is a carbon-intensive energy source, and will have to be either abated with CCS or operated unabated alongside significant renewables in order for the current emission reduction targets to be met. This further underpins the necessity of UK gas-fired power generators to operate their equipment more efficiently and flexibly.

More specific actions and strategies that must be undertaken as a result of the UK Climate Change Act are found in the 2011 UK Carbon Plan. The UK Carbon Plan projects that in order to meet the 80% emissions reduction target by 2050 significant investment is required currently to ensure that the transition to a decarbonized energy sector is maintained, with at least 50% emissions reduction based on 1990 levels by 2027 [10]. The plan covers the first four carbon budgets out to 2027, and provides some projections to 2050, although a degree of uncertainty with those projections is acknowledged. This era out to 2027 can largely be described as one of transition. First, coal-fired power stations will need to close and be replaced primarily by gas and renewables. At least 60-90 GW of new capacity, of which 40-70 GW is new low-carbon power capacity, will be needed in the UK by 2030 [10]. It is projected that at least 100 GW of new low-carbon capacity will be needed by 2050, equating to a build rate of 2.5 GW/year of new low-carbon capacity every year for 40 years [10].

Given the significant level of new low-carbon capacity that remains to be built, the continued use of gas-fired power generation will be required in the short to medium term, and the Carbon Plan directly addresses the future use of gas-fired generation in the UK. Gas-fired power plants are expected to meet both peak demand and intermittent generation from renewables while providing base generation as additional low-carbon capacity is installed [10]. In the short term to 2020, gas is projected to increasingly replace coal for power generation. Unabated gas-fired generation is projected through the 2020s, potentially still producing up to two-thirds of today's generation levels in 2030 [10]. After this point, however, gas generation's role becomes more uncertain, depending on the extent of renewable, nuclear, and CCS installation. In all UK Carbon Plan scenarios, gas-fired generation continues to have a role out to 2050, and the increased flexibility required in its operation will be an absolute requirement in the short term as it covers a transitional period in the UK and out to 2050 when its role may be better suited only for ensuring security of energy supply on a decarbonized grid.

From the regional and local policies described here, it is determined that natural gas and gas-fired power generation will continue to have a role in UK power generation through 2050. Continued deployment of renewable energy sources, increased nuclear production, development of CCS technology, and diversification of gas supplies will all impact how GTs are operated. Meeting future CO₂ emissions targets will be a difficult task with a number of political, economic, social, and environmental uncertainties, but increasing the operational and fuel flexibility of a proven technology such as GT generation will provide the foundation for reaching those targets.

1.1.2 United Kingdom Power Generation – Past, Present, and Future

Within the framework of the European and UK energy policies and regulations presented, it is useful to consider the current and projected state of the UK power and gas sectors. The presented policies and regulations provide the bounds within which the OEMs must design their equipment and the generators must operate it. However, this framework only provides a portion of the influence which drives both the generation portfolio and gas network composition. Certainly economic impacts, such as the recent global recession, or social impacts, such as domestic energy efficiency measures, can play a part in determining which way energy flows within the UK network. Gas-fired generation currently has and will continue to have an important and increasingly flexible role, even as the energy production system is decarbonized to meet established regulations.

A view of UK electricity generation for the 60 year period from 1948 – 2008 is given in Figure 1.1, with increased use of gas for electricity generation from the 1990s. In the late 2000s, a steep decline is noted in the use of nuclear, coal, and other fuels, with gas largely filling the power generation gap [11]. Since 2010, however, the use of gas for electricity generation has been more volatile. This can be linked to a number of factors including fluctuating gas prices, warmer winters, and increasing efforts to improve energy efficiency [12]. Figure 1.2 provides a more recent view of fuel use for electricity generation in the UK from 2014 and 2015. Particular attention should be paid to not only the increasing market share of renewables, but also to the decrease in coal utilization while gas-fired generation remained constant. This is a trend that is expected to continue in the near-term as the EU IED requires the closure of carbon-intensive power generation stations such as those fired by coal and coke.

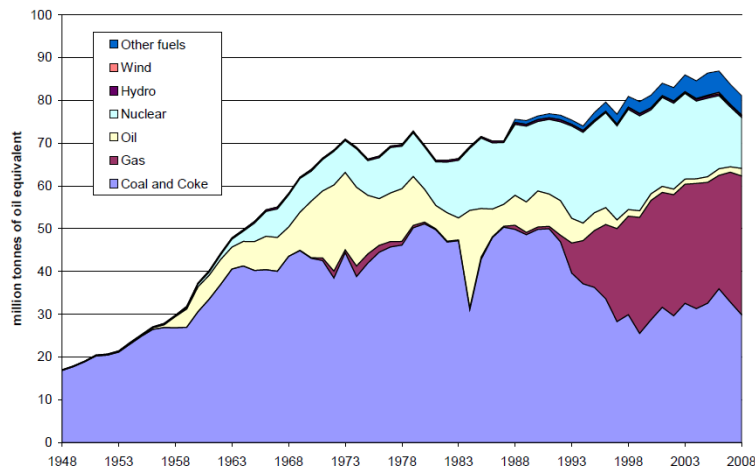


Figure 1.1: Fuels used to generate electricity in the UK from 1948-2008. Reproduced from [11].

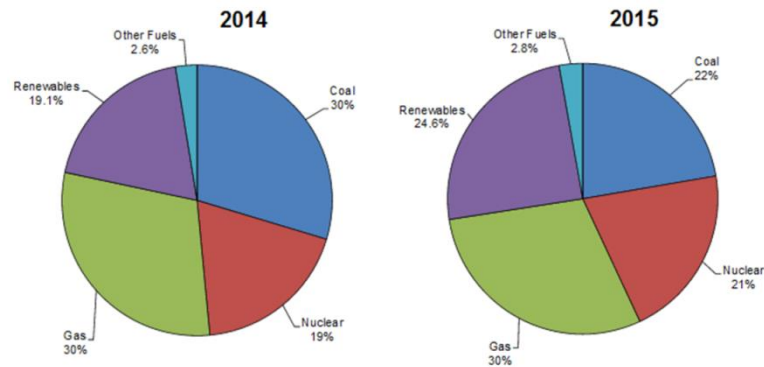


Figure 1.2: Shares of UK electricity generation by fuel type in 2014 and 2015. Reproduced from [3].

The future of power generation and fuel supply in the UK within the constraints of the UK Climate Change Act and the resulting carbon budgets is also important to consider. The most ambitious projection formulated by the UK National Grid Future Energy Scenarios, known as the “Gone Green” scenario, is of significant importance to the gas-fired power generators as it provides a potential view for their future role in the generation landscape. The “Gone Green” scenario assumes that all current UK environmental targets are met, particularly 15% of all energy to be produced in 2022 by renewable energy sources, all established carbon budgets are met, and the 80% reduction in GHG emissions mandated by the UK Climate Change Act is met by 2050 [13]. As can be seen in Figure 1.3, the “Gone Green” scenario arrives at a wide variety of electricity generation sources, with gas, combined heat and power (CHP), and CCS all contributing to the total installed capacity in 2040.

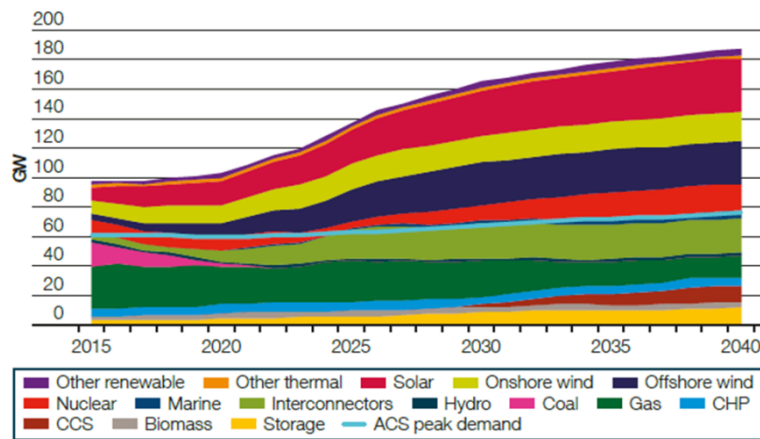


Figure 1.3: Projected UK electricity generation capacities by source in the UK National Grid “Gone Green” scenario. Reproduced from [13].

In the “Gone Green” scenario, the installed capacity of gas-fired power generation remains mostly constant, if it is abated with CCS post-2030. Of course, in the “Gone Green” scenario, there is significantly more renewable energy capacity which allows for even some coal-fired generation to remain in operation beyond 2020. However, after 2022, the generation gap created by the closure of coal-fired power stations is replaced by increased renewable generation. This leads to a potential future generation landscape which relies heavily on gas-fired generation to both meet peak demand and load follow intermittent renewables.

1.1.3 Natural Gas in the UK

In terms of UK power generation, natural gas has played an increasingly important role in the sector for the past 25 years. In fact, across all sectors, the role of natural gas has increased, particularly since the late-1960s with the discovery of natural gas in the southern North Sea [11]. The first combined-cycle GT (CCGT) power station in the UK opened in 1992, and by 2008, CCGT represented 46% of all power generated in the UK, compared with only 5.5% renewables [11].

Perhaps more variable than the use of gas for power generation in the UK over recent years is the source of the natural gas itself. It is widely accepted that offshore domestic gas production has been in decline in the United Kingdom Continental Shelf (UKCS) over the past decade. In fact, UK natural gas production peaked in 2000 [11] and saw its largest annual decline in over 40 years from 2010 to 2011 [12]. This has largely resulted in the UK becoming a net importer of natural gas, whether by pipeline or shipboard LNG, as can be seen in Figure 1.4, which provides the UK gross natural gas flow, with 52% of the gas entering the system imported in 2015. Extensive modeling of future energy scenarios has shown that the UK’s natural gas

import dependency will increase out to 2050 (up to 94%), with LNG meeting most of the demand even in scenarios where UK domestic shale gas production is exploited [14].

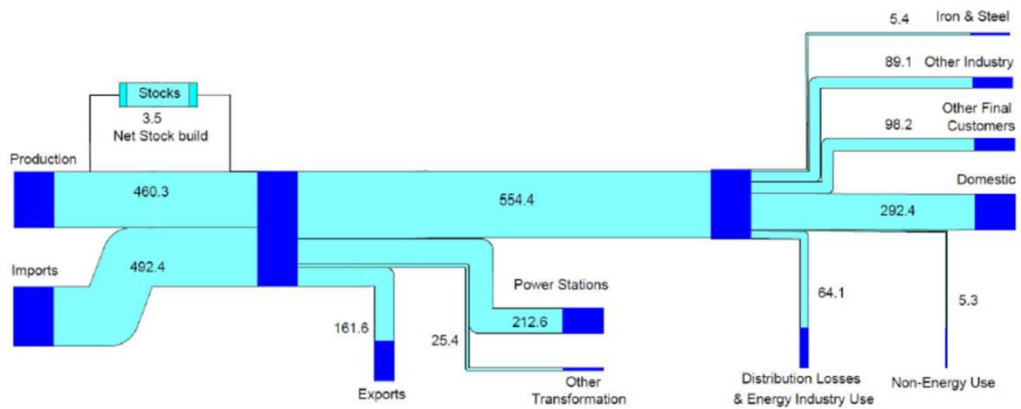


Figure 1.4: UK natural gas flow chart in TWh for 2015. Reproduced from [3].

The focus on varying natural gas compositions is shown to be driven by an increase in the diversity of UK gas supply over the last decade, particularly as LNG imports have increased [3] and hydrogen is projected to play a more pivotal role in the future [15]. Varying natural gas composition has already been shown to impact GT operations by UK GT power generators [16], and GT OEMs are increasingly addressing the wide variety of natural gas blends to be used in GT combustion [17, 18].

1.1.3.1 Liquefied Natural Gas

Considering further the UK's increasing dependence on natural gas imports, LNG is shown to have an expanding role in the balancing of variable pipeline supplies from Norway and continental Europe. First imported from Algeria in the 1960s to the early 1980s, LNG was not imported to the UK again until the opening of the LNG terminal at the Isle of Grain in 2005 [11, 12]. The potential sources of LNG into the UK have since expanded significantly, particularly with the construction of additional LNG export terminals worldwide and the opening of UK import terminals at Teesside, South Hook, and Dragon [19]. The locations of all UK LNG terminals can be seen in the UK gas transmission system shown in Figure A.1 in Appendix A.1. LNG's share of total gas imports rose from 25% in 2009 to 35% in 2010 to 47% in 2011, although declining in recent years due to increased demand for LNG in Asia and increased coal usage [3, 12], as shown in Table 1.1.

Table 1.1 provides details on the wide-ranging sources of LNG into the UK from 2005 to 2015, with countries arranged from top to bottom in terms of total overall imports during that time

period. This again highlights the dominance of Qatar-sourced LNG. The source of LNG coming into the UK is of great importance because often the compositional make-up (e.g. hydrocarbons, CO₂, O₂, etc.) can vary a great deal from source to source. Additional variables such as transit time, pre-processing to remove liquefied petroleum gas (LPG), and post-processing to ballast the gas with nitrogen to ensure it meets pipeline entry requirements, also affect the composition of the LNG as it enters the UK pipeline network and continues on to GT power generators. Given LNG's propensity for having high content of higher hydrocarbons (C₂+) when compared to UK domestic gas [16], this variation and its potential effect on GT power generators is of particular interest to this study. LNG's share of the UK import market is expected to increase in the future. Thus, it will be paramount to understand the impact of its compositional variation on GT combustion characteristics, such as flame shape, stability, operating limits, and potential mitigations. This will also drive the selection of fuel blends for experimental investigation.

Table 1.1: UK annual LNG imports by exporting country from 2005-2015. Compiled from [3].

											GWh
	2005	2006	2007	2008	2009	2010	2011	2012	2013	2014	2015
Imports											
Liquefied Natural Gas	5453	37576	14903	9046	112238	206846	274794	150097	102620	124081	152397
of which:											
Qatar	0	779	2693	0	62076	162384	234077	146431	95204	113769	141143
Algeria	4575	20718	6605	3160	19683	11697	2687	1311	4492	5774	5170
Trinidad & Tobago	878	3614	3854	5886	21873	16896	5903	0	1101	4004	5005
Norway	0	0	0	0	1890	9038	10114	1735	1068	0	601
Egypt	0	12465	1751	0	5891	1282	890	145	755	0	0
Nigeria	0	0	0	0	0	3729	13025	475	0	534	478
Yemen	0	0	0	0	0	1821	6521	0	0	0	0
USA	0	0	0	0	0	0	1575	0	0	0	0
Australia	0	0	0	0	824	0	0	0	0	0	0

1.1.3.2 Natural Gas – Hydrogen Blends

As renewable energy sources such as wind and solar power are expected to contribute increasingly to electricity generation in the UK for the foreseeable future, technologies such as P2G are being developed and implemented as a means of energy storage during times of peak renewable production coupled with reduced demand [7]. Power-to-gas essentially converts the excess electricity into hydrogen (H₂) gas through an electrolysis process for storage in existing natural gas infrastructure [7]. While this technology is still largely under development, it has been successfully implemented since 1991 in California and on larger scales more recently in Germany [7].

In the UK, current legislative limits on hydrogen introduction into the natural gas grid are limited by the Gas Safety (Management) Regulations (GS(M)R) to 0.1% vol [20], however P2G

technology has been evaluated for deployment in various locations [7]. Furthermore, while the addition of hydrogen to the natural gas grid as an energy storage vector through P2G certainly presents an operating scenario worth considering for GT OEMs and power generators, additional work is being undertaken to evaluate the shift of certain natural gas pipeline networks in the UK entirely to hydrogen operation [15]. Instead of being fed by hydrogen produced from excess renewable electricity, it has also been proposed instead to use steam-methane reforming with CCS infrastructure to supply hydrogen into pipelines for domestic and industrial use. A dedicated working group within the H21 Leeds City Gate project is considering blending of hydrogen into natural gas pipelines up to 30 %vol at select locations in the UK [15]. Thus, it will be critical to understand the potential influence that natural gas-hydrogen blends will have on UK GT power generation, in particular as the complexity of hydrogen use in GT combustion has not been fully appreciated in H21's initial report [15].

By considering the policies, regulations, current and future power generation landscape, and projected changes to UK gas networks, it has thus been shown that there are three distinct motivations for this experimental and numerical combustion study, namely:

- 1) GT power generation will continue to be a contributor to the UK power generation landscape through 2050, increasingly utilized in back-up, peak demand, CHP, or coupled with CCS applications.
- 2) Environmental policies and regulations such as the UK Climate Change Act and the European Industrial Emissions Directive drive GT power generation to reduced GHG emissions while maintaining high efficiency and reliability.
- 3) UK gas supplies are currently being drawn from numerous sources, and the diversity of supply is expected to expand, particularly with the slowdown in gas production from the North Sea and the UKCS. Increased imports of globally-sourced LNG, potential harmonization of gas quality specifications across the EU affecting European pipeline imports, the potential for domestic shale gas production, and the introduction of hydrogen as an energy storage vector in the natural gas pipeline will all impact the UK gas supply to industrial power generation stations and the resulting stable combustion regimes in the GTs they operate.

1.2 Thesis Aims and Objectives

The aim of this thesis was to aid GT OEMs and power generators to meet anticipated variation in future natural gas fuel supply composition while maintaining their economic viability and reducing their environmental impact.

To meet this aim, several specific objectives needed to be met:

- A range of representative fuel blends need to be selected for experimental investigation in a premixed swirl combustor at simulated gas turbine operating conditions (at Cardiff University's Gas Turbine Research Centre (GTRC) in Port Talbot, South Wales). These fuel blends will focus on natural gas blends with varying content of hydrogen, higher hydrocarbons (e.g. ethane and propane, further referred to as C₂₊) and diluent (e.g. nitrogen).
- Appropriately scaled generic burners needed to be developed and commissioned.
- A suite of non-invasive combustion diagnostic techniques, such as planar laser induced fluorescence (PLIF) and chemiluminescence (CL), and dynamic pressure sensing techniques need to be developed to enable characterization of the resulting flame structure along with the coupling between pressure fluctuations and heat release resulting from changes in fuel composition.
- Flame structures and heat release characteristics under lean conditions will be quantified to enhance understanding of future GT operating scenarios, when GHG emissions requirements may push operating envelopes closer to current stability limits.
- The data generated will be used to validate chemical kinetic reactor network and computational fluid dynamic (CFD) models, in particular at elevated conditions of ambient temperature and pressure, where data is currently lacking for the fuel blends studied herein.
- The results of this study should support OEMs with swirl burner design considerations for fuels of varying composition, as well as provide GT operators with guidance to help support their plant efficiency, operating flexibility and security, emissions reductions goals, and economic stability.

1.3 Thesis Structure

The thesis is structured to first provide background and motivation for the work presented herein. Following this introductory section, Chapter 2 provides a review of previous research and an evaluation of current ‘state of the art’ in the field of fuel flexibility for GT combustion, including experience from GT OEMs, GT operators, and the academic GT combustion research community. Chapter 2 also includes the theoretical background associated with swirl flame stabilization, thermoacoustics, and emissions, with a particular focus on the influence of elevated ambient conditions of temperature and pressure on these critical combustion parameters. Chapter 3 provides details of the experimental facilities and methodologies employed in this study, with a focus on non-intrusive combustion diagnostics as well as chemical kinetic and acoustic modeling techniques. As the development of non-intrusive combustion diagnostics for Cardiff University’s GTRC High Pressure Combustion Rig (HPCR) has been a key element to this work, Chapter 4 has been dedicated specifically to the implementation, commissioning, and data processing for new CL, PLIF, and dynamic pressure measurement systems. In addition to new diagnostics systems at the GTRC, two new high pressure generic swirl burners (HPGSB and HPGSB-2) have been designed, commissioned, and characterized for this work, and initial results are presented in Chapter 5. Chapters 6 and 7 focus on parametric experimental combustion studies undertaken with the HPGSB-2, examining the influence of higher hydrocarbons (Chapter 6) and hydrogen (Chapter 7) in natural gas on flame stabilization, thermoacoustics, and emissions, each supported by chemical kinetic modeling. Chapter 8 describes the use of an open-source, low order thermoacoustic modeling tool and a comparison with experimental dynamic pressure measurements. Finally, the thesis conclusions, recommendations, and suggestions for future work are given in Chapter 9. Additionally, appendices are provided which detail the burner geometries, numerical coding scripts employed in this study, image analysis procedures, and photographs of key equipment utilized in this study.

CHAPTER 2 – STATE OF THE ART AND LITERATURE REVIEW

From ABB's 4 MW power generation GT installed in Neuchâtel, Switzerland in 1939 [21] to General Electric's 605 MW combined cycle GT installation in Bouchain, France commissioned in 2016 [22], GT combustion technology has accordingly developed to accommodate inlet pressures over 5 MPa, inlet air temperatures up to 900 K, and outlet temperatures approaching 2000 K [1]. With steady technology improvement over the past decades, industrial GTs have been able to achieve thermal efficiencies as a percentage of lower heating value (LHV) of 60% and NO_x emissions below 10 ppm when firing natural gas in CCGT configurations [22-24]. However, with ever-increasing pressure on GT OEMs and operators to increase efficiency and reduce environmental impacts, extensive research and development activities continue to ascertain the impacts of variation in gaseous fuel composition on GT swirl flame stability, thermoacoustics, and GHG emissions formation.

2.1 Gas Turbine Fuel Flexibility

Natural gas quality is a key consideration as many industrial GT combustion systems are tuned for a specific natural gas composition local to the GT installation [16]. As noted in Chapter 1, the UK will become increasingly dependent on gas imports to counter decreasing domestic production and potential short-to-medium term increases in gas-fired power generation. Given the high variability between domestic and international gas compositions, the UK sets limits on the quality of gas that is admissible into the natural gas grid through the GS(M)R [20], impacting both domestic and industrial gas users. One gas quality issue of particular importance is the acceptable Wobbe Index (WI) range. This is particularly crucial for industrial GTs as variation in hydrogen content in natural gas can significantly lower the WI while the presence of higher hydrocarbons can increase the WI. WI is often used in the gas industry as a measure of the energy delivery of a natural gas fuel to a combustion device. It is a calculated value based on a set of reference conditions (combustion and metering temperature, t_1 and t_2 , and pressure, p_2) as shown in Equation (2.1):

$$WI [t_1, V(t_2, p_2)] = \frac{\tilde{H}_s [t_1, V(t_2, p_2)]}{\sqrt{d(t_2, p_2)}} \quad (2.1)$$

where \tilde{H}_s is the real higher (gross) calorific value of the natural gas mixture and d is the real relative density of the mixture with respect to air, with the "real" values differing from the "ideal" values by incorporating a compression factor, Z , as described in the British Standards

Institution (BSI) document for the calculation of calorific values, density, relative density and WI from natural gas composition, BS EN ISO 6976:2005 [25]. All natural gas which enters the UK gas transmission system must meet the standards shown in Table 2.1 [20]. These limits also impact the operation and emissions of industrial users of the natural gas pipelines, including GT power generators.

Table 2.1: Gas quality limits for entry into the UK natural gas system. WI values referenced at $p_2 = 0.101$ MPa and $t_1, t_2 = 288$ K. Compiled from data in [20].

Parameter	
Wobbe Index (MJ/m ³)	47.20 - 51.41
Total Sulfur (mg/m ³)	50 (max)
Hydrogen Sulfide (H ₂ S) + Carbonyl Sulfide (COS) (mg/m ³)	5 (max)
Oxygen (O ₂) (% vol)	0.2 (max)
Hydrogen (% vol)	0.1
Incomplete Combustion Factor	0.48 (max)
Soot Index	0.60 (max)

While the current GS(M)R limits define the useful energy content delivered to industrial GT burners through the WI, it does little to give any indication of the actual chemical composition of the natural gas in the distribution system, which can significantly impact the resulting combustion behavior of those gases at elevated temperature and pressure conditions. Therefore, while fuel flexibility has been highlighted as a key consideration in future GT operations, many GT OEMs, GT operators, and combustion researchers are currently investigating the technological barriers to achieving high efficiency, low emissions combustion as the composition of natural gas varies.

2.1.1 Gas Turbine OEM Experience

Three GT OEMs, Mitsubishi, Siemens, and General Electric, are addressing the issue of variable fuel composition in their GTs through the use of active control systems. Each OEM acknowledges that LNG will continue to have an increasing role as a fuel for GTs worldwide. For example, Figure 2.1 provides a projection of the fuels used in Siemens worldwide GT fleet out to 2020. It can be seen that the percentage of GTs in the Siemens fleet which will be operated on LNG increases in both scenarios, “Steady State” and “High Oil Price”, from 3% in 2005 up to potentially 15% [26]. This increase is in line with the expected increase in LNG’s impact on the UK natural gas market.

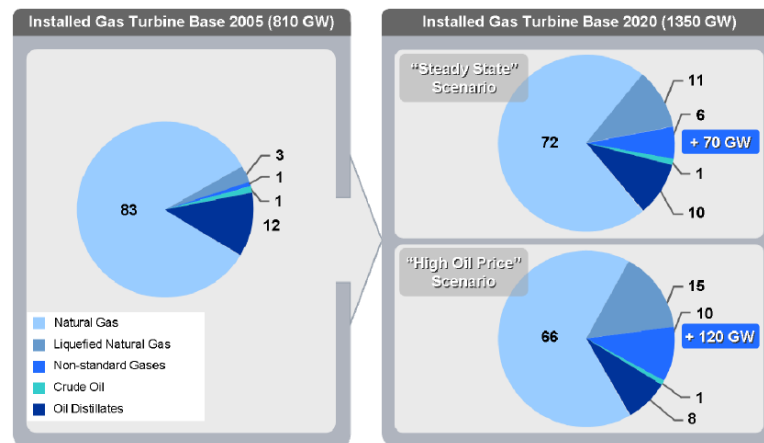


Figure 2.1: Projected fuel types for Siemens installed GT fleet. Reproduced from [26].

In addition to the increased role that LNG will play in the GT fuel market, the OEMs must recognize and address the impact of LNG's compositional variability from various sources around the world. General Electric considers the degree of complexity associated with LNG composition variation to be linked directly to its increased content of inert gases and higher hydrocarbons, especially ethane [27]. Siemens also acknowledges the issues of LNG as a GT fuel by considering the production method of LNG, which can often lead to higher heating values of the fuel as the result of the higher hydrocarbon content [26].

Given that LNG is already being used in GT power generation installations across the world, the OEMs have had to address fuel composition variations in their systems. The GTs designed by these OEMs often employ dry low NO_x (DLN) or dry low emissions (DLE) technology to ensure that the temperatures of premixed fuel and air are controlled to limit the formation of NO_x and carbon monoxide [16]. Compared to diffusion combustion, these premixed systems often introduce a number of complex flow and combustion issues which the fuel composition can greatly affect. For this reason, OEMs will often set their own limits on the composition of fuel to be used in their GTs, and often these are much tighter limits than, for example, the limits provided in GS(M)R. To ensure reliable operation, the OEMs set fuel parameters such as the maximum level of C_2+ , the minimum amount of methane, the maximum inert content, and the maximum allowable excursion from the tuned WI limit [16]. These levels are set not only to maintain the reliability of the combustion equipment, but also to ensure that emissions limits are not exceeded during normal operation.

The GT OEMs have observed combustion instabilities in their machines with variation in gas composition. In one case, Mitsubishi observed that a 4% reduction in the target methane

value lead to high cycle frequency pressure fluctuations during GT operation. Similarly, another fuel gas blend with a 2-3% increase in the target methane resulted in ultrahigh cycle frequency dynamic pressure fluctuations [28]. Siemens has noted that a 10% deviation in the WI from the fuel on which a GT is tuned can lead to combustion instabilities and increased emissions [26].

As will be discussed further in Section 2.1.2, these instabilities have been shown in the field to damage GT combustion equipment. The OEMs therefore have implemented a number of mitigations to address natural gas compositional changes during operation. Siemens' WI Control system [26], General Electric's Modified WI system [27], and Mitsubishi's Automatic Combustion Pressure Fluctuation Monitoring [28] are examples of control systems which have been implemented to respond to natural gas fuel composition changes. These control systems utilize equipment such as valves, acoustic sensors, and gas analysis to augment fuel and air flow to the combustion system. In addition to control systems, the OEMs have also made physical design changes to their combustors to increase the stable operating range. For example, Mitsubishi has introduced acoustic liners in their combustion chambers to help mitigate combustion pressure fluctuations from 500-5000 Hz [28].

Despite these improvements, there are still operational issues experienced by GT operators in the UK as a result of changes in the fuel composition of the UK gas pipeline, the cause for which drives the need for further fundamental combustion research. As additional LNG export markets open and with the potential for hydrogen addition to the natural gas grid, gas-fired generators will face challenges which could affect the security of electricity supply in the UK, the ability to meet UK emissions targets, and the reputation, safety, and profitability of the operators.

2.1.2 Gas Turbine Operator Experience

The study presented in [16] provides operational experience of a GT operator's fleet in the UK and Europe in response to changing natural gas compositions and qualities. It reinforces that the WI is insufficient for the full characterization of the resulting flame behavior. Natural gas can be a particularly difficult fuel blend for which to calculate a WI given that it can contain a large number of chemical species in varying quantities. Also, when accounting for the effects of dilution, it is possible that fuels of widely varying composition can have the same WI. This means that two vastly different fuels with the same WI will deliver the same energy input to

the combustion system, but the fuel composition effects on flame stability, flashback and blowoff limits, chemical reaction mechanisms, and the resulting emissions are unaccounted for [16].

In-field combustion issues that have been experienced and documented include instabilities resulting from both increasing and decreasing fuel WI, rate-of-change of WI, increased dynamics during warmer ambient conditions, and C_2+ increase [16]. In one instance, high combustion dynamics exceeding the control system alarm value resulted from a change in natural gas sourcing as LNG was brought onsite. In another instance, the amount of C_2+ content of a fuel supplied to a UK site increased from 6 % to 9.5% over 4 hours, resulting again in increased combustion dynamics as a result of changing fuel sources to LNG [16]. The results of these issues are largely financial and environmental, as the instabilities lead to machine deloading or shutdown, operation in part load, or even damage to structural components, as shown in Figure 2.2.



Figure 2.2: Photograph of damaged GT combustion chamber due to excessive combustion dynamics. Reproduced from [16].

GT operators have worked to address these combustion issues through control system upgrades, including online fuel composition monitoring, fuel splitting, and fuel heating systems. Enhanced control measures, empirical correlations, and supplementing the WI with other fundamental fuel parameters as a measure of combustion stability and emissions are therefore needed to improve the operability of GTs in future fuel-flexible conditions, as both hydrogen and C_2+ content will impact flame speed, auto-ignition parameters, turbulent response, and chemical kinetics.

2.1.3 Fundamentals of Higher Hydrocarbons in Natural Gas

LNG and unconventional gas (e.g. shale gas) are expected to contribute to the increased movement of natural gas around the world, with the International Energy Agency projecting a doubling of current global LNG trade by 2040 [4]. One important consideration that must accompany this increased global LNG trade is its impact on GT power generation, particularly as LNG typically contains higher concentrations of heavier hydrocarbons (C_2+), e.g. ethane and propane, which can all have an effect on the specific heat, adiabatic flame temperature, chemical kinetic rates, and radiative heat transfer of the gas blend [29].

2.1.3.1 Chemical Kinetics

The research area most dedicated to the study of natural gas blends containing C_2+ components is currently the field of fundamental chemical kinetics experiments and modeling, with emphasis on the influence of both single component fuel properties and interactivity between fuel blend components. It has been noted by Healy et al. [30], as a result of methane, ethane, and propane oxidation testing, that propane exhibits low temperature chemistry, while methane and ethane do not. Mixtures containing higher order hydrocarbons have been shown to cross-over from low-and-intermediate temperature kinetics, which are dependent on the fuel concentration, to high-temperature kinetics, which are dependent on oxygen concentration, at lower temperatures [30]. Won et al. [31] noted that low temperature chemistry was found to change the local fuel/air mixture entering the flame, which would thus impact the local equivalence ratio, ϕ , and subsequently result in a change of turbulent burning velocity and flame structure. Low temperature chemistry of the higher hydrocarbons in natural gas plays an important role in flame stabilization behavior, particularly for swirling flames which utilize the flame stabilizing central recirculation zone (CRZ) to mix hot combustion products with incoming cold reactants. The identification of an increase in local heat release and variations in the local ϕ when introducing higher hydrocarbons could therefore yield evidence of low temperature chemistry effects in the swirling flame.

A number of kinetic modeling efforts have been undertaken with regards to both individual constituents and natural gas blends. Khalil and Karim [32] developed a reaction mechanism containing 1966 elementary reactions and 380 species to model the oxidation of hydrocarbon fuels containing up to eight carbon atoms (C_8). The high temperature reactions of their mechanism focus mainly on the oxidation of hydrogen and carbon monoxide. However, they found that at lower temperatures, below 1000K, the long chain hydrocarbons tended to follow

a sequential breakdown (e.g. C_4 to C_3 to C_2 to C_1), which would correspond to the existence of higher heat content radicals in lower temperature regions of a swirl flame. Khalil and Karim [32] also acknowledge the two-step ignition phenomena in their model as observed by Won et al. [31], which results in a pressure step change that could potentially trigger combustion instabilities in a high-pressure flame. Given that natural gas and LNG is mainly composed of methane, it has been shown that the most significant effect of C_{2+} on methane in the mixture is on the initiation phase of the methane reaction, increasing the rate of reaction due to the abundance of radicals resulting from preignition reactions [32]. For example, the addition of approximately 6% by volume of a mixture of C_{2+} hydrocarbons resulted in an autoignition delay time reduction of 65% compared to pure methane at a temperature of 800 K and pressure of 2.8 MPa [32].

2.1.3.2 Ignition Delay

Higher hydrocarbons have been shown to be highly reactive compared to methane in a number of studies, which could give indication why natural gas blends with C_{2+} content might exhibit thermoacoustic instabilities. Bourque et al. [33] tested two natural gas blends containing less than 82% methane, and the remaining mixture fraction consisting of varying levels of C_{2+} content using two different shock tubes and a rapid compression machine. It is noted that, in general, heavier hydrocarbons tend to have an accelerating effect on ignition [33]. This is supported by shock tube ignition tests which revealed that the blend of natural gas containing the highest level of C_{2+} content lead to faster ignition across all ϕ , temperatures, and pressures [33]. This is in agreement with the work of Holton et al. [34] which found that the addition of only 5-10% of ethane or propane to methane reduced the autoignition time of the binary fuel blend by up to 50%. It should be noted, however, that the work of Holton et al. [34] was only conducted in an atmospheric flow reactor while the work of Bourque et al. [33] was conducted at pressures up to 3.1 MPa. Petersen et al. [35] also conducted shock tube measurements of the ignition delay time, focusing specifically on methane/propane fuel blends. Propane addition was found to increase the ignition speed for all mixtures and conditions. In addition, the ignition delay times decreased as the pressure of the experiments increased [35], an important consideration for premixed swirl combustion at elevated temperature and pressure conditions.

2.1.3.3 Burning Velocity

Laminar flame speed, S_L , is a fundamental measure often used to characterize a key time scale which helps to gauge the effect of fuel variations on both chemistry and mass diffusion [33]. Tseng et al. [36] investigated S_L of the main constituents of natural gas in air, namely methane, ethane, and propane. All tests were conducted at atmospheric pressure and temperature, and reveal that the maximum burning velocity for each hydrocarbon is near stoichiometric ($\varphi = 1$). However, both ethane and propane are shifted towards higher S_L compared to methane in the lean mixture regime ($\varphi < 1$) [36]. S_L measured by Kochar et al. [37] for individual methane and ethane mixtures with air at atmospheric pressure and temperature are in relative agreement with those given in [36]. The influence of preheating is also shown to greatly increase S_L . For example, S_L of a stoichiometric propane-air mixture at atmospheric pressure and 650 K preheat is 1.5 m/s [37], approximately 5 times greater than at atmospheric conditions as presented in [36].

Consideration must also be given to experimental measurements with blended constituents. Numerous methane/ethane and methane/propane mixtures have been investigated in [37], in addition to investigating the impact of dilution, an important consideration as LNG is often ballasted with N_2 to meet UK WI limits. At comparable pressure and temperature conditions, methane/propane mixtures are shown to have higher stoichiometric S_L than methane/ethane mixtures, ~ 1.8 m/s compared to ~ 1.55 m/s, respectively [37]. Bourque et al. [33] also investigated the laminar flame speeds of the natural gas mixtures discussed previously (less than 82% methane). The mixture containing the highest level of higher hydrocarbons is shown to have a higher S_L than the predicted S_L of methane, particularly as the pressure increases up to 0.4 MPa [33]. At atmospheric pressure and temperature, the higher level of high hydrocarbons is shown to result in only a slight increase in the laminar flame speed. However, as mentioned previously, the impact of preheating will significantly influence the flame speed of these mixtures as shown by the increased low temperature chemistry of the higher hydrocarbons and the increase in flame speed noted by Kochar et al. [37] for preheated propane/air mixtures. Finally, both nitrogen and CO_2 have been evaluated as diluents for their impact on S_L of natural gas constituents [37]. Given the higher specific heat capacity of CO_2 compared to nitrogen, it is found that CO_2 dilution decreases the flame speed more than nitrogen for both ethane and propane mixtures [37].

Higher hydrocarbon variation in LNG has been shown to produce potentially damaging combustion instabilities in operational GTs [16] despite the fact that the overall composition met the requirements for entry into the gas distribution system. This highlights the triviality of fuel properties used currently for gas transmission, such as WI, in the prediction of operational GT flame response, particularly if the C_2+ content of the fuel varies widely from the fuel sources specified during GT procurement and tuning. It has been shown that GT OEMs have worked to address these issues in their operational fleets with combustion testing and control systems [17, 18, 26-28, 38]; however there is a lack of experimental research into the underlying causes of observed changes in swirl flame shape, acoustic response, and NO_x emissions with variation in the C_2+ content of natural gas fuels. Fundamental research has been conducted and discussed here for the development and validation of chemical kinetics models of natural gas mixture ignition delay time and laminar flame speed [30, 32-35, 37], but limited applied combustion studies have considered fuel blends containing high C_2+ content in experimental swirl burners [39, 40]. This reinforces the need for further fundamental swirl combustion studies of these fuel blends at elevated temperature and pressure conditions.

2.1.4 Fundamentals of Hydrogen Addition to Natural Gas

Developments in low-carbon hydrogen production have shifted P2G applications from experimental scales to practical integration with existing natural gas pipelines in locations across the world [7]. However, information surrounding admissible concentrations of hydrogen into natural gas networks still varies worldwide, with current legislative limits as low as ≤ 0.1 %vol in the UK as shown in Table 2.1 [20], current hydrogen injection limited to 2 %vol from Thüga Group's operational P2G demonstration facility in Frankfurt, Germany [41], and feasibility studies considering hydrogen blending over 50 %vol in the United States [42]. Hydrogen blending into natural gas pipelines presents challenges to GT power generators due to hydrogen's influence on gaseous fuel combustion parameters such as WI, laminar and turbulent flame speeds, adiabatic flame temperature (AFT), and thermo-diffusive effects under LPM conditions [43, 44].

2.1.4.1 Chemical Kinetics, Ignition Delay, and Burning Velocity

A number of comprehensive numerical [45-47] and experimental [48-50] studies have been undertaken to investigate the influence of hydrogen blending with methane on fundamental flame characteristics such as the ignition delay time and S_L . In the modeling study by

Gauducheau et al. [45], LPM combustion of CH₄-H₂-air flames was investigated at inlet temperatures up to 1000 K and pressures up to 3.0 MPa. The addition of 10-20% H₂ in CH₄ has the effect of reducing the pure methane ignition delay time by two to three times at gas temperatures less than 1000 K at 3.0 MPa and $\phi = 0.6$, with an even more dramatic reduction (order of magnitude) at higher temperatures [45]. Zhang et al. [50] identified similar trends in ignition delay reduction with 20% H₂ addition to CH₄, attributing this to increases in the total chemical kinetic reaction rate with H₂ addition. The increase in reaction rate is attributed to the increased concentrations of the H, O, and OH radicals with H₂ addition through the reactions (1) $\text{H} + \text{O}_2 \leftrightarrow \text{O} + \text{OH}$, (2) $\text{O} + \text{H}_2 \leftrightarrow \text{H} + \text{OH}$, and (3) $\text{OH} + \text{H}_2 \leftrightarrow \text{H} + \text{H}_2\text{O}$ [50]. These radicals promote the oxidation of CH₄, reducing ignition delay times.

H₂ addition to methane has also been shown to increase S_L . In a study of S_L utilizing spherically-expanding flames, Halter et al. [48] note an increase in S_L with H₂ addition of 10 %vol and 20 %vol to CH₄ at each pressure condition of 0.1 MPa, 0.3 MPa, and 0.5 MPa, for all equivalence ratios investigated from $0.7 < \phi < 1.2$. Similar trends were identified in other experimental and numerical studies [45-47, 49]. In addition, an experimental study of turbulent burning rates by Fairweather et al. [49] in a fan-stirred constant volume combustion bomb (CVCB) found that with 20% H₂ addition in CH₄, the turbulent burning velocity increased for lean ϕ . Also, interestingly the ratio of turbulent to laminar flame speeds under lean conditions was observed to be 3-4 times higher than at $\phi = 1$ [49]. The findings in these studies of flame speed reinforce the promotional effect of hydrogen blending on methane reactivity.

Of particular interest in this study is also the influence that H₂ addition has on the thermo-diffusive behavior of methane, and how this may influence its behavior in LPM turbulent swirl flames. In experimental studies by Fairweather et al. [49] and recently by Lapalme et al. [51], the addition of H₂ was shown to not only increase the stretched flame speed of pure CH₄, but also shows that under lean conditions, the stretched flame speed increases with increased stretch rate (κ). Similar results were obtained in the numerical study by Gauducheau et al. [45]. This behavior is characterized by a negative Markstein length, L_b , with H₂ addition under lean conditions, and supports the turbulent burning velocity behavior mentioned previously. This increased flame resistance to stretch under lean conditions is attributed to a reduction in the mixture Lewis number, Le , defined in Equation 2.2 as the ratio of thermal diffusivity, α , to mass diffusivity of the deficient reactant, D_{ij} , where mass diffusion is driven from the deficient reactant i towards j .

$$Le = \frac{\alpha}{D_{ij}} \quad (2.2)$$

It has been shown that Le for methane is near unity ($Le = 1.01$) for lean ϕ , while for pure H_2 it is much less ($Le = 0.29$) under lean conditions [51]. While there is still ongoing debate about the appropriate methods for defining an effective Le for fuel blends, a series of methods were evaluated by Lapalme et al. [51] showing a reduction in methane Le with H_2 addition under lean conditions. As shown in Figure 2.3.a, with lines representing the different blending methods and solid squares representing experimental results, a resulting $Le < 1$ is observed at $\phi = 0.6$ with increase H_2 addition. A Lewis number less than unity will promote diffusion of the fuel (deficient species) into the oxidizer (abundant species), and in the case of H_2 addition, serves to promote the oxidation and reactivity of CH_4 . H_2 addition also has a similar effect on the effective Lewis number in blends with propane [52], shown in Figure 2.3.b. While mixtures of C_3H_8/H_2 are not of direct interest in this study, the influence of H_2 blending with hydrocarbons and the pure C_3H_8 Le (noted in Figure 2.3.b as $Le = 1.9$) are of interest, in particular for C_3H_8 blends with CH_4 .

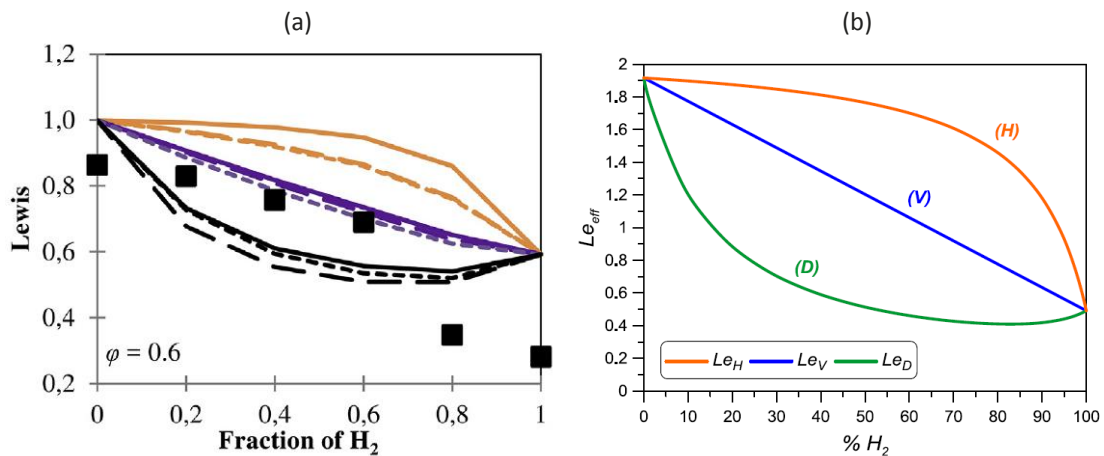


Figure 2.3: Lewis number as a function of H_2 content in CH_4 (a) and C_3H_8 (b) at $\phi = 0.6$ with blending laws (solid line) and experimental values (solid square). Reproduced from [51, 52].

In addition to the fundamental studies discussed here, an extensive body of research exists for the applied study of H_2 addition to CH_4 in practical combustion systems, such as swirl burners. Applied experiments on blended CH_4 - H_2 combustion highlight the potential for its use in GT engines and some necessary fundamental considerations. Previous studies at Cardiff University include pressurized turbulent combustion (up to 0.7 MPa) of 85-15%vol CH_4 - H_2 in a turbulent Bunsen burner [53, 54] and combustion studies in an atmospheric generic swirl burner (AGSB) investigating influences of confinement geometry [55, 56] and swirl number [57] when burning CH_4 - H_2 blends. The current study will therefore extend these previous

studies with experimental investigation of pressurized swirl flames with varying swirl number and burner confinement geometry. Consideration and comparison with additional applied studies are provided in the following Sections as hydrogen blending is considered in terms of flame stability, elevated temperature and pressure effects, and emissions formation.

2.2 Swirl Flame Stability

GT swirl combustors, such as the general can-type configuration shown in Figure 2.4, rely on the interaction between a turbulent flow field and complex chemical reactions within the primary, intermediate, and dilution zones to generate the required turbine inlet temperature for the given load condition while reducing GHG emissions, pressure loss, and instabilities. The design of the generic swirl burners utilized in this study is intended to replicate this flow-through, single can-type combustor operated in a fully premixed configuration. This geometry derives its flame stabilization mechanism mostly through the vortex breakdown structures resulting from the tangential velocity imparted on the flow through the swirler in combination with the sudden expansion into the combustor primary zone.

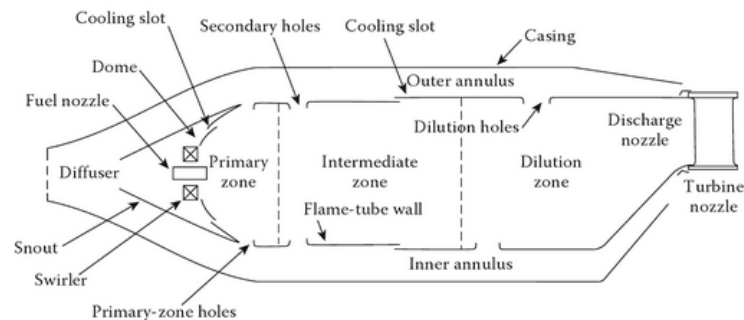


Figure 2.4: General representation of industrial can-type GT combustor. Reproduced from [1].

2.2.1 Flame Stabilization Mechanisms

Flames can be stabilized within a flow field in a number of ways including with a bluff body, sudden expansion, piloted flame, opposed jets, and swirling flows [58]. All of these mechanisms rely on a quasi-steady balance between the flow velocity and the velocity of flame propagation. The generic swirl burners employed in this study utilize a combination of these flame stabilizing methods, in particular swirl flow, sudden expansion, and a recessed bluff body. In a swirling flow, a number of unique features define how the flame stabilizes within the flow field. The most critical feature for flame stabilization in swirling flow is the creation of a central recirculation zone (CRZ) as a result of vortex breakdown [59]. The vast majority of GT combustion systems, such as that shown in Figure 2.5, utilize swirl

configurations with a flame stabilizing CRZ [59]. Figure 2.5 provides a general flow schematic that details the formation of the CRZ in an unconfined swirling flow, where \bar{p} is the centrifugal pressure distribution, r is the radial distance from the burner centerline, \bar{w} is the tangential (or azimuthal) velocity distribution, and \bar{u} is the axial velocity distribution.

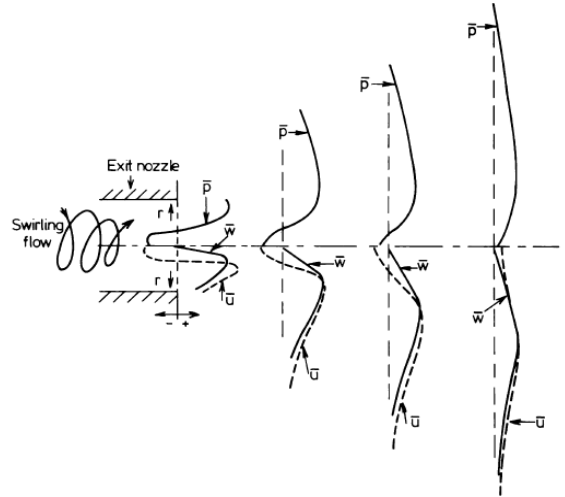


Figure 2.5: Schematic of the formation of the CRZ in unconfined swirl flows. Reproduced from [60].

The observed CRZ formation can be described by the radial momentum equation in Equation 2.3 [59], utilizing the same variables as shown in Figure 2.6 and with ρ as the flow density. Near the burner exit, high centrifugal force and tangential velocity gradient result in a radial pressure gradient with a low pressure region observable along the central axis. The tangential velocity decays as the flow expands and pressure is recovered, creating a negative pressure gradient along the central axis. The combination of this pressure gradient and the low pressure region at the burner exit centerline can create a reverse flow region along the central axis known as the CRZ; granted the swirl component must be sufficiently high for the creation of this pressure distribution [59, 60].

$$\frac{\delta \bar{p}}{\delta r} = \frac{\rho \bar{w}^2}{r} \quad (2.3)$$

The CRZ allows for recirculation of hot combustion products to the root of the flame and is characterized by high shear stresses that exist between the forward propagating reactant flow and the reverse propagating product flow in the CRZ [59]. It is within these low velocity shear layers that the flame is able to stabilize. In addition to the CRZ, swirl flows are often characterized by a sudden expansion from a nozzle or dump plane into the surrounding environment or confinement (e.g. combustion chamber). This sudden expansion creates low pressure outer recirculation zones (ORZ) which also act to stabilize the flame. Shear layers in the flow can also be caused by bluff bodies. A precessing vortex core (PVC) can also form in

swirling flows, characterized by periodic helical movement around the CRZ [60]. A view of these coherent flow structures in confined swirl flames is provided in Figure 2.6. Note that the axial decay of the tangential velocity, \bar{w} , shown in Figure 2.5 for the unconfined case will be directly influenced by the presence of confinement, which in turn increases the size and shape of the CRZ [60].

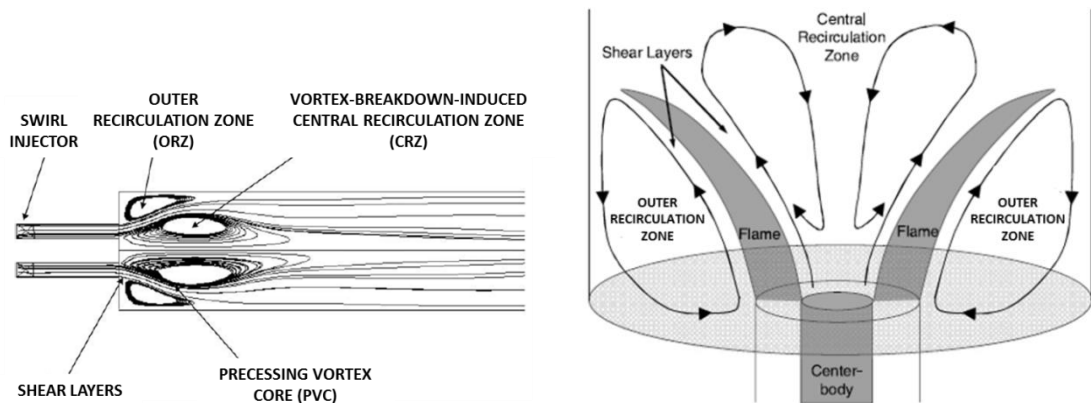


Figure 2.6: Typical mean flow streamlines and coherent flow structures for a confined, swirling, reacting flow. Reproduced from [59, 61].

While Figures 2.5 and 2.6 are in general representative of time-averaged stable flow fields and structures, swirl flames exist within highly turbulent and unsteady instantaneous flow and reaction areas characterized by flow vortices formation and dissipation, flame curvature, and reaction chemistry that occurs on a number of spatial and temporal scales [59, 62]. Recent studies in LPM and partially premixed flame stabilization and dynamics have therefore applied high-speed (kHz repetition and capture rate) diagnostics, including planar laser induced fluorescence (PLIF), particle image velocimetry (PIV), and chemiluminescence (CL) to temporally resolve the fluctuating flow and chemical components in swirling flames [62-64]. By resolving small time scales, phenomena which effect flame stabilization such as flame kernel production, PVC-flame interaction, and flame wrinkling are identified which otherwise would not appear in temporally averaged observations [62-64].

Recent experimental work has also proposed to correlate the fundamental measure of flame extinction strain rate, κ_{ext} , often made in counterflow-type burners, with swirl flame stability and flame shape transitions for varying burner operating conditions [65]. Over a variety of ϕ and H_2 fractions in CH_4 , it was observed that the transition from stable to unstable behavior could be correlated across fuel types with a normalized extinction strain rate that corresponded with a critical flame shape. However, it is noted that this could very well be an

observation that is specific to the studied atmospheric swirl burner and operating condition [65]. Nonetheless, the use of fundamental flame measurements and properties, such as those described here and in previous Sections, to quantify stable flame behavior is a critical consideration for this study.

2.2.2 Flame Instabilities

The balance that must be maintained between the highly turbulent flow field, reaction chemistry, and energy transport in swirl-stabilized flames can often give rise to unsteady processes which influence flame stability [66]. The study of flame instabilities has been a key area of GT combustion research over recent years as modern GT combustors are pushed further towards stability limits, such as in the case of LPM combustion, in order to reduce GHG emissions [59]. In addition to the potential environmental impact, combustion instabilities can also cause damage to GTs [16].

Flame instabilities and combustion noise often involve a coupling of system acoustics, heat release, flame dynamics, and turbulent flow fluctuations [66]. For discussion here, and distinction throughout this study, flame instabilities are described in three broad groups, namely thermoacoustic instabilities, lean blowoff (LBO), and flame flashback. This separation does not portend that these phenomena are mutually exclusive; however, they each exhibit unique qualities which allow for distinct discussions about their occurrence and prevention.

Pressure fluctuations resulting from flame instabilities, hydrodynamic instabilities, and system resonant acoustics can be generally categorized as low frequency ($f < \sim 100$ Hz), mid-frequency (~ 100 Hz $< f < \sim 1000$ Hz), and high frequency ($f > \sim 1000$ Hz) [59, 67]. Low frequency instabilities are often associated with operation near LBO, while mid-frequency instabilities are often associated with longitudinal acoustic system modes and heat release coupling. Higher frequency, “screech” instabilities can be associated with tangential acoustic modes or interactions between flame fluctuations and acoustic disturbances [59]. Reference to these frequency bands will be made throughout this study.

Using these frequencies, dimensionless analytical methods can be applied for quantifying the originating nature of the observed instability. Helmholtz (He) and Strouhal (St) number relationships are utilized in the quantification and comparison of measured frequencies under

isothermal flow and combustion conditions. These relationships are considered in the context of the natural acoustic modes and flow-related modes of the combustor. The Helmholtz number, He , as given in [68] and shown in Equation 2.4, provides a relationship between the measured frequency and the natural acoustic modes of the combustor. It is defined by the observed frequency, f , the length of the combustion chamber, L_{comb} , and the speed of sound, c . A constant Helmholtz number would therefore be indicative of a frequency corresponding to a natural acoustic mode of the burner quartz confinement tube [68].

$$He = \frac{fL_{comb}}{c} \quad (2.4)$$

The Strouhal number, St , as given in [60] and shown in Equation 2.5, provides a relationship between the measured frequency and the potential instabilities arising from oscillations in the fluid flow, such as the Kelvin-Helmholtz shear layer instability, which is responsible for vortex generation in sheared flows [66]. The Strouhal number is defined by the observed frequency, f , the diameter of the burner exit nozzle, D_{noz} , and the mean burner exit velocity, \bar{u} , calculated based on the combustor inlet conditions of total mass flow, burner inlet temperature, T_2 , and burner inlet pressure, P_2 .

$$St = \frac{fD_{noz}}{\bar{u}} \quad (2.5)$$

2.2.2.1 Thermoacoustic Instabilities

Thermoacoustic instabilities are characterized by the coupling of unsteady pressure and heat release fluctuations, often dictated by the geometry of the combustor, the speed of sound distribution within the geometry, and turbulent flow interaction with the flame front [66]. Also referred to as combustion noise, these instabilities can result in reduced combustion efficiency and increased pollutant emissions, with lean thermoacoustic instabilities observed to often occur abruptly with subtle changes in operating conditions [69]. This is classically defined by the Rayleigh criterion, which states that unsteady heat release will add energy to the acoustic field if the product of the pressure, p' , and heat release, q' , fluctuations is greater than zero per Equation 2.6 [70], where Ω is the flow domain, and the phase difference between the two fluctuating quantities is less than 90 degrees [66].

$$\iiint_{\Omega} p'q'd\Omega > 0 \quad (2.6)$$

In practical operating environments, the onset of thermoacoustic instabilities can be generated by entropy waves resulting from area contractions within the combustor geometry, by self-excited oscillations within the primary zone, or by flow-driven fluctuations in the highly turbulent flow field [71]. Each trigger may lead to entry at a location in the general instability loop as illustrated in Figure 2.7. A change in heat release resulting from fluctuations in fuel composition or operating condition (e.g. T_2 , P_2 , mass flow rate) induces a change in the temperature distribution within the combustor, which influences the local speed of sound distribution, leading to a change in the local acoustic field and acoustic pressure fluctuation. The dynamic pressure fluctuation may then influence the local ϕ and flow field, resulting in changes to the stable flame front, which subsequently influences the heat release within the combustor, closing the instability loop. If the system damping is insufficient or corrective actions are not taken, the fluctuating pressure amplitude would increase with time until a limit cycle was reached or system components fail.

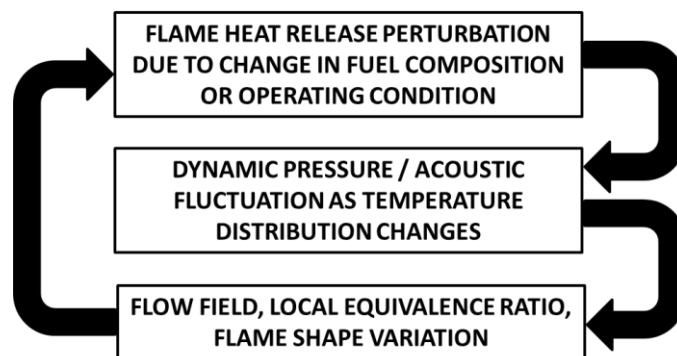


Figure 2.7: Closed-loop diagram of combustion thermoacoustic instability formation

In the context of this study, it is posited that an instability could be triggered by introduction of a natural gas blend containing high levels of C_2+ , resulting in the production of highly reactive intermediate radical species which interact with hot products from the pressurized swirl CRZ. This occurs because higher-order hydrocarbons would tend to dissociate into a pool of radicals as a result of the lower bond dissociation energy of the carbon to carbon (C-C) bonds compared to the carbon to hydrogen (C-H) bonds [32]. Similarly, if hydrogen was introduced into a methane flame, a catalytic effect would be expected as the pool of OH, O, and H radicals available for the chain-branching reactions would be increased [50]. Both scenarios would increase the localized heat release and lead to potentially damaging pressure fluctuations if the system was insufficiently damped.

These instabilities, observed in the mid-frequency range [72, 73], have been studied with a number of techniques in swirling flames including phase-locked PLIF and CL to track the interaction between acoustic waves, flame shape, and heat release [72]. Other studies have utilized stereoscopic PIV in combination with CL and laser Raman scattering to investigate the flow field, heat release, and molecular reaction chemistry parameters that influence thermoacoustic instabilities [73]. Acoustic microphones or dynamic pressure transducers (DPT) are often incorporated to evaluate the acoustic field within the burner and combustion system [72, 73]. Results have shown that oscillations in flow velocity are induced by acoustic pressure fluctuations, which then influence the size, shape, and location of coherent flow structures, such as the CRZ, by changes in axial momentum and swirl number [73]. This was observed to cause oscillations in the heat release rate by augmenting the fuel/air mixture at the base of the swirl flame which was convected downstream to the flame front, with the change in φ dictated by the influence of pressure fluctuations on fuel and air delivery systems with different acoustic impedances [73].

As thermoacoustic instabilities are intricately linked with the system acoustics, these instabilities can be mitigated by physical changes to the burner geometry, which alter its resonant acoustic response, in addition to fuel and air flow controls such as those discussed in Section 2.1.1. One type of physical mitigation, known as a Helmholtz resonator, utilizes a body of fixed volume, V , attached via a short open neck of length, L , and cross-sectional area, A , to the combustion chamber to eliminate certain natural frequencies that may be unstable [66]. A Helmholtz resonator has a natural frequency, f , which depends on its geometry and the speed of sound, c , per Equation 2.7 [66].

$$f = \frac{c}{2\pi} \sqrt{\frac{A}{LV}} \quad (2.7)$$

Helmholtz modes may also arise in locations where area changes occur within the combustion chambers. Thus, it is critical to identify these modes along with other natural resonant frequencies in the combustion system, as both may contribute to the generation of thermoacoustic instabilities.

2.2.2.2 Lean Flame Blowoff

While delivering emissions reduction benefits, LPM GT combustors are inherently susceptible to potentially high amplitude, low frequency pressure fluctuations associated with operation

near the LBO stability limit [74]. This phenomenon results from increasing chemical timescales, τ_{chem} , and decreasing flow timescales, τ_{flow} , under lean conditions ($\varphi < 1$) and is characterized by low AFT and poor combustion efficiency which can manifest within the combustion chamber as localized and periodic flame extinction and reignition events [75].

In reference to Figure 2.8, the LBO instabilities observed and characterized in this study fall within the low frequency range. These low frequency instabilities have been noted to occur in both laboratory scale burners [74-70] and industrial gas turbine engines [81, 82] under operating conditions near LBO. Muruganandam et al. [75] utilized OH* chemiluminescence and acoustic measurements to document that the energy content of the low frequency spectrum (10 – 200 Hz) increased significantly near LBO at an equivalence ratio of $\varphi = 0.75$ in an atmospheric swirl combustor. In a similar experimental setup, Prakash et al. [76] used a number of bandpass acoustic signal frequency filters centered at 15.9, 31.8, and 63.7 Hz as means for LBO detection and subsequent feedback into a pilot fuel injection control system. Bompelly et al. [77] investigated low frequency LBO instabilities in an atmospheric swirl burner which also exhibited thermoacoustic instabilities in the mid-frequency range (245 – 300 Hz) and noted the importance of low-pass signal filtering (< 50 Hz) for the detection of the onset of LBO. Taupin et al. [78] detected a non-acoustic low frequency mode measuring up to $p' = 15$ kPa at 16 Hz near LBO in an atmospheric swirl burner at $\varphi = 0.63$. In a similar swirl burner operating at increased combustor pressure ($P_2 = 0.5$ MPa), Cabot et al. [79] characterized a 32 Hz instability near the lean extinction limit using a combination of CH* chemiluminescence and dynamic pressure measurements. De Zilwa et al. [80] examined the lean extinction limit of a flame stabilized in a rounded duct expansion observing dominant frequencies of near-LBO oscillations of 3-10 Hz which were unique from the acoustic frequencies of the tested geometry. Instead, they observed that these oscillations were related to flame extinction along the reacting shear layer followed by subsequent reignition and flashback, once the fuel/air mixture reached a location of reduced strain further downstream. Stöhr et al. [83] investigated the onset of LBO at $\varphi = 0.55$ using a combination of high-speed CL, PIV, and PLIF in an atmospheric, partially premixed swirl burner, identifying changes in flame stabilization location near the LBO limit, particularly characterized by extinction and reignition of the flame root. Kariuki et al. [84] utilized simultaneous OH and CH₂O PLIF to characterize the heat release in premixed methane-air flames near blow-off in an unconfined, atmospheric bluff-body stabilized burner, noting the transition of the flame location from the outward expanding shear layer to the recirculation zone near LBO. In numerical simulations, Norton and Vlachos

[85] predicted periodic ignition and extinction oscillations near 100 Hz using CFD for a premixed methane-air flame near extinction.

While all of the preceding experimental studies discuss utilized CH₄ only as a fuel, blends of H₂ with CH₄ have also been investigated in terms of lean flame stability. Experimental study with atmospheric swirl flames provides evidence of the potential to extend lean operating limits with H₂ blending [86], noting a reduction in the LBO ϕ for a fixed burner volumetric flow rate as the H₂ fraction in CH₄ is increased. LBO of preheated, pressurized confined swirl flames (up to 80% vol H₂) [61] and Bunsen burner flames (up to 20%vol H₂) [87] has also been examined, with H₂ concentrations noted to have greater influence than pressure on shifting LBO to lower ϕ in both cases.

Finally, a dimensionless Damköhler number ($Da = \tau_{flow} / \tau_{chem}$) relationship for flame extinction, developed by Radhakrishnan et al. [88] and applied recently to premixed CH₄-air swirl flames under atmospheric conditions [89], is proposed as a measure of the competing influences of increasing chemical timescales, τ_{chem} , and decreasing flow time scales, τ_{flow} , at near-LBO and LBO conditions under elevated temperature and pressure conditions. The relationship, shown in Equation 2.8 below, expresses that flame extinction will occur when a product of the chemical timescale, $\tau_{chem} = \nu/S_L^2$, and reciprocal flow timescale, $\tau_{flow} = \bar{u}/D_{lance}$, exceeds a constant value, R , assuming constants C_1 , C_2 , and A hold from flow, geometric, and turbulence scale relationships given in [89]. At LBO, S_L would be expected to reduce with increasing \bar{u} , resulting in a reduction in τ_{chem} coupled with an increase in τ_{flow} , and R would be expected to be on the order of unity at extinction [89]. Further consideration of this parameter is given in Chapter 5.

$$\frac{1}{Da} = \left[\left(\frac{C_1}{C_2} \frac{15}{A} \right) \left(\frac{\bar{u}}{D_{lance}} \right) \left(\frac{\nu}{S_L^2} \right) \right]^{1/2} > R \quad (2.8)$$

2.2.2.3 Lean Flame Flashback

Whereas lean flame blowoff is associated with reduced τ_{chem} and increasing τ_{flow} , lean flame flashback is generally marked by increasing τ_{chem} and decreasing τ_{flow} . This is considered a lean phenomenon in this instance as it can occur at $\phi < 1$, provided the reaction velocity (e.g. S_L) exceeds the local flow velocity. A particular feature of premixed flames, flashback is often characterized by transition of the flame front from a stable location within the flow field

towards the location of fuel and oxidizer mixing, which is often located in LPM GT combustors in areas unsuitable for flame stabilization (e.g. swirler vanes, mixing plenums, etc.) [66, 91]. It is noted that this flame movement often occurs along boundary layers within the swirl flow field, such as the shear layers shown between the CRZ and ORZ in Figure 2.6 [66, 91] as these are areas of locally reduced velocity compared with the mean flow velocity. However, in swirling flows, flashback can also occur as a result of the reverse flow velocity components imparted on the flow field by the vortex breakdown CRZ structure as well as a result of combustion instabilities which may reduce instantaneous flow velocities [66, 91]. Lean flame flashback as a result of variable fuel composition has been observed in operational GTs with C_{2+} variation [16] and in experimental studies, in particular those focused on the addition of H_2 to CH_4 [92].

Flashback is often associated with the turbulent burning velocity, S_t , which can be scaled from the laminar burning velocity, S_L , although much debate still exists about the appropriate scaling to use [91]. Beerer et al. [92] found that S_t was related directly to the fluctuating RMS axial velocity, v'_{RMS} , with pure CH_4 showing a nearly linear $2.1*v'_{RMS}$ correlation and a 90-10 %vol H_2 - CH_4 blend approximated at $4.2*v'_{RMS}$ in a low swirl burner at pressures up to $P_2 = 0.7$ MPa. While H_2 addition has been shown to increase S_L previously, this emphasizes the catalytic effect in turbulent flows, and therefore flashback precaution that must be considered, when blending H_2 with CH_4 . With C_{2+} addition, the influence on autoignition behavior and S_L of CH_4 has been discussed, which may influence the flashback behavior of these blends, however, little current literature is available on the flashback propensity of CH_4 with C_{2+} addition. It is therefore necessary to consider other properties of these blends (such as response to increased stretch) to aid in the characterization of their turbulent flame response and flashback potential.

2.3 Combustion under Elevated Temperature and Pressure Conditions

One of the particular novelties of this study is the experimental evaluation of swirl flame stability and emissions response to variable fuel composition and burner geometry under conditions of elevated burner inlet temperature and pressure.

2.3.1 Turbulence Effects

Turbulence in swirl combustion is dictated by a kinetic energy cascade from length and time scales dominated by inertial forces (known as the integral length, L_T , and time scale, τ_T) down

to length and time scales dominated by viscous forces (known as the Kolmogorov length, η , and time scale, τ_η) [44, 59]. Based on the relative magnitude of these time and length scales, turbulent premixed flames can then be categorized into different regimes as shown in Figure 2.8. In the Broken Reaction Zone, or Well-Stirred Reaction Zone, the turbulent time scales are less than the chemical timescales and thus turbulent eddies interact with the flame across all length and time scales, leading to the destruction of the flame front. In the Thin Reaction Zone, the eddies of size η can penetrate the flame structure and enhance mixing in the preheat zone, although the reaction layer is unimpeded. In the Corrugated Flamelet regime, turbulent eddies interact with the flame front on a purely kinematic level, while chemical and transport processes in the flame are unchanged. Finally, in the Wrinkled Flamelet regime, flame is only influenced by very weak turbulence fluctuation which wrinkles the flame front [44, 59].

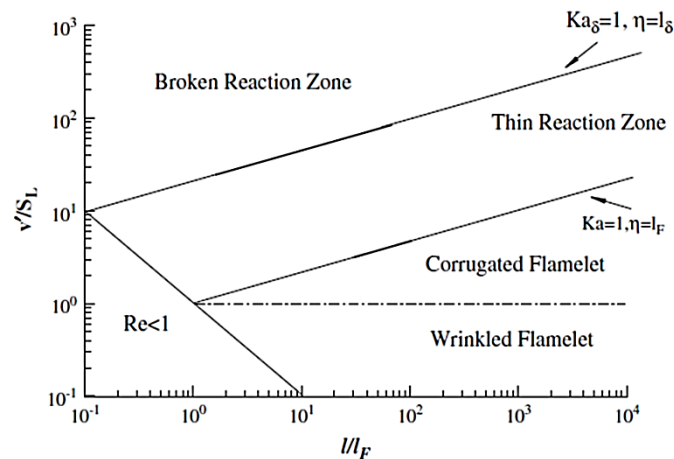


Figure 2.8: Premixed turbulent combustion flame regime diagram. Reproduced from [59].

Under elevated temperature and pressure conditions, the influence between the turbulent flow field and the reacting flame front in premixed flows will be influenced in a number of ways. First, the burning velocity of CH_4 increases by approximately an order of magnitude for a T_2 increase from 300 K to 1000 K with a fixed AFT, and a slight thinning of the flame is observed [66]. Furthermore, with increased pressure, burning velocity decreases, to a first approximation, according to a power law, $P_2^{0.5}$ and the flame thickness decreases approximately linearly with P_2 [66]. Also, with increased pressure, the reactant density will increase, reducing the kinematic viscosity, which will in turn influence the Kolmogorov scales of kinetic energy dissipation. In a study of H_2 addition (40%) to CH_4 in a low swirl burner, Emadi et al. [93] used an OH PLIF measurement system to note an increasingly wrinkled flame front with an increase in pressure from 0.1 MPa to 0.3 MPa (pure CH_4 only) and even further wrinkling still when H_2 was added at 0.3 MPa. This is attributed to the Le effect noted in Figure

2.3, which promotes the local burning rate by increased diffusion with H₂ blending. It is also likely that the influence of pressure on the turbulence scales results in reduced viscous scales while the bulk scales are observed to remain constant, increasing the turbulent range interacting with the flame front.

In a more applied GT swirl combustor investigated experimentally up to 673 K and 0.6 MPa [94, 95] with natural gas containing up to 2.2% C₂₊ and 0.9% N₂, optical diagnostics including PLIF, CL, PIV, and Raman scattering were utilized to characterize the turbulent flow field, reacting flame surface, fluctuating heat release, and chemical species formation under elevated operating conditions. Fluctuations in the turbulent vortices generated along the shear layer between the ORZ and CRZ is noted at $P_2 = 0.3$ MPa and $\varphi = 0.59$. Coherent flow structures were also identified in the instantaneous isothermal flow field. OH PLIF results at $P_2 = 0.15$ MPa and 0.4 MPa show a fragmented flame front, with an increase in the turbulence-related wrinkling with increasing P_2 , as was observed in the case of increased pressure and H₂ addition in [93]. Thermoacoustic instability was also observed in this swirl burner at $P_2 = 0.6$ MPa and $\varphi = 0.60$. This instability was characterized by periodic vortex shedding at the burner nozzle and significant fluctuation in the reverse flow field [95], resulting in variations in the measured fuel/air mixture fractions. It is noted in these studies, however, that the stabilization mechanism at high Reynolds number, Re , still remains ambiguous as the flame front becomes fragmented under these conditions. It is suggested that autoignition plays a role in the stabilization mechanism, however, the destruction of the flame front may be related to the chemical and diffusive effects of the natural gas constituents.

2.3.2 Chemical Kinetic Effects

Elevated temperature and pressure conditions will also have a marked influence on the fundamental chemical kinetics of the reacting fuel blends. For example, Bourque et al. [33] note that for the high C₂₊ natural gas blends tested, the ignition delay time appears to have more pressure dependence than equivalence ratio dependence over the range of temperatures tested, with ignition delay reducing by over 200% with a four-fold increase in pressure, whereas only a 50% change is observed for a four-fold increase in equivalence ratio. As mentioned previously, turbulent burning velocity, S_t , will influence the flame structure and stabilization under elevated conditions, and this will be further influenced by the fuel compositions in the reacting swirl flow. To that end, a study by Kido et al. [96] investigated S_t

of fuel blend mixtures, $\text{CH}_4\text{-H}_2$ and $\text{CH}_4\text{-C}_3\text{H}_8$, which are of significant interest to this study. Results from this study are given in Figure 2.9, with H_2 addition (a) and C_3H_8 addition (b) in CH_4 . S_t is plotted as a function of increased turbulence intensity, u' at $\phi = 0.8$, 298 K, and 0.101 MPa. It can be seen in both plots that S_t increases with increasing turbulence intensity, although it is not necessarily apparent if this trend is nonmonotonic (or saturates). What is perhaps most interesting in this data is the influence of H_2 and C_3H_8 addition at a fixed turbulence intensity. With the addition of H_2 , the turbulent burning velocity increases at constant u' . With the addition of C_3H_8 , however, the opposite trend is apparent, and S_t is observed to reduce compared to pure CH_4 . While this data was captured at atmospheric temperature and pressure conditions, it is indicative of a difference in behavior between these two fuels which, in other fundamental measures such as S_L and AFT, have been observed to increase reactivity. And in a highly turbulent, preheated, and pressurized flow, it is possible that the turbulent burning patterns here could be replicated. This observation of opposite turbulence behavior is further supported by consideration of thermo-diffusive behavior for both for these individual fuels. This behavior is captured in Figure 2.10, which plots the Markstein length, L_b , of CH_4 , C_2H_6 , C_3H_8 , and H_2 mixtures with air as a function of ϕ .

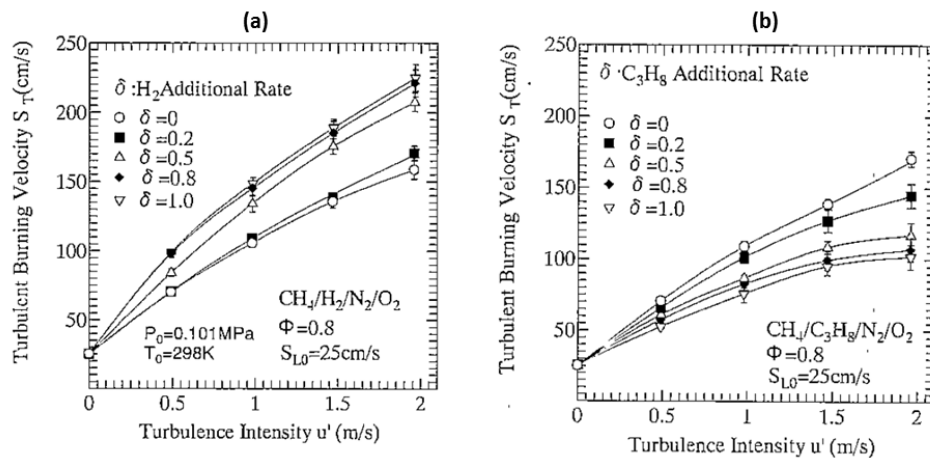


Figure 2.9: Influence of turbulence intensity and H_2 (a) or C_3H_8 (b) addition to CH_4 on the turbulence burning velocity, S_t . Reproduced from [96].

As can be seen in Figure 2.10 (which also provides further support to the discussion of Le in Section 2.1.4.1), the C_2+ fuels have significantly different stretch rate behavior than the CH_4 and H_2 fuels. In this plot, positive L_b values correspond with a negative response of the fuel to increased stretch (i.e. the stretched flame speed decreases with increased stretch rate).

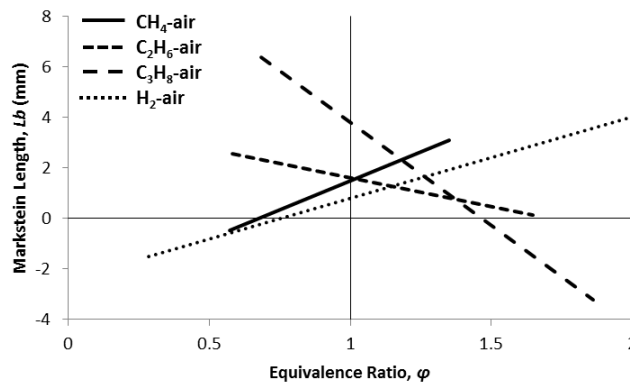


Figure 2.10: Influence of equivalence ratio on measured Markstein length of methane, ethane, propane, and hydrogen-air flames at 293 K and 0.101 MPa. Methane and ethane data from [97], propane data from [98], and hydrogen data from [99].

Thus, for the lean equivalence ratios that are of interest to this study, it would be expected that CH₄-air and H₂-air flames would exhibit accelerating stretched flame speeds with increase stretch rate and the opposite would be true for the C₂+ fuels (unless operated above $\phi > 1.5$). The same caveat must be stated regarding the atmospheric temperature and pressure conditions under which these measurements were taken. However, the combination of Figures 2.9 and 2.10 (and Figure 2.3, for the Le effect), give indication of both how these fuels behave individually as well as when blended with CH₄ in turbulent conditions.

2.4 Exhaust Gas Emissions Formation

For GT OEMs and operators, ensuring that GT combustion systems can meet strict environmental requirements as set out in Chapter 1 is critical to delivering on ambitious climate change targets. As input fuels for GT use vary, a keen awareness of the impact on exhaust gas emissions formation is necessary.

2.4.1 Chemical Kinetics

Of particular interest in this study is the formation of NO_x and CO emissions in preheated, pressurized LPM swirl combustion with varying fuel composition. In lean operation, GT combustors must be operated such that the formation of both NO_x and CO is inhibited while also delivering the required firing temperature at a given load. As can be seen in Figure 2.11, there is a balance that must be struck between firing temperature and NO_x and CO emissions. As the firing temperature decreases, both NO_x and CO emissions are observed to reduce. This would be associated with a decrease in ϕ and an increase in the excess O₂ in the burner.

However, below a certain firing temperature, CO emissions are seen to increase while NO_x emissions continue to decrease.

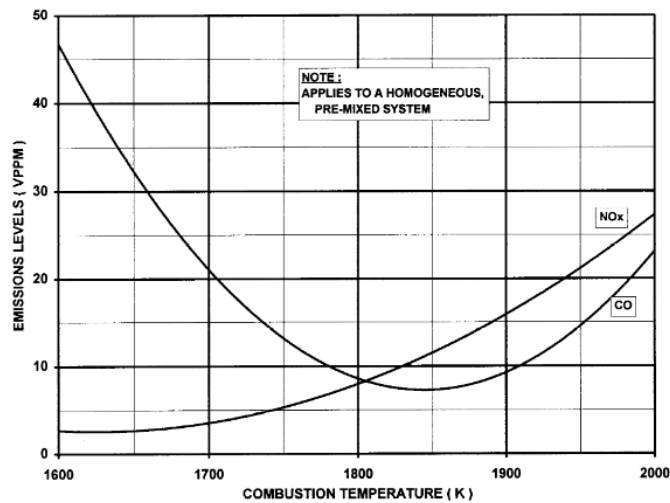


Figure 2.11: Typical NO_x and CO emissions levels from GT combustion as a function of temperature. Reproduced from [100].

This nonmonotonic CO emission behavior is the result of a coupling of effects. First, the increase in CO emissions is related to the reduction in combustion efficiency at lower AFT, thus inhibiting the in-flame oxidation reaction of CO to CO₂, $\text{CO} + \text{OH} \leftrightarrow \text{CO}_2 + \text{H}$ [101]. Also, the residence time required for CO oxidation equilibrium increases significantly with decreasing flame temperature [67]. In this low temperature region, CO emissions are observed to depend exponentially on both temperature and residence time [67]. This is an important consideration for LPM combustors, particularly if operating at part load (i.e. reduced firing temperatures). At higher AFT (and thus higher ϕ), CO emissions increase due to insufficient O₂ available for oxidation to CO₂ and, to a lesser extent, the potential for high-temperature CO₂ dissociation [100].

NO_x emissions are the sum total of NO and NO₂, of which NO usually dominates in LPM GT emissions. There is extensive research regarding the chemical kinetic formation pathways for these GHGs in lean gaseous hydrocarbon combustion, and as indicated by Figure 2.11, are often dictated by flame temperature. The most important pathways for NO_x formation are the thermal NO_x (or Zeldovich) mechanism, the prompt NO_x mechanism, the N₂O mechanism and fuel-based N₂ mechanism [67]. The thermal NO_x formation pathway is observed to dominate NO_x production in LPM combustion if the average temperature in the combustor exceeds 1573 – 1673 K, showing an exponential dependence on temperature [67]. This formation pathway is driven by two reactions (1) $\text{O} + \text{N}_2 \leftrightarrow \text{NO} + \text{N}$ and (2) $\text{N} + \text{O}_2 \leftrightarrow \text{NO} + \text{O}$ [67, 100]. Similar to

CO emissions, the thermal NO_x pathway also has a residence time relationship, but this has been shown to be lower order than the temperature dependence [67]. NO_x formation has also been shown to have a power law pressure dependence with an exponent of 0.2 to 0.5 [67]. The temperature dependence also requires sufficient fuel/air mixing to avoid locally stoichiometric combustion (thus high temperature).

The prompt NO_x mechanism is related to the CH radical by the initiation reaction $\text{CH} + \text{N}_2 = \text{HCN} + \text{N}$ [102]. The HCN then transforms into NO_x where O_2 is available [67]. This has been shown to be an important consideration in the influence of LPM natural gas combustion with C_2 and C_3 compounds on NO_x formation, given the increase in CH radical formation [102]. The fuel-based N_2 mechanism is similar to the prompt NO_x mechanism but its contribution is expected to be minimal. Finally, the N_2O mechanism is initiated by the reaction $\text{O} + \text{N}_2 + \text{M} \leftrightarrow \text{N}_2\text{O} + \text{M}$, and is expected to contribute at higher pressures given the higher probability of the three-body reaction progressing under those conditions [67].

2.4.2 Influence of Fuel Composition

2.4.2.1 Influence of Higher Hydrocarbons in Natural Gas

Both Flores et al. [40] and Hack and McDonnell [103] investigate the effect of higher hydrocarbon content on NO_x and CO emissions. Flores et al. [40] utilized varied amounts of ethane and propane in natural gas to investigate the resulting emissions. Employing a model GT swirl combustor, premixed natural gas and air was blended with either 15 %vol ethane or 20 %vol propane. It was identified that the highest NO_x and CO emissions occurred with propane addition [40]. Given that these experiments are conducted at $\phi = 0.52$, it is noted that the NO_x formation is most likely the result of the N_2O pathway instead of the thermal NO_x pathway, although there is potential for locally high ϕ to develop thermal NO_x through higher temperatures [40]. Hack and McDonnell [103] investigated the impact of ethane and propane content in natural gas in a 60 kW commercial microturbine generator. In [103], ethane was varied up to 17% and propane up to 22%. In agreement with Flores et al. [40], Hack and McDonnell [103] found that the presence of higher hydrocarbons leads to the formation of higher levels of NO_x . However, unlike Flores et al. [40], the production of CO at full load is found to be statistically independent of the fuel composition, suggesting that the overall temperature and residence times are sufficient within the microturbine generator to allow for complete oxidation [103]. Interestingly, the amount of CO produced at part load was greatly

reduced by the presence of higher hydrocarbons [103]. The study by Hack and McDonnell [103] also included one natural gas and higher hydrocarbon blend with up to 5.9% inert content, although the exact constituents (e.g. nitrogen, carbon dioxide, etc.) are not communicated. This particular blend shows that NO_x was reduced when the microturbine was operated at full load, with NO_x levels in line with the baseline natural gas NO_x levels without the additional higher hydrocarbons. This highlights the impact that diluent content has on the combustion characteristics of gaseous fuel blends. Straub et al. [104] also conducted a series of lean premixed combustion experiments at elevated swirl burner inlet pressure ($P_2 = 0.76$ MPa) and temperature ($T_2 = 589$ K) with propane up to 5 %vol in methane, finding no statistically significant effect on NO_x emissions, which suggests a lower limit of acceptable C_3H_8 content to maintain acceptable NO_x emissions levels.

2.4.2.2 Influence of Hydrogen in Natural Gas

Lantz et al. [105] investigated the influence of H_2 -blended natural gas (up to 80%vol) on NO_x formation in a study of a Siemens SGT-700/800 combustor. The study was conducted $T_2 = 693$ K and $P_2 = 0.101$ MPa. By comparison with the baseline natural gas composition, and when holding AFT constant, the NO_x emissions appear to increase exponentially with H_2 addition, with almost 50% increase in the baseline NO_x levels at 80% H_2 [105]. This is attributed to locally high flame temperatures, non-perfect mixing, and reduced mixing of reacted gases into the flame zone.

While the study by Lantz et al. [105] suggests that NO_x emissions would increase for a fixed firing temperature at atmospheric pressure, the study by Griebel et al. [87] in a premixed Bunsen burner shows that the LBO limit can be extended by 9-10% in terms of equivalence ratio with 20 %vol H_2 addition compared with a pure CH_4 flame at $P_2 = 0.5$ MPa and $T_2 = 673$ K. This can be extended even leaner by raising T_2 to 773 K (although higher AFT results in higher NO_x , consequently offset by the lean stability shift). The consequence of this lean operability shift is a corresponding reduction in NO_x emissions due to reduced firing temperatures, with a maximum reduction of 35% compared to pure CH_4 flames. For a fixed lean equivalence ratio ($\varphi < 0.50$), it is noted that there is negligible difference between the CH_4 and $\text{CH}_4\text{-H}_2$ NO_x measurements. At $\varphi > 0.50$, a similar response as identified by Lantz et al. [105] is noted. Griebel et al. [87] attribute this to a chemical kinetic effect given the relatively similar AFT, with additional OH available with H_2 addition to promote NO formation reactions. With H_2

addition at $\varphi = 0.50$, the NO_x emissions appear to be independent of pressure up to 1.4 MPa, while NO_x emissions for the pure CH_4 fuel show a slight downward trend.

2.5 Chapter Summary

In this Chapter, a broad range of current research topics has been discussed in the context of fuel flexible, lean GT combustion. While a number of ongoing research activities are occurring in the field of fuel flexibility for industrial GTs, the need is identified for experimental characterization of swirl flame behavior at elevated temperature and pressure conditions with fuels that are both novel and practically relevant. The following topics have been highlighted:

- An evaluation of the current state of the art in fuel flexible industrial GTs, including an overview of fuel control system parameters.
- Fundamental properties of fuel blends (e.g. Le , L_b , S_L , S_t , AFT, κ_{ext}) have been presented and will be investigated further throughout this study to supplement the use of WI in the characterization of premixed flame behavior.
- A number of nondimensional parameters (e.g. St , He , Da) have been identified in the context of flame stability and will be utilized throughout this study for the identification and classification of observed flame instabilities with varying fuel composition and burner operating conditions.
- A number of combustion diagnostics (e.g. PLIF, CL, PIV, dynamic pressure sensing) have been briefly introduced to highlight the current state of the art in the characterization of experimental flame behavior. Further discussion on the development and use of these methodologies in this study are provided in subsequent Chapters.
- Key considerations for elevated temperature and pressure studies in practical swirl burners have been discussed, including the methods for flame stabilization, instability initialization, and emissions formation.
- Critical exhaust emissions, in particular CO and NO_x , have been identified along with their underlying formation reaction chemistry, which will provide targeted constituents to monitor and measure during the experimental program.

CHAPTER 3 – EXPERIMENTAL FACILITIES AND METHODOLOGIES

3.1 Cardiff University Gas Turbine Research Centre

Cardiff University's GTRC is an industrial-scale experimental combustion research facility in Port Talbot, Wales. The GTRC is capable of performing both atmospheric and pressurized combustion experiments which impact the power generation, propulsion, and industrial heating sectors. A range of experimental rigs for both applied and fundamental research are operated at the GTRC, including the HPCR in which the bulk of this experimental work was undertaken as well as rigs such as the Constant Volume Combustion Bomb (CVCB), used more exclusively for fundamental measures of laminar and turbulent flame speeds. Further detail on the design of these rigs, their capabilities, limitations, and accuracies are first provided. A discussion on the design of the HPGSB and HPGSB-2 is then presented followed by detail regarding the experimental test matrix development, experimental diagnostics, and numerical methods utilized. The reader is directed to Chapter 4 specifically for information on the CL, PLIF, and dynamic pressure measurement systems used in this work. For these specific measurement systems, only the background theory and motivation for their use in this study is provided in this chapter while a detailed discussion has been dedicated to the design, implementation, and commissioning of those systems in Chapter 4.

3.1.1 High Pressure Combustion Rig

The HPCR is designed to deliver air mass flow rates up to 5 kg/s at temperatures up to 900 K and pressures up to 1.6 MPa. Further details concerning the design, capabilities, and utilization of the HPCR test facility can be found in previous studies [53, 54, 106-109]. The critical components that make up the HPCR are the fuel and air delivery systems, the high pressure optical chamber (HPOC) which provides the visual access required for optical combustion diagnostics, the generic swirl burners, and all associated rig instrumentation for experimental condition monitoring. Each of these components are described in detail in the following sections as they allow for the delivery of fundamental combustion studies at elevated temperature and pressure operating conditions.

3.1.1.1 Fuel and Air Delivery System

For this study, the HPCR has been reconfigured for high repeatability and precise control over fuel and air flows through the use of dedicated flow control valves (FCV) and coriolis mass flowmeters (CMF) on a total of 5 delivery lines. For air delivery, 2 of the 5 lines are used, with

mass flows measured with Emerson CMF025M mass flow meters capable of measurement up to 945 g/s. For fuel delivery, another 2 lines are used with mass flows measured with an Emerson CMF010M mass flow meter capable of measurement up to 22.7 g/s. The fuel and air mass flow rates are controlled in a remote location via a PLC system which is operated by inputting the desired FCV position and monitoring the CMF output. Further detail on the accuracies of this system can be found in Section 3.1.1.4. For all experiments with the HPGSB and HPGSB-2, the air flow to the HPCR was provided by an Atlas Copco GA 45 variable speed drive (VSD) air compressor coupled with a Beko Drypoint DPRA960 air dryer to lower the combustion air dew point prior to metering and entering the burner. This VSD compressor is capable of delivering up to 150 g/s air flow at 1.3 MPa. When operating the burners in fully premixed mode, the fuel flow, delivered from multi-cylinder packs stored in a remote onsite location, was split after metering and introduced into the air stream prior to entering the burner.

Rig pressurization was possible with the use of a backpressure valve (BPV) in the water-cooled exhaust piping. After the BPV, exhaust gases are diluted and exit the HPCR through an external combustion stack. For burner operations in which the air mass flow rate through the burner was insufficient to provide the necessary burner inlet pressure, P_2 , a secondary air bypass valve could be opened to allow flow directly from the VSD compressor to the exhaust piping upstream of the BPV. While this bypass flow was unmetered, the flow rate was set by monitoring P_2 while augmenting the BPV position (controlled via PLC) and bypass valve (manually controlled). Combustion testing was conducted, described further in Section 3.2.3, to ensure that the introduction of this bypass air stream into the exhaust piping did not dilute the exhaust gas sample taken from the burner confinement exit. With the commissioning of the 2nd generation high pressure generic swirl burner (HPGSB-2), a 40 kW electric air preheater was installed to allow for elevated burner inlet temperatures, T_2 , up to a target of $573 \text{ K} \pm 5 \text{ K}$. Finally, a coiled fuel heat exchanger capable of operating up to 473 K was added to the HPCR. This fuel heater was installed to counter the Joule-Thomson cooling effect resulting from the pressure reduction from the gaseous fuel cylinders to the fuel delivery pressure, which consequently lowered T_2 in premixed operation. A simplified schematic of the overall HPCR fuel and air delivery system can be seen in Figure 3.1. Note that the HPOC which houses the generic swirl burners and allows for pressurized operation, is not shown in this figure. Photographs of the main elements of the HPCR can be found in Appendix B.2.1, Figure B.7.

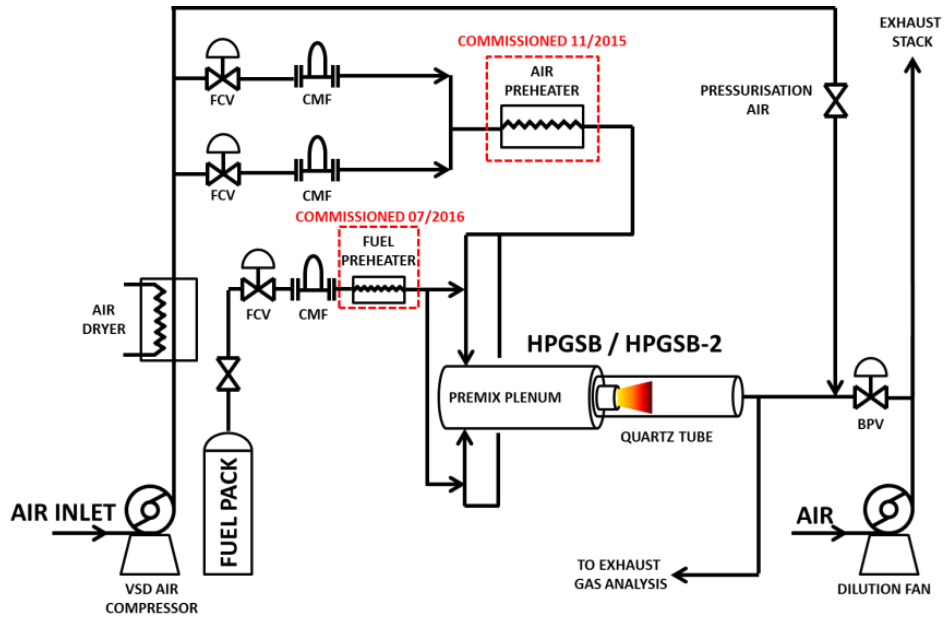


Figure 3.1: Simplified schematic of the fuel and air delivery systems for premixed, preheated, and pressurized operation at the GTRC HPCR. Note that the HPOC is not shown.

3.1.1.2 High Pressure Optical Chamber

The HPOC is the central pressure-containing apparatus of the GTRC's HPCR. The HPOC allows both axial and radial visual access to the burners and operational flames within it. Designed for the full pressure and temperature of the HPCR, the HPOC is 0.716 meters in length with an inside diameter (ID) of 0.315 m. A thermal barrier coating (TBC) has been installed along the entire ID of the HPOC to protect the stainless steel casing from excessive temperatures during combustion experiments. Further thermal management of the HPOC, particularly during high thermal power experiments, is provided by external water-cooled copper coils wrapped around the HPOC OD near the exit flange.

Photographs of the HPOC are shown in Figure 3.2, with the HPOC removed for maintenance (left) and installed in the HPCR (right) with the HPGSB-2. The HPOC has been utilized in past experimental research programs investigating the influence of elevated temperature and pressure conditions up to 0.7 MPa on methane-hydrogen Bunsen burner flames [53, 54] and was successfully operated up to 1.5 MW in the development of a commercial high-hydrogen syngas burner in partnership with Ansaldo Energia [109]. The visual access that the HPOC provides is critical for the non-intrusive optical diagnostics systems that have been developed as part of this work. As shown in Figure 3.2, axial visual and laser sheet access is provided by 50-mm thick quartz windows on the top and sides. Radial visual access is afforded by a window in the water-cooled exhaust section downstream of the HPOC, see Section 3.2.1.3.

During combustion experimentation, the flame is monitored remotely via HD cameras through both the axial and radial windows, and aids in the visual confirmation of flame phenomena such as flame detachment from the burner exit nozzle as well as flame blowoff and flashback.



Figure 3.2: Photographs of HPOC during maintenance (left) and installed in the HPCR (right).

3.1.1.3 HPCR Data Acquisition

During experimental operation of the HPCR, a wide range of data is acquired to aid in characterization and rig operability. This data is captured via a dedicated computer and data acquisition system (MTX Pro-Pack). Data is monitored in real time during rig operation and logged at a rate of 1 Hz for all experiments. For follow-up characterization of observed isothermal and combustion conditions, the following data is logged by the acquisition system:

A) Temperature (K)

- A.1 Burner Inlet Temperature, T_2
- A.2 Burner Outlet Temperature, T_3
- A.3 5 Gas Mixing Line 1 Temperature, T_{Line1}
- A.4 5 Gas Mixing Line 2 Temperature, T_{Line2}
- A.5 5 Gas Mixing Line 3 Temperature, T_{Line3}
- A.6 5 Gas Mixing Line 4 Temperature, T_{Line4}
- A.7 5 Gas Mixing Line 5 Temperature, T_{Line5}
- A.8 Pilot Bluff Body Tip Temperature, T_{pilot}
- A.9 Burner Face Temperature, T_{BF}
- A.10 Quartz Tube Outer Diameter (OD) Temperature, T_{quartz}
- A.11 HPOC TBC Temperature, T_{TBC}

B) Static Pressure (MPa)

- B.1 Burner Inlet Pressure, P_2
- B.2 Burner Outlet (HPOC Casing) Pressure, P_3

B.3 5 Gas Mixing Line 1 Pressure, P_{Line1}

B.4 5 Gas Mixing Line 2 Pressure, P_{Line2}

B.5 5 Gas Mixing Line 3 Pressure, P_{Line3}

B.6 5 Gas Mixing Line 4 Pressure, P_{Line4}

B.7 5 Gas Mixing Line 5 Pressure, P_{Line5}

B.8 Pilot Bluff Body Tip Pressure, P_{pilot}

B.9 Burner Face Pressure, P_{BF}

C) Pressure Drop (kPa)

C.1 Swirler Pressure Drop, ΔP

D) Mass Flow Rate (g/s)

D.1 Air Mass Flow Rate, \dot{m}_{air}

- Sum of the individual air mass flow rate measurements from the 5 gas mixing lines, typically Lines 1 and 2.

D.2 Fuel Mass Flow Rate, \dot{m}_{fuel}

- Sum of the individual fuel mass flow rate measurements from the 5 gas mixing lines, typically Lines 3 and/or 5.

In addition to these measurements, the ambient temperature and barometric pressure are also monitored. A number of other real time measurements are made to ensure the integrity and safety of the HPCR during experimental operation. These measurements include exhaust piping cooling water supply and return temperatures, HPOC cooling coil water return temperature, and HPOC and piping metal temperatures. Electrical signals such as the 40 kW air preheater current draw are also monitored to aid in equipment protection and control during operation. Further information regarding the specific positioning of selected measurements is provided in proceeding sections.

3.1.1.4 HPCR Instrumentation Measurement Accuracy

The accuracy of measurements made during isothermal and combustion experiments in the HPCR is critical for fundamental characterization of burner and flame response to changes in operating conditions and fuel composition. Premixed fuel and air inlet temperature and pressure (T_2 and P_2) are measured by a K-type thermocouple (± 2.2 K) and a Druck PDCR 10/T pressure transducer ($\pm 0.04\%$ full scale to 1.0 MPa), respectively. All other temperature measurements listed in Section 3.1.1.3 are also made with K-type thermocouples (± 2.2 K) with the exception of T_3 , which is measured with an N-type thermocouple (± 1.1 K) with an upper

limit of 1573 K due to the high burner exit temperatures experienced during combustion experiments. All other static pressure measurements are also made with Druck PDCR 10/T pressure transducers ($\pm 0.04\%$ full scale to 1.0 MPa) with the exception of the dedicated swirler pressure drop measurement, ΔP , which is made with a Druck PDCR 10/35L differential pressure transducer (0.04% full scale to 70 kPa). Note that in addition to the standard measurement accuracies provided here, all thermocouples and pressure transducers were calibrated with full traceability of the calibration device and result. Air mass flow measurements are made by Emerson CMF025M coriolis mass flow meters with uncertainty of $\pm 0.35\%$ of measurement. Fuel mass flow measurements are made by Emerson CMF010M coriolis mass flow meters with uncertainty of $\pm 0.35\%$ of measurement. Both the CMF025M and CMF010M would be expected to maintain these uncertainty levels across the experimental range, as flows are typically above 10% of the nominal flow rate for each CMF.

3.1.2 Swirl Burners

As shown in Chapter 2, both experimental and numerical works exist for the understanding of swirl flame stability, thermoacoustics and emissions. However, detailed experimental characterization of the influence of fuel flexibility on LPM combustion in a geometrically generic swirl burner is lacking under representative GT conditions, particularly under preheated and pressurized combustion inlet conditions [75, 90]. The parametric studies afforded by a highly modular swirl burner allow for the validation of both chemical kinetic reactor network and CFD models which approach real-world GT combustion operating conditions. To that end, the HPGSB and HPGSB-2 have been designed and commissioned in this study specifically for the purpose of enhancing the acoustic and optical measurements capable for fully premixed, confined swirl flames under elevated operating conditions. While the reader is directed to Chapter 5 for detailed isothermal and combustion commissioning results for both of these burners, the following sections provide the critical design details.

These generic swirl burners have been increased in scale from the AGSB extensively utilized at Cardiff University [55-57, 110-112] and are designed specifically for the characterization of flame shape, location, and thermoacoustic interactions resulting from changes in burner geometry, fuel composition, and operating conditions typical of an industrial can-type GT combustion chamber. The HPGSB and HPGSB-2 combine the ability to maintain optical access to the internal swirl flame while achieving representative GT combustor parameters of inlet pressure, temperature, and turbulence scales. The HPGSB and HPGSB-2 currently bridge the

gap between the global contingent of atmospheric and pressurized confined swirl research burners, with ongoing work at the GTRC to further extend their demonstrated operational capabilities. A comprehensive view of where these burners fit within the global contingent of experimental confined swirl burners is given in Appendix E, Table E.1 [55-57, 62, 69, 74-79, 89, 90, 95, 112-159].

3.1.2.1 High Pressure Generic Swirl Burner (Mk. I)

The HPGSB utilized in this study is a medium-scale ($P_{therm} < 500$ kW) swirl-stabilized generic burner which can be operated at either atmospheric or pressurized conditions both with and without confinement of the exit nozzle. A cylindrical quartz confinement tube with an expansion ratio of 3.5:1 from the burner exit nozzle to the quartz confinement tube ID (ID = 140 mm) was utilized at the exit nozzle for simulation of a GT combustion chamber and to establish flow structures that would normally be found in a confined swirl burner. The use of confinement with the HPGSB also restricts ingress of surrounding oxygen into the flame while directing the reactants into the exhaust. This burner was only operated when installed in the HPOC within the HPCR. The configuration and components of the HPGSB can be seen in Figure 3.3 as installed in the HPOC. A photograph can be found in Appendix B.2.1, Figure B.8.

When operating the HPGSB in fully premixed mode, fuel is first mixed with the incoming air flow prior to entering the inlet plenum (Figure 3.3.b). All reactants then travel along the flow path (left to right in Figure 3.3) of the premixing chamber (Figure 3.3.d) prior to entering the slot type radial-tangential swirler (Figure 3.3.e) and then out from the exit nozzle (Figure 3.3.f) into the quartz confinement tube (3.3.g) where the swirl flame is stabilized. The quartz confinement tube is 5.5-6 mm thick and directs the exhaust into water-cooled exhaust piping towards the BPV. The radial-tangential swirler insert (Figure 3.3.e) is modular on the HPGSB. The burner exit nozzle diameter is fixed at 40 mm for all swirler inserts while the width of the 9 radial-tangential swirl inlets varies between inserts. This yields a possible geometric swirl number varying from $S_g = 0.5$ to $S_g = 2.0$. The geometric swirl number is defined as in Equation 3.1 below [160]:

$$S_g = \frac{A_{noz} \cdot r_{tan}}{A_{tan} \cdot r_{noz}} \cdot \left(\frac{Q_{tan}}{Q_{tot}} \right)^2 \quad (3.1)$$

where A_{noz} is the exit area of the burner exit nozzle (Fig. 3.3.f), A_{tan} is the area of the tangential inlet, r_{tan} is the effective radius of the tangential inlet, r_{noz} is the radius of the burner exit nozzle, Q_{tan} is the tangential flow rate, and Q_{tot} is the total flow rate. For the experimental

cases in this study, the geometric swirl number for the HPGSB was varied from $S_g = 0.8$ to $S_g = 1.47$. The selected swirler insert is noted where appropriate. In addition to the ability to vary the geometric swirl number of this burner, the burner confinement length can also be manipulated. For all isothermal and combustion experiments in the HPGSB, this length has been fixed at 0.420 m, measured from the ceramic burner face, which protects the swirler insert from combustion temperatures, to the end of the quartz confinement tube.

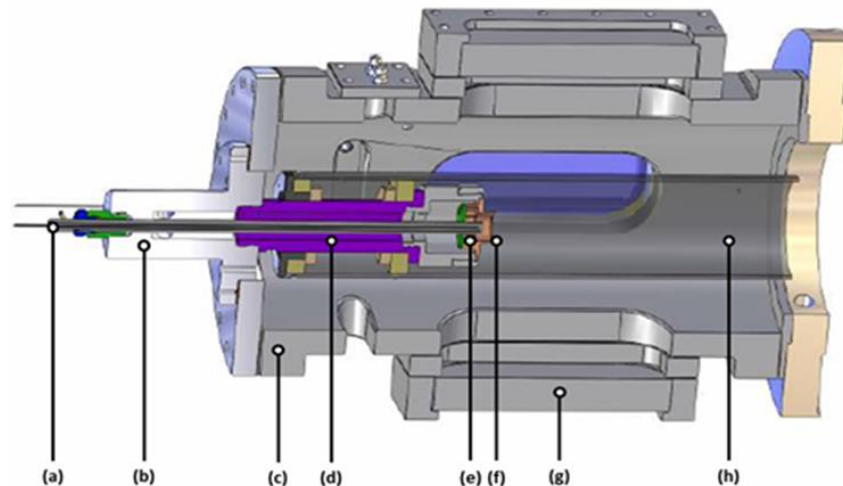


Figure 3.3: Sectioned detail view of the HPGSB/HPOC assembly with (a) instrumentation and pilot lance, (b) inlet plenum, (c) HPOC casing, (d) premixing chamber, (e) radial-tangential swirler, (f) burner exit nozzle, (g) quartz window, and (h) quartz burner confinement tube. Reproduced from [112].

3.1.2.2 High Pressure Generic Swirl Burner (Mk. II)

The HPGSB-2 differs from the 1st generation HPGSB [112-122] in that the combustor expansion ratio has been reduced from 3.5 to 2.5, achieved by a reduction from 140 mm to 100 mm of the quartz burner confinement tube ID while maintaining the burner exit nozzle diameter of 40 mm. A sectioned detail view of the HPGSB-2 and HPOC assembly is shown in Figure 3.4. Photographs of the construction of the HPGSB-2 are provided in Appendix B.2.1, Figure B.9. The HPGSB-2 affords optical access to the flame while achieving representative parameters of inlet pressure, temperature, and turbulence scales typical of a can-type industrial GT combustor.

The HPGSB-2 is modular in its operation and geometry, both of which can be easily manipulated for parametric study of flow and flame phenomena, including both piloted and non-piloted liquid and gaseous fuel operation, varying levels of fuel/air premixing, variable geometric swirl number (S_g , Equation 3.1) combustor confinement length, and combustor outlet geometry. In this study, the burner was operated fully premixed, non-piloted, and with

a geometric swirl number of $S_g = 0.8$ and 0.5 . Similar to the HPGSB, this change in geometric swirl number was achieved by replacing the radial-tangential swirler insert (Figure 3.4.d) to vary the tangential inlet width while maintaining the burner exit nozzle (Figure 3.4.e) diameter, detail of which can be seen in the swirler geometries provided in Figure 3.5 below. The reduction in S_g is achieved by an increase in tangential inlet width from 7.5 mm to 12 mm, thus increasing A_{tan} in Equation 3.1.

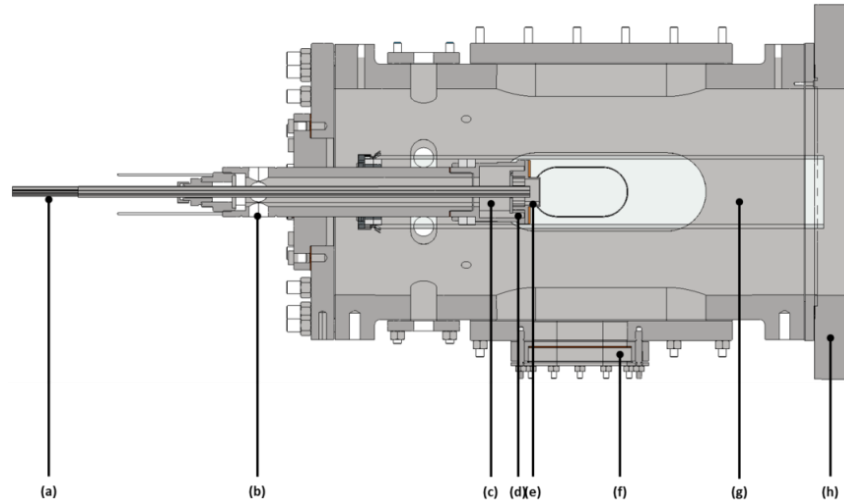


Figure 3.4: Sectioned detail view of the HPGSB-2/HPOC assembly with (a) instrumentation and pilot lance, (b) inlet plenum, (c) mixing chamber, (d) radial-tangential swirler, (e) burner exit nozzle, (f) quartz window, (g) quartz burner confinement tube, and (h) HPOC casing.

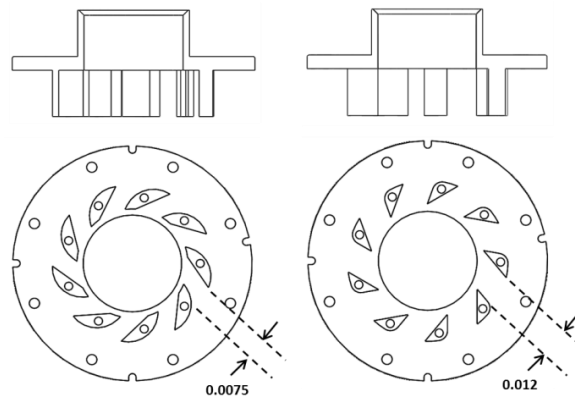


Figure 3.5: Radial-tangential swirler geometries with $S_g = 0.8$ (left) and $S_g = 0.5$ (right). Tangential inlet width dimension in meters.

In fully premixed operation, the fuel flow was split and blended as a jet in crossflow into two inlet air flows approximately 0.3 m before entering diametrically-opposed connections to the burner inlet plenum (Figure 3.4.b). All other flow paths are identical to the HPGSB yielding a total premixing length of approximately 0.7 m and residence time over 20 ms at a flow velocity of 30 m/s. The face of the swirler within the combustor is covered by a 3-mm thick ceramic coating for thermal protection. The flow expands into a quartz confinement tube (Figure

3.4.g) of length $L_{comb} = 407$ mm which directs the combustion products downstream towards an exhaust gas sampling probe. The HPGSB-2 is fitted with an 18-mm OD instrumentation and pilot lance (Figure 3.4.a) inserted down the burner centerline. It contains seven 5 mm OD tubes, with one central tube intended for pilot fuel injection and the remaining six available for instrumentation. The open end of the lance protrudes 8.5 mm into the exit nozzle. Thus, if the exit nozzle was removed from the swirler, the open end of the lance would be in the same axial plane as the burner dump plane and ceramic burner face. This lance provides a bluff-body stabilization location within the burner exit nozzle while also allowing for temperature (T_{pilot}), static pressure (P_{pilot}), and dynamic pressure measurements to be made at this critical location. A limit of $T_{pilot} = 1273$ K was utilized to protect the burner from thermal damage and to indicate the onset of flashback, referred to as a technical flashback (TFB) event because burner operations would be ceased prior to the premixed flame retreating upstream of the swirler.

The HPGSB-2 also utilized a novel quartz confinement with a convergent nozzle exit, seen in Figure 3.6. Both an open-ended cylindrical confinement (Figure 3.6, left) and a convergent nozzle confinement (Figure 3.6, right) were investigated as part of this study. The convergent nozzle confinement has an exit diameter of $D_{exit} = 40$ mm, equaling the burner exit nozzle diameter. Cylindrical confinement can replicate the flame and flow characteristics of an industrial can-type GT combustion chamber, and indeed is widely used in experimental burner systems; however, the use of a convergent nozzle outlet to replicate the influence of the turbine inlet transition piece is less common. Examples include the DLR dual swirl burner ($D_{confine}/D_{exit} = 1.78$) [146] and the CRF combustor ($D_{confine}/D_{exit} = 7.67$) [149]. Therefore, a single construction quartz convergent nozzle ($D_{confine}/D_{exit} = 2.5$) was designed and fabricated to investigate potential flow, flame, and acoustic impacts at elevated temperature and pressure conditions, with relatively low exit Mach numbers ($M < 0.1$) to reduce pressure drop across the quartz tube within the HPOC. Refer to Appendix B.1 for 3D CAD drawings of critical wetted components of the HPGSB-2.

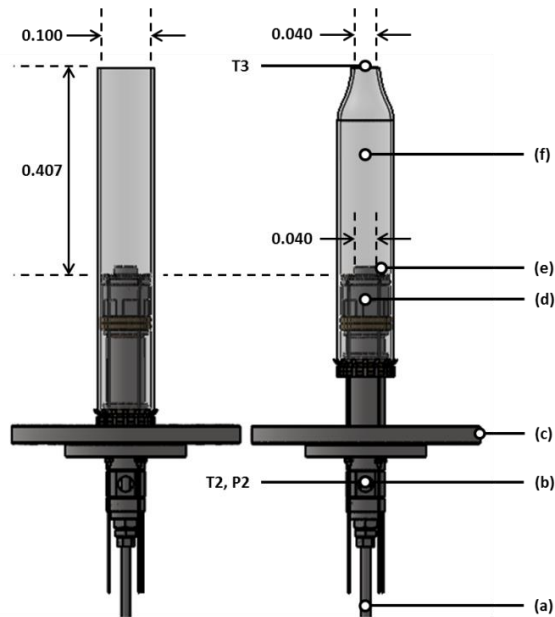


Figure 3.6: Schematic of HPGSB-2 showing the instrumentation and pilot lance (a), inlet plenum (b), HPOC connecting flange (c), mixing chamber (d), burner exit nozzle (e), and quartz confinement (f). Dimensions in meters. Reproduced from [123].

3.2 Non-Intrusive Diagnostics

A number of non-intrusive combustion diagnostics systems are utilized at the GTRC to provide a comprehensive characterization of the influence of burner geometry, fuel composition, and operating conditions on the resulting flame stabilization, thermoacoustic response, and exhaust gas emissions. These diagnostics systems include optical diagnostics such as CL, PLIF, and PIV. Other diagnostics include a dynamic pressure sensing system for monitoring of isothermal and combustion system acoustics as well as an exhaust gas sampling system for combustion emissions monitoring. As the CL, PLIF, and dynamic pressure sensing diagnostic systems were designed, developed, and installed in the course of this study, Chapter 4 has been dedicated specifically to that work, while the fundamental background is presented in this Chapter.

3.2.1 Optical Diagnostics

Non-intrusive optical measurement techniques have been the subject of much research and development over the past few decades in the field of fundamental combustion diagnostics [161-164]. These techniques provide enhanced measurement capability, which results from the undisturbed flow field and lack of reactivity with the flame front. In addition to fundamental studies, these techniques are increasingly being integrated with industrial scale GT combustion technology development and process monitoring [105, 165, 166]. It is

apparent in the reviewed literature that it is often a combination of combustion diagnostic techniques which are employed to characterize the unstable behavior of a GT flame. For example, in their investigation of thermoacoustic instabilities in an atmospheric swirl burner operating on natural gas, Fritsche et al. [69] utilized PLIF of the OH radical to evaluate the flame structure, dynamic pressure sensors for acoustic measurements, and OH* CL to measure the relative flame heat release. Similarly, in measuring the physical and chemical response of an acoustically-driven, atmospheric, swirl stabilized flame operating on natural gas, Hubschmid et al. [72] used OH PLIF, OH CL, and a water-cooled microphone. The study by Stopper et al. [94] combined OH PLIF, OH* CL, and PIV for the characterization of the flow field and combustion response for premixed natural gas/air flames at pressures up to 0.6 MPa. Many authors have also used PLIF to excite alternate species in the flame, in addition to the OH radical, to investigate different in-flame phenomena. For example, Won et al. [31] utilized both OH and formaldehyde (CH₂O) PLIF to measure the burning velocity and flame structure, with the formation of formaldehyde often seen in areas of low temperature fuel oxidation. CL measurements of additional combustion radicals has also been noted, including the CH* radical in addition to the OH* radical [167]. Thus, multiple experimental techniques were applied in this study in light of this literature in which similar flame parameters of interest have been experimentally characterized. The main optical diagnostics in use at the GTRC for this work therefore include CL, PLIF, and PIV. In addition, Schlieren imaging has been utilized in the Constant Volume Combustion Bomb (CVCB) for the evaluation of laminar flame speed and stretch rate effects of selected fuels, however reference should be made to other studies [168, 169] for further information regarding this system.

3.2.1.1 Chemiluminescence

The study of emission spectra of electronically excited species resulting from chemical processes within a flame has progressed significantly from the early 1950s, when Broida and Gaydon [170] required exposure times of up to 30 minutes on medium quartz spectrographs in order to detect OH* and CH* radicals. Recent studies of combustion species CL were carried out both numerically with the use of advanced chemical kinetics models [171, 172] and experimentally, with CL measurements made on industrial GT combustors from both Alstom (EV-10) [173] and Siemens (SGT-700/800) [105]. Typical CL spectra for natural-gas air flames are shown in Figure 3.7, highlighting the key radicals which contribute to lean flame CL emission, particularly OH*, CH*, C₂* and broadband CO₂*.

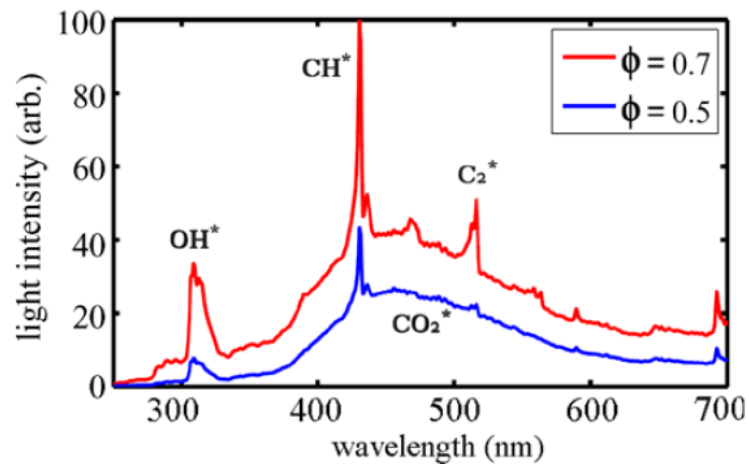


Figure 3.7: Typical CL spectra of atmospheric natural gas-air flames at varying ϕ . Reproduced from [165].

OH* and CH* CL emission are of particular interest for this study as CL imaging of these reactive combustion species has been shown to provide fundamental measures of flame structure [79, 174], heat release [175, 176], and equivalence ratio [177]. As shown in Figure 3.7, OH* CL peaks near $\lambda = 309$ nm. This corresponds to the $A^2\Sigma \rightarrow X^2\Pi$ electronically excited to ground state energy level transition [165]. The dominant chemical production reactions for the formation of OH* are $\text{CH} + \text{O}_2 \leftrightarrow \text{OH}^* + \text{CO}$ [165, 178] and $\text{H} + \text{O} + \text{M} \leftrightarrow \text{OH}^* + \text{M}$ [172]. The CH* CL peaks near $\lambda = 431$ nm, corresponding to the $A^2\Delta \rightarrow X^2\Sigma^-$ energy level transition, with two dominant chemical formation pathways, $\text{C}_2\text{H} + \text{O}_2 \leftrightarrow \text{CH}^* + \text{CO}_2$ and $\text{C}_2\text{H} + \text{O} \leftrightarrow \text{CH}^* + \text{CO}$ [178]. Both OH* and CH* destruction occurs by spontaneous emission of a photon or through collisional quenching to return to the OH and CH radical ground states. The intensity of emitted light from this spontaneous emission can be detected provided that broadband light emission is filtered out. For example, for OH* CL measurements bandpass filters need to be placed on the camera lens corresponding to the peak wavelength of 309 nm. Similarly, CH* CL would require a bandpass filter centered near 431 nm.

Under elevated pressure conditions, OH* CL intensity in experimental and modelled laminar flames has been shown to decrease due to increased collisional quenching and reduction in the reaction zone thickness [172, 179]. Relationships between OH* CL and ϕ under elevated pressure conditions have also been identified. With increasing ϕ , OH* CL is noted to increase due to the increased heat release corresponding to the increase in AFT [179]. In fact, OH* CL has been modeled in pressurized and preheated methane flames, and resulting intensities are observed to increase by 20 times over the equivalence ratio range $0.6 < \phi < 1.0$ at a fixed

pressure condition [172]. Similar trends of increasing OH* CL under elevated inlet temperature conditions have also been shown due to the resulting increase in AFT [172].

3.2.1.2 Planar Laser Induced Fluorescence

The laser induced fluorescence (LIF) technique relies on the use of a high energy density light source, such as an Nd:YAG or dye laser, to electronically excite a target molecule within a reacting flow by absorption of an incident photon. Whereas LIF would provide either line or point excitation of the target molecule, the light source in PLIF is first formed into a sheet before entering the reacting flow to provide a two-dimensional representation of the target species distribution. As the molecule returns to its ground state energy level, it emits light in the form of fluorescence, which can then be captured by a triggered imaging system. A general schematic of the absorption and emission process is found in Figure 3.8. As can be seen, the return to the ground state energy level does not only proceed via fluorescence but is influenced by a number of other atomic and intermolecular processes, including collisional quenching, internal energy transfer, intermediate energy level processes, and spontaneous emission [180].

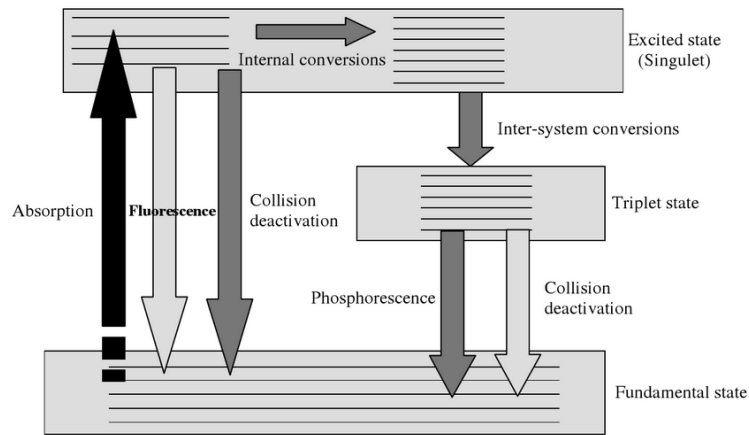


Figure 3.8: Schematic diagram of the PLIF molecular energy states. Reproduced from [180].

The influence of these varying de-energizing pathways on the intensity of the measured fluorescence signal is captured in Equation 3.2, which yields the number of fluorescent photons (N_p) captured by the measurement system [181]:

$$N_p = \eta_{eff} \frac{\Omega}{4\pi} f_1(T) \chi_m n_{tot} V B_{12} E_v \frac{A_{21}}{A_{21} + Q_{21}} \quad (3.2)$$

where η_{eff} is the transmission efficiency of the optical measurement system, Ω is the solid angle of collection between the measurement optics and the fluorescence emission, $f_1(T)$ is the fractional population of the ground state, χ_m is the mole fraction of the absorbing state, n_{tot} is the total gas number density, V is the collection volume (area of the laser sheet multiplied by its thickness) imaged onto one detector pixel, B_{12} is the Einstein coefficient of stimulated absorption, A_{21} is the rate constant for spontaneous emission, and Q_{21} is the rate constant for collisional quenching. Thus, it can be seen that there is a relationship between the measured PLIF intensity and the mole fraction of the absorbing molecule within the measurement volume, and with proper and precise calibration, quantitative PLIF measurements of reacting species concentrations are possible [182]. Calibration is often very difficult with systematic errors, in particular with the quantification of OH radical concentrations in swirl flames given their high reactivity and short lifetime relative to the flow timescales. Thus, it is often sufficient to consider the relative population of OH radicals within a reacting flow rather than the absolute concentration [182]. It is critical to note the temperature dependence in Equation 3.2, which affects the selected excitation wavelength to populate the upper energy levels through the term $f_1(T)$, as well as the pressure dependence which will increase the collisional quenching rate (Q_{21}), effectively lowering the measured PLIF intensity. Q_{21} will also have a dependence on the temperature and local composition.

PLIF imaging relies on the separation between the photon absorption and fluorescence emission wavelengths, and this is particularly critical for the use of PLIF in the imaging of reactive species in swirling flames which, as shown in the previous section, emit broadband CL. Species that have been measured in swirl flames using PLIF include the OH radical, CH radical, C_2 radical, nitrous oxide (NO), and formaldehyde (CH_2O) [180]. Fuel tracers such as acetone can also be used in PLIF studies of fuel/air mixing within a flow field [180]. PLIF measurements of the OH radical are of particular interest in this study because, within the reacting swirl flame, it allows for the qualitative visualization of the flame front, given that high OH radical concentrations are known to exist in this location [181, 183]. For OH PLIF measurements, molecular excitation often occurs via a high-energy planar ultraviolet (UV) light sheet and subsequent fluorescence is measured at a separate wavelength. The resulting emitted light can be imaged directly onto the detector of a CCD camera, and a relative intensity (bright/dark) then indicates the presence or absence of OH radicals in the image. The OH radical is typically stimulated from the $v'' = 0$ vibrational energy level in the $X^2\Pi$ ground state to the $v' = 1$ vibrational energy level in the $A^2\Sigma^+$ excited state, further called the (1,0)

vibrational band [182, 184]. The wavelength energy required for this transition is shown in Figure 3.9 to be approximately 35000 cm^{-1} , which equates to an excitation wavelength of approximately $\lambda = 283 \text{ nm}$, which can be achieved by the use of an Nd:YAG-pumped dye laser. The selection of this vibrational band has also been shown to relate to the high ground state population in the $v'' = 0$ level as well as the reduced temperature dependence of the transitional band near 283 nm [182]. Further information on the selection of precise rotational energy levels near 283 nm for use in this study can be found in Section 4.2.1.

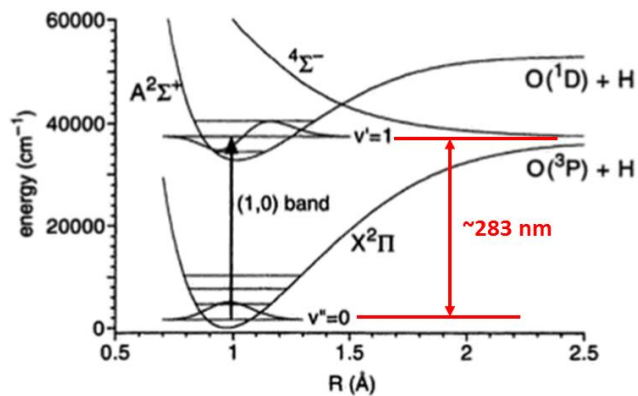


Figure 3.9: OH radical A and X states potential curves. Reproduced from [185].

Another reason for selecting the (1,0) vibration band for OH PLIF excitation is that the excitation wavelength is sufficiently far away from the fluorescence emission wavelength. As the OH radical de-energizes, the strongest transitions occur in the (0,0) and (1,1) vibrational bands, corresponding to 309 nm and 315 nm respectively [182]. This can be seen in Figure 3.10, which is a simulated LIF absorption and emission spectra calculated using the LIFBASE 2.1.1 software package [186]. The OH spectra has been simulated at a pressure of 0.1 MPa and 1700 K to replicate lean, atmospheric pressure combustion conditions in which the OH radical may be present. Given the separation between the laser excitation wavelength and the fluorescence emission, it is then possible to use bandpass filters on the collection optics to eliminate scattered laser light while collecting the fluorescence signal. However, it is necessary to consider that OH* CL emission occurs at approximately the same wavelength ($\sim 309 \text{ nm}$) as OH PLIF emission when stimulated at 283 nm. It is thus critical to control the timing of the PLIF image capture system to synchronize the OH PLIF capture with the light pulse from the laser, noting that fluorescence lifetimes are on the order of $\sim 2 \text{ ns}$ [187]. Otherwise, there is potential for the OH PLIF signal to contain OH* CL intensity. The OH PLIF timing system is discussed further in Chapter 4.

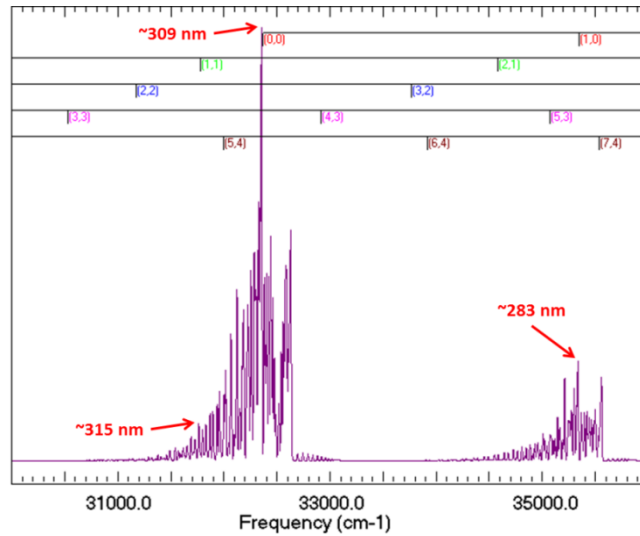


Figure 3.10: Simulated combined LIF absorption and emission spectra from LIFBASE [186] for OH radical at 0.1 MPa and 1700 K, including vibrational bands

Once the PLIF intensity has been captured by the imaging system, it is necessary to utilize image processing techniques to derive meaningful quantities from these images. In the study by Fritsche et al. [69], OH PLIF was used for the definition of the flame shape, flame height, and flame front location. From these measurements, this work concluded that the transition from a stable flame to an unstable flame could be broadly characterized by an abrupt change in both the flame shape and its position [69]. Thus, it was advantageous in this study to utilize OH PLIF as a method for characterization of the flame shape and location as fuel composition, burner geometry, and operating conditions were varied. For swirling flows, the flame shape can be particularly complex, with a number of areas of reverse flow which serves to mix the hot products with the incoming reactants. Even with these highly 3-dimensional structures existing within the flame flow field, it is still possible to identify the flame boundary with OH PLIF. For example, Stopper et al. [94] identified the shear layer flame boundary between areas of forward and recirculating flow in a GT model swirl burner at pressure up to 0.6 MPa. Thus, OH PLIF can also serve as an identifier of complex flow structures that exist within a swirl flame, and will be used to evaluate the effect of changing fuel composition on the size and location of these regions.

3.2.1.3 Particle Image Velocimetry

PIV is one of many techniques utilized for the measurement of fluid flow field velocity, structure, and turbulence characteristics. This measure is critical for determining the influence of changes in flow and turbulence conditions on flame location, acoustic response, and emissions as well as validation of CFD models. The technique relies fundamentally on the

tracking of illuminated seeding particles within the flow field, assuming that the particles are sufficiently buoyant to follow the flow field at the local flow velocity [188]. Similar to PLIF, PIV is predominantly a two-dimensional planar measurement technique. However, studies have utilized stereoscopic PIV techniques to measure velocity components in three dimensions with two off-axis cameras [189]. Dual cavity, pulsed Nd:YAG laser systems are often employed in PIV measurements to illuminate highly reflective seeding particles, typically micro-scale diameter aluminum oxide (Al_2O_3). The laser pulses are synchronized with the camera system to capture consecutive images with mathematical algorithms then employed to detect, track, and calculate the resulting velocity components based on the particle distance traveled and the delay time between consecutive images.

At Cardiff University's GTRC, PIV has been conducted during previous experimental programs in the HPOC [190] as well as the HPGSB [114]. The PIV system utilized in this study is similar to that used in [114], consisting of a frequency-doubled (532 nm) dual cavity Nd:YAG laser (Litron Nano-S-60-15 PIV) operating at 5 Hz. This laser is rated for 60 mJ /pulse at 532 nm with a 4 mm output beam diameter and 5 ns pulse width. A set of sheet forming optics is installed at the immediate outlet of the Nd:YAG laser to create a divergent, 1 mm thick laser sheet, which enters the measurement area within the HPOC in line with the central axial-radial ($y-r$) plane of the burner exit nozzle. For all PIV images presented in this study, the laser was installed so that the light sheet enters through the radial access window in the water-cooled exhaust section, traveling axially upstream towards the burner exit nozzle. This setup was utilized to reduce the amount of internal light reflections as the light sheet enters the burner measurement area parallel with the quartz confinement tube instead of perpendicular, as shown in Figure 3.11. Refer also to the photograph in Appendix B.2.2, Figure B.16. The laser can also be placed such that the light sheet enters the side window of the HPOC, as shown, but this was only used in cases where the burner was operated without confinement. The camera position is fixed, focused on the burner exit nozzle through the top window of the HPOC, perpendicular to the light sheet and axial fluid flow. All images were captured with a Dantec Hi Sense Mk II CCD camera (Model C8484-52-05CP), with 1.38 megapixel resolution (1024 x 1344 pixels) at 12 bits resolution. A 60mm Nikon lens was attached to the CCD camera along with a narrow bandpass filter with high transmissivity at 532 nm to capture the reflected laser light from the seeding particles in the flow. For all PIV measurements, the camera is operated in dual-frame mode, with a delay time between images of 15 μs . This delay time value was selected as it corresponds to a particle displacement per image pair of approximately 5 pixels

given the expected mean velocity at the measured conditions (~ 30 m/s) and image resolution (11.1 pix/mm). This ensures that particle velocity can be accurately calculated within the minimum adaptive correlation interrogation area (32 x 32 pixels). All laser and camera timing were controlled via Dantec DynamicStudio software and a Berkeley Nucleonics BNC 575-8C pulse generator.

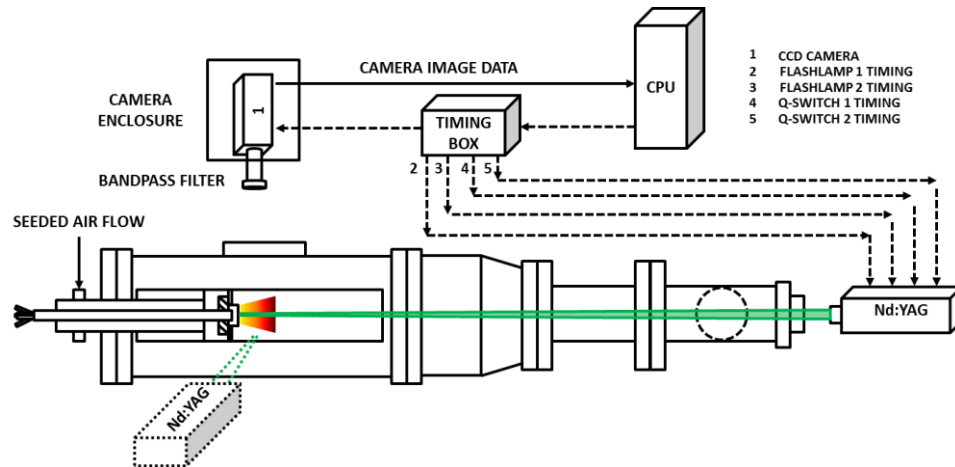


Figure 3.11: Schematic diagram of the PIV image capture and laser timing control system in the HPCR

The camera and lens combination allowed an overall field of view of approximately 90 x 120 mm, in the axial (“y”) and radial (“r”) directions respectively, with a resolution of 11.1 pixels/mm and a depth of view of 1.5 mm (refer to photograph in Appendix B.2.2, Figure B.17). Given that no seeding particle flow would be visible in areas outside of the radial extent (120 mm > quartz tube ID of 100 mm), the subsequent PIV images were masked in these areas to eliminate their influence on the calculated flow field. Note here that for consistency with PLIF and CL images, which have a different field of view as the result of different lenses used, $y = 0$ mm is taken as the edge of the burner exit nozzle and $r = 0$ mm is taken as the centerline of the burner exit nozzle. During PIV measurements, a portion of the burner inlet air mass flow was separately metered and delivered to a rotating fluidized bed seeder vessel. This air flow was seeded with Al_2O_3 particles with approximately 1 μm Sauter mean diameter and delivered into the premixed reactant flow at the inlet plenum.

After acquisition of the PIV data, the images were first masked as described previously within Dantec DynamicStudio. Then, a frame-to-frame adaptive correlation technique was carried out to identify the two-dimensional velocity vector maps. This algorithm utilized a minimum interrogation area of 32 x 32 pixels (2.89 mm x 2.89 mm) and a maximum of 64 x 64 (5.77 mm x 5.77 mm), with adaptability to particle density and velocity gradients. A range validation and

moving average validation were then applied to eliminate outlier velocity vectors. After this step in the image processing, the numerical files were then output and uploaded into MATLAB where bespoke processing scripts (see Appendix C.5) were utilized to calculate a variety of flow measures, including instantaneous, fluctuating, and mean velocity components in the axial and radial direction, turbulence intensity, and integral length scale. For example, each instantaneous velocity component (u_i) will consist of a mean value (U) and a fluctuating value (u'). This fluctuating value can also be described by its root-mean-square value, u'_{RMS} , and is often described as the turbulence intensity. The relative turbulence intensity, T_{int} , is given as the ratio of turbulence intensity and twice the mean burner exit nozzle velocity, \bar{u} . See Equations 3.2, 3.3, 3.4, and 3.5 below where N is the total number of image pairs used in the dataset [191]:

$$u_i = U + u'_i \quad (3.2)$$

$$U = \frac{1}{N} \sum_{i=1}^N u_i \quad (3.3)$$

$$u'_{RMS} = \sqrt{\frac{1}{N} \sum_{i=1}^N u_i'^2} \quad (3.4)$$

$$T_{int} = \frac{u'_{RMS}}{2\bar{u}} \quad (3.5)$$

The integral length scale, L_T , as described in Chapter 2.3.1, is calculated from PIV measurements using the above quantities in the formulation of spatial correlation coefficients, R_{ij} , as defined in [191, 192] and given in Equation 3.6. The integral of the resulting correlation function yields the integral length scale, Equation 3.7.

$$R_{ij}(x, r) = \frac{\overline{u'_i(x)u'_j(x+r)}}{u'_{RMS}(x)u'_{RMS}(x+r)} \quad (3.6)$$

$$L_T = \int_0^{\infty} R(r) dr \quad (3.7)$$

The key consideration in Equation 3.6 is that as the distance, r , between two fluctuating velocity components increases, the components are less correlated and thus turbulence characteristics at each location are increasingly independent. Conversely, at $r = 0$, $R_{ij} = 1$, meaning that a single point in the flow field is perfectly correlated to itself, and $R_{ij} \rightarrow 0$ with

increasing r . These correlation coefficients apply in both the axial and radial directions for each axial and radial velocity component, thus 4 integral length scale components can be calculated for each point in the two-dimensional flow field. These length scales are considered longitudinal when parallel to the velocity component used in the correlation coefficient calculation and transverse when perpendicular to the velocity component. An example of the correlation coefficient plot is given in Figure 3.12, which features the ideal correlation coefficient relationship for the calculation of the integral length scale (black line). However, in practical turbulent flows, the correlation function is typically observed to drop rapidly to its first zero crossing and then oscillate about the x-axis (Figure 3.12, red line) [193].

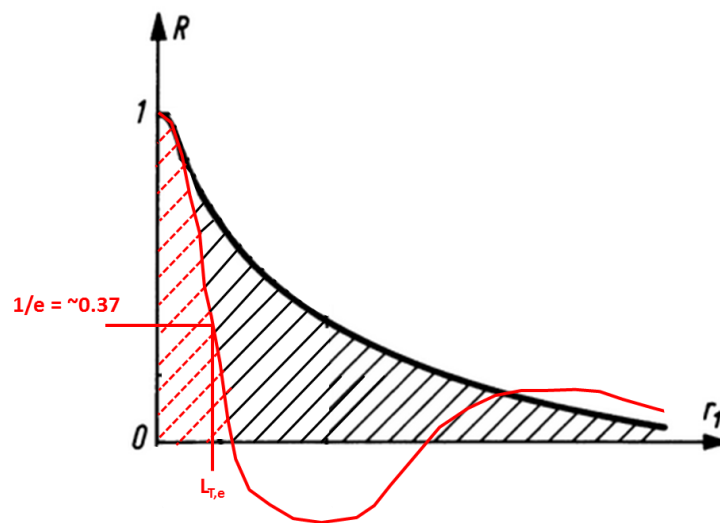


Figure 3.12: Ideal (black) and practical (red) correlation coefficient relationship for determination of integral length scale. Adapted from [192].

Thus, a number of methods for extracting the integral length scale for practical systems are proposed [193], including those shown in Figure 3.12. The first is to estimate the integral length scale, $L_{T,e}$, by the correlation length, r , where $R(r)$ is equal to $1/e$ (~ 0.37) [191] and the second is to estimate the integral length scale, $L_{T,int}$, by integrating $R(r)$ from 0 to the first zero crossing ($R(r) = 0$) [193]. Both methods will be investigated in this study, with results presented in Chapter 5.1.1.2. Characterization of the flow field using these measures allows for further development and understanding of turbulent flame-flow interactions, which is critical for highly turbulent swirling flows in GT combustion systems.

3.2.2 Thermoacoustic Diagnostics

As detailed in Chapter 2.2.2, swirl flame instabilities often arise from the coupling of pressure and heat release fluctuations per the Rayleigh criterion [70]. Whereas the flame heat release

can be monitored and evaluated through the use of optical techniques, pressure fluctuations in combustion chambers are often measured through acoustic systems such as dynamic pressure transducers (DPT) [131, 138, 194] or microphones [69, 73, 195]. Of particular interest to this study is the use of DPTs in strategic locations throughout the HPGSB/HPGSB-2 and HPCR to measure the physical system resonant acoustics in addition to the flow and combustion-induced pressure fluctuations, and their interlinkage with flame stabilization, fuel composition, and emissions under elevated operating conditions. Dynamic pressure sensing has been conducted at the GTRC during previous experimental combustion studies [109, 190]. However, a new system was commissioned for this study and is detailed in Chapter 4.

3.2.2.1 Dynamic Pressure Measurement

Dynamic pressure measurement systems require high sensitivity to high frequency, low amplitude pressure fluctuations, in potentially high static pressure environments. These systems often incorporate piezoelectric DPTs, which utilize a sensitive diaphragm and quartz crystal to convert small changes in diaphragm displacement into a measureable electrical signal through an internal charge amplifier [196, 197]. The time-varying DPT output electrical signal is then converted to a time-varying pressure measurement through a calibration. Subsequent signal analysis of pressure fluctuations incorporates methods in both the time and frequency domains, with varying levels of computational demand required for each. While DPT measurements are made in the time domain, it is often useful to evaluate the measured signal in the frequency domain as well; for combustion systems in particular as unsteady combustion noise is an acoustic emission process containing many distinct frequencies overlaid on broadband acoustic noise [196].

The measurement speed and level of signal analysis are both critical components of dynamic pressure measurement in combustion systems, and their selection depends largely on the nature of the pressure fluctuation being measured. If the dynamic pressure measurement is being utilized in a steady-state operation, the increased computational and temporal requirements of frequency domain analysis may be warranted to monitor combustion stability. However, if the measurement is being used to detect a transition from stable to unstable combustor operation or instability onset, and perhaps even further still incorporated into a stability control system, then time-domain analysis is advantageous, possibly concurrently with frequency analysis [198].

Dynamic pressure measurement allows for the application of various analytical techniques and in this study emphasis has been placed on defining the limitations and benefits of both frequency and time domain signal analysis in the observation of combustion instability events. Analysis of the time-varying dynamic pressure signals in the frequency domain provides discrete evidence of the fluctuating spectral content, amplitude, and phase. This analysis is often conducted through the use of a Fast Fourier Transform (FFT) algorithm, which transforms the time domain signal into the frequency domain [196]. A sampling rate of 4 kHz was used exclusively in this study, thus dynamic pressure signal frequencies up to 2 kHz can be resolved per the Nyquist theorem [196]. This is considered to be sufficient for resolving the combustion, flow, and system acoustic frequencies of interest in this study. A dominant tone extraction algorithm was also used to discretize the dynamic pressure measurement signal into equal length parts sufficient to yield the necessary frequency content information, calculating the FFT of the signal within each interval and extracting the frequency, amplitude, and phase of the signal component with the highest absolute amplitude.

Time domain analysis of the dynamic pressure signal is also of interest in this work. In addition to the monitoring and evaluation of the instantaneous pressure signal (p') and its root-mean-square value (p'_{RMS}), a statistical measure known as kurtosis (K) was also utilized in the identification of transitional states from stable burner operation to LBO instability. Kurtosis is defined as in Equation 3.8 and provides a statistical measure of the sharpness of a peak within a sample distribution [198]. For a continuous input sample, p' , the value of kurtosis is the ratio of the fourth moment about the mean value, p_4 , and the standard deviation, σ , to the fourth power. Thus, it has been suggested for use in the identification of both LBO instabilities [75] and more recently for general thermoacoustic instabilities in premixed swirl-stabilized combustors [198].

$$K = \frac{E(p' - p)^4}{[E(p' - p)^2]^2} = \frac{p_4}{\sigma^4} \quad (3.8)$$

In general, a normal sample distribution such as random Gaussian noise, would have a kurtosis value of 3 while a sinusoidal distribution, such as a purely dominant combustor tone, would have a kurtosis value of 1.5 [198]. These values can therefore be utilized in the identification of high amplitude peaks within a sample distribution of the time-varying dynamic pressure signal. In addition, the input DPT signal was discretized into 0.1 s bins, and the time-varying kurtosis (K') was calculated for each bin, requiring reduced computational time compared with the frequency domain analysis.

3.2.3 Emissions Gas Analysis

Exhaust gas sampling and gas analysis (GA) was conducted via an industry standard system supplied by Signal Gas Analysers Ltd, which has been used in multiple experimental combustion campaigns with the HPGSB [112-121] and HPGSB-2 [122-126]. In the case of the open-ended cylindrical quartz confinement, an equal area (7 holes) exhaust sample probe was placed at the immediate exit of the confinement. In the case of the convergent nozzle quartz confinement, the exhaust sample was taken approximately 0.75 m downstream from the convergent exit using the same probe. The exhaust gas sample line, filter, and distribution manifolds were maintained at 433 K, while a heated pump was used to deliver sample into the analyzer setup. Total NO_x concentrations were measured using a heated vacuum chemiluminescence analyzer (Signal Instruments 4000VM), calibrated in the range of 0-39 ppmV. Total NO_x concentrations were measured hot and wet ($\text{NO}_{x,meas}$) to avoid any losses associated with dropout in condensed exhaust H_2O , with data corrected to the equivalent dry conditions ($\text{NO}_{x,dry}$) using a calculated equilibrium water molar fraction, $X_{\text{H}_2\text{O}}$ (see Section 3.3.1), and then normalized ($\text{NO}_{x,dry, 15\% \text{O}_2}$) to a reference value of 15% O_2 ($\text{O}_{2,ref}$) concentration per Equations 3.9 and 3.10, respectively. Exhaust O_2 measurements ($\text{O}_{2,meas}$) used in Equation 3.10 were made using a paramagnetic analyzer (Signal Instruments 9000MGA). This was calibrated in the range 0-22.52 %vol O_2 .

$$\text{NO}_{x,dry} = \frac{\text{NO}_{x,meas}}{(1-X_{\text{H}_2\text{O}})} \quad (3.9)$$

$$\text{NO}_{x,dry, 15\% \text{O}_2} = \text{NO}_{x,dry} * \left(\frac{20.9 - \text{O}_{2,ref}}{20.9 - \text{O}_{2,meas}} \right) \quad (3.10)$$

In addition to the total NO_x measurement, individual NO and NO_2 measurements were also taken for selected experimental conditions, calibrated for 0-37.1 ppmV NO and 0-1.9 ppmV NO_2 . Both measurements are made hot/wet and corrected similarly to the total NO_x measurement. A chiller was also employed to reduce the exhaust molar H_2O concentration below 1%, with downstream dry CO concentrations measured using a nondispersive infrared analyzer (Signal instruments 9000MGA), calibrated in the range 0-904 ppmV. The same infrared analyzer was used for measurement of exhaust CO_2 concentrations, calibrated for 0-9 %vol CO_2 . Finally, a flame ionization detector (Signal Instruments 3000HM) was used to detect unburned hydrocarbons (UHC) in the exhaust stream, calibrated with propane from 0–890 ppmV. While CO measurements are made dry (and thus normalized using similar inputs to

Equation 3.10 only), UHC exhaust gas emissions are wet and thus must be normalized for exhaust water mole fraction and corrected to 15% excess O₂ option in a similar fashion to NO_x. Typical uncertainties of approximately 5% of measurement account for analyzer specifications, linearization, and accuracy in span gas certification [113].

3.3 Numerical Techniques

In addition to the extensive experimental measurements undertaken in this study, two separate numerical techniques were also utilized in support of the experimental observations. First, chemical kinetics modeling of the experimental conditions was utilized to provide fundamental support to observed changes in flame shape, stability, and emissions. As discussed previously, fundamental fuel quantities such as WI are trivial in their ability to predict flame stability in GT combustion. Thus, the use of chemical kinetics modeling enables the derivation of additional fundamental properties to describe the observed phenomena.

Second, a recently released open-source low order thermoacoustic modeling code [203, 204], based in MATLAB, was investigated for applicability to the prediction of flame stability under varying swirl burner geometry, rig geometry, and operating conditions. This low order code allows for the input of burner and rig geometry along with a flame model to predict system eigenvalues and instability growth rates. The use and validation of this code with observed flame stability at elevated conditions aims to provide a tool for current burner operation prediction and burner design development in the future. A dedicated case study using this program is presented in Chapter 8.

3.3.1 Chemical Kinetics Modeling

Chemical kinetics modeling of the experimental conditions was conducted using three separate modules within CHEMKIN-PRO [199]. First, the equilibrium program was used to model AFT. Second, the PREMIX program was used to model S_L and equilibrium exhaust H₂O concentrations, X_{H_2O} , for use in the correction of wet exhaust gas emissions measurements (Equation 3.9). Solutions in this model are based on an adaptive grid of 1000 points, with mixture-averaged transport properties and trace series approximation. Third, the OPPDIF program was used to model κ_{ext} of the experimental conditions for consideration in the evaluation of its use as suggested by Shanbhogue et al [65], although noting their use of a twin flame model predicts higher extinction strain rates. The model used in this study was based on

a single premixed air/fuel jet flame in opposition with a pure N_2 jet and included the use of multi-component diffusion coefficients and Soret effects. Both the PREMIX and OPPDIF models employed the GRI-Mech 3.0 reaction mechanism [200] which is optimized for use with methane and natural gas compositions (up to propane, C_3) and comprises 53 chemical species and 325 reactions. This mechanism has also been shown to have good agreement with experimental CH_4 - H_2 laminar flame speed measurements at pressures up to 0.5 MPa and H_2 mole fraction up to 0.2 [201]. Thus, GRI-Mech 3.0 has also been used in the evaluation of CH_4 - H_2 flames in this study, as the volume fraction is limited to 15% and maximum operating pressure is 0.33 MPa. These models incorporated all experimental conditions, with molar concentrations of premixed constituents, CH_4 , C_2H_6 , C_3H_8 , H_2 , N_2 , and O_2 (neglecting trace components in air) calculated from measured fuel and air mass flow rates. These molar concentrations were used as model inputs along with measured inlet values of T_2 and P_2 .

3.3.2 Low Order Thermoacoustic System Modeling

GT combustors are inherently difficult to model acoustically given the complex interaction between the physical acoustic environment, given by the combustion chamber, swirler, fuel and air inlets, and turbine inlet transition duct, and the highly turbulent hydrodynamic and thermodynamic processes occurring within them, which modulate the heat release rate, flame shape, speed of sound distribution, and pressure [202]. This makes prediction of unstable operating modes difficult and encourages the use of simplified acoustic modeling tools. In this study, the Open Source Combustion Instability Low Order Simulator (OSCILOS) [203, 204] has been utilized in the validation and prediction of combustion stability in the HPGSB-2. OSCILOS is a MATLAB/Simulink based code for longitudinal acoustic wave modeling in support of can-type (1-D longitudinal) GT combustor development [204]. This code has been validated against experimental measurements of limit cycle frequency and amplitude of both self-excited instabilities in an unsteady swirl burner and forced instabilities in a dump combustor [206]. More recently, OSCILOS has also been used for the examination of Helmholtz resonator location selection in a Rijke tube setup [207] and in the design of a control strategy for combustion instability suppression [208].

The analysis is conducted by representing the combustor and associated connected geometries by a series of consecutive area modules, with conditions of flow velocity, temperature, and pressure varying at the boundary between elements along the longitudinal axis [205]. Both step changes in geometry and gradual changes can be represented within the

MATLAB input. This will allow modelling of both the open and convergent burner confinements. An example of the general geometry input can be seen in Figure 3.13, where A_k represents the upstream and downstream propagation of acoustic waves.

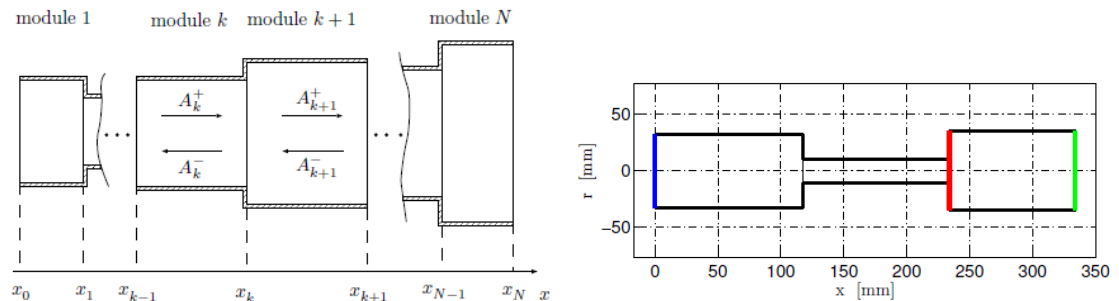


Figure 3.13: Representative combustor geometry input to OSCILOS, mathematical domain (left) and example OSCILOS input (right), flow left to right across flame (red line). Reproduced from [205].

In addition to the geometrical input, the temperature (K), pressure (Pa), fuel, equivalence ratio, combustion efficiency, and flow velocity are also required as inputs, with all fluids assumed to behave as perfect gases. There are a number of pre-loaded fuels from CH_4 to Jet-A available in the program, but a temperature rise across the planar flame can also be input in lieu of a fuel and φ . This is a key consideration as there is not currently functionality in the code for fuel blends, thus either the code must be manipulated (e.g. change fuel properties) or an expected (or measured) temperature change entered for each fuel and condition. Perforated liners or Helmholtz resonators can be added as passive dampers. Inlet and outlet boundary conditions, such as closed ends, open ends, choked ends, or user-defined reflection coefficients and time delays are also required for model initiation.

Finally, and perhaps most importantly, the flame model must be selected. In this program, there are a number of options for the flame model. The available options include a linear n- τ flame transfer function (FTF) to describe linear system response to heat release fluctuations due to velocity fluctuations at the flame front. The selection of the input time delay is critical to these models, and is the subject of further discussion in Chapter 9 as the burner system in use will not be acoustically forced, and thus the time delay between velocity fluctuation and heat release fluctuation must be defined by other methods, including flame shape and flow turbulence characteristics [204]. Nonlinear acoustic models such as the flame describing function (FDF) and the G-equation models are also available to identify limit cycle times and saturation amplitudes. System eigenvalues, mode shapes, and growth rates are calculated both cold or with heat addition from a flame located along the longitudinal axis, represented

by one of the flame models above. This allows for comparison between the OSCILOS model and both isothermal and combustion experimental conditions in the HPGSB-2.

3.4 Experimental Matrix Development

The experimental matrix is intended to provide a wide range of fuel compositions, operating conditions, and burner geometries that are industrially relevant and novel in their application. The fuel blends and operating conditions selected for experimentation were scrutinized to ensure relevancy as well as to provide experimental efficiency. For example, in nearly all experimental conditions, the fuel blends detailed in this Section were delivered from premixed fuel cylinders. As such, the 5-gas mixing facility, described in Section 3.1.1.1 was used for the metering and blending of the premixed air and fuel. This allowed for more precise control of the fuel and air mass flows while simplifying the setup and operation of the experimental facility.

3.4.1 Fuel Selection

While pure methane and pure propane were utilized in the commissioning of the two new generic swirl burners (Chapter 5), a number of fuel blends were selected for study on the influence of higher-hydrocarbon addition to methane (Chapter 6) and hydrogen addition to methane (Chapter 7). Fuel blend selection was not a trivial task as distinct parameters were maintained between fuels, for example two methane-C₂+ blends with identical WI but varying composition were selected amongst others. The fuel blends utilized were also selected to be industrially relevant, focusing on small changes in natural gas composition that may influence GT manufacturers and operators currently and in the near future.

3.4.1.1 Natural Gas Blended with Higher Hydrocarbons and Nitrogen

A report on the security of gas supply to the UK acknowledges that many sources of natural gas produced outside of the UKCS, particularly LNG, have a WI higher than the current UK pipeline admission maximum limit, 51.41 MJ/m³ [209]. With gas supply from the UKCS in decline and import dependence increasing, this will put increasing pressure on GT power generators to operate their equipment on natural gas blends near the UK upper WI limit. The impact of this is two-fold and drives the experimental fuel blend selection to represent LNG fuels. First, natural gas blends near the upper WI limit often contain higher levels of C₂+ molecules. These molecules individually, and their blends with methane, have been shown in

Chapter 2.1.4 to have differing flame properties which could contribute to the production of instabilities in GT swirl combustion. Second, according to GS(M)R regulations, natural gas that does not meet the required WI limit cannot be accepted into the gas network unless special permission is given or in supply emergencies [20]. If the upper WI limit is exceeded, the gas is normally ballasted with nitrogen at the import terminal to reduce the WI [209]. Ballasting of natural gas can result in diluent volume fractions greater than or equal to the concentration of certain higher hydrocarbons within the gas and therefore impact the resulting combustion characteristics. Thus, C_2+ levels and increased nitrogen content are considered critical for LNG fuel selection and characterization of their impact on the resulting flame characteristics at GT operating conditions.

Combining LNG compositional data from [209] with compositional data provided by Josten and Hull [210], Figures 3.14 and 3.15 were produced. The heating value and WI presented in these figures were calculated at 0.101 MPa, 288 K reference conditions utilizing a bespoke Microsoft Excel/Visual Basic computer program developed to the requirements of BS EN ISO 6976-2005 [25]. Figure 3.14 provides the WI for a number of LNG exporting countries as a function of the higher heating value of the fuel blend. It can be seen in Figure 3.14 that almost all LNG blends from exporting countries across the world exceed the current UK WI maximum limit of 51.41 MJ/m³. The countries of particular interest here are those listed in Table 1.1 from Chapter 1.1.3.1, including Qatar, Algeria, and Trinidad and Tobago,, which are the 3 countries from which the UK has imported the most LNG over the past 10 years. Most LNG blends from these countries exceed the upper GS(M)R WI limit, which means that they are most likely ballasted with nitrogen or blended with suitable gas at the import terminal before entering the UK gas network.

Figure 3.15 provides not only a picture of the C_2+ content of LNG from exporting countries around the world, but also the effect of C_2+ content on WI. For example, the blend of Nigerian LNG with the highest WI does not necessarily contain the highest amount of C_2+ molecules on a molar basis. The high WI results from higher levels of butane (C_4H_{10}) which are shown to be normally present in this particular blend of LNG. It can be seen the amount of C_2+ ranges from 3 %vol up to 12 %vol for the LNG exporting countries listed in Table 1.1 with some other countries exceeding 15 %vol. Qatari LNG, which has dominated UK gas imports over the last few years, has a normal range of C_2+ content from 6.6 %vol to 9.6 %vol.

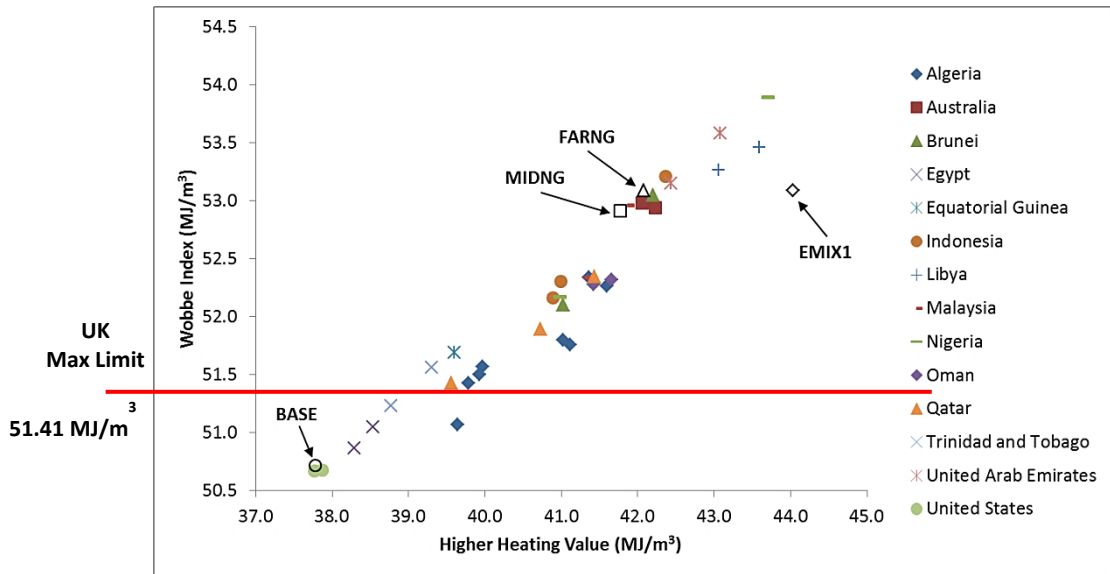


Figure 3.14: WI of LNG from exporting countries as a function of higher heating value, H_5 . UK maximum WI limit and investigated fuel blends shown for reference.

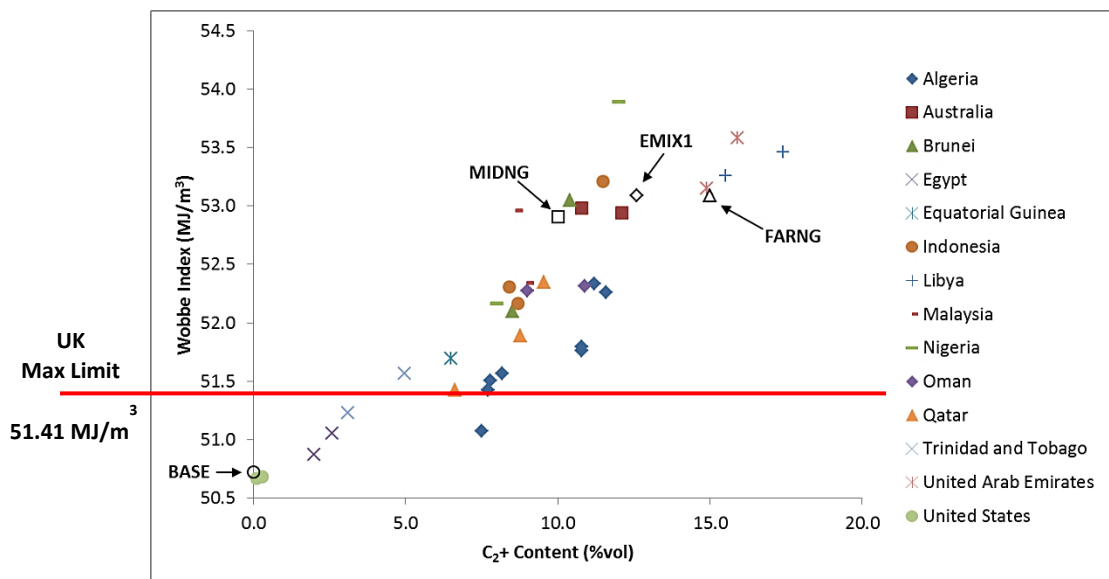


Figure 3.15: WI of LNG from exporting countries as a function of C₂₊ content. UK maximum WI limit and investigated fuel blends shown for reference.

The natural gas fuel blends selected for this study, along with selected characteristics such as molar mass, density (ρ), lower heating value (LHV), and molar and mass hydrogen to carbon (H:C) ratios, are given in Table 3.1. All pressure and temperature dependent values in Table 3.1 are calculated at 0.101 MPa and 288 K. The WI was calculated per BS EN ISO 6976-2005 [25]. The “BASE” fuel is 100% CH₄, widely used in combustion research to represent natural gas, and utilized as a comparison fuel for the remaining three methane blends containing C₂₊ components. The “MIDNG” and “FARNG” blends were formulated based on available global LNG compositional data [209, 210] plotted in Figure 3.15 as a function of country of origin, C₂₊

content, and WI. The fuel blends utilized in this study are also plotted in Figures 3.14 and 3.15 for reference. The CH_4 and C_2H_6 mole fractions of the “MIDNG” fuel blend are derived from the average composition of all LNG fuel blends shown in Figure 3.14. The average remaining C_3+ components have then been combined as C_3H_8 , a methodology that has been shown to be sufficient for the experimental representation of natural gas compositions [211]. A similar ternary composition of methane-ethane-propane (85-10-5%vol, respectively) was used experimentally by Holton et al. [34]. The “FARNG” C_2H_6 mole fraction was derived from the maximum of all LNG fuel blends shown in Figure 3.14 with an additional 10% margin.

Table 3.1: Selected methane and methane- C_2 fuel characteristics for HPGSB-2 study

Fuel Designation	Fuel Blend Components (mol %)				Molar Mass (kg/kmol)	Density, ρ (kg/m ³)	LHV (MJ/kg)	WI (MJ/m ³)	Molar H:C Ratio	Mass H:C Ratio	Stoichiometric AFR _{mass}
	CH ₄	C ₂ H ₆	C ₃ H ₈	N ₂							
BASE	100	0	0	0	16.043	0.680	50.03	50.72	4.000	0.336	17.26
MIDNG	90	6	4	0	18.007	0.764	49.41	52.91	3.754	0.315	16.95
FARNG	85	15	0	0	18.147	0.770	49.38	53.09	3.739	0.314	16.93
EMIX1	85	0	12.61	2.39	19.867	0.843	47.36	53.09	3.589	0.301	16.20

This CH_4 - C_2H_6 fuel blend has been studied by Flores et al. [40] and more recently as a representative composition of shale gas [212]. Finally, the intent of the “EMIX1” fuel blend was to match the WI (53.09 MJ/m³) of the “FARNG” fuel blend by replacing the C_2H_6 content with a combination of C_3H_8 and N_2 , while maintaining the same CH_4 content. By replacing the C_2H_6 with C_3H_8 , the WI is considerably increased, thus the addition of N_2 into the fuel blend is required to reduce the WI to that of the “FARNG” fuel, a methodology that has been employed in a previous study on fuel interchangeability [213] and is often used at the entry point to natural gas pipeline systems to reduce LNG WI within legislative limits [20].

3.4.1.2 Natural Gas Blended with Hydrogen

Guidance on anticipated hydrogen blending limits for use in GT engines from the European Gas Research Group is referenced in this study [214]. The study states that new and upgraded types of GT are expected to be able to handle up to 15% hydrogen by volume in future natural gas systems [214]. Thus, the hydrogen fraction in methane for the study of P2G applications is fixed at 15 %vol. Given that the current limit for hydrogen injection into the natural gas grid in the UK is 0.1 %vol [20], the limit of 15 %vol is considered to be sufficient for near future P2G applications as well as potential application in industrial facilities where excess hydrogen may be available for energy production. The hydrogen fuel blend selected for this study, along with selected characteristics such as molar mass, density (ρ), lower heating value (LHV), stoichiometric air-fuel ratio (AFR_{mass}), and molar and mass hydrogen to carbon (H:C) ratios, are

given in Table 3.2. All pressure and temperature dependent values in Table 3.2 are calculated at 0.101 MPa and 288 K. The WI was calculated per BS EN ISO 6976-2005 [25].

Table 3.2: Selected methane and methane-hydrogen fuel characteristics for HPGSB-2 study

Fuel	Fuel Blend Components (% vol)		Molar Mass (kg/kmol)	Density, ρ (kg/m ³)	LHV (MJ/kg)	WI (MJ/m ³)	Molar H:C Ratio	Mass H:C Ratio	Stoichiometric AFR _{mass}
	CH ₄	H ₂							
BASE	100	0	16.043	0.680	50.03	50.72	4.000	0.336	17.26
FARH2	85	15	13.939	0.590	51.55	48.86	4.353	0.365	17.59

3.4.2 HPCR Operating Conditions

The operating conditions for experimental combustion studies in the HPCR were selected to provide a wide parametric investigation of fuel composition, equivalence ratio, burner geometry, and turbulence scales at elevated temperature and pressure conditions relevant to industrial GT applications. The following list provides a broad overview of the rig operating conditions and geometries employed in this study during isothermal air flow and combustion experiments (note exact conditions will be provided in each results chapter):

1) Premixed Fuel/Air Burner Inlet Temperature, $T_2 = \text{Ambient (280-290 K), 423 K, and 573 K}$

For all experimental conditions at the highest burner inlet temperature, the target temperature was 573 K \pm 5 K.

2) Premixed Fuel/Air Burner Inlet Pressure, $P_2 = 0.101 \text{ MPa, } 0.11 \text{ MPa, } 0.2 \text{ MPa, } 0.22 \text{ MPa, } 0.33 \text{ MPa}$

Atmospheric pressure (0.101 MPa) isothermal and combustion conditions are achieved with the BPV in the fully open position. Slight elevation in P_2 to 0.11 MPa is achieved with the BPV in the fully closed position. This rig geometry was then maintained for subsequent increases in pressure to 0.22 MPa and 0.33 MPa to maintain the same acoustic boundary condition in the exhaust piping. For each pressure condition, the fuel mass flow was fixed while ϕ was varied by changes in air mass flow rate. Air and fuel mass flow rates (and thus P_{therm}) were scaled with combustor inlet pressure to maintain the dimensionless flow parameter, $\dot{m}\sqrt{T_2}/P_2$. Thus, air and fuel mass flows were doubled for increases from 0.11 MPa to 0.22 MPa and tripled for increases from 0.11 MPa to 0.33 MPa. By maintaining this dimensionless flow parameter for a fixed ϕ at each pressure condition, the volumetric flow through the burner exit nozzle is held constant, which in turn maintains the mean

burner exit nozzle velocity, \bar{u} . The intention is to decouple bulk flow effects from the chemical effects of varying fuel blend compositions.

3) Equivalence Ratio, $\varphi = 0.43 - 1.3$

The majority of the following study was conducted under lean, fully premixed operation. For experimental work with the fuel blends, at least three separate equivalence ratios were examined at each pressure condition, although it should be noted that achieving the same set of three equivalence ratios across all fuels was not possible and is the subject of further discussion. For all preheated, pressurized operation, a mean equivalence ratio of $\varphi = 0.55$ was achieved across all fuels. The air mass flow rates between all fuels was held constant for a fixed equivalence ratio, thus nominal changes in the fuel flow rate (based on changes in the stoichiometric AFR_{mass} between fuels) was required. For example, incremental increases in the blended C_2+ fuel mass flow rates with respect to the methane (BASE) flow rate were required to maintain equivalence ratios; 2% for the MIDNG and FARNG blends and 6% for the EMIX1 blend. The lowest equivalence ratios were achieved with the FARH2 hydrogen blend.

4) Burner Confinement Geometry

For all studies with the HPGSB, a cylindrical quartz confinement was used. For studies conducted with the HPGSB-2, both a cylindrical quartz confinement and a convergent nozzle quartz confinement were used. All fuel blend experiments in the HPGSB-2 have been conducted with the convergent quartz confinement, with the exception of selected FARH2 experiments.

5) Burner Radial-Tangential Swirler Insert Geometric Swirl Number, $S_g = 0.5, 0.8, 1.04, 1.47$

For studies with the HPGSB, $S_g = 0.8, 1.04, \text{ or } 1.47$. For studies conducted with the HPGSB-2, $S_g = 0.5 \text{ or } 0.8$. All fuel blend experiments in the HPGSB-2 have been conducted with the $S_g = 0.8$, with the exception of selected FARH2 experiments.

6) Turbulence Scaling Parameter, τ_T / τ_n

As most GT combustors operate at higher air mass flow, $P2$, and $T2$ than achieved experimentally in this study, it is critical to select a parameter which allows for scaling from the experimental system to industrial GT combustors. For the selection of the

baseline air mass flow rates through the HPGSB-2, and to aid in the scaling of the HPGSB/HPGSB-2 to practical GT burner systems, a dimensionless turbulence scaling parameter has been utilized based on the Kolmogorov time scale, τ_η , and integral time scale, τ_T . The integral time scale, related to the integral length scale calculated by Equation 3.7, is a measure of large turbulent eddy turnover time in the kinetic energy transfer range, while the Kolmogorov time scale represents turbulent eddy dissipation at a much smaller scale, where viscous effects dominate rather than inertial effects [215].

From Peters [215], the integral and Kolmogorov time scales can be defined as follows in Equations 3.11 and 3.12, where ν is the kinematic viscosity and ε is the turbulence dissipation rate, defined in Equation 3.13. By algebraic rearrangement, the turbulence scaling parameter τ_T / τ_η is defined in Equation 3.14.

$$\tau_T = \frac{L_T}{u'_{RMS}} \quad (3.11)$$

$$\tau_\eta = \left(\frac{\nu}{\varepsilon}\right)^{1/2} \quad (3.12)$$

$$\varepsilon \sim \frac{u'_{RMS}{}^3}{L_T} \quad (3.13)$$

$$\frac{\tau_T}{\tau_\eta} = \left(\frac{(u'_{RMS})^{3/2}}{(\nu L_T)^{1/2}}\right) \left(\frac{L_T}{u'_{RMS}}\right) = \sqrt{\frac{u'_{RMS} L_T}{\nu}} \quad (3.14)$$

During development of the experimental test matrix, values for the turbulence scaling parameter were calculated based on the mean burner exit nozzle velocity, ($2\bar{u}$), an assumed relative turbulence intensity of, $T_{int} = 0.2$, and an assumed integral length scale of $L_T = 8$ mm. The air mass flow rate was then calculated based on total volumetric air flow through the 40 mm ID burner exit nozzle required to scale the turbulence parameter with industrial GT combustors. As described previously, the dimensionless flow parameter, $\dot{m}_{air}\sqrt{T_2}/P_2$, was then held constant between 0.11 MPa, 0.22 MPa, and 0.33 MPa, for a fixed theoretical equivalence ratio of $\phi = 0.55$. The results of this exercise can be seen in Figure 3.16, which plots the dimensionless turbulence scaling parameter against P_2 for the selected target conditions (Figure 3.16.a) and extended out to a theoretical P_2 of 1.5 MPa (Figure 3.16.b). As the burner

inlet pressure is increased, the kinematic viscosity decreases due to an increase in density, which therefore increases the turbulence scaling parameter. All trends follow a power law relationship with $P2^{0.5}$ dependence. Table 3.3 then presents the selected target conditions for combustion study in the HPGSB-2 including air mass flow rates, φ , $T2$, $P2$, \bar{u} , and dimensionless flow and turbulence parameters. These air mass flow rates are used for all fuel blend testing (Chapters 6 and 7), while an evaluation of the measured turbulence intensity and integral length scale values from isothermal air flow PIV measurements is provided in Chapter 5 to complement the assumed values utilized here.

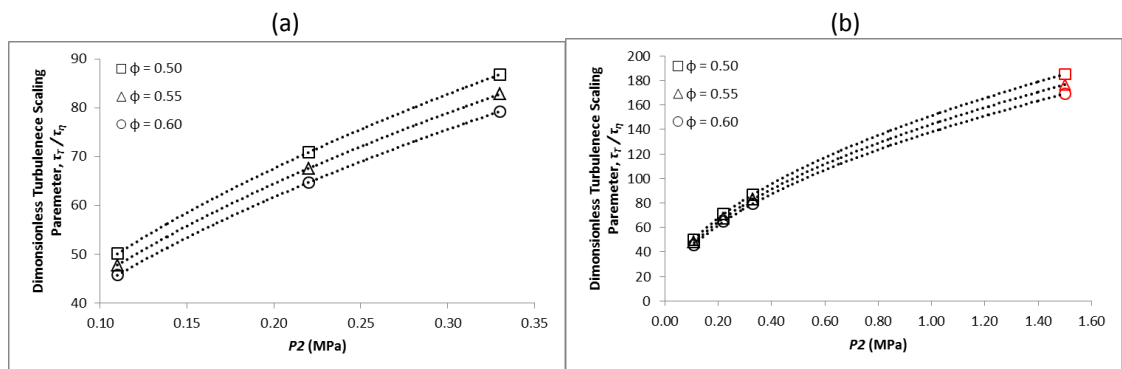


Figure 3.16: HPGSB-2 dimensionless turbulence scaling parameter, τ_T / τ_η , as a function of $P2$ for the selected target operating conditions (a) and extended to theoretical $P2 = 1.5$ MPa (b, red).

Table 3.3: Selected target HPGSB-2 burner operating conditions and dimensionless scaling parameters with theoretical $P2 = 1.5$ MPa values

φ	$T2$ (K)	\dot{m}_{air} (g/s)	$P2$ (MPa)	$\dot{m}_{air}\sqrt{T2}/P2$	\bar{u} (m/s)	τ_T / τ_η
0.60	573	24.063	0.11	0.524	28.63	45.76
0.60	573	48.125	0.22	0.524	28.63	64.72
0.60	573	72.188	0.33	0.524	28.63	79.26
0.55	573	26.250	0.11	0.571	31.24	47.80
0.55	573	52.500	0.22	0.571	31.24	67.59
0.55	573	78.750	0.33	0.571	31.24	82.78
0.50	573	28.875	0.11	0.628	34.36	50.13
0.50	573	57.750	0.22	0.628	34.36	70.89
0.50	573	86.625	0.33	0.628	34.36	86.82
0.60	573	328.125	1.5	0.524	28.63	168.98
0.55	573	357.955	1.5	0.571	31.24	176.50
0.50	573	393.750	1.5	0.628	34.36	185.11

CHAPTER 4 – NEW DIAGNOSTIC SUITE FOR PRESSURIZED COMBUSTION FACILITY

In order to characterize sufficiently the influence of changes in fuel composition, burner geometry, and burner operating conditions on experimental swirl flames in the HPGSB and HPGSB-2, a new suite of non-intrusive diagnostics was developed, installed, and commissioned at Cardiff University's GTRC during the course of this study. New optical combustion diagnostics focus specifically on the measurement of flame CL, as described in Section 3.2.1.1, and PLIF as described in Section 3.2.1.2. In addition, a new dynamic pressure measurement system, as described in Section 3.2.2.1 was installed for system acoustic and flow stability characterization of isothermal and combustion experimental conditions. The CL and PLIF systems, used at Cardiff University from 2006-2013 [216, 217], were installed and commissioned from 2013-2014 at the GTRC and have since contributed to the evaluation of flame characteristics in the HPGSB and HPGSB-2 operating with a variety of fuel blends including humidified high-CO syngas [113, 126], diluted oxymethane [114], propane [118], methane-hydrogen [123, 124], and methane-C₂+ blends [125]. The CL system has further contributed to the evaluation of heat release distribution in experimental combustion studies in the HPGSB with pure methane and high-CO syngas [119], ammonia [115, 117, 121], as well as biodiesel and Jet-A liquid fuels [116, 120]. Additional experimental tests in the HPGSB-2 of methane with EGR [122] also utilized the new chemiluminescence system. The dynamic pressure system, used in previous test campaigns at the GTRC [109, 190], was upgraded with new, higher sensitivity DPTs installed in new locations within the HPGSB-2 and HPCR. The DPT system was commissioned in 2015 for use in the HPGSB-2, and has since contributed to combustion dynamics measurements in multiple experimental campaigns [123-125]. Complete descriptions of these non-intrusive measurement systems, experimental commissioning, and associated data processing and analysis methods are presented in this Chapter to complement the theoretical background and motivation for their use provided in Chapter 3.

4.1 Chemiluminescence Measurement Facility

At Cardiff University's GTRC, a chemiluminescence imaging system was commissioned for use with the HPGSB and HPSBG-2 installed in the HPOC to provide qualitative measures of localized heat release and flame stabilization mechanisms under varying conditions of fuel

composition, swirl burner geometry, and operating conditions. The system is based on a CCD camera and high-speed gated image intensifier with associated optics for wavelength filtering of combustion species CL emission. In the HPCR, the ICCD is placed at a 90° angle to the direction of flow, and thus is positioned to capture images through the top window of the HPOC. It is fixed in place for all measurements.

The OH* and CH* chemiluminescence measurement system was commissioned with swirl-stabilized methane flames in the HPGSB to identify the optimal settings of image intensifier gate timing, gain, and UV lens f-stop. Measurements with gate widths down to $100 \mu\text{s}$ were achieved on methane flames with ambient inlet temperature ($T_2 = 283 - 285 \text{ K}$), inlet pressures up to $P_2 = 0.3 \text{ MPa}$, thermal powers up to $P_{therm} = 100 \text{ kW}$, and global equivalence ratios of $\varphi = 0.6$ to 1.2 . OH* and CH* chemiluminescence intensities are shown to vary with each parameter and yield sufficient spatial information to confirm visual evidence of stable flame operation as well as both lean and rich stability limits. Further OH* and CH* chemiluminescence measurements were made on Basic Oxygen Steelmaking (BOS) gas (65 %vol CO, 34 %vol N₂, 1 %vol H₂) flames at comparable conditions to the CH₄ flames to investigate the change in chemiluminescence intensities, with marked variation identified between the two fuels as expected due to the significant variation in composition and fundamental properties such as S_L . In addition to developing measurement capability, chemiluminescence image processing and Abel deconvolution techniques have also been developed.

4.1.1 System Setup and Components

The GTRC's chemiluminescence system is based on an intensified charge-couple device (ICCD) camera system with a bandpass filtered UV lens. The camera is a Dantec Hi Sense Mk II CCD camera (Model C8484-52-05CP), with 1.38 megapixel resolution (1024 x 1344 pixels) at 12 bits resolution. The maximum frame rate at full resolution is 12.2 Hz. This CCD camera has 70% peak quantum efficiency, a measure of the conversion of incident photons into electrons at the CCD, from 460 – 560 nm [218].

This CCD camera is coupled via a relay lens to a Hamamatsu high-speed gated image intensifier (Model C9546-C03L). This intensifier is capable of gate times as low as $t_{gate} = 3 \text{ ns}$ and repetition rates up to 30 kHz. It utilizes a multialkali photocathode material with a spectral response from 185 nm to 900 nm, and a peak response wavelength of 430 nm to convert the

incident photons into electrons [219]. The quantum efficiency of the image intensifier is 15% at 430 nm [219]. The image intensifier contains a P43 phosphor screen. With this phosphor screen type, “ghosting” is a potential issue if sufficient time is not allowed between consecutive images for the incident image imprint to decay. If insufficient time between frames is not provided, the next image could potentially have remnant intensity captured from the previous image. The P43 phosphor screen exhibits typical decay times on the order of 0.001 to 0.01 seconds to achieve approximately 95% intensity reduction, depending on the input gate time, t_{gate} [219]. This limits the maximum repetition rate of the image intensifier to obtain clean instantaneous images between 1000 and 100 Hz. This timing is controlled via Dantec DynamicStudio software and pulse generator, discussed in further detail below. The image intensifier gain can be controlled either by remote control or via USB connection to the unit through DynamicStudio. For all experimental results where chemiluminescence images are compared, the image intensifier gain was held constant.

A Pentax 78 mm UV lens (Model C91698) is installed on the Hamamatsu image intensifier coupled with narrow band-pass filters to detect the chemiluminescence emission from the OH* and CH* radicals. This lens has a variable aperture ($f/16 - f/3.8$). A photograph of the ICCD and lens assembly is provided in Appendix B.2.2, Figure B.12. The lens is manually focused using a scaled calibration target plate installed in the burner exit nozzle mid-plane (refer to Appendix B.2.2, Figure B.15). Each image is 1024 x 1344 pixels in the axial (y) and radial (r) directions, respectively, with a resolution of 13.6 pixels/mm ($0.0054 \text{ mm}^2/\text{pix}$) yielding a field of view of approximately 75 mm x 100 mm. This results in the ability to image from the edge of the burner exit nozzle to 75 mm downstream and from the burner exit nozzle centerline to 50 mm in either radial direction. Thus, in all proceeding images, $r = 0$ mm represents the burner exit nozzle centerline and $y = 0$ mm represents the edge of the burner exit nozzle. Note that the field of view described here is different from the PIV field of view described in Chapter 3.2.1.3 due to the different lenses utilized.

For detection of the discrete combustion radical chemiluminescence, optical wavelength bandpass filters are installed on the UV lens. The bandpass filter used for the measurement of OH* chemiluminescence is centered at 315 nm (15 nm FWHM) while the bandpass filter for the CH* radicals is centered at 430 nm (15 nm FWHM). The OH* and CH* bandpass filters were tested for bandpass width and transmissivity with the use of a Bentham wide spectrum light source and a Macam fiber optic spectroradiometer. The OH* filter was found to have a

maximum transmissivity of approximately 65% while the CH* filter has a maximum transmissivity of almost 100% at the wavelength of interest.

All images are captured via a remote computer outside of the experimental testing hall via dedicated software program, Dantec's DynamicStudio. This software also controls the image intensifier gain and timing for both the image intensifier gating and camera exposure. For measurements with the HPGSB, the image capture system consisted of a timing box (Dantec Timer Box) which provides the trigger signal at a rate of 10 Hz to the CCD camera. The image intensifier requires a gate signal, which was produced externally by a pulse generator (AMF Venner 728), with the gate pulse synced to the trigger pulse sent to the CCD camera. A digital oscilloscope (Tektronix TDS 2024B) was used to monitor the trigger and gate pulses sent to the ICCD system. In June 2015, a new Berkeley Nucleonics BNC 575-8C pulse generator was purchased to replace the Dantec Timer Box and AMF Venner 728 pulse generator. The BNC 575-8C pulse generator provides 250 ps resolution timing, delaying, gating, pulsing, and synchronization with each channel capable of delivering TTL or 2-20 V signals. It is connected to the image capture system via USB and controlled directly within the DynamicStudio software. The BNC 575-8C pulse generator was commissioned along with the HPGSB-2, and the corresponding setup is shown in Figure 4.1.

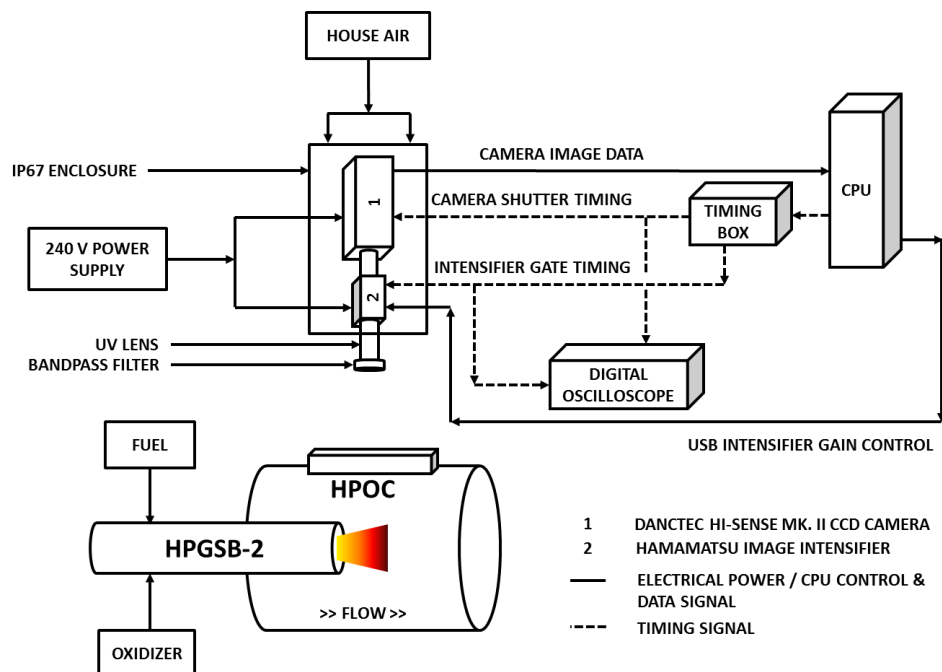


Figure 4.1: CL measurement system timing, image capture, and utility setup at Cardiff University's GTRC as used for measurements with the HPGSB-2.

4.1.2 Image Processing and Data Analysis

An evaluation of the literature presented in Chapter 3.2.1.1 indicates that there are not only multiple approaches to the measurement of OH* and CH* CL, but also numerous methods utilized for the processing and presentation of chemiluminescence measurements, with the reporting of time-averaged intensity values [174, 179] common along with both background correction and the use of a variety of deconvolution algorithms, including the Abel transformation [94, 105, 167]. The general method applied here involves noise filtering using a 3x3 pixel median filter, background removal, temporal averaging, and the use of an Abel inversion for deconvolution of the OH* and CH* CL signals. While images are captured via Dantec's DynamicStudio software, all image processing was conducted using new MATLAB codes, which can be found in Appendix C.1 (Chemiluminescence Image Temporal Average and Integral Intensity MATLAB code) and Appendix C.2 (Chemiluminescence Abel Deconvolution MATLAB code).

As described in [176], chemiluminescence is a line-of-sight technique, meaning that the measured light intensities are integrated, including signal contributions from both in front of and behind the focal plane of the ICCD UV lens. As such, the resulting image requires deconvolution in order to obtain spatially-resolved localization of the average heat release zones [95]. An open-source MATLAB algorithm developed by Killer [220], based on the Abel inversion method described by Pretzler [221], has been modified to provide spatial representation of the OH* and CH* chemiluminescence measurements. This Abel inversion is based on a Fourier-series-like expansion which projects the radial pixel intensity distribution function onto a theoretical 2-D plane through cosine expansions. The selection of the number of cosine expansions utilized in the reconstruction is critical to both intensity distribution filtering effects and computation time. For this work, 5 cosine expansions were used. The application of an Abel inversion assumes that the radial distribution being processed is symmetric about a central axis [221]. Given the highly variable structure of the instantaneous turbulent swirl flames investigated here, only the time-averaged OH* and CH* chemiluminescence images were used to ensure symmetry about the burner central axis. The quartz confinement tube provides a boundary for the flame, and the swirler imparts a conical shape on the flame front, thus it is assumed here to be axisymmetric. As such, the right half of the temporally-averaged image is extracted for use in the row-wise Abel inversion, although either half can be selected for use in the image processing algorithm. The resulting image is then mirrored about the axis of symmetry.

An example of this image processing technique's capability is given in Figure 4.2. Figure 4.2 shows a 50 kW BOS gas-air flame at $\phi = 0.98$. The resulting image in Figure 4.2.a is only background corrected and time-averaged, while the image in Figure 4.2.b is the resulting spatially-resolved OH* chemiluminescence image after Abel inversion. In Figure 4.2.a, the line-of-sight integration of OH* chemiluminescence from the BOS gas flame provides only an outline of the expected conical swirl flame shape, while Figure 4.2.b gives a more representative shape of the flame and planar OH* distribution, which could be confirmed visually during testing. Note that the pixel intensity scales, representing regions of higher heat release, differ between the two images, as the intensities in Figure 4.2.a are integrated along the line-of-sight.

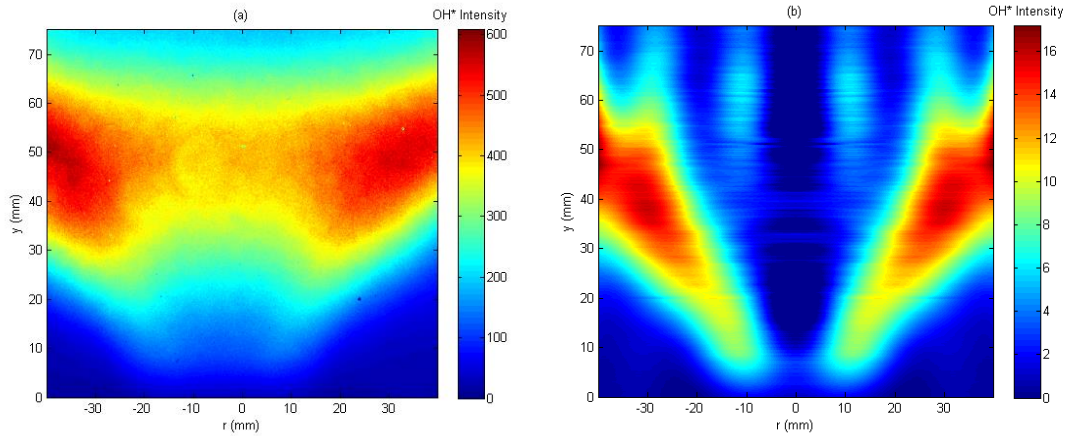


Figure 4.2: Time-averaged OH* chemiluminescence image before (a) and after (b) Abel inversion for 50 kW BOS gas flame at $T_2 = 285$ K, $P_2 = 0.101$ MPa, and $\phi = 0.98$.

For further comparison between chemiluminescence intensity levels and heat release under varying rig operating conditions, an integral intensity was utilized, defined in Equation 4.1 as a pixel-wise summation of the chemiluminescence intensity values from the temporally averaged and background corrected images. Instantaneous values of the filtered raw image integral intensity, II'_{OH^*} , were tracked throughout an image capture set to monitor OH* chemiluminescence and heat release fluctuations from frame to frame.

$$II_{OH^*} = \sum_{i=1}^{1344} \sum_{j=1}^{1024} \bar{I}_{OH^*_{i,j}} \quad (4.1)$$

A systematic evaluation of the appropriate equipment settings which impact the intensity of the measured chemiluminescence signal, namely the image intensifier gain (equipment-specific setting), image intensifier gate signal pulse width, and the UV lens f-stop, was performed to identify the ideal settings for OH* and CH* chemiluminescence measurements

under the combustion conditions described herein. Previous studies have varied the intensifier gate signal pulse width times for chemiluminescence measurement from $t_{gate} = 10 \mu s$ [105] to $t_{gate} = 400 \mu s$ [222]. To minimize the impact of multiple parameters in the initial experiments, the equipment settings were held constant for all OH* and CH* measurements. Then, a parametric study was initiated with the HPGSB operated at atmospheric pressure with a stable 50 kW methane-air flame at $\phi = 1$. Each system parameter was varied independently, and both OH* and CH* measurements taken to determine the effect of each parameter on the signal intensity.

To measure the effect of image intensifier gain and gate signal pulse widths on the measurements taken, the integral intensity from Equation 4.1 was used. Figure 4.3 shows the effect of image intensifier gain and two intensifier gate signal pulse widths, 1000 μs and 100 μs , on the 2D integral pixel intensity of time-averaged OH* and CH* images. Each measurement is made using an average of 200 images captured at 10 Hz. These images were not background corrected as the intent is to show relative intensities only.

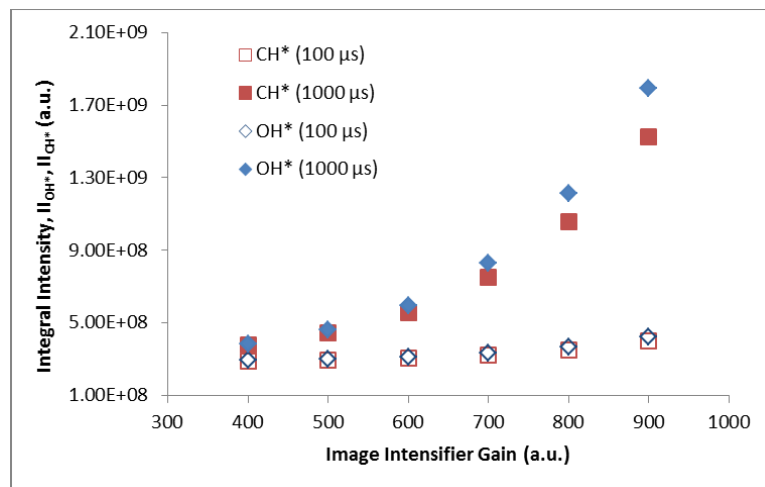


Figure 4.3: Effect of image intensifier gain and intensifier gate signal pulse width on the integral intensity of OH* and CH* signal in CH₄-air and BOS gas flames at $\phi = 1.0$.

Figure 4.3 shows that the gain setting of the intensifier has a greater effect on the measured OH* and CH* signal intensity at higher image intensifier gate times. Also, it appears that the image intensifier gain has a greater effect on the OH* intensity at both pulse widths, particularly above a gain setting of 700. As a result of this analysis, the image intensifier gate pulse width was set to 100 μs to reduce the noise introduced by the intensifier gain, and this value is consistent with that used in [174] for swirl-stabilized flames. To reduce the noise impact of the image intensifier gain further, the intensifier gain is set to 680 (equipment-specific value), while the f-stop of the UV lens was set to f/3.8, the largest aperture possible to

enhance the measured signal. Note that the image intensifier gain and gate timing are increased for lean operation with reduced OH* production. It should be noted also that the broadband CO₂* chemiluminescence which has been shown to contribute to both measured OH* and CH* chemiluminescence [167, 172, 176] has not been accounted for in these or further measurements in this work, as only relative trends are presented.

For all stable operating conditions, 200 instantaneous chemiluminescence images are captured and temporally averaged before the Abel deconvolution is applied. This total image number value was selected by statistical analysis of the signal to noise ratio (SNR) of the chemiluminescence integral intensity, which can be found in Appendix D.1. For transient operations, the chemiluminescence system was operated in a constant capture operation at a repetition rate of 10 Hz. This allowed for observation of changes in OH* chemiluminescence as a known phenomenon, such as LBO, was approached by varying the air mass flow rate through the burner.

4.1.3 System Commissioning

The experimental study presented in [119] aims to fill an identified gap in combustion chemiluminescence research of varying fuel compositions at elevated P_2 in a generic swirl burner while also demonstrating new fundamental combustion diagnostic capabilities at the GTRC. Chemiluminescence imaging of the electronically-excited combustion radicals, OH* and CH*, has been carried out experimentally across a wide range of test conditions, with P_{therm} up to 100 kW and $0.6 < \varphi < 1.2$. Two separate fuels were used for comparison, with results presented from CH₄-air flames and a high-CO syngas-air flame representative of BOS gas. The dry BOS gas blend used here is unique in both its industrial origin and resulting flame characteristics. Others such as Sadanandan et al. [159] and Kutne et al. [174] have studied OH* chemiluminescence in hydrogen-rich syngas, but CO-rich syngas has not received as much attention, despite its potential use in the steelworks industry for power and heat generation.

Combustion testing in the HPGSB was first conducted on CH₄-air flames with P_{therm} from 25 to 100 kW, P_2 up to 0.3 MPa, and $0.62 < \varphi < 1.27$. For all experimental cases here, a radial-tangential swirler insert with a set geometric swirl number of $S_g = 1.04$ was utilized. Both OH* and CH* measurements were taken at each test condition by replacing the bandpass filter on the end of the UV lens (see Figure 4.1). OH* chemiluminescence measurements taken on CH₄-air flames at two pressures can be seen in Figure 4.4. Figure 4.4.a is a 50 kW atmospheric

pressure methane-air flame at $\varphi = 0.8$. A comparable 50 kW flame at $\varphi = 0.77$ and $P_2 = 0.2$ MPa is shown in Figure 4.4.b. It can be seen that the increase in pressure serves to compact the overall flame as areas of increased heat release move radially inward along the shear layer. This is most likely due to the drop in overall volumetric flow rate through the burner as well as changes in thermal and mass diffusion due to an increase in density, as the BPV is closed.

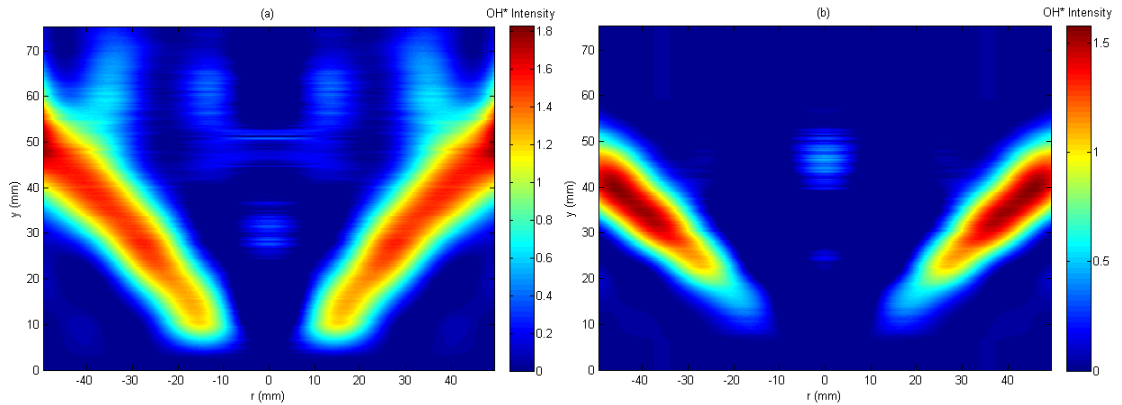


Figure 4.4: Abel inversion of OH^* chemiluminescence images for 50 kW CH_4 -air flame at atmospheric pressure (a) and 0.2 MPa (b) and $\varphi = 0.8$.

Combustion testing in the HPGSB was then conducted on high-CO BOS gas-air flames at atmospheric pressure, 50 kW thermal power, and $0.49 < \varphi < 1.34$. Both OH^* and CH^* chemiluminescence measurements were taken at each test condition. Figure 4.5 shows the CH^* chemiluminescence image for the same 50 kW BOS gas-air flame ($\varphi = 0.98$) as Figure 4.2 (OH^* chemiluminescence). The image in Figure 4.5.a is only background corrected and time-averaged, whilst the image in Figure 4.5.b was the resulting spatially-resolved CH^* chemiluminescence image after Abel inversion. Comparing Figure 4.2.a and Figure 4.5.a shows that there is an increase in signal intensity from OH^* to CH^* chemiluminescence, most likely due to the higher transmissivity of the CH^* lens and quantum efficiency of the image intensifier and CCD camera in the wavelength range of CH^* production (~ 430 nm). The conical flame shape in Figure 4.5.a is seen to move upstream compared to that in Figure 4.2.a, expected as the concentration of CH radicals peaks in the pre-reaction flame zone while OH radicals are typically present within the reaction zone and post-flame region. Given that CH^* chemiluminescence emittance is in the visible spectrum, impurities in the cylindrical quartz confinement tube are also visible.

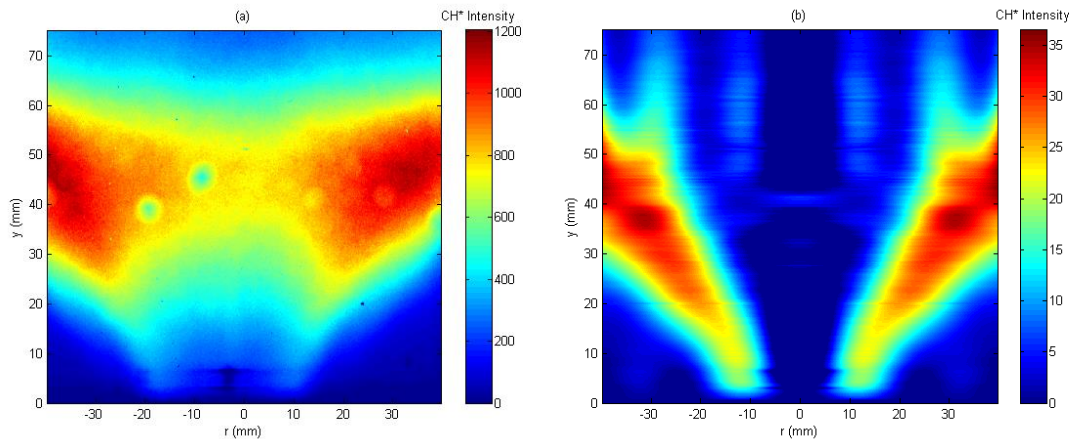


Figure 4.5: Time-averaged CH* chemiluminescence image (a) and after Abel inversion (b) of a 50 kW atmospheric BOS gas flame at $\phi = 0.98$.

Finally, it has been documented that the equivalence ratio can be correlated to the OH* and CH* chemiluminescence intensity for CH₄-air flames [171, 173, 177]. As can be seen in Figure 4.6, the OH* and CH* chemiluminescence integral intensity (calculated per Equation 4.1) peaks near $\phi = 1$, showing good agreement with trends identified in [171] and [173].

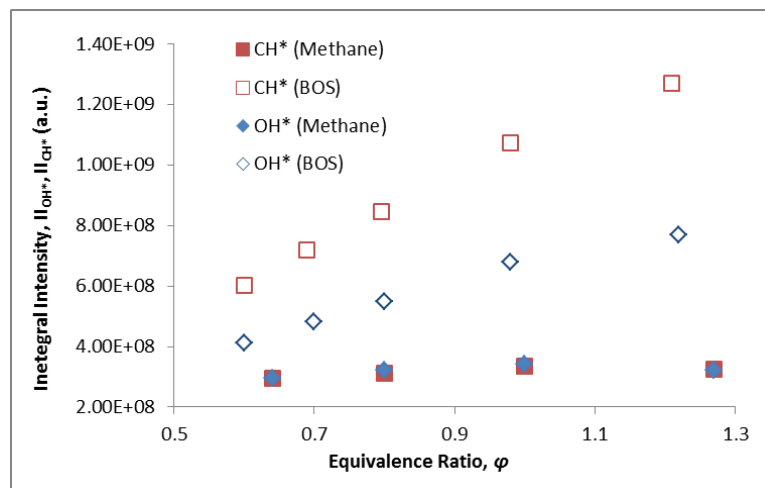


Figure 4.6: Effect of ϕ on the integral intensity of OH* (diamond) and CH* (square) for both CH₄ and BOS gas flames at $T_2 = 285$ K and $P_2 = 0.101$ MPa.

However, it can be seen that the BOS gas flames do not exhibit the same behavior, with the intensity of both OH* and CH* chemiluminescence increasing well past $\phi = 1$. If each of the integral intensity values is normalized by the maximum value observed for that fuel in the dataset, the trend of OH* and CH* variation with ϕ matches the modeled S_L dependence on ϕ , as shown in Figure 4.7.

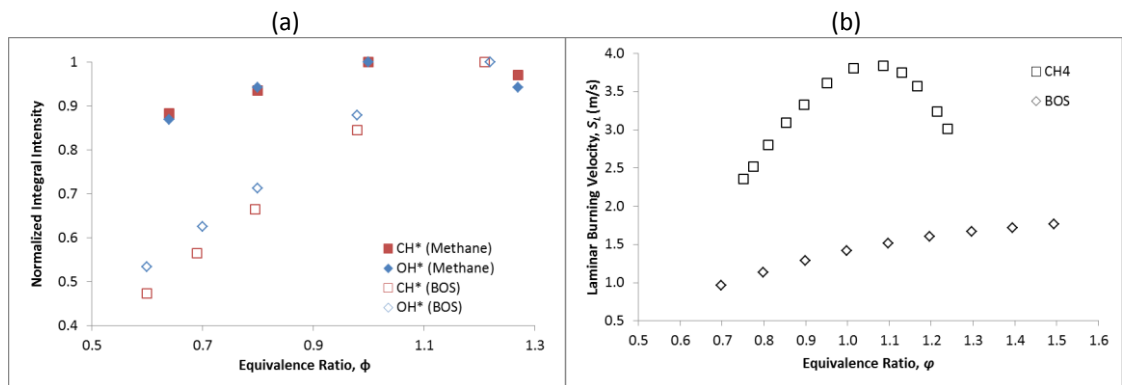


Figure 4.7: Effect of ϕ on normalized integral intensity (a) and S_L (b) of CH_4 and BOS flames at atmospheric temperature and pressure.

The modeled S_L values (Figure 4.7.b) have been compiled from [168], which modeled CH_4 -air flames at 303 K and 0.101 MPa using the GRI Mech 3.0 chemical kinetics mechanism [200] and BOS gas-air flames at 303 K and 0.101 MPa using the Davis mechanism [223]. Note that while the BOS gas composition in [168] varies from that utilized here, the same general response would be expected for high-CO, low H_2 syngas flames. The nonmonotonic dependence of I_{OH^*} and S_L on ϕ for CH_4 -air flames at ambient temperature and pressure can be seen between Figures 4.7.a and 4.7.b, although it should be noted that the CL values peak just below $\phi = 1$ while the modeled S_L peaks just above $\phi = 1$. The modeled laminar flame speed of BOS gas appears to peak at approximately $\phi = 1.5$. While this ϕ was not tested experimentally, the CL trend appears to be similar. The shift in overall flame speed between the two fuels, with methane exhibiting over twice the S_L as BOS gas, also supports the observed heat release distributions shown in Figures 4.2.b and 4.4.a. The heat release distribution represented by OH^* CL is spread over a much wider area in the BOS flame as a result of its slower chemical kinetics compared with the much more compact CH_4 flame.

4.2 Planar Laser Induced Fluorescence Measurement Facility

At Cardiff University's GTRC, an OH PLIF imaging system has been commissioned for use with the HPGSB and HPSBG-2 installed in the HPOC to provide qualitative measures of flame stabilization location, shape, and movement under varying conditions of fuel composition, swirl burner geometry, and operating conditions. The system is based on a dye laser pumped by the frequency-doubled fundamental output of an Nd:YAG laser for species excitation and an intensified CCD camera with associated optics for wavelength filtering of combustion species fluorescence emission. The output beam of the dye laser can be tuned to the desired excitation wavelength before entering sheet forming optics and further into the HPOC and

swirl burner. Additional system design considerations include temperature stability of the laser and imaging system, remote operation during experimentation, and laser safety interlocks.

The PLIF measurement system was first commissioned with swirl-stabilized methane flames in the HPGSB to identify the optimal settings of image intensifier gate timing and gain. PLIF measurements of the OH radical with gate widths down to $t_{gate} = 0.1 \mu s$ were achieved on methane flames with ambient inlet temperature ($T_2 = 288 \text{ K}$), atmospheric inlet pressure ($P_2 = 0.101 \text{ MPa}$), $P_{therm} = 55 \text{ kW}$, and $\phi = 0.7$ and 0.8 . While the laser sheet is used at a fixed location near the burner exit nozzle in the HPGSB, further OH PLIF measurements were made in the HPGSB-2 to commission a scanning PLIF system in which the laser sheet can be traversed via a servo-controlled prism through the camera field of view to image the full flame shape. A parametric study on the use of this servo was undertaken at comparable conditions to the CH_4 flames used in the HPGSB PLIF commissioning. In addition to developing measurement capability, PLIF image processing techniques have also been developed to extract flame characteristic shape, thickness, and area.

4.2.1 System Setup and Components

The PLIF system shown in Figure 4.8 consists of a Quantel TDL-90-NBP2-UVM3 dye laser pumped by the 532 nm output beam of a Spectra Physics GCR 170-10 Nd:YAG laser operating at 10 Hz. The Nd:YAG laser has a pulse duration of 7-10 ns at 532 nm and the resulting linewidth of the TDL-90 dye laser at 560 nm is $\pm 0.005 \text{ nm}$. In order to achieve the required output wavelength for excitation of the OH radical, a solution of Rhodamine 590 dye powder and ethanol was used in the dye laser. This dye solution has a fundamental frequency of 562 nm when pumped by the 532 nm output from the Nd:YAG laser. Through the use of a diffraction grating (2400 lines/mm), the fundamental frequency can be shifted in the dye laser using a remote control with resolution of 0.001 nm. The fundamental frequency is then directed through a frequency-doubling crystal and a Pellin-Broca prism for separation of the required UV wavelength for OH PLIF. The output beam of the TDL-90 was tuned to the excitation wavelength by changing the diffraction grating position to yield a fundamental output frequency near 566 nm from the dye laser. The wavelength of $\sim 283 \text{ nm}$ is used to excite the (1,0) vibrational band of the OH radical, as discussed in Chapter 3.2.1.2. Given the temperature and pressure dependence of the OH ground state population distribution, the dye laser output was tuned near to a specific rotational energy transition, $Q_1(6)$ at 283.010 nm

[186], which has been shown to have a weak temperature dependence of the Boltzmann factor related to the total OH number density [244]. The excitation wavelengths utilized for each fuel blend given in Chapter 3.4.1 at $T_2 = 573$ K and varying P_2 can be found in Table 4.1.

Table 4.1: Dye laser excitation wavelengths for OH PLIF with varying P_2 and fuel type

	P2 (MPa)		
	0.11	0.22	0.33
Fuel	PLIF Excitation Wavelength (nm)		
BASE	283.027	283.027	283.029
FARNG	282.926	282.966	282.919
MIDNG	282.957	282.957	283.029
EMIX1	282.936	282.958	283.029
FARH2	282.929	282.957	282.947

The dye laser output beam is then directed through a set of sheet-forming optics to provide a laser sheet approximately 25 mm in width and 2-3 mm thick. The laser sheet entered the flame volume through a side window of the HPOC with the capture camera focused through the top window of the HPOC, 90° relative to the laser sheet and axial fluid flow. The laser sheet elevation is fixed in the same plane as the burner exit nozzle centerline. Identical to the chemiluminescence measurements, the resulting fluorescence signal was captured through the use of a CCD camera (Dantec HiSense Mk II, 1.3 megapixel resolution) coupled with an image intensifier (Hamamatsu C9546-C03L), 78 mm focal length UV lens (Pentax C91698, f/3.8), and narrow bandpass filter (300-330 nm). Thus, the same 75 mm x 100 mm ($y \times r$) field of view and 13.6 pixels/mm resolution is achieved for PLIF measurements.

The Nd:YAG laser produces pulse energies at 532 nm of 450 mJ/pulse to pump the dye laser at a repetition rate of 10 Hz. The shot-to-shot stability of the Nd:YAG laser energy is 1.5%. Given the significant optical path in the dye laser, the PLIF system produces pulse energies of 10-12 mJ/pulse at 283 nm, which is critical for the experimental rig setup given the size and shape of the HPOC quartz windows and the HPGSB/HPGSB-2 quartz confinement tube. While these laser energy levels have been shown to be sufficient for measurement within the field of view, the shot-to-shot stability of the dye laser is approximately 25%, which influences the output beam profile and resulting laser sheet energy distribution. This is discussed further in terms of PLIF image correction in Section 4.2.2. Refer to Appendix B.2.2, Figure B.14 for the PLIF system utility setup.

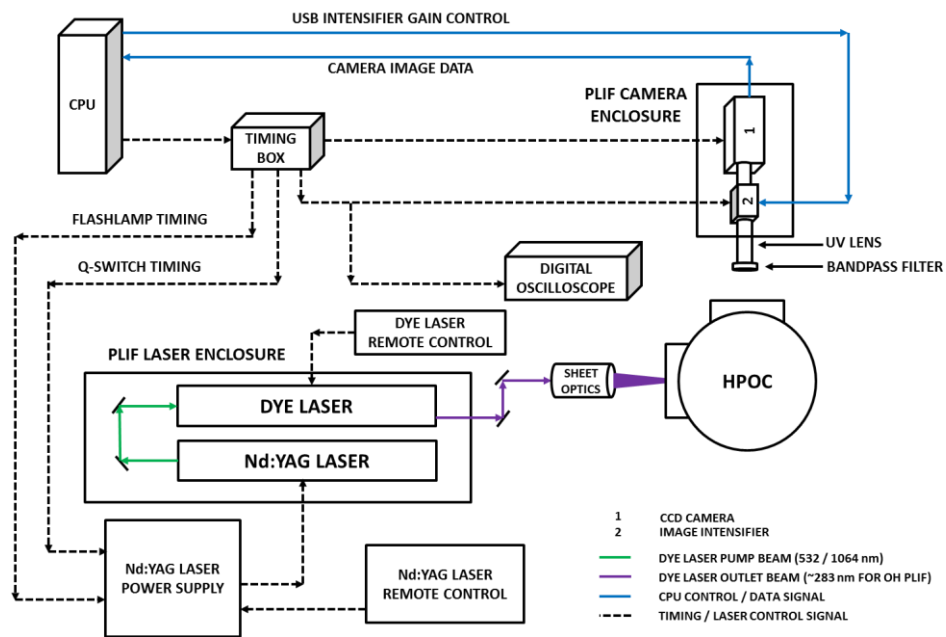


Figure 4.8: Fixed laser sheet PLIF measurement system timing and image capture setup at Cardiff University's GTRC.

Given the short lifetime of the OH radical fluorescence signal (~ 2 ns) and the potential influence of quenching effects, the gate timing of the image intensifier must be significantly lower than for OH* chemiluminescence measurements, and it must be synchronized with the output laser light pulse from the dye laser. The synchronization of the camera shutter, image intensifier gate, Nd:YAG flashlamp, and Nd:YAG Q-switch is controlled by Dantec DynamicStudio software and a Berkeley Nucleonics BNC 575-8C pulse generator to ensure that signal capture was appropriately timed with the dye laser excitation light pulse. A parametric study on the effects of t_{gate} on measured intensity values was conducted and presented in Section 4.2.3. The PLIF system at the GTRC can be fully operated from a remote data capture and timing control computer system outside of the experimental area. For personnel safety, the laser is contained within a bespoke, climate controlled enclosure in the experimental area. A photograph can be found in Appendix B.2.2, Figure B.13.

4.2.2 Image Processing and Data Analysis

Whereas chemiluminescence is a line-of-sight integrated imaging technique, the benefit of PLIF measurements is that the light intensity that is captured by each CCD pixel is the result of a response to an excitation planar light source and therefore yields a real-time representation of the excited species concentration at the location of the light sheet. Therefore, no deconvolution methods must be utilized. The most often utilized method of PLIF image processing and analysis applied here, and described below, involves noise filtering with a 3x3

pixel median filter, background correction, correction for laser light sheet intensity distribution, and temporal averaging. In addition, an edge detection algorithm has also been developed to extract the temporally averaged flame shape and thickness. While images are captured through the use of Dantec's DynamicStudio software, all image processing is conducted using bespoke MATLAB codes, which can be found in Appendix C.3.

Background removal from each instantaneous image was conducted after image filtering. This was achieved by capturing images of the field of view with the laser firing, but without a flame present in the burner. Typically 500 images were captured at 10 Hz and then temporally averaged. This allowed for instantaneous image correction for both the background image intensity and laser light reflections from the cylindrical quartz tube. Note that for PLIF measurements in the HPGSB, the light sheet enters the measurement volume through a side window in the HPOC, perpendicular to the axial flow in the burner. In the HPGSB-2, the laser sheet was angled ($\sim 15^\circ$) to pass through the HPOC side window and the cylindrical quartz confinement from downstream to upstream in the flow direction to reduce the amount of reflected light imposed on the images due to the smaller confinement ID. Both methods still required correction for these reflections.

PLIF images were also corrected for variation in the laser intensity distribution along the planar light sheet. This was required because the laser light intensity across the light sheet does not follow a top-hat distribution and is instead more Gaussian, with higher intensities towards the middle of the light sheet and lower intensity towards the edge of the light sheet. As PLIF intensity is a function of the input laser energy (Equation 3.2), it is therefore necessary to correct the measured intensity values for this energy distribution. This was accomplished first by measuring the laser light sheet profile, fitting a Gaussian distribution to the measured intensity distribution, and then systematically correcting the measured intensity values using this distribution. The Gaussian fit was utilized because it provides a statistically symmetric representation of averaged sheet intensity with a significant fluctuating component due to the shot-to-shot variation in the dye laser energy (25%) which also influences the laser sheet profile shape. The normalized sheet profile was calculated using the average of 500 sheet images. In Figure 4.9, the average laser sheet intensity distribution (Figure 4.9.a) and the Gaussian fit used for image correction (Figure 4.9.b) are given. Note that when applying the normalized Gaussian correction, the extent to which the correction is applied is marked by the

green hashed lines in Figure 4.9.b. These extents are determined by the location of maximum gradient in the Gaussian fit, and correspond to a length along the laser sheet of 24.35 mm.

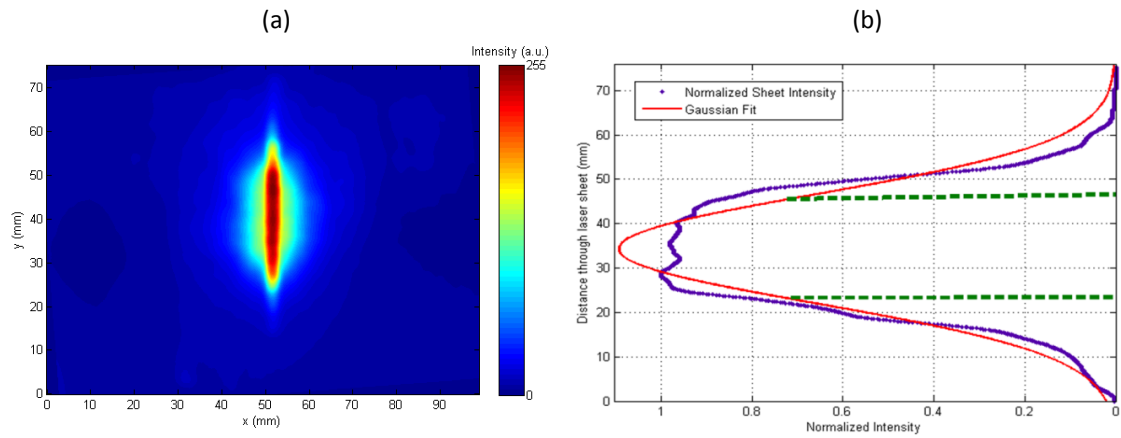


Figure 4.9: PLIF laser sheet intensity (a) and Gaussian fit to intensity distribution (b) for image correction

For all stable operating conditions, 500 instantaneous OH PLIF images are captured and temporally averaged after the correction processes described above are applied. This total image number was selected by statistical analysis of the SNR of the measured maximum OH PLIF intensity, which can be found in Appendix D.2. Note that the number of images used for OH PLIF measurements ($N = 500$) is greater than the number of images used for OH* CL measurements ($N = 200$), thus the measurements have different sampling times (50 s and 20 s, respectively). The shot-to-shot variation in dye laser energy is thought to contribute to the longer PLIF sampling time required for settlement of the SNR ratio, when compared to the CL measurements. In addition, the energy of each laser pulse during the PLIF sampling is not measured, which further requires a longer sampling time as this correction cannot then be applied to the maximum instantaneous OH PLIF intensity value.

Finally, a bespoke image processing technique for the extraction of key flame features has been developed for use with the temporally averaged images. This technique binarizes the OH PLIF image by identifying the location of the maximum OH PLIF intensity in each row of the image and then locating the maximum gradient of OH PLIF intensity on either side of that maximum location. This yields a flame brush thickness, δ_{flame} , for each row which is then averaged over all rows where the maximum OH PLIF intensity level is at least 50% of the overall image maximum OH PLIF intensity. This maximum flame brush thickness corresponds to a reaction progress variable, $\langle c \rangle$, of 0.5, in a usage similar to [93]. The value to $\langle c \rangle$ can be input into the algorithm ($0 < \langle c \rangle < 0.5$) as well to measure different flame surface locations, where $\langle c \rangle = 0$ is the line of maximum OH PLIF intensity and $\langle c \rangle = 0.5$ is the full flame brush

thickness as described above. A flame surface is developed by applying this technique to each image row in which this criterion is satisfied. Using the known image pixel resolution, 13.6 pixels/mm, a pixel area of 0.0054 mm^2 is calculated and a flame area can then be derived from the constructed flame surface. An example of this technique is given in Figure 4.10, for a 42 kW CH_4 -air flame at $T_2 = 573 \text{ K}$, $P_2 = 0.11 \text{ MPa}$, and $\varphi = 0.7$ in the HPGSB-2 with the convergent confinement. In Figure 4.10.a, the OH PLIF intensity distribution has been measured at $t_{gate} = 0.1 \mu\text{s}$ using the scanning OH PLIF method described in Section 4.2.3. The extracted flame surface for a reaction progress variable of $\langle c \rangle = 0.5$ is plotted in Figure 4.10.b and yields a mean flame brush thickness of $\delta_{flame} = 8.58 \text{ mm}$ and a flame area of $A_{flame} = 950 \text{ mm}^2$.

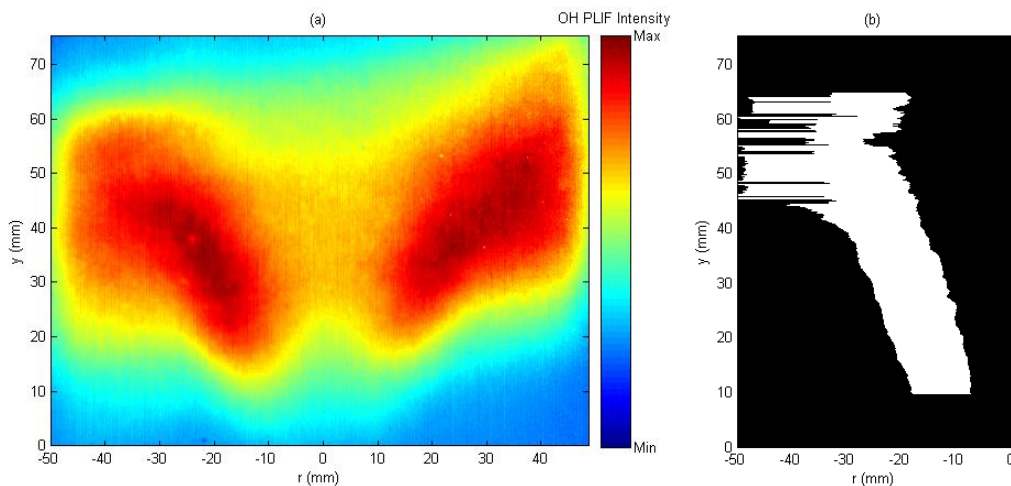


Figure 4.10: Average OH PLIF measurement (a) and extracted flame surface (b) for a 42 kW CH_4 -air flame at $T_2 = 573 \text{ K}$, $P_2 = 0.11 \text{ MPa}$, and $\varphi = 0.7$ in the HPGSB-2 with convergent confinement

4.2.3 System Commissioning

4.2.3.1 PLIF Commissioning in the HPGSB

The OH PLIF system was commissioned first to examine the influence of varying intensifier gate timing on the resulting OH PLIF intensity measurement. This is a critical system parameter as the intensifier gate timing must be synchronized with the excitation laser light pulse while the gate opening time itself, t_{gate} , must be sufficiently long to capture the fluorescence signal yet limited to eliminate the background chemiluminescence signal. This setup is known as “pulsed excitation and integrated detection”, and is the most commonly encountered setup with the distinct advantage of higher laser pulse energies, but limited to lower repetition rates, such as 10 Hz used in this study [162]. Experimental characterization of 55 kW premixed CH_4 -air swirl flames was conducted at $T_2 = 288 \text{ K}$, $P_2 = 0.101 \text{ MPa}$, and $S_g = 0.8$ while studying two equivalence ratios at $\varphi = 0.7$ and $\varphi = 0.8$. The image intensifier gate

timing was varied from $t_{gate} = 1.5 \mu\text{s}$ to $0.75 \mu\text{s}$ to $0.1 \mu\text{s}$ to evaluate statistically its influence on SNR (refer to Appendix D.2) as well as the background chemiluminescence intensity contribution, as the OH PLIF and CL capture wavelengths are nearly identical ($\sim 309 \text{ nm}$) and therefore utilize the same bandpass filter. For all OH PLIF measurements in the HPGSB, the laser sheet is fixed at the burner exit nozzle ($y = 0 \text{ mm}$). Temporally averaged OH PLIF images of the two flames studied is presented in Figure 4.11, with $\varphi = 0.7$ (Figure 4.11.a) and $\varphi = 0.8$ (Figure 4.11.b), captured with $t_{gate} = 0.1 \mu\text{s}$. Figure 4.11 shows two shear layer stabilized flames typical of this swirl burner geometry [113, 114]. An increase in φ leads to increased reactivity in the CH_4 -air flame and thus the areas of highest OH intensity are seen to move radially outward, reducing the amount of OH observed in the CRZ along the burner centerline ($r = 0 \text{ mm}$). A combination of increased S_L and reduced bulk exit nozzle velocity leads to a slight upstream shift in the flame brush as well. The increase in reactivity also reduces the averaged flame brush thickness from 5.98 mm to 5.69 mm and the overall flame area by almost 20%.

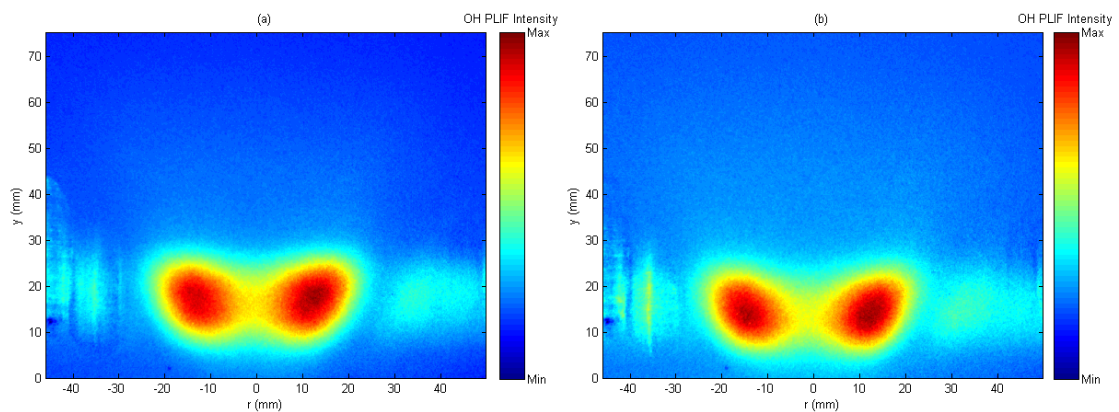


Figure 4.11: Average OH PLIF measurements for a premixed 55 kW CH_4 -air flame at $T_2 = 288 \text{ K}$ and $P_2 = 0.101 \text{ MPa}$, with $\varphi = 0.7$ (a) and $\varphi = 0.8$ (b) in the HPGSB

The gate timing used for evaluation of the flames in Figure 4.12 was selected because it increases the SNR while reducing the chemiluminescence signal captured. From statistical analysis (refer to Appendix D.2), the overall SNR for $t_{gate} = 1.5 \mu\text{s}$ and $0.1 \mu\text{s}$ at $N = 500$ images is seen to be nearly similar, with $t_{gate} = 0.75 \mu\text{s}$ showing the lowest SNR. While a high SNR is advantageous, the longer gate time will result in higher CL signal, which will interfere with the measured PLIF intensity, as shown in Figure 4.12, which plots I_{OH^*} against t_{gate} for the two flames shown in Figure 4.11, with a more significant reduction up to 20% of the CL signal that could interfere with the measured PLIF signal at $\varphi = 0.8$ as t_{gate} is reduced. As a result of this study, the gate timing was set at $t_{gate} = 0.1 \mu\text{s}$ for all further OH PLIF measurements in both the HPGSB and HPGSB-2.

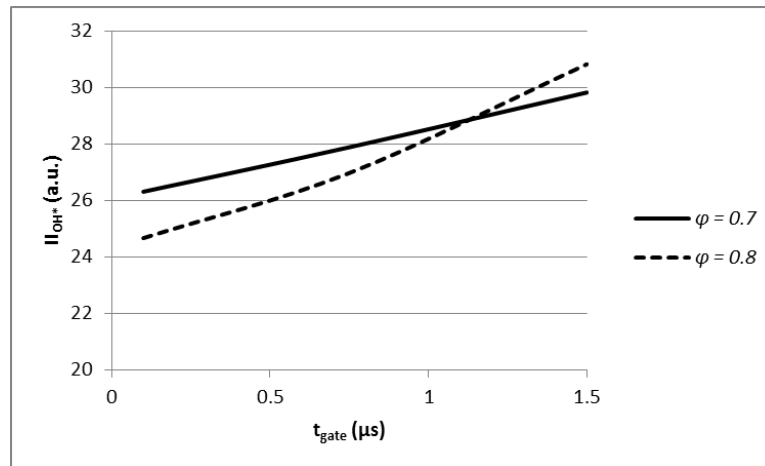


Figure 4.12: I_{OH^*} measurements as a function of t_{gate} for a premixed 55 kW CH₄-air flame at $T_2 = 288$ K, $P_2 = 0.101$ MPa, and $\phi = 0.7$ (a) and 0.8 (b)

4.2.3.2 PLIF Commissioning in the HPGSB-2

While OH PLIF measurements in both the HPGSB and HPGSB-2 can be made with the laser sheet fixed at the immediate burner exit, a scanning OH PLIF system was commissioned in the HPGSB-2 to capture the variation in OH PLIF intensity along the axial direction of the field of view. This technique was accomplished by installing a servo on the output prism of the TDL-90 dye laser. All other components were the same as in Figure 4.8. This servo manipulates the angle of the output prism of the dye laser, effectively scanning the resulting laser sheet from the burner exit nozzle in the downstream direction. A schematic of the scanning OH PLIF system and a photograph of the servo installation can be found in Appendix B.2.2, Figure B.18.

At the start of each scanning PLIF measurement, a trigger signal from the image capture system is sent through the BNC 575-8C pulse generator to a Pololu Maestro servo controller, for which a script has been written to accept the trigger pulse and accurately control the servo position during image capture. The servo controller is capable of driving the PLIF laser sheet through multiple passes in the field of view based on user input. The system was commissioned for use with the HPGSB-2 (open cylindrical confinement) with a 42 kW premixed CH₄-air swirl flame at $T_2 = 288$ K, $P_2 = 0.11$ MPa, and $S_g = 0.8$ while studying the influence of multiple laser sheet passes at equivalence ratios of $\phi = 0.64, 0.7,$ and 0.8 . Given the image capture rate of 10 Hz and the need for at least 500 images, a sweep rate of 1.5 mm/s allowed a single pass from the burner exit nozzle to the downstream edge of the field of view ($y = \sim 75$ mm). A sweep rate of 3 mm/s yielded two passes from the burner exit nozzle to the downstream edge before returning to the burner exit nozzle. A final sweep rate of 4.5 mm/s was also examined, which yielded three passes through the field of view. The captured

images are then corrected and averaged using the techniques described previously, with example OH PLIF images captured with two passes shown in Figure 4.13 at $\varphi = 0.64$ (Figure 4.13.a), 0.7 (Figure 4.13.b), and 0.8 (Figure 4.13.c). Note that only one half of the temporally averaged OH PLIF image is shown from each flame in Figure 4.13. In comparison with the fixed laser image in Figure 4.11, it was possible to image the entire shear-layer stabilized flame brush within the field of view with this method. This includes the identification of increased flame brush thickness and OH PLIF intensity shift into the ORZ as the flame moves towards LBO, resulting in a transition in overall flame shape from a V-shape to an M-shape as reactivity decreases and bulk exit velocity increases (moving from Figure 4.13.c to Figure 4.13.a).

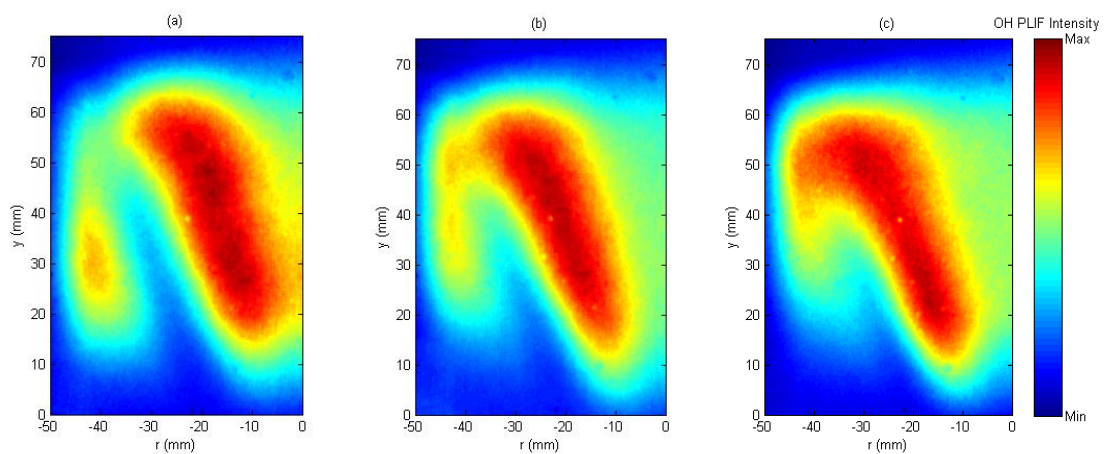


Figure 4.13: Averaged images using scanning OH PLIF method (with 2 passes) of a 42 kW CH₄-air flame at $T_2 = 288$ K, $P_2 = 0.11$ MPa, and $\varphi = 0.64$ (a), 0.70 (b), and 0.80 (c)

The number of sweeps utilized in the measurement of the averaged flame brush in Figure 4.13 was selected as two based on a comparison between measured flame characteristics and fundamental flame properties predicted by chemical kinetics modeling as described in Chapter 3.3.1. For this comparison, the modeled reaction zone thickness, δ_r , is compared with the flame brush thickness at the location of maximum OH PLIF intensity for each laser sheet sweep rate given previously. Traditionally defined by the normalized maximum temperature gradient in the premixed and reaction zones [224], a new definition of reaction zone thickness is proposed in Figure 4.14 as the one-dimensional axial distance between the preheat zone (represented by the peak CH molar concentration) and the reaction zone (represented by the peak OH molar concentration). Figure 4.14 represents the modeled conditions for the CH₄-air flame in Figure 4.13.c (42 kW, $T_2 = 288$ K, $P_2 = 0.11$ MPa, and $\varphi = 0.80$). Further discussion on the use of this definition is provided in Chapter 6 in regards to the influence of C₂₊ molecules in natural gas on combustion measurements, particularly NO_x emissions.

A comparison between flame brush thickness at the location of maximum OH PLIF intensity and reaction zone thickness is presented in Figure 4.15.a along with a comparison between the axial location of the maximum OH PLIF intensity and the 1-D axial location of the modeled maximum OH PLIF mole fraction, Figure 4.15.b. While the intention is not for these compared quantities to be equivalent, instead the physical trends can be identified. As φ increases, the S_L increase is coupled with lowered bulk flow velocity, shifting the location of the maximum OH PLIF intensity upstream. In addition, with increased reactivity, the flame brush thickness would be expected to reduce with increased φ as well.

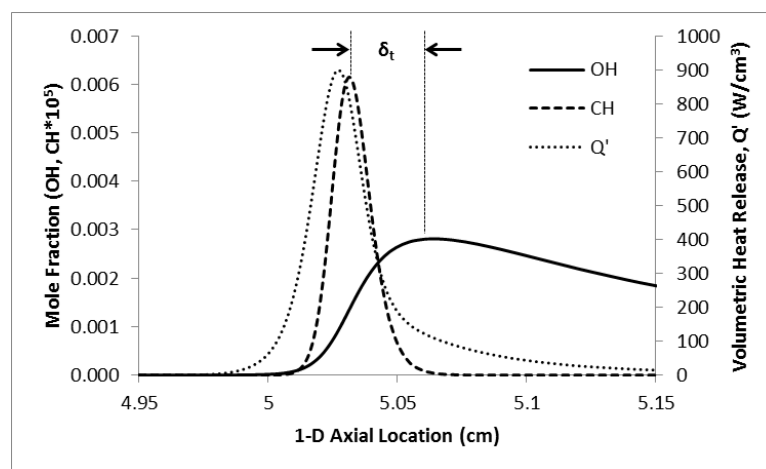


Figure 4.14: Defining the reaction zone thickness, δ_t , based on maximum CH and OH mole fraction location in one-dimensional flame model from CHEMKIN PREMIX code. Modeled conditions for CH_4 -air flame shown in Figure 4.22.c.

These physical phenomenon are best represented by the mean flame brush and OH PLIF intensity distribution constructed from the two pass scanning OH PLIF measurement, both of which show positive correlation (represented by the positive slope between modeled value and measured value) with the modeled reaction zone thickness, Figure 4.15.a, and the modeled maximum OH mole fraction location, Figure 4.15.b. While the resulting averaged OH PLIF distribution and flame brush from all three sweep rates are able to capture the modeled flame response at $\varphi = 0.8$, the response diverges as the equivalence ratio decreases, with only the two pass method following the expected physical trends. Not only does this brief study support the use of two passes for all subsequent scanning OH PLIF measurements, it also supports the use of the reaction zone thickness, δ_t , defined in Figure 4.23 for further study.

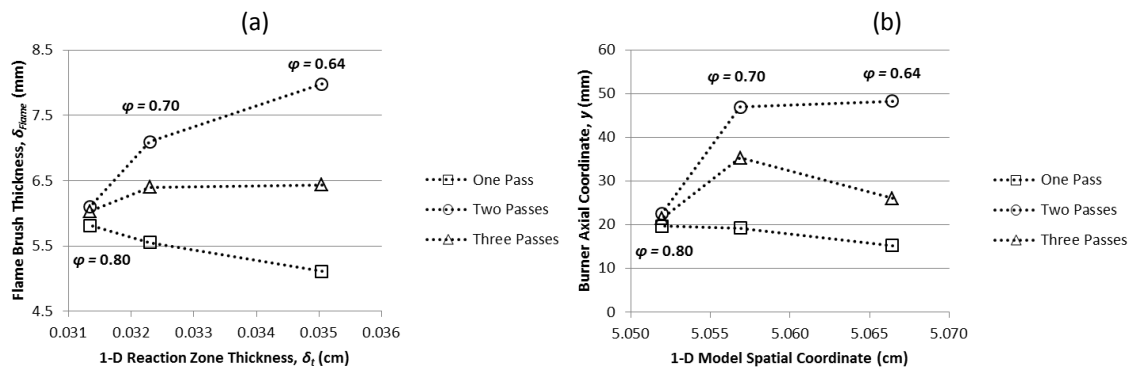


Figure 4.15: Comparisons between measured δ_{flame} at the maximum OH PLIF intensity location and modeled δ_t (a) and between axial location of maximum OH PLIF intensity and modeled maximum OH mole fraction location (b) for a 42 kW CH₄-air flame with varying number of scanning PLIF passes

4.3 Dynamic Pressure Measurement Facility

At Cardiff University's GTRC, a new dynamic pressure measurement facility has been commissioned for use with the HPGSB and HPSBG-2 installed in the HPOC to provide quantitative measures of combustion, flow, and rig acoustics, including dynamic pressure spectra, dominant frequencies, amplitudes, and thermoacoustic instability indicators with varying fuel composition, swirl burner geometry, and operating conditions. The system is based on four DPTs placed at strategic locations within the swirl burner and HPCR. Measurements are made by a dedicated computer system that performs real-time signal analysis while post-processing is performed in MATLAB. Additional system design considerations include proper electrical grounding and isolation of each DPT as well as the use of semi-infinite tubing coils to dampen the influence of reflected waves passing the DPT.

The dynamic pressure measurement system was commissioned with isothermal air flow experimentation in the HPGSB, with a single DPT installed in the HPGSB pilot lance. In addition to identifying the need for appropriate electrical grounding of the DPT, this study also investigated the influence of burner geometric swirl number on measured dominant frequencies, and suggests a mechanism for collapsing frequency measurements across varying geometric swirl numbers. An isothermal flow characterization of the HPGSB-2 was also conducted for two geometric swirl numbers with a fixed convergence nozzle confinement. For isothermal air flow characterization of the HPCR and open-confinement HPGSB-2, refer to Chapter 5.2.1.1.

4.3.1 System Setup and Components

In addition to the non-intrusive optical techniques described previously, four DPTs were installed at critical locations throughout the HPGSB-2 and HPCR in order to adequately characterize flame dynamics and acoustic response within the system, as shown in Figures 4.25 and 4.26. The four locations are designated as “Plenum” with the DPT measurement location at the fuel/air inlet to the HPGSB-2, “Pilot” with the DPT measurement location within the instrumented bluff body pilot lance in the burner exit nozzle, “Burner Face” with the DPT measurement location in the same axial plane as the “Pilot” DPT on the OD of the ceramic coating covering the swirler within the combustor, and finally “Exhaust” with the DPT measurement location at the exit of the quartz confinement tube. Each DPT was fixed in a machined Swagelok tee and separated from the measurement location by an impulse line of 980 mm length for thermal protection of the DPT, as shown in Figure 4.16. Further detail on the location of the “Pilot” and “Burner Face” DPTs can be seen in Figure 4.17. As can also be seen in Figure 4.16, each DPT utilizes a semi-infinite tubing connection made from 3 mm x 10 m (D x L) copper tubing capped at one end for attenuation of reflected acoustic waves [225-227].

The “Plenum”, “Pilot”, and “Burner Face” DPTs are PCB 113B28 with 500 kHz resonant frequency, 14.5 mV/kPa sensitivity ($\pm 15\%$), and 0-350 kPa range. The “Exhaust” DPT is a PCB 112A22 with 250 kHz resonant frequency, 14.5 mV/kPa ($\pm 15\%$), and 0-350 kPa range. Each DPT was connected via low noise coaxial cable to a PCB 482C05 signal conditioner and output voltages are measured via a dedicated National Instruments DAQ (PXI-6123) and processed in for real-time viewing in a bespoke National Instruments LabVIEW program. Photographs of the installation are also provided in Appendix B.2.1, Figures B.10 and B.11.

for monitoring of the experiment and identifying transitions from stable to unstable conditions as the burner operation is manipulated. For each stable experimental condition, 240000 dynamic pressure measurements were captured at a rate of 4 kHz for a total sampling time of 60 seconds at each of the 4 measurement locations. In addition, at selected stability transitions, the DPT system was placed into a constant 4 kHz capture mode in order to resolve the transition from stable to unstable operation as φ was changed. This measurement technique allows for the application of various analytical techniques and emphasis is placed on defining the limitations and benefits of both frequency and time domain signal analysis in the observation of thermoacoustic instabilities.

In addition to the real-time signal processing performed in LabView, bespoke MATLAB codes were created for post-processing of the captured dynamic pressure values in both the frequency and time domains. This code can be found in Appendix C.4 and performs both frequency and time domain analysis on the captured dynamic pressure signal. The code allows for bandpass and high pass filtering of the measured signal, but also performs all time and frequency domain analysis on the full input signal. The code includes a dominant frequency extraction algorithm using a peak-finding function, to extract the dominant frequency and amplitude in a given frequency band (or the entire signal). The function also outputs the full signal pressure RMS (p'_{RMS}) and kurtosis (K) value, as described in Chapter 3.2.2.1. Furthermore, a time division can be input for which the time varying RMS ($p'_{RMS}(t)$) and kurtosis ($K(t)$) values of each bin is calculated. Full signal, bandpass, and high pass FFTs and PSDs are created and plotted. The dominant frequencies are identified in all FFT and PSD plots, along with their corresponding amplitudes.

4.3.3 System Commissioning

The DPT measurement system was first commissioned with a single DPT (PCB 112A22) installed in the HPGSB at the “Pilot” location. Isothermal air flow ($T_2 = 293$ K, $P_2 = 0.101$ MPa) testing was first conducted with a variety of swirl numbers ($S_g = 0.8, 1.04, \text{ and } 1.47$) to observe the measured dominant frequency response at air flows from $\dot{m}_{air} = 17.3 - 96.3$ g/s. The Pilot DPT output was monitored with a Tektronix TDS 2024B digital oscilloscope, which performs a FFT of the input voltage signal and uses a Hanning window to plot the output. The peak frequency was then noted from the oscilloscope output, yielding the dominant frequency (f_{peak}) response plotted versus the mean burner exit nozzle velocity, \bar{u} , in Figure 4.18.a. The linear relationship between \bar{u} and f_{peak} yields an approximately constant Strouhal number for

each swirl number, $St = 1.6, 1.9,$ and 2.3 for $S_g = 0.8, 1.04,$ and $1.47,$ respectively. This is indicative of a Kelvin-Helmholtz shear layer instability, possibly related to vortex shedding from the burner exit nozzle [68], with an obvious S_g influence. The measured f_{peak} can be corrected for swirl number by considering that the mean flow velocity is composed of both an axial and tangential component and the swirl number broadly represents the ratio of angular to axial momentum flux. Thus, normalization by $\sqrt{1 + S_g^2}$ results in collapse across swirl numbers in both the dominant frequency, as shown in Figure 4.18.b, and the Strouhal number, $St = 1.3$.

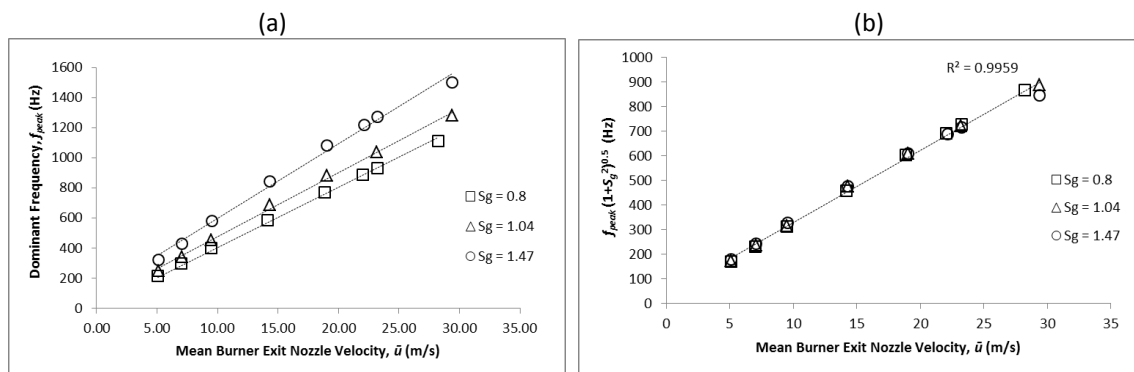


Figure 4.18: Influence of \bar{u} and S_g on measured Pilot DPT f_{peak} for isothermal air flow study in the HPGSB, with values unscaled (a) and correct (b) to account for swirl.

The full DPT measurement system was similarly commissioned in the HPGSB-2, with ambient and preheated isothermal air flow experimentation conducted with swirl numbers of $S_g = 0.5$ and 0.8 and air mass flow conditions matching those presented in Table 3.3 up to $P2 = 0.33$ MPa. For the results in Figure 4.19, the convergent nozzle confinement was utilized, which is expected to result in a different flow field within the burner compared with the open confinement due to the influence on coherent structures in the flow field [128]. The FFT of the Burner Face DPT measurement for $\varphi = 0.55$ air mass flow (78.75 g/s) at $T2 = 573$ K and $P2 = 0.33$ MPa is presented in Figure 4.19 for both $S_g = 0.5$ and 0.8 .

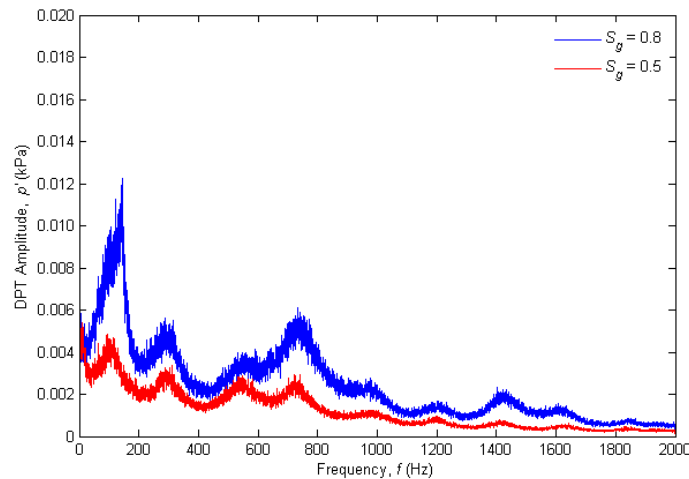


Figure 4.19: FFT of Burner Face DPT measurement for isothermal air flow in the HPGSB-2 with varying swirl number

The bulk exit nozzle velocity is held constant between these two conditions, $\bar{u} = 31$ m/s, but variation in pressure amplitude is apparent with $p'_{RMS} = 0.964$ kPa and 0.531 kPa for $S_g = 0.8$ and 0.5, respectively. This suggests that the swirl component dominates the flow fluctuation in the convergent nozzle case, instead of the vortex shedding observed in Figure 4.31. This is supported by considering the normalized pressure amplitude, p'_{RMS}/P_2 for all air flow cases and both swirl numbers in Figure 4.20. The normalized pressure amplitude can be directly scaled by $1/S_g$ to improve the collapse between both swirl numbers, differing from the $\sqrt{1 + S_g^2}$ scaling used in the case of an open cylindrical confinement. Variation within each pressure band is due to the three air temperatures examined, 293 K, 493 K, and 573 K. The trend of increased DPT amplitude with increasing pressure is expected due to higher turbulence with increased Reynolds number. Further isothermal work characterizing the HPCR resonant acoustics and the response of the HPGSB-2 with open confinement is presented in Chapter 5.2.1.1 as it pertains specifically to the LBO study presented as part of the commissioning of the HPGSB-2.

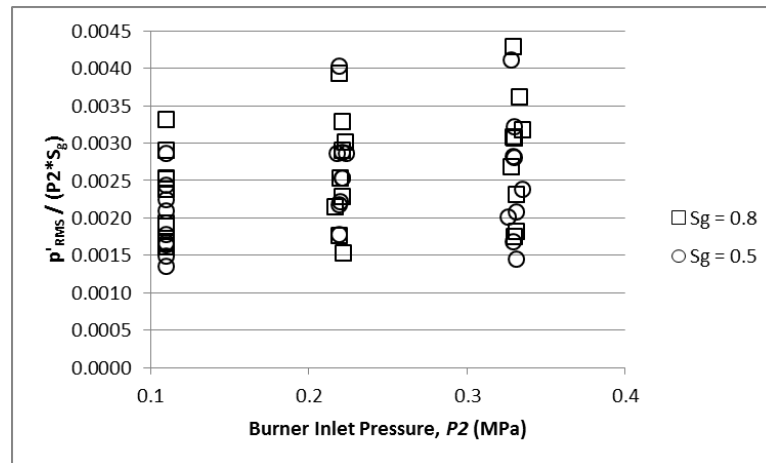


Figure 4.20: Swirl-corrected normalized pressure amplitude as a function of P_2 and S_g for isothermal air flow at 0.11 MPa, 0.22 MPa, and 0.33 MPa

4.4 Chapter Summary

The development and commissioning of a chemiluminescence imaging system for the study of atmospheric and pressurized swirl flames at Cardiff University's GTRC was completed through experimental combustion studies of both premixed CH_4 -air and high CO syngas-air flames in the HPGSB. Both OH^* and CH^* measurements were taken to demonstrate the following:

- 1) Validation of system equipment settings and image processing procedure, including background removal, temporal averaging, and deconvolution using an Abel inversion algorithm.
- 2) The influence of fuel composition, equivalence ratio, and pressure on chemiluminescence signal intensity, flame shape, and stabilization location.
- 3) Comparison of chemiluminescence signal intensity between two fuels that differ greatly in composition and reactivity shows that variation in integral intensity with equivalence ratio follows the same trend as the variation in modeled S_L with ϕ .

An OH PLIF system has also been installed and commissioned for the study of swirl flames in the HPCR. Commissioning was completed in two phases. First, the fixed laser sheet OH PLIF system was commissioned on atmospheric pressure, ambient temperature premixed CH_4 -air flames in the HPGSB to evaluate flame stabilization at the burner exit nozzle. Second, the scanning laser sheet OH PLIF system was commissioned on atmospheric pressure, ambient temperature premixed CH_4 -air flames in the HPGSB-2 for imaging of the entire flame volume within the field of view. OH PLIF measurements were taken to demonstrate the following:

- 1) Validation of system equipment settings and image processing procedure, including image intensifier gate timing, appropriate number of samples, image correction for variations in laser light sheet intensity distribution, temporal averaging, and extraction of physical flame details using a maximum intensity gradient algorithm.
- 2) The introduction of a new reaction zone thickness which is positively correlated with the mean flame brush thickness resulting from two passes of the scanning OH PLIF system.
- 3) The influence of equivalence ratio on atmospheric CH₄-air flame shape and stabilization location, including the observed transition from V-shape to M-shape as LBO is approached, and an increase observed in the OH PLIF intensity in the ORZ.

Finally, a dynamic pressure measurement facility has been significantly upgraded from a previous system for the study of flame and rig acoustics in the HPGSB/HPGSB-2. Isothermal air flow testing was first conducted in the HPGSB and HPGSB-2. Dynamic pressure measurements were made, demonstrating the following:

- 1) Validation of system equipment settings and signal processing procedure, including pressure transducer electrical isolation, semi-infinite line setup, frequency domain analysis (e.g. FFT and dominant tone extraction), and time domain analysis.
- 2) The influence of swirl number on the dominant frequency extracted from isothermal air flow testing in the HPGSB, and suggested scaling methodology to account for velocity components in swirling flows.
- 3) The influence of confinement geometry on measured dynamic pressure amplitudes and frequency content, in particular the dominant isothermal flow frequency, which appears to be driven by vortex shedding in the open confinement case and tangential velocity in the convergent confinement case.

CHAPTER 5 – CHARACTERIZATION OF NEW GENERIC SWIRL BURNERS

In addition to the commissioning of new non-intrusive combustion diagnostics systems at Cardiff University's GTRC as detailed in Chapter 4, two new high pressure generic swirl burners (HPGSB and HPGSB-2) have also been commissioned as part of this work. The reader is referred to Chapter 3.1.2 for detail regarding the design of these swirl burners. In this chapter, a brief experimental combustion study [118] undertaken during the commissioning of the HPGSB is first presented. In this study, pure methane and propane, both important constituents in natural gas and LNG, were burned under ambient conditions of inlet temperature and pressure to evaluate the change in flame stabilization and exhaust emissions. For further experimental characterization of the HPGSB, the reader is directed to additional studies [112-117, 119-121].

Given that a majority of the remaining experimental fuel flexibility work presented in this study utilized the HPGSB-2 exclusively, a comprehensive isothermal and pure methane combustion characterization is presented in this Chapter, including the identification of both a repeatable LBO instability and thermoacoustic instability. Isothermal characterization is carried out with acoustic, flow structure, and turbulence measurements. Combustion characterization is conducted at ambient and elevated conditions of temperature up to 573K and pressure up to 0.2 MPa. This study of the behavior of the HPGSB-2 operating on pure methane informs the fuel flexibility studies in Chapters 6 and 7, as well as providing a case study for comparison with low-order thermoacoustic modeling in Chapter 8.

5.1 High Pressure Generic Swirl Burner (Mk. I)

The 1st generation HPGSB was commissioned at the GTRC in 2014 after extensive design and development to increase the geometric scale of this burner from the AGSB [55-57, 110-112], and has supported numerous experimental campaigns [112-121]. As previously detailed in Chapter 3.1.2, the HPGSB is a radial-tangential swirl burner capable of pressurized operation with a cylindrical quartz confinement that allows optical access when installed in the HPOC. As part of the HPGSB commissioning, an experimental study on the flame stability and exhaust gas emissions of fully premixed methane and propane flames at ambient conditions was undertaken. This provides a baseline for comparison with the 2nd generation high pressure

generic swirl burner (HPGSB-2) which is detailed further in this Chapter. In addition, a scaling factor based on fuel molar hydrogen-to-carbon ratio (H:C) is identified for collapse of OH* chemiluminescence intensity measurements between CH₄-air and C₃H₈-air flames, which is then further validated for the variety of natural gas blends of these pure constituents (and thus variable H:C ratios) in Chapter 6 as well as CH₄-H₂ mixtures in Chapter 7.

5.1.1 Combustion Characterization

For the methane and propane fuels used in this commissioning study, selected characteristics such as molar mass, density (ρ), lower heating value (LHV), stoichiometric air-fuel ratio (AFR_{mass}) as well as molar and mass hydrogen to carbon (H:C) ratios, are given in Table 5.1. All pressure and temperature dependent values in Table 5.1 are calculated at 0.101 MPa and 288 K. WI was calculated per BS EN ISO 6976-2005 [25].

Table 5.1: Selected methane and propane fuel characteristics for HPGSB commissioning

Fuel	Fuel Blend Components (% vol)		Molar Mass (kg/kmol)	Density, ρ (kg/m ³)	LHV (MJ/kg)	WI (MJ/m ³)	Molar H:C Ratio	Mass H:C Ratio	Stoichiometric AFR_{mass}
	CH ₄	C ₃ H ₈							
CH ₄	100	0	16.043	0.680	50.03	50.72	4.000	0.336	17.26
C ₃ H ₈	0	100	44.097	1.899	46.34	76.83	2.667	0.224	15.66

Table 5.2 specifies the main HPCR operating condition ranges for these fully premixed fuel-air combustion experiments. Note that the mean burner exit nozzle velocity, \bar{u} , is calculated based on the total premixed volumetric flow through the burner exit nozzle with diameter of $D_{noz} = 40$ mm. The subsequent Reynolds number is calculated per Equation 5.1 below,

$$Re = \frac{\bar{u}D_{noz}\rho_{premix}}{\mu_{premix}} \quad (5.1)$$

where ρ_{premix} is the total premixed reactant density and μ_{premix} is the total premix dynamic viscosity calculated per the Wilke correlation [228] and utilizing individual component viscosities from the NIST Chemistry WebBook [229].

Table 5.2: HPCR conditions for methane and propane commissioning of the HPGSB

Fuel Type (%vol)	Confinement	S_g	P_2 (MPa)	T_2 (K)	P^{therm} (kW)	ϕ	\bar{u} (m/s)	Re ($\times 10^3$)	$\dot{m}\sqrt{T_2/P_2}$
CH ₄ (100)	Open Cylindrical	0.8	0.101	288	55	0.53 - 0.8	17 - 25	45 - 67	0.42 - 0.63
C ₃ H ₈ (100)	Open Cylindrical	0.8	0.101	288	56	0.53 - 0.8	16 - 24	45 - 67	0.42 - 0.63

Chemical kinetics modeling of the laminar flame speed, S_L , and adiabatic flame temperature (AFT) for the as-tested experimental conditions was conducted per Chapter 3.3.1 to provide a fundamental reference for the observed changes in flame stabilization location, heat release indicators, and exhaust gas emissions. The resulting S_L for these two fuels is plotted against AFT in Figure 5.1 along with the experimental equivalence ratio. Under these conditions, propane is observed to have a 60-80% increase in S_L compared to methane under lean conditions below $\phi = 0.7$, with a slight increase in propane AFT for a fixed equivalence ratio, a trend which has been observed by others [37].

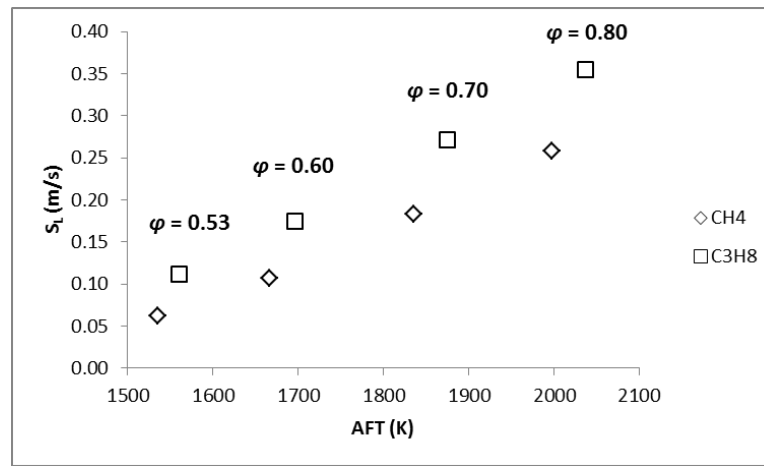


Figure 5.1: Chemical kinetics modeling of S_L as a function of AFT for LPM CH₄-air and C₃H₈-air flames

The increase in fundamental reactivity from methane to propane as suggested by the chemical kinetics model influences the measured flame stabilization characteristics under the given experimental conditions. Fixed laser sheet OH PLIF measurements at the immediate outlet of the burner exit nozzle ($y = 0$ mm) are given for all conditions investigated in Figure 5.2. Note that OH PLIF measurements of the CH₄-air flame at $\phi = 0.53$ and $\phi = 0.60$ could not be made because the flame stabilization location moved from the burner exit nozzle into the cylindrical quartz confinement, out of the plane of the excitation laser sheet. This is supported by the full field of view OH* chemiluminescence results presented in Figure 5.3, which show that localized heat release areas have stabilized more than 25 mm downstream of the burner exit nozzle. At $\phi = 0.70$, the CH₄-air flame transitions back to a stabilization location at the burner exit nozzle, along the shear layer between the CRZ and ORZ. Further increase in ϕ sees the area of high OH PLIF intensity shift further upstream towards the burner exit nozzle. This is in contrast to the behavior of the C₃H₈-air flame under lean conditions ($\phi < 0.7$), which appears to transition from a CRZ/ORZ stabilized flame at low ϕ to a shear-layer stabilized flame at increased ϕ . In all cases, the C₃H₈-air flame stabilizes further upstream than the CH₄-air flame, which has been noted for laminar flame experiments where the bulk velocity has been

maintained [230], and may be linked to the low temperature oxidation chemistry of propane, which promotes intermediate radical (including OH) formation [230, 231].

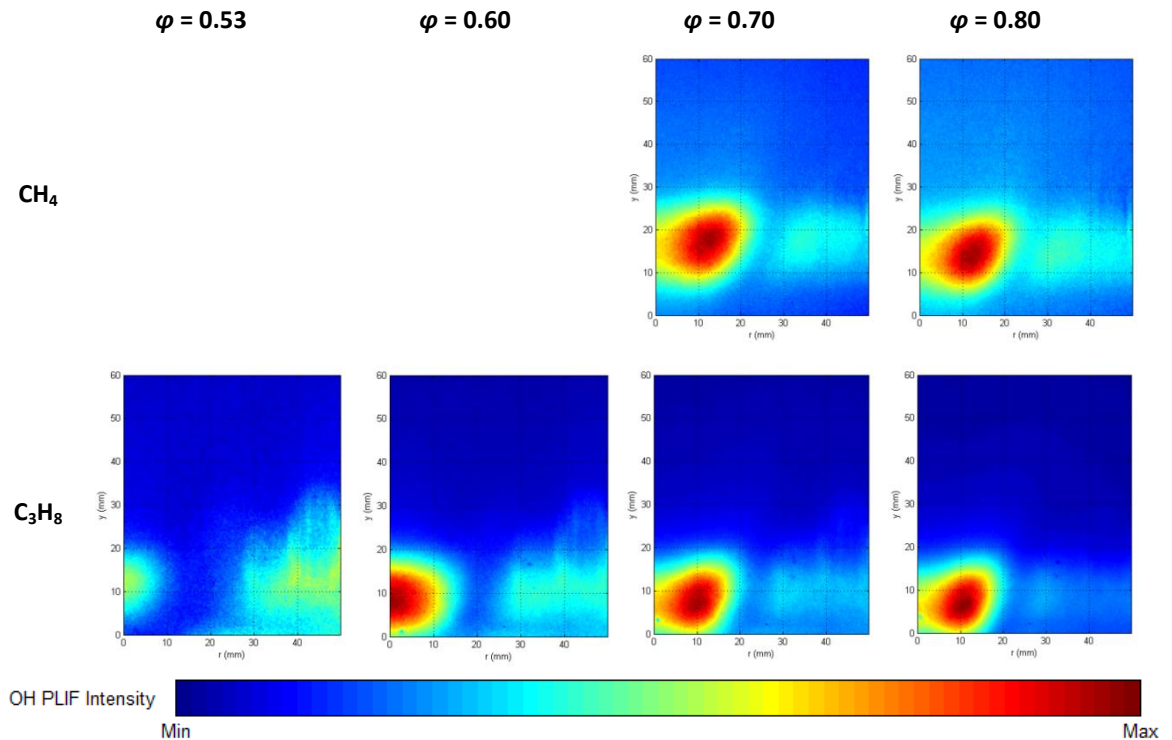


Figure 5.2: Fixed sheet OH PLIF measurement of LPM CH₄-air and C₃H₈-air flames in the HPGSB at $T_2 = 288$ K, $P_2 = 0.101$ MPa, $S_j = 0.8$, and varying ϕ

The overall transition of the areas of localized heat release with an increase in equivalence ratio (and corresponding reduction in \bar{u} and Re) is visible in the Abel-transformed OH* chemiluminescence images in Figure 5.3. A similar upstream shift between CH₄ and C₃H₈ is noted as in Figure 5.2 as well as the transition from CRZ stabilized to CRZ/ORZ stabilized to shear layer stabilized with increasing equivalence ratio, with nearly identical heat release structure between the two fuels at $\phi = 0.8$.

From the temporally-averaged OH* chemiluminescence images, an integral intensity is calculated per Equation 4.1 and related to the equilibrium AFT calculated via kinetics modeling in Figure 5.4. As expected based on the increased heat release rate and increased CH radical formation in the C₃H₈-air flame, the measured OH* intensity is higher across all conditions compared to the CH₄-air flame. It is possible to account for the influence of fuel composition that yields the offset seen in Figure 5.4.a by scaling the integral intensity by the fuel molar hydrogen to carbon ratio (H:C)³, with the cubic exponent selected as this results in a correlation coefficient close to unity. This collapse highlights the potential for this fundamental fuel property to characterize premixed flame response.

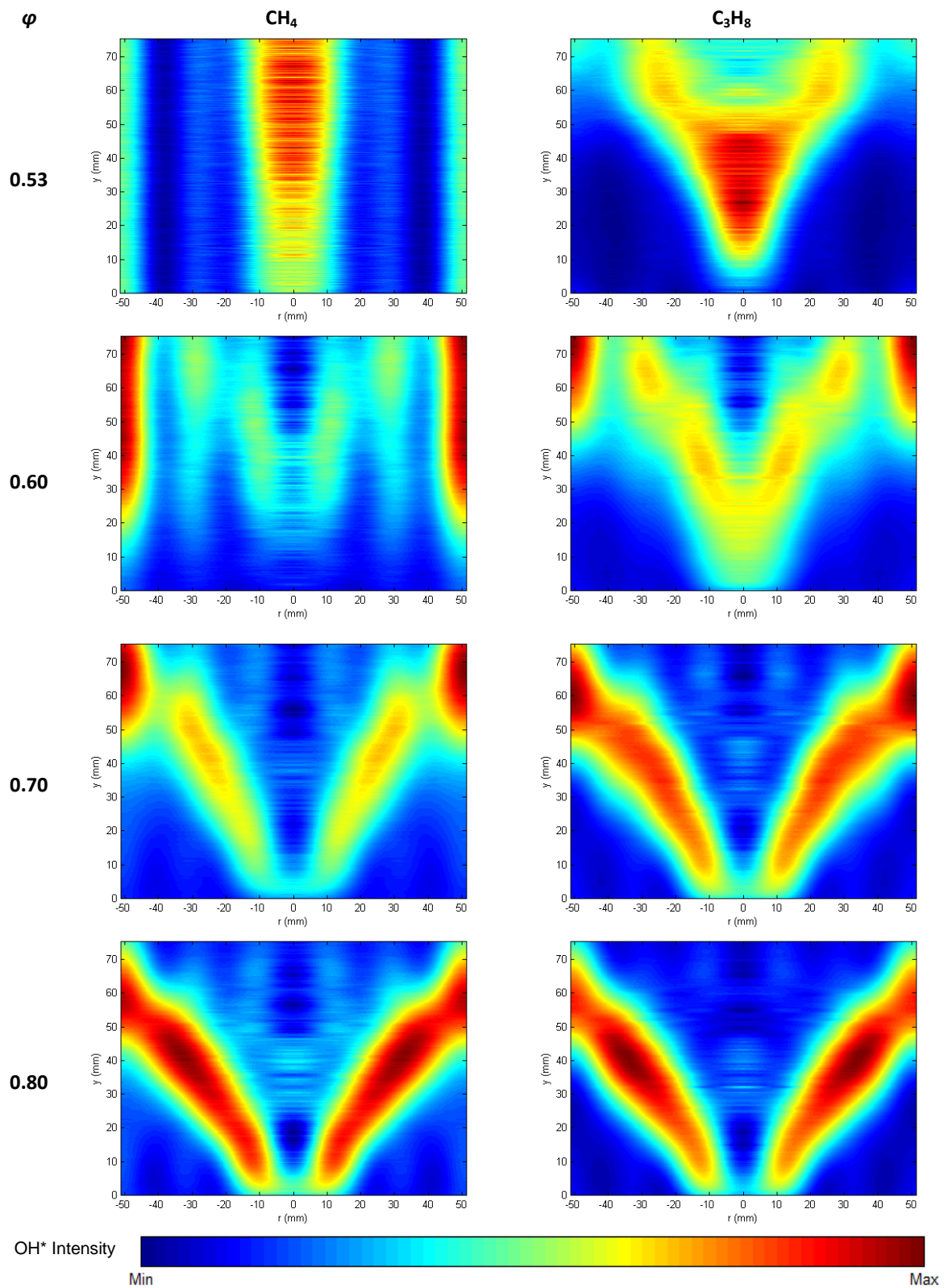


Figure 5.3: Abel transformed OH^* chemiluminescence of LPM CH_4 -air and C_3H_8 -air flames in the HPGSB at $T_2 = 288 \text{ K}$, $P_2 = 0.101 \text{ MPa}$, $S_g = 0.8$, and varying φ

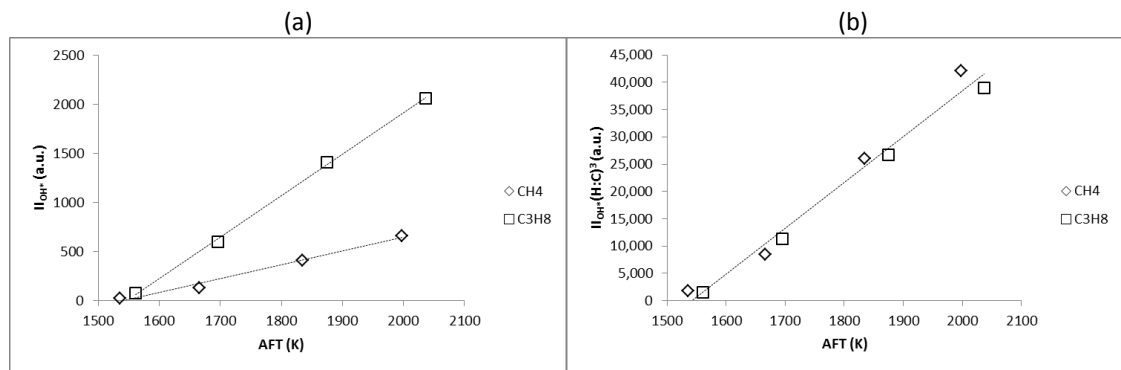


Figure 5.4: I_{0H^*} as a function of AFT (a) and scaled by the fuel H:C ratio (b) for CH₄-air and C₃H₈-air flames

Finally, the exhaust gas emissions from this premixed combustion study are presented as a function of AFT in Figure 5.5, with O₂ / CO₂ (%vol, open/closed) in Figure 5.5.a and CO / NO_x (ppmV, 15% O₂, open/closed) in Figure 5.5.b. The O₂/CO₂ response is as expected with increasing equivalence ratio, and C₃H₈-air flames result in higher exhaust CO₂ for nominally similar AFT compared to CH₄-air flames. NO_x and CO measurements below 10 ppmV are made with AFT < 2000, with NO_x emissions formed by the dominant thermal NO_x mechanism, resulting in an exponential response with increasing AFT. CO emissions for C₃H₈-air flames show a nonmonotonic response for the experimental range as discussed in Chapter 2.4, with an increase in CO emissions observed below 1600 K, which gives an indication of propane's behavior in lean mixtures with increasing turbulence, in which thermo-diffusive effects may begin to dominate the flame response and thus emissions formation mechanisms.

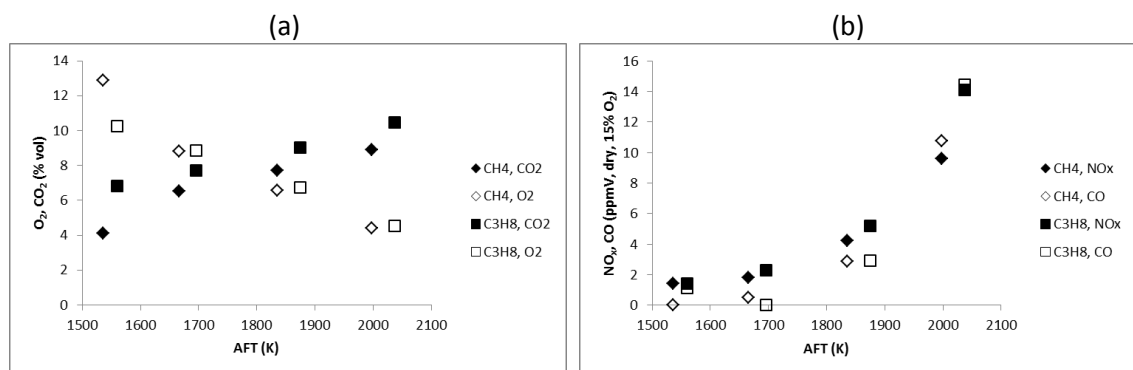


Figure 5.5: Exhaust gas measurements for premixed CH₄-air and C₃H₈-air flames as a function of AFT, showing CO₂ (closed) / O₂ (open) (a), and NO_x (closed) / CO (open) (b)

5.2 High Pressure Generic Swirl Burner (Mk. II)

The 2nd generation HPGSB-2 was commissioned in 2015 for use in this study [123-125] in addition to other experimental combustion studies undertaken at the GTRC [122, 126]. As previously detailed in Chapter 3.2.1, the main geometric difference between the HPGSB and HPGSB-2 is the reduction in expansion ratio from the burner exit nozzle ID to the quartz

confinement ID. Where the HPGSB had an expansion ratio of 3.5, this has been reduced to 2.5 in the HPGSB-2 with a reduction in the quartz confinement ID from 140 mm to 100 mm. All other critical geometric dimensions (swirler geometry, burner exit nozzle, etc.) have been maintained between the two designs.

5.2.1 Isothermal Characterization

5.2.1.1 Isothermal Acoustic Characterization

Isothermal acoustic characterization of the overall combustion rig, including the HPGSB-2, HPOC, and ancillary equipment is critical to the identification of system resonant frequencies and flow-driven instabilities which could potentially influence flame stability. Prior to combustion experiments, two isothermal characterization procedures were undertaken to allow isolation of critical acoustic signatures in the rig. First, a loudspeaker was installed in the exhaust piping directly in line with the burner centerline, replacing the window which normally provides end-on radial visual access to the burner. This setup and technique are similar to those undertaken for the acoustic characterization of both industrial gas turbine combustors [232] and piping systems [233]. Using this speaker with a tone generator, a linear frequency sine sweep from 40-1000 Hz was conducted at a rate of 17.45 Hz/s with the HPCR at ambient temperature (286 K). Figure 5.6 shows the temporal variation in the dynamic pressure measurement for each of the four DPTs, first with the BPV in the fully open position (Figure 5.6.a) and then in the fully closed position (Figure 5.6.b).

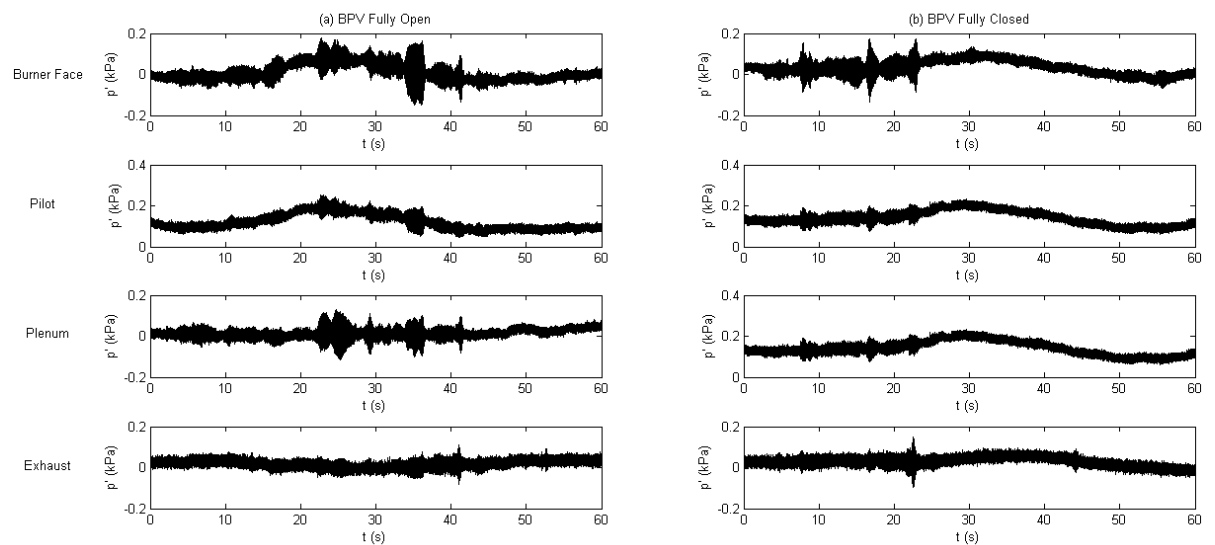


Figure 5.6: Temporal variation of dynamic pressure measurement for all four DPTs during an isothermal loudspeaker 40-1000 Hz linear tone sweep with the BPV in the fully open (a) and fully closed (b) positions

With the BPV fully open (Figure 5.6.a) the burner face, pilot, and plenum DPTs exhibit amplitude spikes in the 20-40 second range of the tone sweep. Closing the BPV (Figure 5.6.b) has the effect of damping the higher frequency tones seen in the fully open case. Within the first 25 seconds of the time series, the burner face, pilot, and plenum DPTs exhibit three distinct harmonic peaks. In both cases, the exhaust DPT is shown to exhibit only a single dominant peak suggesting that the physical location undergoes higher damping compared to the other DPT locations as it is located within the HPOC casing outlet flange.

The frequency and magnitude spectra during the tone sweep are plotted using spectrograms of the Burner Face DPT measurement in Figure 5.7, with the BPV fully open (Figure 5.7.a) and fully closed (Figure 5.7.b). With the BPV in the fully open position (Figure 5.7.a), the rig exhibits resonance that falls within three groups, the first near 133 Hz, the second at 280 Hz, and the third near 400 Hz. With the BPV in the fully closed position (Figure 5.7.b), the rig exhibits harmonic resonances as noted in Figure 5.6.b, the first near 133 Hz, the second at 292 Hz, and the third at 394 Hz. The three resonant groups show comparable dominant frequency results between the two BPV positions, although as expected the amplitudes have been reduced as a result of the increased system damping with the BPV closed. It is interesting to note the high dominant frequency density in the 150-400 Hz range in the fully open case compared with the fully closed case. In the fully closed case, the dominant frequency correlates nearly linearly with the input 40-1000 Hz tone sweep, however, in the fully open case, the natural resonant frequencies dominate when the tone sweep passes through the harmonic frequencies of these resonances. For example, as the tone sweep passes through 400 Hz ($t = 23$ s) in the fully open case, the measured dominant frequency is approximately 3 times less (133 Hz), corresponding to the high intensity region shown in Figure 5.7.a. Whereas the input of a harmonic frequency acts as an amplifier of the resonant frequency in the fully open BPV case, the effect of the resonant harmonic frequencies is diminished by acoustically isolating the system by closing the BPV.

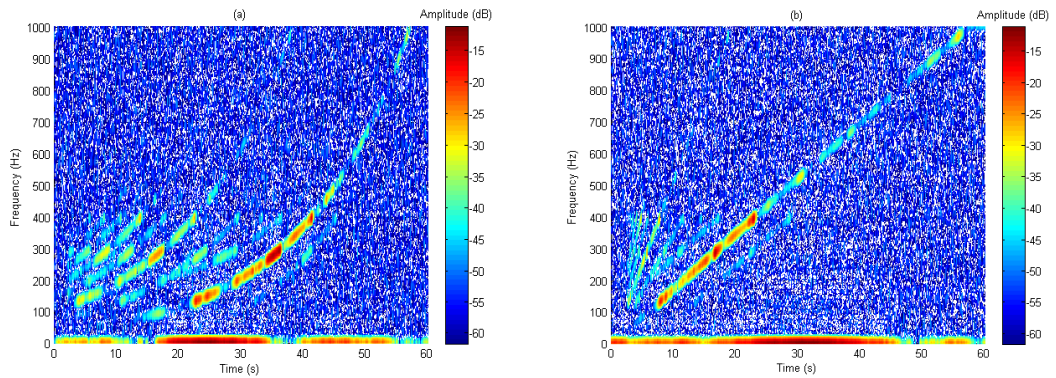


Figure 5.7: Spectrograms of the Burner Face DPT measurement during an isothermal loudspeaker 40-1000 Hz linear tone sweep with the BPV in the fully open (a) and fully closed (b) positions

An isothermal air flow experimental study was also conducted to provide baseline acoustic characteristics of flow through the HPGSB-2 with an open confinement and $S_g = 0.8$. Nine separate isothermal air flow conditions were investigated, a combination of air flow rates at three combustor inlet temperatures, $T_2 = 286$ K, 423 K, and 573K, and three combustor inlet pressures, $P_2 = 0.101$ MPa, 0.2 MPa, and 0.4 MPa. For each data set of constant T_2 , the air flow rate was increased by a factor equal to the increase in P_2 , maintaining constant $(\dot{m}_{air}\sqrt{T_2})/P_2$, and thus an approximately constant \bar{u} . Using the Burner Face DPT dominant frequency, f_{peak} , the resulting Helmholtz (He) and Strouhal (St) numbers for all experimental cases are calculated per Equations 2.4 and 2.5 and plotted as a function of f_{peak} in Figure 5.8. Note first that f_{peak} falls in the mid-frequency range ($100 < f < 1000$ Hz) as discussed in Chapter 2.2.2. It is also apparent from Figure 5.8 that the burner exhibits a constant $St = 0.8$ across all experimental conditions of temperature and pressure, while He is shown to vary linearly with the three unique groupings identified by constant T_2 , increasing from left to right. The constant Strouhal number is indicative of a dominant frequency corresponding to vortex shedding from the shear layer as the swirling flow exits the burner nozzle [68]. The dominant frequencies are thus found to collapse along a single line, dependent only on \bar{u} .

Further support that the measured dominant frequency is the result of a vortex shedding phenomena is provided in Figure 5.9, where the measured Helmholtz number is plotted as a function of the air flow Reynolds number, calculated in Equation 5.1. For a fixed T_2 and P_2 , He is shown to vary linearly with Reynolds number, which has also been shown to be indicative of vortex shedding in other work [68].

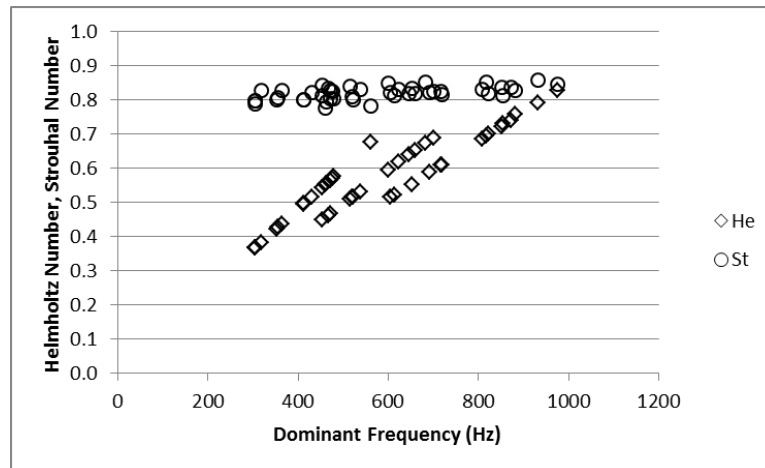


Figure 5.8: Isothermal air flow Helmholtz and Strouhal numbers as a function of f_{peak} for $T_2 = 286$ K, 423 K, and 523 K and $P_2 = 0.101$ MPa, 0.2 MPa, and 0.4 MPa with open confinement and $S_g = 0.8$

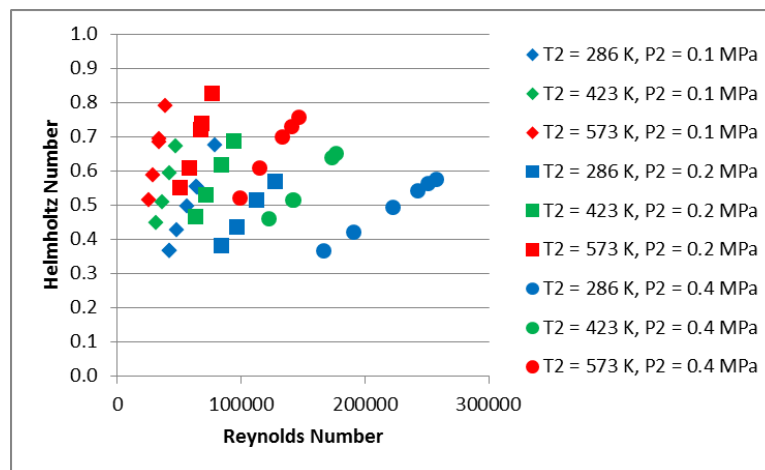


Figure 5.9: Helmholtz number as a function of Re for fixed T_2 and P_2 isothermal air flow tests in the HPGSB-2 with open confinement and $S_g = 0.8$

5.2.1.2 Isothermal Flow Characterization Using PIV

Isothermal air flow PIV measurements were conducted to characterize the flow velocity profile, identify coherent flow structures, and calculate turbulence characteristics for the HPGSB-2 flow field at the baseline $\varphi = 0.55$, $T_2 = 573$ K, and $P_2 = 0.11$ MPa, 0.22 MPa, and 0.33 MPa air flow conditions given in Table 3.4 with swirl number of $S_g = 0.8$. Both the open cylindrical confinement and convergent nozzle confinement were utilized for these measurements, in particular as the isothermal acoustic response differs significantly between confinements, despite holding \bar{u} constant for these conditions ($\bar{u} = 31$ m/s). The following results, measured and calculated using the methodology described in Chapter 3.2.1.3, are based on 200 image pairs captured at a rate of 5 Hz. The number of images utilized for the extraction of key flow field features from PIV measurements is critical, particularly in the case of confined flows using quartz, as these are inevitably coated with the seeding material, introducing noise into the PIV image pairs by representing zero-velocity particles and limiting

measurement times. However, a sufficient number of images must also be captured for the extracted values to converge. This process is detailed further in Appendix D.3. Key velocity and turbulence measures converge near to their final value after 200 image pairs, thus this value was selected for all further measurements.

The resultant velocity vector maps for each of the examined conditions are presented in Figures 5.10 and 5.11 for each pressure and confinement, open (Figure 5.10) and convergent (Figure 5.11). Each vector map is then overlaid with colored contours of mean axial velocity, v . Note that the radial field of view is reduced between the open and convergent confinement PIV results as the width of the laser light sheet reduces as it passes through the end of the convergent quartz tube. For all conditions with the open cylindrical confinement (Figure 5.10), a number of coherent flow structures are visible, including a CRZ along the burner central axis (with upstream flow velocities up to -17 m/s) and two radially symmetric ORZs near the flow expansion from the burner exit nozzle at $r = \pm 40$ mm, $y = 25$ mm. The vortex breakdown structure along the central axis is seen to increase in size radially as the pressure is increased from 0.11 to 0.33 MPa, with flow velocities remaining relatively similar as the bulk volumetric flow is held constant. Separating these two coherent structures, an outward-expanding shear layer of zero axial velocity is also present, and it is this highly turbulent, low velocity area where the swirl flame stabilizes, as discussed in Chapter 2.

As a result of temporal averaging, the vortices shed from the burner exit nozzle along the shear layer (and predicted by the previous acoustic analysis) cannot be seen in Figures 5.10 and 5.11; however they are visible in the instantaneous velocity vector maps. As expected from the isothermal acoustic analysis, and as predicted numerically by Wu et al. [128], the addition of the convergent nozzle confinement significantly alters the flow field. With a reduction in the outlet diameter of the confinement to a contraction ratio of 0.4 ($D_{\text{exit}}/D_{\text{confine}} = 40$ mm/100 mm), the tangential (swirl) velocity is enhanced compared to the open confinement case and thus the axial pressure gradient is impacted, with the location of the lowest pressure along the centerline expected to move downstream towards the convergence [128]. In numerical studies, a strong, twisted vortex core along the swirl burner central axis has been predicted at a contraction ratio of 0.4 to 0.325 [128]. This is visible in each of the PIV vector maps in Figure 5.11, as an asymmetric area of positive axial velocity can be seen near the central axis which increases in size with increasing P_2 . The CRZ is seen to significantly change in size and magnitude of reverse axial velocity.

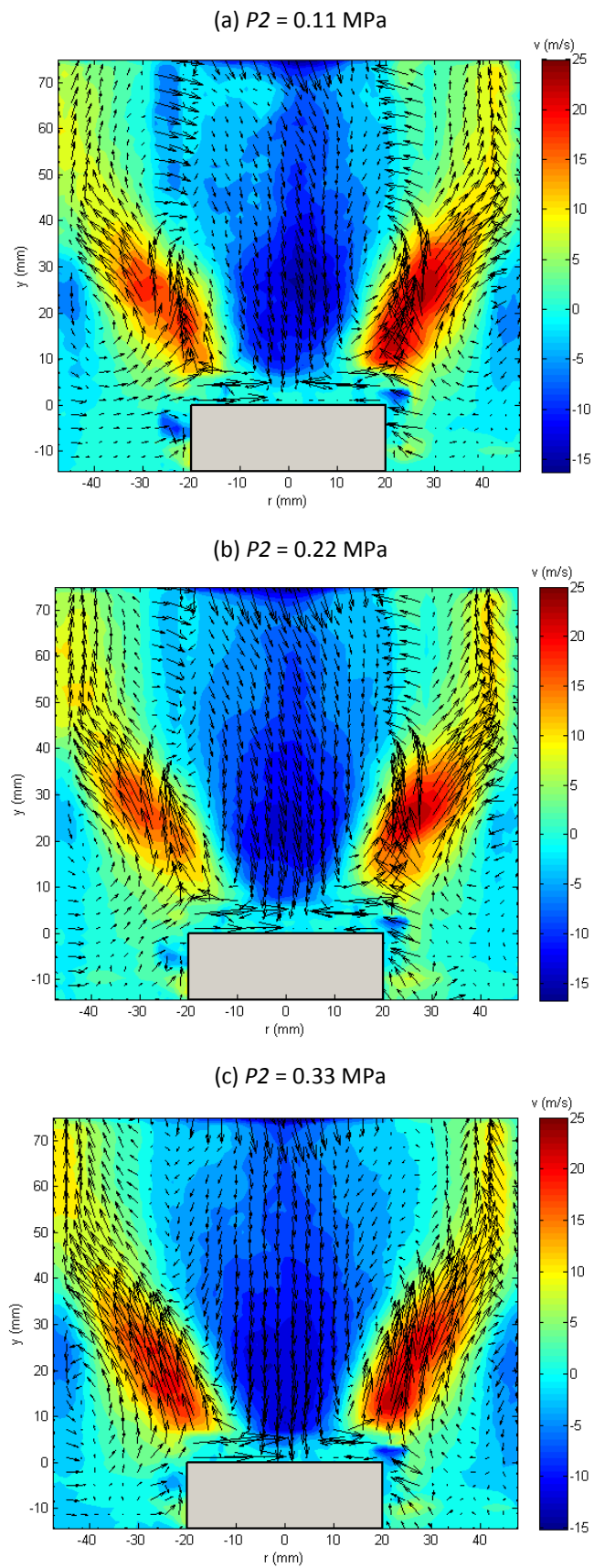


Figure 5.10: Isothermal air flow PIV velocity vector maps with axial velocity contours for the HPGSB-2 (open confinement) at varying P_2 and $T_2 = 573$ K

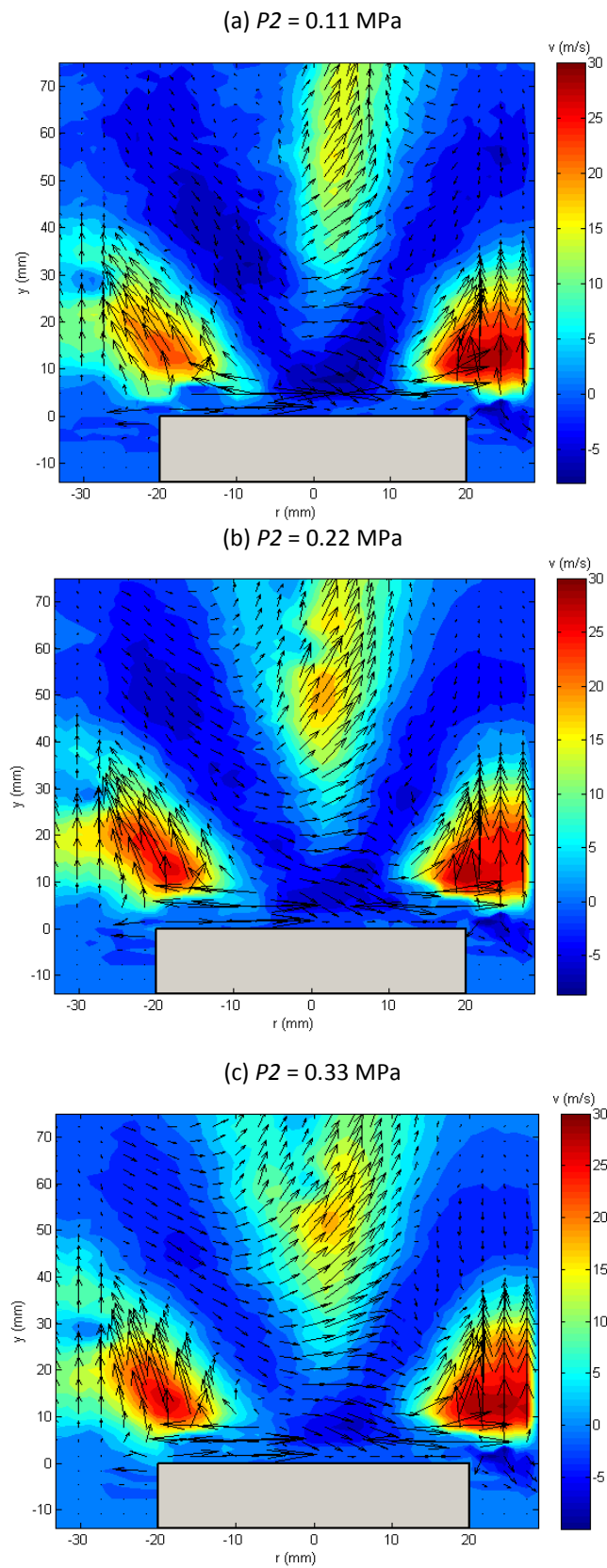


Figure 5.11: Isothermal air flow PIV velocity vector maps with axial velocity contours for the HPGSB-2 (convergent nozzle confinement) at varying P_2 and $T_2 = 573$ K

Although the field of view here is limited, Wu et al. [128] predict numerically that the ORZ is not affected by the change in convergent nozzle outlet. This change in flow structure is particularly evident in the axial velocity profiles plotted in Figure 5.12 at an axial distance of $y = 32$ mm above the burner exit nozzle, with results plotted for the open confinement (Figure 5.12.a) and convergent confinement (Figure 5.12.b). The CRZ and radial shear layers are identified by negative axial velocity and zero axial velocity, respectively, in Figure 5.12.a. The similarity between pressure conditions confirms that the bulk flow field has been maintained. The magnitude of axial velocity in the convergent nozzle case (Figure 5.12.b) is reduced in both the upstream and downstream directions, and a third shear layer near the central axis is observed along with the positive axial velocity core identified in Figure 5.12.

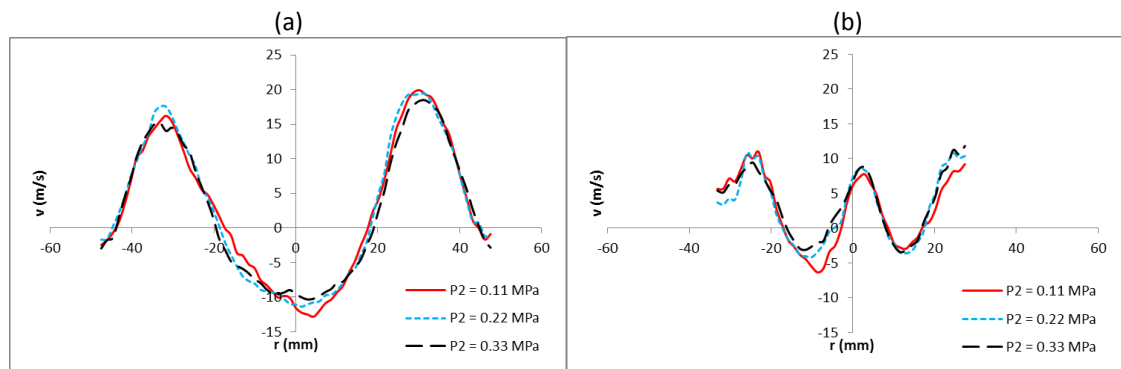


Figure 5.12: Axial velocity profiles of isothermal air flow in the HPGSB-2 open (a) and convergent (b) confinement at $y = 32$ mm with varying P_2 .

As discussed in Chapter 3.4.2 in regards to selection of the HPGSB-2 operating conditions, an assumed relative turbulence intensity (T_{int}) and integral length scale (L_T) were used in the calculation of the dimensionless turbulence scaling parameter. This scaling parameter allows for comparison between industrially relevant GT combustor conditions and those in the experimental swirl burner. Thus, it was critical to verify these assumed values of $L_T = 8$ mm and $T_{int} = 0.2$ (= 20%). Understandably, the turbulence intensity varies across the flow field as the RMS velocity values vary in areas of high turbulence, as can be seen in Figure 5.13, which presents the axial velocity contours of T_{int} as a function of P_2 and confinement geometry. A significant difference in the turbulence distribution is evident between the two confinements, with the introduction of the third shear layer in the convergent nozzle cases resulting in an asymmetric turbulence distribution along the burner centerline. The central axis turbulence distribution is significantly affected by the addition of the convergent confinement, with an approximately 30% increase in the turbulence intensity in the central core flow from open to convergent confinement. Maximum relative turbulence intensity near to the flow shear layers

identified in Figures 5.10 and 5.11 approach 30% and 35% in the open and convergent confinements, respectively. Mean values calculated from each contour plot range from 11% to 16%. Thus, the use of 20% for the assumed turbulence intensity for dimensionless turbulence scaling to an industrial GT combustor is adequate considering mean and maximum values observed.

Similarly, the integral length scale (L_T) will vary within the flow field. At each point in the flow field, four length scales are calculated using the two methods ($L_{T,e}$ and $L_{T,int}$) described in Chapter 3.2.1.3. These are the radial longitudinal and transverse length scales ($L_{r,u}$ and $L_{r,v}$) and the axial longitudinal and transverse length scales ($L_{y,u}$ and $L_{y,v}$). These are then combined per Equations 5.2-5.4 to yield the radial and axial integral length scales (L_r and L_y) and thus the overall integral length scale, L_T .

$$L_r = \sqrt{L_{y,u}^2 + L_{r,u}^2} \quad (5.2)$$

$$L_y = \sqrt{L_{y,v}^2 + L_{r,v}^2} \quad (5.3)$$

$$L_T = \sqrt{L_r^2 + L_y^2} \quad (5.4)$$

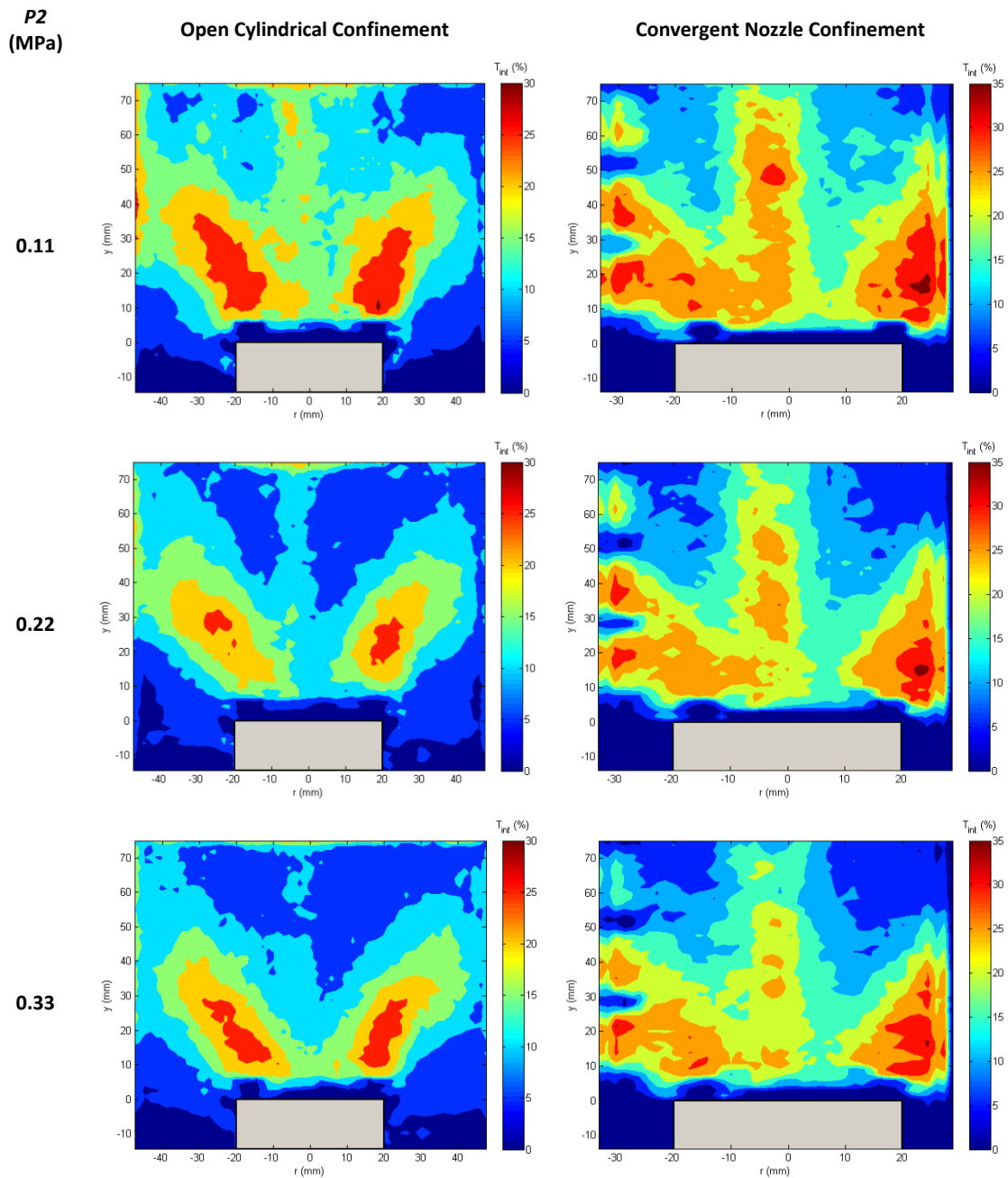


Figure 5.13: Isothermal air flow axial relative turbulence intensity (T_{int}) contours for the HPGSB-2 at $T_2 = 573$ K, with varying burner confinement and P_2 . Note change in colormap scaling.

Figure 5.14 compares the calculated integral length scale for varying points in the flow field, burner confinement, and P_2 . In Figure 5.14.a, the variation in L_T along the burner central axis ($r = 0$ mm) is presented at different values of y ($y = 5$ mm and $y = 19$ mm) above the burner exit nozzle in the open and convergent confinement cases. Similarly in Figure 5.14.b, the variation in L_T along a fixed height above the burner exit nozzle ($y = 32$ mm) is presented at different values of r ($r = -13$ mm and $r = -26$ mm) from the burner exit nozzle centerline. In both plots, the open symbols represent the open cylindrical confinement and the closed symbols

represent the convergent nozzle confinement. $L_{T,e}$ is plotted with a solid connecting line while $L_{T,int}$ is plotted with a hashed line. All inlet pressure conditions ($P_2 = 0.11$ MPa, 0.22 MPa, and 0.33 MPa) are also identified for each length scale. As expected, L_T is observed to vary in both the radial and axial directions, showing higher variation in the axial direction than the radial direction, and an apparent pressure influence as well, presumably as the bulk flow Reynolds number increases with increased air flow density, which will influence the fluctuating velocity components in the correlation function. Across all conditions and locations in the flow field, the mean integral length scale as calculated by the 1/e method is equal to 9.65 mm with a standard deviation of 3.83 mm. The mean integral length scale as calculated by the integration method is equal to 9.95 mm with a standard deviation of 3.04 mm. As can be seen, both methods produce approximately equal integral length scale measurements. It should be noted that the integration method could not be used at all conditions (1 of 30) presented in Figure 5.14 if the correlation function, $R(r)$ or $R(y)$, did not have a zero crossing, thus the calculation of the mean and standard deviation values differs slightly between methods. An assumed value of $L_T = 8$ mm was used for the dimensionless turbulence scaling factor, which falls within a 98% confidence interval of the overall $L_{T,e}$ dataset using a statistical t-test.

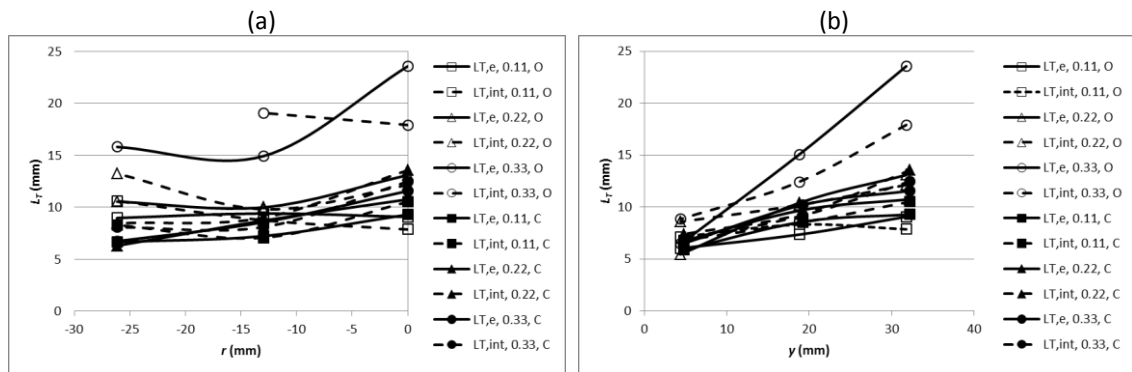


Figure 5.14: Integral length scale ($L_{T,e}$ and $L_{T,int}$) variation in the axial direction along the burner centerline (a) and in the radial direction fixed at height $y = 32$ mm above the burner exit nozzle (b). Note varying P_2 (0.11, 0.22, 0.33 MPa) and confinement: open ("O", open symbols) and convergent ("C", closed symbols)

5.2.2 Combustion Characterization

The new HPGSB-2 was commissioned as part of this study specifically for the purposes of enhancing the acoustic and optical measurements capable for fully premixed, confined swirl flames under elevated operating conditions. The aim of this commissioning study was to experimentally characterize the stable operation, onset, and occurrence of high amplitude, low frequency combustion instabilities observed under lean, fully premixed and near-blowoff conditions in the HPGSB-2. In addition to providing a comprehensive data set for validation of

computational fluid dynamics (CFD) and chemical kinetics reactor network models, this study also aims to provide further development of tools for the prediction of the onset of near-blowoff instabilities in practical operating environments. A combination of techniques is therefore investigated based on the acoustic and optical measurements taken under combustion conditions with the goal of reducing near-LBO operating margins.

Methane-air combustion experimentation was first conducted at ambient temperature and atmospheric pressure (ATAP) to identify stable burner operation in addition to LBO precursor events and LBO instabilities. These experiments were conducted with fully premixed CH₄-air flames at $P_{therm} = 55$ kW and $T_2 = 290$ K, an example of which can be seen in the photograph in Figure 5.15 for a flame at $\phi = 0.80$. However, focus has been placed here on the experimental results from the elevated temperature and pressure conditions, and reference is made to observations from the ATAP experiments. The elevated temperature and pressure experiments were conducted with fully premixed CH₄-air flames at $P_{therm} = 42$ kW to 110 kW, P_2 up to 0.2 MPa, and T_2 up to 584 K. For all experimentation presented here, the HPGSB-2 is operated with the open cylindrical confinement and $S_g = 0.8$. The resulting flames are studied experimentally through a combination of measurement techniques, most notably dynamic pressure, OH* CL, and OH PLIF. Additionally, a chemical kinetic modeling approach was undertaken along with nondimensional analysis to provide fundamental support for the flame characteristics observed in relation to LBO stability.

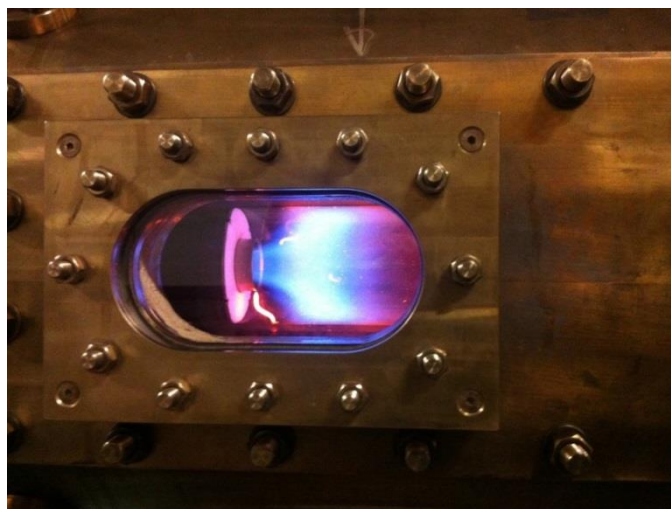


Figure 5.15: Color photograph of 55 kW CH₄-air flame at $P_2 = 0.105$ MPa, $T_2 = 287$ K, and $\phi = 0.8$

5.2.2.1 Elevated Inlet Temperature and Pressure Combustion

Table 5.4 below specifies the main rig operating condition ranges for each of the experiments undertaken in this Section. Reference is first made to ATAP combustion conditions. In addition, elevated temperature, atmospheric pressure (ETAP) and elevated temperature, elevated pressure (ETEP) combustion conditions are introduced. Note that \bar{u} is calculated based on the total premixed (air and fuel) volumetric flow through the burner exit nozzle with diameter, $D_{noz} = 40$ mm. The Reynolds number is calculated per Equation 5.1.

Table 5.3: HPCR conditions for ATAP, ETAP, and ETEP combustion experiments in the HPGSB-2

Rig Parameter	Experimental Conditions		
	ATAP	ETAP	ETEP
Air Mass Flow, \dot{m}_{air} (g/s)	12 - 30	26 - 38	64 - 78
CH ₄ Mass Flow, \dot{m}_{CH_4} (g/s)	1.1	0.8 - 1.1	2.2
Equivalence Ratio, Φ	0.64 - 1.54	0.49 - 0.75	0.49 - 0.60
Combustor Inlet Temperature, T_2 (K)	285 - 292	423 - 584	559 - 568
Combustor Inlet Pressure, P_2 (bara)	1.03 - 1.06	1.05 - 1.12	1.95 - 2.04
Thermal Power, P_{therm} (kW)	55	42 - 55	110
Mean Burner Nozzle Exit Velocity, \bar{u} (m/s)	9 - 20	29 - 48	43 - 53
Reynolds Number, Re	25000 - 56000	29000 - 46000	73000 - 88000

The burner stability envelope was evaluated for a selected number of rig operating conditions to aid in the identification of stable operation, LBO, and technical flashback (TFB, Chapter 3.1.2.2). In the ETAP case, with $T_2 = 573$ K and $P_{therm} = 55$ kW, the stable operating limits were defined by the LBO instability at $\phi = 0.50$ and TFB at $\phi = 0.75$, with a lean shift in LBO equivalence ratio compared to the ATAP case due to the increased S_L with increased T_2 as indicated by chemical kinetics modeling. Thus, although the burner appeared stable at $\phi = 0.75$ under ETAP conditions, it was not driven to higher ϕ as the bluff body tip temperature, T_{pilot} , approached the TFB operating limit of 1273 K at this ϕ , and further reduction in air flow would potentially have caused propagation of the flame upstream into the swirler. The LBO instability was also investigated under ETAP conditions for different fuel flow rates ($P_{therm} = 42$ kW and 49 kW) and T_2 (423 K, 560 K, and 573 K). In the ETEP experimental case, with $T_2 = 573$ K and $P_2 = 0.2$ MPa, the stable operating limits were defined by the LBO instability at $\phi = 0.49$ and TFB at $\phi = 0.60$. A comparison of stable operating curves for the ATAP, ETAP, and ETEP cases are presented in Figure 5.16 as a function of ϕ and Re . The limited influence of pressure on the LBO instability equivalence ratio is apparent between the ETAP and ETEP case, where the dimensionless flow parameter, $(\dot{m}_{premix}\sqrt{T_2})/P_2$, has been held nominally constant across these conditions.

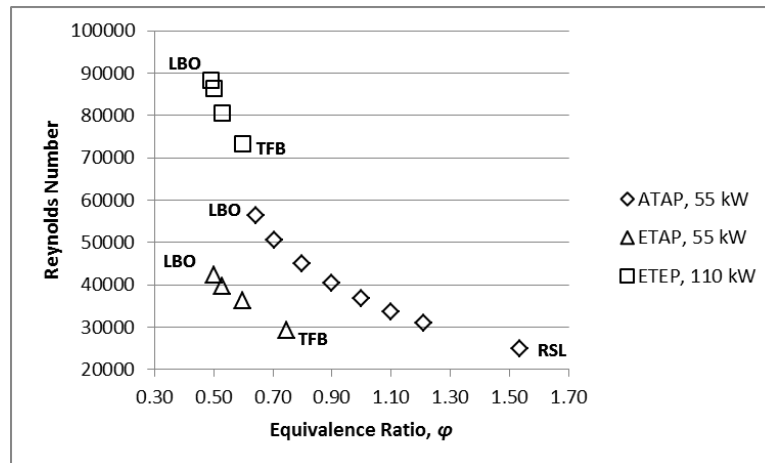


Figure 5.16: Stable operating curves for selected ATAP, ETAP, and ETEP combustion cases in the HPGSB-2

ETAP experimental work in the HPGSB-2 focused on the influence of increased T_2 under atmospheric pressure conditions. A stable operation curve, as shown in Figure 5.16, was generated at $T_2 = 573$ K, with a constant fuel flow rate of $\dot{m}_{CH_4} = 1.1$ g/s, yielding $P_{therm} = 55$ kW. In addition to investigating the LBO instability under these conditions, the influence of varying T_2 and P_{therm} was also considered. Thus, the LBO instability was repeated at $T_2 = 423$ K ($P_{therm} = 49$ kW and 55 kW) and at $T_2 = 560$ K ($P_{therm} = 42$ kW). For the results presented herein, focus is placed first on the stability curve generated in the $T_2 = 573$ K, $P_{therm} = 55$ kW ETAP case, particularly the high-amplitude, low frequency LBO instability observed at $\phi = 0.50$. Results of the LBO instabilities observed at varying T_2 and P_{therm} are subsequently presented.

Abel transformed OH* chemiluminescence results ($t_{gate} = 400$ μ s) are presented in Figure 5.17 for three selected equivalence ratios, $\phi = 0.50$ (Figure 5.17.a), 0.60 (Figure 5.17.b), and 0.75 (Figure 5.17.c). The image shown in Figure 5.17.a has been calculated using 100 images immediately prior to the onset of the observed LBO instability. With an increase in T_2 from ATAP to ETAP conditions, the maximum heat release zones in Figure 5.17.b and Figure 5.17.c extend into the burner exit nozzle and attach to the bluff body instrumentation and pilot lance. This is evident in the increase in measured T_{pilot} values, with the $\phi = 0.75$ case (Figure 5.17.c) reaching the defined TFB limit of 1273 K. For comparison, TFB was not observed under ATAP conditions due to reduced T_2 and thus reduced S_L and AFT. In Figures 5.17.b and 5.17.c, the areas of maximum heat release are shown to lie along the shear layer between the ORZ and CRZ, yielding a V-shape flame structure which extends into the burner exit nozzle. As LBO is approached (bottom to top in Figure 5.17), the transition to an M-shape flame can be seen,

with maximum heat release shown in the CRZ, suggesting the flame stabilization location has transitioned from the shear layer to the CRZ. Thus, the flame is no longer stabilized within the burner exit nozzle and instead stabilizes downstream in the quartz confinement tube. A similar transition in the suggested flame stabilization location and shift from V-shape to M-shape near LBO was also observed under ATAP conditions.

Temporally-averaged OH PLIF results are shown in Figure 5.18 for two selected equivalence ratios, $\varphi = 0.53$ (Figure 5.18.a) and 0.60 (Figure 5.18.b) at $T_2 = 573$ K and $P_{therm} = 55$ kW. Note that each image has been mirrored about the burner centerline ($r = 0$ mm) for identification of the flame shape with a fixed laser sheet position. Figure 5.18.a shows OH PLIF intensity is high in the CRZ and ORZ. The reduced OH PLIF intensity along the shear layer expanding from the burner exit nozzle is also similar to that seen under ATAP conditions prior to the onset of LBO. The flame stabilization location moves from the shear layer to the CRZ with less than 10% increase in air mass flow rate between Figures 5.18.a and 5.18.b. This shift in flame stabilization location as the LBO instability is approached is in agreement with that shown generally by heat release zone movement in the OH* chemiluminescence images at corresponding equivalence ratios in Figure 5.17.

The 55 kW ETAP case was also seen to exhibit a potential thermoacoustic instability near the TFB limit at $\varphi = 0.75$. This is evident in Figure 5.19, which shows the effect of φ on II'_{OH^*} as LBO is approached from $\varphi = 0.75$ to 0.50. There is a reduction in II'_{OH^*} as the φ is reduced towards LBO corresponding to a reduction in Q'_{max} . However, there is significant fluctuation in intensity at $\varphi = 0.75$, implying that a second instability mode exists under ETAP conditions. Increased peak to peak II'_{OH^*} fluctuation is also present at $\varphi = 0.60$, compared with the $\varphi < 0.60$ experimental conditions, suggesting the onset of this second instability mode begins prior to TFB.

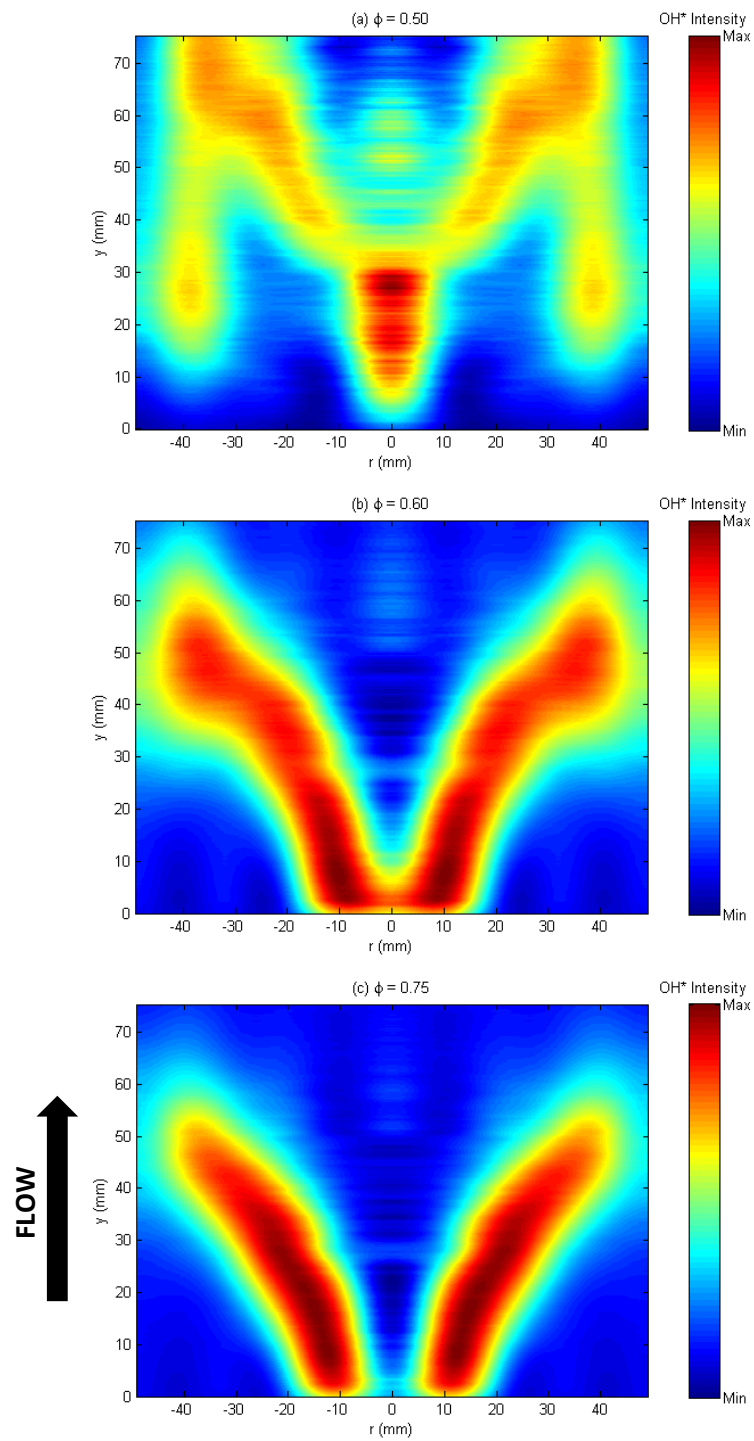


Figure 5.17: Abel transformed OH^* chemiluminescence images for ETAP CH_4 -air flames ($T_2 = 573$ K, $P_2 = 0.101$ MPa, $P_{therm} = 55$ kW) at $\phi = 0.50$ (a), 0.60 (b), and 0.75 (c)

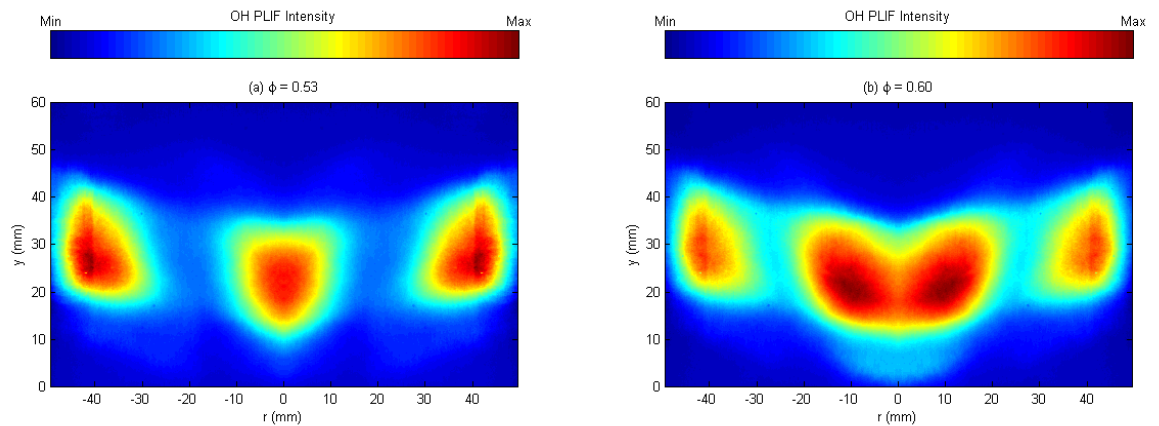


Figure 5.18: Time-averaged OH PLIF images for ETAP CH₄-air flames ($T_2 = 573$ K, $P_2 = 0.101$ MPa, $P_{therm} = 55$ kW) at $\phi = 0.53$ (a) and 0.60 (b).

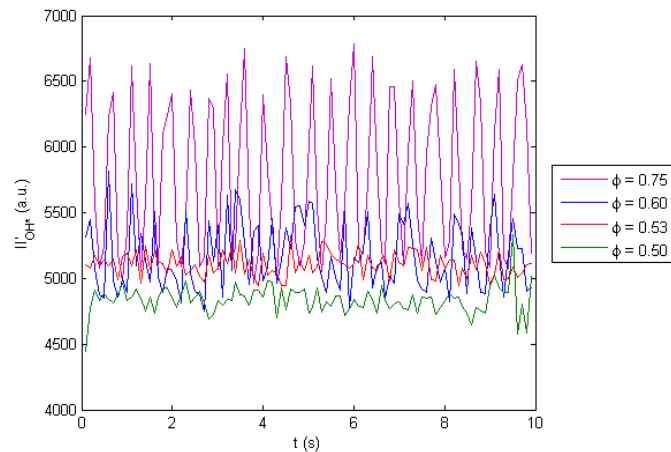


Figure 5.19: Effect of ϕ on II'_{OH^*} for ETAP CH₄-air flames ($T_2 = 573$ K, $P_2 = 0.101$ MPa, $P_{therm} = 55$ kW)

The observation of a second instability mode in the $T_2 = 573$ K, 55 kW ETAP case is further confirmed by the Burner Face DPT measurements, as shown in Figure 5.20, with $\phi = 0.50$ (Figure 5.20.a) and 0.60 (Figure 5.20.b). During burner operation at $\phi = 0.60$, a set of harmonic frequencies is apparent in the resulting PSD plot. The first peak of this set has a frequency of 479 Hz, which results in $St = 0.48$, suggesting that the measured frequency is not due to vortex shedding, which has been shown to dominate at $St = 0.8 - 1.0$ in this burner. Instead, the frequency measured here appears to correspond to the first harmonic frequency of a longitudinal standing wave within the burner, assuming open ends. The fundamental frequency of the burner can be calculated using the distance from the premixed air/fuel inlet to the combustor exit (0.814 m) and an estimated speed of sound based on the average air ($\gamma = 1.4$) speed of sound calculated at AFT (866 m/s) and burner outlet temperature, T_3 (712 m/s). It has been found that this speed of sound estimation (789 m/s) falls within 2% of the speed of sound (779.8 m/s) required to generate this measured fundamental frequency. Using

Equation 2.4, the resulting Helmholtz number at this condition is $He = 0.25$. During the LBO instability (Figure 5.20.a), the harmonic content has shifted to the low end of the frequency spectrum below 200 Hz. The dominant frequency at the LBO instability is measured at ~ 20 Hz with a total pressure fluctuation during the LBO instability of $p'_{RMS} = 2.9$ kPa.

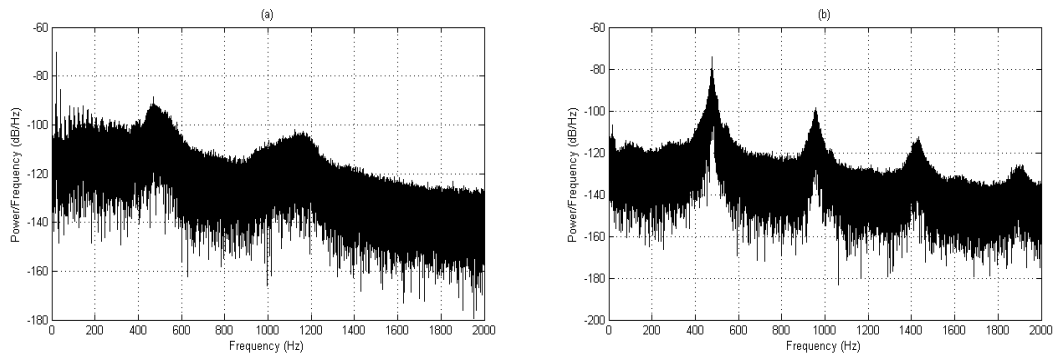


Figure 5.20: PSD of Burner Face DPT measurement during LBO instability at $\varphi = 0.50$ (a) and operation at $\varphi = 0.60$ (b) for ETAP CH_4 -air flames ($T_2 = 573$ K and $P_{therm} = 55$ kW)

Pressure fluctuations during these two distinct instability modes are approximately equal, as seen in Figure 5.21, at just over 2.5% of P_2 . The pressure fluctuation level is shown to collapse prior to the onset of the LBO instability, a trend also identified in the ATAP case. At $\varphi = 0.53$, the frequency spectrum no longer shows the harmonics seen in Figure 5.20.b, instead appearing multimodal with peaks at 20 Hz corresponding to partial extinction and reignition events, 430 Hz ($St = 0.38$) related to the standing wave, and 1070 Hz ($St = 0.95$) consistent with flow-driven vortex shedding. As the air mass flow rate is further increased from 36 g/s to 38 g/s, the flame transitions into the LBO instability and the pressure fluctuation levels increase as low frequency harmonics are established.

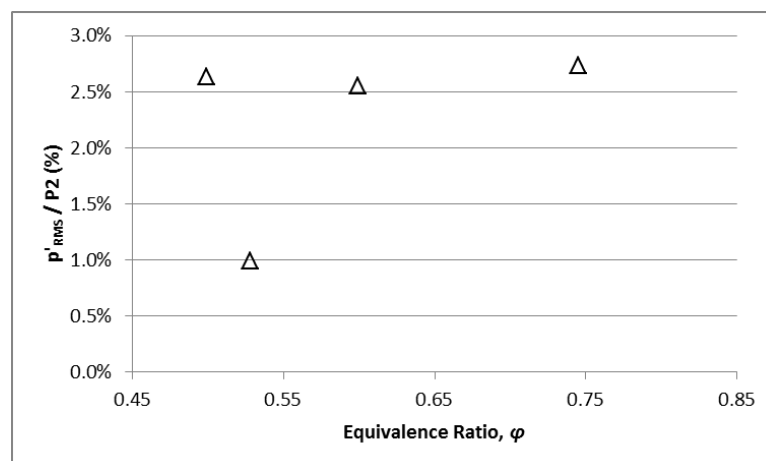


Figure 5.21: Effect of φ on the observed dynamic pressure fluctuation of the Burner Face DPT for ETAP CH_4 -air flames ($T_2 = 573$ K and $P_{therm} = 55$ kW)

Under ETAP operating conditions, the LBO instability was also investigated at varying T_2 and P_{therm} , with the resulting bandpass filtered PSDs plotted in Figure 5.22. With $T_2 = 423$ K, the LBO instability was observed at $P_{therm} = 49$ kW (Figure 5.22.a) and 55 kW (Figure 5.22.b). With further increase to T_2 , the LBO instability was observed at $T_2 = 560$ K and $P_{therm} = 42$ kW (Figure 5.22.c). Finally, the harmonic content of the high-amplitude, low frequency LBO instability at $T_2 = 573$ K and $P_{therm} = 55$ kW, discussed in detail previously in this Section, is seen in the PSD plot in Figure 5.22.d. The LBO instability in the $T_2 = 423$ K cases occurred at $\varphi = 0.57$ compared to $\varphi = 0.50$ for the $T_2 = 560$ K and 573 K cases, attributed to reduced S_L and AFT laminar flame speed as T_2 was reduced. For the $T_2 = 573$ K, 55 kW ETAP case, the dominant 20.6 Hz frequency can be identified in Figure 5.22.d, along with its harmonics. For all other ETAP cases, the dominant frequency is ~ 16 Hz across varying T_2 and P_{therm} while approximately equal in magnitude as well. This agreement in dominant frequency appears to be a function of the chemical time scale, τ_{chem} , which will be discussed further in terms of a blowoff Damköhler number relationship in Section 5.2.2.3.

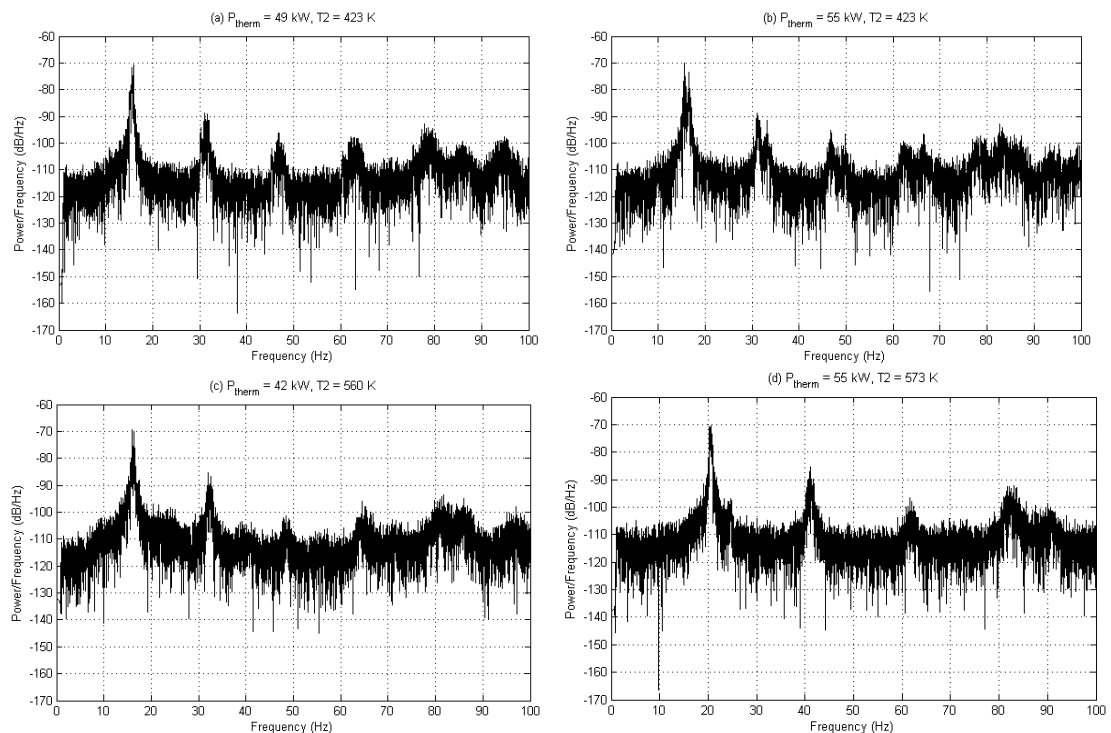


Figure 5.22: Bandpass filtered PSD for Burner Face DPT during LBO instability in ETAP CH_4 -air flames at $T_2 = 423$ K and $P_{therm} = 49$ kW (a), $T_2 = 423$ K and $P_{therm} = 55$ kW (b), $T_2 = 560$ K and $P_{therm} = 42$ kW (c), and $T_2 = 573$ K and $P_{therm} = 55$ kW (d)

ETAP experimental conditions in the HPGSB-2 focused on an increase in both combustor inlet temperature ($T_2 = 573$ K) and pressure ($P_2 = 0.2$ MPa), while maintaining $\dot{m}_{premix}\sqrt{T_2}/P_2$ with the $T_2 = 573$ K, $P_{therm} = 55$ kW ETAP case. The stable operation curve shown in Figure

5.16 was generated at $T_2 = 573\text{K}$, with a constant fuel flow rate of $\dot{m}_{CH_4} = 2.2\text{ g/s}$, yielding $P_{therm} = 110\text{ kW}$, with the high-amplitude, low frequency LBO instability observed at $\varphi = 0.49$. Abel transformed OH^* chemiluminescence ($t_{gate} = 400\ \mu\text{s}$) results are presented in Figure 5.23 for three selected equivalence ratios, $\varphi = 0.50$ (Figure 5.23.a), 0.53 (Figure 5.23.b), and 0.60 (Figure 5.23.c). The maximum heat release zone in Figure 5.23.c is shown to extend into the burner exit nozzle and attach to the bluff body instrumentation and pilot lance. This is evident in the increase in measured T_{pilot} values, with the $\varphi = 0.60$ case (Figure 5.23.c) reaching the defined TFB limit of 1273 K , compared with TFB at $\varphi = 0.75$ in the ETAP case. Similar to results shown in the ETAP case (Figure 5.17), however, the heat release stabilization location is shown to move downstream as the burner operation moves towards the LBO instability. In Figure 5.23.c, the area of maximum heat release is shown to stabilize along the shear layer yielding a V-shape flame structure. As LBO is approached (from bottom to top in Figure 5.23), the transition to an M-shape flame can be seen again in Figure 5.23.b, as noted prior to LBO in the ATAP and ETAP cases, with stabilization influenced by the quartz confinement wall. Given the higher air mass flow rates at the increased P_{therm} condition, up to 78 g/s at the LBO instability, the air mass flow control system allows enhanced control on the approach to LBO (as a percentage of overall flow). Thus, an intermediate stabilization structure is noted between the M-shape structure ($\varphi = 0.53$) and the LBO instability ($\varphi = 0.49$). At $\varphi = 0.50$ (Figure 5.23.a), the structure appears to resemble flame shapes described by Muruganandam and Seitzman [234] and similarly by Bradley et al. [235] prior to LBO in atmospheric swirl flames, where the flame is stabilized by the combustor walls instead of by the burner exit nozzle with little influence from the ORZ.

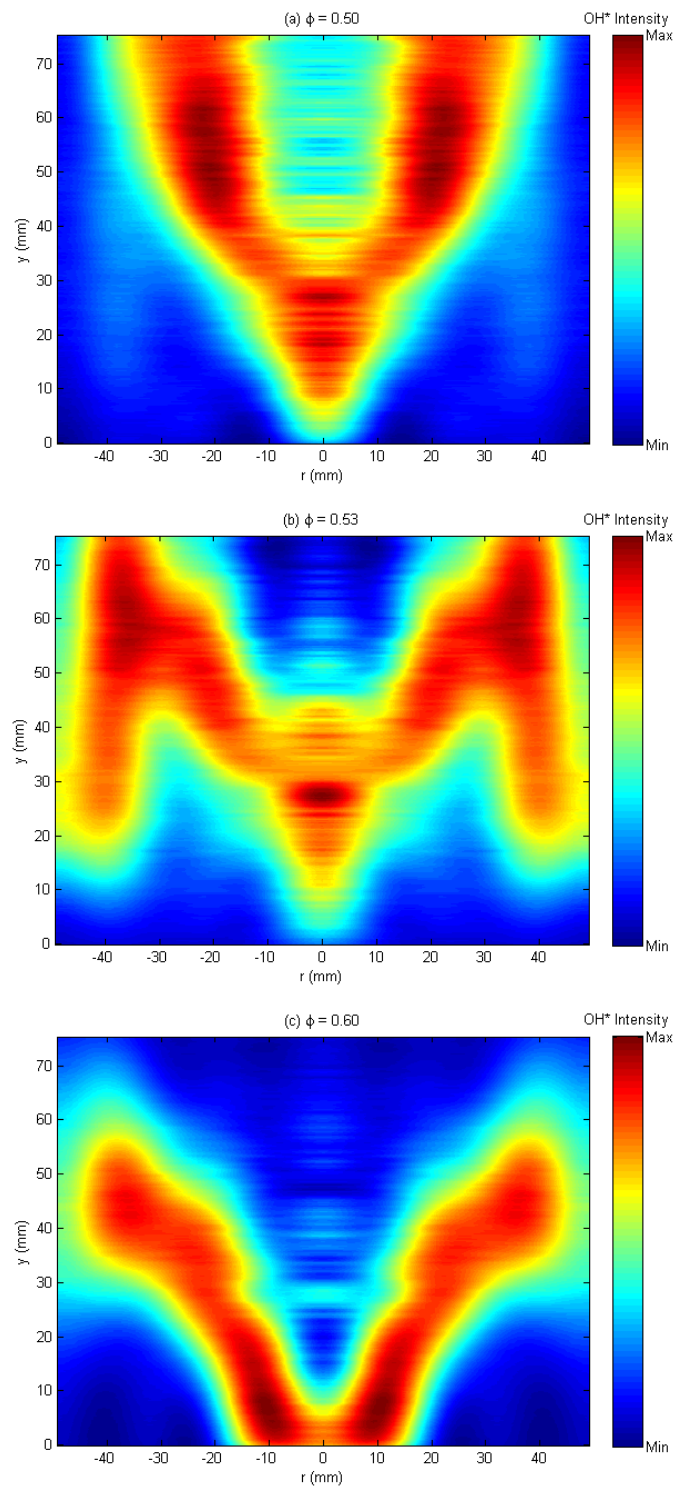


Figure 5.23: Abel inverted OH* chemiluminescence images for ETEP CH₄-air flames at $\phi = 0.50$ (a), 0.53 (b), and 0.60 (c)

A temporally-averaged OH PLIF image at $\phi = 0.53$ is shown in Figure 5.24. Note that the image has been mirrored about the burner centerline ($r = 0$ mm) for identification of the flame shape with a fixed laser sheet. Supporting the observed M-shaped area of heat release from the

corresponding OH* chemiluminescence image in Figure 5.32.b, OH PLIF intensity is seen to be highest in the ORZ with the dominant flame structure downstream ($y > 20$ mm) of the laser sheet excitation plane. A non-reacting shear layer expanding from the burner exit nozzle is also similar to that seen in Figure 5.26.a (ETAP) at the same equivalence ratio and similar burner exit nozzle velocity (45 – 48 m/s), suggesting similar stabilization modes and limited influence of pressure prior to LBO.

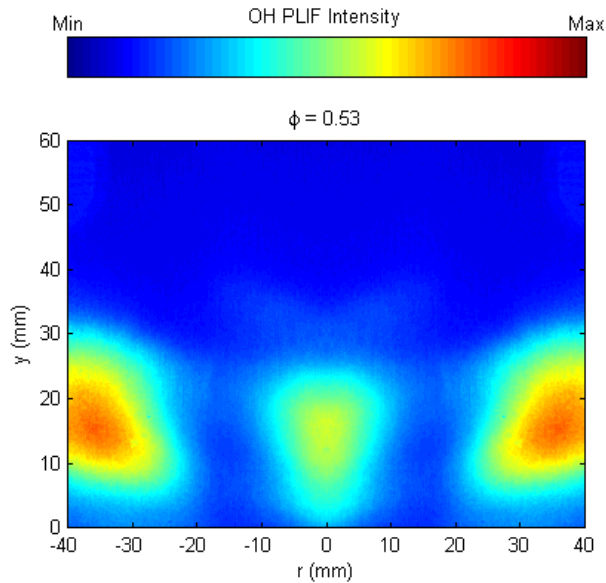


Figure 5.24: Time-averaged OH PLIF image for an 110 kW ETEP CH₄-air flame at $\phi = 0.53$

Similar to the $T_2 = 573$ K, 55 kW ETAP case, the ETEP case was seen to exhibit potential thermoacoustic instability near the TFB limit at $\phi = 0.60$. This is evident in Figure 5.25, which shows the effect of ϕ on II'_{OH^*} as LBO is approached from $\phi = 0.60$ to $\phi = 0.50$. As seen in the ETAP case, there is a reduction in II'_{OH^*} (thus HRR) as ϕ is reduced towards LBO. However, significant intensity fluctuation is evident at $\phi = 0.60$, implying that a second instability mode exists under ETEP conditions. Note again that this fluctuation was not apparent in the flame visually and was not marked by complete flameout and reignition as in the case of the LBO instability. Thus, similar to ETAP conditions, stable operation under ETEP conditions appears to be bounded by an LBO instability at $\phi = 0.50$ and a thermoacoustic instability between $\phi = 0.53$ and $\phi = 0.60$.

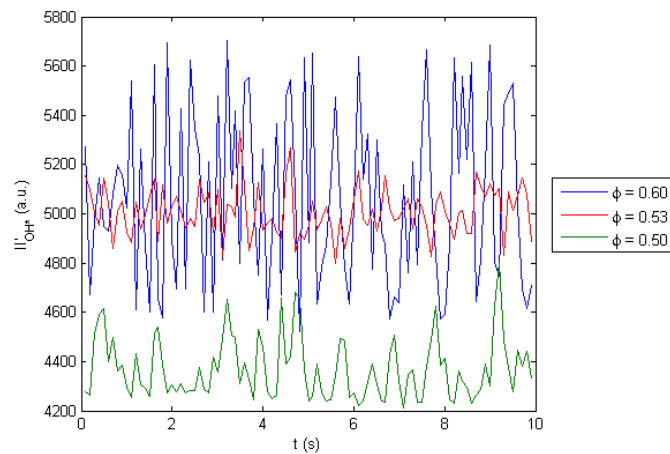


Figure 5.25: Effect of φ on II'_{OH^*} for 110 kW ETEP CH_4 -air flames

By reducing the equivalence ratio below $\varphi = 0.50$, the flame is observed to undergo an LBO instability marked first by partial extinction and reignition events and followed by complete flameout and reignition, as seen in Figure 5.26. When the intensity levels reach $II'_{OH^*} = 5200$ - 5600 , similar to levels at $\varphi = 0.60$ in Figure 5.25, the flame is seen to temporarily stabilize along the shear layer near the burner exit. Subsequent partial reignition events occur in various locations including the CRZ and ORZ with full flame extinction below $II'_{OH^*} = 4200$. Despite the influence of aliasing, the fluctuation frequency of reignition and extinction events shown here is similar compared with the ATAP case, a point supported by dynamic pressure sensing during the ETEP LBO instability.

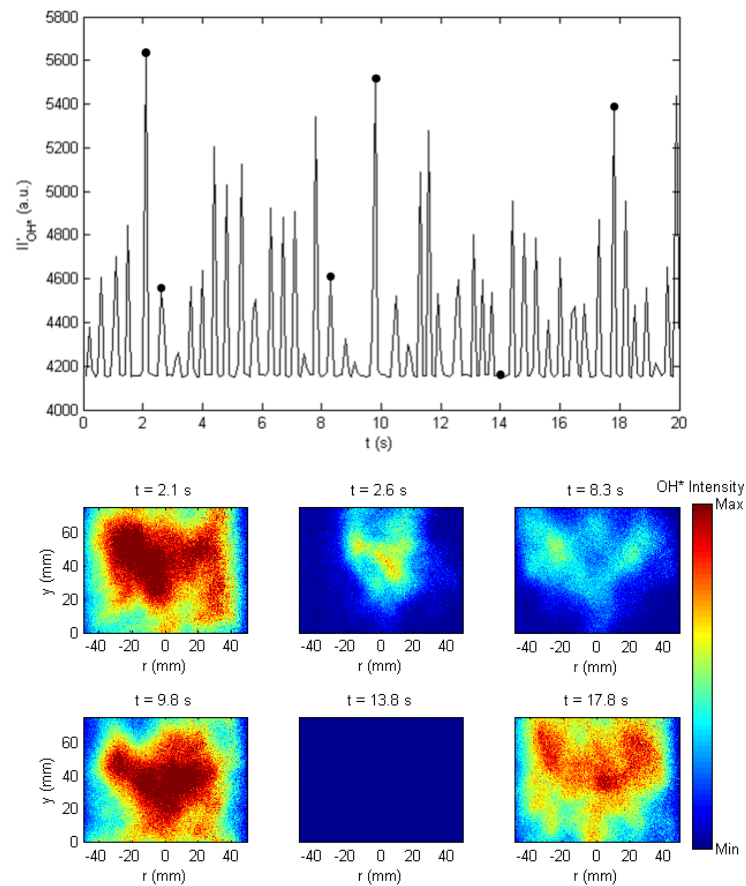


Figure 5.26: OH* chemiluminescence intensity fluctuation (left) with solid markers corresponding to selected instantaneous OH* chemiluminescence images (right) for a 110 kW ETEP CH₄-air flame during LBO instability at $\phi = 0.49$

The observation of a second instability mode in the ETEP case is confirmed by dynamic pressure measurement from the Burner Face DPT, as shown in Figure 5.27, with $\phi = 0.49$ (Figure 5.27.a) and 0.60 (Figure 5.27.b). During burner operation at $\phi = 0.60$, a set of harmonic frequencies is apparent in the resulting PSD, similar to the ETAP case in Figure 5.27.b. The first peak has a frequency of 511 Hz, matching the ETAP Strouhal number at $\phi = 0.60$, $St = 0.48$. Similar to the ETAP, $\phi = 0.60$ case shown in Figure 5.20, the frequency measured here appears to correspond to the first harmonic frequency of a longitudinal standing wave within the burner. Using the same estimation method for the speed of sound based on AFT and T_3 under these conditions, it was found that the estimated value (835 m/s) falls within 1% of the speed of sound (830.3 m/s) required to generate this measured fundamental frequency. Further support for this instability representing an acoustic mode of the combustor is provided by a constant Helmholtz number, $He = 0.25$, identical to the ETAP, $\phi = 0.60$ case [68]. During the LBO instability (Figure 5.27.a), the harmonic content shifts to the low end of the frequency

spectrum below 200 Hz. The dominant frequency at the LBO instability is measured at ~ 12 Hz with a total pressure fluctuation during the LBO instability of $p'_{RMS} = 4.4$ kPa.

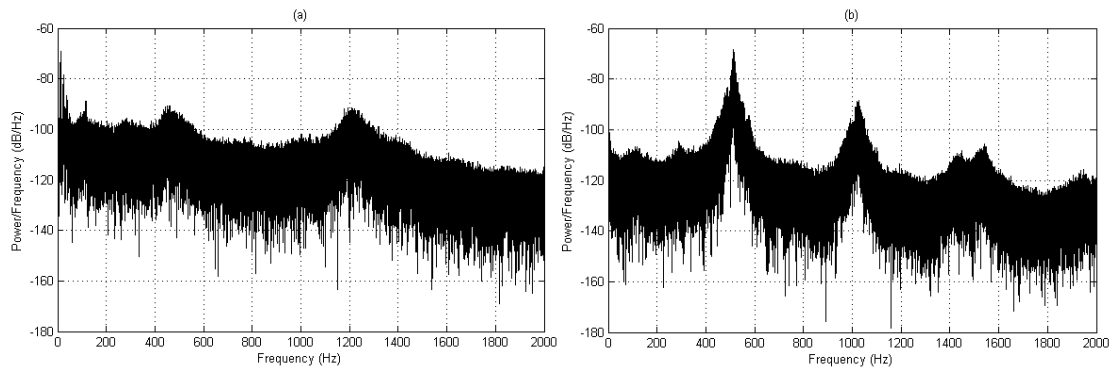


Figure 5.27: PSD of Burner Face DPT measurement for 110 kW ETEP CH₄-air flames during LBO instability at $\varphi = 0.49$ (a) and operation at $\varphi = 0.60$ (b)

Pressure fluctuations during these two distinct instability modes both exceed 2% of the combustor inlet pressure of 0.2 MPa, as seen in Figure 5.28. As shown in both the ATAP and ETAP cases, the pressure fluctuation level is shown to collapse prior to the onset of the LBO instability at $\varphi = 0.50$. At $\varphi = 0.50$, the frequency spectrum no longer shows the harmonics seen in Figure 5.27.b, appearing multimodal with peaks at 20 Hz corresponding to localized extinction and reignition events, 416 Hz ($St = 0.32$) related to the standing wave, and 1221 Hz ($St = 0.94$) consistent with flow-driven vortex shedding. As the air mass flow rate is further increased, the flame transitions into the LBO instability and the pressure fluctuations increase as low frequency harmonics are established.

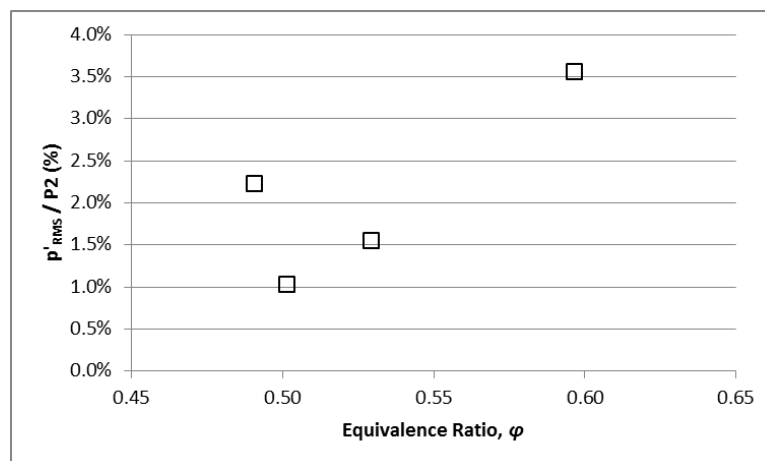


Figure 5.28: Effect of φ on the total dynamic pressure fluctuation of the Burner Face DPT for 110 kW ETEP CH₄-air flames

The harmonic content of the high-amplitude, low frequency LBO instability under ETEP conditions is further evident when the Burner Face DPT signal is bandpass filtered, as shown in

the PSD plot in Figure 5.29. The dominant frequency of the LBO instability is 12.5 Hz, also observed in the ATAP case, an interesting point given that \bar{u} at LBO in the ETEP case is approximately 3 times (53.4 m/s) that of the ATAP case (19.5 m/s), suggesting a link instead with chemical effects, similar to the chemical influence suggested in the ETAP case (Figure 5.22).

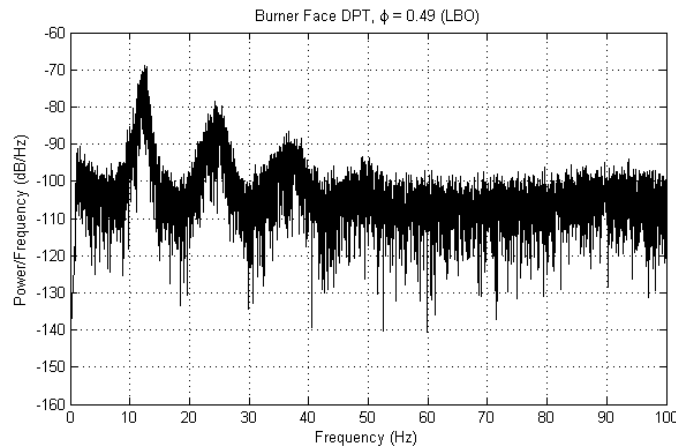


Figure 5.29: Bandpass filtered PSD for Burner Face DPT during LBO instability for an 110 kW ETEP CH₄-air flame at $\phi = 0.49$

5.2.2.2 Application of LBO Instability Prediction Methods

Given the detailed experimental characterization of LBO instabilities in Sections 5.2.2.1 and 5.2.2.2, it is useful to investigate the potential for predicting these instabilities in a manner that can be extended to general use in practical systems. Two analysis methods are considered. The first, based on the time-varying dynamic pressure signal, applies the kurtosis method introduced in Chapter 3.2.2.1. The second, based on generic burner geometric scales and chemical kinetic modeling, applies the dimensionless Strouhal and Damköhler relationships described in Chapter 2.2

In the three operational cases where stability curves were developed, 55 kW ATAP, $T_2 = 573$ K, 55 kW ETAP, and 110 kW ETEP, the kurtosis value at each equivalence ratio was calculated from the full, unfiltered Burner Face DPT data set, which consists of 240000 data points generated at 4 kHz for 60 seconds. In the case of each LBO instability, the kurtosis value was calculated from a smaller data set (~40000 – 60000 data points) as the instability was not sustained for the same duration to protect the experimental apparatus. The variation in the kurtosis value as a function of ϕ is presented in Figure 5.30. Note that data points are connected simply to highlight the trends. In the 55 kW ATAP case, it can be seen that for $\phi \geq 0.70$ the kurtosis of the dynamic pressure signal is approximately 3, while the value drops to

1.8 at the LBO instability at $\varphi = 0.64$. This is in agreement with trends identified in Section 5.2.2.1 which gave evidence of stable operation under ATAP conditions except very near the LBO limit. In the 55 kW ETAP and 110 kW ETEP cases, in which potential thermoacoustic instabilities were observed in addition to the LBO instability, the dynamic pressure kurtosis analysis is able to identify both instabilities. In the 55 kW ETAP case, kurtosis values below $K = 2$ can be seen on either side of $\varphi = 0.53$, providing further evidence of multiple instability modes under these conditions. A kurtosis value of 1.7 can be seen at $\varphi = 0.60$ in the 110 kW ETEP case, supporting the claim of thermoacoustic instability suggested by the PSD shown in Figure 5.27.b.

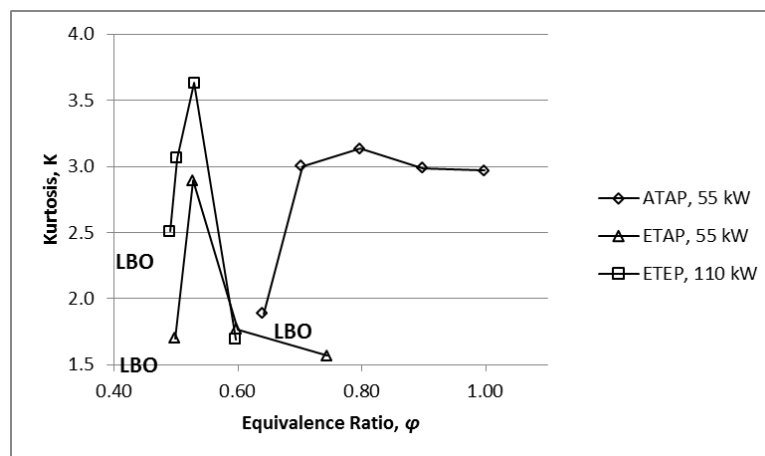


Figure 5.30: Effect of φ on the measured Burner Face DPT kurtosis across 3 operating cases in the HPGSB-2

The LBO kurtosis value of $K = 2.5$ for the 110 kW ETEP case highlights one critical caveat of this particular analysis technique. All kurtosis values at LBO plotted in Figure 5.39 are calculated from the bandpass filtered ($1 \text{ Hz} < f < 100 \text{ Hz}$) signal only, while all other equivalence ratio kurtosis values are calculated using the unfiltered dynamic pressure signal. If the unfiltered dynamic pressure signal is used in the LBO cases, the kurtosis value tends towards 3 because of the multimodal frequency content that has been identified and described previously. Whereas the kurtosis analysis is able to identify the thermoacoustic instability because the instability depends on a single sinusoidal standing wave, the analysis is limited when the dominant frequency is overlaid with other modes, as in the ETEP LBO case. The importance of this filtering process in the identification of high-amplitude, low frequency LBO instabilities, which has also been highlighted by Bompelly et al. [77], is shown in Figure 5.31 for the ETEP operating case specifically. As can be seen, without bandpass filtering, the measured kurtosis value of the Burner Face DPT signal during the LBO instability is approximately $K = 2.8$. The kurtosis of 2.5 plotted in Figure 5.39 for the ETEP case is calculated when the bandpass filter

cutoff frequency is 100 Hz ($1 \text{ Hz} < f < 100 \text{ Hz}$). By decreasing the cutoff frequency towards the actual instability frequency of 12.5 Hz, the kurtosis trends towards 1.5, as would be expected with the signal less influenced by other higher-frequency modes. Thus, the filtering cutoff frequency is a critical component to consider when applying this analysis technique to LBO instabilities, which may occur within multimodal systems.

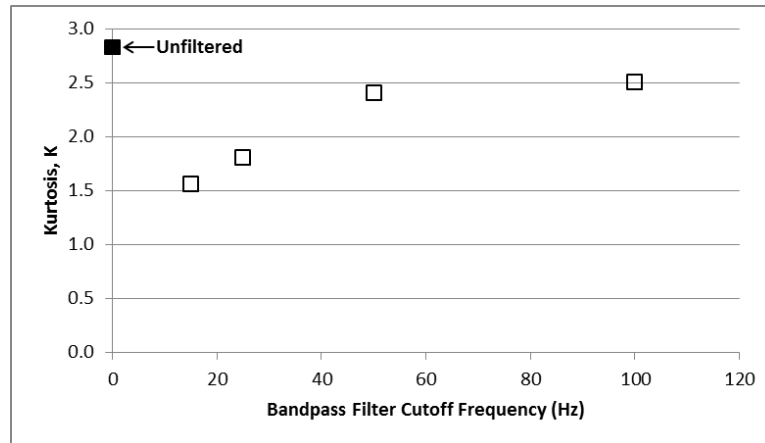


Figure 5.31: Effect of bandpass maximum cutoff frequency on the measured Burner Face DPT kurtosis during LBO instability of an 110 kW ETEP CH₄-air flame at $\varphi = 0.49$

It is also useful to consider the time-varying Burner Face DPT kurtosis value, seen in Figure 5.32.a. In Figure 5.32, the time series of LBO onset and LBO instability from the 55 kW ATAP and $T_2 = 573 \text{ K}$, 55 kW ETAP cases are overlaid. The onset of the LBO instability is identified in Figure 5.32.b at $t = 5 \text{ s}$ by the significant rise in p'_{RMS} , calculated for the same bin size ($t = 0.1 \text{ s}$) as the kurtosis value. A reduction in the kurtosis value (Figure 5.32.a) towards 1.5 is seen at the onset of LBO in both operating cases. Prior to the onset of the LBO instability ($t < 5 \text{ s}$), both the ATAP and ETAP kurtosis values are observed to undergo significant fluctuations. When considering the time-varying kurtosis under "stable" conditions (for example $\varphi = 0.70$ in the ATAP case and $\varphi = 0.53$ in the ETAP case), similar fluctuations are seen as that observed prior to the onset of LBO. This suggests that the time-varying fluctuation in kurtosis could be utilized as a measure of flame stability given that the level of fluctuation in time-varying kurtosis drops significantly once the instability is established.

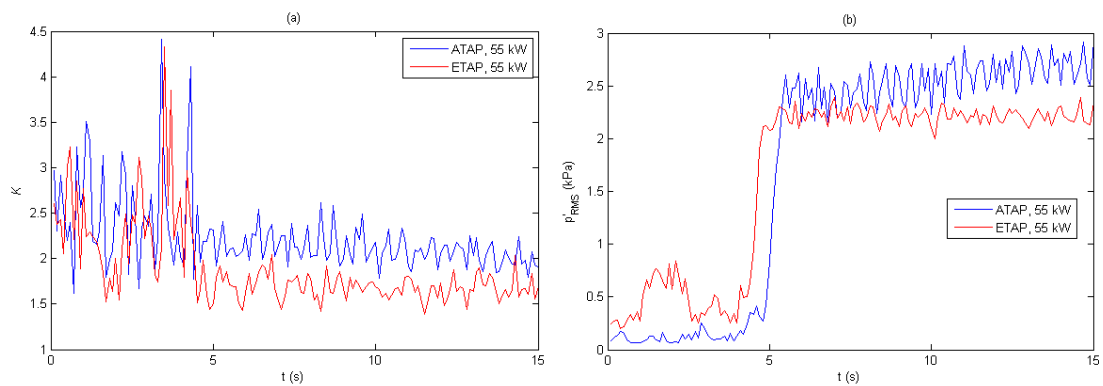


Figure 5.32: Time series of measured Burner Face DPT kurtosis (a) and p'_{RMS} (b) at the approach to LBO instability in the 55 kW ATAP and $T_2 = 573$ K, 55 kW ETAP operating cases

Further to the kurtosis analysis, which may provide an operational instability diagnosis tool, a dimensionless analysis of the LBO conditions is conducted to inform potential burner design implications. By considering only the LBO instability points observed in this study, the Strouhal number, St , is first plotted as a function of the measured LBO dominant frequency in Figure 5.33 to investigate potential flow and acoustic effects on the observed phenomena. Due to the low frequency nature of the LBO instability, the Strouhal number range ($St = 0.009 - 0.027$) is significantly less than those associated with the flow-driven vortex shedding ($St = 0.8-1.0$) and the standing wave instability ($St = 0.4-0.5$). For a fixed combustor inlet pressure condition, the LBO instability Strouhal number is shown to vary linearly with the measured instability frequency, implying that the instability is not necessarily flow driven. This suggests that the instability frequency may be controlled more by chemical effects than flow field or acoustic effects. The Strouhal analysis is also unable to capture the effect of increased combustor inlet pressure, with the ETEP operating case an obvious outlier. However, it is possible to observe that similar dominant LBO frequencies were measured for the ATAP and ETEP operating conditions (~ 12.5 Hz) as well as selected ETAP conditions (~ 16 Hz).

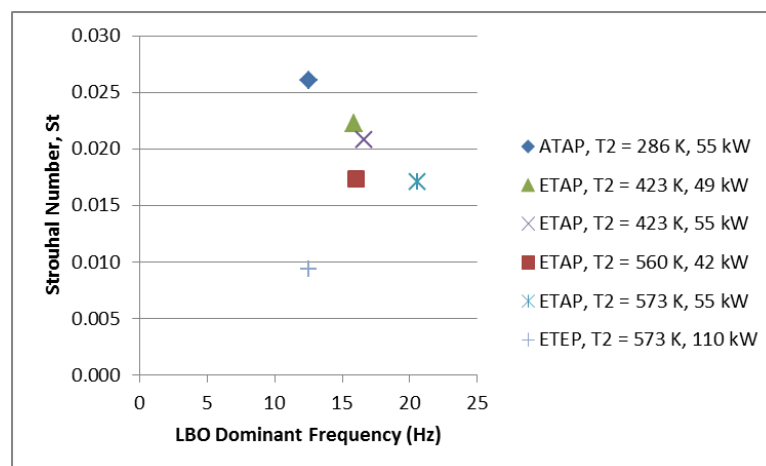


Figure 5.33: Strouhal number as a function of LBO dominant frequency in the HPGSB-2

To investigate the potential influence of chemical effects on the LBO instability frequency, the measured frequency is plotted in Figure 5.34 as a function of the chemical time scale defined in Chapter 2.2.2.2, $\tau_{chem} = \nu/S_L^2$, where $\nu = \mu_{premix}/\rho_{premix}$ and S_L is calculated from chemical kinetics modeling. Compared to Figure 5.33, this relationship provides improved collapse of all observed LBO instability frequencies as the pressure effect is captured in both ν and S_L . It also appears physically relevant that as the chemical timescale decreases, the LBO instability frequency increases, as the extinction and reignition events are able to proceed on reduced timescales. This also provides support for the measured ~ 16 Hz LBO instability frequency for the selected ETAP conditions shown in Figure 5.22. In the 42 kW ETAP case, the combination of reduced HRR and reduced combustor inlet temperature ($T_2 = 560$ K) has the effect of reducing S_L , which consequently increases the chemical timescale for that particular flame to the point where the 16 Hz LBO instability frequency matches the 49 kW and 55 kW ETAP cases at $T_2 = 473$ K. Thus, similar chemical timescales for all three of these ETAP points are observed in Figure 5.34, despite LBO occurring at different equivalence ratios, $\phi = 0.57$ ($T_2 = 423$ K) and $\phi = 0.50$ ($T_2 = 560$ K).

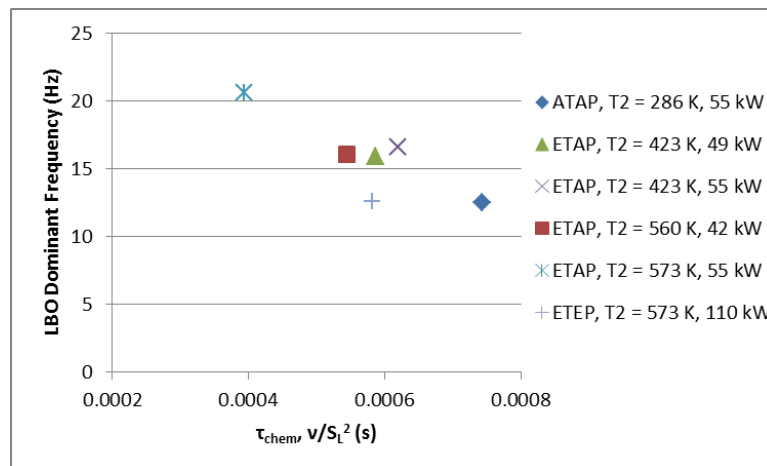


Figure 5.34: Effect of τ_{chem} on the LBO f_{peak} in the HPGSB-2

Cavaliere et al. [89] suggest that the success of the Damköhler correlation (Equation 2.8) in predicting LBO for their burner implies it could potentially be used in other configurations. Extending the previous analysis of τ_{chem} to this extinction Damköhler relationship, Figure 5.35 supports this claim, that a minimum blowoff Da relationship may exist for a given burner configuration and operating condition. The main point of comparison between the two burner systems would be the ATAP point, given that Cavaliere et al. [89] conducted their LBO work at atmospheric temperature and pressure. It is interesting to note that despite similar bluff body diameter (19.6 mm [89] and 18 mm, HPGSB-2), confinement diametric expansion ratio (2.57

[89] and 2.5, HPGSB-2), and burner exit nozzle velocity at LBO (19.6 m/s [89] and 19.5 m/s, HPGSB-2), the LBO equivalence ratio differs from $\varphi < 0.60$ [89] to $\varphi = 0.64$ in the HPGSB-2 under ATAP conditions. As shown in Figure 5.35, Cavaliere et al [89] measured Damköhler relationship values of 1.19 to 1.34 for premixed ATAP flames at varying thermal power. Values of the Damköhler relationship in the HPGSB-2 vary from 0.92 (ATAP) to 1.31 (ETEP), with an obvious increase between groupings of constant P_2 . The difference between the published results and the HPGSB-2 is suggested to be due to differences in the swirler geometry, which will influence the flow field and allow for the observed lean shift in the LBO φ . This will most significantly affect the LBO S_L (hence, τ_{chem}) in Equation 2.8. This is considered the primary reason for the downward shift in the value of $\left[\left(\frac{\bar{u}}{D_{lance}} \right) \left(\frac{v}{S_L^2} \right) \right]^{1/2}$ between the ATAP condition and those of Cavaliere et al. [89]. The burner used by Cavaliere et al. [89] utilized an axial swirler with $S_g = 1.23$. To accommodate this change in swirler configuration more generally, the utilization of a scaled axial exit velocity based on swirl number, $\bar{u}_y = \frac{\bar{u}}{\sqrt{1+S_g^2}}$, allows for better LBO data collapse between burners, as shown in Figure 5.35.b. This scaling factor is identical to that used in Chapter 4.3.3 for collapsing isothermal dynamic pressure dominant frequency measurements with varying swirl number in the HPGSB.

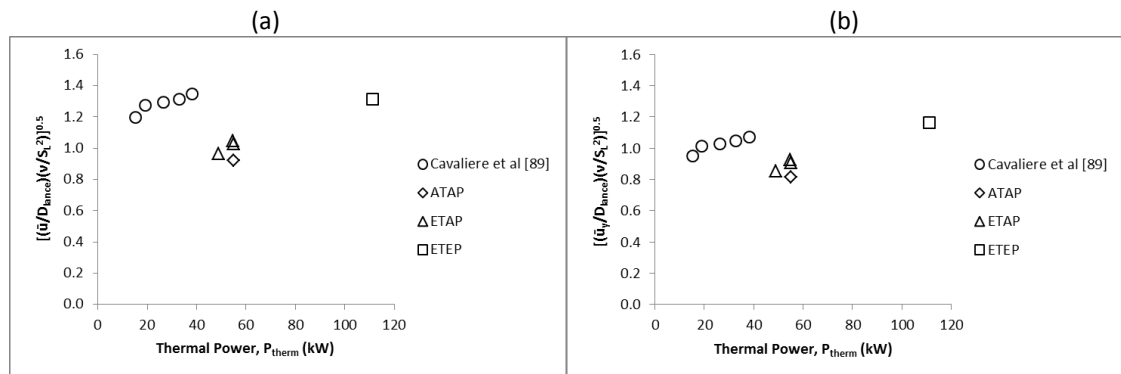


Figure 5.35: Comparison of Da relationship applied by Cavaliere et al. [89] with the observed LBO instability (a) and with swirl-corrected exit velocity (b)

5.3 Chapter Summary

Two new generic swirl burners (HPGSB and HPGSB-2) have been designed and commissioned at Cardiff University's Gas Turbine Research Centre (GTRC) for the study of flame stability in fully premixed flames.

In the HPGSB, a brief study of pure methane and propane combustion was conducted at atmospheric temperature and pressure conditions at 55-56 kW. Both flames are observed to change shape and stabilization location as ϕ is reduced and LBO is approached, supported by OH* CL and OH PLIF measurements. Exhaust gas emissions show that under these lean operating conditions, sub-10 ppmV NO_x and CO measurements are possible, with the thermal NO_x formation pathway observed to dominate, showing an exponential relationship with AFT. CO emissions are shown to be nonmonotonic and increasing with reduced equivalence ratio. For C₃H₈-air flames, this occurs at higher AFT than CH₄-air flames, suggesting that thermo-diffusive effects may begin to dominate under LPM conditions, leading to incomplete combustion despite higher S_L and AFT than methane. Finally, a scaling factor based on hydrogen-to-carbon ratio is suggested for OH* chemiluminescence intensity measurements between differing hydrocarbon fuels, which will be further explored in Chapter 6 for a variety of H:C ratios and elevated operating conditions.

In the HPGSB-2, in addition to extensive isothermal and stable flame characterization, a low-frequency, high-amplitude combustion instability associated with the onset of LBO was identified and investigated experimentally under varying conditions up to $T_2 = 573$ K $P_2 = 0.2$ MPa, and $P_{therm} = 110$ kW using a combination of OH* CL, OH PLIF, and dynamic pressure sensing techniques. In addition, chemical kinetics modelling, statistical analysis, and dimensionless analysis were utilized to enhance the experimental study undertaken. The following conclusions are therefore made:

- Extensive characterization of the combustion rig and burner through isothermal loudspeaker excitation and air flow testing in combination with Strouhal and Helmholtz dimensionless analysis facilitates the identification of natural resonant acoustic and flow-driven instability modes. The influence of BPV position in the experimental rig is such that, under atmospheric conditions (BPV fully open), harmonic excitation of natural resonant modes appears to occur, while under pressurized conditions (BPV closed) the system is sufficiently damped to avoid harmonic excitation. The first acoustic mode of the rig appears in both cases at approximately 133 Hz. Across all isothermal flow conditions, a constant Strouhal number ($St = 0.8$) as a function of dominant frequency and a linearly-varying Helmholtz number as a function of air flow Reynolds number indicates Kelvin-Helmholtz vortex shedding from the burner exit nozzle.

- Isothermal PIV identifies coherent flow structures such as the CRZ and ORZ within the flow field. PIV measurements with the HPGSB-2 with convergent confinement confirms the flow field changes predicted numerically and suggested by isothermal acoustic analysis, with an asymmetric area of positive axial velocity identified along the burner central axis. This reduces the strength and size of the CRZ compared to the open confinement case. This analysis also confirms the use of assumed turbulence intensity and integral length scale values in the turbulence scaling parameter which links the HPGSB-2 to industrially-relevant GT combustor conditions.
- Flame stabilization and shape transitions at elevated operating conditions are consistent with complementary work under atmospheric ambient conditions. Flame transition from a V-shape flame attached to the instrumentation and pilot lance bluff body and stabilized along the shear layer from the burner exit nozzle to an M-shape flame which stabilizes downstream in the quartz confinement tube, with significant influence from the quartz confinement walls, CRZ and ORZs. In the ETEP case, an intermediate flame stabilization location is observed between the M-shape flame and LBO, identified as a highly unstable mode in which the lifted flame is stabilized only by the combustor confinement walls.
- Instantaneous measurements of OH* chemiluminescence integral intensity and dynamic pressure provide evidence of the nature of the LBO instability in addition to other flow and acoustic instabilities at elevated conditions. Strouhal number and Helmholtz number analysis allows for the separation of the observed instabilities into three distinct categories: resonant acoustic ($St = 0.4-0.5$, $He = 0.25$), flow-driven vortex shedding ($St = 0.8-1.0$), and chemically-driven extinction and reignition ($St < 0.01$). Partial flame extinction and reignition events are evident prior to the onset of the low frequency, high amplitude LBO instability, which is characterized in all operating cases by periodic complete flame extinction and reignition. LBO instability frequencies of ~ 12.5 Hz (ATAP/ETEP), ~ 16 Hz (ETAP), and 20 Hz (ETAP) are identified with observed amplitudes up to 2.5% of the combustor inlet pressure.
- Kurtosis analysis of the measured time-domain dynamic pressure signal is shown to be a viable method for the identification of multiple instability modes. In the ETAP and ETEP cases, potential thermoacoustic instabilities were identified at the TFB limit by

both instantaneous II'_{OH^*} and dynamic pressure measurements, although visually the flame did not appear unstable. Overall signal kurtosis values near 1.5 were identified in both cases, suggesting that indeed the burner experienced thermoacoustic instability under these conditions. The LBO instability was also marked by a reduction in kurtosis from 3 to 1.5, although frequency filtering has been highlighted as a critical element to the application of this method for the identification of instability modes which may exist within a multimodal, unstable system. This multimodal system was characterized prior to the onset of the LBO instability by partial extinction and reignition frequency, thermoacoustic frequency (in the ETAP and ETEP cases only), and vortex shedding frequency. Time-varying kurtosis fluctuation has also been shown to be a potential LBO instability indicator.

- Given that a Strouhal number analysis is unable to collapse all measured LBO instability frequencies, the instability is suggested to be dictated primarily by the τ_{chem} developed for use within an existing extinction Damköhler relationship. This τ_{chem} , the ratio of ν to S_L^2 , is able to better capture the effect of $P2$ on the LBO instability across all operating conditions. Comparison of the Damköhler relationship with published burner data confirms its potential use across burner geometries, although it is suggested that the bulk axial velocity is scaled to a resultant velocity by the burner swirl number to capture the potential effect of changes in swirler geometry across burners. This is an area for future work given the variety of swirl numbers possible with the HPGSB-2.

CHAPTER 6 – FUEL FLEXIBILITY FOR GAS TURBINES – HIGHER HYDROCARBONS

With ever-increasing pressure on conventional natural gas supplies, resulting from fluctuating domestic production and demand in concert with stricter economic and environmental conditions, global gas mobility is becoming more important for the security and development of flexible energy systems. In recent years, demand for increased operational flexibility from GT power generation has coupled with increased global trade of LNG and the development of unconventional gas sources (e.g. shale gas). While this increase in global gas trade has been known to cause local GT operational issues [16], little experimental research at elevated ambient conditions is available which characterizes the influence of higher hydrocarbon (C_2+) content typical of these fuels in swirl burners. Thus, an experimental characterization of the influences of LNG fuel composition and elevated operating conditions on LPM flames has been conducted in the HPGSB-2. Combustion stability and flame stabilization, chemical kinetics, and NO_x emissions are considered parametrically at a fixed T_2 of 573 K, P_2 of 0.11 – 0.33 MPa, P_{therm} of 382 kW/MPa, and ϕ of 0.50 – 0.65. LNG fuel compositions were varied up to 15% ethane and 13% propane in methane, as described in Chapter 3.4.1.1, while in some cases fuel parameters such as WI are held constant. Flame dynamic pressure amplitudes, OH^* chemiluminescence intensity, and NO_x emissions are shown generally to scale with pressure and fuel molar hydrogen to carbon ratio. The use of a reaction zone thickness derived from chemical kinetic modeling is proposed to collapse combustion noise and NO_x emissions measurements across fuel blends and pressures. Chemical kinetic modeling of AFT and S_L of the experimental conditions also supports the characterization of the observed flame response to changes in C_2+ content, with propane addition specifically observed to influence lean flame stability. The influence of propane on the thermo-diffusive behavior of methane is further studied with flame speed measurements in the CVCB, and stretch rate results support the observation in the more practical HPGSB-2 combustion environment that propane-containing blends cannot be operated stably under the same lean conditions and turbulence as a pure methane fuel, despite fundamental properties such as S_L and AFT which suggest these fuels have higher reactivity. This finding highlights the trivality of parameters such as WI at predicting the combustion behavior of natural gas blends with high C_2+ content and emphasizes the need to utilize other fundamental properties of these fuels used in operational GTs. It also provides a steer for LPM GT combustor designs to take into consideration the

effects of both a thinning of the combustion reaction zone as pressures increase and the influence of high turbulence levels on C_2+ containing fuels.

6.1 Chemical Kinetics Modeling and Flame Speed Measurements

6.1.1 Chemical Kinetics Modeling

Table 6.1 provides the full range of experimental conditions evaluated in this study. Note that all values are calculated based on the full premixed reactant flows, in particular the Reynolds number, which accounts for changes in premixed dynamic viscosity through use of the Wilke correlation [228] using Equation 5.1. The experimental designations in Table 6.1 refer to the fuel type (e.g. BASE, FARNG, MIDNG, EMIX1). All experimental combustion results presented in this Chapter were captured in the HPGSB-2 with a fixed convergent nozzle confinement and a fixed geometric swirl number of $S_g = 0.8$ to isolate the chemical kinetic effects of the change in fuel composition as the convergent confinement is shown to decouple the thermoacoustic instability identified with the open cylindrical confinement at the rig operating conditions of interest (refer to Chapter 7.3.1, Figure 7.17). As can be seen, a variety of elevated inlet operating conditions were investigated, including fixed T_2 at 573 K, increased P_2 up to 0.33 MPa, P_{therm} up to 126 kW and a variety of flow turbulence levels. Fuel characteristics for BASE (100% CH_4), FARNG (85%-15% $CH_4-C_2H_6$), MIDNG (90%-6%-4% $CH_4-C_2H_6-C_3H_8$), and EMIX1 (85%-12.6%-2.4% $CH_4-C_3H_8-N_2$) can be found in Table 3.1 (Chapter 3.4.1.1).

Table 6.1: HPCR operating ranges for C_2+ combustion experiments

Fuel Designation	T_2 (± 5 K)	P_2 (MPa)	P_{therm} (kW)	ϕ	\bar{u} (m/s)	Re ($\times 10^3$)	$\dot{m}\sqrt{T_2}/P_2$	AFT (K)	S_L (m/s)
BASE	573	0.11 - 0.33	42 - 126	0.52 - 0.65	29 - 35	27 - 91	0.51 - 0.62	1732 - 1954	0.20 - 0.54
FARNG	573	0.11 - 0.33	42 - 126	0.52 - 0.60	30 - 35	27 - 92	0.54 - 0.63	1732 - 1889	0.24 - 0.57
MIDNG	573	0.11 - 0.33	42 - 126	0.52 - 0.65	28 - 35	25 - 92	0.50 - 0.63	1737 - 1967	0.22 - 0.67
EMIX1	573	0.11 - 0.33	42 - 126	0.53 - 0.65	28 - 34	25 - 93	0.50 - 0.62	1748 - 1982	0.22 - 0.73

Chemical kinetics modeling of the experimental conditions was conducted with CHEMKIN-PRO [199] using the equilibrium tool to provide adiabatic flame temperatures (AFT) and the PREMIX program to provide laminar flame speed (S_L), volumetric heat release rate distribution (Q'), equilibrium exhaust H_2O concentrations, X_{H_2O} , for NO_x emissions correction, and OH (X_{OH}) and CH radical (X_{CH}) 1-D profiles for calculation of the theoretical reaction zone thickness, δ_v , per Figure 4.23. The model employed the GRI-Mech 3.0 [200] reaction mechanism per the methods described in Chapter 3.3.1.

The influence of AFT, $P2$, and fuel composition on S_L and burner operability was evaluated for all experimental conditions, with kinetics modeling results presented in Figure 6.1. As expected, an increase in AFT increases S_L , thus reactivity, of all fuels, with quasi-linear relationships for lean ($\varphi < 1$) conditions at a fixed $P2$ which are further expected to be nonmonotonic for rich conditions ($\varphi > 1$). This plot also gives indication of the influence of $P2$ on the modeled S_L , with an observable decrease in S_L with increasing $P2$, a point which influences the balance of chemical and flow timescales required for stable burner operation at GT relevant conditions. As for the influence of increased C_2+ content in the fuels, modeled S_L results indicate a slight increase with the addition of ethane and propane to methane at a fixed $P2$. This is in agreement with the discussion and literature results presented in Chapter 2.1.3.3.

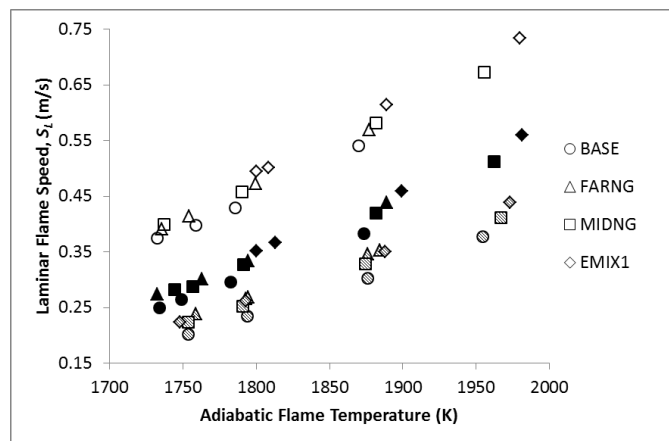


Figure 6.1: Modeled S_L of all experimental conditions as a function of AFT with varying $P2$, 0.11 MPa (open), 0.22 MPa (closed), 0.33 MPa (hashed)

Of particular interest and novelty in this study is to examine the effect of elevated $P2$ and $T2$ on the resulting flame stability and fuel reactivity. Thus, the influence of C_2+ addition to methane on the modeled S_L at varying $P2$ is further highlighted in Figure 6.2, which plots normalized S_L values against $P2$. Each individual fuel S_L has been normalized by the equivalent 100% CH_4 (BASE) S_L at the same condition of elevated temperature ($T2 = 573$ K) and $P2$. These results are plotted for two fixed equivalence ratios, $\varphi = 0.55$ and $\varphi = 0.60$, with AFTs across all fuels of 1791 ± 9 K and $AFT = 1884 \pm 15$ K, respectively. These two conditions of fixed φ are selected for presentation here, and further presentation throughout this Chapter as they represent comparable conditions which could be achieved across all fuels and rig operating conditions. For example, EMIX1 could not be stably operated below $AFT = 1800$ K at $P2 = 0.11$ and 0.22 MPa, whereas BASE, MIDNG, and FARNG could be operated much leaner ($AFT < 1800$ K), as shown in Figure 6.1.

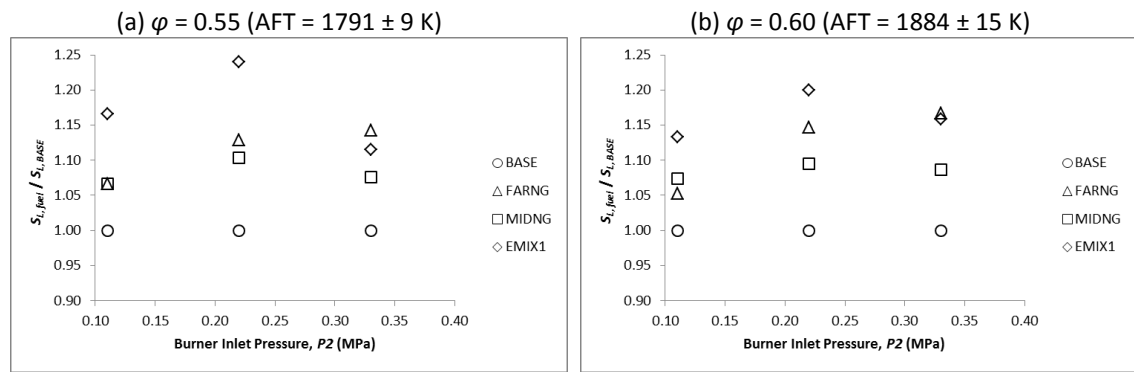


Figure 6.2: Normalized modeled S_L of selected experimental conditions as a function of P_2 at varying ϕ , 0.55 (a) and 0.60 (b).

From Figure 6.2, the modeled S_L increases for all fuels containing C_2+ constituents compared to the BASE S_L , with EMIX1 showing the highest increase of up to 25% at $P_2 = 0.22$ MPa and $\phi = 0.55$. The P_2 response of the propane containing fuels (MIDNG and EMIX1) appears nonmonotonic with increasing P_2 , while the FARNG blend appears to follow a power law correlation, an observed trend that appears to be replicated in the measured NO_x emissions presented in Section 6.4. This relationship suggests competing fundamental influences between propane and ethane blended fuels, whereas the low temperature chemistry effects of propane addition may have a catalytic effect on methane reactivity, this effect under elevated pressure conditions may be limited compared to ethane-blended fuels due to differences in molecular diffusivity (Le effects). Thus, compared with the BASE fuel, the addition of specific C_2+ molecules may have opposing effects on both the blends' reactivity and its diffusivity, which may begin to shift and slow the reaction pathways in highly turbulent, pressurized flow fields.

As suggested by the brief study of pure methane and pure propane flames in the HPGSB in Chapter 5.1.1, the molar fuel hydrogen to carbon ratio (H:C) may be a key fundamental fuel property from which relationships across fuels with varying composition may be drawn. For the conditions presented in Figure 6.2, the modeled S_L has also been considered in terms of H:C ratio, and plotted in Figure 6.3 for varying P_2 and ϕ . As suggested by the relative ordering of fuels for a fixed P_2 in Figure 6.2, Figure 6.3 shows that the modeled S_L values generally increase with decreasing H:C ratio under all conditions of P_2 . While this suggests increased reactivity with increasing H:C ratio, experimental work counters this in terms of the lean operability limits, which suggest that thermo-diffusive effects begin to dominate with increasing H:C ratio and turbulence levels.

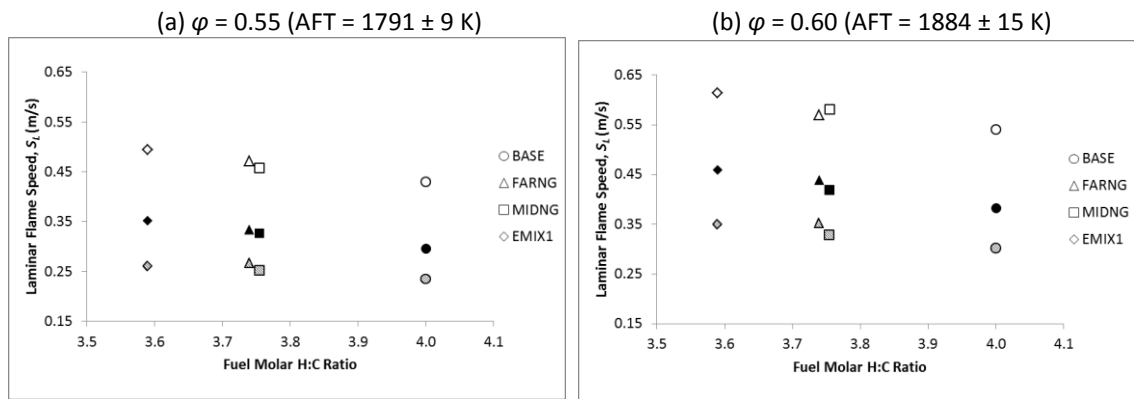


Figure 6.3: Modeled S_L of selected experimental conditions as a function of fuel molar H:C ratio at varying ϕ , 0.55 (a) and 0.60 (b), and P_2 , 0.11 MPa (open), 0.22 MPa (closed), 0.33 MPa (hashed)

Whereas Figures 6.1 and 6.3 give some indication of the influence of P_2 on the modeled S_L , Figure 6.4 compares the fuels directly with a fixed geometry (convergent confinement and $S_g = 0.8$) to evaluate the influence of P_2 . Figure 6.4 provides modeled S_L as a function of P_2 at $\phi = 0.55$ (open symbols) and $\phi = 0.60$ (closed symbols). For a fixed AFT, C_2+ addition is shown consistently to increase flame speed above the BASE case, as expected. All fuels show a marked reduction in S_L with increasing P_2 , following a power law correlation with a P_2^x relationship with $0.43 < x < 0.58$, with x increasing from top to bottom, suggesting that flame reactivity is increasingly dependent on P_2 as the combustion process is shifted to reduced ϕ . It is interesting to note that for a fixed ϕ , the addition of ethane (FARNG) results in the lowest power law exponent of all fuels ($x = 0.43$ at $\phi = 0.60$ and 0.51 at $\phi = 0.55$), suggesting that ethane addition, while increasing reactivity compared to BASE, results in S_L that is less influenced by P_2 , a key point for consideration of this fuel at representative GT operating conditions.

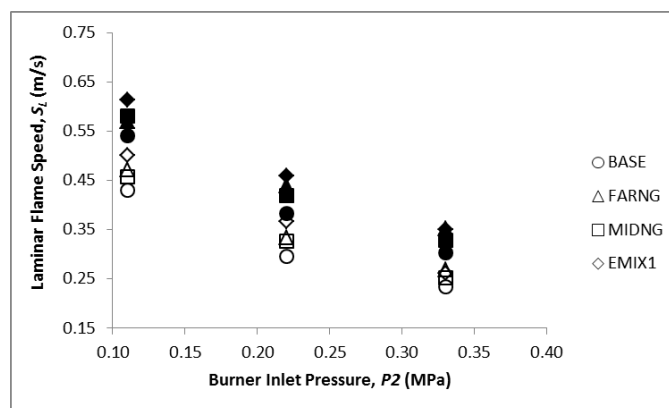


Figure 6.4: Pressure influence on modeled S_L of selected experimental conditions at $\phi = 0.55$ (open symbols) and 0.60 (closed symbols)

6.1.2 Flame Speed Measurements

Given the observed shift in lean operability between EMIX1 and BASE fuels, a brief fundamental study on flame speed and stretch effects was conducted in the CVCB. In a similar manner to the BASE and FARH2 flame speed measurements presented in Chapter 7, S_L , stretch rate (κ), and Markstein length (L_b) for BASE and EMIX1 fuels have been measured. S_L measurements of spherically-expanding BASE and EMIX1 flames were conducted at 298 K and 0.101 MPa, for a lean equivalence ratio range of $0.6 \leq \varphi \leq 0.8$. The results are found in Figure 6.5. Note that the S_L values presented in Figure 6.5 are calculated by correcting the projected unstretched, spherically-expanding flame speed (e.g. Figure 6.6.a at $\kappa = 0$) with the adiabatic density ratio of products to reactants [168]. The measured BASE S_L is in good agreement with the modeled results shown in Figure 7.1 at $T = 290$ K and show a similar quasi-linear trend for lean φ . Note that the reader is directed to Figure 7.1 as the modeled S_L results in this Chapter were conducted at $T = 573$ K, which explains the offset between the values measured here and modeled in Figure 6.1 at $P_2 = 0.11$ MPa. In addition, for a fixed φ , the addition of C_3H_8 and N_2 to CH_4 consistently increases S_L also in agreement with works cited in Chapter 2 and as modeled in Figure 6.2, albeit at higher T .

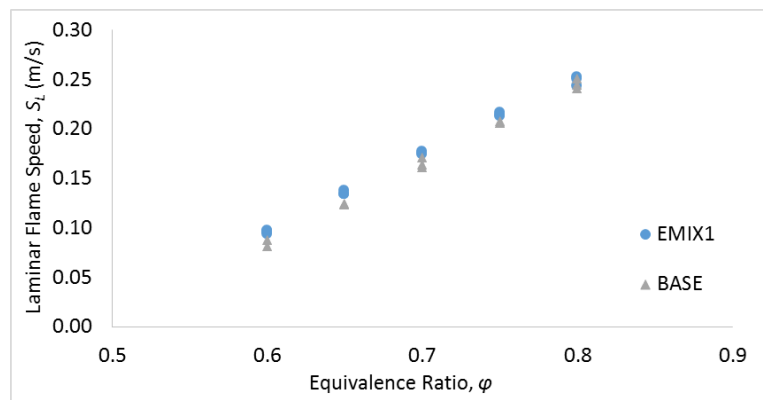


Figure 6.5: S_L measurements for BASE and EMIX1 flames at 298 K and 0.101 MPa

The S_L measurements presented in Figure 6.5 are derived from measures of stretched flame speed as a function of κ as shown in Figure 6.6.a for an equivalence ratio of $\varphi = 0.60$. While the derived S_L is a useful output to categorize flame reactivity, the flame response to increased stretch is also of particular significance due to the lean, turbulent conditions typical of a GT combustor. As can be seen in Figure 6.6.a, the BASE and EMIX1 fuels have opposing slopes at $\varphi = 0.6$. The positive slope exhibited by the BASE fuel means that with increased stretch rate, the stretched flame speed increases, while the opposite is true for the EMIX1 fuel. This gradient is described numerically by the Markstein length, L_b , plotted for the BASE and EMIX flame speed measurements in Figure 6.6.b. Thus, the positive slope for the BASE fuel in Figure

6.6.a corresponds to a negative L_b at $\varphi = 0.6$ in Figure 6.6.b. The negative slope in Figure 6.6.a for the EMIX1 fuel corresponds to a positive L_b at $\varphi = 0.6$ in Figure 6.6.b. The zero-crossing for the BASE fuel in Figure 6.6.b indicates a change in positive stretched flame speed correlation with stretch rate to negative correlation (i.e. reduced flame speed with stretch), while L_b is positive for all measured φ in the EMIX1 case, indicating a negative correlation across the measured range. Thus, the addition of only 12.6% C_3H_8 and 2.4% N_2 to CH_4 has changed completely the response to stretch of the BASE fuel, and would be expected to exhibit decelerating flame speeds in turbulent (i.e. stretched) flames operating under lean conditions. This change in measured fundamental thermo-diffusive behaviour supports the lean stability observations made in the more practical HPGSB-2 operating environment.

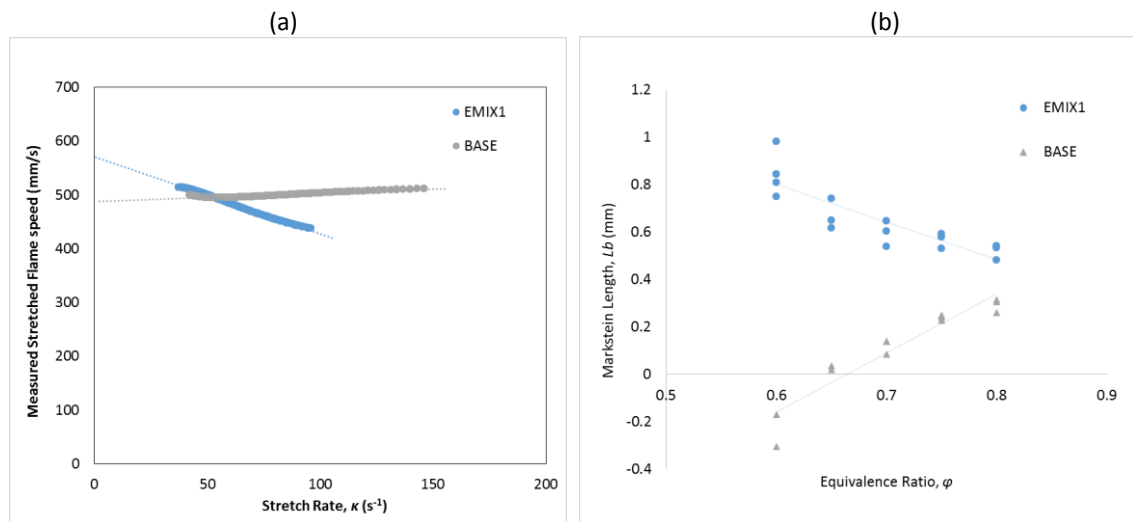


Figure 6.6: Measured stretched flame speed (at $\varphi = 0.60$, a) and Markstein length (at varying φ , b) for BASE and EMIX1 flames at $T_2 = 298$ K and $P_2 = 0.101$ MPa

It is interesting to note here as well that by comparison with the results presented in Chapter 7 for the FARH2 fuel, the addition of H_2 to CH_4 is seen to have the opposite thermo-diffusive influence as the addition of C_3H_8 , not unexpected due to their different Lewis numbers ($Le < 1$ for H_2 and $Le > 1$ for C_3H_8). It is their influence when mixed in relatively small quantities with methane that is remarkable. Whereas the addition of 12.6% C_3H_8 results in a decrease in the stretched flame speed, the addition of only 15% H_2 to CH_4 instead shifts the Markstein length zero-crossing of the BASE fuel to higher φ , promoting an increase in the stretched flame speed under lean conditions (see Figure 7.6.b). Further discussion on this point is provided in Chapter 7.1.2 in the context of the lean stability shift promoted by H_2 addition, as this difference in thermo-diffusive effects is a key finding of this study.

6.2 Flame Stabilization

To isolate the influence of C_2+ addition on premixed methane flame stabilization mechanisms, a series of combustion experiments were conducted with a fixed HPGSB-2 burner geometry and nominally similar flow and turbulence conditions (e.g. fixed Re at each P_2 and φ). For all results presented in this Section, the HPGSB-2 was configured with the convergent nozzle confinement and $S_g = 0.8$, in a configuration identical to that used for the H_2 blended combustion experiments presented in Chapter 7.2.1. BASE, FARNG, MIDNG, and EMIX1 flame stabilization is evaluated based on Abel-transformed OH^* chemiluminescence and OH PLIF measurements with flames at $\varphi = 0.55$ and $\varphi = 0.60$ at $T_2 = 573$ K and three burner inlet pressures, $P_2 = 0.11$ MPa, 0.22 MPa, and 0.33 MPa. For all OH^* CL images presented, the image intensifier gate timing was $t_{gate} = 400$ μs with gain held constant for each dataset. For all OH PLIF measurements, $t_{gate} = 0.1$ μs with gain held constant. In combination with the acoustic measurements presented in Section 6.3, a comprehensive evaluation of C_2+ influence on preheated, pressurized swirl combustion is thus made. For all experimental results, the reader is referred to Table 3.3 for air mass flow rates.

For the $\varphi = 0.55$, $T_2 = 573$ K flames, the AFT across all fuels is 1791 ± 9 K. The dimensionless flow parameter $\dot{m}_{premix}\sqrt{T_2}/P_2$ has been held constant at 0.59, effectively fixing the mean burner exit nozzle velocity at $\bar{u} = 33$ m/s. Scaling the premixed reactant flow rate with pressure yields a thermal power scaling of approximately 382 kW/MPa for thermal powers of $P_{therm} = 42$ kW, 84 kW, and 126 kW. In order to match φ between fuels while holding the air mass flow rates constant, incremental increases in the blended C_2+ fuel mass flow rates with respect to the methane (BASE) flow rate were required; 2% for the MIDNG and FARNG blends and 6% for the EMIX1 blend due to the reduction in FARNG, MIDNG, and EMIX1 stoichiometric AFR compared to the BASE fuel. As the pressure increases, the Reynolds number also increases due to a reduction in premixed reactant density, however, it is nominally constant between fuels at a fixed P_2 , approximately $Re = 30000$, 60000, and 90000 at $P_2 = 0.11$ MPa, 0.22 MPa, and 0.33 MPa, respectively. Thus under fixed P_2 conditions, observed changes in the results can be attributed to chemical influences resulting from changing fuel composition.

For the $\varphi = 0.60$, $T_2 = 573$ K flames, the AFT across all fuels is 1884 ± 15 K. The dimensionless flow parameter $\dot{m}_{premix}\sqrt{T_2}/P_2$ has been held constant at 0.54, effectively fixing the mean burner exit nozzle velocity at $\bar{u} = 31$ m/s. The thermal powers are identical to the $\varphi = 0.55$

conditions. Due to the reduction in premixed air flow rate to achieve $\varphi = 0.60$, the bulk flow Reynolds number is reduced to approximately $Re = 27000$, 54000 , and 81000 at $P_2 = 0.11$ MPa, 0.22 MPa, and 0.33 MPa, respectively.

6.2.1 Influence of Ethane Addition

Comparison is first made between the BASE and FARNG fuels to evaluate the influence of 15% C_2H_6 addition to methane on flame stabilization location and heat release distribution. As discussed previously, this level of ethane content is considered to be at the upper specification of LNG fuel compositions. BASE and FARNG flame stabilization is evaluated based on Abel-transformed OH^* chemiluminescence and scanning OH PLIF measurements in Figures 6.7 and 6.8, respectively. First, in Figure 6.7, a series of BASE and FARNG OH^* CL images are presented with flames at $\varphi = 0.55$ and varying P_2 from 0.11 MPa to 0.33 MPa (comparable with MIDNG and EMIX1 fuels in Figure 6.9). Then, in Figure 6.8, a series of BASE and FARNG scanning OH PLIF images are presented with flames at $P_2 = 0.33$ MPa (126 kW) and varying φ from 0.53 to 0.60 .

At $\varphi = 0.55$ in Figure 6.7, both BASE and FARNG flames are observed to stabilize along the outward expanding shear layer between the CRZ and ORZ observed in the isothermal PIV results in Chapter 5.2.1.2, yielding conical, V-shaped flames which expand radially outward from the burner exit nozzle centerline ($r = 0$ mm). However, the influence of ethane addition is notable. The mean area of localized heat release is observed to transition upstream along the shear layer towards the burner exit nozzle at each pressure condition. This compacts the heat release zone and reduces the influence of the quartz confinement walls which is more apparent under BASE conditions. This is the result of increased chemical reactivity as shown in Figure 6.2.a, with modeled FARNG S_L approximately 7% higher than 100% CH_4 . Thus, the heat release reactions proceed on a reduced chemical time scale while the flow time scale has been held nominally constant between fuels. The BASE flame reaction zone extends axially downstream and radially outward compared with the FARNG flames, with little change in flame angle observed across all pressure conditions. However, the FARNG flame is observed to shift upstream towards the burner exit nozzle with increased P_2 . The distribution of maximum OH^* chemiluminescence intensity is interesting to note between both fuels. At $P_2 = 0.11$ MPa (the lowest Re condition), the areas of highest heat release are quite narrow and reside axially upstream near the burner exit nozzle. At $P_2 = 0.22$ MPa (thus increased Re), the area of maximum intensity appears almost uniform along the flame brush in the FARNG case

as increased vortex interaction resulting from the increased turbulence promotes improved mixing.

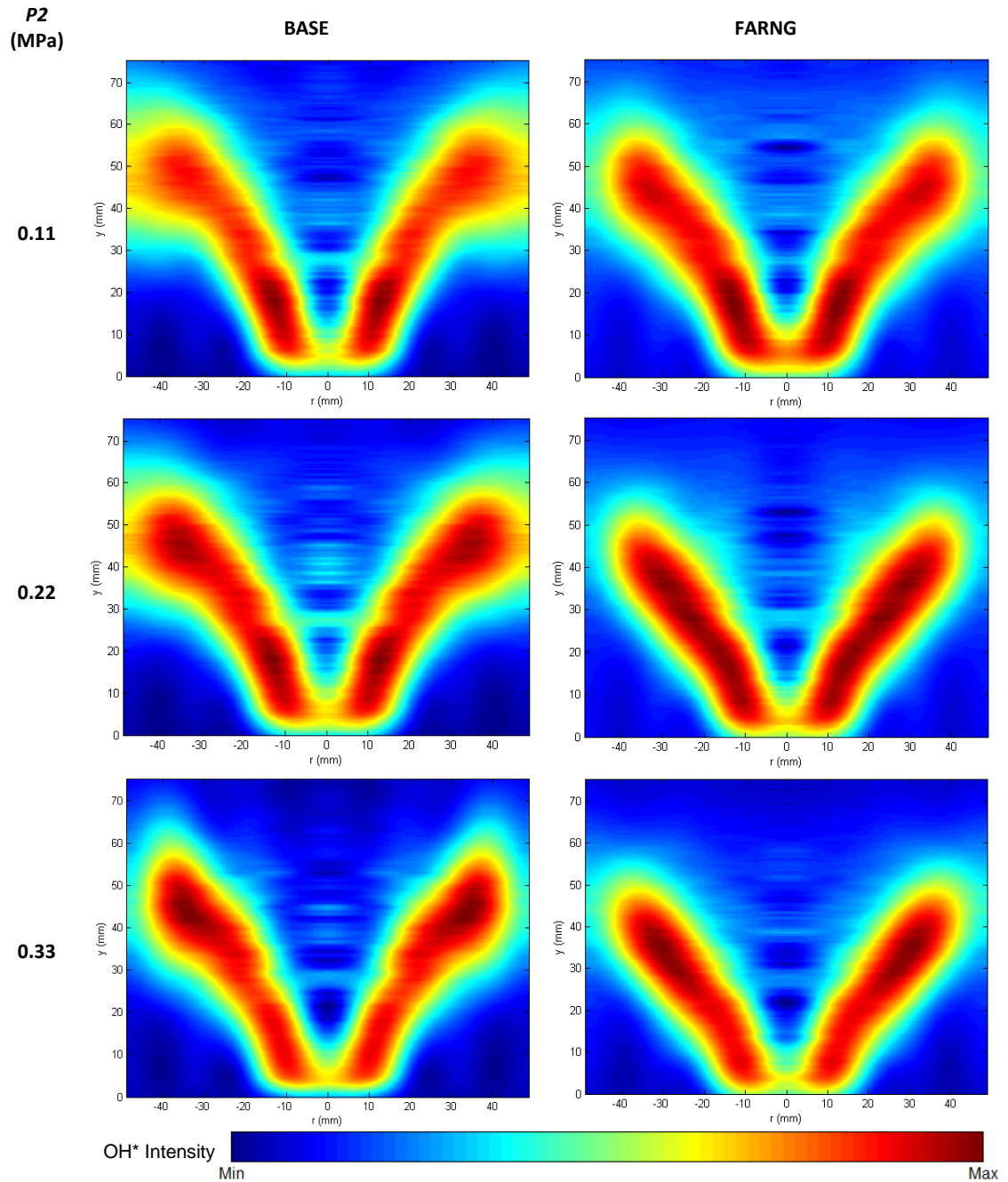


Figure 6.7: Abel-transformed OH* chemiluminescence images for BASE and FARNG flames at $\phi = 0.55$ with varying P_2

A similar extension of the BASE heat release zones is noted, but is not as uniform as the FARNG blend, again as the result of increased reactivity on the part of the FARNG fuel (10% increase in S_L at $P_2 = 0.22$ MPa). At $P_2 = 0.33$ MPa (highest Re condition), the location of maximum intensity is compacted once again, but is now located further downstream from the burner

exit nozzle in both BASE and FARNG cases. The structure of the heat release zones influences the thermoacoustic stability of the flame as the local speed of sound is influenced and the exhaust gas composition, in particular NO_x emissions in which temperature and residence time in areas of highest heat release are critical considerations. Further discussion on both points is provided in Sections 6.3 and 6.4.

The scanning OH PLIF results for BASE and FARNG fuels at $P_2 = 0.33$ MPa (126 kW) and varying φ conditions are presented in Figure 6.8. Note that for ease of presentation, only half of each temporally averaged and corrected OH PLIF image has been shown, assuming the flame is symmetric about the burner centerline ($r = 0$ mm). Each image presented has been normalized against its own image maximum and then fit to the same false colormap. In the BASE case, LBO was observed at $\varphi = 0.52$, thus a similar transition in flame shape as LBO is approached can be seen in Figure 6.8 as was presented under 100% CH_4 elevated temperature and pressure conditions in Chapter 5.2.2.2, albeit for $P_2 = 0.2$ MPa and $P_{therm} = 110$ kW in that case. In both 100% CH_4 cases, the flame is observed to transition from a V-shaped flame to an M-shaped flame prior to LBO. This transition results from reduced reactivity as flame temperatures and speeds reduce and the reaction zone increasingly interacts with the ORZ and confinement wall, resulting in further heat loss. In the FARNG case, LBO was also observed at $\varphi = 0.52$, but the flame shape transition prior to LBO is not evident, suggesting that the FARNG fuel is unable to stabilize in regions of high flame stretch as \bar{u} and Re increase prior to LBO, unlike the BASE fuel. The reaction zone also appears to shift upstream while increasing in thickness with ethane addition for a fixed φ condition, with a wider distribution of OH radicals, particularly in the post-flame zone (e.g. CRZ) in the FARNG case.

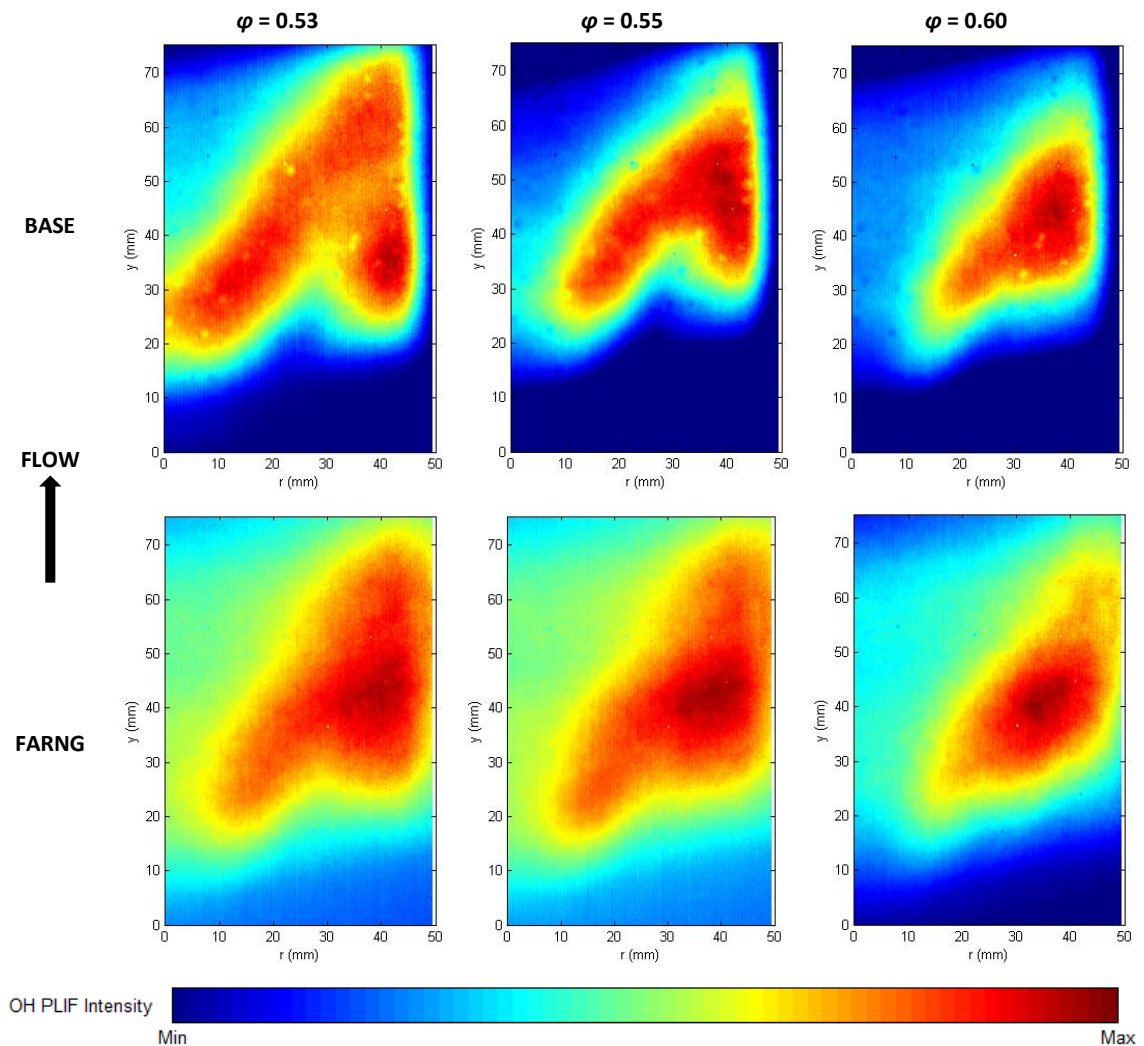


Figure 6.8: Scanning OH PLIF measurements of BASE and FARNG flames at $T_2 = 573$ K, $P_2 = 0.33$ MPa, and varying ϕ

6.2.2 Investigation of Ternary Natural Gas Mixtures

Similar to the evaluation presented in Section 6.2.1, ternary natural gas mixtures, MIDNG ($\text{CH}_4\text{-C}_2\text{H}_6\text{-C}_3\text{H}_8$) and EMIX1 ($\text{CH}_4\text{-C}_3\text{H}_8\text{-N}_2$), are compared here to evaluate the influence of propane-containing fuels on flame stabilization location and heat release distribution. The MIDNG fuel blend represents an averaged LNG fuel composition while the EMIX1 fuel blend has been selected specifically to match the Wobbe Index of the FARNG fuel (specific comparison between those fuels is found in Section 6.2.3). MIDNG and EMIX1 flame stabilization is evaluated based on Abel-transformed OH^* chemiluminescence and scanning OH PLIF measurements in Figures 6.9 and 6.10, respectively. First, in Figure 6.9, a series of MIDNG and EMIX1 OH^* CL images are presented with flames at $\phi = 0.55$ and varying P_2 from 0.11 MPa to 0.33 MPa. Then, in Figure 6.10, a series of MIDNG and EMIX1 scanning OH PLIF images are presented with flames at $P_2 = 0.33$ MPa (126 kW) and varying ϕ from 0.55 to 0.65.

At $\varphi = 0.55$ in Figure 6.9, both MIDNG and EMIX1 flames are observed to stabilize along the outward expanding shear layer between the CRZ and ORZ observed in the isothermal PIV results in Chapter 5.2.1.2, yielding conical, V-shaped flames which expand radially outward from the burner exit nozzle centerline ($r = 0$ mm), similar to the BASE and FARNG flames in Figure 6.7. Per Figure 6.2.a, the MIDNG fuel blend is most similar to the BASE fuel in terms of S_L across all $P2$ conditions, as expected given the 90% CH_4 content in MIDNG. Thus, by comparison between Figures 6.7 and 6.9, it can be observed that the localized areas of heat release are quite similar between the MIDNG and BASE fuels across all pressure conditions. The similarity in heat release distribution is worthy of note, particularly at $P2 = 0.11$ MPa, where the EMIX1 S_L is 17% higher than BASE S_L at $\varphi = 0.55$. Unlike the FARNG fuel blend, which shows an upstream shift in the flame stabilization location with only a 7% increase in S_L , the EMIX1 blend is seen to extend downstream, interacting with the quartz confinement wall. In fact, at $P2 = 0.11$ MPa and 0.22 MPa, the EMIX1 fuel blend experienced LBO with just a 1-2% increase in air flow rate from the $\varphi = 0.55$ condition presented in Figure 6.9. This was unexpected given the assumed increased reactivity implied by the elevated S_L and AFT for similar operating conditions between the EMIX1 and BASE fuels and is considered to be a consequence of the opposing thermo-diffusive effects between EMIX1 and BASE as shown in Figure 6.6. This leads to the conclusion that high propane content fuels will not be able to operate as lean as pure CH_4 fuels without potentially altering the turbulence characteristics of the flow field to reduce the effects of stretch. The MIDNG fuel experienced LBO at $\varphi = 0.52$, similar to both BASE and FARNG, which further suggests that heat release distributions can be maintained across fuels of varying C_2+ content up to a certain level of C_3H_8 (4% in MIDNG), before lean operational issues may be experienced. Similar to the observation made in the BASE and FARNG cases, the area of maximum OH^* CL intensity appears most uniform along the flame brush at $P2 = 0.22$ MPa in both the MIDNG and EMIX1 cases, resulting from improved mixing with increased Re . With increased Re at $P2 = 0.33$ MPa, both MIDNG and EMIX heat release areas shift away from the burner exit nozzle.

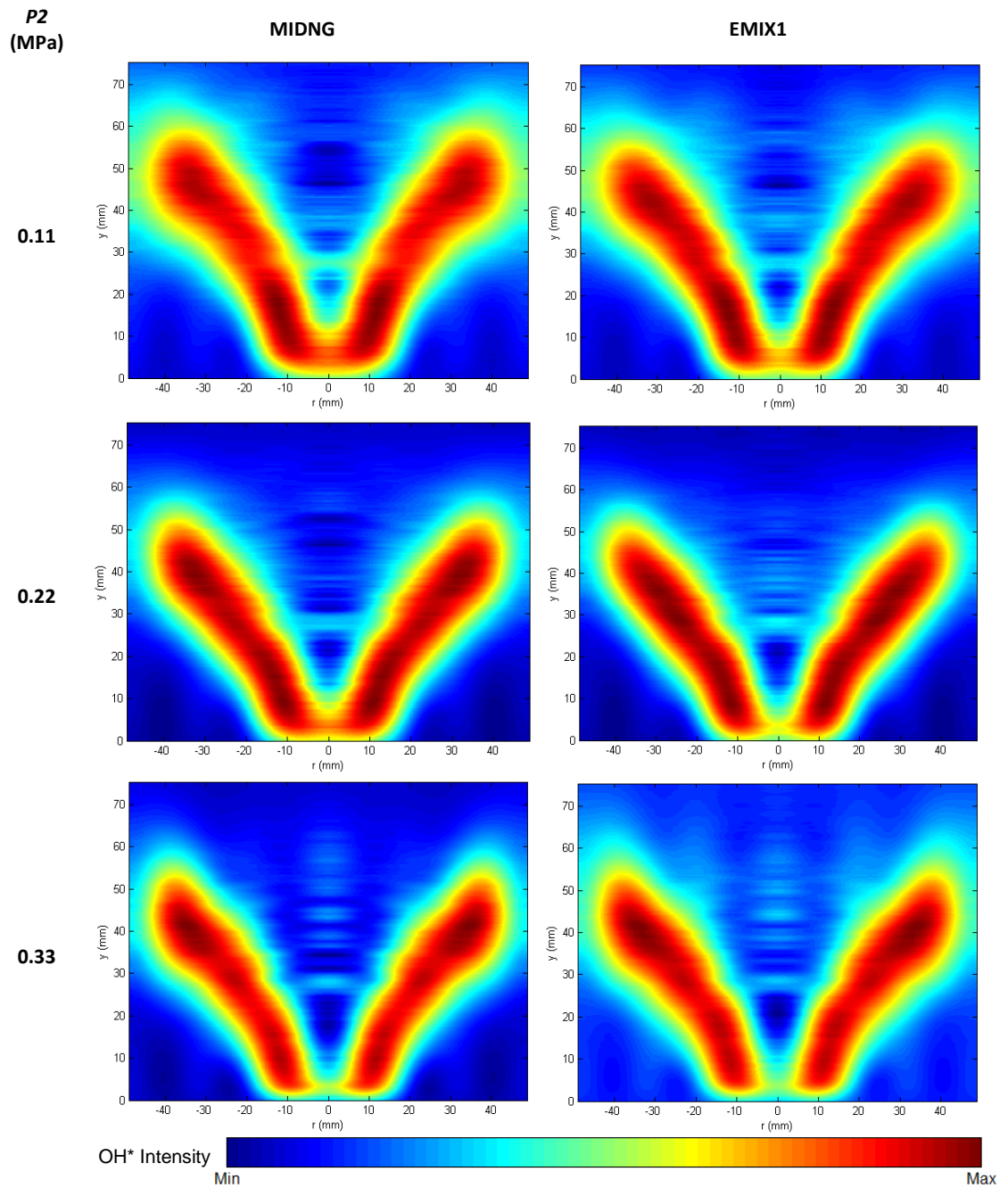


Figure 6.9: Abel-transformed OH* chemiluminescence images for MIDNG and EMIX1 flames at $\phi = 0.55$ with varying P_2

The scanning OH PLIF results for MIDNG and EMIX1 fuels at $P_2 = 0.33$ MPa (126 kW) and varying ϕ conditions is presented in Figure 6.10. Note that for ease of presentation, only half of each temporally averaged and corrected OH PLIF image has been shown, assuming the flame is symmetric about the burner centerline ($r = 0$ mm). In both the MIDNG and EMIX1 cases, the OH radical distribution is nearly identical across the examined ϕ conditions, appearing to shift downstream with reduced ϕ . Note that the equivalence ratio range examined here is shifted to higher ϕ from that in Figure 6.8 for the BASE and FARNG cases as

EMIX1 could not be stably operated at the same lean conditions as those fuels. Subtle differences in the reaction zone thickness are noted as the EMIX S_L is higher than the MIDNG S_L for all conditions, per Figure 6.2.b, particularly at $\phi = 0.60$. At $\phi = 0.55$, however, the EMIX1 reaction zone appears larger in area than the MIDNG flame, extending to $y = 65$ mm, and highlighting the increased influence of stretch under these high turbulence ($Re = 90000$) conditions.

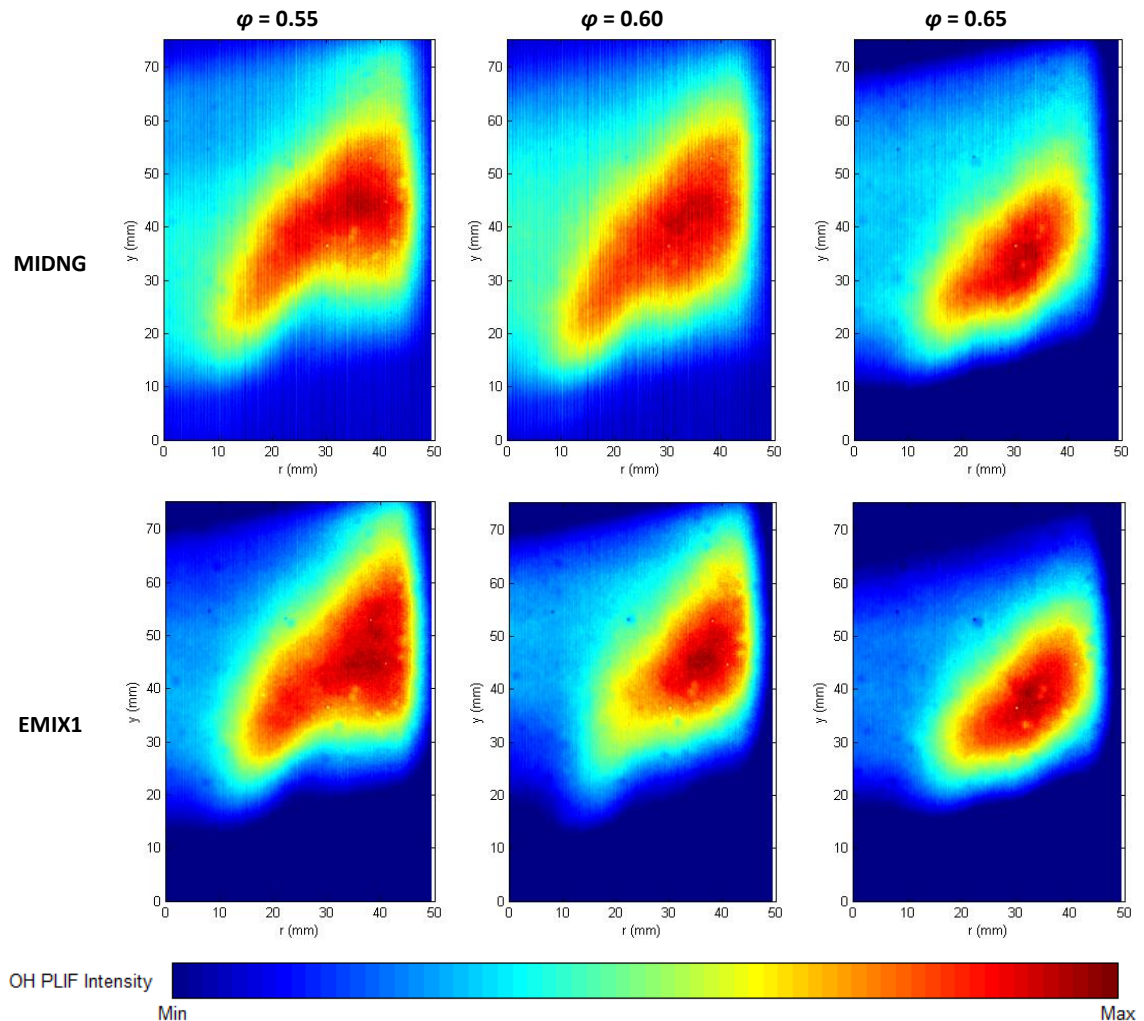


Figure 6.10: Scanning OH PLIF measurements of MIDNG and EMIX1 flames at $T_2 = 573$ K, $P_2 = 0.33$ MPa, and varying ϕ

6.2.3 Constant Wobbe Index Evaluation

Experimental evaluation has also been made between the FARNG and EMIX1 fuels to investigate the influence of variable C_2+ content for two fuels specified such that their WI is equal at 53.09 MJ/m³. To achieve this, the EMIX1 fuel replaces the 15% ethane content (in 85% CH₄) in the FARNG fuel with 12.6% propane and 2.4% N₂. FARNG and EMIX1 flame stabilization is evaluated based on Abel-transformed OH* chemiluminescence measurements

in Figure 6.11. In Figure 6.11, a series of FARNG and EMIX1 OH* CL images are presented with flames at $\varphi = 0.60$ and varying $P2$ from 0.11 MPa to 0.33 MPa. For comparison between these fuels at $\varphi = 0.55$, reference should be made to Figures 6.7-6.10, which show a difference in heat release location, flame shape, and post-flame zone OH radical concentrations between these fuels of near-identical WI. At $\varphi = 0.60$, however, the FARNG and EMIX1 flames appear nearly identical in terms of overall flame shape and heat release distribution. Only subtle differences are apparent in reaction zone thickness at $P2 = 0.11$ MPa and in the slight downstream movement of the EMIX1 heat release areas at $P2 = 0.33$ MPa, most likely influenced by stretch effects as the fuels have nearly identical S_L at this condition.

Given the similarity in flame shape and heat release distribution between these two fuels of similar WI, one might conclude that the parameter could provide a good indication of their operability despite their varying C_2+ content. While the similarities in Figure 6.11 are notable, these two fuels are observed to behave differently in practical operation, particularly near LBO. This is highlighted in Figure 6.12, which provides the stable operating curves for FARNG and EMIX1 flames at varying φ , Re , and $P2$. At $P2 = 0.11$ MPa and 0.22 MPa, the flames were driven to LBO by increasing the air mass flow rate (thus lowering φ and AFT while increasing \bar{u} and Re). The FARNG flames are able to stabilize at notably lower AFT and higher Re than the EMIX1 flames. At $P2 = 0.33$ MPa, the flames were not driven to LBO to protect the HPCR from potential damage. It is noted at $P2 = 0.33$ MPa that the EMIX1 fuel could stabilize at a lower AFT than at $P2 = 0.11$ MPa and 0.22 MPa, however the FARNG blend presumably could be operated below $\varphi = 0.53$ if rig operations were extended in the future. While this difference in lean behavior is in part attributed to the thermo-diffusive effect of propane addition on methane, these two fuels appear to have opposing S_L trends at $P2 = 0.33$ MPa (see Figure 6.2.a), which warrants further investigation at increased pressure conditions.

Further comparisons between these two fuels of similar WI are made throughout the rest of this Chapter in regards to their influence on reaction zone thickness, flame area, dynamic pressure measurements, and NO_x emissions. While in some cases (such as Figure 6.11) WI may provide an indication of the flame response, observed differences between these fuels (both fundamentally and in practical operation) highlight the need to establish improved criteria for the characterization of natural gas swirl flame behavior with varying C_2+ content.

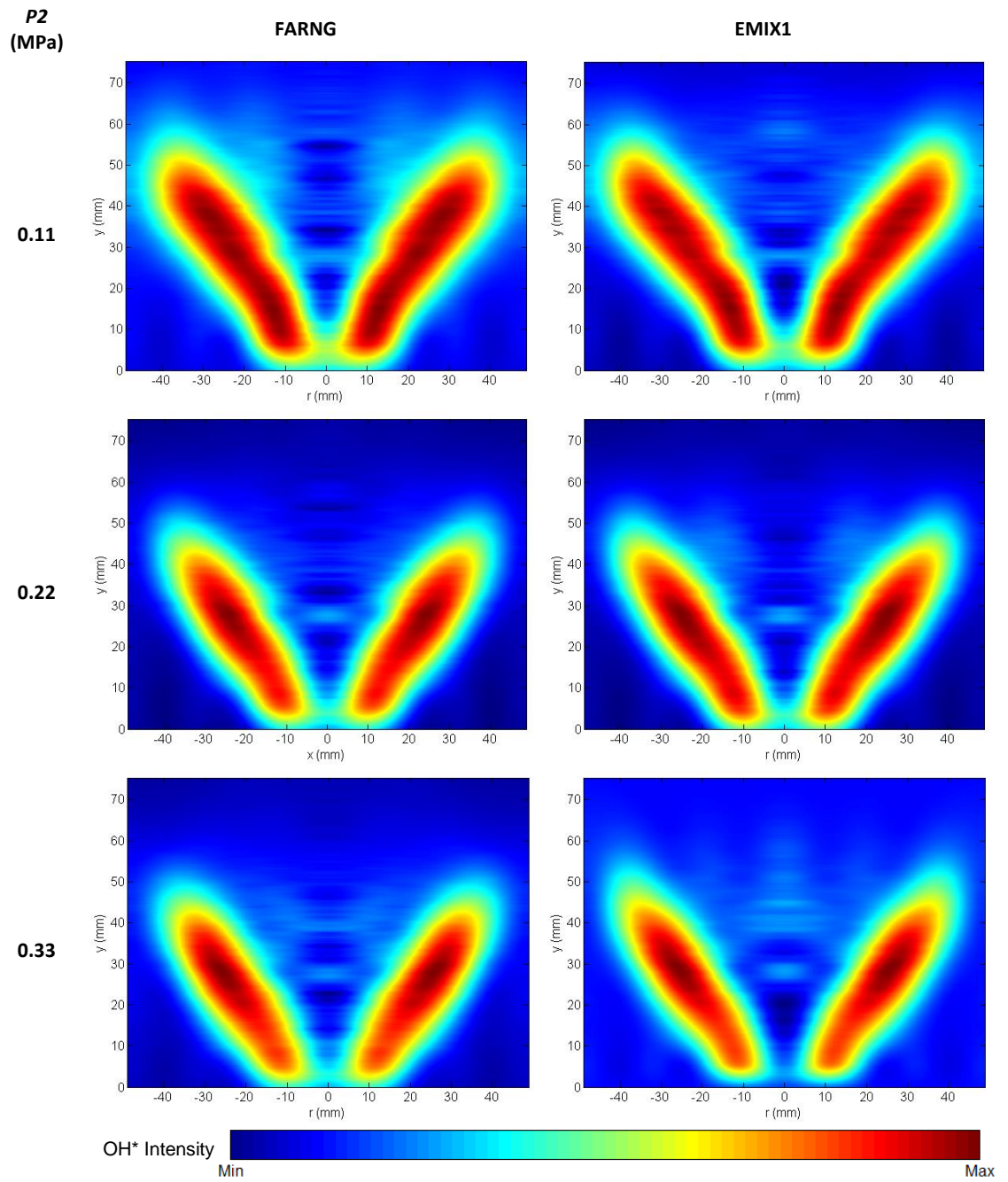


Figure 6.11: Abel-transformed OH* chemiluminescence images for FARNG and EMIX1 flames at $\varphi = 0.60$ with varying $P2$

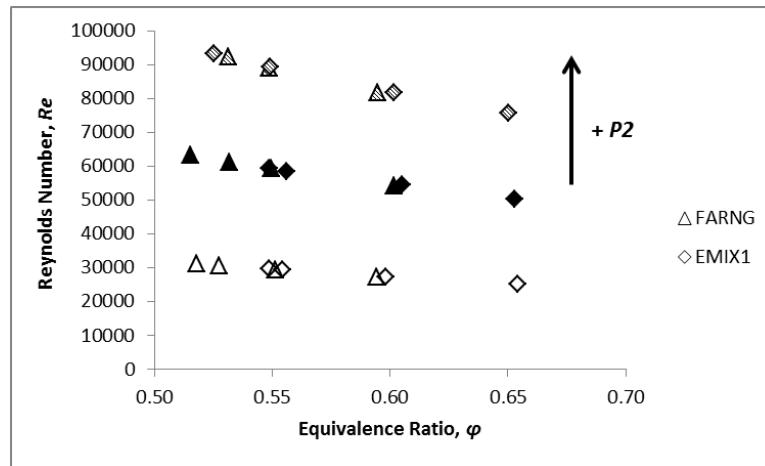


Figure 6.12: Lean operating curves for FARNG and EMIX1 flames as a function of ϕ and P_2 , 0.11 MPa (open), 0.22 MPa (closed), and 0.33 MPa (hashed).

6.2.4 Influence of Heat Release and Reaction Zone Thickness

Utilizing non-intrusive measurements and numerical chemical kinetic modeling, a series of evaluations of the influence of fuel composition on fundamental characteristics such as the localized heat release and reaction zone thickness has been conducted. While the two are intricately linked, it has been shown that their individual contribution is significant to experimentally measured values such as chemiluminescence integral intensity (I_{OH^*}), flame stabilization location, and further to NO_x emissions production (see Section 6.4).

6.2.4.1 Evaluation of Experimental and Numerical Heat Release Measurements

As a comparison between the varying fuel compositions and the distribution of heat release areas and flame shape, Figure 6.13 plots the axial and radial locations of the binarized OH^* chemiluminescence intensity centroid from the Abel-transformed images presented in this Chapter (Figures 6.7 and 6.9) at $\phi = 0.55$. The arrows show the centroid movement from $P_2 = 0.11$ MPa (open symbols) to $P_2 = 0.22$ MPa (closed symbols). This provides a quantitative measure of the mean heat release distribution within the field of view and highlights the influence of variable fuel composition, pressure, and turbulence on observed flame stabilization locations. Further information on this methodology can be found in the work by Han and Hochgreb [236]. Flame angles of 30° and 45° are imposed for reference. The influence of C_2+ addition is observed at $P_2 = 0.11$ MPa (open symbols), as the heat release centroid shifts upstream and radially inward for all conditions compared to the BASE flames, which show very little movement across all operating conditions for a fixed \bar{u} , despite increased P_2 causing a drop in reactivity and increased Re with increased P_2 . This is attributed

to methane's thermo-diffusive response under lean conditions shown in Figure 6.6. For the C_2+ containing fuels at $P_2 = 0.11$ MPa, the heat release zones appear stabilized approximately along the same shear layer (little change in flame angle), simply moving upstream along that shear layer. Quite a similar shift is observed at $P_2 = 0.22$ MPa, with the BASE flame stabilizing at the furthest radial location and all C_2+ containing flames shifting upstream and radially inward, given the increase in reactivity with C_2+ addition. At $P_2 = 0.33$ MPa, however, there is a more dramatic shift from BASE to MIDNG and EMIX1 (propane containing fuels), resulting in an increase in flame angle as the level of turbulence increases. The FARNG blend has a less marked response to increased turbulence, suggesting that the thermo-diffusive effect of ethane addition is not as remarkable as propane addition, warranting further study.

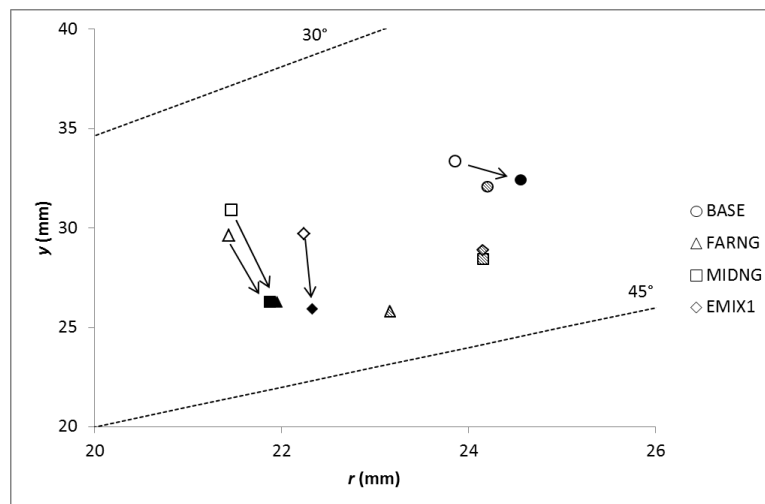


Figure 6.13: OH^* chemiluminescence intensity centroid locations and flame angles at $T_2 = 573$ K, $\phi = 0.55$, and varying P_2 , 0.11 MPa (open), 0.22 MPa (closed), 0.33 MPa (hashed). Arrows indicate the transition from $P_2 = 0.11$ MPa to 0.22 MPa.

In addition to utilizing the Abel-transformed OH^* chemiluminescence intensity centroid as a marker of flame stabilization location, OH^* integral intensity (I_{OH^*}) has also been utilized per Equation 4.1 as a measure of the variation in heat release relative to the addition of C_2+ content to methane. The use of I_{OH^*} has been shown in Chapter 4 to scale with S_L and Chapter 5 to scale with AFT and Q'_{max} , highlighting its usefulness in fundamental characterization of LPM swirl flames. A similar comparison is made here between the measured I_{OH^*} intensity and chemical kinetics modeling results. The results of this comparison are provided in Figure 6.14, with I_{OH^*} compared to AFT (Figure 6.14.a), Q'_{max} (Figure 6.14.b), and Q (Figure 6.14.c) for all experimental conditions evaluated in this study. In Figure 6.14.a, I_{OH^*} is again shown to vary in a quasi-linear fashion with modeled AFT, as was shown in Figure 5.4 for pure methane and

pure propane flames. However, there is an obvious effect based on increased $P2$ (thus P_{therm}), which separates the three $P2$ groupings. In addition, within those groupings of constant $P2$ there are fuel variations which result in changes in the measured I_{OH^*} . This is expected given both OH^* dependence on pressure (Chapter 3.2.1.1) and the OH^* formation equation, $CH + O_2 \leftrightarrow OH^* + CO$, which will be influenced by increased CH radical formation with increased C_2+ content (see Figure 6.19). To account for this change in fuel composition and pressure, the measured I_{OH^*} is plotted against the modeled maximum volumetric heat release rate, Q'_{max} , in Figure 6.14.b. This value is taken as the maximum value from the 1-D modeled heat release distribution using the CHEMKIN PREMIX code.

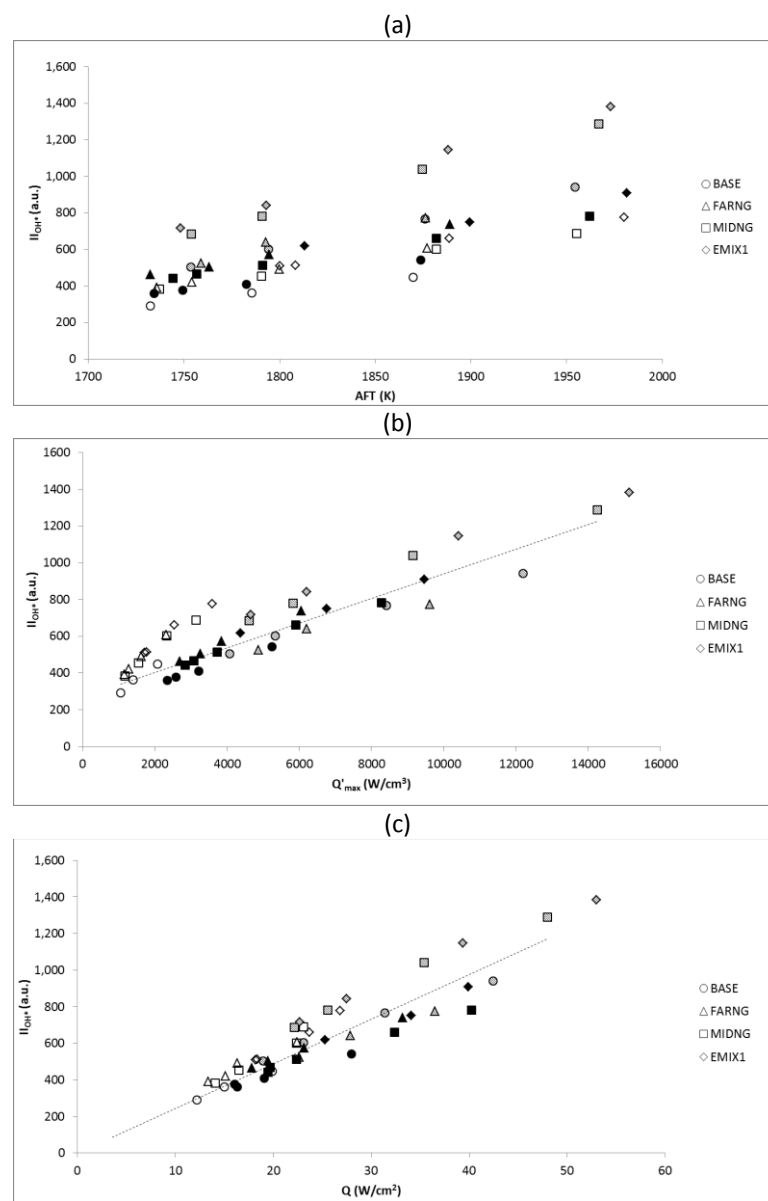


Figure 6.14: Measured I_{OH^*} as a function of AFT (a), Q' (b), and Q (c) for all experimental conditions with varying $P2$, 0.11 MPa (open), 0.22 MPa (closed), 0.33 MPa (hashed)

The relationship between II_{OH^*} and Q'_{max} also appears linear, with improved collapse between fuels, however there are still quite distinct nonlinear groupings of constant $P2$, particularly at $P2 = 0.11$ MPa (open symbols). To account for the change in $P2$, which would be expected to thin the reaction zone [172, 179], the volumetric heat release, Q' , is integrated along the 1-D axial distance that defines the reaction zone thickness, δ_t , per Figure 4.14 to yield Q (W/cm²) per Equation 6.1 below.

$$Q = \int_{x_{CH,max}}^{x_{OH,max}} Q' dx \quad (6.1)$$

The value of Q is estimated with a summation series of rectangular area sections defined by the local value of Q' and the corresponding axial segment distance from the 1-D chemical kinetics simulation. The measured II_{OH^*} is then plotted against Q in Figure 6.14.c, and shows further improved collapse between fuels and $P2$ as the reaction zone thickness accounts for the change in pressure (see Figure 6.20). This not only highlights the usefulness of this suggested modeled reaction zone thickness, but also the ability of a global non-intrusive measurement such as flame OH^* chemiluminescence to provide indication of the fundamental heat release changes resulting from changes in fuel composition and operating conditions.

OH^* chemiluminescence measurements can also be utilized for evaluation of fuel characteristics, as shown in Figures 6.15 and 6.16. In Figure 6.15, II_{OH^*} is plotted against fuel molar H:C ratio, which has been suggested in Chapter 5 as a fundamental fuel property of interest, in particular with fuels of varying hydrocarbon composition. For a fixed $\varphi = 0.55$ and varying $P2$, II_{OH^*} is shown in general to increase with a reduction in H:C ratio, with the exception of FARNG at $P2 = 0.33$ MPa (hashed symbol). This measurement was repeated on two separate experimental test days, with the same result obtained in both cases, suggesting a potential chemical kinetic quenching reaction at increased pressure with an ethane blended fuel, rather than an experimental anomaly. II_{OH^*} is also seen to increase with $P2$, attributed to the scaled thermal power with increased $P2$, whereas OH^* measurements have been shown in other fundamental studies to decrease with pressure due to quenching [179].

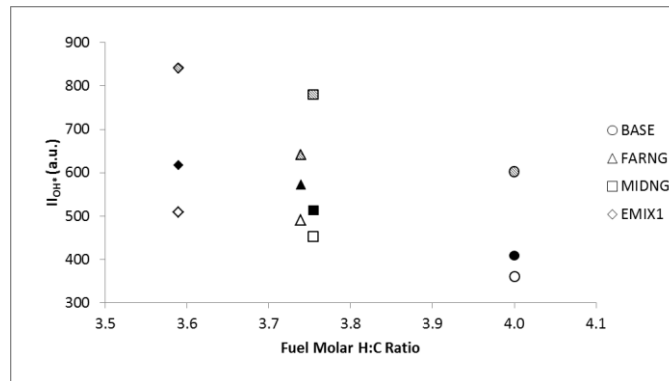


Figure 6.15: Measured I_{OH^*} as a function of fuel molar H:C ratio at $\varphi = 0.55$ with varying P_2 , 0.11 MPa (open), 0.22 MPa (closed), and 0.33 MPa (hashed).

The influence of pressure on I_{OH^*} is more apparent in Figure 6.16, which plots the same points from Figure 6.15 against P_2 instead of fuel H:C ratio. The BASE, MIDNG, and EMIX1 fuels appear to follow exponential relationships while the FARNG (ethane) fuel blend follows a linear or power law correlation. Interestingly, the FARNG fuel demonstrated a similar relationship with pressure and normalized modeled S_L in Figure 6.2.a, suggesting as in Figure 6.15 that pressure influence on methane-ethane blended fuels may be unique kinetically from pure methane and ternary fuel blends. This further reinforces the observations made in Section 6.2.3, in which fuels of similar Wobbe Index (FARNG and EMIX1) were shown to exhibit different behavior in a more practical combustion environment.

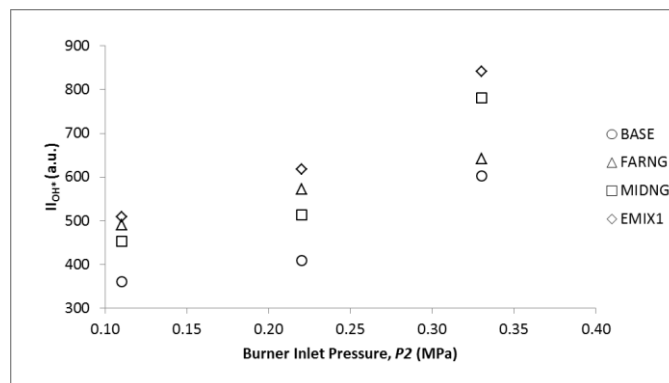


Figure 6.16: Measured I_{OH^*} as a function of P_2 for varying fuel composition at $\varphi = 0.55$

Finally, as suggested in Chapter 5.1.1 from atmospheric pressure and ambient temperature combustion of pure methane and propane, the fuel molar H:C ratio can be utilized in the scaling of OH^* intensity measurements to account for changes in fuel composition. Given that improved collapse between AFT and pure methane and propane I_{OH^*} could be achieved under those conditions (see Figure 5.4), it is advantageous to validate that analysis at conditions of variable fuel H:C ratio as well as elevated temperature and pressure. Similar to Figure 5.4.b,

the measured I_{OH^*} values have been scaled by $(H:C)^3$ and plotted in Figure 6.17.a for all experimental conditions. As can be seen in Figure 6.17.a, collapse is again achievable between fuels of varying hydrocarbon composition yielding a quasi-linear relationship under lean conditions, albeit for a fixed $P2$, as three groupings of $P2 = 0.11$ MPa, 0.22 MPa, and 0.33 MPa are discernable. It is interesting to note that the relationship in Figure 6.17.a is unable to collapse the FARNG measurements at $P2 = 0.33$ MPa, suggesting again that there is another influence with ethane addition that is unaccounted for in this analysis. As the previous analysis in Chapter 5.1.1 was only conducted at atmospheric pressure, the influence of varying $P2$ was unaccounted for. When plotted against normalized $P2$ ($P2 / P_{atm}$), where $P_{atm} = 0.101$ MPa, the scaled $I_{OH^*}(H:C)^3$ value varies exponentially. By normalizing the scaled OH^* intensity for this pressure effect, collapse along a single line between fuels of varying H:C ratio and burner operating conditions ($P2$ and AFT) can be achieved. The improved collapse is significantly enhanced under lean operating conditions ($\phi < 0.60$). The resulting relationship is plotted in Figure 6.17.b and given in Equation 6.2.

$$I_{OH^*} = \frac{(AFT)e^{(0.21 \frac{P2}{P_{atm}})}}{(H:C)^3} \quad (6.2)$$

While this exact relationship will certainly be specific to this particular burner (including confinement) and OH^* chemiluminescence measurement setup, it does provide an indication of possible use in more practical burner systems for the identification of burner operations at elevated pressure conditions with fuels of varying composition, and may perhaps even be utilized in the monitoring of fuel H:C ratio if the correlation can be extended for a further variety of fuels and operating conditions. This would then require calibration for a specific OH^* chemiluminescence measurement system, for example in-combustor fiber optic chemiluminescence measurement or perhaps pre-burner fuel characterization for feed-forward into a burner control system. An example of this is provided in Figure 6.18, which gives theoretical I_{OH^*} values from Equation 6.2 as a function of lean AFT for a variety of H:C fuels at $P2 = 1.5$ MPa (573 kW). The utilization of the H:C ratio to scale heat release measurements between variable fuels, both pure constituents and their blends, at ambient and elevated conditions, is a key finding of this study and provides an unique and simple fundamental fuel property for consideration in the characterization of natural gas fuel blends, where perhaps Wobbe Index has been used previously without success.

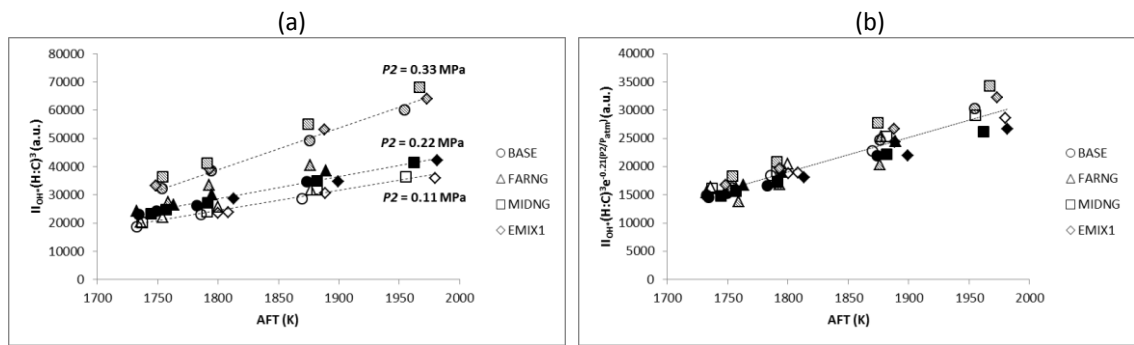


Figure 6.17: Measured II_{OH^*} as a function of AFT and P_2 , 0.11 MPa (open), 0.22 MPa (closed), 0.33 MPa (hashed), for all experimental conditions, scaled by fuel molar H:C ratio (a) and then additionally by the exponential pressure influence (b)

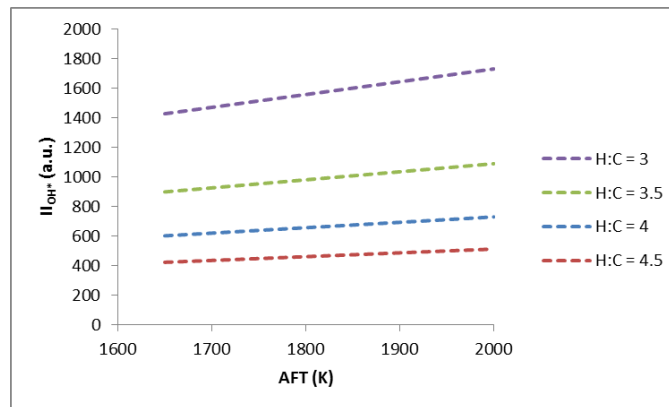


Figure 6.18: Projected II_{OH^*} levels in the HPGSB-2 as a function of AFT and fuel molar H:C ratio at $P_2 = 1.5$ MPa (573 kW).

6.2.4.2 Evaluation of Experimental and Numerical Reaction Zone Thickness Measurements

As suggested in Chapter 4 (Figure 4.23) and discussed briefly in Section 6.2.4.1, a theoretical reaction zone thickness, δ_t , based on the numerical 1-D axial location of the maximum CH mole fraction and OH mole fraction has been evaluated and utilized for the characterization of changes in natural gas fuel compositions in this study. As has been discussed previously, both OH* production and prompt NO_x production are related to CH radical production, which in turn is a function of the fuel composition, as shown in Figure 6.19. Figure 6.19 plots the maximum modeled CH mole fraction as a function of fuel composition and P_2 using CHEMKIN PREMIX code for experimental flames at $\phi = 0.55$. This plot shows the influence of H:C ratio on CH production, particularly at $P_2 = 0.11$ MPa, in agreement with the OH* measurements in Figure 6.16. With increasing pressure, however, the maximum CH mole fraction appears to become independent of fuel composition, following a negative power law correlation, with P_2^{-x} relationship and $x = 1.4$, which will consequently influence CH-based reactions such as OH* production (Chapter 3.2.1.1) and prompt NO_x formation (Chapter 2.4.1).

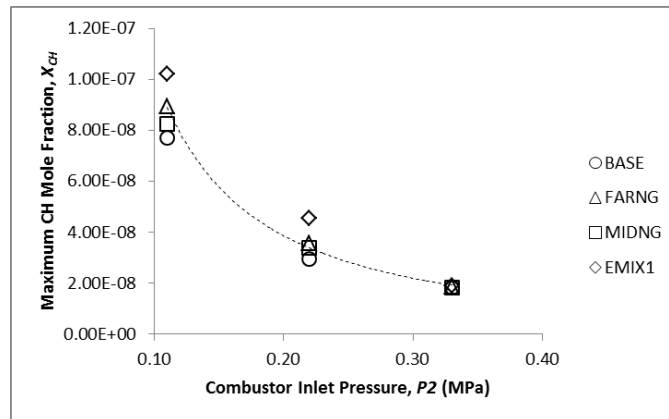


Figure 6.19: Modeled maximum CH mole fraction, X_{CH} , as a function of P_2 at $\varphi = 0.55$

Similar to the influence of pressure on maximum CH mole fraction, the influence of pressure on the theoretical reaction zone thickness, δ_t , is plotted in Figure 6.20 for $\varphi = 0.55$ (open symbols) and $\varphi = 0.60$ (closed symbols), showing a thinning of the reaction zone with increased P_2 , as expected. This also follows a negative power law correlation with P_2^x relationship and $x = 1.1$. Thus, the maximum CH mole fraction and δ_t are seen to vary linearly with each other, that is, as the maximum CH mole fraction increases, the reaction zone thickness increases. In addition to showing reduced dependence on fuel composition with increasing P_2 , this relationship also shows reduced dependence on AFT, as both φ datasets converge to a nearly equal value of $\delta_t = 0.010$ cm at $P_2 = 0.33$ MPa.

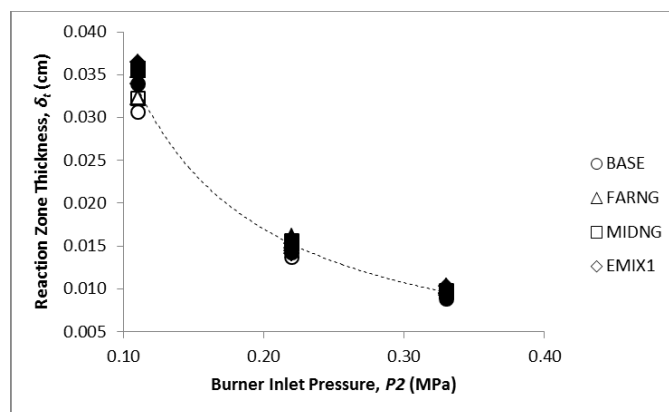


Figure 6.20: Modeled reaction zone thickness, δ_t , as a function of P_2 at $\varphi = 0.55$ (open) and 0.60 (closed)

In addition to the chemical kinetics evaluation of reaction zone, the image processing technique described in Chapter 4.2.2 was also applied to the scanned and temporally averaged OH PLIF images captured at each experimental condition. This technique extracts a mean flame brush thickness, δ_{flame} , and flame brush area, A_{flame} , from each binarized OH PLIF image, the results of which can be found in Figure 6.21 and 6.22, respectively, as a function of P_2 . In both figures, the measured quantity is presented at two values of $\varphi = 0.55$ (open symbols) and 0.60 (closed symbols). In Figure 6.21, the mean flame brush thickness is seen to vary

nonmonotonically with P_2 , first increasing with increased pressure to 0.22 MPa and then decreasing at $P_2 = 0.33$ MPa, with the exception of the BASE flame at $\varphi = 0.55$, which appears to follow a more expected negative power law correlation as seen in the thinning of the modeled reaction zone thickness in Figure 6.20. It is important to note that while it has been shown in Figure 4.24 that the measured flame brush thickness is positively correlated with the modeled reaction zone thickness, the influence of increased turbulence with increasing P_2 is not accounted for in Figure 6.20, which would result in an increased temporally averaged reaction zone. Thus, δ_t and δ_{flame} are offset by an order of magnitude. While δ_{flame} is able to capture the overall trend of thinning with increased P_2 , the nonmonotonic behavior at $P_2 = 0.22$ MPa can be directly related to the observed heat release distribution in Figures 6.7 and 6.9, which show broad heat release distribution along the flame front. This correlates with an increased number of rows with wide OH PLIF gradients contributing to the mean flame brush thickness calculation than in the 0.11 MPa and 0.33 MPa cases. Further support to this nonmonotonic observation of increased reactivity with increased P_2 (and Re) followed by subsequent decreased reactivity with further increased P_2 and Re is provided by the axial location of maximum OH PLIF intensity. For example, in the FARNG, $\varphi = 0.55$ case, the axial location of maximum OH PLIF intensity moves upstream from $y = 22.9$ mm (downstream of the burner exit nozzle) at $P_2 = 0.11$ MPa to $y = 21.0$ mm at $P_2 = 0.22$ MPa. However, as P_2 is further increased, the location of maximum PLIF intensity moves back downstream again to $y = 31.0$ mm at $P_2 = 0.33$ MPa. This suggests an optimal turbulence level exists for uniform OH radical and heat release distribution for C_2+ containing fuels, above which the benefits of enhanced mixing are offset by thermo-diffusive effects related to increased stretch rate behavior as suggested in Figure 6.6.

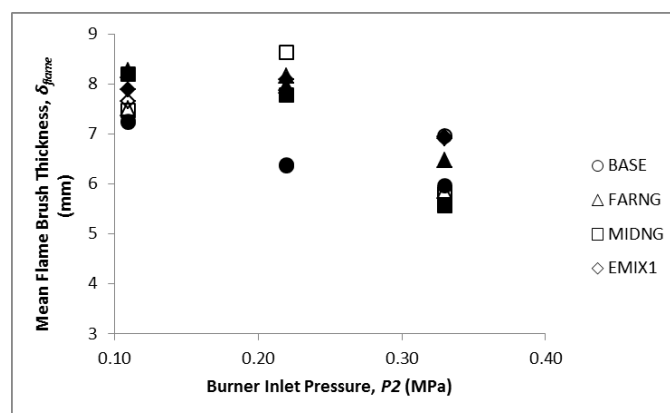


Figure 6.21: Measured mean flame brush thickness, δ_{flame} , as a function of P_2 at $\varphi = 0.55$ (open) and 0.60 (closed)

As can be seen in Figure 6.22, the measurement of A_{flame} extracted from OH PLIF measurements also decreases generally with increasing $P2$, as would be expected with a thinning of the reaction zone and flame thickness as shown in Figures 6.20 and 6.21. However, it is interesting to note the confluence of A_{flame} measurements seen at $P2 = 0.22$ MPa for varying fuel composition and operating conditions (e.g. AFT, Re , and \bar{u}). This again suggests that a uniformity in reaction zone thickness (and thus A_{flame}) can be achieved by selection of optimal operating conditions and turbulence levels with C_2+ containing fuel blends. For example, the flame area is seen to dramatically decrease with the EMIX1 fuel blend for increasing $P2$ and Re , which may result in the development of broken reaction zones and partial extinction under lean operating conditions if the turbulence levels are not scaled sufficiently to counter the thermo-diffusive behavior of this propane-containing blend. Furthermore, the limited reduction in FARNG fuel blend A_{flame} suggests a different stretch rate response with ethane blending compared to propane blending. This difference in behavior between ethane and propane blended fuels under elevated operating conditions warrants further parametric investigation to identify blending concentrations levels which may change the thermo-diffusive behavior, and thus turbulent response, of the BASE fuel.

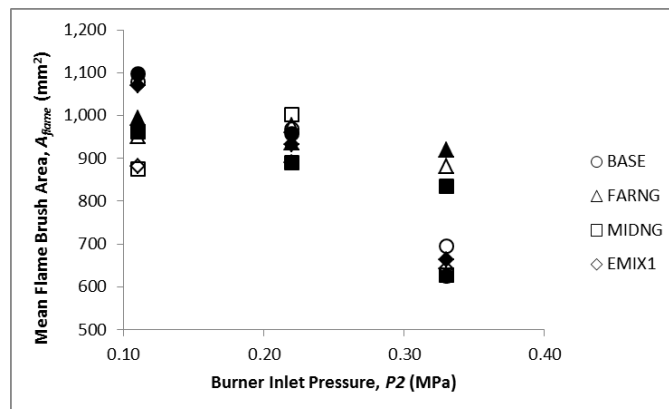


Figure 6.22: Measured mean flame brush area, A_{flame} , as a function of $P2$ at $\phi = 0.55$ (open) and 0.60 (closed)

6.3 Thermoacoustics

As shown in further detail in Chapter 7.3.1, the use of the convergent nozzle confinement and $S_g = 0.8$ radial-tangential swirler input effectively decouples the thermoacoustic instability observed in the open cylindrical confinement case. This is largely due to the change in heat release fluctuation that results from reduced recirculation of hot reactants as the CRZ size is observed to be considerably affected by the introduction of the convergent nozzle confinement. This was validated with isothermal PIV (Chapter 5.2.1.2) and is in agreement

with numerical swirl burner simulation [128]. As such, no high amplitude thermoacoustic combustion oscillations were observed in this study of C_2+ content in natural gas fuels, which therefore allows for isolation of the chemical and turbulent flow field effects with changes in fuel composition and elevated operating conditions. Results of a frequency domain analysis are first presented followed by a time domain analysis of overall combustion noise amplitudes, including proposed H:C ratio and δ_t scaling.

6.3.1 Frequency Domain Analysis

With the observation that the convergent confinement decouples potential thermoacoustic instabilities under the experimental operating conditions, the resulting combustion noise measurements therefore contain a broadband frequency spectrum of flow, acoustic, and chemical reactivity contributions, similar to those observed in the low amplitude valleys between LBO and thermoacoustic instabilities identified in the study of the HPGSB-2 presented in Chapter 5.2.2. The resulting FFTs of the Burner Face DPT measurement at varying P_2 are presented in Figures 6.23 and 6.24, with $\varphi = 0.55$ and 0.60 , respectively.

Noting the change in y-axis scaling in Figure 6.23 at $\varphi = 0.55$, the Burner Face DPT amplitudes are seen to increase with increasing P_2 (thus P_{therm}), but the overall shape of the broadband noise frequency spectra remain nominally similar. Furthermore, with the exception of only a few points across all FFTs, the addition of C_2+ is seen to reduce the peak amplitudes observed with the BASE fuel, providing a noise damping function which was similarly observed with an increase in reactivity resulting from the addition of H_2 as discussed in Chapter 7. The addition of C_2+ molecules is also observed to shift the identified peaks towards higher frequencies, which was also observed with H_2 addition in Chapter 7, and is attributed to higher localized flame temperatures which contribute to a shift in the local speed of sound for acoustic frequencies.

At $P_2 = 0.11$ MPa, the dominant frequency peak of all fuels exists in the low frequency range, at approximately $f_{peak} = 25-27$ Hz. This is indicative of localized extinction and reignition events as identified in the study in Chapter 5.2.2, with similar harmonic peaks beginning to establish. Although it must be noted that when φ was reduced further towards LBO, the burner with convergent confinement did not experience the high-amplitude, low-frequency LBO instability observed with the open confinement.

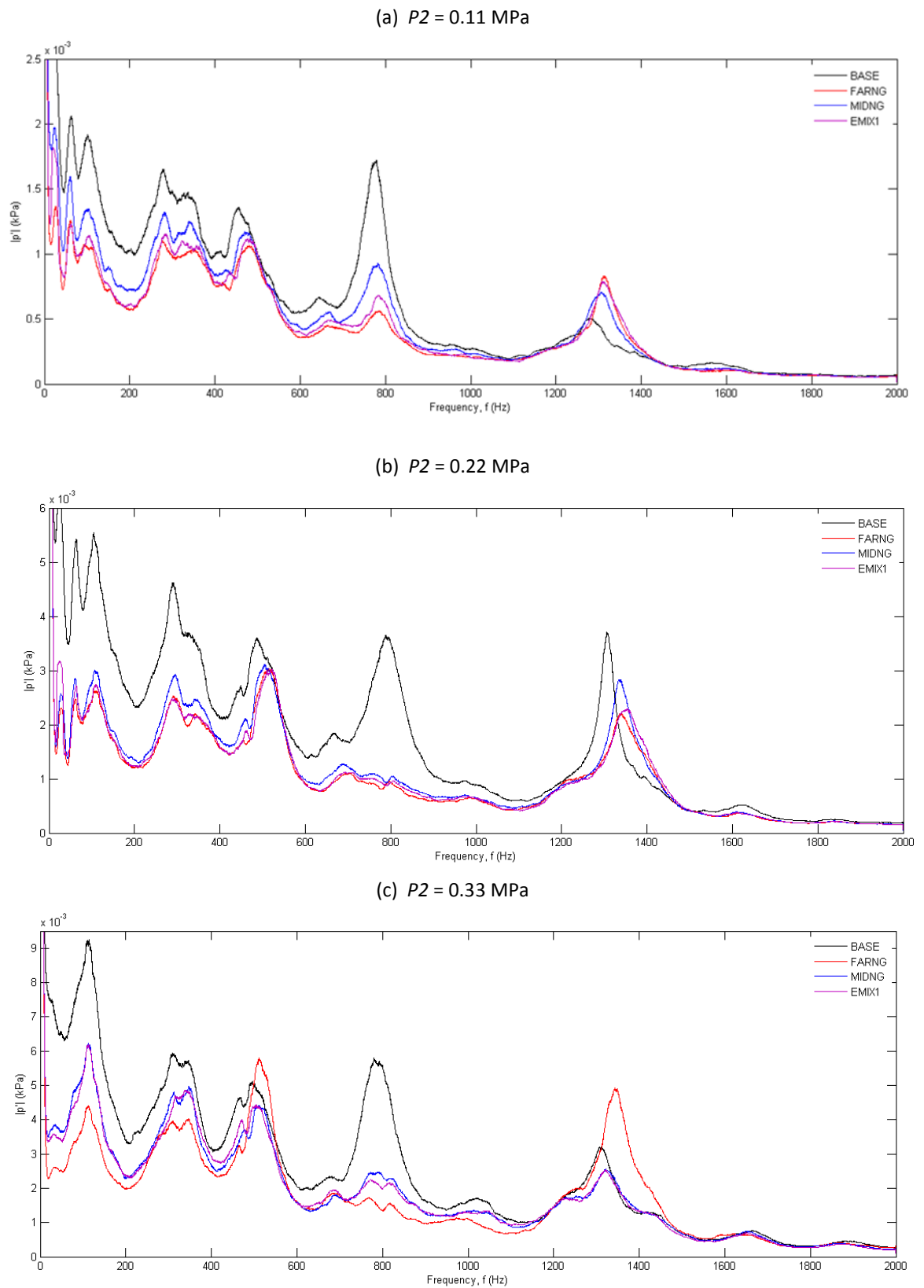


Figure 6.23: FFT of Burner Face DPT measurement for varying fuel composition and P_2 at $\phi = 0.55$. Note the change in y-axis scaling for each plot.

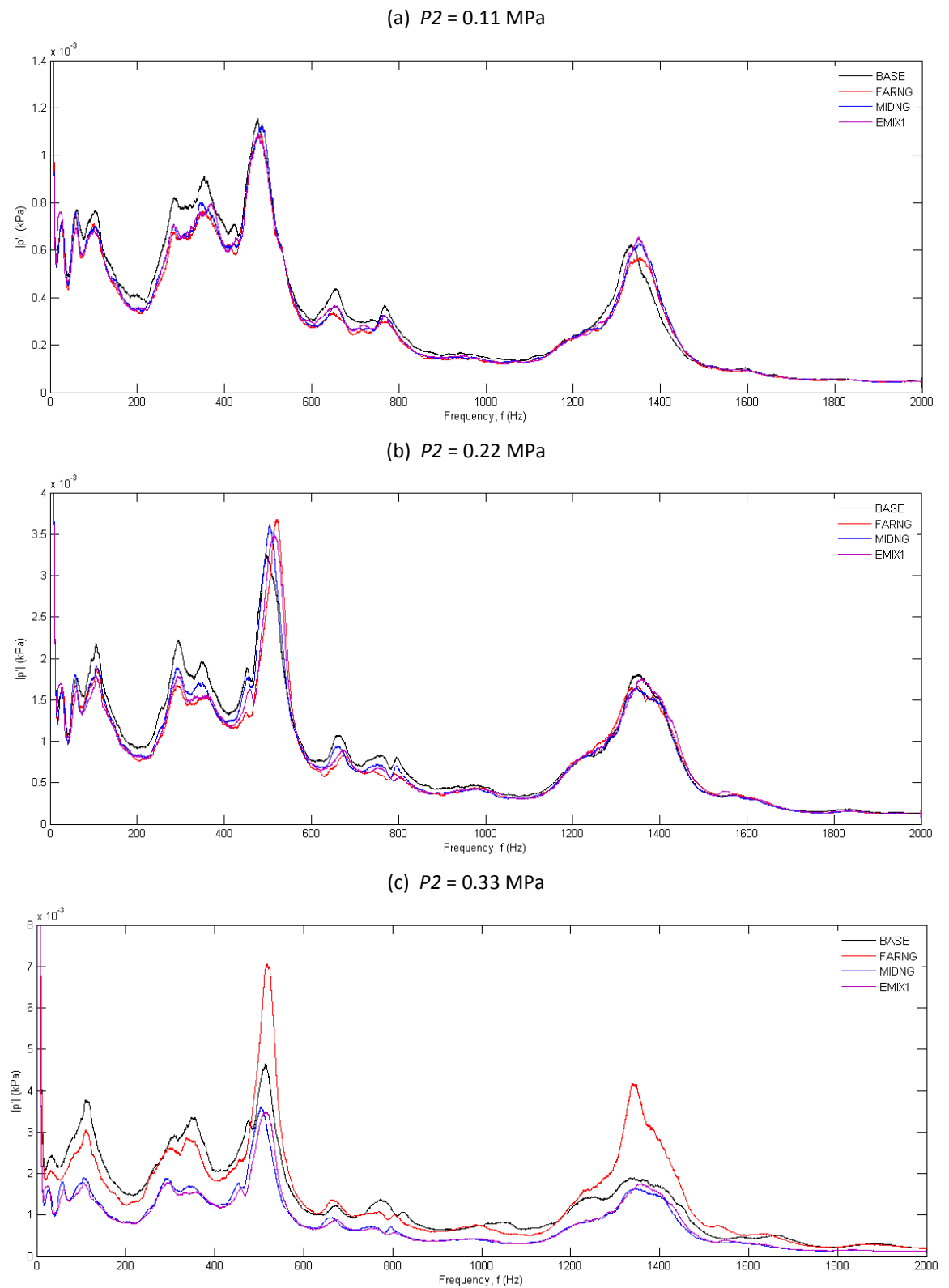


Figure 6.24: FFT of Burner Face DPT measurement for varying fuel composition and P_2 at $\phi = 0.60$.
Note the change in y-axis scaling for each plot.

Instead, the flame detached from its stabilized location along the outward expanding shear layer from the burner exit nozzle and extinguished. This is most likely due to the weaker CRZ, which limits heat input to the root of the flame to allow for full flame reignition as observed in Chapter 5.2.2. Nevertheless, the transition towards LBO follows a similar pattern between confinements. This is further supported by the spectra in Figure 6.24, which shows reduced low frequency contribution as the burner is moved away from LBO.

In Figure 6.23, three peaks are also identified in the mid-frequency range at approximately 280 – 285 Hz, 450 – 480 Hz, and 780 Hz – 785 Hz. A single high frequency range peak is identified at 1280 – 1315 Hz. The peak at 450 – 480 Hz yields a Strouhal number of $St = 0.54 – 0.58$ using Equation 2.5, which was shown in Chapter 5 to be related to the first resonant quarter wave frequency of the HPGSB-2 burner and confinement. The peak at 780-785 Hz yields a Strouhal number of $St = 0.94 – 0.95$, which was shown in Chapter 5 to be related to a Kelvin-Helmholtz shear layer vortex shedding instability. At $\varphi = 0.55$, this fluctuation is suppressed with the addition of C_2+ and, as can be seen in Figure 6.24, provides a significantly reduced peak at $\varphi = 0.60$ (with subsequent reduction in \bar{u} as the air mass flow rate is reduced).

The two main frequency peaks that dominate the $\varphi = 0.60$ case in Figure 6.24 are approximately 500 Hz and 1350 Hz. The first peak is again related to the resonant quarter wave frequency of the burner configuration, showing little flow velocity dependence. Instead, it appears to be related directly to the increase in AFT, which consequently influences the local speed of sound, increasing the measured f_{peak} . As for the high frequency peak, this was also observed in the $\varphi = 0.55$ case in Figure 6.23. In both cases, the Strouhal number for this frequency ranges from $St = 1.5$ to 1.7 , and it appears to vary with changes in AFT resulting from the increase in φ and or from changes in fuel composition at a fixed φ . It has been considered that the convergent nozzle confinement may behave like a Helmholtz resonator, and thus utilizing Equation 2.7 for a fixed confinement length of 407 mm, exit diameter of 40 mm, and an assumed internal speed of sound equal to the average of the local AFT speed of sound and measured $T3$ speed of sound, the observed high-frequency peak can be resolved as the Helmholtz frequency assuming a short neck length ($L_{neck} = 0.1 * D_{exit}$). This assumption is considered to be adequate given the tapered transition to the abrupt exit of the convergent confinement, as shown in Figure 3.9.

One additional unique observation regarding the $\varphi = 0.60$ case is the increased amplitude observed at both observed peaks in the FARNG case at $P2 = 0.33$ MPa (Figure 6.24.c). A similar increase is also noted in Figure 6.23.c at the quarter wave frequency and Helmholtz frequency, while the MIDNG and EMIX1 fuels are shown to dampen the BASE fluctuation amplitude at these frequencies. As was shown in Figure 6.22, the measured FARNG flame area, A_{flame} , was the largest amongst all fuels at $P2 = 0.33$ MPa at both $\varphi = 0.55$ and $\varphi = 0.60$, which may highlight the relationship between the observed DPT amplitudes of these resonant frequencies and measured heat release distribution. This observation holds at $P2 = 0.11$ MPa as well, where the BASE fuel was observed to have the highest A_{flame} for both $\varphi = 0.55$ and $\varphi = 0.60$.

A view of the dominant Burner Face DPT frequency, f_{peak} , extracted for all experimental conditions is provided in Figure 6.25, with f_{peak} plotted against Q , shown in 6.14.c to account for the effect of $P2$ on the thinning reaction zone. As can be seen in Figure 6.25, as the heat release rate decreases, there is an abrupt transition in dominant frequency from approximately 500 Hz (associated with the quarter wave frequency of the burner) to 25 Hz (associated with localized extinction and reignition events). This transition appears to occur at higher values of Q as the H:C ratio decreases and $P2$ is increased. This plot also highlights an intermediate transitional location for the $P2 = 0.33$ MPa fuel cases near $f_{peak} = 100$ Hz.

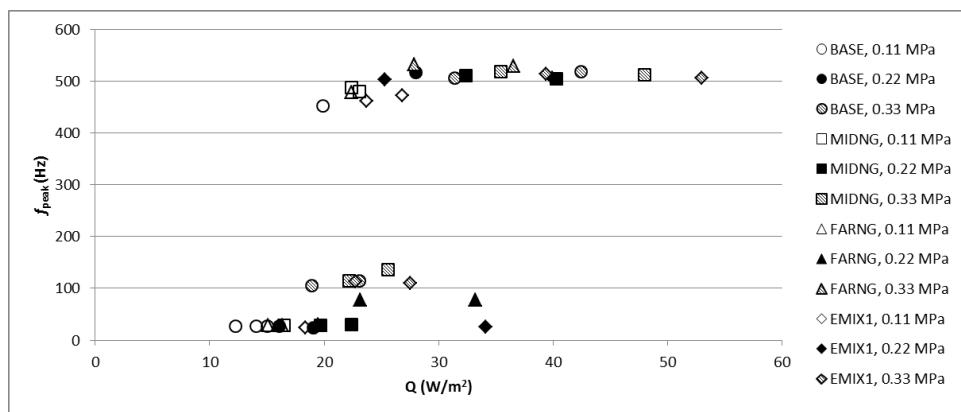


Figure 6.25: Dominant Burner Face DPT frequency, f_{peak} , plotted against Q

6.3.2 Time Domain Analysis

Combustion noise was also evaluated in the time domain by considering the RMS values of pressure fluctuation amplitude of the Burner Face DPT. The RMS amplitude normalized by $P2$ is plotted for all experimental conditions against the maximum modeled volumetric heat release rate, Q'_{max} , in Figure 6.26. Not only does this plot confirm that all measurements were conducted in an acoustically decoupled system ($p'_{RMS} / P2 < 1\%$ for all conditions), three

distinct groupings of constant $P2$ are also observed. For a fixed $P2$, it is seen that above a certain value of Q'_{max} the combustion noise amplitudes appear to be independent of heat release rate. It is only as the burner is moved toward LBO that the dynamic pressure amplitudes begin to increase significantly. A similar response is observed if the same plot is repeated with Q instead of Q'_{max} which indicates that the DPT amplitudes are influenced by additional parameters compared with those associated with $P2$ and δ_t .

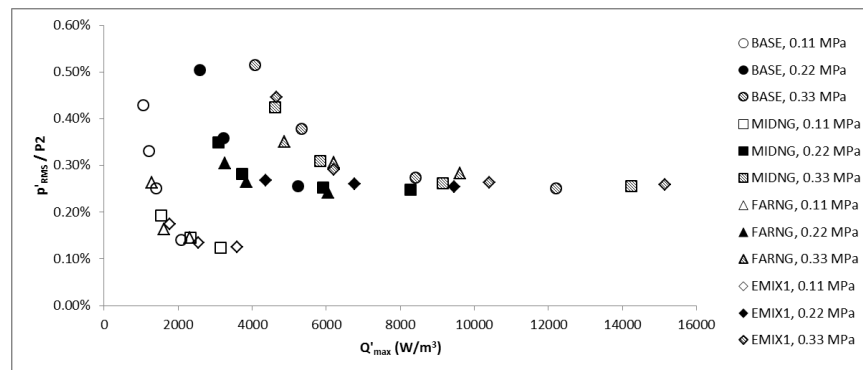


Figure 6.26: Normalized Burner Face DPT amplitude as a function of Q'_{max}

Thus, in order to extend the characterization of measured Burner Face DPT amplitude, the direct influence of fuel composition is considered, with the normalized amplitudes plotted against fuel molar H:C ratio at $\varphi = 0.55$ and varying $P2$ in Figure 6.27. As was seen generally in the FFT plots at the same condition (Figure 6.23), the pressure amplitudes, while increasing with $P2$, are dampened as H:C ratio is increased. The increased H:C ratio fuel counteracts the asymptotic increase in DPT amplitude by increasing the volumetric heat release rate, shifting the flame stabilization position, and effectively moving the BASE flame away from LBO.

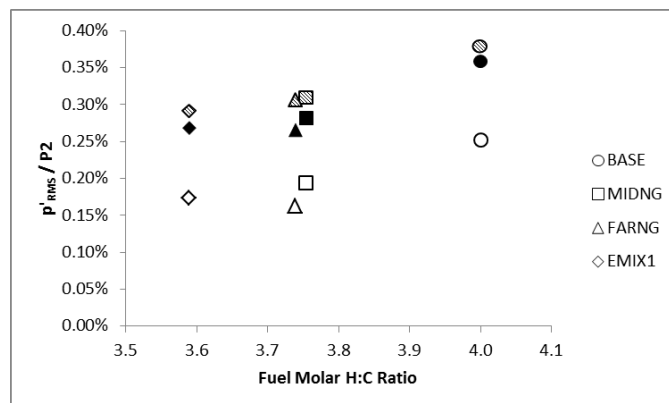


Figure 6.27: Influence of fuel molar H:C ratio on normalized Burner Face DPT amplitudes at $\varphi = 0.55$ and varying $P2$, 0.11 MPa (open), 0.22 MPa (closed), and 0.33 MPa (hashed).

Whereas Figure 6.27 suggests that there is a fuel composition influence on combustion noise amplitudes, Figure 6.28 extends the characterization by considering the effect of normalized

$P2$ ($P2/P_{atm}$) at $\phi = 0.55$, where $P_{atm} = 0.101$ MPa. Normalized Burner Face DPT amplitudes are shown to follow a power law correlation with increasing $P2$ in Figure 6.28.a, with an obvious offset between fuel types, particularly at low $P2$. In a similar fashion to the scaling of I_{OH^*} in Figure 6.17.a, the fuel H:C ratio is used to account for the fuel composition influence identified in Figure 6.27, and thus the improved collapse between combustion noise levels and fuel compositions can be seen in Figure 6.28.b, where a $1/(H:C)^3$ scaling has been implemented. This yields an estimation of combustion noise levels in the HPGSB-2 with convergent confinement at elevated pressure conditions per Equation 6.3 and as plotted in Figure 6.29 up to $P2 = 1.5$ MPa (573 kW) for varying H:C ratio.

$$\frac{p'_{RMS}}{P2} = 4 \times 10^{-5} \left(\frac{P2}{P_{atm}} \right)^{0.4736} (H:C)^3 \quad (6.3)$$

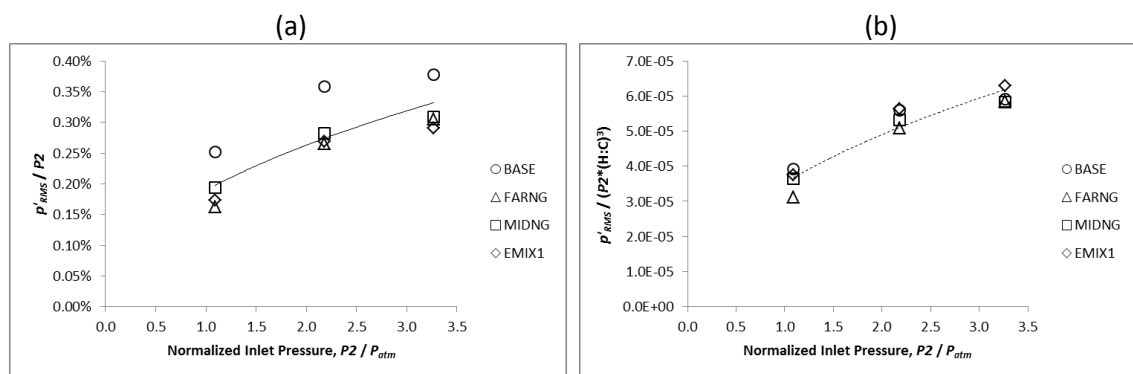


Figure 6.28: Normalized Burner Face DPT amplitude as a function of normalized $P2$ at $\phi = 0.55$, unscaled (a) and scaled by fuel $(H:C)^3$ (b)

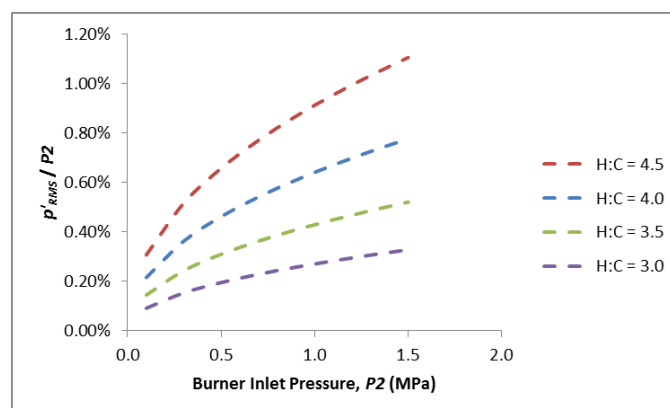


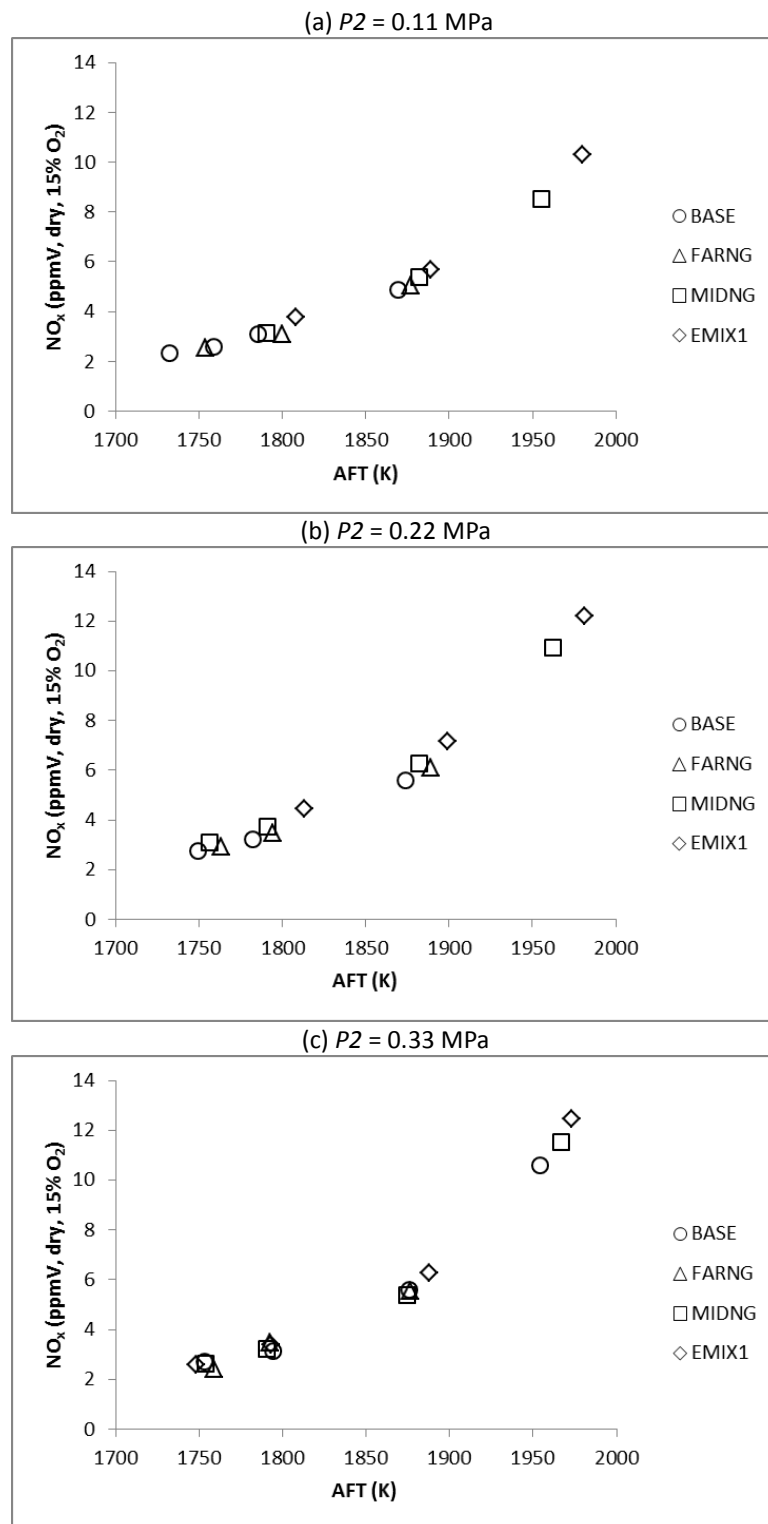
Figure 6.29: Projected combustion noise levels in the HPGSB-2 as a function of $P2$ and fuel molar H:C ratio up to $P2 = 1.5$ MPa (573 kW).

6.4 Exhaust Gas Emissions

It is critical to evaluate the influence of changing fuel compositions on emissions given the current and projected legal requirements facing GT manufacturers and operators, as discussed in Chapter 1. By maintaining constant burner geometry, and operating the HPGSB-2 in a mode which is considered to be thermoacoustically stable, the chemical kinetic and turbulent influences of C_2+ addition to methane can be isolated for evaluation of their contributions to emissions formation, with a particular focus on NO_x emissions given the shift towards LPM operation and low NO_x GT combustor designs.

NO_x emissions corrected to 15% excess O_2 for all experimental conditions at $T_2 = 573$ K are plotted against AFT for varying P_2 in Figure 6.30. The exponential trend of NO_x formation with increasing AFT is typical of the thermal NO_x formation mechanism as discussed in Chapter 2.4.1. Measured NO_x emissions for $AFT \leq 1900$ K ($\varphi < 0.6$) are below 10 ppmV across all conditions and fuels when normalized, resulting from a reduction in the thermal NO_x formation pathway under such lean operating conditions, and thus potentially featuring a contribution, albeit limited, from the prompt NO_x mechanism under these lean conditions [102]. Similarly low NO_x measurements with no statistically significant dependence on fuel composition were made at $P_2 = 0.76$ MPa and $T_2 = 589$ K with propane addition up to 5% by Straub et al. [104] at similar AFT, although higher overall NO_x values were obtained in their study due to the use of a diffusion pilot creating locally stoichiometric areas in the flow field. The EMIX1 fuel blend could not be operated stably below $AFT < 1800$ K ($\varphi < 0.55$) at $P_2 = 0.11$ MPa and 0.22 MPa, in part due to thermo-diffusive effects as shown in Figure 6.6. However, the other fuel blends are capable of achieving sub-4 ppmV NO_x levels under these conditions.

While the low NO_x measurements overall make it difficult to draw conclusions within the measurement uncertainty in Figure 6.30, trends of higher NO_x emissions with C_2+ addition can be identified by the plot in Figure 6.31 of NO_x against the fuel molar H:C ratio at varying P_2 , $T_2 = 573$ K, and $\varphi = 0.55$. This is in agreement with the findings of Flores et al. [40] with C_2+ addition, and may be related to the increase in AFT for a fixed φ , as well as the contribution from the N_2O pathway, identified with increased propane blending [40].

Figure 6.30: NO_x emissions versus AFT at varying P_2 for all experimental conditions at $T_2 = 573$ K

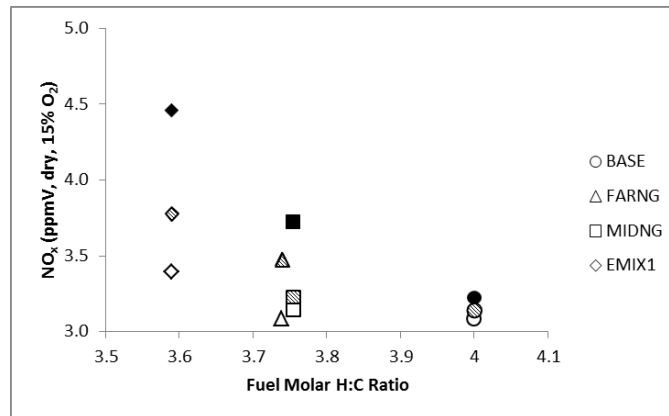


Figure 6.31: NO_x emissions versus fuel molar H:C ratio at $\phi = 0.55$ and varying P_2 , 0.11 MPa (open), 0.22 MPa (closed), 0.33 MPa (hashed)

While the overall trend of increasing NO_x emissions with decreasing H:C ratio is evident in Figure 6.30, a more subtle trend is also evident, notably the nonmonotonic response of NO_x emissions with increasing P_2 . For all fuels shown in Figure 6.31, the measured NO_x emissions are highest at $P_2 = 0.22$ MPa (closed symbols). To highlight this nonmonotonic trend, Figure 6.32 shows the influence of P_2 on NO_x emissions for all flames at $\phi = 0.55$ (AFT = 1791 K \pm 9 K) and $\phi = 0.60$ (AFT = 1884 K \pm 15 K). The nonmonotonic trend identified in Figure 6.31 is observed in Figure 6.32 for a fixed ϕ , noting the overall upward shift in NO_x emissions corresponding to the increase in AFT from $\phi = 0.55$ (Figure 6.32.a) to $\phi = 0.60$ (Figure 6.32.b). The nonmonotonic trend is most apparent in the propane-containing fuel blends (EMIX and MIDNG), while the increase in P_2 appears to have limited effect on FARNG NO_x emissions at $\phi = 0.55$ and BASE NO_x emissions at $\phi = 0.60$. NO_x production would be expected to scale generally with the square root of combustor pressure [237] under these conditions. A similar nonmonotonic trend with increasing pressure was observed in Figure 6.2 with regards to the normalized S_L of the fuel blends with respect to the BASE fuel. This suggests an overall increase in reactivity at $P_2 = 0.22$ MPa, and supports the observation in heat release distribution which appear to be the most uniform (and compact, if axial location of heat release centroid is considered from Figure 6.13). This distribution of heat release in a flow field shown to have a CRZ (although weakened) by isothermal PIV measurements, would ensure that the flow residence time in areas of maximum heat release would be maximized compared to the other flow conditions. It is also possible that the level of turbulence generated at $P_2 = 0.22$ MPa ($Re = 60000$ at $\phi = 0.55$ and $Re = 54000$ at $\phi = 0.60$), is sufficient to increase reactant and product mixing compared to the $P_2 = 0.11$ MPa condition, but yet suppresses the stretch influence as may be observed at higher Re in the $P_2 = 0.33$ MPa condition. This is supported by the flame brush and flame area measurements presented in Figures 6.21 and 6.22, which show

both an increase in mean flame brush thickness and a decrease in overall flame area at $P2 = 0.22$ MPa. Note that a similar nonmonotonic trend has also been identified with H_2 addition and is presented in Chapter 7.4.

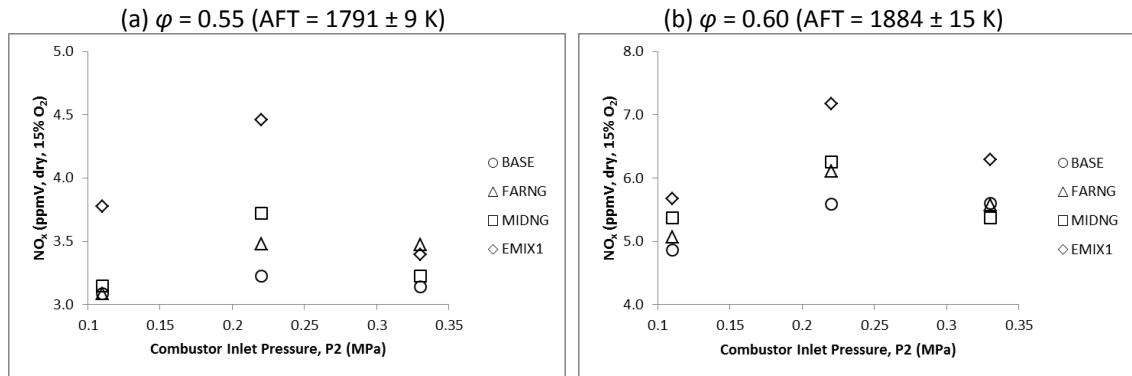


Figure 6.32: NO_x emissions plotted versus $P2$ at varying ϕ , 0.55 (a) and 0.60 (b). Note difference in y-axis scaling.

Finally, the relationship between modeled reaction zone thickness and the measured NO_x emissions is considered in Figure 6.33 at $\phi = 0.55$ and varying $P2$. First, the NO_x measurement of the given fuel blend is normalized against the corresponding BASE NO_x measurement under that condition ($NO_{x, fuel} / NO_{x, BASE}$). This normalized NO_x value is then compared with a similarly normalized maximum modeled CH mole fraction ($X_{CH, fuel} / X_{CH, BASE}$) in Figure 6.33.a and reaction zone thickness ($\delta_{t, fuel} / \delta_{t, BASE}$) in Figure 6.33.b. As discussed previously in Section 6.2.4.1, the reaction zone thickness, δ_t , varies nearly linearly with maximum modeled CH mole fraction, X_{CH} , and so a similar response between these fundamental parameters and the measured NO_x emissions was expected. As can be seen in Figure 6.33, the measured NO_x values, although varying nonmonotonically with pressure, appear to vary linearly with both X_{CH} and δ_t , as both fundamental modeled parameters account for the change in burner inlet pressure, and also vary nonmonotonically with increased $P2$ when normalized. However, as evidenced by the gradient of each linear relationship, it appears that NO_x emissions measurements would be more sensitive to reaction zone thickness (and thus residence time at the region of highest temperature) than by maximum CH mole fraction (which may promote the prompt NO_x mechanism under lean conditions). This supports the use of the suggested reaction zone thickness definition for evaluation of NO_x production, as further nonintrusive optical techniques could be utilized (e.g. CH PLIF) in the future for experimental validation. This may also allow for NO_x emissions prediction for fuels of varying C₂₊ content, if only limited CH₄ NO_x emissions are available (e.g. in cases of burner experimental design validation), greatly simplifying the process of expanding burner designs from low C₂₊ to high C₂₊ fuels where limiting NO_x emissions are a critical design criterion.

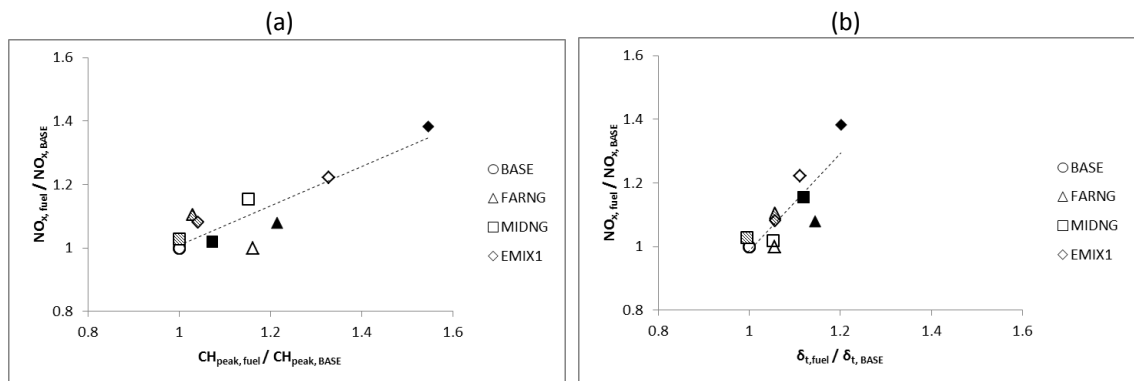


Figure 6.33: Normalized NO_x emissions plotted against normalized maximum CH mole fraction (a) and normalized modeled reaction zone thickness (b) at $\phi = 0.55$ and varying P_2 , 0.11 MPa (open), 0.22 MPa (closed), 0.33 MPa (hashed)

6.5 Chapter Summary

This Chapter presents an experimental and chemical kinetics analysis of the influence of (i) variable C_2+ fuel content, (ii) flow turbulence parameters, and (iii) elevated ambient conditions on fully premixed CH_4/air and $\text{CH}_4\text{-C}_2+\text{air}$ flames in terms of flame location, stability, and NO_x emissions in the HPGSB-2. Elevated operating conditions range from P_{therm} to 126 kW, T_2 to 573 K and P_2 to 0.33 MPa. In addition to providing a parametric dataset for chemical kinetics reactor network and CFD modeling, the following conclusions are deduced:

- The most dramatic effect on flame shape was identified with the FARNG fuel (15% ethane in 85% methane), as ethane appears to have a catalytic effect, promoting methane oxidation and resulting in upstream flame movement compared with 100% CH_4 fuel. The addition of C_2+ molecules was observed to have an overall damping effect on combustion noise amplitudes. NO_x emissions appear to show a correlation with fuel H:C ratio and a nonmonotonic trend with P_2 . Similar nonmonotonic trends with P_2 were identified with normalized S_L , normalized theoretical reaction zone thickness, δ_t , and mean flame brush thickness calculated from OH PLIF measurements, δ_{flame} .
- The addition of C_2+ fuels to methane enhances fundamental measurements such as S_L and AFT. Modeled S_L is seen to increase by up to 20% with the addition of propane in the EMIX1 fuel blend. Modeled S_L of BASE and EMIX1 fuels have been further supported by experimental measurements in the CVCB. A key finding from this experimental work is the shift in thermo-diffusive behavior between pure CH_4 , which exhibits increased stretched flame speed with increased stretch rate, and EMIX1, which exhibits decreased stretch flame speed

with increased stretch rate. At the lean premixed conditions studied here, these opposing trends are even more pronounced.

- OH* chemiluminescence and OH PLIF have been utilized to examine the flame stabilization location and heat release distribution resulting from changes in natural gas C₂₊ content. At comparable operating conditions of T_2 , P_2 , and turbulence, the BASE, MIDNG, and EMIX1 fuels are shown to have broadly similar flame stabilization mechanisms, while the FARNG fuel shows the greatest effect on localized heat release distribution. A similar effect with EMIX1 was expected given its significant increase in S_L compared to the BASE fuel, however, this was not observed, and in fact EMIX1 exhibited an unexpected lean response compared to the other fuels. As the flame transitions towards LBO, the observed change in flame shape from V-shape to M-shape by the BASE flame was not replicated by any other fuel, suggesting that fuels with increased C₂₊ content are unable to stabilize in areas of high stretch, such as the ORZ, despite increased S_L .
- The EMIX1 fuel containing 12.6% propane and 2.4% nitrogen in 85% methane could not be operated at the same lean equivalence ratios and turbulence levels as the other fuels, despite having consistently higher S_L and AFT for nominally similar AFR. This observation is attributed to changes in fundamental properties of the mixture, in particular thermo-diffusive effects which promote decelerated burning rates and positive Markstein lengths under lean, turbulent conditions. This is a key consideration with fuels with high C₂₊ content, in particular propane, and warrants further investigation to identify an acceptable propane limit for highly turbulent burner operations.
- A correlation between OH* chemiluminescence integral intensity, AFT, fuel H:C ratio, and P_2 is derived. Utilizing this correlation, theoretical I_{OH^*} values at 1.5 MPa (572 kW) in the HPGSB-2 could be predicted for a given C₂₊ containing fuel type and a range of AFT. This correlation could potentially provide support for onboard condition monitoring or fuel characterization.
- A power law correlation between combustion noise amplitudes and operating pressure (thus thermal power) is derived, taking into account the influence of fuel type (represented by H:C ratio). Utilizing this correlation, combustion noise amplitudes at 1.5 MPa (572 kW) in the HPGSB-2 could be predicted for a given C₂₊ containing fuel type.

CHAPTER 7 – FUEL FLEXIBILITY FOR GAS TURBINES – HYDROGEN ADDITION

A variety of low carbon intensity hydrogen production methods are currently being explored to enable the use of hydrogen as an energy vector within existing natural gas infrastructure. However, the introduction of hydrogen into natural gas systems presents potential operational issues for GT combustion and power generation applications; in particular as acceptable blending concentrations are still widely debated. The HPGSB-2 was therefore used in experimental investigation of CH₄-H₂ swirl flame stability and exhaust gas emissions at T_2 up to 573 K, P_2 up to 0.33 MPa, and P_{therm} up to 126 kW [123, 124] to provide evidence of potential design modifications necessary for future GT operation on hydrogen-blended fuels as well as to validate chemical kinetics reactor network and CFD model predictions. The geometry of the modular burner is augmented under isothermal and combustion conditions to investigate separately the influence of combustor outlet geometry and the effect of S_g . The burner confinement is varied to include both a cylindrical tube and a novel quartz tube with a tapered convergent exit, as shown in Chapter 3.1.2.2. Two inlet geometric swirl numbers are utilized, with values of $S_g = 0.8$ and 0.5 (Figure 3.8). The investigation of chemical effects of H₂ addition has been isolated by maintaining nominally similar turbulence characteristics within the combustor flow field across comparable experimental conditions. Combustion stability and heat release locations of LPM CH₄-air and CH₄-H₂-air combustion are evaluated by a combination of OH PLIF, OH* CL, and dynamic pressure measurements. Notable differences in flame stabilization and acoustic response are evident, in particular near the lean operating limit as H₂ blending is observed to shift the LBO of CH₄-air flames to lower ϕ with corresponding reduction in NO_x emissions. The influence of increased pressure on the lean operating point stability and emissions appears to be limited. Indicators of flame flashback are considerably affected, as well as burner acoustic response, by the use of a convergent combustor outlet geometry, which has been shown numerically [128] as well as in isothermal PIV measurements in Chapter 5.2.1.2 to alter the influence of the CRZ as a flame stabilizing coherent flow structure. Turbulence and thermo-diffusive effects of H₂ blending with CH₄ are studied with S_L measurement experiments in the CVCB and results support the observed lean stability behavior of the fuel blend in the more practical HPGSB-2 combustion environment. Chemical kinetic modeling, including an investigation of modeled extinction strain rate, K_{ext} , was also conducted to provide support to the experimental observations that stable CH₄ burner operation can be achieved with blended H₂ up to 15% by volume.

7.1 Chemical Kinetics Modeling and Flame Speed Measurements

7.1.1 Chemical Kinetics Modeling

Table 7.1 provides the full range of experimental conditions evaluated in this study. Note that all values are calculated based on the full premixed reactant flows, in particular the Reynolds number, which accounts for changes in premixed dynamic viscosity through use of the Wilke correlation [228] using Equation 5.1. The experimental designations in Table 7.1 refer to the fuel type, confinement, and geometric swirl number, e.g. BASE-O-8 for 100% CH₄, open cylindrical confinement, and $S_g = 0.8$. As can be seen, a large number of parametric influences, including burner inlet conditions, burner confinement, geometric swirl number, and turbulence characteristics are investigated as part of this study. Fuel characteristics for BASE (100% CH₄) and FARH2 (85%-15% CH₄-H₂) can be found in Table 3.2 (Chapter 3.4.1.2).

Table 7.1: HPCR operating ranges for isothermal, CH₄, and CH₄-H₂ combustion study

Experimental Designation	Fuel Type (%vol)	Confinement	S_g	$P2$ (MPa)	$T2$ (± 5 K)	P_{therm} (kW)	ϕ	\bar{u} (m/s)	Re ($\times 10^3$)	$\dot{m}\sqrt{T2}/P2$
ISO-O-8	---	Open	0.8	0.11 - 0.22	290 - 573	---	---	14 - 35	25 - 103	0.37 - 0.64
ISO-CQ-8	---	Convergent	0.8	0.11 - 0.33	290 - 573	---	---	14 - 35	25 - 152	0.37 - 0.63
ISO-CQ-5	---	Convergent	0.5	0.11 - 0.33	290 - 573	---	---	14 - 35	25 - 152	0.37 - 0.64
BASE-O-8	CH ₄ (100)	Open	0.8	0.11 - 0.33	290, 573	42 - 126	0.5 - 0.8	12 - 36	27 - 88	0.29 - 0.65
BASE-O-5	CH ₄ (100)	Open	0.5	0.11 - 0.33	573	42 - 126	0.47 - 0.65	27 - 38	25 - 90	0.49 - 0.69
BASE-CQ-8	CH ₄ (100)	Convergent	0.8	0.11 - 0.33	290, 573	42 - 126	0.52 - 1.0	10 - 35	24 - 91	0.25 - 0.62
BASE-CQ-5	CH ₄ (100)	Convergent	0.5	0.11	290, 573	42	0.5 - 1.0	10 - 36	23 - 46	0.24 - 0.64
FARH2-O-8	CH ₄ -H ₂ (85-15)	Open	0.8	0.11 - 0.22	573	42 - 84	0.43 - 0.6	30 - 41	27 - 71	0.54 - 0.74
FARH2-CQ-8	CH ₄ -H ₂ (85-15)	Convergent	0.8	0.11 - 0.33	573	42 - 126	0.5 - 0.6	30 - 36	27 - 97	0.54 - 0.64
FARH2-CQ-5	CH ₄ -H ₂ (85-15)	Convergent	0.5	0.11 - 0.33	573	42 - 126	0.46 - 0.6	30 - 39	27 - 89	0.54 - 0.70

Chemical kinetics modeling of the experimental conditions was conducted using three separate modules within CHEMKIN-PRO [199]. First, the equilibrium program was used to model AFT. Second, the PREMIX program was used to model laminar flame speeds (S_L) and equilibrium exhaust H₂O concentrations, X_{H2O} for wet emissions correction. Finally, the OPPDIF program was used to model extinction strain rates (κ_{ext}) of the experimental conditions for consideration in the evaluation of its use as suggested by Shanbhogue et al. [65] in Chapter 2.2.1, although noting their use of a twin flame model predicts higher extinction strain rates overall than the single flame model detailed in Chapter 3.3.1.

The influence of $T2$ on S_L and burner operability was evaluated with 100% CH₄-air flames at $P2 = 0.11$ MPa with both confinements and swirl numbers, and kinetics modeling results are presented in Figure 7.1. As expected, an increase in $T2$ significantly increases S_L , thus reactivity, of the BASE flames, with approximately linear relationships for lean ($\phi < 1$) conditions which are expected to be nonmonotonic for rich conditions ($\phi > 1$). This plot also

gives indication of the influence of confinement on burner operability, as an observable shift in lean operability equivalence ratios (thus AFT) afforded by the convergent nozzle confinement. In the $T_2 = 573$ K case, the BASE-O-8 points are bounded by LBO at AFT = 1700 K ($\varphi = 0.50$) and TFB at AFT = 1890 K ($\varphi = 0.60$). With the addition of the convergent nozzle confinement in the $T_2 = 573$ K case, e.g. BASE-CQ-8, burner operation is bounded by LBO at a higher AFT (1730 K at $\varphi = 0.52$) and does not experience TFB under any conditions, extending the upper lean operating range. This is considered to be a consequence of the change in CRZ size and strength from open to convergent confinement, as the stronger CRZ in the open confinement case allows for stabilization at lower AFT. This also causes operational issues as φ is increased and hot recirculated products increase the metal temperature of the bluff body within the burner exit nozzle. The reduction in swirl number from $S_g = 0.8$ and 0.5 is also observed to extend LBO limits in both the open and convergent confinements.

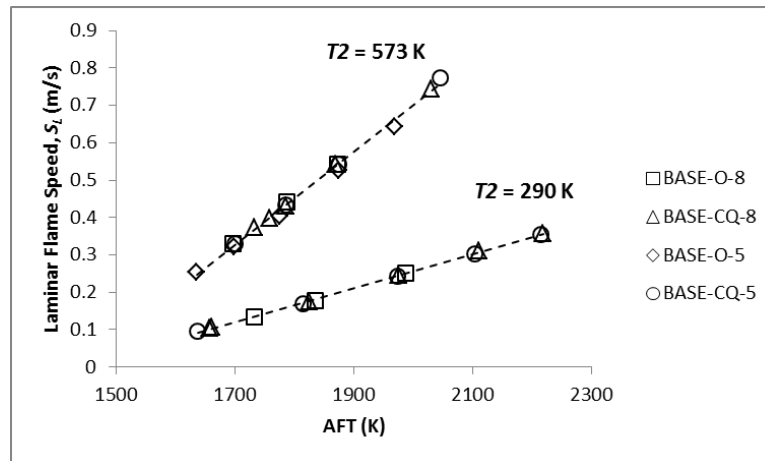


Figure 7.1: Modeled S_L of experimental BASE flames as a function of AFT at $P_2 = 0.11$ MPa with varying T_2 , burner confinement, and S_g

Of particular interest and novelty in this study is to examine the effect of elevated P_2 and temperature T_2 on the resulting flame stability and fuel reactivity. The results of chemical kinetics modeling of the elevated P_2 and T_2 experimental conditions are presented in Figures 7.2 and 7.3. First, in Figure 7.2, the influence of P_2 on each individual fuel, BASE (Figure 7.2.a) and FARH2 (Figure 7.2.b) is examined at $T_2 = 573$ K with varying confinement and S_g . Again, approximately linear relationships between AFT and S_L are observed for a fixed P_2 as in Figure 7.1. However, with increasing P_2 , S_L is seen to reduce for a fixed AFT, indicating a reduction in reactivity at increased pressure. For the BASE fuel, this results in an increase in the LBO point, as can be seen in the BASE-CQ-8 case. Comparing the two fuels, it is observed that the addition of hydrogen shifts the LBO point to lower AFT (thus φ) for a fixed P_2 . This lean shift is considered to be the result of two contributing factors, increased S_L for a fixed φ , as seen in

Figure 7.3, and increased thermo-diffusive effects as discussed in Section 7.1.2. Similar trends of lean operability range extension as seen in Figure 7.1 with the convergent confinement compared with the open cylinder and with a reduction in swirl number from $S_g = 0.8$ to 0.5 are observed in both BASE and FARH2 cases.

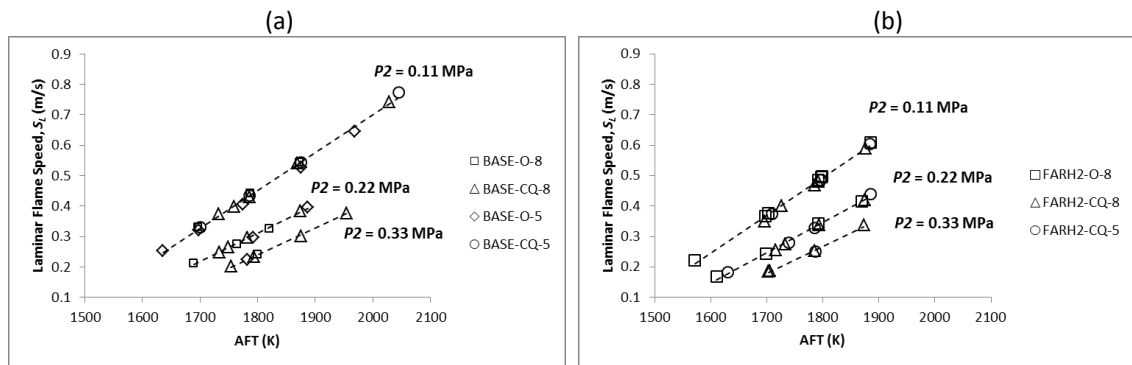


Figure 7.2: Modeled S_L of experimental BASE (a) and FARH2 (b) flames as a function of AFT at $T_2 = 573$ K with varying P_2 , burner confinement, and S_g

Whereas Figure 7.2 considered the BASE and FARH2 fuels individually for a wide range of operating conditions and burner configurations, Figure 7.3 compares the fuels directly with a fixed geometry (convergent confinement and $S_g = 0.8$) to evaluate the influence of P_2 and hydrogen addition. Figure 7.3 provides modeled S_L as a function of P_2 at $\varphi = 0.55$ (open symbols) and $\varphi = 0.60$ (closed symbols).

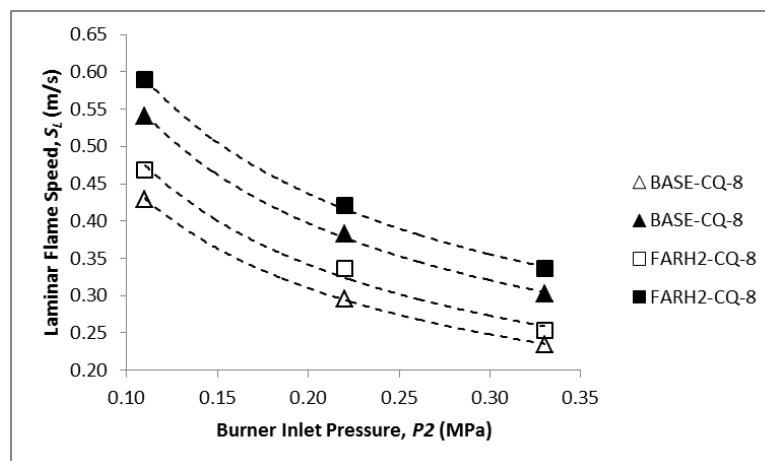


Figure 7.3: Pressure influence on modeled S_L of experimental BASE and FARH2 flames at $\varphi = 0.55$ (open symbols) and $\varphi = 0.60$ (closed symbols) with $T_2 = 573$ K, convergent confinement, and $S_g = 0.8$

These experimental conditions were selected because they represent overlapping rig operating conditions and show the effect of H_2 addition at nominally similar AFT. The calculated AFT is significantly less pressure dependent than S_L , with AFTs for both fuels falling within $1788 \text{ K} \pm 6 \text{ K}$ ($\varphi = 0.55$) and $1873 \text{ K} \pm 3 \text{ K}$ ($\varphi = 0.60$) across the experimental pressure range. For a fixed AFT, H_2 addition is shown consistently to increase flame speed above the

pure CH₄ case, as expected. Both fuels show a marked reduction with increasing $P2$, following a power law correlation with a $P2^{-x}$ relationship with $0.5 < x < 0.55$, with x increasing from top to bottom, suggesting that flame reactivity is increasingly dependent on $P2$ as the combustion process is shifted to reduced φ .

In addition to modeling of the experimental AFT and S_L , the extinction strain rate, κ_{ext} , was also modeled for selected experimental conditions. Shanbhogue et al. [65] observed that the transition between stability modes relative to changes in equivalence ratio in cylindrically confined CH₄-H₂ swirl flames can be represented by κ_{ext} , although their experimental analysis is limited to atmospheric temperature and pressure flames. Figure 7.4 provides indication of the influence of hydrogen addition, equivalence ratio, and operating pressure on the modeled κ_{ext} of experimental conditions with the convergent quartz confinement and $S_g = 0.8$. Figure 7.4.a and 7.4.c provide the CHEMKIN OPPDIF output for each fuel at $T2 = 573$ K and $\varphi = 0.55$. From these plots of maximum flame temperature and extinction strain rate, the curve turning point represents the maximum extinction strain rate under those conditions. For the BASE case (Figure 7.4.a), the extinction strain rates are 315 s^{-1} , 337 s^{-1} , and 357 s^{-1} at $P2 = 0.11$ MPa, 0.22 MPa, and 0.33 MPa, respectively. For the FARH2 case (Figure 7.4.c), the extinction strain rates are 450 s^{-1} , 529 s^{-1} , and 487 s^{-1} at $P2 = 0.11$ MPa, 0.22 MPa, and 0.33 MPa, respectively. With the addition of only 15% H₂ in CH₄, a 30-40% increase in extinction strain rate is seen across all pressure conditions. A similar effect is observed with an increase in equivalence ratio to $\varphi = 0.60$ for a fixed fuel composition, as shown in Figure 7.4.b for CH₄ and Figure 7.4.d for CH₄-H₂. Interestingly, there appears to be a nonmonotonic effect of pressure on extinction strain rate in the hydrogen addition case at $\varphi = 0.55$, Figure 7.4.d. This effect was recently noted above 0.3 MPa by Niemann et al. [238] in pure H₂-air counterflow diffusion flame experiments and warrants consideration in the context of its use as a flame stability predictor [65] in the case of H₂ addition in pressurized premixed natural gas combustion.

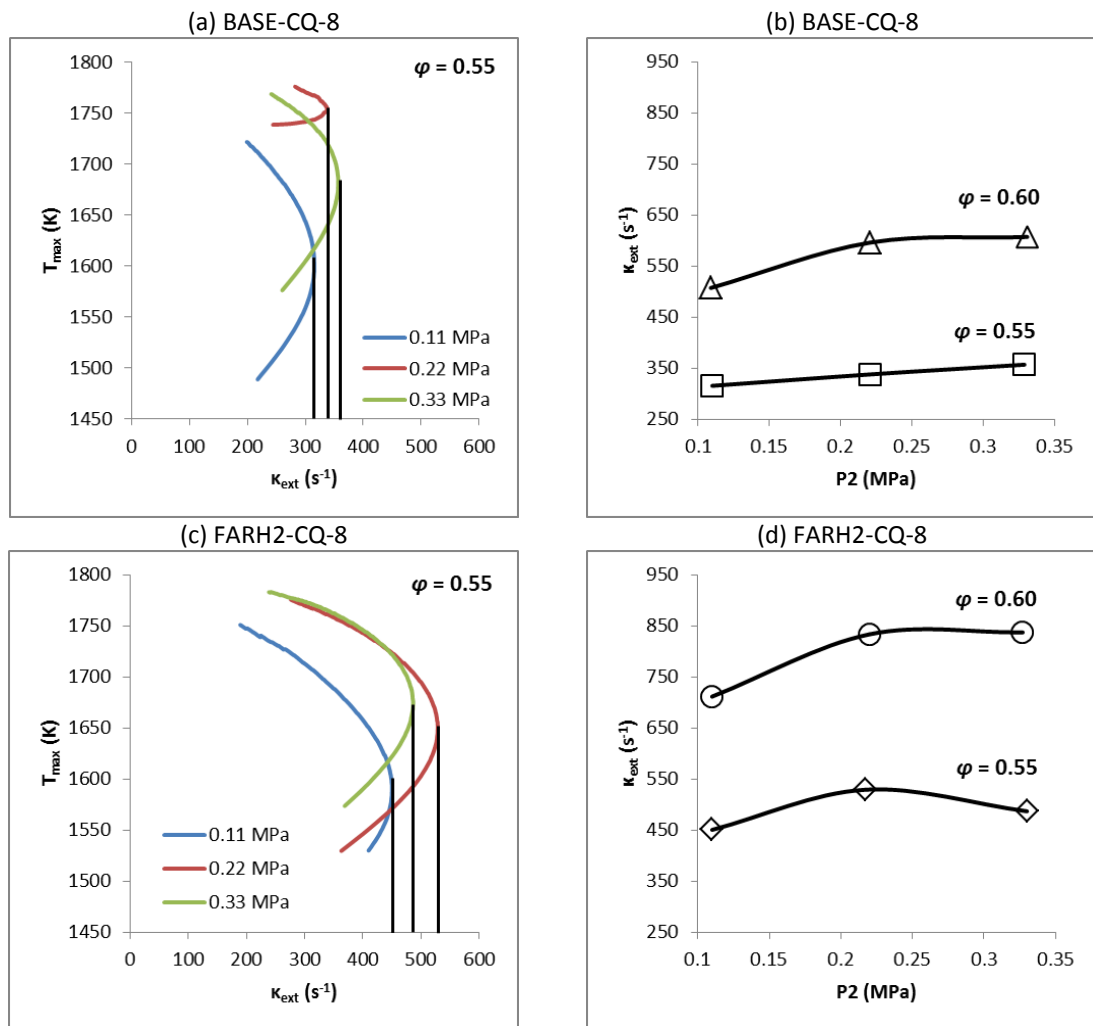


Figure 7.4: Modeled κ_{ext} plots for experimental BASE and FARH2 flames at $T_2 = 573$ K, convergent confinement, and $S_g = 0.8$ with varying ϕ and P_2

7.1.2 Flame Speed Measurements

In a similar manner to the BASE and EMIX1 flame speed measurements presented in Chapter 6, measurements of S_L , stretch rate, and Markstein length, L_b , for BASE and FARH2 fuels have been conducted in the CVCB. S_L measurements of spherically-expanding BASE and FARH2 flames were conducted at 298 K and 0.101 MPa, for an equivalence ratio range of $0.6 \leq \phi \leq 0.8$. The results are found in Figure 7.5. Note that the S_L values presented in Figure 7.5 are calculated by correcting the projected unstretched, spherically-expanding flame speed (e.g. Figure 7.6.a at $\kappa = 0$) with the adiabatic density ratio of products to reactants [168]. The measured BASE S_L is in good agreement with the modeled results shown in Figure 7.1 at $T = 290$ K and show a similar quasi-linear trend for lean ϕ . In addition, for a fixed ϕ , the addition of H_2 to CH_4 increases S_L also predicted by the modeling work in Figure 7.3, although at a higher temperature the upward shift is more pronounced.

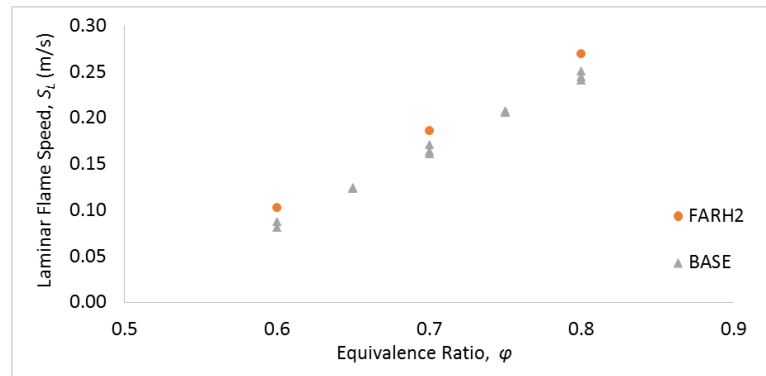


Figure 7.5: S_L measurements for BASE and FARH2 flames at 298 K and 0.101 MPa

The S_L measurements presented in Figure 7.5 are derived from measures of stretched flame speed as a function of stretch rate, κ , as shown in Figure 7.6.a for an equivalence ratio of $\phi = 0.6$. While the derived S_L is a useful output to categorize flame reactivity, the flame response to increased stretch is also of particular significance due to the lean, turbulent conditions typical of a GT combustor and used in the HPGSB-2. As can be seen in Figure 7.6.a, both the BASE and FARH2 have positive slopes at $\phi = 0.6$, meaning that with increased stretch rate, the stretched flame speed increases. This gradient is described numerically by the L_b , plotted for the BASE and FARH2 flame speed measurements in Figure 7.6.b. Thus, the positive slope in Figure 7.6.a corresponds to the negative L_b at $\phi = 0.6$ in Figure 7.6.b. As the FARH2 fuel is observed to have a higher slope at $\phi = 0.6$ in Figure 7.6.a, it has a lower L_b at $\phi = 0.6$ in Figure 7.6.b. The zero-crossing in Figure 7.6.b, indicating a change in positive stretched flame speed correlation with stretch rate to negative correlation (i.e. reduced flame speed with stretch), has shifted to higher ϕ with H₂ addition ($\phi = 0.65$ to 0.75). Thus, while both BASE and FARH2 fuels would be expected to exhibit accelerating flame speeds at $\phi < 0.65$ with increased stretch rate, the effect is even greater for the H₂-blended fuel.

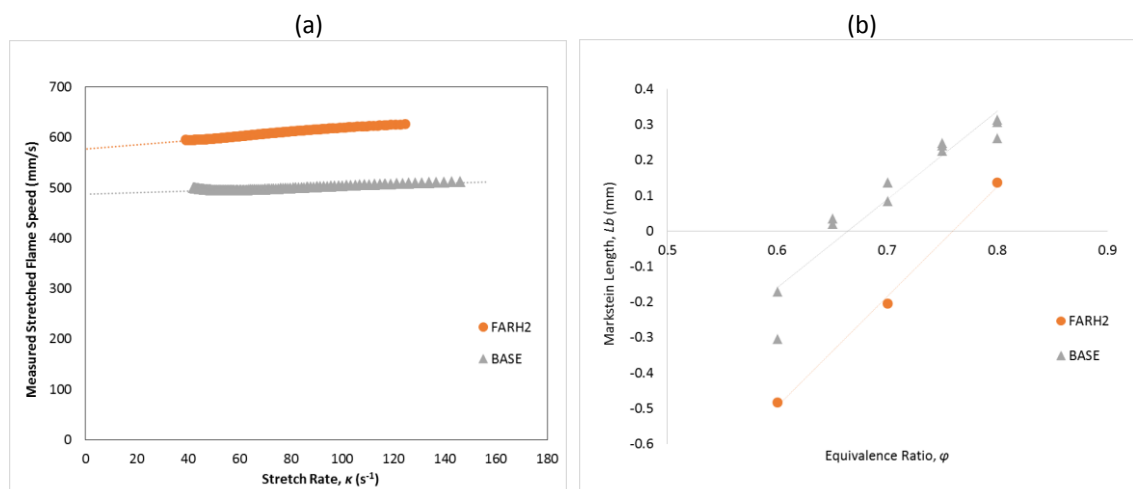


Figure 7.6: Measured stretched flame speed (at $\phi = 0.60$, a) and Markstein length (at varying ϕ , b) for BASE and FARH2 flames at $T_2 = 298$ K and $P_2 = 0.101$ MPa

It is interesting to note here as well that by comparison with the results presented in Chapter 6 for the EMIX1 fuel, the addition of H₂ to CH₄ is seen to have the opposite thermo-diffusive influence as the addition of C₃H₈, not unexpected due to their different Lewis numbers ($Le < 1$ for H₂ and $Le > 1$ for C₃H₈). It is their influence when mixed in relatively small quantities with methane that is remarkable. Whereas the addition of 15% H₂ promotes an increase in the flame speed, and correspondingly shifts the Markstein length zero-crossing to higher φ (as seen in Figure 7.6.b), the addition of only 12.6% C₃H₈ to CH₄ changes the stretch rate response completely, resulting in a positive L_b for all lean conditions (see Figure 6.6.b). This is particularly interesting because EMIX1 and FARH2 have nominally similar S_L and AFT across the experimental range considered, and as such were expected to behave similarly under lean operating conditions in the HPGSB-2, assuming those fundamental properties were to provide the basis of their reactivity relative to pure methane. However, the lean operability of the FARH2 fuel is shifted to far lower φ than could be achieved with the EMIX1 fuel blend under any operating conditions, and in some cases the EMIX1 lean operability limit was shifted to higher φ than the BASE fuel despite the assumed increase in reactivity. This was unexpected and highlights the need to consider thermo-diffusive effects such as Le and L_b to provide indication of how a fuel mixture may behave in a more applied combustion system, particularly preheated, pressurized GT combustion which operate under lean, turbulent conditions where flame stretch effects may be enhanced. This is a key finding of this study and warrants future investigation, particularly as this study has only initially considered ambient temperature and pressure conditions in the CVCB.

7.2 Flame Stabilization

Flame stabilization in the HPGSB-2 was evaluated experimentally through the use of OH PLIF and OH* CL measurements, considering first the influence of H₂ addition to CH₄ in a fixed burner geometry and then subsequently varying the burner confinement geometry and S_g . In combination with the acoustic measurements presented in Section 7.3, a comprehensive evaluation of H₂ influence on preheated, pressurized swirl combustion is thus made. For all following experimental results, the reader is referred to Table 3.3 for air mass flow rates.

7.2.1 Influence of Premixed Fuel Composition

To isolate the influence of hydrogen addition on premixed methane flame stabilization mechanisms, a series of combustion experiments were conducted with a fixed HPGSB-2 burner

geometry and nominally similar flow and turbulence conditions. For all results presented in this Section, the HPGSB-2 was configured with the convergent nozzle confinement and $S_g = 0.8$, in a configuration identical to that used for the C_2+ blended combustion presented in Chapter 6. BASE and FARH2 flame stabilization is evaluated based on Abel-transformed OH^* chemiluminescence measurements in Figures 7.7 and 7.8, with flames at $\varphi = 0.55$ in Figure 7.7 and $\varphi = 0.60$ in Figure 7.8 at three burner inlet pressures, $P_2 = 0.11$ MPa, 0.22 MPa, and 0.33 MPa.

For the $\varphi = 0.55$, $T_2 = 573$ K flames in Figure 7.7, the AFT for both BASE and FARH2 fuels is approximately equal at $1788 \text{ K} \pm 6 \text{ K}$. In addition, as the dimensionless flow parameter $\dot{m}_{premix}\sqrt{T_2}/P_2$ has been held constant across all conditions presented at 0.59, this effectively fixes the mean burner exit nozzle velocity at $\bar{u} = 33$ m/s. Scaling the premixed reactant flow rate with pressure yields a thermal power scaling of approximately 382 kW/MPa for $P_{therm} = 42$ kW, 84 kW, and 126 kW. In order to match φ between fuels while holding the air mass flow rates constant, a slight reduction in FARH2 fuel flow rate ($\sim 2\%$) was necessary due to the increase in FARH2 stoichiometric AFR compared to the BASE fuel. As the pressure increases, the Reynolds number also increases due to a reduction in premixed reactant density, however, it is nominally constant between fuels at a fixed P_2 , approximately $Re = 30000$, 60000, and 90000 at $P_2 = 0.11$ MPa, 0.22 MPa, and 0.33 MPa, respectively.

At $\varphi = 0.55$, both BASE and FARH2 flames are observed to stabilize along the outward expanding shear layer between the CRZ and ORZ observed in the isothermal PIV results in Chapter 5.2.1.2, yielding conical, V-shaped flames which expand radially outward from the burner exit nozzle centerline ($r = 0$ mm). However, the influence of hydrogen addition is immediately apparent, as the flames are observed to transition upstream towards the burner exit nozzle at each pressure condition, compacting the heat release zones. This is the result of the compounding effect of the thermo-diffusive behavior of CH_4 - H_2 blends with increased turbulence (thus stretch) described in Section 7.1.2 and increased chemical reactivity as the hydrogen encourages chain-branching reactions, thus the heat release proceeds on a reduced chemical time scale while the flow time scale has been held nominally constant. The BASE flame reaction zone appears elongated axially, to the point of interaction with the quartz confinement walls and ORZ, and it is only under the $P_2 = 0.33$ MPa condition that the areas of heat release are found strictly along the shear layer.

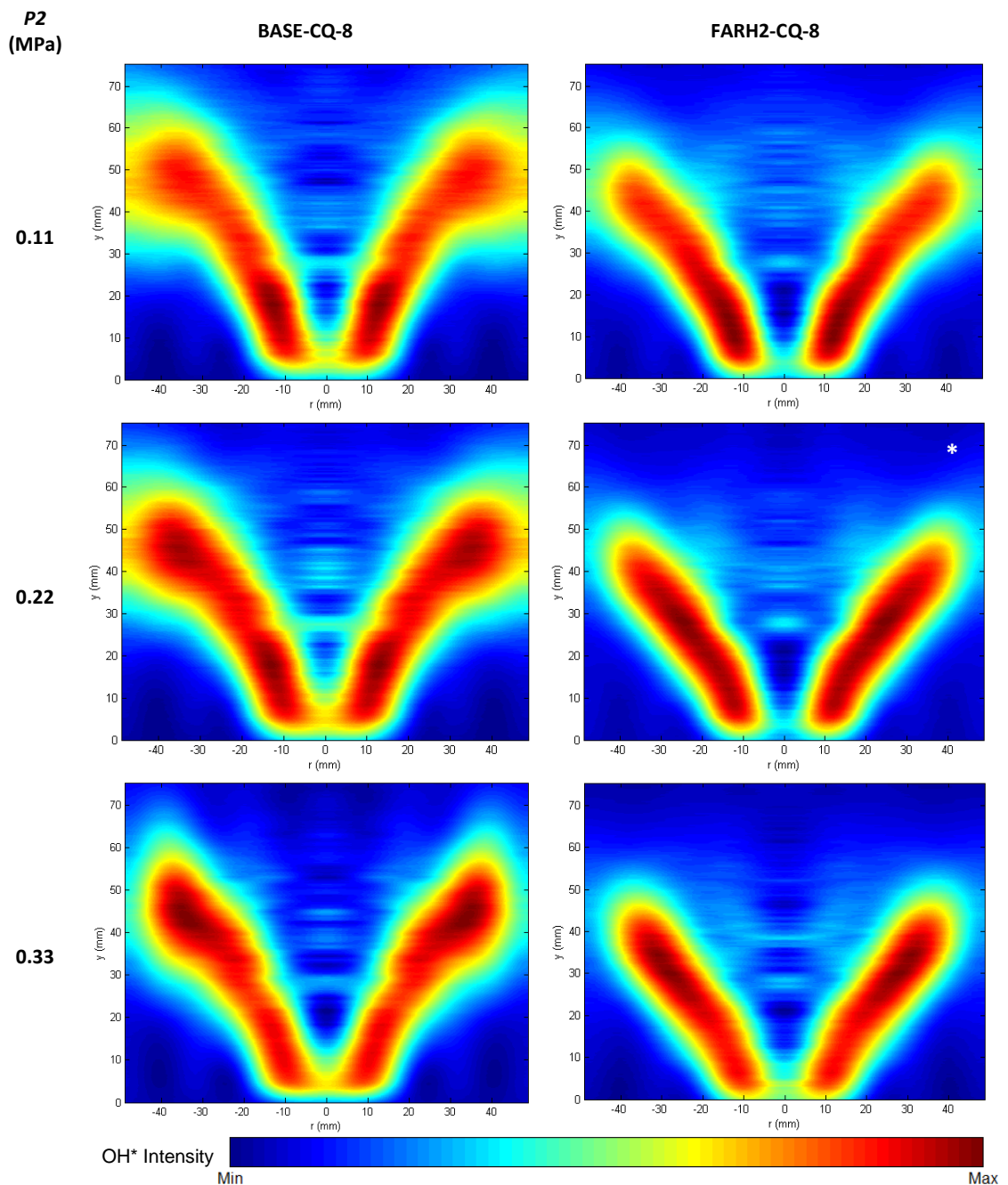


Figure 7.7: Abel-transformed OH* chemiluminescence images for BASE and FARH2 flames in the HPGSB-2 with convergent confinement at $T_2 = 573$ K, $\phi = 0.55$, and $S_g = 0.8$ with varying P_2

The distribution of maximum OH* CL intensity is also interesting to note between both fuels, as it appears to follow the same pattern with increasing pressure. At $P_2 = 0.11$ MPa, the areas of highest heat release are quite narrow and reside axially at $y = 10 - 20$ mm (BASE) and at $y = 5 - 30$ mm (FARH2). At $P_2 = 0.22$ MPa, the area of maximum intensity appears almost uniform along the flame brush. At $P_2 = 0.33$ MPa, the location of maximum intensity is compacted once again, but is now located at $y = 40 - 50$ mm (BASE) and at $y = 20 - 35$ mm (FARH2). The structure of the heat release zones will influence both the thermoacoustic

stability of the flame as the local speed of sound is influenced and the exhaust gas emissions, in particular NO_x emissions in which temperature and residence time play key formation roles.

For the $\varphi = 0.60$, $T_2 = 573$ K flames in Figure 7.8, the AFT for both BASE and FARH2 fuels is approximately equal at $1873 \text{ K} \pm 3 \text{ K}$. In addition, as the dimensionless flow parameter $\dot{m}_{\text{premix}}\sqrt{T_2}/P_2$ has been held constant across all conditions presented at 0.54, this effectively fixes the mean burner exit nozzle velocity at $\bar{u} = 31 \text{ m/s}$. The thermal powers are identical to the $\varphi = 0.55$ conditions. Due to the reduction in premixed air flow rate to achieve $\varphi = 0.60$, the bulk flow Reynolds number is reduced to approximately $Re = 27000$, 54000 , and 81000 at $P_2 = 0.11 \text{ MPa}$, 0.22 MPa , and 0.33 MPa , respectively. As expected with the upward shift in S_L shown in Figure 7.3 (and reduced \bar{u}), the $\varphi = 0.60$ flames have all transitioned upstream along the shear layer compared with the $\varphi = 0.55$ flames. A similar effect for hydrogen addition is noted as in Figure 7.7 with the flame area observed to move towards the burner exit compared to the BASE flame at similar conditions. The change in flame shape from BASE to FARH2 in Figure 7.8 is not as remarkable as in Figure 7.7, further reinforcing the effect of H_2 on lean methane flame reactivity.

While the change in bulk velocity from Figure 7.7 and 7.8 makes a direct comparison between the two figures difficult, the flames of FARH2-CQ-8, $P_2 = 0.22$, $\varphi = 0.55$ (Figure 7.7, marked with white asterisk) and BASE-CQ-8, $P_2 = 0.22$, $\varphi = 0.60$ (Figure 7.8, marked with white asterisk) are almost identical in both overall flame brush shape and heat release distribution. From Figure 7.3, FARH2 S_L at $P_2 = 0.22$, $\varphi = 0.55$ is 0.35 m/s (middle open square in Figure 7.3) while BASE S_L at $P_2 = 0.22$, $\varphi = 0.60$ is 0.40 m/s (middle closed triangle in Figure 7.3). In addition, Re for the FARH2 case is approximately 60000 while $Re = 54000$ for this BASE condition due to reduced \bar{u} at $\varphi = 0.60$. However, despite the reduced reactivity indicated by a lower S_L and a more turbulent flow condition, the addition of H_2 allows for the same overall flame shape and heat release distribution at leaner conditions, which consequently could inhibit the thermal NO_x pathway given the reduced AFT. This is in part attributable to the lower projected Markstein length of the FARH2 blend at $\varphi = 0.55$ than the measured BASE L_b at $\varphi = 0.60$ as shown in Figure 7.6.b.

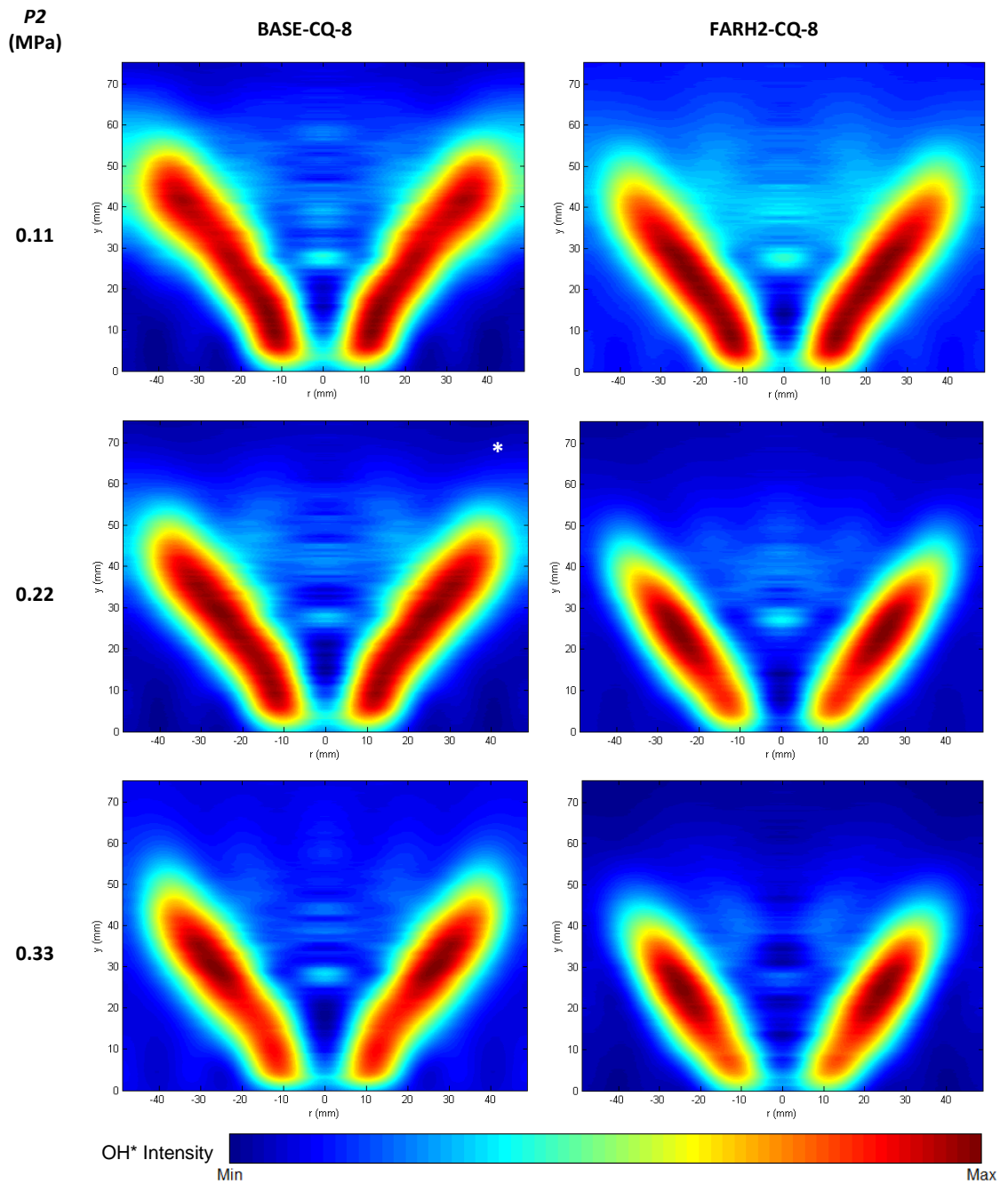


Figure 7.8: Abel-transformed OH* chemiluminescence images for BASE and FARH2 flames in the HPGSB-2 with convergent confinement at $T_2 = 573$ K, $\varphi = 0.60$, and $S_g = 0.8$ with varying P_2

7.2.2 Influence of Burner Confinement Geometry

Further experimental work in the HPGSB-2 focused on the influence of burner confinement geometry on flame stabilization characteristics, dynamic response, and emissions. Both an open cylindrical confinement (Figure 3.6, left) and a convergent nozzle confinement (Figure 3.6, right) were investigated as part of this study at a fixed swirl number of $S_g = 0.8$. While cylindrical confinement can in many ways replicate the flame and flow characteristics of an industrial can-type gas turbine combustion chamber, and indeed is widely used in

experimental burner systems, the use of a convergent nozzle outlet to replicate the influence of the turbine inlet transition piece on flow structure and acoustic response is less common. Examples include the DLR dual swirl burner ($D_{\text{confine}}/D_{\text{exit}} = 1.78$) [146] and the CRF combustor ($D_{\text{confine}}/D_{\text{exit}} = 7.67$) [149]. Therefore, a single construction quartz convergent nozzle ($D_{\text{confine}}/D_{\text{exit}} = 2.5$) has been designed and fabricated to investigate potential flow, flame, and acoustic impacts at elevated temperature and pressure conditions, with relatively low exit Mach numbers ($M < 0.1$) to reduce pressure drop across the quartz tube within the HPOC.

Figures 7.9 and 7.10 provide evidence of the influence of using a convergent nozzle confinement on 100% CH₄ (BASE) flames under ambient inlet conditions of $T_2 = 290$ K, $P_2 = 0.11$ MPa (Figure 7.9) and elevated inlet conditions of $T_2 = 573$ K, $P_2 = 0.11$ – 0.22 MPa (Figure 7.10) through the use of OH PLIF and Abel-transformed OH* chemiluminescence images. Figure 7.9 details the OH* chemiluminescence intensity distribution, while Figure 7.10 provides a split measurement of OH PLIF (left) and OH* CL (right). While the OH PLIF images provide qualitative indication of actual in-flame OH radical concentration as a measure of flame front location, the Abel-transformed OH* chemiluminescence images are numerical planar projections of localized heat release areas. In Figure 7.9, a well-defined flame structure along the shear layer between the CRZ and ORZ is visible for varying equivalence ratio and confinement type. With a reduction in equivalence ratio from $\varphi = 0.8$ to $\varphi = 0.7$, the flame is shown to extend further downstream with increased influence from the confinement walls and ORZ, as would be expected given the drop in flame speed ($S_L = 0.25$ m/s to 0.18 m/s, see Figure 7.1) combined with the increased \bar{u} . Generally, there appears to be limited influence of the confinement outlet geometry on the overall flame shape as only a slight retraction towards the burner exit nozzle is evident. Also, a small increase in flame angle relative to the burner centerline ($r = 0$ mm) can be seen in the convergent nozzle case (Figure 7.9.c and 7.9.d) relative to the open confinement, evidenced by the solid and hashed lines drawn along the burner centerline and flame brush, respectively. This effect is more pronounced under elevated temperature and pressure conditions shown in Figure 7.10.

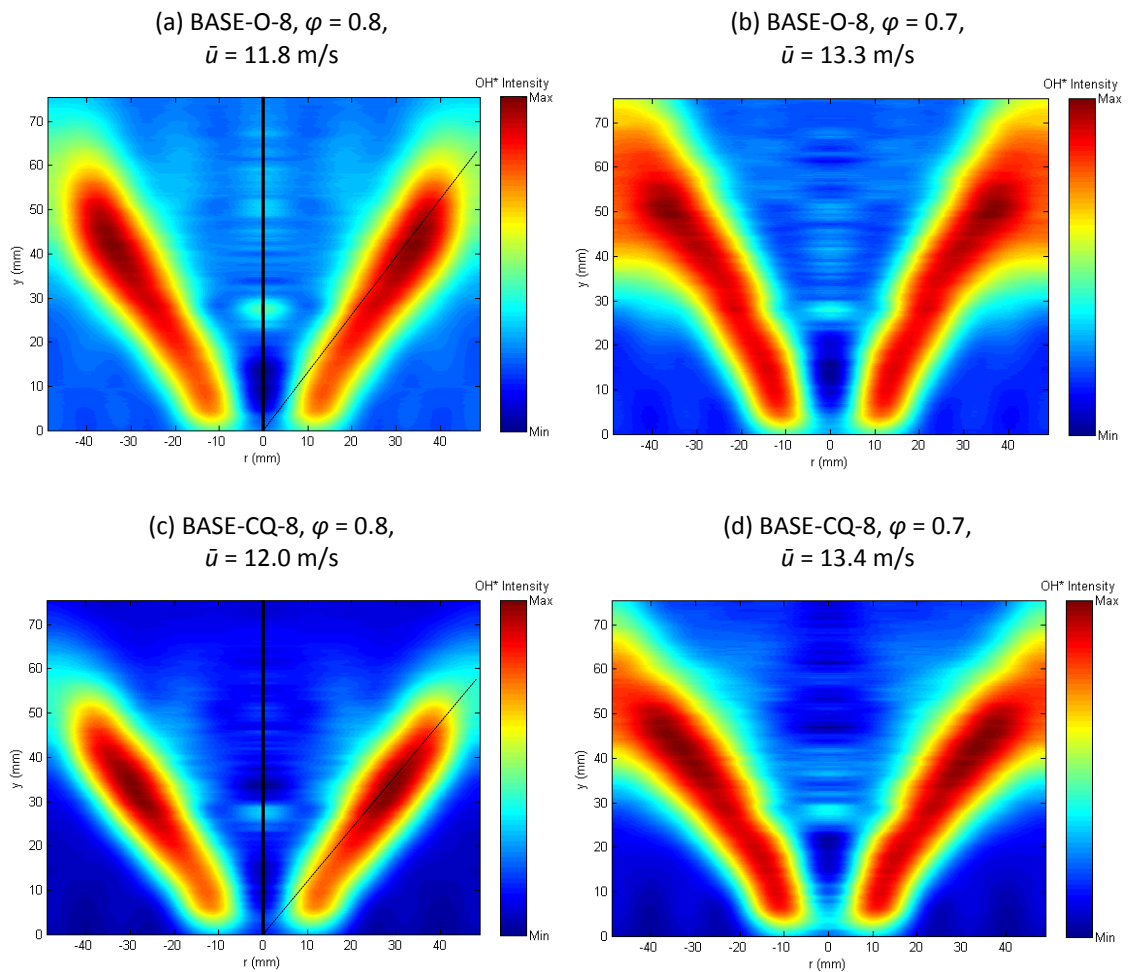


Figure 7.9: Abel-transformed OH* chemiluminescence for BASE flames at $T_2 = 290$ K and $P_2 = 0.11$ MPa with varying ϕ and burner confinement: open, (a) and (b), convergent, (c) and (d)

With an increase in burner inlet temperature and pressure, the influence of the exhaust confinement was apparent both operationally and as shown in Figure 7.10 for $T_2 = 573$ K and $\phi = 0.55$. In the open confinement case (Figure 7.10.a and 7.10.b), the burner was not operated above $\phi = 0.6$ as it reached the TFB operating limit, described in Chapter 3.1.2.2, resulting from flame stabilization location and strength of the CRZ which appears to extend into the burner exit nozzle, thus heating the bluff body and increasing T_{pilot} . When operating the burner with the convergent confinement (Figure 7.10.c and 7.10.d), however, the TFB limit was not reached under any operating condition. This is attributed to the effect of the nozzle exit area restriction on the CRZ size and strength as detailed in [128] and shown in the isothermal PIV measurements in Chapter 5.1.2.2. With an open confinement, the CRZ is observed to be larger and extend along the axis of the cylindrical quartz tube. As the confinement exit area is reduced in the convergent nozzle case, the CRZ reduces in size and shifts downstream towards the convergence. While the existence and influence of the ORZ

does not appear to alter the flame dramatically, the increase in flame angle in the convergent case is evident, see hashed lines in Figure 7.10.a and 7.10.c. This is attributed to increased tangential velocities with reduction in CRZ size, as noted in [128]. In Figure 7.10, it is also possible to observe the influence of pressure on the flame stabilization location. By maintaining approximately constant $\dot{m}\sqrt{T_2}/P_2 = 0.59$ (thus $\bar{u} = 33$ m/s) with increasing pressure, changes to the overall flow field shape are limited and as such changes in flame shape and location are attributable to turbulent (increased Re) and chemical (e.g. S_L , K_{ext}) effects. In the open confinement case, the areas of heat release transition from V-shape to M-shape with increasing pressure while the flame moves slightly downstream. With an increase in pressure from 0.11 MPa to 0.22 MPa, S_L reduces by approximately 30% as shown in Figure 7.3, and thus the flame stabilizes both along the shear layer and partially within the CRZ and ORZ. With increased Re , the CH_4 flame would also become increasingly stretched, which would serve to thicken the mean flame brush in combination with the drop in S_L , as observed in both confinement cases.

The influence of confinement geometry on flame location and heat release in the case of hydrogen addition (85-15% CH_4 - H_2) is shown in Figure 7.11. Comparing Figures 7.10 and 7.11 directly is useful, as $\varphi = 0.55$ in both cases and $\dot{m}\sqrt{T_2}/P_2$ has been held nominally constant across both fuels with approximately 1% increase in P_{therm} in the CH_4 - H_2 case to maintain burner exit nozzle velocities at approximately 33 m/s. With the addition of 15% H_2 , the laminar flame speed of CH_4 increases by 8% at 0.11 MPa and 12% at 0.22 MPa, while the extinction strain rate increases by 30% and 36%, respectively. This increased reactivity is evident as the flame stabilized further upstream near the burner exit ($y = 0$ mm) while also reducing in thickness compared to the 100% CH_4 flame. The increase in flame angle relative to the burner centerline between the open (Figures 7.11.a and 7.11.b) and convergent (Figures 7.11.c and 7.11.d) cases is also observed as in Figures 7.9 and 7.10. A comparison of the flame stabilization locations between fuels in the open confinement, Figure 7.10.b (BASE) with 7.11.b (FARH2), and convergent confinement, Figure 7.10.d (BASE) with 7.11.d (FARH2), yields an interesting consideration with respect to hydrogen addition. With increased Re , the 0.22 MPa cases will be further influenced by thermo-diffusive effects in addition to the S_L effects mentioned previously. With increased stretch rate, lean CH_4 - H_2 flames have been shown to exhibit accelerated burning rates in Figure 7.6, reducing the flame's sensitivity to aerodynamic stretch [47, 49]. While consideration of this influence should be given in the context of flame flashback, H_2 addition has been shown in this study to extend stable lean operational limits,

which provides a potential offsetting mechanism to avoid flashback. The thermo-diffusive effect of H_2 addition, and its influence on turbulent flame speed, is significant when operating the burner along a constant $\dot{m}\sqrt{T_2}/P_2$ line and at a fixed equivalence ratio, as nominally similar flow field and AFT will not necessarily be indicative of similar operation to a methane burner.

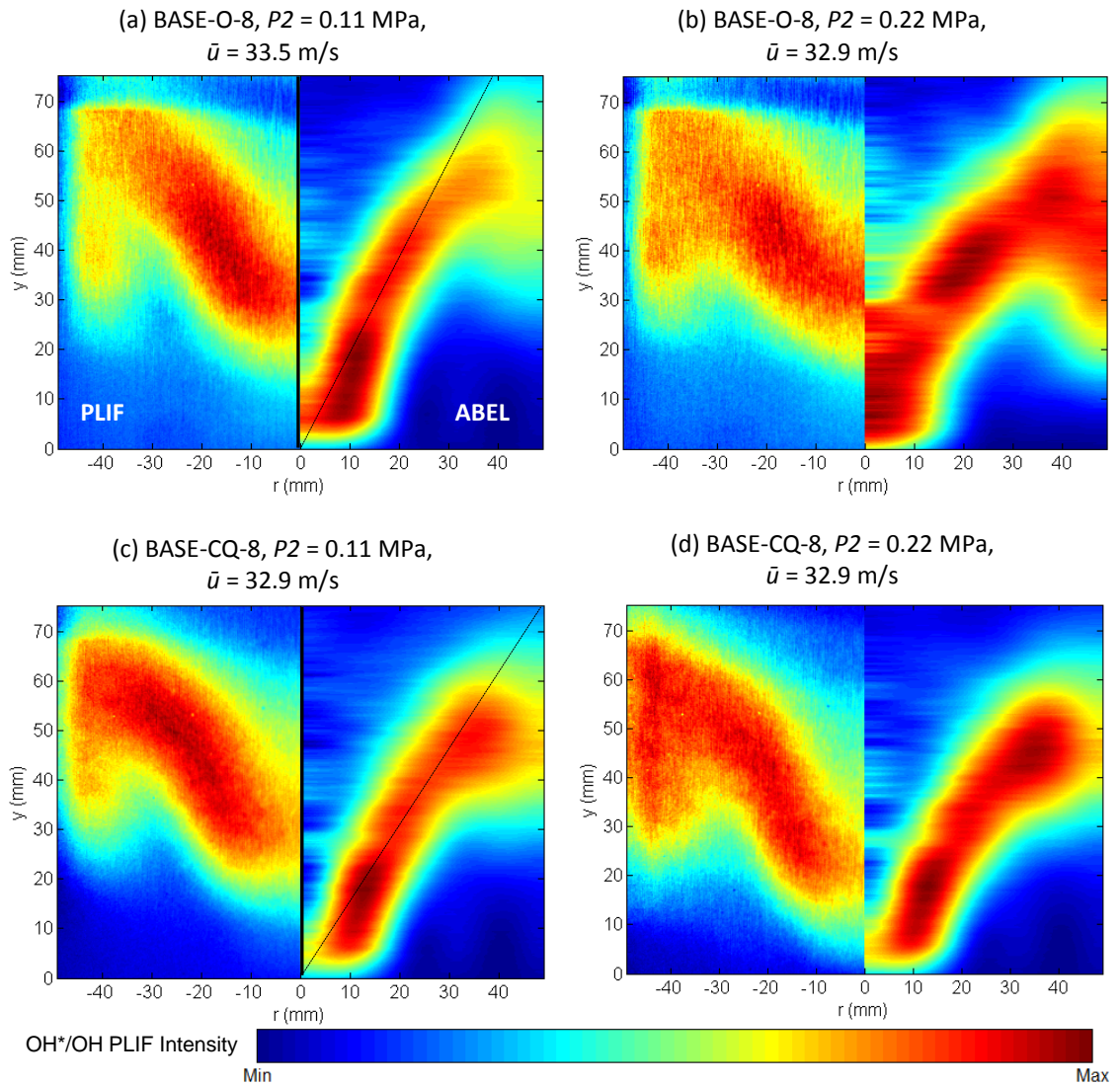


Figure 7.10: Combined PLIF (left) and Abel-transformed OH^* chemiluminescence (right) images for BASE flames at $T_2 = 573$ K and $\varphi = 0.55$ with varying P_2 and burner confinement: open, (a) and (b), convergent, (c) and (d)

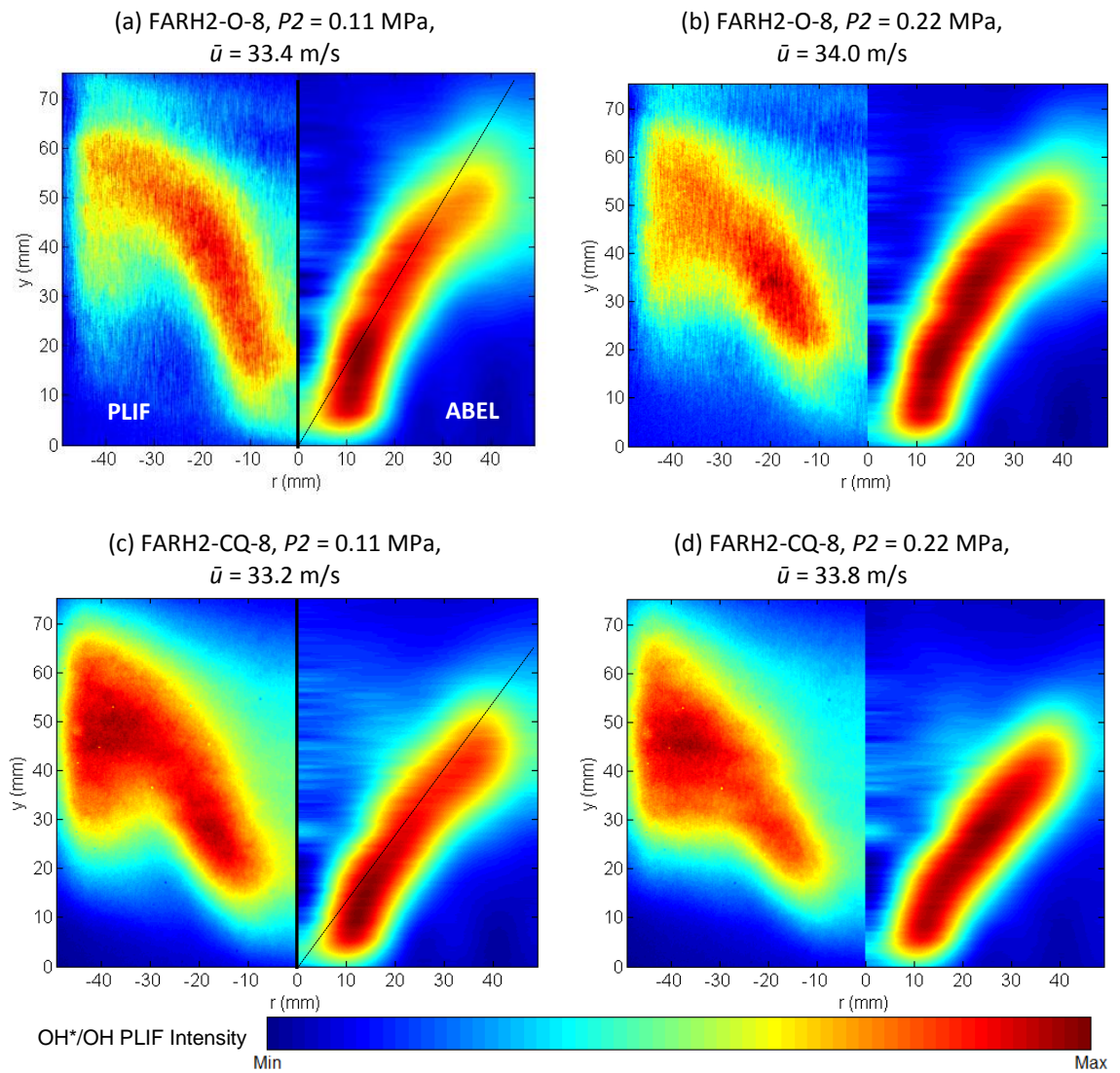


Figure 7.11: Combined OH PLIF (left) and Abel-transformed OH* chemiluminescence (right) images for FARH2 flames at $T_2 = 573$ K, $\varphi = 0.55$ with varying P_2 and burner confinement: open, (a) and (b), convergent, (c) and (d)

7.2.3 Influence of Burner Geometric Swirl Number

Isothermal and combustion experiments in the HPGSB-2 also investigated the influence of S_g on CH_4 and $\text{CH}_4\text{-H}_2$ flame location, stability, and emissions. Two radial-tangential swirl nozzle inserts with $S_g = 0.5$ and 0.8 (Figure 3.8) were utilized with both an open cylindrical and convergent nozzle confinement for experiments at $T_2 = 573$ K and pressures up to $P_2 = 0.33$ MPa.

Results from an experimental study of the influence of geometric swirl number in the open cylindrical confinement are presented for BASE flames at $\varphi = 0.55$ and varying P_2 in Figure 7.12. Some results (BASE-O-8 at $P_2 = 0.11$ MPa and 0.22 MPa) are reproduced here from

Figure 7.11.a and 7.11 b for direction comparison with the same BASE-O-5 conditions, but the BASE-O-8 condition is also extended to $P_2 = 0.33$ MPa. With a reduction in S_g in the open confinement case, a different flame stabilization mechanism is visible. While the tangential velocity imparted on the flow by the $S_g = 0.8$ swirler insert is sufficient to result in a vortex breakdown structure such as the CRZ, the same cannot be said at $S_g = 0$.

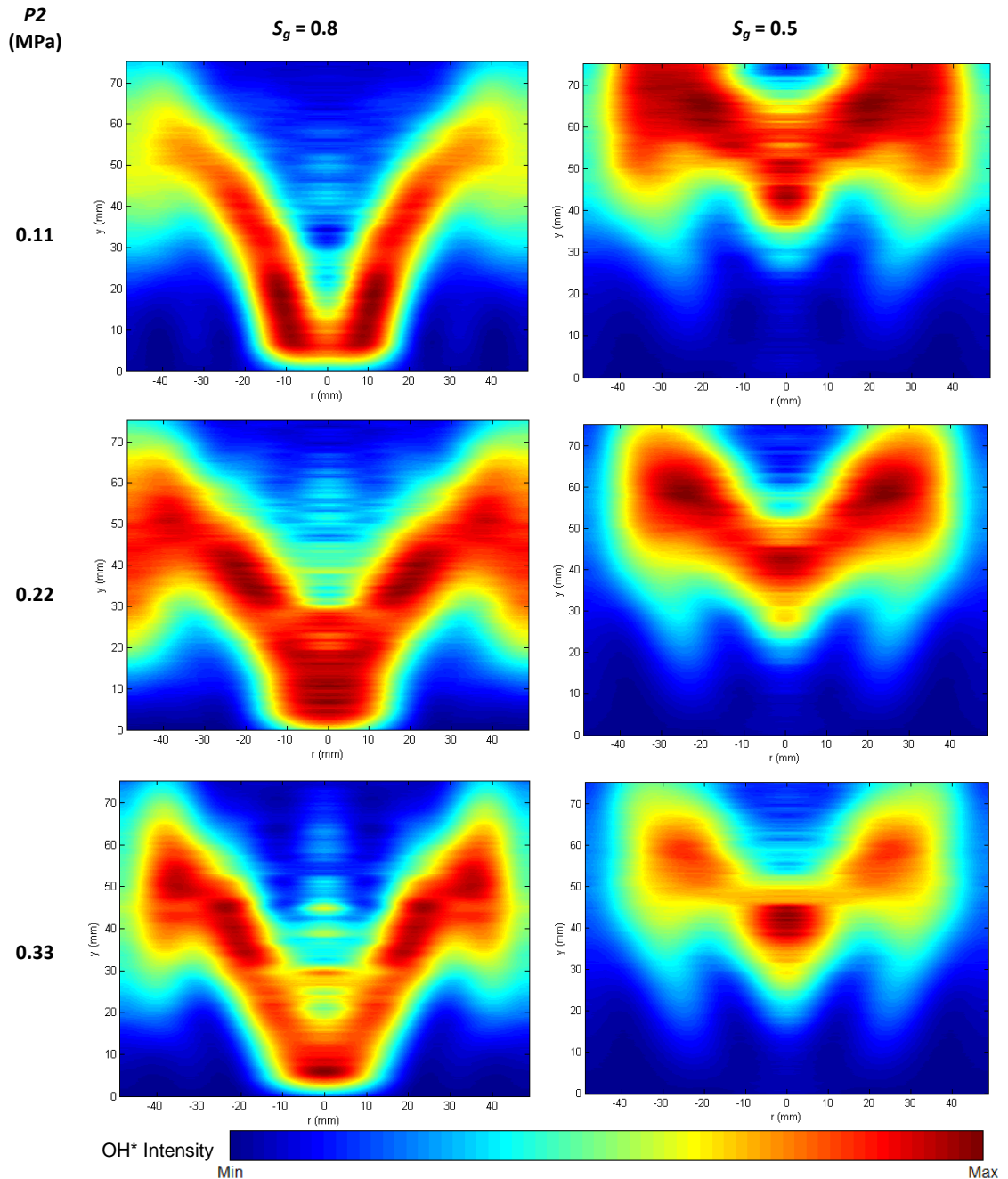


Figure 7.12: Abel-transformed OH* chemiluminescence images for BASE flames in the HPGSB-2 with open confinement at $T_2 = 573$ K and $\varphi = 0.55$ with varying P_2 and S_g

With the formation of the CRZ in the $S_g = 0.8$, the change in axial flow velocity results in a low velocity shear layer between the CRZ and ORZ where the flame speed and flow velocity normal

to the flame front are equal. This shear layer extends into the burner exit nozzle and thus the flame stabilizes close to the burner exit. In the $S_g = 0.5$ case, the reduced tangential velocity component and increased axial velocity component results in a flame stabilization location that is centered on the burner axis and lifted from the burner exit nozzle, in some cases stabilizing the flame root at $y = 20 - 30$ mm. The flame appears to be stabilized by the reduction in axial velocity caused by the flow expansion and a weak swirl component, resulting in a toroidal shaped flame. Whereas the open confinement flame at $S_g = 0.8$, $T_2 = 573$ K could not be operated above $\varphi = 0.60$ due to TFB, the $S_g = 0.5$ did not result in any TFB events due to the change in flame stabilization location. It has been previously noted that the $S_g = 0.8$, convergent confinement case also did not experience TFB, but this is considered to be due to a change in the CRZ size and strength, not necessarily from a complete change in flame stabilization location as seen in the $S_g = 0.5$ case in Figure 7.12. This change in flame stabilization location may alleviate flashback concerns with H_2 addition, but also makes the flame more susceptible to LBO due to the lack of anchoring. The change in overall heat release area and the reduced residence time due to low recirculation also influence emissions formation, discussed further in Section 7.4.

Figure 7.13 compares BASE flame OH PLIF/OH* CL measurements using the convergent confinement at $T_2 = 573$ K, $P_2 = 0.11$ MPa, and $\varphi = 0.6$, with varying swirl number, $S_g = 0.8$ (Figure 7.13.a) and 0.5 (Figure 7.13.b). Figure 7.13.a is comparable with Figure 7.10.c (BASE, $\varphi = 0.55$), with the flame seen to move upstream towards the burner exit with increased φ , resulting from a combined effect of reducing \bar{u} and increasing S_L and AFT. With a reduction in S_g , Figure 7.13.b, a new flame stabilization location is evident as seen in the open confinement case, Figure 7.12. Whereas the convergent confinement was shown previously to reduce the CRZ size and shift its location downstream, this effect is more pronounced with the reduction in swirl number. Instead of stabilizing along the shear layer between the ORZ and CRZ, the flame is located around the center axis, completely detached from the burner exit nozzle, and more compact in overall flame shape.

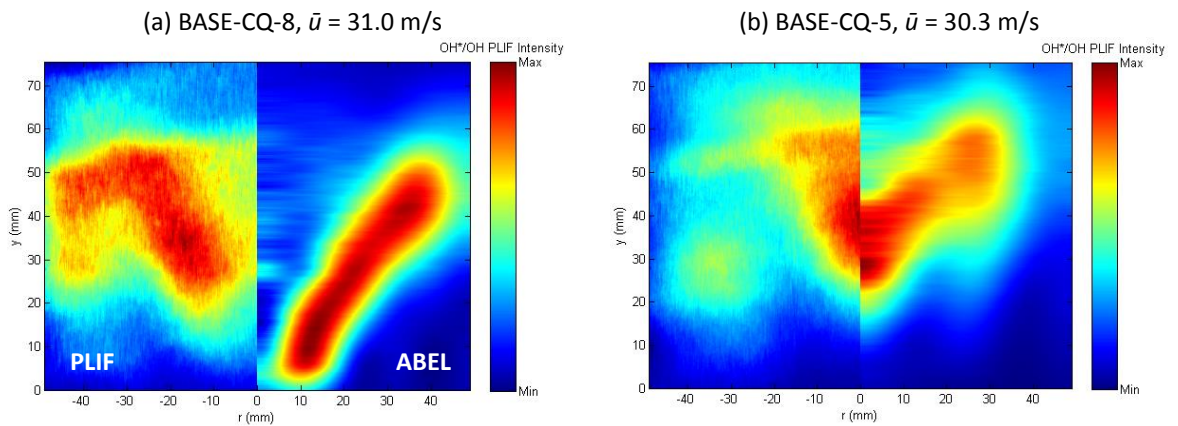


Figure 7.13: Combined OH PLIF (left) and Abel-transformed OH* chemiluminescence (right) images for BASE flames at $T_2 = 573$ K, $P_2 = 0.11$ MPa, and $\varphi = 0.6$ with convergent confinement and varying S_g : 0.8 (a) and 0.5 (b)

A reduction in S_g has been shown to increase the axial velocity profiles in $\text{CH}_4\text{-H}_2$ combustion under ambient temperature and pressure conditions [239]. This effect would be enhanced with increased T_2 . Thus, the influence of S_g on flame location and heat release in the case of hydrogen addition (85-15% $\text{CH}_4\text{-H}_2$) was also investigated at $\varphi = 0.60$ with the convergent confinement as shown in Figure 7.14 with $S_g = 0.8$ (Figures 7.14.a and 7.14.b) and $S_g = 0.5$ (Figures 7.14.c and 7.14.d). It is particularly useful to compare Figures 7.11 and 7.14 directly, as Figure 7.14.a and 7.14.b (FARH2, $\varphi = 0.60$) are related to Fig. 7.11.c and 7.11.d (FARH2, $\varphi = 0.55$), respectively, with the flame observed to move upstream towards the burner exit with increased φ in both cases, resulting from a combined effect of reducing \bar{u} and increasing S_L and AFT. In Figure 7.14, $\dot{m}\sqrt{T_2}/P_2$ has been held nominally constant across all conditions to maintain exit nozzle velocities at $\bar{u} = 31$ m/s. A similar shift in flame stabilization location for the FARH2 case from the shear layer to the central axis is evident with a reduction in swirl number as seen for the BASE case. Comparing Figure 7.13.b (BASE-CQ-5) with Figure 7.14.c (FARH2-CQ-5), hydrogen addition is shown to cause flame movement upstream towards the burner exit. This has the effect of reducing the local flame swirl number, as noted in [239], which causes the flame to extend axially, reducing the flame angle. Similar to the pressure effects observed in Figure 7.11, an upstream shift in flame area can be seen for $S_g = 0.8$ (Fig. 7.14.b). In the $S_g = 0.5$ case (Figure 7.14.d), however, increased pressure has the effect of increasing OH production in the area surrounding the center axis, increasing the flame area potentially due to increase Reynolds number.

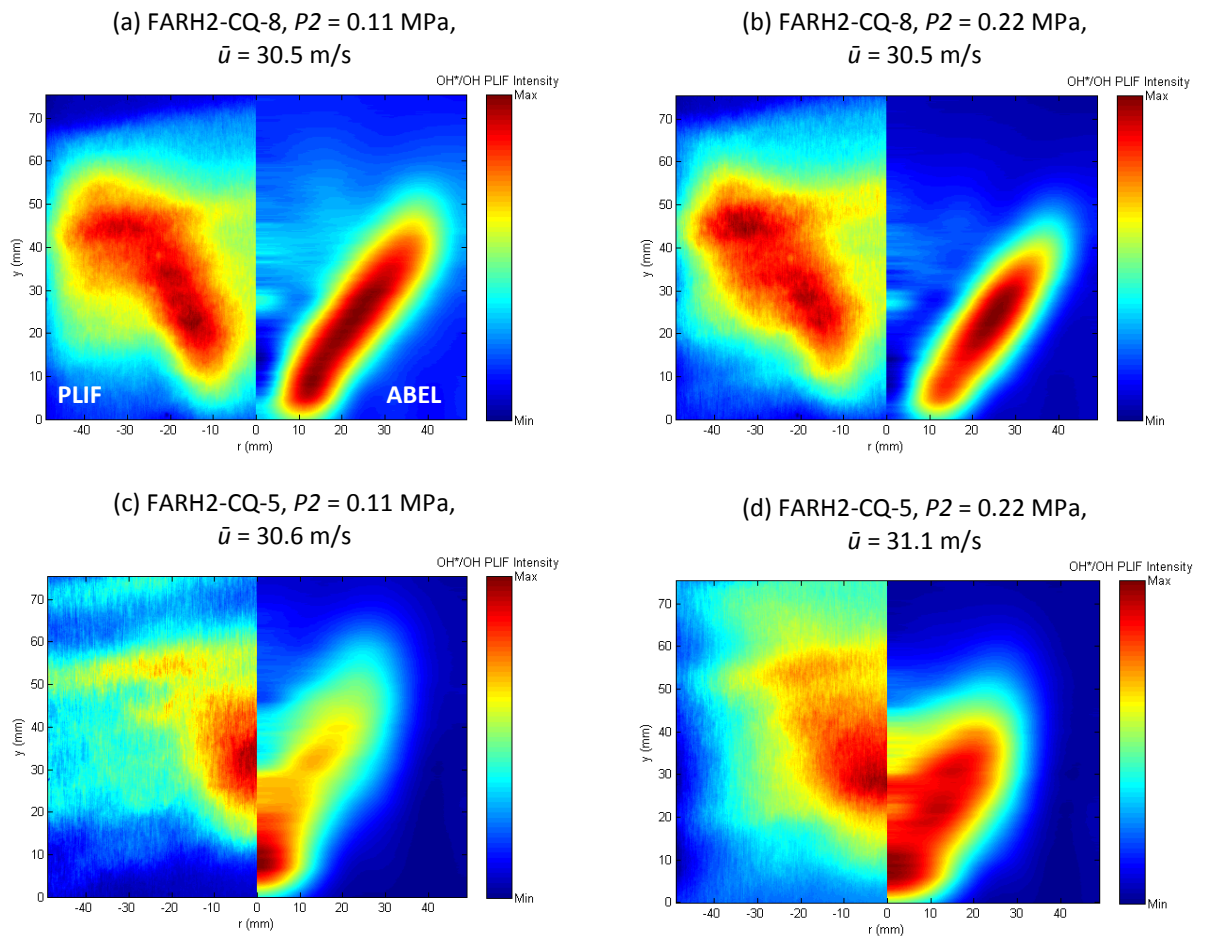


Figure 7.14: Combined OH PLIF (left) and Abel-transformed OH* chemiluminescence (right) images for FARH2 flames at $T_2 = 573$ K and $\varphi = 0.6$ with varying P_2 and S_g : 0.8, (a) and (b), 0.5, (c) and (d)

Comparison was also made at $P_{therm} = 126$ kW, $T_2 = 573$ K, and $P_2 = 0.33$ MPa between FARH2 flames with varying swirl number and convergent nozzle confinement, as shown in Figure 7.15. At $\varphi = 0.55$, flames were imaged at $S_g = 0.8$ (Figure 7.15.a) and 0.5 (Figure 7.15.b). Figure 7.15.a can be related to Figures 7.10.c and 7.10.d at the same equivalence ratio ($\varphi = 0.55$) and burner exit velocity. The Abel-transformed OH* chemiluminescence half image in Figure 7.15.a suggests further contraction of the heat release area with increasing pressure compared to Figure 7.10.d. However, the OH PLIF result shows the influence of high turbulence ($Re = 90000$) in a flame with a CRZ. While there is limited OH production in the CRZ, the flame stabilized further downstream along the shear layer as S_L continues to reduce with increased pressure and the flame brush is thickened by increasing turbulence. With a reduction in swirl number (Figure 7.15.b), the flame is again seen to transition to a stabilized location about the center axis, as noted in Figures 7.12-7.14, taking on a toroidal shape. The extinction strain rates calculated using the experimental conditions for these flames are also presented, noting

their similarity given the fixed φ . This highlights the need for additional considerations when using this value to identify flame stabilization modes as suggested by Shanbhogue et al. [65].

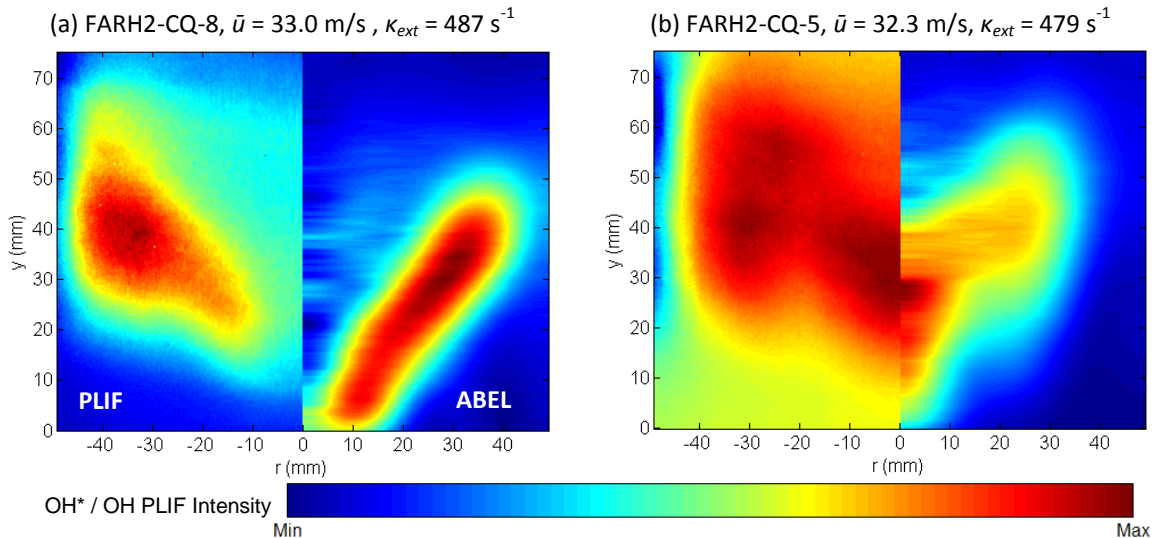


Figure 7.15: Combined OH PLIF (left) and Abel-transformed OH* chemiluminescence (right) images for FARH2 flames at $T_2 = 573$ K, $P_2 = 0.33$ MPa, and $\varphi = 0.55$ with varying S_g : 0.8 (a) and 0.5 (b)

As a final comparison between the swirl stabilization influences of fuel composition, burner confinement, and geometric swirl, Figure 7.16 plots the axial and radial locations of the binarized OH* chemiluminescence intensity centroid from the Abel-transformed images presented in this Section at an equivalence ratio of $\varphi = 0.55$. This provides a quantitative measure of the mean heat release distribution within the field of view and highlights the influence of hydrogen addition, pressure, confinement, and swirl number on observed flame stabilization locations. Further information on this methodology can be found in the work by Han and Hochgreb [236]. Flame angles of 15°, 30°, and 45° are imposed for reference. First, the influence of hydrogen addition is observed as the FARH2 heat release centroid shifts upstream and radially inward for all conditions compared to the BASE flames. The increased flame angle relative to the burner centerline ($r = 0$ mm) observed when moving from an open to convergent confinement at $S_g = 0.8$ is supported by the measured heat release centroid. The open confinement cases have a centroid location at a flame angle nearer to 30° while the convergent nozzle cases shift axially upstream and radially outward towards a flame angle of 45°. Finally, the pronounced change in flame stabilization location from $S_g = 0.8$ to 0.5 is also evident as the heat release centroid is seen to shift downstream and towards the burner centerline in all $S_g = 0.5$ cases.

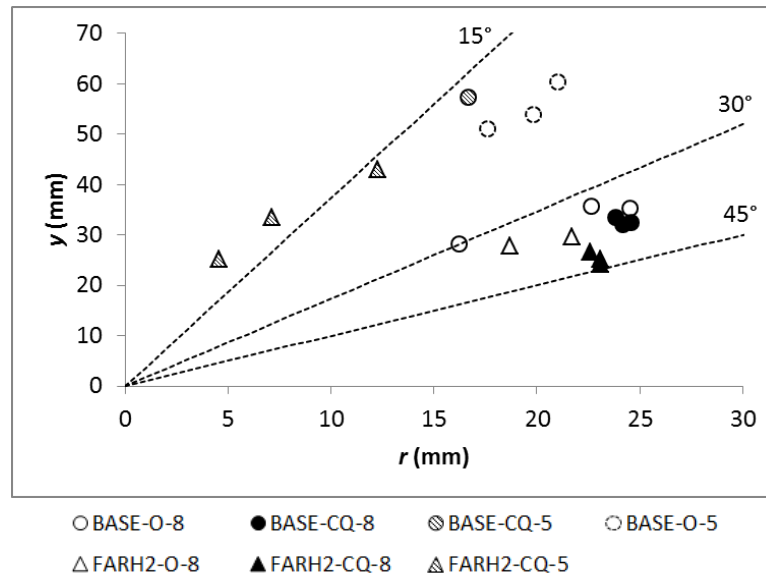


Figure 7.16: OH* chemiluminescence intensity centroid locations and flame angles for BASE and FARH2 flames at $T_2 = 573$ K, $\phi = 0.55$, and varying P_2

7.3 Thermoacoustics

7.3.1 Influence of Burner Confinement Geometry

In general, the influence of the convergent nozzle on the flame stabilization location and localized heat release areas in both fuels appears to be somewhat limited to changes relative to CRZ shape and location. However, there is a dramatic influence in the measured dynamic pressure amplitude and frequency spectra between the two confinements as shown in Figure 7.17, for the open (Figures 7.17.a and 7.17.b) and convergent (Figures 7.17.c and 7.17.d) cases with BASE and FARH2 flames at $T_2 = 573$ K, $\phi = 0.55$, and $P_2 = 0.11$ MPa and 0.22 MPa. Figure 7.17 shows the FFT plots of the Burner Face DPT measurement when sampled at 4 kHz for 60 seconds. These data were taken simultaneously at the same experimental conditions shown in the combined OH PLIF/OH* CL images in Figures 7.10 and 7.11, in addition to matching isothermal air flow ($T_2 = 573$ K) conditions. As seen in Figures 7.17.a and 7.17.b, both CH₄ and CH₄-H₂ flames are acoustically coupled at $\phi = 0.55$ with the open cylindrical burner confinement geometry, evident in the harmonic peaks established. Hydrogen addition has the effect of increasing the dominant frequencies from 438 Hz (red, CH₄) to 467 Hz (blue, CH₄-H₂) in the $P_2 = 0.11$ MPa case and 439 Hz to 494 Hz in the $P_2 = 0.22$ MPa case.

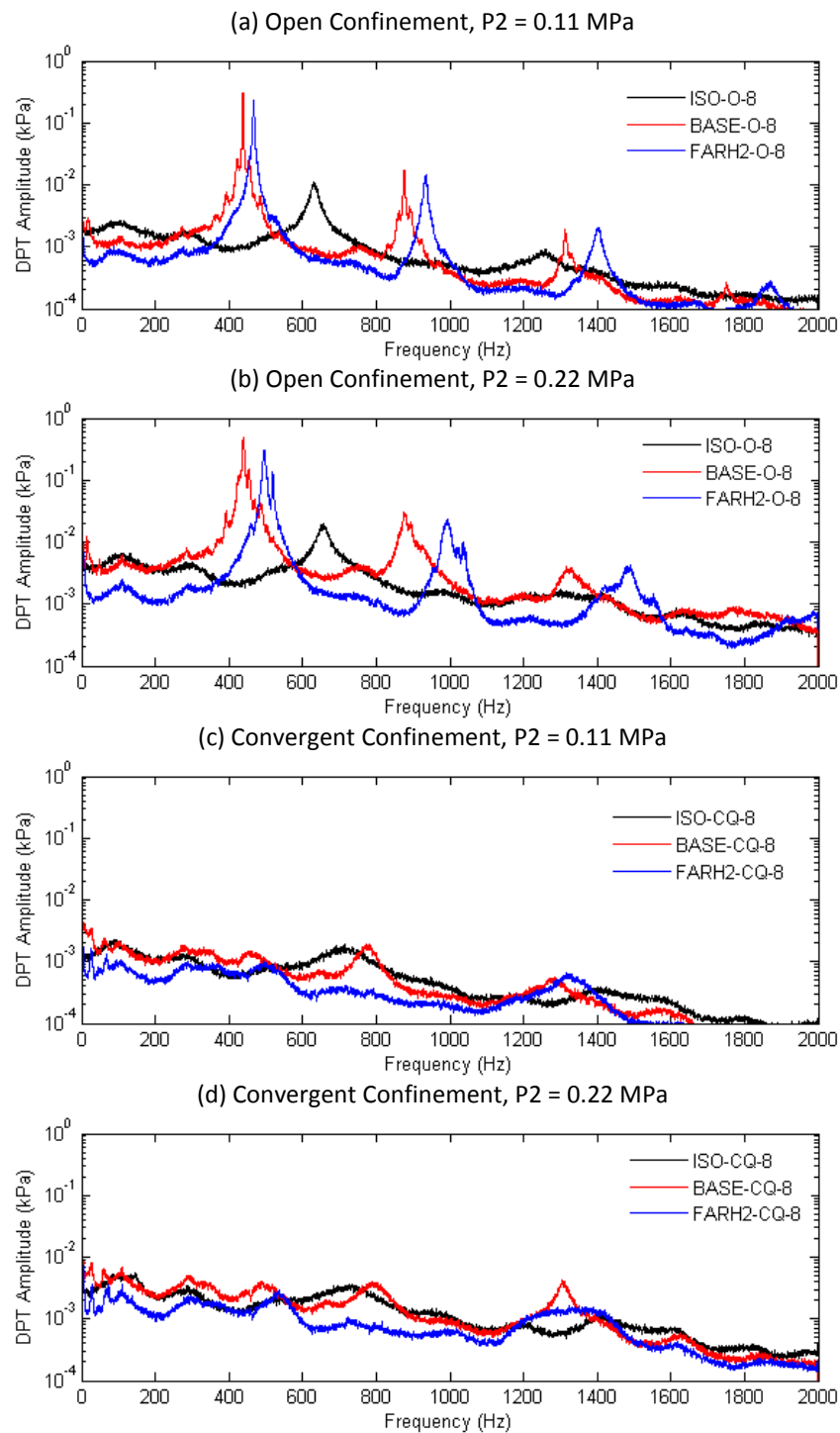


Figure 7.17: FFT of Burner Face DPT measurements for isothermal air flow, BASE, and FARH2 flames at $T_2 = 573$ K, $\phi = 0.55$, and $S_g = 0.8$ with varying P_2 and confinement: open, (a) and (b), convergent, (c) and (d)

These dominant resonant frequencies are similar to those observed during thermoacoustic instability in the ETAP and ETEP HPGSB-2 commissioning study in Chapter 5.2.2. The reader will recall that the Helmholtz number of the ETAP and ETEP thermoacoustic instability

condition was based on an average speed of sound, c , calculated using the AFT and measured burner outlet temperature, T_3 , yielding $He = 0.25$ in both cases. For the instabilities shown in Figures 7.17.a and 7.17.b, He is nearly identical at 0.22 – 0.25, despite the change in φ and the introduction of H_2 , and further supporting the argument that the observed pressure fluctuations are related to an acoustic mode of the burner geometry. The increase in f_{peak} with H_2 addition was observed by Hirsch et al. [240] in a 60 kW swirl burner, attributed to the shortening of the flame due to the increase in S_L , in agreement with the results presented in Figures 7.10 and 7.11. The local flame temperature may also be higher with H_2 addition despite maintaining overall AFT due to the reduction in flame size, particularly with increased pressure, as suggested by Lantz et al. [105]. In the acoustically-coupled case, this increase in local flame temperature would act to increase the local speed of sound, which may also contribute to the increase in peak frequency. Furthermore, DPT amplitudes are observed to reduce with hydrogen addition across all cases in Figure 7.17. A similar reduction was observed by Lantz et al. [105] in a single-can Siemens SGT-700/800 burner with H_2 addition up to 30% due to axial mode damping. Overall combustion noise amplitudes are seen to increase with combustor inlet pressure due to higher heat release rates as fuel flows are scaled with increased pressure, in agreement with the scaling suggested by Lieuwen [66].

When the burner is operated with the convergent nozzle confinement, the harmonics observed with the open confinement are no longer apparent and there is a significant reduction in overall DPT amplitude, as can be seen in both Figures 7.17 and 7.18. As discussed previously, the convergent nozzle confinement affects the flow field, which will in turn affect the heat release fluctuation within the burner. In the operating cases presented here, this change in flow field structure decouples the heat release fluctuation from the burner resonant acoustics. Figure 7.18 highlights the influence of φ , confinement, and P_2 on normalized dynamic pressure amplitudes of the Burner Face DPT. With the open confinement flame at $\varphi = 0.55$, shown in Figure 7.17 to be acoustically coupled, observed pressure fluctuations of up to 4% of P_2 are measured. As φ is reduced in the open confinement case, pressure amplitudes are observed to reduce; the opposite is noted for the convergent nozzle cases. The trend in the open confinement, $P_2 = 0.11$ MPa CH_4 - H_2 case suggests that its transition from stable to resonant operation occurs below $\varphi = 0.50$, in agreement with the results shown for H_2 addition in [105]. With increased pressure, the CH_4 open confinement flames exhibit similar responses in transition to resonant operation. With hydrogen addition, the pressure influence would appear to shift the transition to even leaner equivalence ratios below $\varphi = 0.45$. While this lean

shift may be attributed to increased extinction strain rate as suggested by Shanbhogue et al. [65] and the chemical kinetics modeling in Figure 7.4, it may be necessary to consider the nonmonotonic behavior of $\text{CH}_4\text{-H}_2$ K_{ext} with increasing pressure above 0.22 MPa as the transition between stable and unstable operation may shift to higher ϕ .

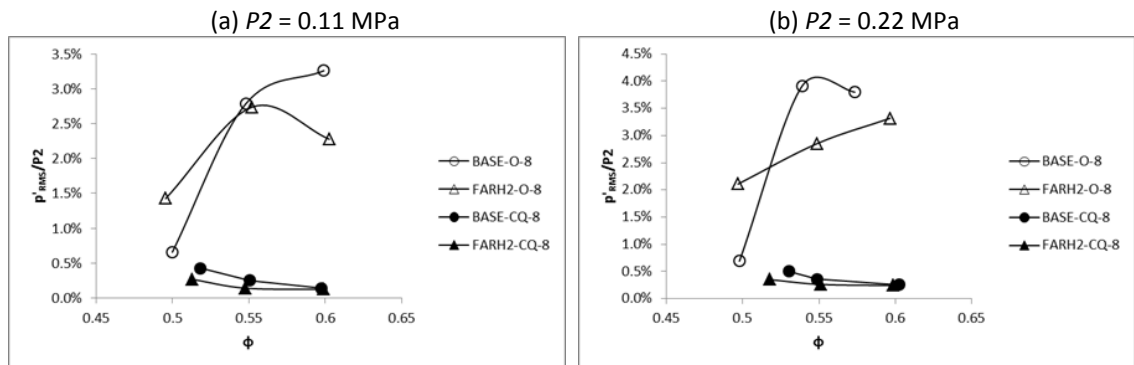


Figure 7.18: Confinement and ϕ effects on normalized Burner Face DPT pressure fluctuation for BASE and FARH2 flames at $T_2 = 573$ K, with varying P_2 : 0.11 MPa (a) and 0.22 MPa (b)

7.3.2 Influence of Burner Geometric Swirl Number

Dynamic pressure measurements were also recorded at reduced S_g operation, with an example FFT in Figure 7.19 comparing isothermal air flow, CH_4 , and $\text{CH}_4\text{-H}_2$ combustion with the convergent confinement for $T_2 = 573$ K, $P_2 = 0.11$ MPa, and $\phi = 0.55$. This FFT plot from the Burner Face DPT can be compared directly with Figure 7.17.c ($S_g = 0.8$). While the use of the convergent confinement broadly reduces the dynamic pressure amplitudes, there are similar peaks around 200 Hz and 1300 Hz between the two swirl numbers. Under these conditions, the burner was generally stable, although it is interesting to note that the trend of reduced amplitudes with hydrogen addition appears to be marginally reversed with reduced swirl number.

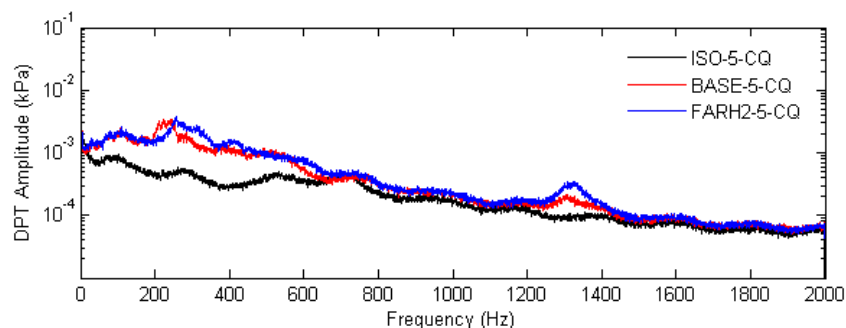


Figure 7.19: FFT of Burner Face DPT measurement for isothermal air flow, BASE, and FARH2 flames at $T_2 = 573$ K, $P_2 = 0.11$ MPa, $\phi = 0.55$, $S_g = 0.5$, and convergent confinement

In addition to the acoustic decoupling introduced by a change in confinement from open to convergent nozzle as shown in Figure 7.17, a reduction in swirl number also has a similar decoupling effect between the heat release rate, flame dynamics, and burner acoustics. This is most evident in the Burner Face DPT amplitudes plotted in Figure 7.20 for BASE and FARH2 flames at $T_2 = 573$ K and $\varphi = 0.55$ with an open confinement. As shown in Figure 7.17, the open confinement, $S_g = 0.8$ BASE and FARH2 cases are acoustically coupled at $P_2 = 0.11$ and 0.22 MPa. This trend continues when operating up to $P_2 = 0.33$ MPa as shown in Figure 7.20, with p'_{RMS} approaching 4% of P_2 . However, with a reduction in swirl number to $S_g = 0.5$, the pressure fluctuations are reduced by an order of magnitude, suggesting a potential burner design consideration reduction of longitudinal thermoacoustic instability amplitudes.

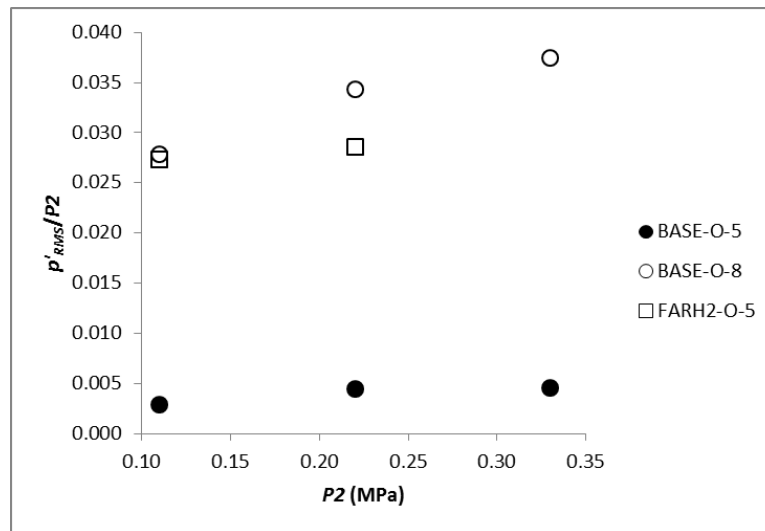


Figure 7.20: P_2 and S_g effect on Burner Face DPT amplitudes for BASE and FARH2 flames with open confinement at $T_2 = 573$ K and $\varphi = 0.55$

Given the combustion dynamic pressure measurements at 0.11 MPa, 0.22 MPa, and 0.33 MPa for the FARH2-CQ-8 and FARH2-CQ-5 cases, it is possible to derive a power law correlation between measured dynamic pressure fluctuation and increased normalized P_2 (and thus, P_{therm}), where P_2 is normalized by $P_{atm} = 0.101$ MPa. Scaling of uncoupled combustion noise levels with heat release has been suggested for atmospheric swirl flames [66], but the current analysis also considers increased operating pressure and resultant velocity influences. This relationship is shown in Figure 7.21, where normalized pressure fluctuation of the Burner Face DPT is plotted as a function of P_2 and S_g for $T_2 = 573$ K and $\varphi = 0.55$ $\text{CH}_4\text{-H}_2$ flames. In Figure 7.21.a, the influence of swirl number on the overall pressure fluctuation is evident, as dynamic pressure measurements are consistently higher at $S_g = 0.5$. This is attributed to the flame stabilization location of the $S_g = 0.5$ flame as it is detached from the burner exit nozzle and

stabilized completely by the turbulent flow field within the convergent confinement. If the normalized dynamic pressure measurement is scaled by S_g , which accounts for the change in resultant velocities in the flow field, the dynamic pressure values collapse along a single exponential line as seen in Figure 7.21.b. Note that a similar scaling factor ($1/S_g$) was utilized in Chapter 4.3.3 for the collapse of dynamic pressure amplitudes measured for isothermal air flow in the convergent nozzle confinement with S_g of 0.5 and 0.8.

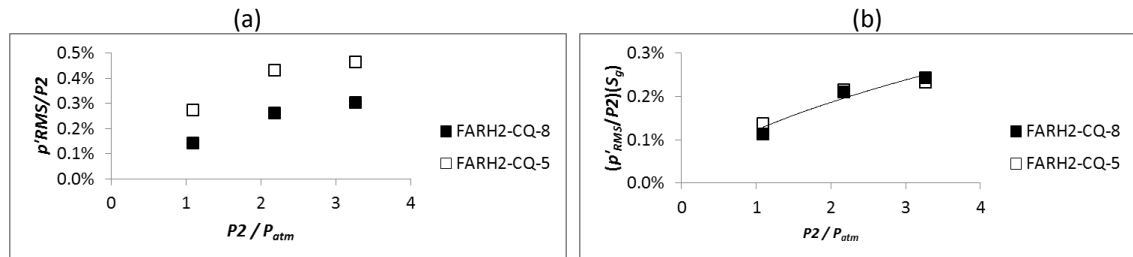


Figure 7.21: P_2 and S_g effect on Burner Face DPT amplitude for FARH2 flames with convergent confinement at $T_2 = 573$ K and $\phi = 0.55$ with values ununscaled (a) and scaled (b) by S_g

The resulting power law relationship is as shown in Equation 7.1, and has the potential to be used for the prediction of uncoupled combustion noise levels at increased thermal power and pressure conditions.

$$\frac{p'_{RMS}}{P_2} = \left(\frac{0.0012}{S_g} \right) \left(\frac{P_2}{P_{atm}} \right)^{0.6059} \quad (7.1)$$

Further evaluations indicate, however, that this relationship alone cannot collapse the dynamic pressure effect across fuel types and ϕ , but that similar power law trends may exist. Thus, while this relationship appears to hold for a fixed fuel type and ϕ , its application across fuel types and S_g requires further evaluation. For example, the correlation in Equation 7.1 is unable to collapse the BASE combustion noise measurements under the same burner confinement and operating conditions, as shown in Figure 7.22.a. While the BASE-CQ-8 combustion noise levels still appear to follow a power law correlation, there is an obvious offset between the BASE and FARH2 fuels, even after accounting for the change in resultant velocities with the swirl number scaling. Thus, an additional factor must be considered to account for the influence of fuel type. As has been shown in Chapters 5 and 6, the fuel H:C ratio improves experimental correlation between differing fuel types. Thus, this factor is utilized similarly in Figure 7.22.b. This results in near-identical response between both fuels when scaled by $(H:C)^3$, and further supports the use of this fundamental fuel property to characterize premixed flame response.

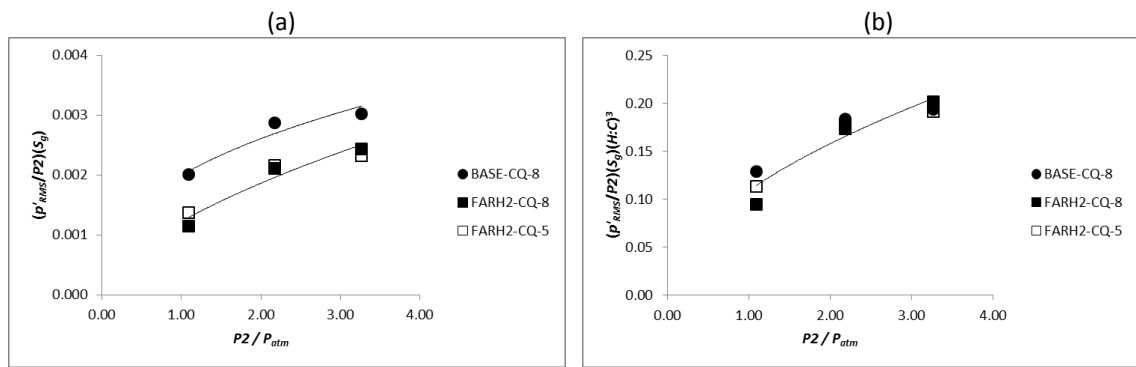


Figure 7.22: P_2 and S_g effect on Burner Face DPT amplitude for BASE and FARH2 flames with convergent confinement at $T_2 = 573$ K and $\phi = 0.55$ with values unscaled (a) and scaled (b) by $(H:C)^3$

The resulting power law correlation for uncoupled combustion noise prediction with varying swirl number and fuel type, including the H:C scaling, is given in Equation 7.2.

$$\frac{p'_{RMS}}{P_2} = \left(\frac{0.109}{S_g(H:C)^3} \right) \left(\frac{P_2}{P_{atm}} \right)^{0.5326} \quad (7.2)$$

Extending this correlation to higher P_2 allows for predicted combustion noise values to be calculated for this burner. In Figure 7.23, the correlation in Equation 7.2 is evaluated up to 1.5 MPa ($P_{therm} = 572$ kW), operating on both BASE and FARH2 fuels with varying swirl number. Generally, it can be seen that combustion noise levels are below 1% of burner inlet pressure up to 1.5 MPa, suggesting combustion noise levels would be at industrially accepted levels. This also highlights the potential advantages of blending H_2 into CH_4 , as the lowest combustion noise levels at 1.5 MPa are observed with H_2 blending and $S_g = 0.8$, with an almost 50% reduction in combustion noise levels from the pure CH_4 fuel with $S_g = 0.5$. Although additional consideration would need to be given to offset potential flashback mechanisms introduced by using the higher swirl number, which shows a different flame stabilization mechanism than the low swirl number flame.

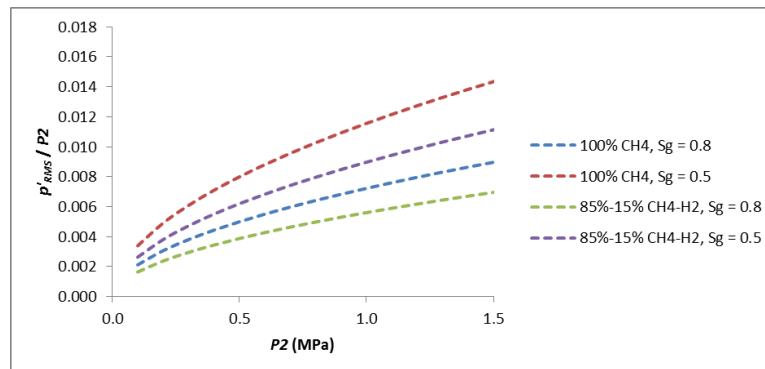


Figure 7.23: Predicted combustion noise amplitudes in the HPGSB-2 for BASE and FARH2 flames up to $P_2 = 1.5$ MPa at $T_2 = 573$ K and $\phi = 0.55$ with varying S_g

An important caveat to the use of this correlation is that the operating conditions examined in the cases for its development are at a fixed equivalence ratio ($\varphi = 0.55$) and thus nominally similar AFT ($1788 \text{ K} \pm 6 \text{ K}$). Thus, it is useful to consider the combustion noise response as the φ varies. As can be seen in Figure 7.24.a, the correlation in Equation 7.2 is unable to capture the shift in combustion noise levels, as seen in Figure 7.18, for increasing $\varphi = 0.60$. However, it is interesting to note that a similar increase in combustion noise amplitude is observed in the FARH2 $S_g = 0.5$ case compared to $S_g = 0.8$, as seen in Figure 7.21.a. The offset between the predicted values (lines) based on Equation 7.2 and the measured values (symbols) in Figure 7.24.a. is considered to be influenced by the change in reactivity and flame stabilization location when the equivalence ratio increases from $\varphi = 0.55$ to $\varphi = 0.60$. By accounting for this change in reactivity with an additional scaling factor based on the change in modeled S_L as a function of equivalence ratio and pressure per Equation 7.3, the correlation between the predicted values and the measured values improves, as shown in Figure 7.23.b.

$$\frac{p'_{RMS}}{P2} = \left(\frac{S_{L,\varphi=0.55}(f(P2))}{S_L(f(\varphi, P2))} \right) \left(\frac{0.109}{S_g(H:C)^3} \right) \left(\frac{P2}{P_{atm}} \right)^{0.5326} \quad (7.3)$$

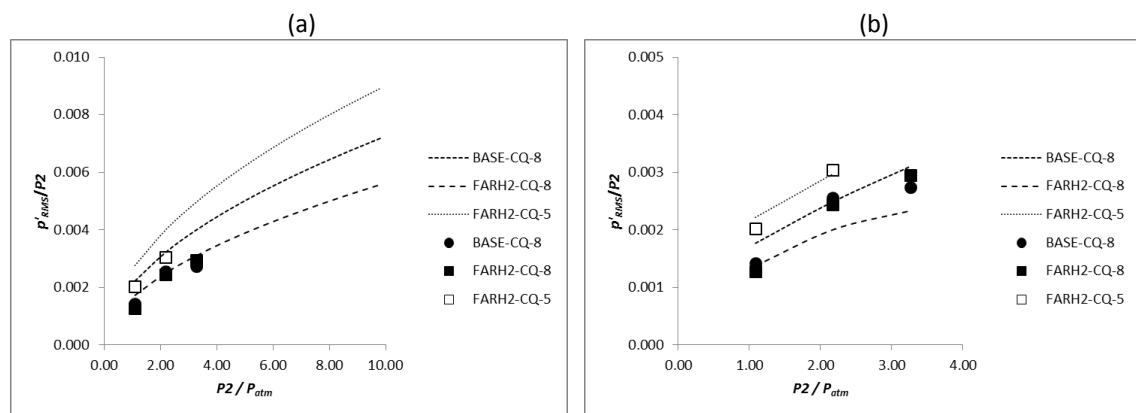


Figure 7.24: Measured and predicted combustion noise amplitudes for BASE and FARH2 flames with convergent confinement at $T_2 = 573 \text{ K}$ and $\varphi = 0.55$ with predicted values using Equation 7.2 (a) and after S_L scaling (b).

7.4 Exhaust Gas Emissions

As flame shape and thermoacoustic stability will certainly influence GT operability, they are also both intrinsically linked with the fundamental reaction chemistry and resulting exhaust gas emissions. It is thus important to evaluate the emissions measurements, including the influence of H_2 addition and burner geometry, with a particular focus on NO_x emissions given the drive for LPM and low NO_x GT combustor designs to meet environmental regulations.

NO_x emissions corrected to 15% excess O₂ are first presented in Figure 7.25 for BASE flames at a fixed combustor geometry (convergent nozzle and $S_g = 0.5$), $P_2 = 0.11$ MPa, and varying inlet temperature ($T_2 = 290$ K and 573 K). With this configuration, NO_x emissions below 5 ppmV can be achieved at AFT up to 1900 K. The exponential trend of NO_x formation with increasing AFT is typical of the thermal NO_x formation mechanism as discussed in Chapter 2.4.1. Referring to Figure 7.13.b, the reaction zone in the BASE-CQ-5, $T_2 = 573$ K case is quite flat both axially and radially. In fact, the convergent nozzle has been shown to alter the flow field by reducing the CRZ strength in $S_g = 0.8$ cases. This observation coupled with the reduction in S_g further reduces the influence of recirculated flow within the burner, thus the residence time within the areas of highest heat release and temperature is limited, and therefore the thermal NO_x formation pathway is inhibited. This is further supported by the measured burner outlet temperature, T_3 , between comparable BASE-CQ-8 and BASE-CQ-5 conditions, which show a trend of lower temperatures in the $S_g = 0.5$ case for similar AFT.

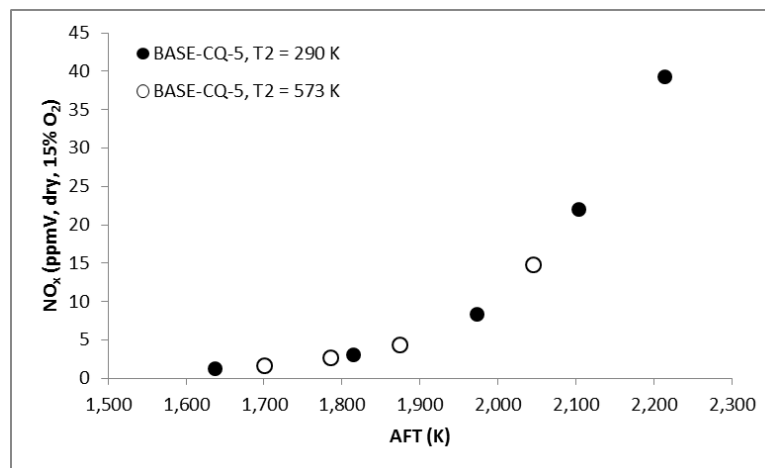


Figure 7.25: NO_x emissions versus AFT for BASE flames with convergent confinement, $P_2 = 0.11$ MPa, $S_g = 0.5$, and varying T_2

The NO_x emissions for all experimental conditions at $T_2 = 573$ K are plotted against AFT for varying P_2 in Figure 7.26. Measured NO_x emissions for $AFT \leq 1900$ K are below 7 ppmV across all conditions when normalized, resulting from a reduction in the thermal NO_x formation pathway under such lean operating conditions, as observed in Figure 7.25.

While the low values overall make it difficult to draw conclusions within the measurement uncertainty, trends of higher NO_x emissions with hydrogen addition can be identified at fixed AFT, particularly at $P_2 = 0.11$ MPa (Figure 7.26.a). This was also observed by Lantz et al. [105]

with increasing H₂ concentration in natural gas and is attributed to locally high flame temperatures resulting from increased heat release density. This assessment would also agree with the acoustically-coupled frequency peak shift discussed in Section 7.3.1. However, the addition of hydrogen allows for stable burner operation at reduced AFT compared to the CH₄ flames. This lean shift reduces NO_x emissions relative to CH₄ in nearly all cases due to lower flame temperatures, as shown previously [61, 86, 87]. In practical applications, it appears that H₂ addition allows for stable, low NO_x operation at the same AFT with increased pressure compared to 100% CH₄, due to its increased reactivity and thermo-diffusive effects. For example in Figure 7.26, at a selected AFT of ~1700-1720 K, the CH₄-H₂ blend (FARH2-CQ-8) can be burned stably with < 3 ppm NO_x while the CH₄ blend (BASE-CQ-8) cannot operate at the same AFT without approaching LBO, particularly at $P_2 = 0.33$ MPa in Figure 7.26.c.

The change in burner confinement appears to have little influence on NO_x emissions. This is not unexpected given the largely similar flame structures shown in the OH PLIF and OH* chemiluminescence measurements and the dominance of the thermal NO_x pathway. Of particular note in Figures 7.26 – 7.28 is that NO_x was consistently lower in the $S_g = 0.5$ cases. The reduction in swirl number has the effect of reducing or eliminating CRZ, thereby reducing the residence time of combustion products in the post-flame region, effectively reducing the thermal NO_x pathway [241]. This is evident in the change in flame shape from $S_g = 0.8$ to 0.5 observed in Figures 7.12 – 7.15 and supported by other experimental work with variable swirl numbers [242]. Figure 7.27 provides selected BASE and FARH2 NO_x measurements with convergent confinement and varying swirl number at $P_2 = 0.11$ MPa, which confirms this general trend. A similar trend between FARH2-CQ-8 and FARH2-CQ-5 was also observed at $P_2 = 0.22$ MPa.

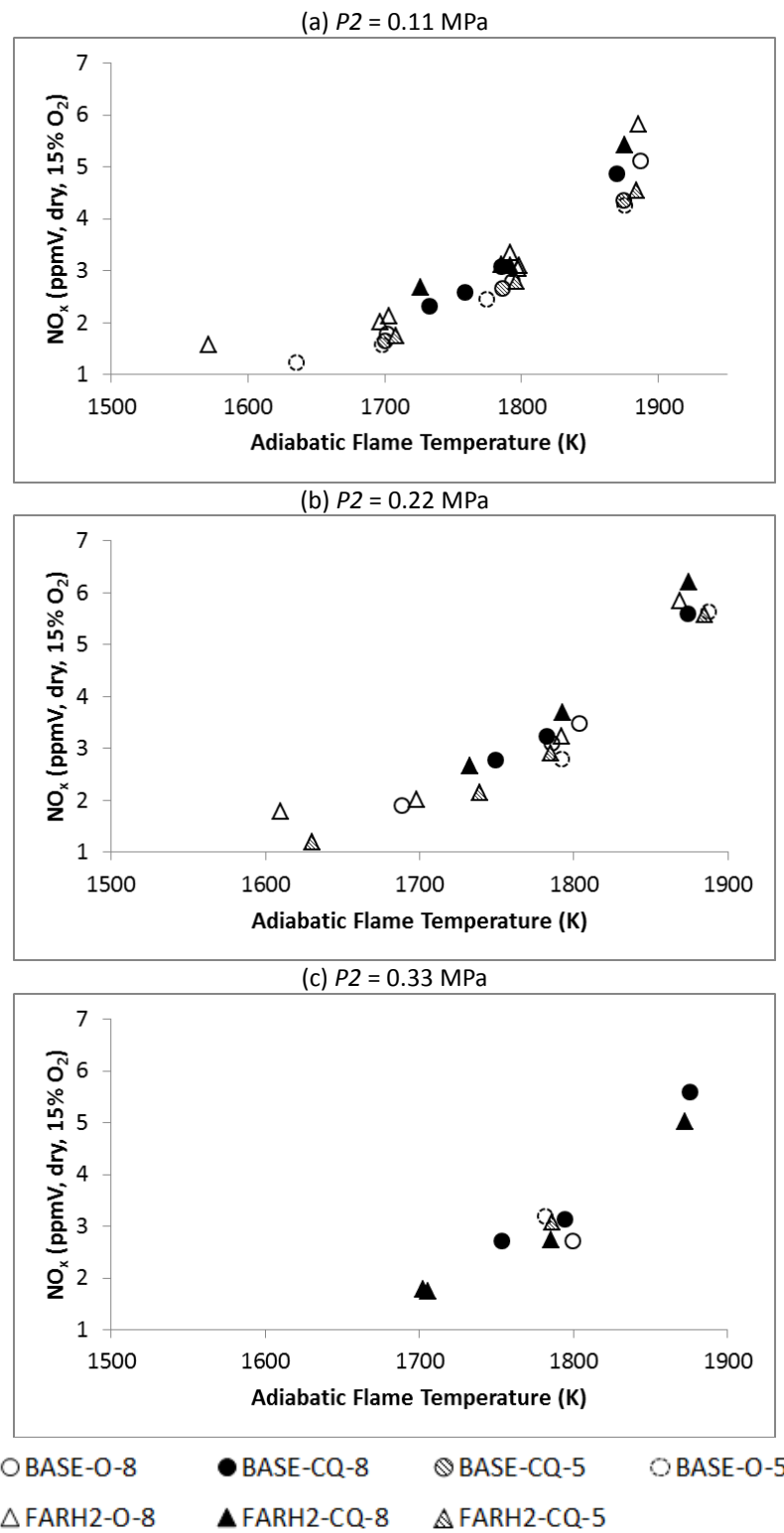


Figure 7.26: NO_x emissions versus AFT at varying P_2 for all experimental conditions at $T_2 = 573$ K

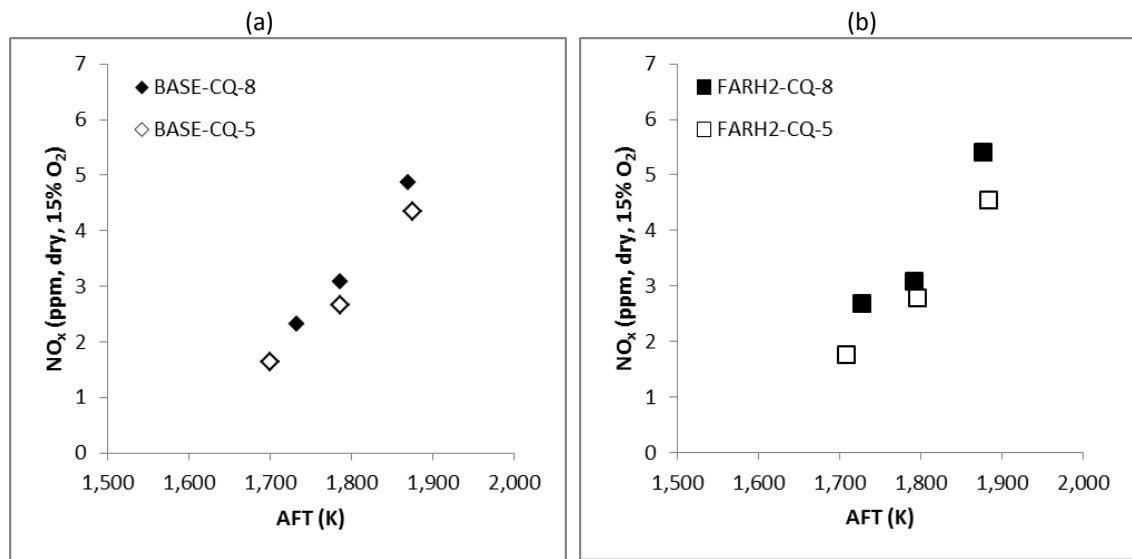


Figure 7.27: NO_x emissions versus AFT for BASE (a) and FARH2 (b) flames with convergent confinement and varying S_g at $P_2 = 0.11$ MPa

Figure 7.28 shows the influence of P_2 on NO_x emissions for both BASE and FARH2 flames at $\varphi = 0.55$ (AFT = 1788 K \pm 6 K) with varying confinement and swirl geometry. NO_x measurements below 4 ppm at this AFT suggest that there is adequate premixing among the reactants and that the thermal NO_x formation pathway dominates [237]. Under these conditions, NO_x production would be expected to scale generally with the square root of combustor pressure [237]. A trend of increasing NO_x emissions with pressure is evident between 0.11 MPa and 0.22 MPa, most significant in the FARH2-CQ-8 case. However, the measured NO_x is nonmonotonic above $P_2 = 0.22$ MPa in all cases except FARH2-CQ-5 and BASE-O-5. This is attributed to a combination of heat release distribution within the flow field and heat losses in the experimental rig. For example in Figures 7.7 and 7.8, the heat release distribution is observed to be well-distributed at $P_2 = 0.22$ MPa, and coupled with the stronger CRZ in the $S_g = 0.8$ cases, would increase the residence time of the combustion products in the areas of highest heat release. Heat losses in the experimental rig may also contribute to the observed nonmonotonic behaviour, which would be reduced in the $S_g = 0.5$ case as the flame stabilizes completely within the confinement tube, detached from the burner exit nozzle and thus reducing conduction heat losses and increasing heat input to the reaction chemistry. Note that a similar nonmonotonic trend was observed with C₂₊ addition and is presented in Chapter 6.4.

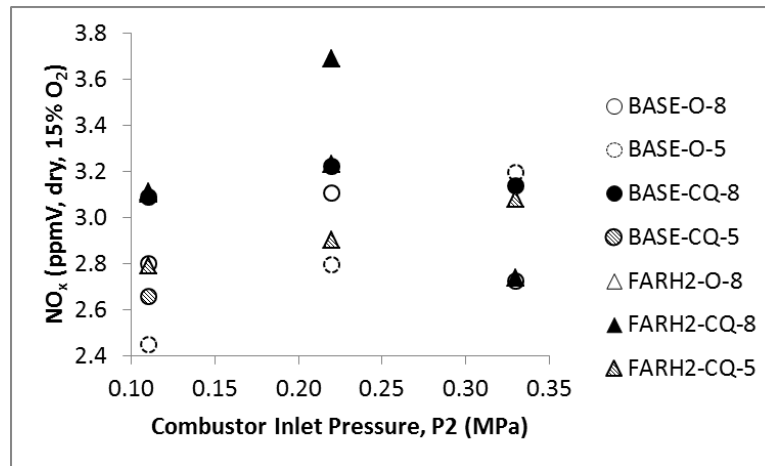


Figure 7.28: P_2 effect on NO_x emissions for BASE and FARH2 flames at $\phi = 0.55$ (AFT = $1788 \text{ K} \pm 6 \text{ K}$)

7.5 Chapter Summary

This Chapter presents an experimental and chemical kinetics analysis of the influence of (i) burner confinement geometry, (ii) geometric swirl number, and (iii) elevated ambient conditions on fully premixed CH_4/air and $\text{CH}_4\text{-H}_2/\text{air}$ (85-15% vol) flames in terms of flame location, stability, and NO_x emissions in the HPGSB-2. Elevated operating conditions range from P_{therm} to 126 kW, T_2 to 573 K and P_2 to 0.33 MPa. In addition to providing a parametric dataset for chemical kinetics reactor network and CFDE modeling, the following conclusions are deduced:

- For a fixed fuel type, changes in experimental burner confinement geometry from an open cylinder to convergent nozzle is shown to have a limited influence on flame stabilization location, with only a slight increase in flame angle attributed to a reduction of CRZ size, its downstream movement, and increased radial velocities, all consistent with numerical predictions and isothermal PIV measurements. However, a significant reduction in pressure fluctuation levels is observed as the convergent confinement decouples heat release and pressure fluctuations observed with the open confinement. Hydrogen addition is generally shown to increase the dominant resonant frequency and reduce overall pressure fluctuation amplitudes due to upstream shift in flame stabilization location and changes to the local speed of sound.
- Significant changes in flame stabilization location were observed for both fuel types and both confinements as the burner geometric swirl number was reduced from 0.8 to 0.5. The flame is observed to stabilize along the shear layer between the ORZ and CRZ in the $S_g =$

0.8 case, but stabilizes near the burner centerline due to a much weaker CRZ established in the $S_g = 0.5$ case.

- Hydrogen addition to methane generally allows for stable operation at reduced φ , and these flames are observed to shift upstream with increasing pressure for nominally similar bulk flow conditions and turbulence levels. This observation is attributed to changes in fundamental properties of the mixture, particularly increased S_L and thermo-diffusive effects which promote accelerated burning rates and aerodynamic stability under lean conditions.
- The influence of confinement geometry on NO_x emissions appears to be limited; however there is a consistent trend across fuels showing reduced NO_x production with reduced S_g , although corrected NO_x measurements are shown to be less than 7 ppmV at all conditions below $\text{AFT} \leq 1900$ K. This is an important combustor design consideration for $\text{CH}_4\text{-H}_2$ fuels, as it would allow operation at similar firing temperatures and air flow rates with reduced combustor pressure drop, provided there is adequate fuel-air premixing.
- A power law correlation between combustion noise amplitudes and $P2$ (thus thermal power) is derived, taking into account the influence of S_g on bulk flow resultant velocities, the influence of fuel type (represented by H:C ratio), and the influence of fuel reactivity (represented by S_L). Utilizing this correlation, predicted combustion noise amplitudes at 1.5 MPa (572 kW) in the HPGSB-2 would be reduced by almost 50% by the blending of up to 15% H_2 in CH_4 and operation at a higher burner swirl number compared to a low swirl burner operating on pure CH_4 .

CHAPTER 8 – REVIEW OF A GAS TURBINE THERMOACOUSTIC MODELING TOOL

In this Chapter, a thermoacoustic modeling tool known as the Open Source Combustion Instability Low Order Simulator (OSCILOS) is used in the evaluation of selected isothermal and combustion case studies in the HPGSB-2. Focus has been given to the observed thermoacoustic instabilities and combustion noise measurements as described in Chapters 5 and 7. The version of the OSCILOS modeling tool utilized in this study (Version 1.4.5) only considers longitudinal acoustic modes within the input geometry. Further detail on OSCILOS can be found in Chapter 3.3.2. In this modeling effort, a frequency domain analysis is made between the output eigenvalues of the acoustic system model and the frequency spectra for each of the selected conditions, along with estimations of limit cycle frequencies and velocity perturbations. A time domain analysis of limit cycle oscillation amplitudes has not been undertaken, but would be warranted in future study based on the frequency domain results presented here. Both isothermal air flow and combustion conditions are considered in this analysis. It is critical to note that this analysis only concerns self-excited thermoacoustic fluctuations in the HPGSB-2, as controlled flame or flow modulation (e.g. with a siren or loudspeaker) has not been conducted in this study.

Three separate experimental conditions have been modeled as case studies in this Chapter. First, the 110 kW CH₄-air flame instability identified and discussed in Chapter 5.2.2.2 under elevated temperature ($T_2 = 573$ K) and pressure ($P_2 = 0.20$ MPa) inlet conditions with the open cylindrical confinement is considered. Second, the instability observed with 84 kW CH₄-air and CH₄-H₂-air flames discussed in Chapter 7.3.1 at $T_2 = 573$ K and $P_2 = 0.22$ MPa with the open cylindrical confinement is evaluated. Finally, the influence of the convergent nozzle confinement, seen experimentally to decouple the heat release and pressure fluctuations in the HPGSB-2, is considered for the same conditions as the 84 kW CH₄-air and CH₄-H₂-air flames from Chapter 7.3.1. For all experimental combustion conditions, the corresponding isothermal conditions are also presented and evaluated. A brief evaluation is also made of the predicted limit cycle oscillation frequency at theoretical GT burner inlet conditions.

The current model employed shows relatively good agreement between predicted unstable eigenvalues and observed dominant instability frequencies, in particular those observed with the open cylindrical confinement. The model is also able to capture the shift in dominant instability frequency with changes in burner operating conditions (e.g. changing φ and P_{therm})

and fuel composition (e.g. CH₄ to CH₄-H₂). The model also shows a shift in unstable modes with change in confinement (e.g. open to convergent nozzle), but is unable to resolve the low dominant frequencies ($f_{peak} < 100$ Hz) in the convergent nozzle combustion cases.

8.1 Model Initialization

The OSCILOS thermoacoustic modeling tool is a MATLAB-based program which requires a series of model initializations, namely the combustor geometry, passive damper specifications (e.g. Helmholtz resonator), inlet mean flow properties (e.g. T_2 , P_2 , \bar{u}), heat addition (e.g. ΔT or fuel type with φ) selected flame model parameters (e.g. gain and time delay, τ), and inlet and outlet boundary conditions (e.g. open, closed, choked). All required inputs must be satisfied before proceeding to the frequency and time domain analysis.

8.1.1 Geometry Input

For this analysis, the HPGSB-2 geometry was used exclusively, as this has been shown to exhibit thermoacoustic instabilities, particularly when operated under preheated, pressurized conditions with the cylindrical quartz burner confinement tube. The required geometric input for OSCILOS requires only the geometric radius of components along a central axis. OSCILOS allows for the input of both straight tube cylindrical sections as well as sections with linearly varying radii, such as the outlet of the convergent nozzle quartz confinement tube. One particular limitation of the geometry input is that OSCILOS is currently unable to incorporate annular geometries, such as the instrumentation and pilot lance which is placed down the burner centerline through the fuel/air inlet plenum, mixing plenum, and swirler, protruding into the burner exit nozzle (see Figure 4.26). To account for this, the equivalent annular area has been converted into an equivalent circular area with the resulting radius entered as the required input for those affected sections of the HPGSB-2. Furthermore, OSCILOS is unable to resolve more complex geometries such as the radial-tangential swirler. While the swirler geometry is not expected to influence the longitudinal acoustic modes of the system, the change in area as the flow passes through the radial inlets must be accounted for. Thus, for the geometry input, the radial inlet area (width x height) of the $S_g = 0.8$ swirler has been multiplied by the number of inlets ($N = 9$) and converted into an equivalent circular area for input into the burner model. Figures 8.1 and 8.2 show the HPGSB-2 geometry input into OSCILOS for the open and convergent confinements, respectively.

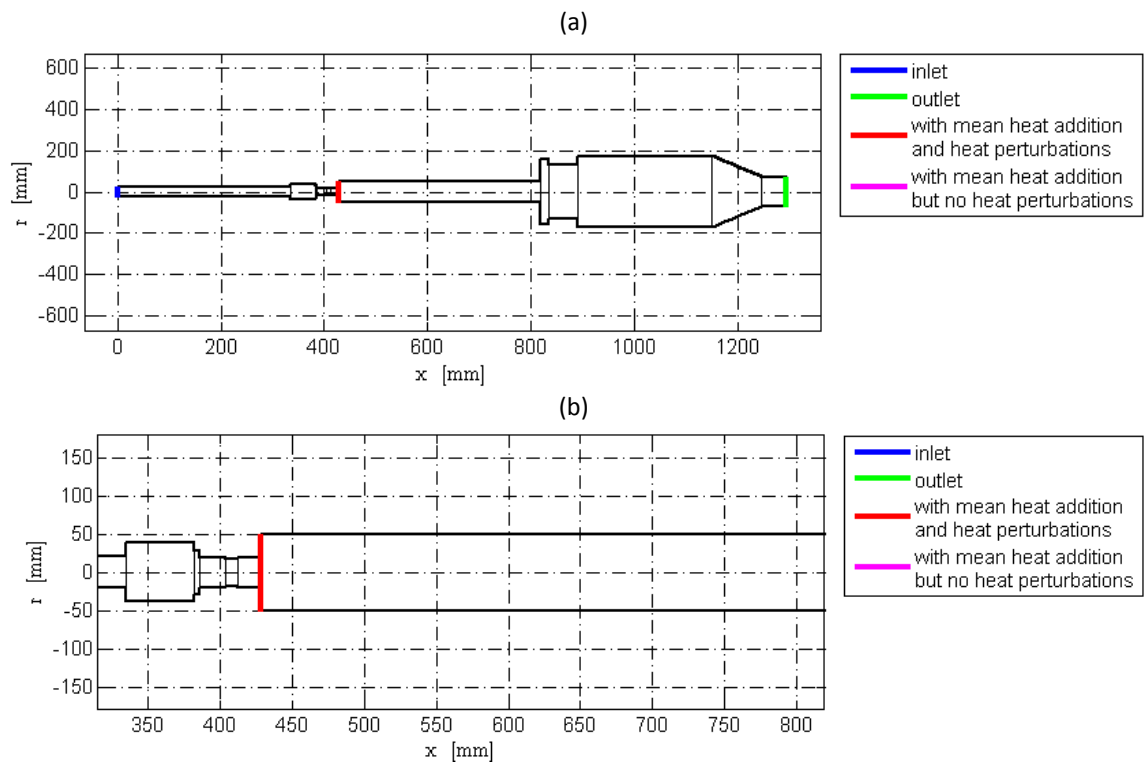


Figure 8.1: OSCILOS geometry input for the HPGSB-2 with open cylindrical confinement including inlet plenum and water-cooled exhaust piping (a) and highlighting the mixing plenum, swirler, and confinement tube (b). Flame location marked in red.

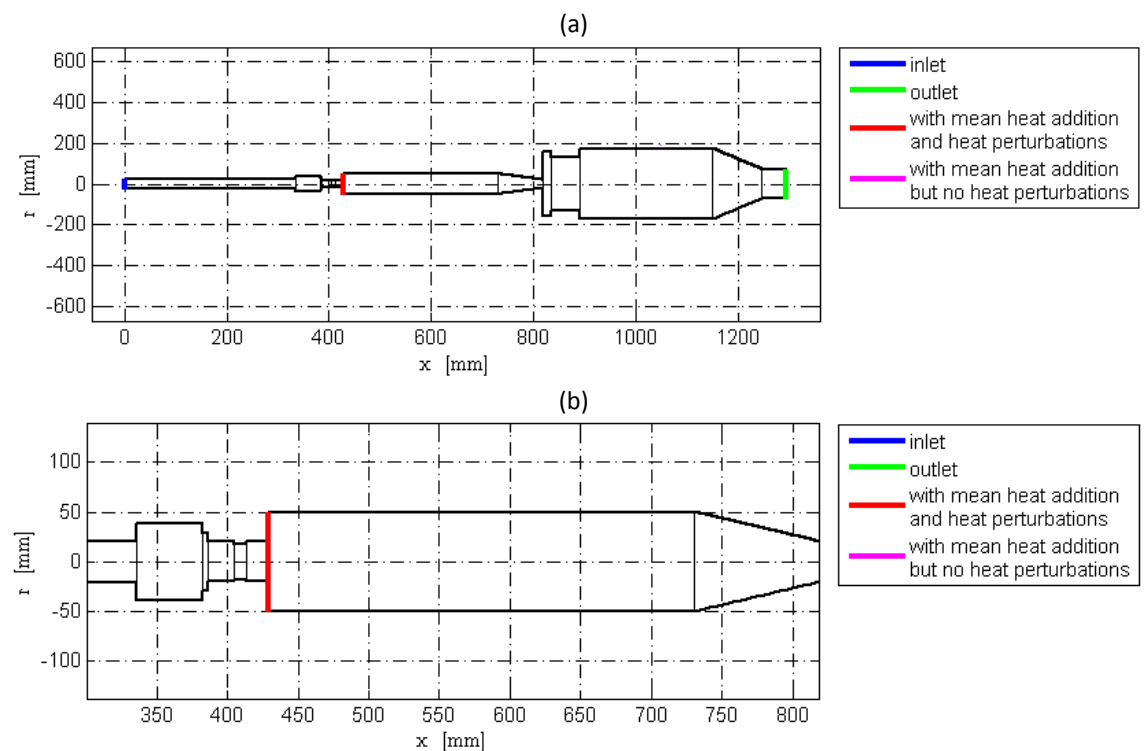


Figure 8.2: OSCILOS geometry input for the HPGSB-2 with convergent nozzle confinement including inlet plenum and water-cooled exhaust piping (a) and highlighting the mixing plenum, swirler, and confinement tube (b). Flame location marked in red.

OSCILOS cannot directly account for the annular area between the HPGSB-2 and the ID of the HPOC which is also open to the burner exhaust, and thus is not pictured in Figures 8.1 and 8.2. The model geometry begins at the fuel/air inlets to the inlet plenum (Figure 3.9.b) and terminates after a reducer in the water-cooled exhaust piping section. OSCILOS has currently only been validated for two burner geometries, both of which are open to the atmosphere at the outlet [206]. Thus, this study provides an evaluation of the application of the code to pressurized burner systems. In the HPCR, the overall geometry is more complex than the Cambridge and EM2C combustor systems in [206], and discussion about the selection of inlet and outlet boundary conditions is provided in Section 8.1.2.

8.1.2 Flame Model and Boundary Conditions

8.1.2.1 Flame Model Selection and Inputs

With the burner geometry input into OSCILOS, the burner inlet conditions of temperature, pressure, flow, and heat input must be initialized. Note that isothermal modeling does not require heat input or selection of a flame model. These conditions are provided in Tables 8.1, 8.2, and 8.3 in the respective Section for each experimental condition investigated. It should be noted that in order to achieve the required mean burner exit nozzle velocity, \bar{u} at the appropriate axial location, the inlet velocity input into OSCILOS was reduced by approximately 2 m/s in each condition. The increase in velocity to \bar{u} was then achieved by the reduction in flow area at the burner exit nozzle. In all cases, fuel combustion was selected as the heat source (rather than a differential temperature across the flame), which required selection of the fuel type, e.g. CH₄, the equivalence ratio as given Tables 8.1 – 8.3, and a combustion efficiency. The selected value of combustion efficiency ranged from 0.96 to 0.99 to achieve the P_{therm} values listed in Tables 8.1 – 8.3. As OSCILOS does not have the FARH2 fuel blend (85-15 %vol CH₄-H₂) as a fuel choice, the fuel was manually entered into the source code by changing the CH₄ molecular weight from 16.0425 to 13.939, and the C_xH_y values (x = 1, y = 4 for CH₄) to x = 0.85 and y = 3.7. The heat of formation, Δh_f , of CH₄ (-74800 J) was not augmented as Δh_f of H₂ = 0.

The flame model selected for initial evaluation is a linear (n- τ) flame transfer function (FTF) [205]. This model requires input of a gain (a) and time delay (τ) for a linear transformation in the Laplace domain between velocity fluctuations upstream of the flame, u' , and resulting heat release fluctuations, q' . This flame model is represented in Equation 8.1.

$$\mathcal{T}_u(s) = ae^{-\tau s} \quad (8.1)$$

The gain has been held constant at $a = 1$ for all presented results, as used in [204]. The definition of the time delay between the upstream velocity fluctuation and heat release fluctuation, however, is not trivial. The definition has been related to both convective time of coherent flow structures and the center of gravity of heat release [243] as well as flame height [204]. Thus, a time delay is proposed for use in this model based on experimental measurements of the flames to be evaluated. This time delay is defined in Equation 8.2 as the ratio of the axial height of the OH* chemiluminescence intensity centroid (e.g. from Figure 7.16, calculated per [236]) and the measured turbulence intensity (or large eddy turnover time).

$$\tau = \frac{y_{II_{OH^*},centroid}}{u'} \quad (8.2)$$

Physically, this is interpreted as the time taken for a vortex originating from the burner exit nozzle to traverse axially to interact with the location of mean heat release. The OH* centroid will vary for each condition, while the selected turbulence intensity has been held constant for each confinement, $u' = 8.43$ m/s in the open confinement and $u' = 15.75$ m/s in the convergent confinement case. This was measured by PIV at the $P2 = 0.22$ MPa cases shown in Figure 5.14 at $r = 0$ mm and $y = 32$ mm (only $P2 = \sim 0.22$ MPa cases investigated in this Chapter). The resulting τ therefore varies for the flames evaluated from $\tau = 1.6$ ms to $\tau = 4.2$ ms, and is listed in Tables 8.1 – 8.3. Reduced time delay is obvious with change in burner confinement due to increased u' and with H₂ addition due to reduced axial location of OH* CL centroid as the CH₄-H₂ flames stabilize further upstream than the equivalent CH₄ flame. These values are considered reasonable given that ranges of 3.5 – 4 ms have been identified in the literature for various burner configurations [204, 243].

While certainly an oversimplification of the complex flame-flow interactions in this highly turbulent, swirling flow, the linear (n- τ) FTF allows examination of the input geometry and simple flame response to arbitrary velocity perturbations. To evaluate the influence of variable normalized velocity perturbations, \hat{u}_u / \bar{u}_u , on the establishment of a limit cycle, a flame describing function (FDF) can instead be used. For the limit cycle results presented here, the FDF has been selected as a combination of the same linear (n- τ) FTF given in Equation 8.1 and a nonlinear model proposed by Li and Morgans [204]. The use of this nonlinear model

requires selection of coefficients, α_1 and β , and the same values as selected for use in the modeling work of [204] have been utilized here, $\alpha_1 = 0.85$ and $\beta = 40$. The α_1 coefficient influences the normalized velocity limit at which heat release fluctuation saturation occurs and β effects the sharpness of the corner between the linear flame response (for weak velocity perturbations) and the saturated response (for stronger velocity perturbations) [204]. Also, nonlinear effects on the time delay have been neglected.

8.1.2.2 Boundary Conditions Selection and Inputs

The outlet boundary condition was held constant for all tests, modeled as open-ended with minor reflection (reflection coefficient, $R = -0.95$, where $R = -1$ for fully open and $R = 1$ for fully closed ends). This was selected due to the reduction in flow velocity (thus low Mach number) assumed in this area due to expansion from the confinement exit into the exhaust piping as well as the temperature reduction due to contact with the water-cooled piping. For the inlet boundary condition, however, a study was undertaken utilizing only the (n- τ) linear FTF to evaluate the influence of the selected reflection coefficient. The inlet boundary condition was first thought to behave as a closed-ended tube with almost complete reflection ($R = 0.95$). This assumed that the fuel/air inlet piping to the inlet plenum was sufficiently small compared to the inlet plenum such that acoustic waves would tend to reflect at the end of the inlet plenum chamber. Thus, all experimental conditions, both isothermal and combustion, presented in this Chapter were first modeled with an inlet boundary condition of closed, $R = 0.95$ and outlet boundary condition of open, $R = -0.95$. However, the model response was comparatively poor in terms of identifying the dominant unstable frequencies, the range of stable and unstable frequencies, as well as the observed shift in dominant unstable frequencies with H_2 addition or change in confinement. Other unexpected observations, such as positive growth rate frequencies (thus, unstable) were identified in the isothermal flow cases.

Thus, the inlet boundary condition was reevaluated, and it is proposed to instead model the inlet boundary condition as open-ended with $R = -0.95$ (matching the outlet boundary condition). This has been proposed because Mach numbers at the burner inlet piping connections are low under these operating conditions ($M = \sim 0.1$) and the diameter of the inlet piping connections to the plenum ($D = 25.4$ mm) are approximately twice the diameter required for choked flow under these conditions. Thus, it may very well be possible that acoustic waves are able to travel upstream of the burner inlet plenum. The evaluation of all

conditions was again conducted with the new inlet boundary condition, and a comparison of the raw residuals between the predicted eigenvalues and the measured frequency spectra is presented in Figure 8.3 for the closed inlet boundary (Figure 8.3.a) and open inlet boundary (Figure 8.3.b). This change in inlet boundary condition reduces the root-mean-square error of the OSCILOS predicted frequencies by 35%, evident in the increased population of residual points near to zero in Figure 8.3.b compared with Figure 8.3.a. In addition, the model is able to better replicate the observed dominant frequency trends with changes in operating conditions and fuel composition. Also, all isothermal condition eigenvalues are observed to be negative (thus, stable) when using this boundary condition. Thus, this inlet boundary condition ($R = -0.95$) has been used for all further modeling. This assumption will require experimental validation in future work.

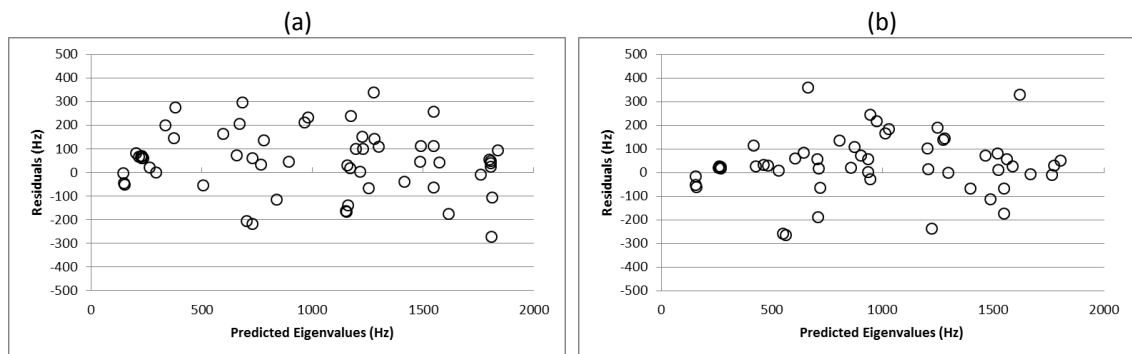


Figure 8.3: Raw residual plots of OSCILOS predicted eigenvalues with closed (a) and open (b) burner inlet boundary conditions

8.2 Acoustic Modeling of Selected Experimental Conditions

8.2.1 CH₄ Combustion Thermoacoustic Instability (Chapter 5.2.2.2)

In Chapter 5.2.2.2, a thermoacoustic instability was identified in the HPGSB-2 with an 110 kW CH₄-air flame using an open cylindrical confinement. The operating conditions were $T_2 = 573$ K, $P_2 = 0.2$ MPa, and $\varphi = 0.6$. The instability was identified by high DPT amplitudes and a harmonic FFT spectrum with a dominant frequency of 510 Hz. The full range of HPCR operating conditions as well as inputs for the corresponding OSCILOS model can be found in Table 8.1 for both the combustion and equivalent isothermal air flow conditions. The designation in Table 8.1 (and subsequent Tables) refers to the operating condition, confinement, swirl number, and P_2 (MPa), e.g. “BASE-O-8-0.2” for CH₄-air flame, open cylindrical confinement, $S_g = 0.8$, and $P_2 = 0.2$ MPa.

Table 8.1: HPGSB-2 OSCILOS isothermal and CH₄ combustion input conditions at P₂ = 0.20 MPa with open cylindrical confinement

Rig Parameter	Experimental Conditions	
	ISO-O-8-0.2	BASE-O-8-0.2
Combustor Inlet Temperature, T_2 (K)	573	573
Combustor Inlet Pressure, P_2 (MPa)	0.20	0.20
Air Mass Flow, \dot{m}_{air} (g/s)	63.72	64.01
CH ₄ Mass Flow, \dot{m}_{CH_4} (g/s)	---	2.21
Equivalence Ratio, φ	---	0.60
Thermal Power, P_{therm} (kW)	---	110
Mean Burner Nozzle Exit Velocity, \bar{u} (m/s)	41.7	42.7
Reynolds Number, Re	68725	73382
$\dot{m}\sqrt{T_2}/P_2$	0.76	0.77
Dominant Frequency, f_{peak} (Hz)	871	510
Time Delay, τ (ms)	---	3.315

For comparison with the OSCILOS predicted eigenvalues, the FFT plots of the Burner Face DPT measurement from both isothermal and combustion conditions are presented in Figure 8.4. Note the difference in y-axis scaling (thus DPT amplitudes) between both plots. The isothermal condition (Figure 8.4.a) exhibits a single dominant frequency peak at $f_{peak} = 871$ Hz, which was shown in Chapter 5.2.1.1 to be most likely related to a vortex shedding phenomenon. The combustion condition (Figure 8.4.b) exhibits harmonic frequencies with the dominant frequency peak at $f_{peak} = 510$ Hz, which was suggested in Chapter 5.2.2.2 to be the first harmonic of a standing wave in the burner geometry, using an average speed of sound based on AFT and T_3 .

Using only the (n- τ) FTF (or no flame model for the isothermal case), the resulting contour plot of eigenvalues and growth rate for the isothermal and combustion conditions are presented in Figure 8.5. In these plots, a negative growth rate (left of zero on the x-axis) is indicative of a stable frequency while a positive growth rate (right of zero on the x-axis) is indicative of an unstable frequency, meaning that a perturbation would likely oscillate at that frequency. The eigenvalues of the system are marked by white circles on each contour plot. For the isothermal case (Figure 8.5.a), all eigenvalues have a negative growth rate, as would be expected with no heat addition. While the dominant frequency is flow related in the isothermal case, the model does appear able to identify other peaks in the FFT plot (such as those near 1400 Hz, 1600 Hz, and 1800 Hz), although it appears to under predict the frequency. In the combustion case (Figure 8.5.b), the eigenvalue distribution has shifted along the x-axis, with a number of positive growth rate (unstable) modes identified.

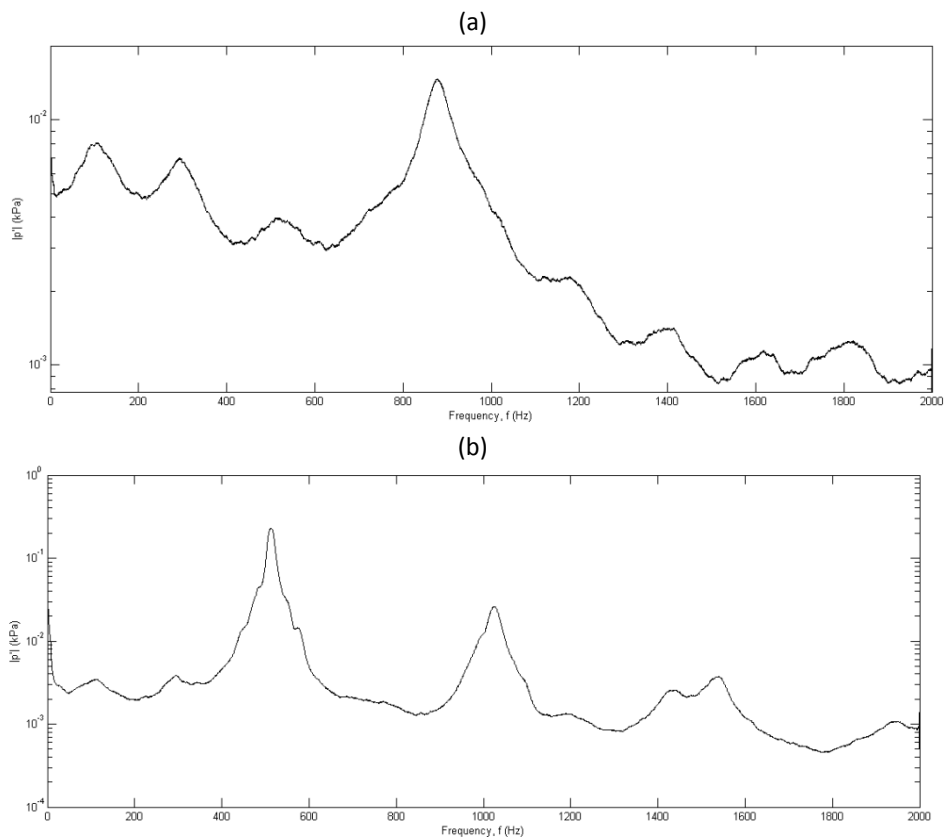


Figure 8.4: FFT of Burner Face DPT measurement for ISO-O-8-0.2 (a) and BASE-O-8-0.2 (b). Note the difference in y-axis scaling.

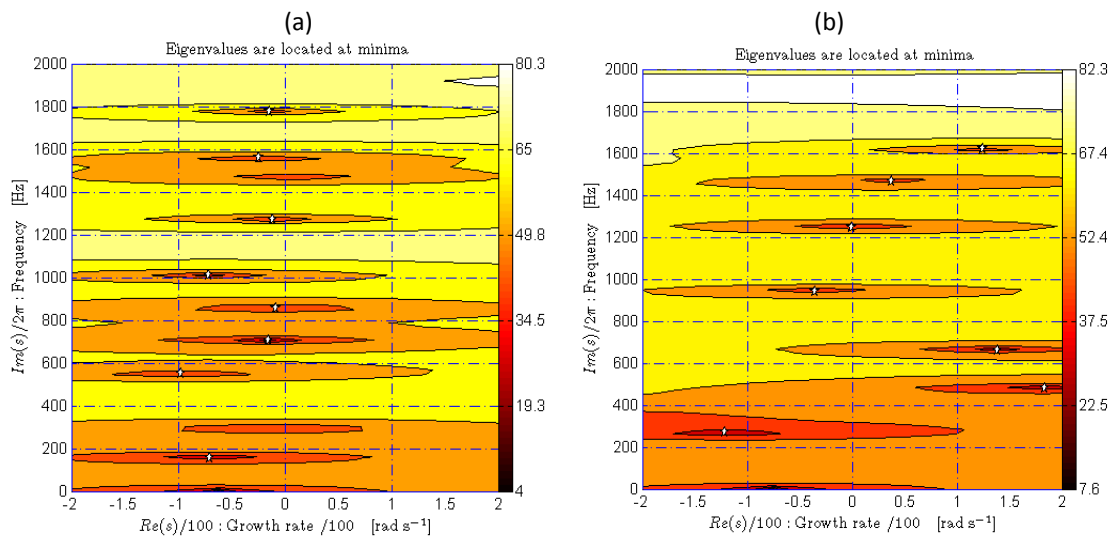


Figure 8.5: Contour plots of eigenvalues and growth rates predicted by OSCILOS for ISO-O-8-0.2 (a) and BASE-O-8-0.2 (b). The main modes of the system are indicated by white circles.

The eigenfrequency with the highest growth rate (184 rad/s) in Figure 8.5.b is 481.5 Hz, within 5% of the measured f_{peak} , 510 Hz. It is interesting to note here that the model which utilized a closed inlet boundary condition identified the frequency with the highest growth rate (100 rad/s) at 731 Hz, which does not appear in Figure 8.4.b. The model also identifies approximate

harmonic frequencies at 943 Hz (2nd harmonic) and 1466 Hz (3rd harmonic). Similar to the isothermal case, other peaks appear to be identified, such as that near 300 Hz, and again the model appears to under predict the frequency values. A comparison between the isothermal and combustion cases (in both Figures 8.4 and 8.5) indicate common acoustic markers (peaks in similar locations aside from the dominant frequencies), which further supports the selection of the open inlet boundary condition.

The results from the combined FDF model are found in Figures 8.6 and 8.7, and identify the frequency and velocity fluctuation amplitude at which a limit cycle would be established. Similar to the contour plot in Figure 8.5 for an arbitrary velocity perturbation, contour plots are generated for varying velocity fluctuation amplitudes when conducting the nonlinear analysis. Figure 8.6 presents the eigenvalue and growth rate contour plots at two velocity fluctuation levels, $\hat{u}_u / \bar{u}_u = 0.50$ (Figure 8.6.a) and $\hat{u}_u / \bar{u}_u = 0.75$ (Figure 8.6.b). If the previously identified peak frequency (~ 480 Hz) is tracked from Figure 8.6.a to Figure 8.6.b, it is observed to pass through a growth rate of 0 rad/s. Thus, as the velocity perturbation increases, the unstable mode at ~ 480 Hz transitions from an unstable mode to a stable mode. This zero-crossing in growth rate therefore indicates the establishment of a limit cycle.

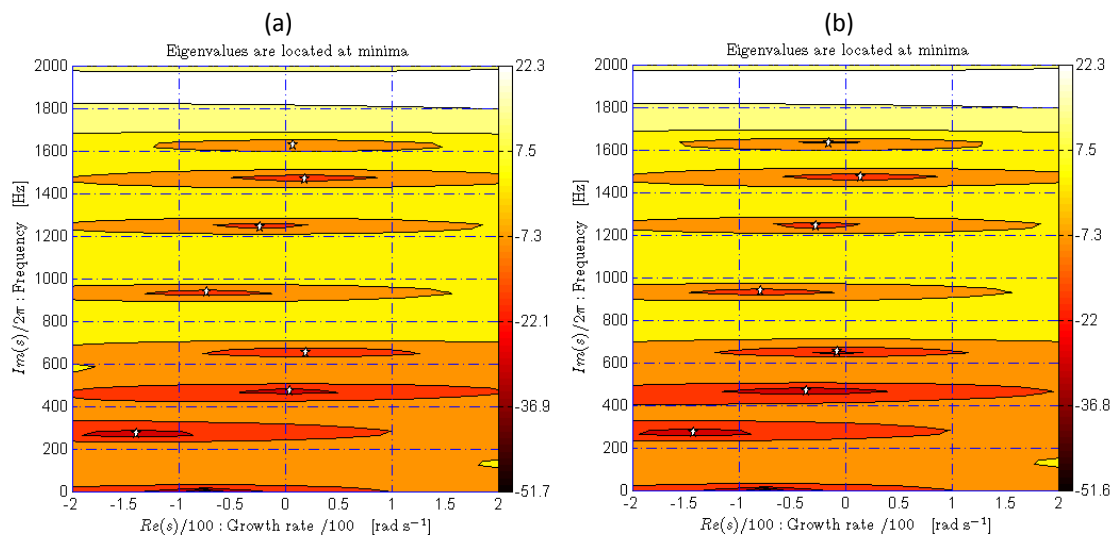


Figure 8.6: Contour plots of eigenvalues and growth rates predicted by OSCILOS for BASE-O-8-0.2 with different velocity perturbations: $\hat{u}_u / \bar{u}_u = 0.50$ (a) and $\hat{u}_u / \bar{u}_u = 0.75$ (b). The main modes of the system are indicated by white circles.

By evaluating the frequency and growth rate as a function of the velocity perturbation, it is possible to predict where the limit cycle would be established. This analysis is plotted in Figure 8.7, with the selected eigenvalue of ~ 480 Hz (circles, left y-axis) and its growth rate (triangles, right y-axis) tracked with increasing velocity perturbation. The growth rate zero crossing is

where the limit cycle is established, which can then be projected down to the x-axis for the velocity perturbation amplitude and projected onto the corresponding frequency curve. For the establishment of the limit cycle, the model predicts this would occur at $f = 473.1$ Hz with an amplitude of $\hat{u}_u / \bar{u}_u = 0.527$. Given the current under prediction of the model with measured values, this frequency value is most likely an under prediction as well, but a downward shift from the established harmonic gives an indication of the conditions under which the limit cycle may be established in the burner. For example, this may indicate that the harmonic limit cycle is established at a lower AFT than at $\varphi = 0.6$ as the harmonic frequency appears to be a function of the local speed of sound. This would be in agreement with Figure 5.38, which identified increasing dynamic pressure amplitudes in the burner prior to $\varphi = 0.6$.

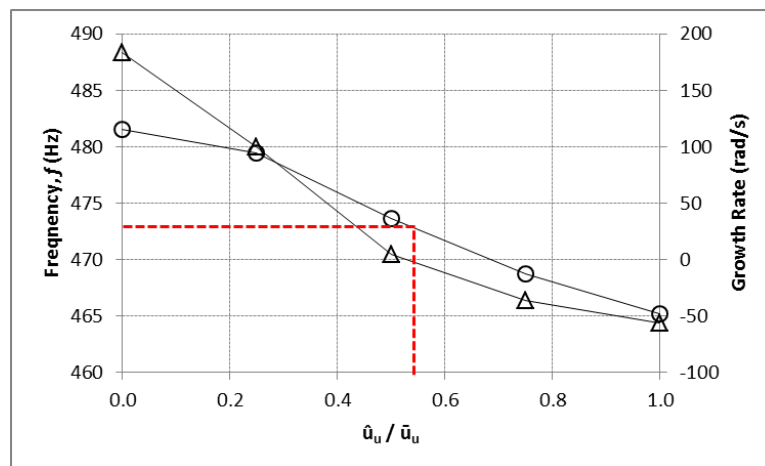


Figure 8.7: Predicted eigenvalues (circles) and growth rate (triangles) plotted against normalized velocity perturbation. Red lines mark the predicted limit cycle frequency and velocity perturbation.

8.2.2 CH₄ / CH₄-H₂ Combustion Thermoacoustic Instability (Chapter 7.3.1)

In Chapter 7.3.1, a thermoacoustic instability was identified in the HPGSB-2 with 84 kW CH₄-air and CH₄-H₂-air flames using an open cylindrical confinement. The operating conditions were $T_2 = 573$ K, $P_2 = 0.22$ MPa, and $\varphi = 0.55$. The instability was identified by high DPT amplitudes and a harmonic FFT spectrum with dominant frequencies of 455 Hz (CH₄-air) and 494 Hz (CH₄-H₂-air). The full range of HPCR operating conditions as well as inputs for the corresponding OSCILOS model can be found in Table 8.2 for both the combustion and equivalent isothermal air flow conditions.

Table 8.2: HPGSB-2 OSCILOS isothermal and CH₄/CH₄-H₂ combustion input conditions at P₂ = 0.22 MPa with open cylindrical confinement

Rig Parameter	Experimental Conditions		
	ISO-O-8-0.22	BASE-O-8-0.22	FARH2-O-8-0.22
Combustor Inlet Temperature, T_2 (K)	593	575	578
Combustor Inlet Pressure, P_2 (MPa)	0.22	0.22	0.22
Air Mass Flow, \dot{m}_{air} (g/s)	52.59	52.30	52.49
Fuel Mass Flow, \dot{m}_{fuel} (g/s)	---	1.67	1.64
Equivalence Ratio, φ	---	0.55	0.55
Thermal Power, P_{therm} (kW)	---	83	84
Mean Burner Nozzle Exit Velocity, \bar{u} (m/s)	32.5	33.2	34.0
Reynolds Number, Re	55010	58675	58618
$\dot{m}\sqrt{T_2}/P_2$	0.58	0.59	0.60
Dominant Frequency, f_{peak} (Hz)	650	455	494
Time Delay, τ (ms)	---	4.179	3.525

For comparison with the OSCILOS predicted eigenvalues, the FFT plots of the Burner Face DPT measurement from both isothermal and combustion conditions are presented in Figure 8.8. Note the difference in y-axis scaling (thus DPT amplitudes) between each plot. The isothermal condition (Figure 8.8.a) exhibits a single dominant frequency peak at $f_{peak} = 650$ Hz, which was shown to be most likely related to a vortex shedding phenomenon due to the corresponding Strouhal number of $St = \sim 0.8$. The combustion conditions exhibit harmonic frequencies with the dominant frequency peak at $f_{peak} = 455$ Hz in the CH₄-air case (Figure 8.8.b) and $f_{peak} = 494$ Hz in the CH₄-H₂-air case (Figure 8.8.c), both of which were suggested in Chapter 7.3.1 to be related to the first harmonic of a standing wave in the burner geometry, using an average speed of sound based on AFT and T_3 , with the observed shift with H₂ addition attributed to a more compact flame shape and locally higher temperatures influencing the local speed of sound. In comparison with the case study presented in Section 8.2.1, the dominant harmonic frequency is seen to reduce from 510 Hz to 455 Hz for the CH₄-air flames, attributed to the reduction in AFT (due to shift from $\varphi = 0.60$ to $\varphi = 0.55$) and operation at a lower P_{therm} and \bar{u} . Similar peaks near 100 Hz, 300 Hz, and 1400 Hz – 1600 Hz are also identifiable between isothermal conditions, suggesting that while the dominant frequency may scale with \bar{u} , other modes exist which are consistent (e.g. acoustic modes which are constant as T_2 and burner geometry are held constant between both cases).

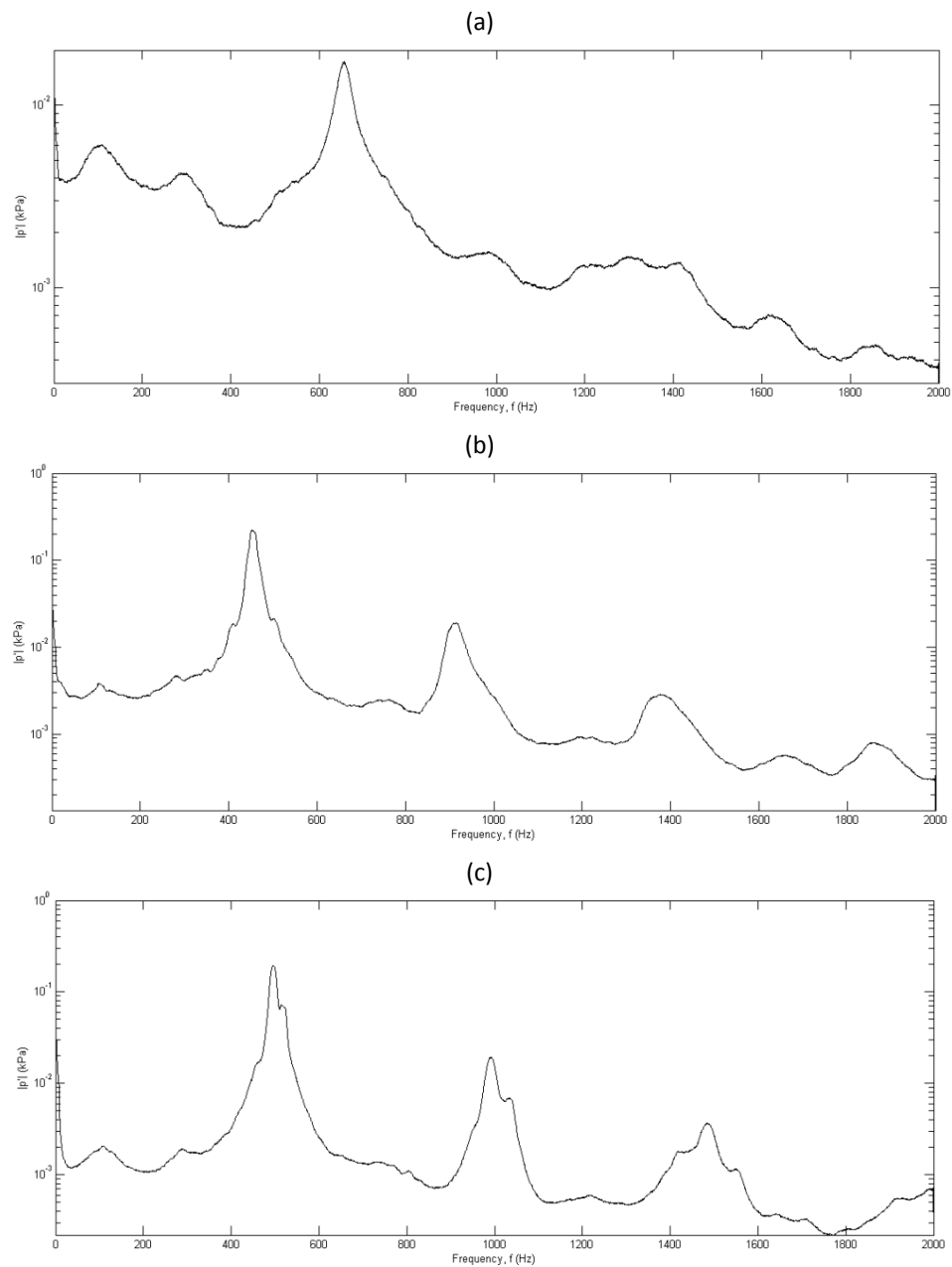


Figure 8.8: FFT of Burner Face DPT measurement for ISO-O-8-0.22 (a), BASE-O-8-0.22 (b), and FARH2-O-8-0.22. Note the difference in y-axis scaling.

Using only the $(n-\tau)$ FTF (or no flame model for the isothermal case), the resulting contour plot of eigenvalues and growth rate for the isothermal and combustion conditions are presented in Figure 8.9. The eigenvalues of the system are marked by white circles on each contour plot. For the isothermal case (Figure 8.9.a), all eigenvalues have a negative growth rate, as would be expected with no heat addition. While the dominant frequency is flow related in the isothermal case, the model does appear able to identify other peaks in the FFT plot (such as those near 1400 Hz, 1600 Hz, and 1800 Hz), although it appears to under predict the frequency, as was noted in Section 8.2.1. In the combustion cases (Figures 8.9.b and 8.9.c),

the eigenvalue distribution has again shifted along the x-axis, with a number of positive growth rate (unstable) modes identified.

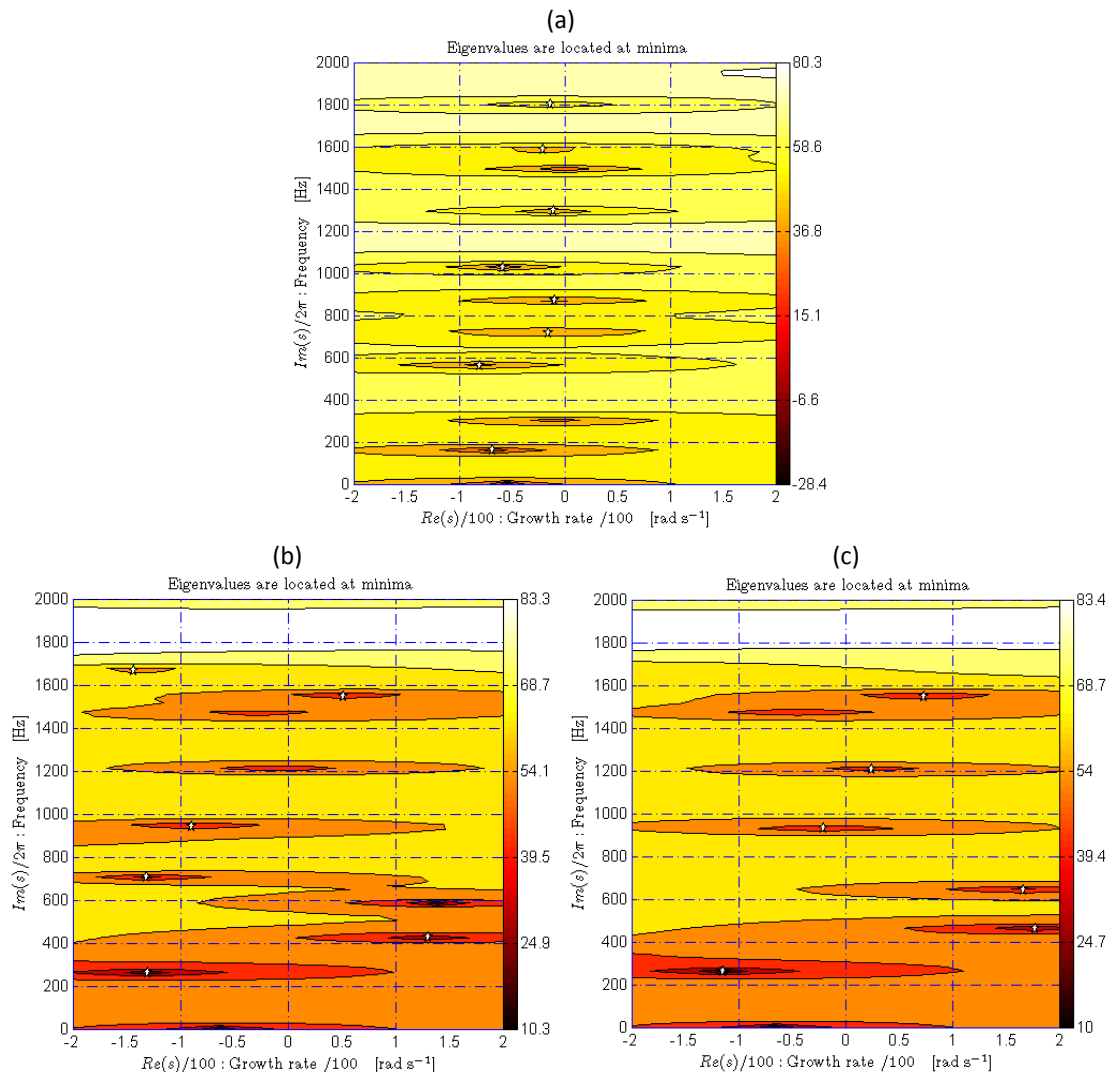


Figure 8.9: Contour plots of eigenvalues and growth rates predicted by OSCILOS for ISO-O-8-0.22 (a), BASE-O-8-0.22 (b), and FARH2-O-8-0.22 (c). The main modes of the system are indicated by white circles.

The eigenfrequency with the highest growth rate (130.2 rad/s) in the CH₄-air case (Figure 8.9.b) is 427.6 Hz, within 6% of the measured f_{peak} , 455 Hz. The model also identifies an approximate harmonic frequency at 944 Hz (2nd harmonic) as well as a non-harmonic frequency near 1600 Hz, which appears to be present in the FFT plot (Figure 8.9.b). The eigenfrequency with the highest growth rate (177.3 rad/s) in the CH₄-H₂ case (Figure 8.9.c) is 462.2 Hz, again within 6% of the measured f_{peak} , 494 Hz. Similar to the previous case study, other peaks appear to be identified, such as that near 300 Hz and 1600 Hz, and again the model appears to under predict the observed frequency values. OSCILOS appears to capture the influence of changing fuel composition with a relatively simple linear flame model, which

will be critical to further model development with other fuel blends. As was observed in the HPGSB-2 experiments, the addition of H₂ increases the dominant frequency, and the predicted model values appear to show a similar trend (427.6 Hz to 462.2 Hz). Also, the reduction between the measured dominant CH₄-air frequency in the previous case study (510 Hz) and this study (455 Hz) with changing operating conditions is replicated by the model (481.5 Hz to 427.6 Hz), which suggests the model is also able to sufficiently resolve changes in P_2 , P_{therm} , φ , and \bar{u} .

Similar to Section 8.2.1, the limit cycle frequency and velocity perturbation were evaluated with the nonlinear FDF, with the analysis plotted in Figure 8.10 for the CH₄-air (Figure 8.10.a) and CH₄-H₂-air (Figure 8.10.b) flames. In Figure 8.10.a, the selected eigenvalue of ~430 Hz (circles, left y-axis) and its growth rate (triangles, right y-axis) are tracked with increasing velocity perturbation amplitude. For the establishment of the limit cycle with the CH₄-air flame, the model predicts this would occur at $f = 437.7$ Hz with an amplitude of $\hat{u}_u / \bar{u}_u = 0.836$. Tracking the ~460 Hz eigenvalue in the CH₄-H₂-air flame, the model predicts the limit cycle would occur at $f = 455$ Hz with an amplitude of $\hat{u}_u / \bar{u}_u = 0.750$, showing a reduction in limit cycle amplitude of 10% with H₂ addition under these operating conditions. Note that for the CH₄-air flame, the unexpected trend of increasing frequency with velocity perturbation appears to be sensitive to the delay time, $\tau = 4.179$ ms, which is particularly influenced in this case by the change in flame shape observed (refer to Figure 7.10.b). Under this condition, the CH₄-air flame has taken on an M-shape, which weights the OH* CL centroid further downstream than the V-shaped flame, increasing τ . At lower τ , the same trend of decreasing frequency with increasing velocity amplitude, as observed in Figure 8.7 and 8.10.b (both V-shaped flames), can be replicated.

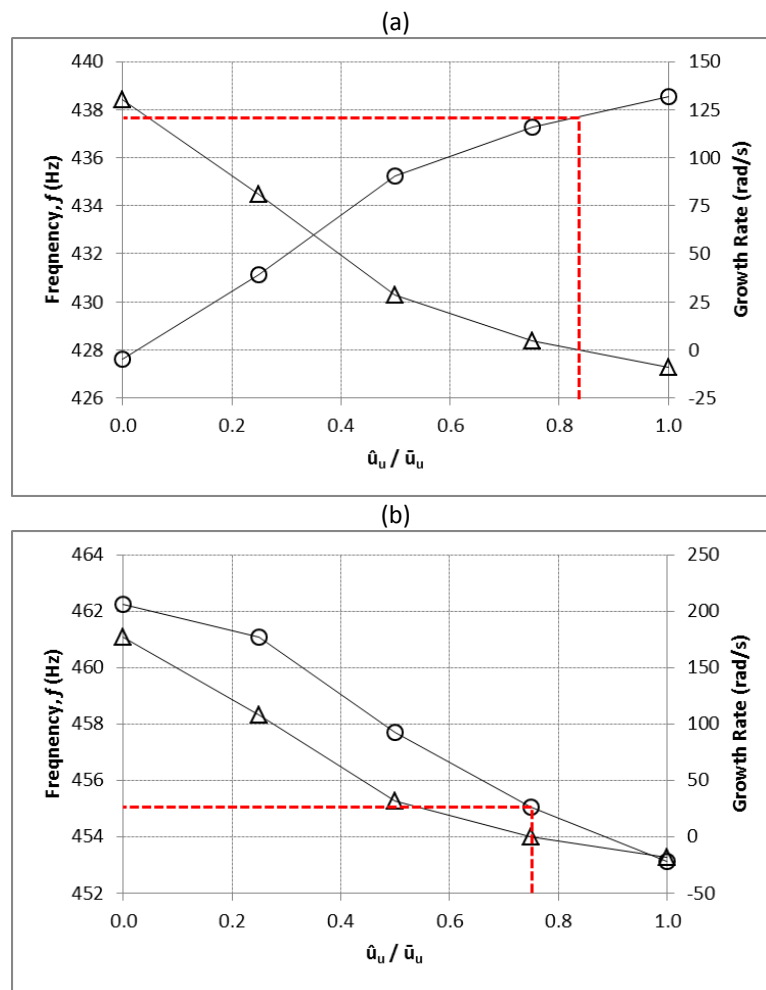


Figure 8.10: Predicted eigenvalues (circles) and growth rate (triangles) plotted against normalized velocity perturbation for BASE-O-8-0.22 (a) and FARH2-O-8-0.22 (b). Red lines mark the predicted limit cycle frequency and velocity perturbation.

8.2.3 CH₄ / CH₄-H₂ Combustion Noise (Chapter 7.3.1)

In Chapter 7.3.1, it was observed that a change in the burner confinement from open cylinder to convergent nozzle effectively decoupled the heat release and pressure fluctuations, resulting in a significant reduction in combustion noise levels (see Figures 7.17.c and 7.17d). For an evaluation of this effect in OSCILOS, similar HPGSB-2 conditions are considered as in Section 8.2.2 with 84 kW CH₄-air and CH₄-H₂-air flames using the convergent nozzle confinement. The operating conditions are identical at $T_2 = 573$ K, $P_2 = 0.22$ MPa, and $\varphi = 0.55$. The combustion noise was marked by an order of magnitude reduction in combustion noise levels compared to the acoustically coupled case identified with the open cylindrical confinement, with dominant frequencies of 24 Hz (CH₄-air) and 73 Hz (CH₄-H₂-air). The full range of HPCR operating conditions as well as inputs for the corresponding OSCILOS model can be found in Table 8.3 for both the combustion and equivalent isothermal air flow conditions.

Table 8.3: HPGSB-2 OSCILOS isothermal and CH₄/CH₄-H₂ combustion input conditions at P₂ = 0.22 MPa with convergent nozzle confinement

Rig Parameter	Experimental Conditions		
	ISO-CQ-8-0.22	BASE-CQ-8-0.22	FARH2-CQ-8-0.22
Combustor Inlet Temperature, T_2 (K)	570	573	573
Combustor Inlet Pressure, P_2 (MPa)	0.22	0.22	0.22
Air Mass Flow, \dot{m}_{air} (g/s)	52.44	52.54	52.64
Fuel Mass Flow, \dot{m}_{fuel} (g/s)	---	1.67	1.64
Equivalence Ratio, ϕ	---	0.55	0.55
Thermal Power, P_{therm} (kW)	---	83	84
Mean Burner Nozzle Exit Velocity, \bar{u} (m/s)	31.0	32.9	33.8
Reynolds Number, Re	56381	59152	59087
$\dot{m}\sqrt{T_2}/P_2$	0.57	0.59	0.6
Dominant Frequency, f_{peak} (Hz)	137	24	73
Time Delay, τ (ms)	---	2.059	1.604

For comparison with the OSCILOS predicted eigenvalues, the FFT plots of the Burner Face DPT measurement from both isothermal and combustion conditions are presented in Figure 8.11. Note the difference in y-axis scaling (thus DPT amplitudes) between each plot. The isothermal condition (Figure 8.11.a) appears to exhibit numerous modes with a dominant frequency peak at $f_{peak} = 137$ Hz. In comparison with the combustion FFTs in Figure 8.8, the combustion FFTs in Figure 8.11 no longer exhibit the established harmonic frequencies with the dominant frequency peak now at $f_{peak} = 24$ Hz in the CH₄-air case (Figure 8.11.b) and $f_{peak} = 73$ Hz in the CH₄-H₂-air case (Figure 8.11.c), confirming the decoupling observation. The high frequency peaks near 1300 Hz appear related to the Helmholtz resonance of the burner confinement. As discussed in Chapter 5, the low frequency dynamics appear to be related to localized flame extinction and reignition events, which appears to be confirmed in this case, as no low frequency dynamics are observed in the isothermal flow case. In addition, with the geometric change to a convergent nozzle confinement, the flow field is considerably affected, such that for the same \bar{u} , the convergent confinement flames are more likely to blowoff due to reduced CRZ size. This is supported by the measured bluff body temperature (T_{pilot}) value for these conditions, $T_{pilot} = 1234$ K for BASE-O-8-0.22 reducing to $T_{pilot} = 1069$ K for BASE-CQ-8-0.22.

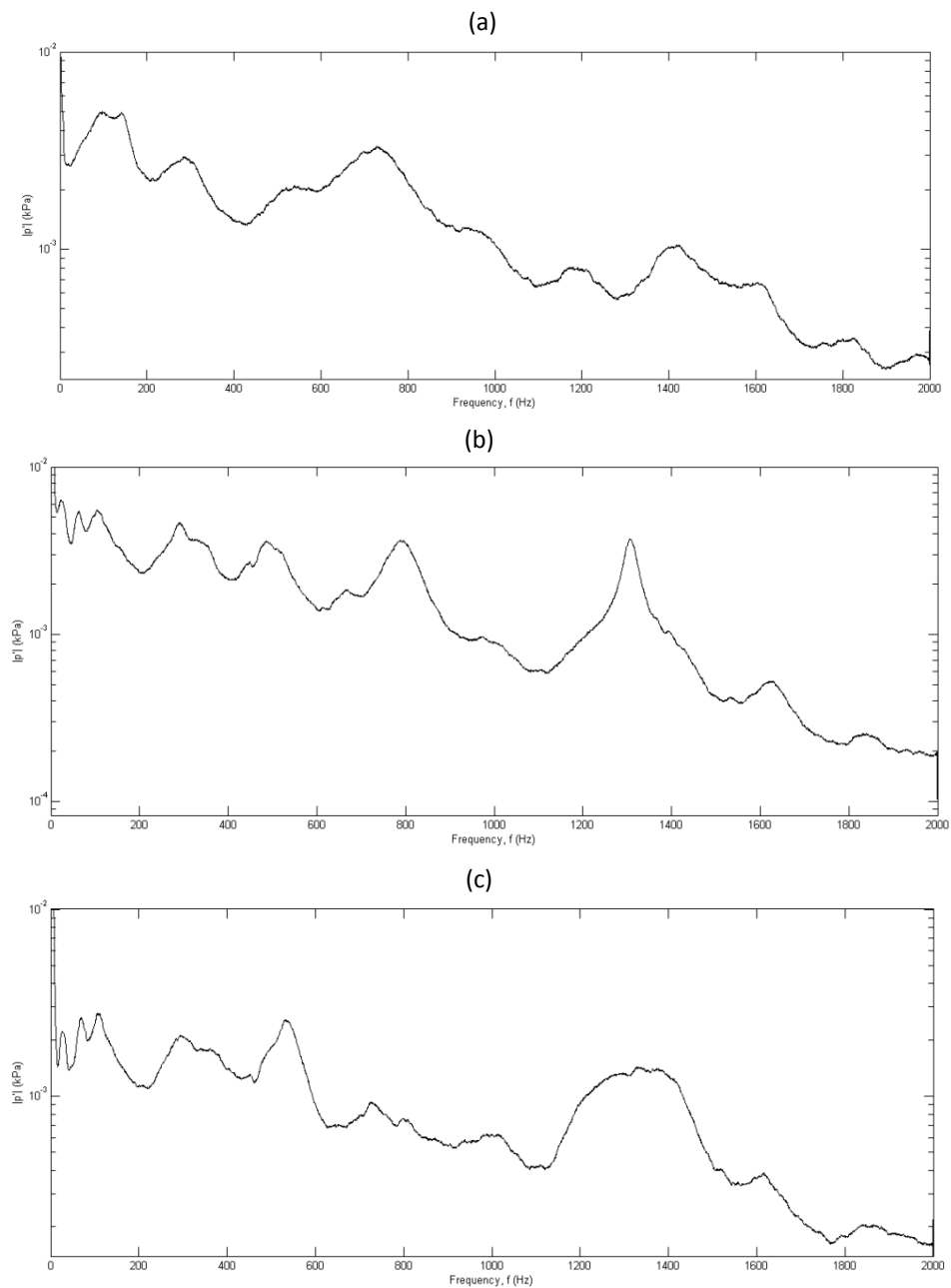


Figure 8.11: FFT of Burner Face DPT measurement for ISO-CQ-8-0.22 (a), BASE-CQ-8-0.22 (b), and FARH2-CQ-8-0.22 (c). Note the difference in y-axis scaling.

Using only the $(n-\tau)$ FTF (or no flame model for the isothermal case), the resulting contour plot of eigenvalues and growth rate for the isothermal and combustion conditions are presented in Figure 8.12. The eigenvalues of the system are marked by white circles on each contour plot. For the isothermal case (Figure 8.12.a), all eigenvalues have a negative growth rate, as would be expected with no heat addition. The model appears able to identify many of the frequency peaks in the isothermal FFT plot in Figure 8.11.a, notably at 150 Hz (near f_{peak}), 530 Hz, 700 Hz, and near 1800 Hz. However, given the complex flow field, it is expected that a number of

modes in the convergent confinement FFT are unrelated to longitudinal acoustic modes. In the combustion cases (Figures 8.12.b and 8.12.c), the eigenvalue distribution appears to significantly differ from the open confinement, acoustically coupled cases in Figures 8.5 and 8.9.

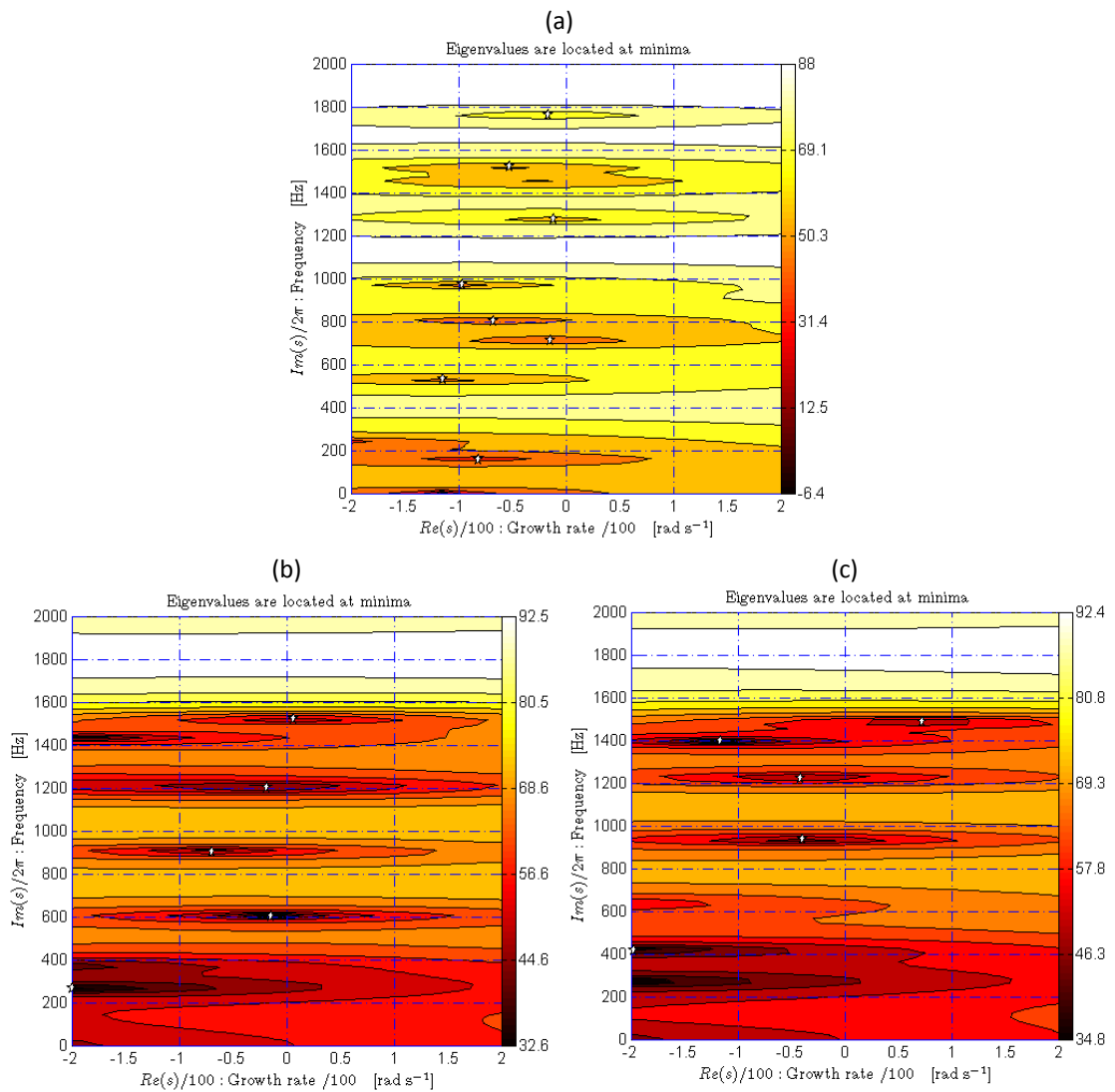


Figure 8.12: Contour plots of eigenvalues and growth rates predicted by OSCILOS for ISO-CQ-8-0.22 (a), BASE-CQ-8-0.22 (b), and FARH2-CQ-8-0.22 (c). The main modes of the system are indicated by white circles.

In the CH_4 -air case (Figure 8.12.b), the eigenfrequency with the highest growth rate (6.76 rad/s) is 1522.4 Hz, compared with unstable growth rates of 184 rad/s at 481 Hz and 130.2 rad/s at 428 Hz in the acoustically-coupled conditions presented in Section 8.2.1 and 8.2.2, respectively. The eigenfrequency with the highest growth rate (72.9 rad/s) in the CH_4 - H_2 case (Figure 8.12.c) is 1487 Hz, compared with unstable growth rates of 177.3 rad/s at 462 Hz in the acoustically-coupled case presented in Section 8.2.2. The unstable modes identified were

unexpected given the measured pressure amplitudes; however, it may be indicative that the linear (n - τ) FTF is insufficient for representing this decoupled, multimodal system, and warrants further work. Thus, while it appears that the model is unable to resolve the dominant low frequency modes in the convergent confinement cases (which may not be acoustically related as previously discussed), it does appear to capture the decoupling effect of the convergent confinement observed in the measured FFTs.

8.3 Model Prediction at Gas Turbine Relevant Conditions

Having utilized the OSCILOS model for prediction of the experimentally observed thermoacoustic and combustion noise behavior of the HPGSB-2, a brief study was also conducted to evaluate the thermoacoustic stability of both input geometries at GT relevant conditions of temperature and pressure. As such, elevated burner inlet conditions have been evaluated at $T_2 = 900$ K at $P_2 = 1.5$ MPa. Maintaining similar flow conditions as those presented in Section 8.2.2 and 8.2.3 yields $P_{therm} = 573$ kW at 1.5 MPa. The equivalence ratio has been maintained at $\varphi = 0.55$ in the acoustic model along with the corresponding time delays given in Tables 8.2 and 8.3, with CH_4 as the fuel.

The results from the combined FDF model are given in Figures 8.13 and 8.14. Contour plots of the eigenvalues and growth rates at $\hat{u}_u / \bar{u}_u = 0$ are given in Figure 8.13, with the open (Figure 8.13.a) and convergent (Figure 8.13.b) confinements. The eigenfrequency with the highest growth rate (101.15 rad/s) in the open confinement case (Figure 8.13.a) is 764.7 Hz. The model also predicts a number of other unstable modes at 466 Hz, 600 Hz 1140 Hz, and 1290 Hz, some of which are near to the established limit cycle, suggesting that this geometry would be highly unstable, but also that limit cycle amplitudes for those frequencies would be low. The eigenfrequency with the highest growth rate (17.83 rad/s) in the convergent confinement case (Figure 8.13.b) is 1555 Hz. Similar to the previous case study with the convergent confinement, many of the unstable modes in the open confinement case have been eliminated, with only two unstable modes at 1555 Hz and 687 Hz. The established limit cycle amplitudes in this case would be low, as all modes show negative growth rates at $\hat{u}_u / \bar{u}_u > 0.25$.

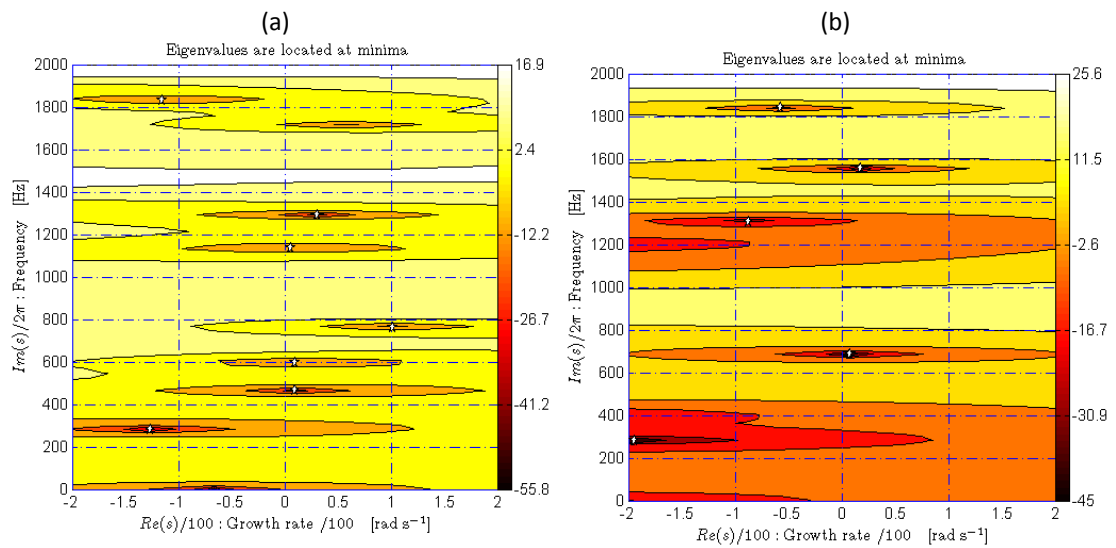


Figure 8.13: Contour plots of eigenvalues and growth rates predicted by OSCILOS at $T_2 = 900$ K, $P_2 = 1.5$ MPa, and $\hat{u}_u / \bar{u}_u = 0.0$ with open (a) and convergent nozzle (b) confinement. The main modes of the system are indicated by white circles.

The limit cycle frequency and velocity perturbation were evaluated with the nonlinear FDF, with the analysis plotted in Figure 8.14 for the open (Figure 8.14.a) and convergent (Figure 8.14.b) confinement. In Figure 8.14.a, the selected eigenvalue of ~ 760 Hz (circles, left y-axis) and its growth rate (triangles, right y-axis) are tracked with increasing velocity perturbation amplitude. For the establishment of the limit cycle with the open confinement, the model predicts this would occur at $f = 757.6$ Hz with an amplitude of $\hat{u}_u / \bar{u}_u = 0.5$. This upward shift in limit cycle frequency (757.6 Hz) from the BASE-O-8-0.22 case (437.7 Hz) is to be expected due to the increase in T_2 and P_{therm} . Tracking the ~ 687 Hz eigenvalue in the convergent confinement case, the model predicts the limit cycle would occur at $f = 687.5$ Hz with an amplitude of $\hat{u}_u / \bar{u}_u = 0.025$, showing a significant reduction in limit cycle amplitude with the convergent confinement.

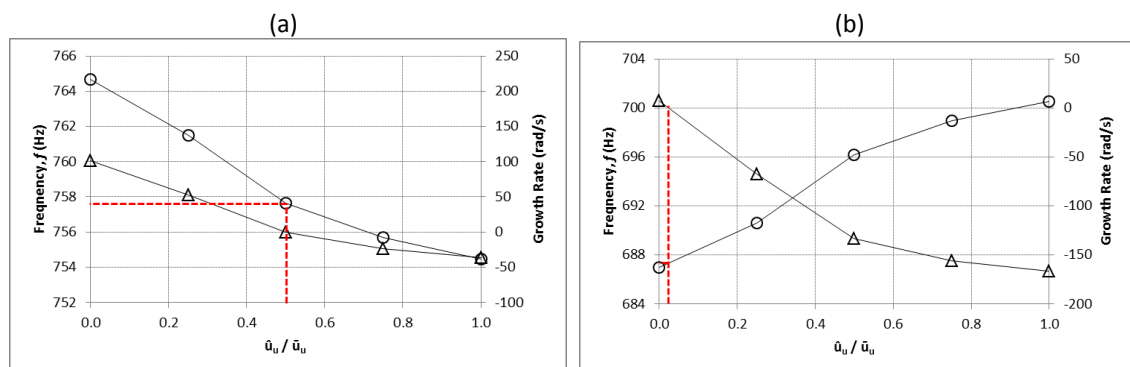


Figure 8.14: Predicted eigenvalues (circles) and growth rate (triangles) plotted against normalized velocity perturbation for HPGSB-2 at $T_2 = 900$ K, $P_2 = 1.5$ MPa with open (a) and convergent nozzle (b) confinement. Red lines mark the predicted limit cycle frequency and velocity perturbation.

8.4 Chapter Summary

An open source low order thermoacoustic modeling tool has been utilized to evaluate the longitudinal acoustic modes of the HPGSB-2 and downstream water-cooled piping under a number of operating conditions. Observed self-excited thermoacoustic instabilities in the HPGSB-2 have been selected for evaluation under conditions of varying P_2 , P_{therm} , \bar{u} , and fuel composition. In addition, the influence of burner confinement geometry has also been investigated with both cylindrical and convergent nozzle confinements input into the OSCILOS model to evaluate the experimentally observed decoupling of burner and flame acoustics with the convergent confinement. Both isothermal air flow and combustion conditions have been considered with both confinement geometries to identify system acoustics as well as flame-related acoustics. An n - τ linear FTF model was used to identify system eigenvalues and growth rates, and was found to show good agreement with the experimental observations using a time delay, τ , derived from experimental measurements of turbulence intensity, u' (from PIV), and heat release location (from OH* CL centroid calculation). Other key findings of this modeling study include:

- The n - τ model is able to predict the dominant frequencies in the acoustically coupled cases with the HPGSB-2 operated with open confinement within 5-6%, but under predicts the frequency values. It is also able to resolve the decoupling influence of the convergent confinement, showing an overall frequency shift towards negative growth rates (thus stable modes). However, it is unable to resolve the low frequency peaks in the decoupled cases. An improved FTF may be used in future work to better resolve the observed behavior of the convergent nozzle confinement.
- The model is able to resolve the observed shift in frequency with varying operating conditions, such as the reduction in peak harmonic frequency with a reduction in φ and P_{therm} . The model is also able to resolve the observed increase in instability frequency with H₂ addition. A number of non-resonant acoustic frequencies, which appear across burner operating conditions, can be approximated by the model.
- An FDF model which utilized a combination of the linear n - τ model and a nonlinear model was utilized to predict the amplitude and frequency for limit cycle establishment, with limit cycle frequency of 473 Hz in the BASE-O-8-0.2 case, 437 Hz in

the BASE-O-8-0.22 case, and 455 Hz in FARH2-O-8-0.22 case. These limit cycle frequencies, although under predicting the observed instability frequencies, follow the observed trends. In the $P_2 = 0.22$ MPa cases, 15% H_2 addition in CH_4 was predicted to reduce the limit cycle velocity perturbation amplitude by 10%.

- Extension of the FDF model to relevant GT operating conditions with a CH_4 -air flame at $\varphi = 0.55$ indicates an upward shift in limit cycle frequency (757.6 Hz) from the $P_2 = 0.22$ MPa case (437.7 Hz), which is to be expected due to the increase in T_2 and P_{therm} . A reduction in the velocity perturbation amplitude is noted. The use of the convergent confinement appears to dampen a number of unsteady modes identified in the open confinement case, with limit cycle amplitudes less than 0.05 for all modes.
- This study has only considered self-excited thermoacoustic instabilities. Further validation is warranted, including measurement of dynamic pressure fluctuations upstream of the burner inlet to validate the open boundary condition.

CHAPTER 9 – CONCLUSIONS AND FUTURE WORK

Gas turbine fuel flexibility will become even more important in years to come as domestic gas production declines and imports rise. And not only that, gas turbines will have to operate more flexibly as well, utilized for demand management in a generation landscape that is increasingly diverse and, perhaps not fully appreciated in its intermittency with renewable generation on the rise. It is no surprise, then, that GT operators and OEMs are currently designing and implementing engine control measures to adapt to variations in fuel composition. With LNG imports continuing to provide security of UK gas supply, and developing technologies such as P2G further integrated with the natural gas pipeline network, this thesis aimed to provide GT operators and OEMs with a comprehensive study of variable natural gas composition behavior under elevated operating conditions of temperature and pressure in an industrially-relevant swirl burner. In this brief Conclusion, the key findings of this study are highlighted along with a look forward to the future of gas turbine combustion study.

9.1 Facilities

The parametric experimental studies in this thesis were conducted in full at Cardiff University's Gas Turbine Research Centre. In the course of this study, new facilities have been designed, implemented, and optimized for the fundamental characterization of natural gas flame behavior under conditions of varying fuel composition and elevated operating conditions. These include the following:

- Two new generic swirl burners (HPGSB and HPGSB-2) have been designed and commissioned for the study of fully premixed flames at elevated temperature and pressure. In addition to isothermal and combustion experimentation on a full range of swirl numbers from $S_g = 0.5$ to $S_g = 1.47$, a novel quartz confinement with a convergent nozzle was designed and implemented for the enhanced representation of the turbine inlet transition duct influence on the flow field and acoustics. This apparatus was successfully commissioned and used for an extent of the experimental work, as it was identified to decouple the thermoacoustic instabilities observed with the cylindrical confinement, thus allowing for the isolation of fuel chemistry effects and turbulence effects on flame location, stability, and emissions.
- A highly repeatable and reliable experimental rig with precise control over air and fuel mass flow rates, burner inlet temperature, and burner inlet pressure.

9.2 Methodologies

A range of methodologies, both experimental and numeric, have been developed and utilized for the characterization of flame behavior, stability, thermoacoustics, and emissions. These include:

- Non-intrusive optical diagnostics, including OH* and CH* chemiluminescence and OH PLIF, which were utilized at the GTRC for the first time in the course of this study.
- A new dynamic pressure measurement system for quantification of burner and flame stability. This system aided in the observation of both LBO and thermoacoustic instabilities in the HPCR. The time varying dynamic pressure kurtosis was found to be adequate for identifying thermoacoustic and LBO instabilities at elevated temperature and pressure conditions.
- Image processing techniques have been developed for the quantification of key flame and flow characteristics under lean conditions including OH radical distribution within the reacting flame front, localized areas of heat release, flame thickness and area, as well as flow velocity, turbulence length scales and intensities. These measures have been utilized to quantify flame location, flame stabilization mechanisms, and stability transitions.
- Numerical methods including chemical kinetics modeling and thermoacoustic system model have been found to predict the experimental rig behavior. A new reaction zone thickness definition has been proposed based on modeled OH and CH mole fraction in a 1-D flame which is found to correlate positively with quantitative PLIF measures of flame thickness, area, and maximum intensity location. Thermoacoustic modeling with an open-source code was in good agreement with observed self-excited instabilities and peak frequency trends, although further refinement is needed.
- Non-dimensional Strouhal and Helmholtz number analysis has identified acoustic and hydrodynamic modes in the experimental burner, and support the use of the geometric swirl number as a method for data collapse across different burner geometries as a result of its influence on mean resultant flow velocities. This has allowed for dominant dynamic pressure frequency data collapse across swirl numbers, dynamic pressure amplitude collapse with varying swirl number, and improvement of an existing extinction Damkohler relationship modified to account for the influence of swirl on the LBO point.

9.3 Fuel Blends

In addition to studies with pure methane, propane, and a high-CO syngas, the focus of this study was natural gas fuel blends containing methane blended with higher hydrocarbons (typical of LNG) and hydrogen (for P2G applications). The following conclusions are made as a result of the combined experimental and numerical study of these fuel blends.

9.3.1 Methane-Higher Hydrocarbons

An experimental and chemical kinetics analysis was conducted on the influence of (i) variable C_2+ fuel content, (ii) flow turbulence parameters, and (iii) elevated ambient conditions on fully premixed CH_4 /air and CH_4-C_2+ /air flames. Elevated operating conditions range from P_{therm} to 126 kW, T_2 to 573 K and P_2 to 0.33 MPa. In addition to providing a parametric dataset for chemical kinetics reactor network and CFD modeling, the following conclusions are deduced:

- The fuel molar hydrogen to carbon ratio (H:C) appears to be a promising fundamental fuel property for the characterization of the flame behavior of fuel blends with varying composition. Data collapse across pure hydrocarbon fuels, fuel blends, operating conditions, and measures of interest (e.g. OH^* chemiluminescence intensity or dynamic pressure amplitude) was achieved with $(H:C)^3$ scaling.
- Ethane addition to methane appears to have a catalytic effect, promoting methane oxidation and resulting in upstream flame movement compared with 100% CH_4 fuel.
- The addition of C_2+ molecules was observed to have an overall damping effect on combustion noise amplitudes in an acoustically-uncoupled system.
- NO_x emissions appear to show a correlation with fuel H:C ratio and a nonmonotonic trend with P_2 . Similar nonmonotonic trends with P_2 were identified with normalized S_L , normalized theoretical reaction zone thickness, δ_t , and mean flame brush thickness calculated from OH PLIF measurements, δ_{flame} .
- The addition of C_2+ fuels to methane enhances fundamental measurements such as S_L and AFT. Modeled S_L is seen to increase by up to 20% with the addition of propane in the EMIX1 fuel blend. A key finding from this experimental work is the shift in thermo-diffusive behavior between pure CH_4 , which exhibits negative Markstein length at the equivalence ratio of interest while the blend with 13% propane has a positive Markstein length at the same condition. This thermo-diffusive behavior is thought to contribute to burner stability issues when operating with high C_2+ content fuel under lean conditions. LBO behavior suggests that fuels with increased C_2+ content are

unable to stabilize in areas of high stretch, such as the ORZ, despite increased S_L .

- A correlation between OH* chemiluminescence integral intensity, AFT, fuel H:C ratio, and P_2 is derived. Utilizing this correlation, theoretical I_{OH^*} values at 1.5 MPa (572 kW) in the HPGSB-2 could be predicted for a given C_{2+} containing fuel type and a range of AFT. This correlation could potentially provide support for onboard condition monitoring or fuel characterization.
- A power law correlation between combustion noise amplitudes and operating pressure (thus thermal power) is derived, taking into account the influence of fuel type (represented by H:C ratio). Utilizing this correlation, combustion noise amplitudes at 1.5 MPa (572 kW) in the HPGSB-2 could be predicted for a given C_{2+} containing fuel type.

9.3.2 Methane-Hydrogen

This study presents an experimental analysis of the influence of (i) burner confinement geometry, (ii) geometric swirl number, and (iii) elevated ambient conditions on fully premixed CH_4 /air and CH_4 - H_2 /air (85-15% vol) flames in terms of flame location, stability, and NO_x emissions in a new generic swirl-stabilized burner. Ambient operating conditions range from at P_{therm} to 126 kW, T_2 to 573 K and P_2 to 0.33 MPa. The following conclusions are deduced:

- H_2 addition to CH_4 allows for a lean shift in operability, attributed to its positive stretch rate influence and Lewis number effects. This lean shift could be utilized to offset the higher NO_x anticipated with H_2 blended fuels.
- A consistent trend across fuels showing slightly reduced NO_x production with reduced swirl number was identified. This is an important combustor design consideration for CH_4 - H_2 fuels, as it would allow operation at similar firing temperatures with reduced combustor pressure drop, provided there is adequate fuel-air premixing.
- For a fixed fuel type, changes in experimental burner confinement geometry from an open cylinder to convergent nozzle is shown to have a limited influence on flame stabilization location, with only a slight increase in flame angle attributed to a reduction of CRZ size, its downstream movement, and increased radial velocities, all consistent with numerical predictions. However, a significant reduction in pressure fluctuation levels is observed as the convergent confinement decoupled heat release and pressure fluctuations observed with the open confinement. This is thought to be the result of changes to the bulk flow field and CRZ influence, as shown by PIV measurements.

- Significant changes in flame stabilization location were observed for both fuel types as the geometric swirl number was reduced from 0.8 to 0.5. The flame is observed to stabilize along the shear layer in the $S_g = 0.8$ case, but stabilizes near the burner centerline with a much weaker CRZ established in the $S_g = 0.5$ case.
- A power law correlation between combustion noise amplitudes and $P2$ (thus thermal power) is derived, taking into account the influence of S_g on bulk flow resultant velocities, the influence of fuel type (represented by H:C ratio), and the influence of fuel reactivity (represented by S_L). Utilizing this correlation, predicted combustion noise amplitudes at 1.5 MPa (572 kW) in the HPGSB-2 would be reduced by almost 50% by the blending of up to 15% H_2 in CH_4 and operation at a higher burner swirl number compared to a low swirl burner operating on pure CH_4 .

9.4 Future Work

As a result of this thesis, a number of further studies are being considered. These include:

1. Further development of the OSCILOS acoustic model using nonlinear flame models or FDF developed from LES modeling.
2. Validation of the suggested reaction zone thickness model using CH/OH PLIF measurements.
3. Further validation of the H:C ratio and OH* correlation to determine if this could potentially be used as a burner control technique.
4. Parametric study of the influence of C_2+ molecules on the thermo-diffusive behavior of methane blends to identify the turning point in stretch rate behavior. This will perhaps inform GT operators who are monitoring their natural gas inlet compositions of an acceptable limit of C_2+ content in methane before thermo-diffusive behavior may affect the combustion process.
5. NO PLIF study of the generic swirl burner with varying natural gas fuel composition to determine NO_x formation locations in the reaction flow for validation of chemical reactor network models.
6. Nonmonotonic extinction strain rate behavior with CH_4-H_2 blends at pressure has been identified as part of the chemical kinetic modeling in this study. Validating this behavior fundamentally in a counterflow burner and in the swirl burner under pressurized conditions may help to identify instability transitions at elevated operating conditions.

REFERENCES

- [1] Lefebvre AH, Ballal, DR. *Gas Turbine Combustion: Alternative Fuels and Emissions*. 3rd ed. Boca Raton: CRC Press; 2010.
- [2] Flexible and Efficient Power Plant – Flex-E-Plant Consortium. Case for Support and Technical Annex. UK EPSRC Project EP/K021095/1.
- [3] United Kingdom Department for Business, Energy and Industrial Strategy. *Digest of UK Energy Statistics*. London; 2016.
- [4] International Energy Agency. *World Energy Outlook 2016 Executive Summary*. Paris; 2016.
- [5] United Nations Framework Convention on Climate Change. Paris Agreement. Article 2. Paris; 2015.
- [6] European Commission. Communication from the Commission to the European Parliament, the Council, the European Economic and Social Committee and the Committee of the Regions *Energy Roadmap 2050*. COM(2011) 885 Final. Brussels; 2011.
- [7] Gahleitner G. Hydrogen from renewable electricity: An international review of power-to-gas pilot plants for stationary applications. *Int J Hydrogen Energ*. 2013; 38(5): 2039-2061.
- [8] European Parliament. Directive 2010/75/EU of the European Parliament and of the Council of 24 November 2010 on Industrial Emissions (Integrated Pollution Prevention and Control). *Official Journal of the European Union*. OJ L334/17; 2010.
- [9] United Kingdom Parliament. *Climate Change Act 2008*. Chapter 27. London; 2008.
- [10] United Kingdom Department of Energy and Climate Change. *The Carbon Plan: Delivering our Low Carbon Future*. London; 2011.
- [11] United Kingdom Department of Energy and Climate Change. *60th Anniversary Digest of UK Energy Statistics*. London; 2009.
- [12] United Kingdom Department for Business, Energy and Industrial Strategy. *Digest of UK Energy Statistics*. London; 2012.
- [13] National Grid. *Future Energy Scenarios*. Warwick, United Kingdom; 2016.
- [14] Qadrdan M, Chaudry M, Jenkins N, Baruah P, Eyre N. Impact of transition to a low carbon power system on the GB gas network. *Appl Energ*. 2015; 151: 1-12.
- [15] Sadler D. H21 Leeds City Gate Report. Northern Gas Networks; 2016. [cited 08 Mar 2017]. Available from: <http://www.northerngasnetworks.co.uk/archives/document/h21-leeds-city-gate>
- [16] Abbott DJ, Bowers JP, James SR. The Impact of Natural Gas Composition Variations on the Operation of Gas Turbines for Power Generation. In: *The Future of Gas Turbine Technology*, 6th International Gas Turbine Conference; 2012 Oct 17-18; Brussels, Belgium.

- [17] Nag P, LaGrow M, Wu J, Abou-Jaoude K, Engel J. LNG Fuel Flexibility in Siemens' Land-Based Gas Turbine Operations. In: Electric Power Conference; 2007 May 1-3; Chicago, Illinois.
- [18] Zucca A, Forte A, Giannini N, Romano C, Modi R. Enlarging Fuel Flexibility for Frame 5 DLN: Combustor Operability and Emissions with High C₂₊ Content. In: Proceedings of ASME Turbo Expo 2015: Turbine Technical Conference and Exposition; 2015 Jun 15-19; Montréal, Canada.
- [19] United Kingdom Department for Business, Energy and Industrial Strategy. Digest of UK Energy Statistics. London; 2013.
- [20] United Kingdom Health and Safety Executive. Gas Safety (Management) Regulations 1996 – GS(M)R; 1996. [cited 18 May 2014] Available from: <http://www.legislation.gov.uk/uksi/1996/551/contents/made>
- [21] Armagnac, AP. Gas Turbines Promise – How searing flames are harnessed. Pop Sci. 1939; 135(6): 80-81, 236, 238.
- [22] GE Power. Powering a new record at EDF – 9HA.01 sets efficiency world record. GEA32885, General Electric Company. Schenectady (NY); 2016.
- [23] Siemens. Trail-blazing power plant technology. Fossil Power Generation Division Press Release. Erlangen (Germany); 2011.
- [24] Chase, DL, Kehoe PT. GE Combined-Cycle Product Line and Performance. GER-3574G, GE Power Systems. Schenectady (NY); 2000.
- [25] British Standards Institution. Natural gas — Calculation of calorific values, density, relative density and Wobbe index from composition. BS EN ISO 6976:2005. London; 2007.
- [26] Poloczek V, Hermsmeyer H. Modern Gas Turbines with High Fuel Flexibility. In: POWER-GEN Asia; 2008 Oct 21-23; Kuala Lumpur, Malaysia.
- [27] Jones R, Goldmeier J, Monetti B. Addressing Gas Turbine Fuel Flexibility. GER 4601(05/11) revB. GE Energy. Schenectady (NY); 2011.
- [28] Tanaka K, Nishida K, Akizuki W. Gas Turbine Combustor Technology Contributing to Environmental Conservation. Mitsubishi Heavy Industries Technical Review. 2009; 46:6-12.
- [29] Lieuwen T, McDonell V, Petersen E, Santavicca D. Fuel Flexibility Influences on Premixed Combustor Blowout, Flashback, Autoignition, and Stability. J Eng Gas Turb Power. 2008; 130(1): 011506-1-10.
- [30] Healy D, Curran HJ, Simmie JM, Kalitan DM, Zinner CM, Barrett AB, et al. Methane/ethane/propane mixture oxidation at high pressures and at high, intermediate and low temperatures. Combust Flame. 2008; 155(3): 441-448.
- [31] Won SH, Windom B, Jiang B, Ju Y. The role of low temperature fuel chemistry on turbulent flame propagation. Combust Flame. 2014; 161(2): 475-483.

- [32] Khalil EB, Karim G. A Kinetic Investigation of the Role of Changes in the Composition of Natural Gas in Engine Applications. *J Eng Gas Turb Power*. 2002; 124(2): 404-411.
- [33] Bourque G, Healy D, Curran H, Zinner C, Kalitan D, de Vries J, et al. Ignition and Flame Speed Kinetics of Two Natural Gas Blends With High Levels of Heavier Hydrocarbons. *J Eng Gas Turb Power*. 2009; 132(2): 021504-1-11.
- [34] Holton MM, Gokulakrishnan P, Klassen MS, Roby RJ, Jackson GS. Autoignition Delay Time Measurements of Methane, Ethane, and Propane Pure Fuels and Methane-Based Fuel Blends. *J Eng Gas Turb Power*. 2010; 132(9): 091502-1-9.
- [35] Petersen EL, Kalitan DM, Simmons S, Bourque G, Curran HJ, Simmie J. Methane/propane oxidation at high pressures: Experimental and detailed chemical kinetic modeling. *P Combust Inst*. 2007; 31(1): 447-454.
- [36] Tseng LK, Ismail MA, Faeth GM. Laminar burning velocities and Markstein numbers of hydrocarbon air flames. *Combust Flame*. 1993; 95(4): 410-426.
- [37] Kochar Y, Lieuwen T, Seitzman J. 2009. Laminar Flame Speeds of C1-C3 Alkanes at Elevated Pressure and Temperature. In: *Proceedings of the 6th U.S. National Combustion Meeting*; 2009 May 17-20; Ann Arbor, Michigan.
- [38] Blomstedt M, Larsson A. SGT-700 DLE Combustion System Extending the Fuel Flexibility. In: *21st Symposium of the Industrial Application of Gas Turbines Committee*; 2015 Oct 19-21; Banff, Alberta, Canada.
- [39] Ferguson D, Straub D, Richards G, Robey E. Impact of Fuel Variability on Dynamic Instabilities in Gas Turbine Combustion. In: *Proceedings of the 5th U.S. National Combustion Meeting*; 2007 Mar 25-28; San Diego, California.
- [40] Flores R, McDonnell V, Samuelsen G. Impact of Ethane and Propane Variation in Natural Gas on the Performance of a Model Gas Turbine Combustor. *J Eng Gas Turb Power*. 2003; 125(3): 701-708.
- [41] ITM electrolyser adds first P2G hydrogen to German gas grid. *Fuel Cells Bulletin*. 2014; 1: 8-9.
- [42] Melaina M, Antonia O, Penev M. Blending Hydrogen into Natural Gas Pipeline Networks: A Review of Key Issues. Technical Report NREL/TP-5600-51995, US Department of Energy National Renewable Energy Laboratory; 2013.
- [43] Ajayi-Oyakhire O. Hydrogen - Untapped Energy? Institution of Gas Engineers and Managers. Kegworth (UK); 2012.
- [44] Benim AC, Syed KJ. Flashback Mechanisms in Lean Premixed Gas Turbine Combustion. Boston: Academic Press; 2015.
- [45] Gauducheau JL, Denet B, Searby G. A Numerical Study of Lean CH₄/H₂/Air Premixed Flames at High Pressure. *Combust Sci Technol*. 1998; 137: 81-99.

- [46] Chen Z. Effects of hydrogen addition on the propagation of spherical methane/air flames: A computational study. *Int J Hydrogen Energ.* 2009; 34(15): 6558-6567.
- [47] Bradley D, Lawes M, Mumby R. Burning velocity and Markstein length blending laws for methane/air and hydrogen/air blends. *Fuel.* 2017; 187: 268-275.
- [48] Halter F, Chauveau C, Gökalp I. Characterization of the effects of hydrogen addition in premixed methane/air flames. *Int J Hydrogen Energ.* 2007; 32(13): 2585-2592.
- [49] Fairweather M, Ormsby M, Sheppard C, Woolley R. Turbulent burning rates of methane and methane-hydrogen mixtures. *Combust Flame.* 2009; 156(4): 780-790.
- [50] Zhang Y, Huang Z, Wei L, Zhang J, Law CK. Experimental and modeling study on ignition delays of lean mixtures of methane, hydrogen, oxygen, and argon at elevated pressures. *Combust Flame.* 2012; 159(3): 918-931.
- [51] Lapalme D, Lemaire R, Seers P. Assessment of the method for calculating the Lewis number of H₂/CO/CH₄ mixtures and comparison with experimental results. *Int J Hydrogen Energ.* Article in Press 2017.
- [52] Bouvet N, Halter F, Chauveau C, Yoon Y. On the effective Lewis number formulations for lean hydrogen/hydrocarbon/air mixtures. *Int J Hydrogen Energ.* 2013; 38(14): 5949-5960.
- [53] Bagdanavicius A, Bowen P, Bradley D, Lawes M, Mansour M. Stretch rate effects and flame surface densities in premixed turbulent combustion up to 1.25 MPa. *Combust Flame.* 2015; 162(11): 4158-4166.
- [54] Bagdanavicius A, Bowen P, Syred N, Crayford A. Turbulent Flame Structure of Methane-Hydrogen Mixtures at Elevated Temperature and Pressure. *Combust Sci Technol.* 2013; 185(2): 350-361.
- [55] Syred N, Giles A, Lewis J, Abdulsada M, Valera-Medina A, Marsh R, Bowen P, et al. Effect of Inlet and Outlet Configurations on Blow-off and Flashback with Premixed Combustion for Methane and a High Hydrogen Content Fuel in a Generic Swirl Burner. *Appl Energ.* 2014; 116: 288-296.
- [56] Abdulsada M, Syred N, Bowen P, O'Doherty T, Griffiths A, Marsh R, et al. Effect of exhaust confinement and fuel type upon the blowoff limits and fuel switching ability of swirl combustors. *Appl Therm Eng.* 2012; 48: 426-435.
- [57] Syred N, Abdulsada M, Griffiths A, O'Doherty T, Bowen P. The effect of hydrogen containing fuel blends upon flashback in swirl burners. *Appl. Energ.* 2012; 89(1): 106-110.
- [58] Lieuwen, TC. Physics of Premixed Combustion-Acoustic Wave Interactions. In: Lieuwen, TC, Yang, V editors. *Combustion Instabilities in Gas Turbine Engines. Progress in Astronautics and Aeronautics.* 2005; 210: 315-366.
- [59] Huang Y, Yang V. Dynamics and stability of lean-premixed swirl-stabilized combustion. *Prog Energy Combust.* 2009; 35(4): 293-364.

- [60] Syred, N. A review of oscillation mechanisms and the role of the precessing vortex core (PVC) in swirl combustion systems. *Prog Energ Combust.* 2006; 32(2): 93-161.
- [61] Strakey, P, Sidwell, T, Ontko, J. Investigation of the effects of hydrogen addition on lean extinction in a swirl stabilized combustor. *P Combust Inst.* 2007; 31(2): 3173-3180.
- [62] Boxx I, Carter CD, Stöhr M, Meier W. Study of the mechanisms for flame stabilization in gas turbine model combustors using kHz laser diagnostics. *Exp Fluids.* 2013; 54(5): 1532.
- [63] Boxx I, Arndt C, Carter C, Meier W. Highspeed LASER diagnostics for the study of flame dynamics in a lean premixed gas turbine model combustor. In: 15th International Symposium on the Applications of Laser Techniques in Fluid Mechanics; 2010 Jul 5-8; Lisbon, Portugal.
- [64] Boxx I, Slabaugh C, Kutne P, Lucht RP, Meier W. 3 kHz PIV/OH-PLIF measurements in a gas turbine combustor at elevated pressure. *P Combust Inst.* 2015; 35(3): 3793-3802.
- [65] Shanbhogue SJ, Sanusi YS, Taamallah S, Habib MA, Mokheimer EMA, Ghoniem AF. Flame macrostructures, combustion instability, and extinction strain scaling in swirl-stabilized premixed CH₄/H₂ combustion. *Combust Flame.* 2016; 163: 494-507.
- [66] Lieuwen TC. *Unsteady Combustor Physics.* Cambridge: Cambridge University Press; 2012.
- [67] Brade, P. Gas turbine operation and combustion performance issues. In: Jansohn, P, editor. *Modern gas turbine systems: high efficiency, low emission, fuel flexible power generation.* Cambridge: Woodhead Publishing; 2013.
- [68] Chakravarthy SR, Shreenivasan OJ, Boehm B, Dreizler A, Janicka J. Experimental characterization of onset of acoustic instability in a nonpremixed half-dump combustor. *J Acoust Soc Am.* 2007; 122(1): 120-127.
- [69] Fritsche D, Füre M, Boulouchos K. An experimental investigation of thermoacoustic instabilities in a premixed swirl-stabilized flame. *Combust Flame.* 2007; 151(1-2): 29-36.
- [70] Nicoud F, Poinot T. Thermoacoustic instabilities: Should the Rayleigh criterion be extended to include entropy changes? *Combust Flame.* 2005; 142(1-2): 153-159.
- [71] Keller J. Thermoacoustic Oscillations in Combustion Chambers of Gas Turbines. *AIAA J.* 1995; 33(12): 2280-2287.
- [72] Hubschmid W, Bombach R, Inauen A, Güthe F, Schenker S, Tylli N, et al. Thermoacoustically driven flame motion and heat release variation in a swirl-stabilized gas turbine burner investigated by LIF and chemiluminescence. *Exp Fluids.* 2008; 45(1): 167-182.
- [73] Arndt C, Severin M, Dem C, Stöhr M, Steinberg A, Meier W. Experimental analysis of thermo-acoustic instabilities in a generic gas turbine combustor by phase-correlated PIV, chemiluminescence, and laser Raman scattering measurements. *Exp Fluids.* 2015; 56: 69.
- [74] Nair S, Lieuwen T. Acoustic Detection of Blowout in Premixed Flames. *J Propul Power.* 2005; 21(1); 32-39.

- [75] Muruganandam T, Nair S, Neumeier Y, Lieuwen T, Seitzman J. Optical and Acoustic Sensing of Lean Blowout Precursors. In: 38th AIAA/ASME/SAE/ASEE Joint Propulsion Conference and Exhibit; 2002 Jul 7-10; Indianapolis, Indiana.
- [76] Prakash S, Nair S, Muruganandam T, Neumeier Y, Lieuwen T, Seitzman J, et al. Acoustic Sensing and Mitigation of Lean Blow Out In Premixed Flames. In: 43rd Aerospace Sciences Meeting; 2005 Jan 10-13; Reno, Nevada.
- [77] Bompelly R, Lieuwen T, Seitzman J. Lean Blowout and its Sensing in the Presence of Combustion Dynamics in a Premixed Swirl Combustor. In: 47th Aerospace Sciences Meeting; 2009 Jan 5-8; Orlando, Florida.
- [78] Taupin B, Vauchelle D, Cabot G, Boukhalfa A. Experimental study of lean premixed turbulent combustion. In: 11th International Symposium on Applications of Laser Techniques to Fluid Mechanics; 2002 Jul 8-11; Lisbon, Portugal.
- [79] Cabot G, Vauchelles D, Taupin B, Boukhalfa A. Experimental study of lean premixed turbulent combustion in a scale gas turbine chamber. *Exp Therm Fluid Sci.* 2004; 28: 683-690.
- [80] De Zilwa SRN, Uhm JH, Whitelaw JH. Combustion Oscillations Close to the Lean Flammability Limit. *Combust Sci Tech.* 2000; 160(1): 231-258.
- [81] Mongia HC, Held TJ, Hsiao GC, Pandalai RP. Incorporation of Combustion Instability Issues into Design Process: GE Aero-derivative and Aero Engines Experience. In: Lieuwen T, Yang V, editors. *Combustion Instabilities in Gas Turbine Engines: Operational Experience, Fundamental Mechanisms, and Modeling.* Prog Astronaut Aero. 2005; p. 43-64.
- [82] Sewell JB, Sobieski PA. Monitoring of Combustion Instabilities: Calpine's Experience. In: Lieuwen T, Yang V, editors. *Combustion Instabilities in Gas Turbine Engines: Operational Experience, Fundamental Mechanisms, and Modeling.* Prog Astronaut Aero. 2005; p. 147-162.
- [83] Stöhr M, Boxx I, Careter C, Meier W. Dynamics of lean blowout of a swirl-stabilized flame in a gas turbine model combustor. *P Combust Inst.* 2011; 33(2): 2953-2960.
- [84] Kariuki J, Dowlut A, Yuan R, Balachandran R, Mastorakos E. Heat release imaging in turbulent premixed methane-air flames close to blow-off. *P Combust Inst.* 2015; 35(2): 1443-1450.
- [85] Norton DG, Vlachos DG. Combustion characteristics and flame stability at the microscale: a CFD study of premixed methane/air mixtures. *Chem Eng Sci.* 2003; 58(21): 4871-4882.
- [86] Tuncer O, Acharya S, Uhm J. Dynamics, NO_x and flashback characteristics of confined premixed hydrogen-enriched methane flames. *Int J Hydrogen Energ.* 2009; 34(1): 496-506.
- [87] Griebel P, Boschek E, Jansohn P. Lean Blowout Limits and NO_x Emissions of Turbulent, Lean Premixed, Hydrogen-Enriched Methane/Air Flames at High Pressure. *J Eng Gas Turb Power.* 2006; 129(2): 404-410.
- [88] Radhakrishnan K, Heywood JB. Premixed turbulent flame blowoff velocity correlation based on coherent structures in turbulent flows. *Combust Flame.* 1981; 42: 19-33.

- [89] Cavaliere DE, Kariuki J, Mastorakos E. A Comparison of the Blow-Off Behaviour of a Swirl-Stabilized Premixed, Non-Premixed and Spray Flames. *Flow Turb Combust.* 2013; 91(2): 347-372.
- [90] Al-Abdeli YM, Masri AR. Review of laboratory swirl burners and experiments for model validation. *Exp Therm Fluid Sci.* 2015; 69: 178-196.
- [91] McDonell V. Lean Combustion in Gas Turbines. In: Dunn-Rankin D, editor. *Lean Combustion Technology and Control.* Burlington: Academic Press; 2008. p. 121-160.
- [92] Beerer D, McDonell V, Therkelsen P, Cheng R. Flashback and Turbulent Flame Speed Measurements in Hydrogen/Methane Flames Stabilized by a Low-Swirl Inject at Elevated Pressures and Temperatures. *J Eng Gas Turb Power.* 2013; 136(3): 031502-1-9.
- [93] Emadi M, Karkow D, Salameh T, Gohil A, Ratner A. Flame structure changes resulting from hydrogen-enrichment and pressurization for low-swirl premixed methane-air flames. *Int J Hydrogen Energ.* 2012; 37(13): 10397-10404.
- [94] Stopper U, Aigner M, Meier W, Sadanandan R, Stöhr M, Kim, IS. Flow Field and Combustion Characterization of Premixed Gas Turbine Flames by Planar Laser Techniques. *J Eng Gas Turb Power.* 2008; 131(2): 021504-1-8.
- [95] Stopper U, Meier W, Sadanandan R, Stöhr M, Aigner M, Bulat G. Experimental study of industrial gas turbine flames including quantification of pressure influence on flow field, fuel/air premixing and flame shape. *Combust Flame.* 2013; 160(10): 2013-2118.
- [96] Kido H, Nakahara M, Hashimoto J, Barat D. Turbulent Burning Velocities of Two-Component Fuel Mixtures of Methane, Propane, and Hydrogen. *JSME Int J B-Fluid T.* 2002; 45(2): 355-362.
- [97] Tseng, LK, Ismail, MA, Faeth, GM. Laminar Burning Velocities and Markstein Numbers of Hydrocarbon / Air Flames. *Combust Flame.* 1993; 95(4): 410-426.
- [98] Aung, KT, Tsend, LK, Ismail, MA, Faeth, GM. Response to comment by S.C. Taylor and D.B. Smith on "Laminar Burning Velocities and Markstein Numbers of Hydrocarbon / Air Flames." *Combust Flame.* 1995; 102(4): 526-530.
- [99] Aung, KT, Hassan, MI, Faeth, GM. Flame Stretch Interactions of Laminar Premixed Hydrogen/Air Flames at Normal Temperature and Pressure. *Combust Flame.* 109(1-2): 1-24.
- [100] Walsh, PP, Fletcher, P. *Gas Turbine Performance.* 2nd ed. Oxford: Blackwell Science; 2004.
- [101] Schefer RW, White C, Keller J. Lean Hydrogen Combustion. In: Dunn-Rankin D, editor. *Lean Combustion Technology and Control.* Burlington: Academic Press; 2008. p. 121-160.
- [102] Pillier L, El Bakali A, Mercier X, Rida A, Pauwels JF, Desgroux P. Influence of C2 and C3 compounds of natural gas on NO formation: an experimental study based on LIF/CRDS coupling. *P Combust Inst.* 2005; 30(1): 1183-1191.

- [103] Hack R, McDonell V. Impact of Ethane, Propane, and Diluent Content in Natural Gas on the Performance of a Commercial Microturbine Generator. *J Eng Gas Turb Power*. 2008; 130(1): 011509-1-7.
- [104] Straub D, Ferguson D, Castleton K, Richards G. Effects of Propane/Natural Gas Blended Fuels on Gas Turbine Pollutant Emissions. In: *Proceedings of the 5th U.S. National Combustion Meeting*; 2007 Mar 25-28; San Diego, California.
- [105] Lantz A, Collin R, Aldén M, Lindholm A, Larfeldt J, Lörstam D. Investigation of Hydrogen Enriched Natural Gas Flames in a SGT-700/800 Burner Using OH PLIF and Chemiluminescence Imaging. *J Eng Gas Turb Power*. 2015; 137(3): 031505-1-8.
- [106] Sevensco Y, Mojarrad MG, Marsh R, Morris S, Bowen PJ, Syred N. Integrating Hypersonics into a Combustion Test Facility with 3D Viewing Capability. In: *20th AIAA International Space Planes and Hypersonic Systems and Technologies Conference*; 2015 Jul 6-9; Glasgow, Scotland.
- [107] Syred N, Morris SM, Bowen PJ, Valera-Medina A, Marsh R. Preliminary Results from a High Pressure Optical Gas Turbine Combustor Model with 3D Viewing Capability. In: *53rd AIAA Aerospace Sciences Meeting*; 2014 Jan 5-9; Kissimmee, Florida.
- [108] Lewis J, Marsh R, Valera-Medina, A, Morris S, Baej H. The Use of CO₂ to Improve Stability and Emissions of an IGCC Combustor. In: *Proceedings of ASME Turbo Expo 2014: Turbine Technical Conference and Exposition*; 2014 Jun 16-20; Düsseldorf, Germany.
- [109] Morris, S. Cardiff University Progress Report July 2013. European Turbine Network FP7 H2-IGCC Project. 2013.
- [110] Giles A, Marsh R, Bowen PJ, Valera-Medina A. Applicability of the Peclet number approach to blow-off and flashback limits of common steelworks process gases. *Fuel*. 2016; 182: 531-540.
- [111] Valera-Medina A, Baej H. Hydrodynamics During the Transient Evolution of Open Jet Flows from/to Wall Attached Jets. *Flow Turbul Combust*. 2016; 97(3): 743-760.
- [112] Runyon J, Marsh R, Valera-Medina A, Giles A, Morris S, Pugh D, et al. Methane-Oxygen Flame Stability in a Generic Premixed Gas Turbine Swirl Combustor at Varying Thermal Power and Pressure. In: *Proceedings of ASME Turbo Expo 2015: Turbine Technical Conference and Exposition*; 2015 Jun 15-19; Montreal, Canada.
- [113] Pugh DG, Bowen PJ, Marsh R, Crayford AP, Runyon J, Morris S, et al. Dissociative influence of H₂O vapour/spray on lean blowoff and NO_x reduction for heavily carbonaceous syngas swirling flames. *Combust Flame*. 2017; 177: 37-48.
- [114] Marsh R, Runyon J, Giles A, Morris S, Pugh D, Valera-Medina A, et al. Premixed methane oxycombustion in nitrogen and carbon dioxide atmospheres: measurement of operating limits, flame location and emissions. *P Combust Inst*. 2017; 36(3): 3949-3958.
- [115] Valera-Medina A, Marsh R, Runyon J, Pugh D, Beasley P, Hughes T, et al. Ammonia-methane combustion in tangential swirl burners for gas turbine power generation. *Appl Energ*. 2017; 185(2): 1362-1371.

- [116] Kurji H, Valera-Medina A, Runyon J, Giles A, Pugh D, Marsh R, et al. Combustion characteristics of biodiesel saturated with pyrolysis oil for power generation in gas turbines. *Renew Energ.* 2016; 99: 443-451.
- [117] Valera-Medina A, Morris S, Runyon J, Pugh DG, Marsh R, Beasley P, et al. Ammonia, Methane and Hydrogen for Gas Turbines. *Energ Proced.* 2015; 75: 118-123.
- [118] Runyon J, Marsh R, Morris S, Giles A, Pugh D, Bowen P. Fuel Flexibility for Industrial Gas Turbine Generation: Effects of Higher-Hydrocarbon Variation in Natural Gas on Swirling Flame Stability. In: 9th International Charles Parsons Turbine and Generator Conference; 2015 Sep 15-17; Loughborough, United Kingdom.
- [119] Runyon J, Marsh R, Sevcenco Y, Pugh D, Morris S. Development and Commissioning of a Chemiluminescence Imaging System for an Optically-Accessible High-Pressure Generic Swirl Burner. In: Proceedings of the 7th European Combustion Meeting; 2015 Mar 30 – Apr 2; Budapest, Hungary.
- [120] Buffi, M, Valera-Medina A, Runyon J, Pugh D, Giles A, Marsh R, et al. Evaluation of Combustion Behavior of Renewable Jet Fuel in a Combustor Rig: Influence of HEFA and its Blends on Flame Stability and Emissions Compared to Aviation Kerosene. In: 24th European Biomass Conference & Exhibition; 2016 Jun 6-9; Amsterdam, Netherlands.
- [121] Valera-Medina A, Morris S, Runyon J, Pugh D, Marsh R, Beasley P. Ammonia, Methane and Hydrogen for Gas Turbines. In: Clean, Efficient and Affordable Energy for a Sustainable Future: The 7th International Conference on Applied Energy (ICAE2015); 2015 Mar 28-31; Abu Dhabi, United Arab Emirates.
- [122] Marsh R, Giles A, Runyon J, Pugh D, Bowen P, Valera-Medina A, et al. Selective exhaust gas recycling for carbon capture applications: combustion and operability measurement. In: 8th International Gas Turbine Conference – The Future of Gas Turbine Technology; 2016 Oct 12-13; Brussels, Belgium.
- [123] Runyon J, Marsh R, Pugh D, Bowen P, Giles A, Morris S, et al. Experimental Analysis of Confinement and Swirl Effects on Premixed CH₄-H₂ Flame Behavior in a Pressurized Generic Swirl Burner. In: Proceedings of ASME Turbo Expo 2017: Turbomachinery Technical Conference and Exposition; 2017 Jun 26-30; Charlotte, North Carolina.
- [124] Runyon J, Marsh R, Bowen P, Pugh D, Giles A, Morris S. Premixed CH₄-H₂ flame behavior in pressurized generic swirl burner for power-to-gas applications. In: International Flame Research Foundation Topic Oriented Technical Meeting (TOTeM) 44; 2017 Mar 14-15; Essen, Germany.
- [125] Runyon J, Marsh R, Bowen P, Pugh D, Giles A, Morris S. Influence of higher hydrocarbons in LNG on natural gas flame stability under elevated conditions. In: International Flame Research Foundation Topic Oriented Technical Meeting (TOTeM) 44; 2017 Mar 14-15; Essen, Germany.

- [126] Pugh D, Bowen P, Crayford A, Marsh R, Runyon J, Morris S, et al. Catalytic Influence of Water Vapour on Lean Blowoff and NO_x Reduction for Pressurised Swirling Syngas Flames. In: Proceedings of ASME Turbo Expo 2017: Turbomachinery Technical Conference and Exposition; 2017 Jun 26-30; Charlotte, North Carolina.
- [127] Orbay RC, Nogenmyr KJ, Klingmann J, Bai XS. Swirling turbulent flows in a combustion chamber with and without heat release. *Fuel*. 2013; 104: 133-146.
- [128] Wu Y, Carlsson C, Szasz R, Peng L, Fuchs L, Bai, XS. Effect of geometrical contraction on vortex breakdown of swirling turbulent flow in a model combustor. *Fuel*. 2016; 170: 210-225.
- [129] Fritsche, D. Origin and Control of Thermoacoustic Instabilities in Lean Premixed Gas Turbine Combustion [PhD Thesis]. Swiss Federal Institute of Technology Zurich; 2005.
- [130] De Rosa AJ, Peluso SJ, Quay BD, Santavicca DA. The Effect of Confinement on the Structure and Dynamic Response of Lean-Premixed, Swirl-Stabilized Flames. *J Eng Gas Turb Power*. 2015; 138(6): 061507-1-10.
- [131] Taamallah S, LaBry ZA, Shanbhogue SJ, Ghoniem AF. Thermo-acoustic instabilities in lean premixed swirl-stabilized combustion and their link to acoustically coupled and decoupled flame macrostructures. *P Combust Inst*. 2015; 35(3): 3273-3282.
- [132] Kewlani G, Shanbhogue S, Ghoniem A. Investigation into the Impact of the Equivalence Ratio on Turbulent Premixed Combustion using Particle Image Velocimetry and Large Eddy Simulation Techniques: "V" and "M" Flame Configurations in a Swirl Combustor. *Energ Fuel*. 2016; 30(4): 3451-3462.
- [133] Weigand P, Meier W, Duan XR, Giezendanner-Thoben R, Meier U. Laser Diagnostic Study of the Mechanism of a Periodic Combustion Instability in a Gas Turbine Model Combustor. *Flow Turbul Combust*. 2005; 75(1): 275-292.
- [134] Komarek T, Polifke W. Impact of Swirl Fluctuations on the Flame Response of a Perfectly Premixed Swirl Burner. *J Eng Gas Turb Power*. 2010; 132(6): 061503-1-7.
- [135] Tay-Wo-Chong L, Polifke W. Large Eddy Simulation-Based Study of the Influence of Thermal Boundary Condition and Combustor Confinement on Premix Flame Transfer Functions. *J Eng Gas Turb Power*. 2013; 135(2): 021502-1-9.
- [136] Mordaunt, CJ, Pierce WC. Design and preliminary results of an atmospheric-pressure model gas turbine combustor utilizing varying CO₂ doping concentration in CH₄ to emulate biogas combustion. *Fuel*. 2014; 124: 258-268.
- [137] Bedick CR, Weiland NT, Strakey PA. Swirling and Non-Swirling Diffusion Flame Velocity Measurements in a Model Validation Combustor. In: Proceedings of the 8th U.S. National Combustion Meeting; 2013 May 19-22; Park City, Utah.
- [138] Kim KT. Combustion instability feedback mechanisms in a lean-premixed swirl-stabilized combustor. *Combust Flame*. 2016; 171: 137-151.

- [139] Schildmacher KU, Hoffmann A, Selle L, Koch R, Schulz C, Bauer HJ, et al. Unsteady flame and flow field interaction of a premixed model gas turbine burner. *P Combust Inst.* 2007; 31(2): 3197-3205.
- [140] Chong CT, Kew CW, Jo-Han N, Tee BT, Jaafar MNM. Effect of Nitrogen Dilution on the Lean Blowout Limit and Emissions of Premixed Propane/Air Swirl Flame. *Jurnal Teknologi.* 2014; 71(2): 79-84.
- [141] Reichel TG, Terhaar S, Paschereit O. Increasing Flashback Resistance in Lean Premixed Swirl-Stabilized Hydrogen Combustion by Axial Air Injection. *J Eng Gas Turb Power.* 2015; 137(7): 071503-1-9.
- [142] Therkelsen PL, Portillo JE, Littlejohn D, Martin SM, Cheng RK. Self-induced unstable behaviors of CH₄ and H₂/CH₄ flames in a model combustor with a low-swirl injector. *Combust Flame.* 2013; 160(2): 307-321.
- [143] Palies P, Durox D, Schuller T, Candel S. Experimental Study on the Effect of Swirler Geometry and Swirl Number on Flame Describing Functions. *Combust Sci Tech.* 2011; 183(7): 704-717.
- [144] Park J, Lee MC. Combustion instability characteristics of H₂/CO/CH₄ syngases and synthetic natural gases in a partially-premixed gas turbine combustor: Part I – Frequency and mode analysis. *Int J Hydrogen Energ.* 2016; 41(8): 7484-7493.
- [145] Kraus C, Harth S, Bockhorn H. Experimental investigation of combustion instabilities in lean swirl-stabilized partially-premixed flames in single- and multiple-burner setup. *Int J Spray Combust.* 2016; 8(1): 4-26.
- [146] Meier W, Dem C, Arndt, CM. Mixing and reaction progress in a confined swirl flame undergoing thermo-acoustic oscillations studied with laser Raman scattering. *Exp Therm Fluid Sci.* 2016; 73: 71-78.
- [147] Sayad P, Schönborn A, Klingmann J. Experimental investigation of the stability limits of premixed syngas-air flames at two moderate swirl numbers. *Combust Flame.* 2016; 164: 270-282.
- [148] Mokheimer EMA, Sanusi YS, Habib MA. Numerical study of hydrogen-enriched methane-air combustion under ultra-lean conditions. *Int J Energ Res.* 2016; 40(6): 743-762.
- [149] Williams TC, Schefer RW, Oefelein JC, Shaddix CR. Idealized gas turbine combustor for performance research and validation of large eddy simulations. *Rev Sci Instrum.* 2007; 78(3): 035114.
- [150] Galley D, Ducruix S, Lacas F, Veyante D. Mixing and stabilization study of a partially premixed swirling flame using laser induced fluorescence. *Combust Flame.* 2011; 158(1): 155-171.

- [151] Hedman PO, Fletcher TH, Flores DV, Graham SG, Haslam JK, Murray RL, et al. Observations of Flame Behavior in a Laboratory-Scale Premixed Natural Gas/Air Gas Turbine Combustor From Planar Laser Induced Fluorescence Measurements of OH, Laser Doppler Anemometer Velocity Measurements, and Coherent Anti-Stokes Raman Spectrometer Temperature Measurements. *J Eng Gas Turb Power*. 2004; 127(4): 724-739.
- [152] Tao W, Mazur M, Huet M, Richecoeur F. Indirect Combustion Noise Contributions in a Gas Turbine Model Combustor with a Choked Nozzle. *Combust Sci Tech*. 2016; 188(4-5): 793-804.
- [153] Zhang Q, Noble DR, Lieuwen T. Characterization of Fuel Composition Effects in H₂/CO/CH₄ Mixtures Upon Lean Blowout. *J Eng Gas Turb Power*. 2006; 129(3): 688-694.
- [154] Noble DR, Zhang Q, Shareef A, Tootle J, Meyers A, Lieuwen T. Syngas Mixture Composition Effects Upon Flashback and Blowout. In: *Proceedings of ASME Turbo Expo 2006: Power for Land, Sea, and Air*; 2006 May 8-11; Barcelona, Spain.
- [155] Broda JC, Seo S, Santoro RJ, Shirhattikar G, Yang V. An experimental study of combustion dynamics of a premixed swirl injector. *Symposium (International) on Combustion*. 1998; 27(2): 1849-1856.
- [156] Lartigue G, Meier U, Bérat, C. Experimental and numerical investigations of self-excited combustion oscillations in a scaled gas turbine combustor. *App Therm Eng*. 2004; 24(11-12): 1583-1592.
- [157] Sidwell T, Richards G, Casleton K, Straub D, Maloney D, Strakey P, et al. Optically Accessible Pressurized Research Combustor for Computational Fluid Dynamics Model Validation. *AIAA J*. 2006; 44(3): 434-443.
- [158] Strakey PA, Woodruff SD, Williams TC, Schefer RW. OH-Planar Fluorescence Measurements of Pressurized, Hydrogen Premixed Flames in the SimVal Combustor. *AIAA J*. 2008; 46(7): 1604-1613.
- [159] Sadanandan R, Kutne P, Steinberg A, Meier W. Investigation of the Syngas Flame Characteristics at Elevated Pressures Using Optical and Laser Diagnostic Methods. *Flow Turb Combust*. 2012; 89(2): 275-294.
- [160] Syred N, Beér JM. Combustion in Swirling Flows: A Review. *Combust Flame*. 1974; 23(2): 143-201.
- [161] Kychakoff G, Howe RD, Hanson RK, Drake MC, Pitz RW, Lapp M, et al. Visualization of Turbulent Flame Fronts with Planar Laser-Induced Fluorescence. *Science*. 1984; 224(4647): 382-384.
- [162] Daily JW. Laser Induced Fluorescence Spectroscopy in Flames. *Prog Energy Combust*. 1997; 23(2): 133-199.
- [163] Barlow RS. Laser diagnostics and their interplay with computations to understand turbulent combustion. *P Combust Inst*. 2007; 31(1): 49-75.

- [164] Wolfrum J. Lasers in combustion: From basic theory to practical devices. Symposium (International) on Combustion. 1998; 1-41.
- [165] Guethe F, Guyot D, Singla G, Noiray N, Schuermans B. Chemiluminescence as a diagnostics tool in the development of gas turbines. *Appl Phys B-Lasers O*. 2012; 107(3): 619-636.
- [166] Witzel B, Huth M, Schulz C. Application of optical diagnostics as an experimental tool for the development of combustors for stationary gas turbines. *VGB PowerTech*. 2014; 12: 39-45.
- [167] Lauer M, Zellhuber M, Sattelmayer T, Aul CJ. Determination of the Heat Release Distribution in Turbulent Flames by a Model Based Correction of OH* Chemiluminescence. *J Eng Gas Turb Power*. 2011; 133(12): 121501-1-8.
- [168] Pugh D. Combustion Characterisation of Compositionally Dynamic Steelworks Gases [PhD Thesis]. Cardiff University; 2013.
- [169] Pugh DG, Crayford AP, Bowen PJ, Al-Naama M. Parametric investigation of water loading on heavily carbonaceous syngases. *Combust Flame*. 2016; 164: 126-136.
- [170] Broida HP, Gaydon AG. The Mechanism of Formation of OH, CH, and HCO in Flame Spectra, Using Deuterium as Tracer. *Proc R Soc Lond A*. 1953; 218(1132): 60-69.
- [171] Panoutsos CS, Hardalupas Y, Taylor AMKP. Numerical evaluation of equivalence ratio measurement using OH* and CH* chemiluminescence in premixed and non-premixed methane-air flames. *Combust Flame*. 2009; 156(2): 273-291.
- [172] Nori V, Seitzman J. Evaluation of Chemiluminescence as a Combustion Diagnostic under Varying Operating Conditions. In: 46th AIAA Aerospace Sciences Meeting; 2008 Jan 7-10, Reno, Nevada.
- [173] Guyot D, Guethe F, Schuermans B, Lacarelle A, Paschereit CO. CH*/OH* Chemiluminescence Response of an Atmospheric Premixed Flame Under Varying Operating Conditions. In: Proceedings of ASME Turbo Expo 2010: Power for Land, Sea, and Air; 2010 Jun 14-18; Glasgow, United Kingdom.
- [174] Kutne P, Boxx I, Stöhr M, Meier W. Experimental analysis of the combustion behaviour of a low calorific syngas mixture in a gas turbine model combustor. In: Proceedings of the 3rd European Combustion Meeting; 2007 Apr 11-13; Crete, Greece.
- [175] Haber LC, Vandsburger U, Saunders WR, Khanna VK. An Experimental Examination of the Relationship between Chemiluminescence Light Emissions and Heat-release Rate Under Non-Adiabatic Conditions, Report No. RTO-MP-051. U.S. Department of Defense; 2001.
- [176] Lauer M, Sattelmayer T. Heat Release Calculation in a Turbulent Swirl Flame from Laser and Chemiluminescence Measurements. In: 14th International Symposium on Applications of Laser Techniques to Fluid Mechanics; 2008 Jul 7-10; Lisbon, Portugal.

- [177] Hardalupas Y, Panoutsos CS, Skevis G, Taylor AMKP. Numerical Evaluation of Equivalence Ratio Measurement Using OH* and CH* Chemiluminescence in Premixed Iso-Octane/Air Flames. In: Proceedings of the 2nd European Combustion Meeting; 2005 Apr 3-6; Louvain-la-Neuve, France.
- [178] Walsh KT, Long MB, Tanoff MA, Smooke MD. Experimental and computational study of CH, CH*, and OH* in an axisymmetric laminar diffusion flame. *Symposium (International) on Combustion*. 1998; 27(1): 615-623.
- [179] Higgins B, McQuay MQ, Lacas F, Rolon JC, Darabiha N, Candel S. Systematic measurements of OH chemiluminescence for fuel-lean, high-pressure, premixed, laminar flames. *Fuel*. 2001; 80(1): 67-74.
- [180] Lemoine, F, Grisch, F. Laser-Induced Fluorescence. In: Boutier, A, editor. *Laser Metrology in Fluid Mechanics*. London: ISTE Ltd; 2013.
- [181] Grisch F, Orain M. Role of Planar Laser-Induced Fluorescence in Combustion Research. *Aerospace Lab Journal*. 2009; Issue 1: 1-14.
- [182] McManus K, Yip B, Candel S. Emission and laser-induced fluorescence imaging methods in experimental combustion. *Exp Therm Fluid Sci*. 1995; 10(4): 486-502.
- [183] Lee JG, Santavicc DA. Experimental Diagnostics for the Study of Combustion Instabilities in Lean Premixed Combustors. *J Propul Power*. 2003; 19(5): 735-750.
- [184] Eckbreth AC. *Laser Diagnostics for Combustion Temperature and Species*. Amsterdam: Gordon and Breach Publishers; 1996.
- [185] Dagdigian PJ. Reactive scattering. In: Spencer ND, Moore JH, editors. *Encyclopedia of Chemical Physics and Physical Chemistry: Fundamentals*. Bristol: Institute of Physics Publishing; 2001.
- [186] Luque, J, Crosley, D. LIFBASE (version 2.1.1). SRI report No. MP 99-009. SRI International; 1999. Available from: <https://www.sri.com/engage/products-solutions/lifbase>
- [187] Guttenfelder WA, Renfro MW, Laurendeau NM, Ji J, King GB, Gore JP. Hydroxyl time series and recirculation in turbulent nonpremixed swirling flames. *Combust Flame*. 2006; 147(1-2): 11-21.
- [188] Riethmuller, M, David, L, Lecordier, B. Particle Image Velocimetry. In: Boutier, A, editor. *Laser Velocimetry in Fluid Mechanics*. London: ISTE Ltd; 2012.
- [189] Prasad AK. Stereoscopic particle image velocimetry. *Exp Fluids*. 2000; 29(2): 103-116.
- [190] Lewis J. *The Behaviour of Swirling Flames Under Variable Fuel Composition [PhD Thesis]*. Cardiff University; 2014.

- [191] Nomura T, Iizuka T, Ishima T, Obokata T. PIV Measurements and Numerical Simulation on In-Cylinder Flow Under Steady State Flow Condition. In: Proceedings of 12th International Symposium on Applications of Laser Techniques to Fluid Mechanics; 2004 Jul 12-15; Lisbon, Portugal.
- [192] Eder, A, Durst, B, Jordan, M. Laser-Doppler Velocimetry. In: Feldman, O, Mayinger, F, editors. Optical Measurements: Techniques and Applications. 2nd Edition. Verlag: Springer; 2001.
- [193] O'Neill PL, Nicolaides D, Honnery D, Soria J. Autocorrelation Functions and the Determined of Integral Length Scale with Reference to Experimental and Numerical Data. In: 15th Australasian Fluid Mechanics Conference; 2004 Dec 13-17. Sydney, Australia.
- [194] Lieuwen TC. Experimental Investigation of Limit-Cycle Oscillations in an Unstable Gas Turbine Combustor. *J Propul Power*. 2002; 18(1): 61-67.
- [195] Meier W, Weigand P, Duan XR, Giezendanner-Thoben R. Detailed characterization of the dynamics of thermoacoustic pulsations in a lean premixed swirl flame. *Combust Flame*. 2007; 150(1-2): 2-26.
- [196] Jacobsen, F, Juhl PM. Fundamentals of General Linear Acoustics. West Sussex: Wiley; 2013.
- [197] Bicking, RE. Pressure Fundamentals of Pressure Sensor Technology [Internet]. *Sensors Online*. 1998 [cited 15 Jun 2015]. Available from: <http://www.sensormag.com/sensors/pressure/fundamentals-pressure-sensor-technology-846>
- [198] Song WJ, Cha DJ. Temporal kurtosis of dynamic pressure signal as a quantitative measure of combustion instability. *Appl Therm Eng*. 2016; 104: 577-586.
- [199] Reaction Design. CHEMKIN-PRO 15092. San Diego, California; 2009.
- [200] Smith G, Golden D, Frenklach M, Moriarty N, Eiteneer B, Goldenberg M, et al. GRI-Mech 3.0, http://www.me.berkeley.edu/gri_mech/; 1999.
- [201] Halter F, Chauveau C, Djebaïli-Chaumeix N, Gökalp I. Characterization of the effects of pressure and hydrogen concentration on laminar burning velocities of methane-hydrogen-air mixtures. *P Combust Inst*. 2005; 30(1): 201-208.
- [202] Emmert T, Bomberg S, Polifke W. Intrinsic thermoacoustic stability of premixed flames. *Combust Flame*. 2015; 162(1): 75-85.
- [203] Li J, Yang D, Luzzato C, Morgans AS. OSCILOS: The Open Source Combustion Instability Low Order Simulator; 2014 (<http://www.oscilos.com>)
- [204] Li J, Morgans AS. Time domain simulations of nonlinear thermoacoustic behaviour in a simple combustor using a wave-based approach. *J Sound Vib*. 2015; 346: 345-360.

- [205] Li J, Yang D, Luzzato C, Morgans AS. Open Source Combustion Instability Low Order Simulator (OSCILOS) Technical Report. Department of Aeronautics, Imperial College London; 2014 (http://www.oscilos.com/download/OSCILOS_Long_Tech_report.pdf)
- [206] Han X, Li J, Morgans AS. Prediction of combustion instability limit cycle oscillations by combining flame describing function simulations with a thermoacoustic network model, *Combust Flame*. 2015; 162(10): 3632–3647.
- [207] Yang D, Morgans AS. Helmholtz Resonators for Damping Combustor Thermoacoustics. In: 22nd International Congress on Sound and Vibration (ICSV22); 2015 Jul 12-15; Florence, Italy, 2015
- [208] Li J, Morgans AS. Feedback control of combustion instabilities from within limit cycle oscillations using H^∞ loop-shaping and the v -gap metric. *P Roy Soc A-Math Phy*. 2016; 472(2191): 20150821.
- [209] ILEX Energy Consulting Limited. Importing Gas into the UK – Gas Quality Issues. A report to Department of Trade and Industry, Ofgem and the Health and Safety Executive. Oxford; 2003.
- [210] Josten M, Hull S. 2006-2009 Triennium Work Report Program Committee D1: LNG Quality and Interchangeability. In: 24th World Gas Conference; 2009 Oct 5-9; Buenos Aires, Argentina.
- [211] Dagaut P. On the kinetics of hydrocarbons oxidation from natural gas to kerosene and diesel fuel. *Phys Chem Chem Phys*. 2002; 4: 2079-2094.
- [212] Vargas AC, Arrieta AA, Arrieta CE. Combustion characteristics of several typical shale gas mixtures. *J Nat Gas Sci Eng*. 2016; 33: 296-304.
- [213] Ferguson D, Richard G, Straub D. Fuel Interchangeability for Lean Premixed Combustion in Gas Turbine Engines. In: Proceedings of ASME Turbo Expo 2008: Power for Land, Sea, and Air; 2008 Jun 9-13; Berlin, Germany.
- [214] Altfeld K, Pinchbeck D. Admissible hydrogen concentrations in natural gas systems. *Gas for Energy* DIV Deutscher Industrieverlag; 2013.
- [215] Peters N. *Turbulent Combustion*. Cambridge: Cambridge University Press; 2000.
- [216] Bagdanavicius A. Premixed combustion of alternative fuels under varying conditions of temperature and pressure [PhD Thesis]. Cardiff University; 2010.
- [217] Simis S. Application of the Planar Laser Induced Fluorescence imaging technique of the hydroxyl radical in the qualitative investigation of Bunsen burner flames at atmospheric conditions [MSc Thesis]. Cardiff University; 2011.
- [218] Dantec Dynamics. HiSense 11M, 4M and MkII Cameras – CCD cameras for demanding imaging applications. Publication No. PI334v1. Skovlunde (Denmark).
- [219] Hamamatsu Photonics. High-speed gated image intensifier units – C9016-2x, C9546, C9547 series. Iwata City (Japan); 2015.

- [220] Killer C. Abel Inversion Algorithm. MATLAB Central File Exchange <http://www.mathworks.com/matlabcentral/fileexchange/43639-abel-inversion-algorithm>; 2014.
- [221] Pretzler G. A New Method for Numerical Abel-Inversion. *Z Naturforsch.* 1991; 46a: 639-641.
- [222] Kutne P, Kapadia B, Meier W, Aigner M. Experimental analysis of the combustion behaviour of oxyfuel flames in a gas turbine model combustor. *P Combust Inst.* 2011; 33(2): 3383-3390.
- [223] Davis, SG, Joshi AV, Wang H, Egolfopoulos, F. An optimized kinetic model of H₂/CO combustion. *P Combust Inst.* 2005; 30(1): 1283- 1292.
- [224] Cant S, Mastorakos E. *An Introduction to Turbulent Reacting Flows.* London: Imperial College Press; 2008.
- [225] Englund, DR, Richards, WB. The Infinite Line Pressure Probe. In: 39th International Instrumentation Symposium; 1984 May 7-10; Denver, Colorado.
- [226] Straub DL, Ferguson DH, Rohrssen R, Perez E. Design considerations for remote high-speed pressure measurements of dynamic combustion phenomena. In: 45th AIAA Aerospace Sciences Meeting; 2007 Jan 8-11; Reno, Nevada.
- [227] Christman M. *Taking the Pulse of Combustion.* PCB Piezotronics. Depew, New York.
- [228] Wilke C. A Viscosity Equation for Gas Mixtures. *J Chem Phys.* 1950; 18(4): 517-519.
- [229] Lemmon EW, McLinden MO, Friend DG. Thermophysical Properties of Fluid Systems. In: Lindstrom PJ, Mallard WG, editors. NIST Chemistry WebBook, NIST Standard Reference Database Number 69. National Institute of Standards and Technology; Gaithersburg Maryland; <http://webbook.nist.gov>.
- [230] Mishra TK, Datta A, Mukhopadhyay A. Comparison of the structures of methane-air and propane-air partially premixed flames. *Fuel.* 2006; 85(9): 1254-1263.
- [231] Gokulakrishnan P, Fuller C, Klassen MS, Joklik RG, Kochar YN, Vaden SN, et al. Experiments and modeling of propane combustion with vitiation. *Combust Flame.* 2014; 161(8): 2038-2053.
- [232] Yu L, Cashmore M. An Acoustic Modal Analysis of a DLE Combustion System. In: *Proceedings of ASME Turbo Expo 2008: Power for Land, Sea, Air*; 2008 Jun 9-13; Berlin, Germany.
- [233] Tao L, Groves K, Lennox B. The Simulation of Acoustic Wave Propagation Within Networked Pipe Systems – Development and Experimental Validation. In: *22nd International Congress on Sound and Vibration (ICSV22)*; 2015 Jul 12-16; Florence, Italy.

- [234] Muruganandam TM, Seitzman JM. Characterization of extinction events near blowout in swirl-dump combustors. In: 41st AIAA/ASME/SAE/ASEE Joint Propulsion Conference and Exhibit; 2005 Jul 10-13; Tuscon, Arizona.
- [235] Bradley D, Gaskell PH, Gu XJ, Lawes M, Scott MJ. Premixed turbulent flame instability and NO formation in a lean-burn swirl burner. *Combust Flame*. 1998; 115(4): 515-538.
- [236] Han Z, Hochgreb S. The response of stratified swirling flames to acoustic forcing: Experiments and comparison to model. *P Combust Inst*. 2015; 35(3): 3309-3315.
- [237] Richards G, Weiland N, Strakey P. Combustion Strategies for Syngas and High-Hydrogen Fuel. In: *Gas Turbine Handbook*. U.S. National Energy Technology Laboratory; 2006
- [238] Niemann U, Seshadri K, Williams F. Effect of pressure on structure and extinction of near-limit hydrogen counterflow diffusion flames. *P Combust Inst*. 2013; 34(1): 881-886.
- [239] Kim H, Arghode V, Linck M, Gupta A. Hydrogen addition effects in a confined swirl-stabilized methane-air flame. *Int J Hydrogen Energ*. 2009; 34(2): 1054-1062.
- [240] Hirsch C, Wäsle J, Winkler A, Sattlemayer T. A spectral model for the sound pressure from turbulent premixed combustion. *P Combust Inst*. 2007; 31(1): 1435-1441.
- [241] Cheng R. Low Swirl Combustion. In: *Gas Turbine Handbook*. U.S. National Energy Technology Laboratory; 2006.
- [242] Alkabile H, Andrews G. Reduced NO_x Emissions Using Low Radial Swirler Vane Angles. In: *ASME 1991 International Gas Turbine and Aeroengine Congress and Exposition*; 1991 Jun 3-6; Orlando, Florida.
- [243] Ćosić, B, Terhaar S, Moeck JP, Paschereit CO. Response of a swirl-stabilized flame to simultaneous perturbations in equivalence ratio and velocity at high oscillation amplitudes. *Combust Flame*. 2015; 162(4): 1046-1062.
- [244] Saint FP, Lacost DA, Kirkpatrick MJ, Odic E, Laux CO. Temporal evolution of temperature and OH density produced by nanosecond repetitively pulsed discharges in water vapour at atmospheric pressure. *J Phys D Appl Phys*. 2014; 47(7): 075204.

APPENDIX A – UNITED KINGDOM GAS TRANSMISSION NETWORK



Figure A. 1: UK gas transmission network including LNG import facilities and interconnectors. Reproduced from [19].

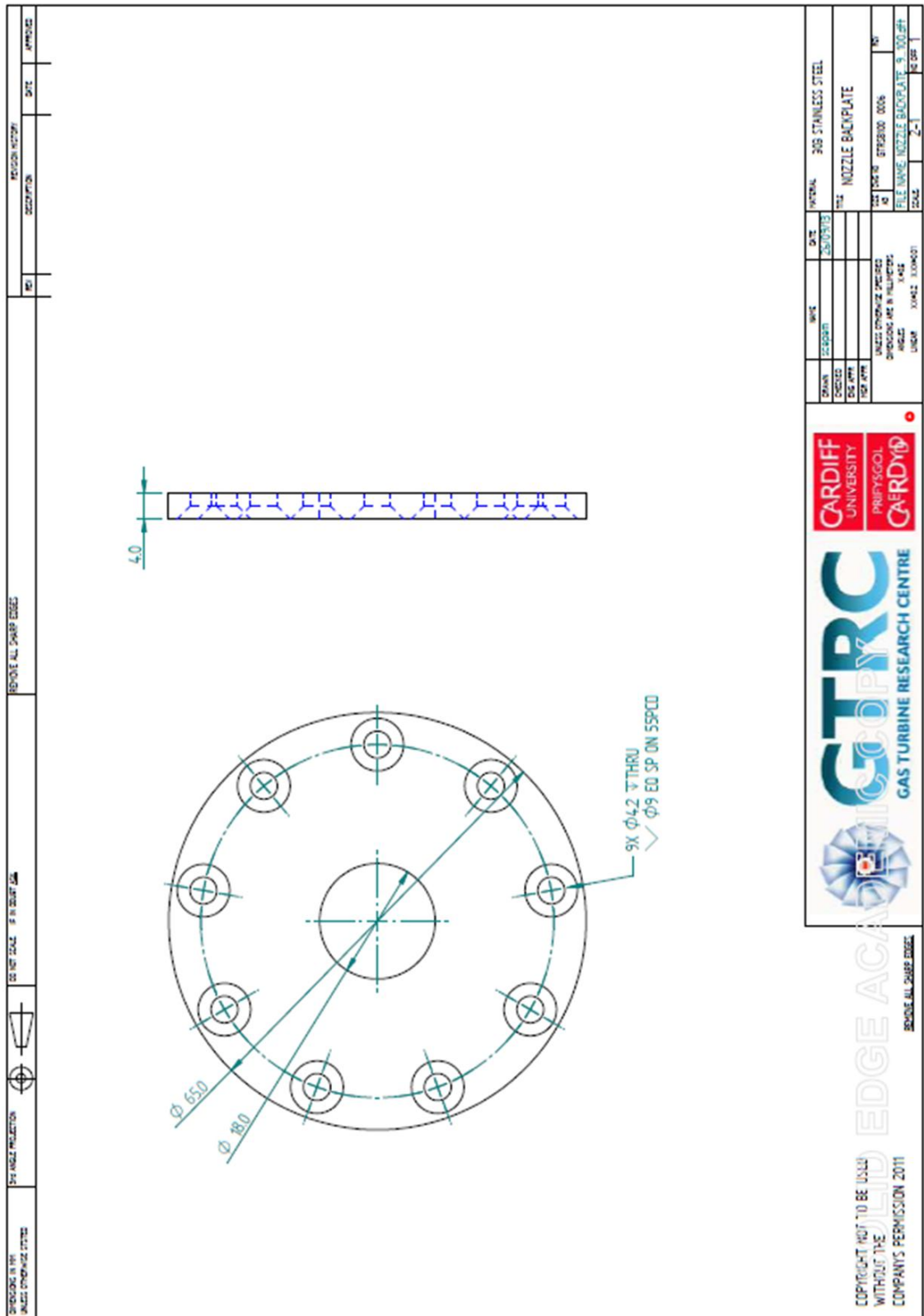


Figure B.4: HPGSB-2 Radial Tangential Swirler Insert Back Plate (Figure 3.4.d)

Appendix B.2 – Photographs and Diagrams

Appendix B.2.1 – HPCR and HPGSB/HPGSB-2 Photographs and Diagrams

Photographs of the main elements of the HPCR are given in Figure B.7 with the HPCR as setup for use with the HPGSB (prior to November 2015) in the top photograph. The bottom photograph of Figure B.7 shows the HPCR as configured for use with the HPGSB-2, including the fuel heat exchanger, commissioned in July 2016. In both images, key elements of the HPCR are visible, including the 5 gas mixing lines, the HPOC, and the camera system for optical diagnostics.

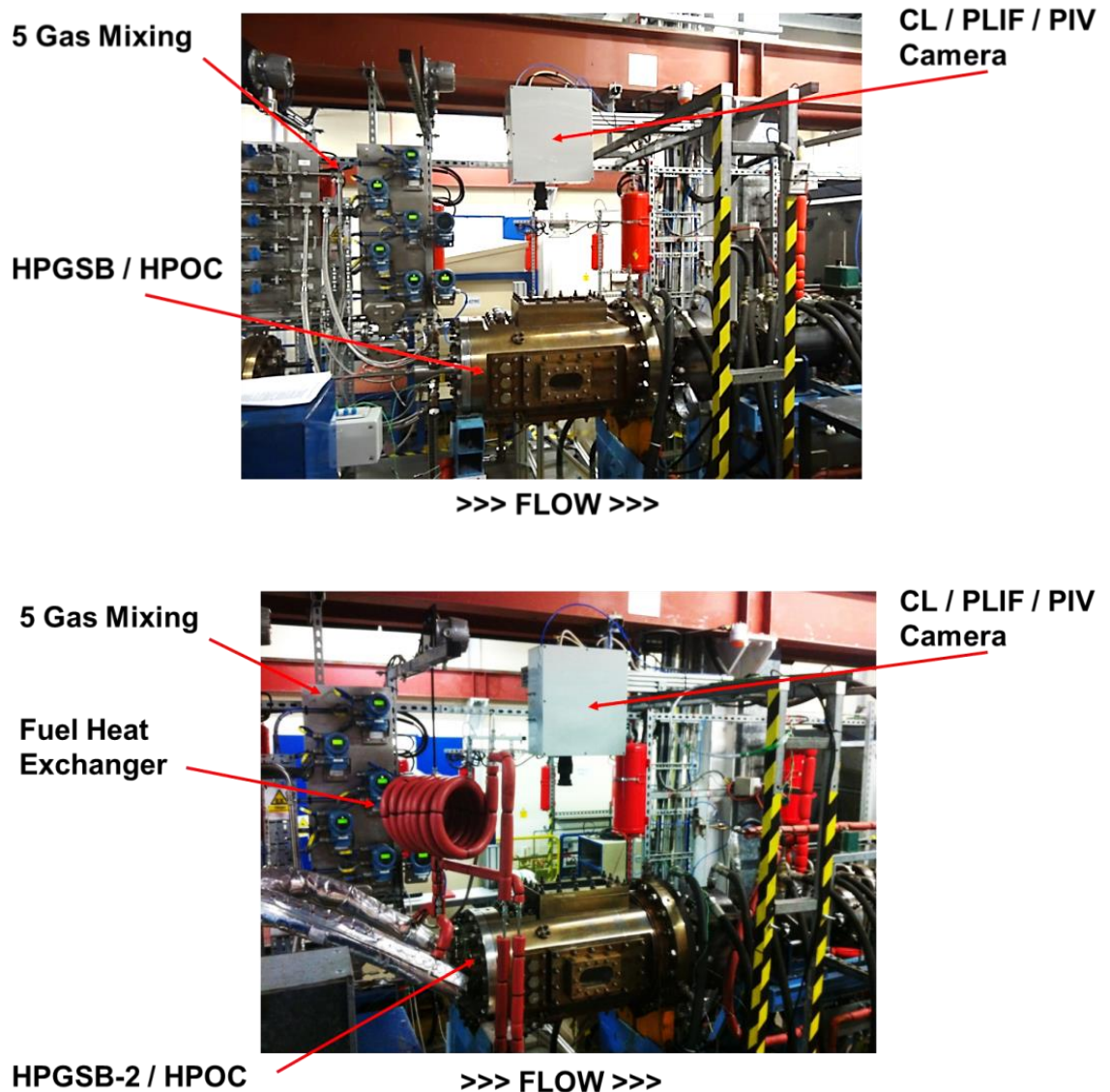


Figure B.7: Photographs of HPCR setup prior to installation of the air and fuel preheating systems with the HPGSB (top) and after installation of these systems with the HPGSB-2 (bottom).

Photographs of the HPGSB and HPGSB-2 are provided in Figures B.8 and B.9. In Figure B.9, the HPGSB-2 is shown during construction (Figure B.9.a) and completed with open cylindrical confinement, prior to installation in the HPOC (Figure B.9.b)

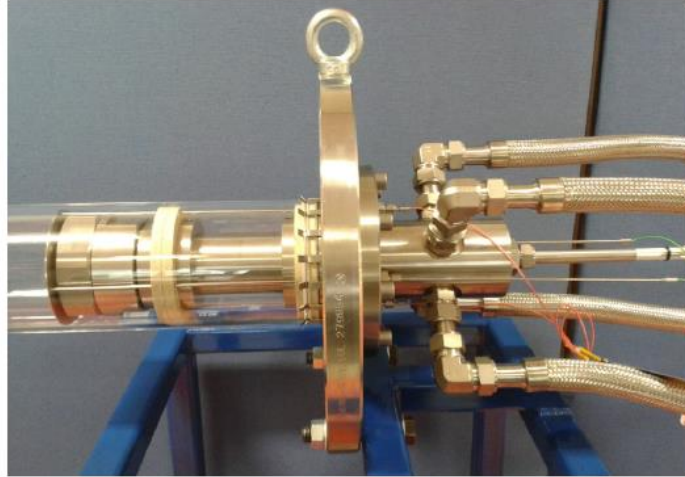


Figure B.8: Photograph of assembled HPGSB prior to installation in the HPOC. Reproduced from [115].



Figure B.9: Photographs of HPGSB-2 during construction (a) and complete, fully instrumented (b)

Photographs of the HPGSB-2 burner and dynamic pressure installation are provided in Figures B.10 and B.11. Figure B.10.a provides an end-on view of the burner face and exit nozzle with the instrumentation lance installed. Figure B.10.b provides a side view of the burner face and exit nozzle through a side window in the HPOC, and also features the spark igniter installed through a hole drilled in the bottom of the quartz confinement tube. In Figure B.11, the back end of the HPGSB-2 is shown as installed in the HPOC. The instrumentation lance is shown in the foreground while the HPGSB-2 inlet plenum and HPOC connection flange are shown in the background. Also visible in the foreground are the DPTs for the “Pilot” (left) and “Burner Face” (right).



Figure B.10: Photographs of HPGSB-2 burner components with an end-on view of the burner face, exit nozzle, and instrumentation/pilot lance prior to installation in the HPOC (a) and after installation in the HPOC with the spark igniter installed (b).

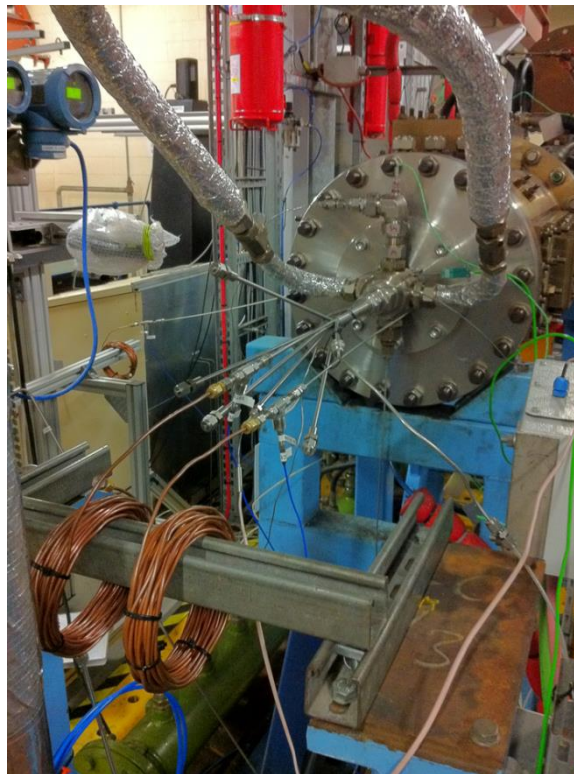


Figure B.11: Photograph of the instrumentation at the front end of the HPGSB-2 as installed in the HPOC, including DPTs for the "Pilot" (left semi-infinite line) and "Burner Face" (right semi-infinite line). The exhaust DPT semi-infinite line can be seen in the background (back left).

Appendix B.2.2 – Optical Diagnostics Photographs and Diagrams

The ICCD camera system used for PLIF and CL is shown in Figure B.12. Due to its proximity to the HPOC, the ICCD system requires cooling and consideration of potential explosive environments as the system itself is not intrinsically safe. Both design criteria are met by placing the ICCD in an IP-67 rated enclosure and purging the enclosure with cool, filtered air.



Figure B.12: Photograph of the ICCD camera system as installed in the IP-67 enclosure. Refer to Figure 3.2 for installed location in the HPCR.

The bespoke PLIF system enclosure is found in Figure B.13 and is used for temperature control and control of potential explosion hazard areas. The dye laser output beam exits the right-hand side of the enclosure before entering the sheet forming optics and the HPOC (not shown).



Figure B.13: Photograph of PLIF laser system as installed at Cardiff University's GTRC.

The PLIF diagnostic system utility setup (e.g. electrical and cooling water requirements) is given in Figure B.14.

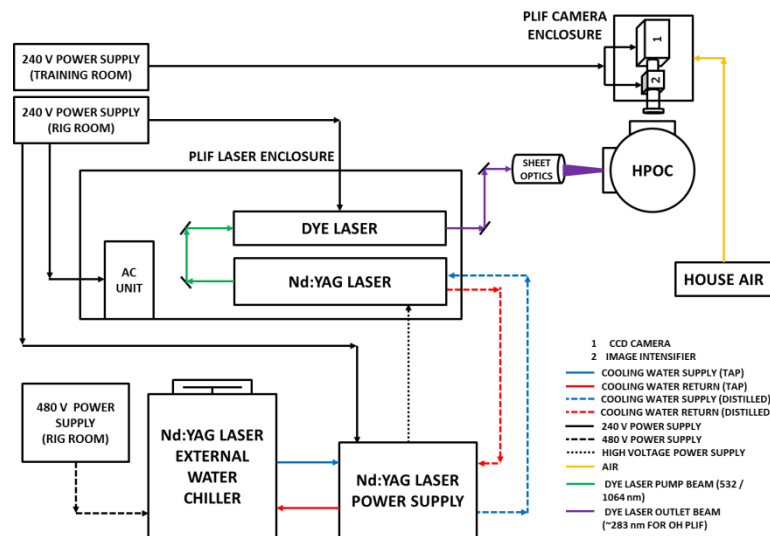


Figure B.14: PLIF measurement system utility setup at Cardiff University's GTRC.

Figure B.15 provides photographs of the scaled imaging targets used for PLIF/CL measurements as installed in the HPGSB (Figure B.15.a) and HPGSB-2 (Figure B.15.b). The field of view limitation of 100 mm in the radial direction explains the imposed shift in camera position for the HPGSB in Figure B.15.a. As the ID of the HPGSB quartz confinement tube is 140 mm, the flame area extends out of the field of view if the focal plane is centered on the burner exit nozzle centerline. Thus, the camera is focused off center to capture one half of the flame image, which is critical for the subsequent chemiluminescence image Abel deconvolution process described in Chapter 4.1.2.

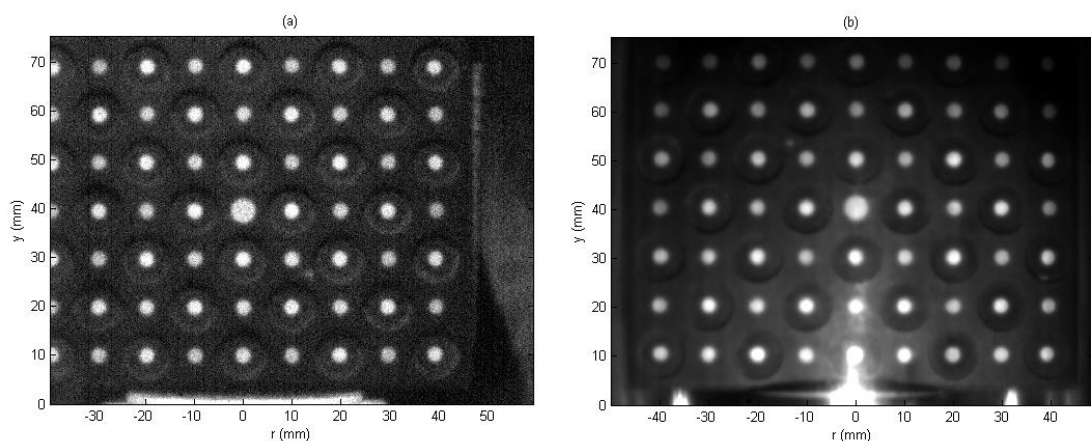


Figure B.15: Images of scaled calibration targets installed in the HPGSB (a) and HPGSB-2 (b)

A photograph of the Nd:YAG laser mounted at the back end of the HPOC for PIV measurements in the HPGSB-2 is shown in Figure B.16.

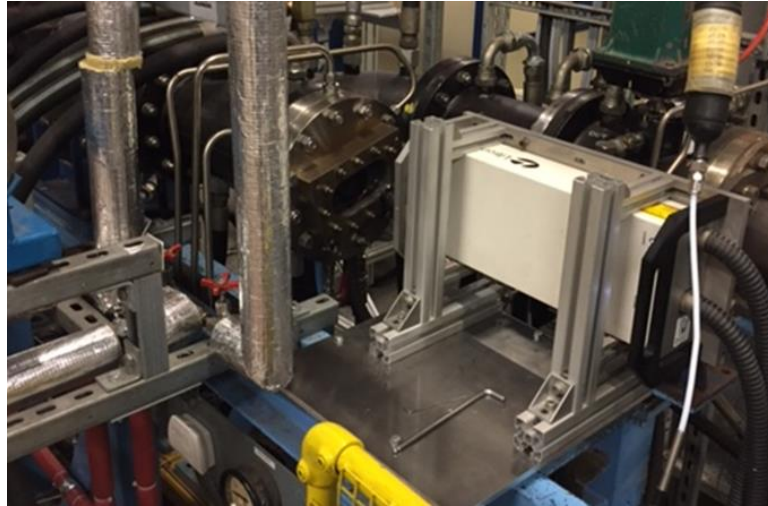


Figure B.16: Photograph of the Nd:YAG laser mounted for PIV measurements in the HPCR as shown in Figure 3.15.

Figure B.17 provides photographs of the scaled imaging target used for PIV measurements as installed in the HPGSB-2 open (Figure B.17.a) and convergent (Figure B.17.b) confinements. Also visible in Figure B.7 is the burner exit nozzle and boundaries of the quartz confinement ID ($D_{confine} = 100$ mm).

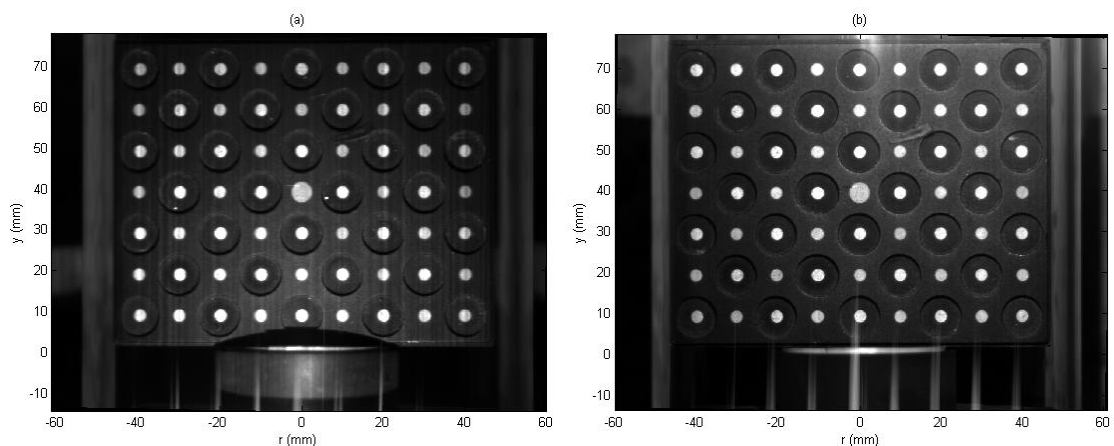


Figure B.17: Images of scaled calibration targets installed in the HPGSB-2 for PIV measurements with the open cylindrical confinement (a) and convergent nozzle confinement (b)

A schematic and photograph of the scanning OH PLIF system can be found in Figure B.18.

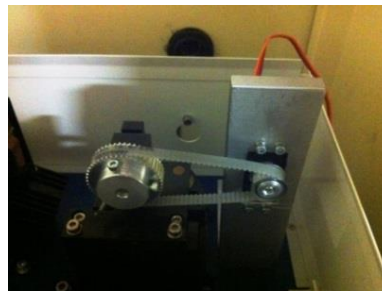
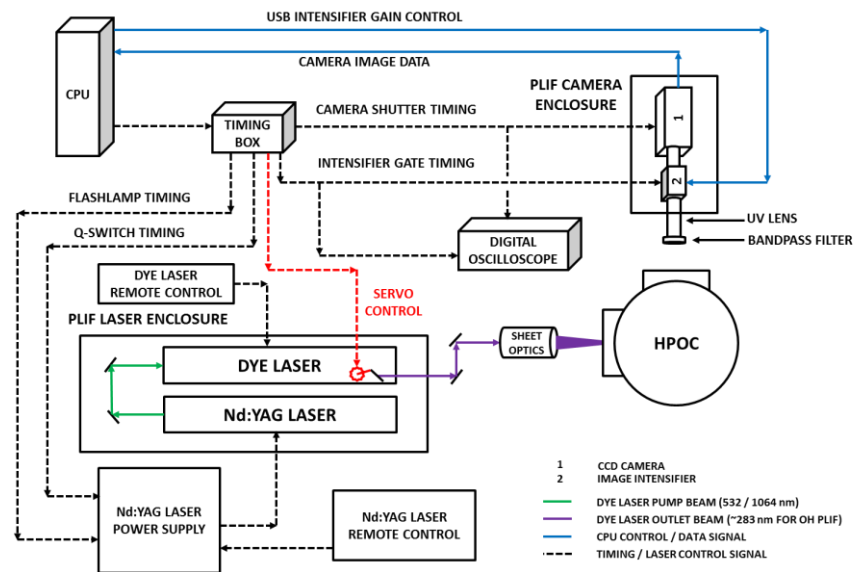


Figure B.18: Schematic of scanning laser sheet PLIF measurement system timing and image capture setup at Cardiff University's GTRC (top) and photograph of servo installation in the TDL-90 dye laser (bottom).

APPENDIX C – COMPUTATIONAL CODES

Appendix C.1 – Chemiluminescence Image Temporal Average and Integral Intensity MATLAB code

The “CHEMI_AVG.m” function calculates a temporal average chemiluminescence intensity image from an input set of instantaneous .TIF image files. It also outputs the original image grayscale colormap and calculates the integral image intensity of each instantaneous chemiluminescence image as well as the final temporal average image. First, the user must input the number of images to be processed. The function then requests the user to select the .TIF files for processing and checks that the number of files selected is equal to the number of images input by the user. Each .TIF image file is read in, converted to double precision and filtered using a 3x3 median filter. The pixel intensity values for each image are summed in an empty image matrix and then divided by the total number of images to yield the temporal average image. This average image is then background corrected using the calculated statistical mode of the final temporal average image and also corrected by the minimum %intensity value after background correction.

```
function [CHEMI_AVGout, CHEMI_cmap, Img_IntenINSTAN, Img_IntenAVG] =
CHEMI_AVG(NumImages)

%Open dialogue box for user to select .TIF image files
[listOfFiles, folder] = uigetfile ('*.tif', 'Select your image',
'MultiSelect', 'on');
fullFileName = fullfile(folder, listOfFiles{1});
[I cmap] = imread(fullFileName);
[rows columns] = size(I);

%Initialize output matrix and vector variables
CHEMI_AVGout_zero = zeros(rows,columns);
Img_IntenINSTAN = zeros(1, NumImages);

%Check number of images selected matches number input by user
if NumImages ~= length(listOfFiles)
    msg = 'Error Occured - Image Number Mismatch';
    error(msg);
else
    for j=1:length(listOfFiles)
        fullFileName = fullfile(folder, listOfFiles{j});
        I2 = imread(fullFileName);
        %Convert .TIF image to double precision
        I2_double = im2double(I2);
        %Filter the image with a 3x3 median filter
        I2_double_filt = medfilt2(I2_double, 'symmetric');
        %Add each image to the proceeding image
        CHEMI_AVGout_zero = CHEMI_AVGout_zero + I2_double_filt;
        %Calculate and store the instantaneous image integral
        intensity
```

```
        Img_IntenINSTAN(1,j) = sum(I2_double_filt(:));
    end
end
%Calculate the temporal average image
CHEMI_AVG_1 = CHEMI_AVGout_zero ./ NumImages;
CHEMI_AVG_mode = mode(CHEMI_AVG_1(:));
%Background correction using the statistical mode of the temporal
average
CHEMI_AVGout = CHEMI_AVG_1 - CHEMI_AVG_mode;
%Minimum value correction
CHEMI_AVGout = CHEMI_AVGout - min(CHEMI_AVGout(:));
CHEMI_cmap = cmap;
%Calculate the integral intensity of the temporal average image after
%correction
Img_IntenAVG = sum(CHEMI_AVGout(:));
```

Appendix C.2 – Chemiluminescence Abel Deconvolution MATLAB code

The “HalfAbel.m” function calculates the Abel deconvolution of one half of a full resolution input chemiluminescence image, presumably the temporal average, assuming that the input image is symmetric about its central axis. The function requires the user to input the chemiluminescence image as a matrix. It also requires the horizontal (left-right) central pixel location (e.g. column index), “CentXPix”. The user must also indicate if the half image used for analysis should be defined from the central pixel of the image to the right edge (WhichWay = 1) or from the left edge of the image to the central pixel (WhichWay = 2). Finally, the user must input the radius of the image, R, in mm, which should be calculated based on the half image to be entered and the image resolution (pix/mm). The “HalfAbel.m” code below makes a call to “abel_inversion.m”, which in turn calls “compute_expansion.m” and “solve_lsq.m.” All three of these called functions are available open source from [X] and thus have not been included here for brevity.

```
function [ImAbel] = HalfAbel(Image, R, CentXPix, WhichWay)

[i j] = size (Image);
n = (j/2) + 1;

if WhichWay == 1
    NewEdge = (2*(j-CentXPix));
    %Initialize output image matrix
    ImAbel = zeros(i, NewEdge);
    k = (NewEdge/2) - 1;
    %For loop cycles through each row of the input image
    for z = 1:i
        %Extract single image row
        A = Image(z, CentXPix:j);
        %Convert image row to double precision
        A2 = im2double(A, 'indexed');
        %Calls the Abel inversion function one row at a time with an
        %input of 5 cosinus expansions in the Fourier-series-like
        %expansion
        [f_rec , X] = abel_inversion(A2,R,5);
        %Add the Abel deconvoluted row to the output matrix
        ImAbel(z, (NewEdge/2):NewEdge) = f_rec(:,1);
        %Rotate the Abel deconvoluted row about the central axis
        f_rec = flipud(f_rec);
        ImAbel(z, 1:k) = f_rec(2:(NewEdge/2),1);
    end
end

if WhichWay == 2
    NewEdge = (2*CentXPix);
    ImAbel = zeros(i, NewEdge);
    k = (NewEdge/2) - 1;
    %For loop cycles through each row in the input image
    for z = 1:i
```

```
%Extract single image row
A = Image(z, 1:(CentXPix+1));
A = fliplr(A);
%Convert image row to double precision
A2 = im2double(A, 'indexed');
%Calls the Abel inversion function one row at a time with an
input
%of 5 cosinus expansions in the Fourier-series-like expansion
[f_rec , X] = abel_inversion(A2,R,5);
%Add the Abel deconvoluted row to the output matrix
ImAbel(z, (NewEdge/2):NewEdge) = f_rec(:,1);
%Rotate the Abel deconvoluted row about the central axis
f_rec = flipud(f_rec);
ImAbel(z, 1:k) = f_rec(2:(NewEdge/2),1);
end
end
end
```

Appendix C.3 – Planar Laser Induced Fluorescence Image Processing MATLAB codes

The “PLIF_AVG_SHEETNORM.m” function calculates the temporal average of a set of instantaneous OH PLIF images. The instantaneous images are first filtered and background corrected from the input “PLIF_BG” input (average of PLIF background without flame). The images are then corrected for variation in the laser sheet intensity by normalizing the intensity values in each column, starting from the maximum OH PLIF intensity and proceeding in both upstream and downstream directions until the point at which the Gaussian fit has its maximum gradient (24.35 mm, or approximately 12.175 mm in either direction. After laser sheet intensity correction, the instantaneous images are temporally averaged and output as “PLIF_AVGout.” The colormap “PLIF_cmap” is also output as the input images are “.tif” files that cannot be plotted in MATLAB with the “imshow” function without also inputting the colormap. The function requires the user to input the number of images to be used in the calculation, “NumImages” as well as the background image “PLIF_BG.”

```
function [PLIF_AVGout, PLIF_cmap] = PLIF_AVG_SHEETNORM(NumImages,
PLIF_BG)

% Open dialog box to prompt for .TIF OH PLIF file selection
[listOfFiles, folder] = uigetfile ('*.tif', 'Select your image',
'MultiSelect', 'on');
fullFileName = fullfile(folder, listOfFiles{1});
[I cmap] = imread(fullFileName);
[rows columns] = size(I);
PLIF_AVGout_zero = zeros(rows,columns);
PLIF_Sheet_Norm_zero = zeros(rows,columns);
PLIF_BG_double = im2double(PLIF_BG);

%Error check if the number of selected images is equal NumImages
if NumImages ~= length(listOfFiles)
    msg = 'Error Occured - Image Number Mismatch';
    error(msg);

else
    for j=1:length(listOfFiles)
        fullFileName = fullfile(folder, listOfFiles{j});
        % Read in first instantaneous OH PLIF image
        I2 = imread(fullFileName);
        % Convert the image to double precision
        I2_double = im2double(I2);
        % Apply 3x3 pixel median filter to reduce noise
        I2_double_filt = medfilt2(I2_double, 'symmetric');
        % Correct the instaneous OH PLIF image for the input
background
        % image
        I2_double_NoBG = I2_double_filt - PLIF_BG_double;
```

```

% Apply laser sheet intensity distribution correction
for i = 1:columns
    % Find the maximum OH PLIF intensity value in each column
    [ColMax Loc] = max(I2_double_NoBG(:,i));
    % Convert the column pixel location to "mm" distance
    LocMM = Loc/13.6;
    LocNorm = LocMM / (LocMM / 34.338);
    GaussInten = 1.093*exp(-((LocNorm-34.33)/17.23)^2);
    % Normalize the maximum OH PLIF intensity value
    IntenNorm = ColMax/GaussInten;
    PLIF_Sheet_Norm_zero(:,i) = I2_double_NoBG(:,i);
    PLIF_Sheet_Norm_zero(Loc, i) = IntenNorm;

    % Apply the Gaussian normalization in upstream direction
from
    % the maximum OH PLIF intensity location
    for l = 1:165
        if (Loc - l) == 0
            break
        end
        LocNormL = 34.338-((Loc-(Loc-l))*(1/13.6));
        GaussIntenL = 1.093*exp(-((LocNormL-34.33)/17.23)^2);
        IntenNormL = I2_double_NoBG((Loc-l), i)/GaussIntenL;
        PLIF_Sheet_Norm_zero((Loc-l), i) = IntenNormL;
    end

    % Apply the Gaussian normalization in the downstream
    % direction from the maximum OH PLIF intensity location
    for k = 1:165
        if (Loc + k) > 1024
            break
        end
        LocNormK = 34.338+(((Loc+k)-Loc)*(1/13.6));
        GaussIntenK = 1.093*exp(-((LocNormK-34.33)/17.23)^2);
        IntenNormK = I2_double_NoBG((Loc+k), i)/GaussIntenK;
        PLIF_Sheet_Norm_zero((Loc+k), i) = IntenNormK;
    end
    end
    PLIF_AVGout_zero = PLIF_AVGout_zero + PLIF_Sheet_Norm_zero;
end
end

%Calculate the temporal average OH PLIF image
PLIF_AVGout = PLIF_AVGout_zero ./ NumImages;

%Output the .TIF file colormap for easier image plotting
PLIF_cmap = cmap;

end

```

The “PLIF_FLAME_MAX.m” function calculates a number of flame properties from an input temporally averaged PLIF image, “PLIF_AVG”. The function also requires the input image pixel value, “CenterLinePixel,” which corresponds to the centerline of the burner exit nozzle in the “r” direction as well as the pixel resolution, “PixScale” in pixels/mm. Finally, a reaction progress variable, “ProgVar” must be input as a value between 0 and 0.5, where 0 corresponds to the line of maximum OH PLIF intensity and 0.5 corresponds to the flame thickness from the maximum intensity value to the maximum intensity gradient.

This function converts the input averaged PLIF image into a binary image by identifying the line of maximum OH PLIF intensity extending out from the burner exit nozzle, and setting the pixel intensity at that location to 1. The OH PLIF intensity distribution along each pixel row is then fit with a 9th order polynomial function, for which the 1st derivative is calculated. A peak finding algorithm is used to identify the peaks in the 1st derivative, corresponding to the highest PLIF intensity gradient, considered to be a flame edge. If a peak cannot be located, then the 2nd derivative is calculated, and the near-zero locations are identified. The pixel location in each row from the maximum to the identified maximum gradient is set to 1. All other values in the image are set to 0. From this binary image, the flame surface can be output, “FlameSurf” as well as the flame area, “FlameArea” (in mm²), using the known pixel area from “PixScale”. Other outputs from the function include the locations of the maximum OH PLIF intensity in each row, “I_PLIF_MAX_LOCS”, and the locations of the maximum gradient, “LFT_EDGE_LOCS” and “RHT_EDGE_LOCS”. The mean flame thickness, “FlameThk” (in mm), and each individual row flame thickness “ROW_FLM_THK” are also output. A binary image containing only the line of maximum OH PLIF intensity is also output, “FlameMax”.

```
function [FlameMax, FlameSurf, FlameThk, FlameArea, I_PLIF_MAX_LOCS,
LFT_EDGE_LOCS, RHT_EDGE_LOCS, ROW_FLM_THK] = PLIF_FLAME_MAX(PLIF_AVG,
CenterLinePixel, PixScale, ProgVar)
```

```
[rows columns] = size(PLIF_AVG);
X = 1:CenterLinePixel;
X = X.';
% Select half of the average OH PLIF image to evaluate
PLIF_AVG_Half = imcrop(PLIF_AVG, [0 0 CenterLinePixel rows]);
% Find the maximum OH PLIF intensity value in the selected half image
I_PLIF_MAX_Crop = max(PLIF_AVG_Half(:));
FlameMax = zeros(rows, CenterLinePixel);
FlameSurf = zeros(rows, CenterLinePixel);
I_PLIF_MAX_LOCS = zeros(rows,1);
LFT_EDGE_LOCS = zeros(rows,1);
RHT_EDGE_LOCS = zeros(rows,1);
ROW_FLM_THK = zeros(rows,1);
```

```

% Calculate the pixel area (mm^2) from the input pixel scale (pix/mm)
PixelArea = (1/PixScale)^2;

for k = 1:rows
    % Find the maximum OH PLIF intensity value in each row
    [I_PLIF_MAX I_PLIF_MAX_LOC] = max(PLIF_AVG_Half(k,:));

    % If the maximum value is less than 50% of the overall image
    % maximum PLIF intensity, move to the next row
    if I_PLIF_MAX/I_PLIF_MAX_Crop < 0.5
        continue
    end

    FlameMax(k, I_PLIF_MAX_LOC) = 1;
    I_PLIF_MAX_LOCS(k) = ((CenterLinePixel/PixScale)-
(I_PLIF_MAX_LOC/PixScale));
    % Extract the entire row distribution of OH PLIF intensity
values
    I_PLIF_ROW = PLIF_AVG_Half(k,:);
    I_PLIF_ROW = I_PLIF_ROW.';
    % Fit a 9th order polynomial to the row OH PLIF intensity
    % distribution
    [P,~,MU] = polyfit(X,I_PLIF_ROW, 9);
    F = polyval(P,X,[],MU);
    % Calculate the 1st derivative of the row OH PLIF intensity
    distribution
    Fx = gradient(F);

    % Extract OH PLIF intensity values from the left edge of the
row
    % to the maximum location
    Fx_LR = flipud(Fx(1:I_PLIF_MAX_LOC-1));
    % Error checking
    FX_LR_EMPCHK = isempty(Fx_LR);
    if FX_LR_EMPCHK == 1 || numel(Fx_LR) < 3
        continue
    end
    % Find the locations of the peaks in the 1st derivative
    % distribution from the left edge to the maximum location
    [Fx_LR_PK, Fx_LR_LOC] = findpeaks(Fx_LR);
    % If no peaks are found, take 2nd derivative and find
    Locations closest to 0
    if numel(Fx_LR_LOC)==0
        Fx2 = gradient(Fx);
        [P2,~,MU2] = polyfit(X,Fx2, 9);
        F2 = polyval(P2,X,[],MU2);
        Fx2_LR = flipud(Fx2(1:I_PLIF_MAX_LOC-1));
        Fx_LR_LOC = find(abs(Fx2_LR-0)==min(abs(Fx2_LR-0)));
    end

    % Calculate the left edge location
    LFT_EDGE_LOC = (I_PLIF_MAX_LOC -
ceil(2*ProgVar*Fx_LR_LOC(1)));
    if LFT_EDGE_LOC < 0
        continue
    end
end

```

```

    % Convert the left edge location to mm
    LFT_EDGE_LOCS(k) = ((CenterLinePixel/PixScale)-
(LFT_EDGE_LOC/PixScale));

    % Extract OH PLIF intensity values from the maximum location
to
    % the right edge of the row
    Fx_RL = Fx((I_PLIF_MAX_LOC+1):CenterLinePixel);
    % Error checking
    FX_RL_EMPCHK = isempty(Fx_RL);
    if FX_RL_EMPCHK == 1 || numel(Fx_RL) < 3
        continue
    end
    % Find the locations of the peaks in the 1st derivative
    % distribution from the maximum location to the right edge
    [Fx_RL_PK, Fx_RL_LOC] = findpeaks(-Fx_RL);
    % If no peaks are found, take 2nd derivative and find
    % Location closest to 0
    if numel(Fx_RL_LOC)==0
        Fx3 = gradient(Fx);
        [P3,~,MU3] = polyfit(X,Fx3, 9);
        F3 = polyval(P3,X,[],MU3);
        Fx3_RL = Fx3((I_PLIF_MAX_LOC+1):CenterLinePixel);
        Fx_RL_LOC = find(abs(Fx3_RL-0)==min(abs(Fx3_RL-0)));
    end

    % Calculate the right edge location
    RHT_EDGE_LOC = (I_PLIF_MAX_LOC +
ceil(2*ProgVar*Fx_RL_LOC(1)));
    if RHT_EDGE_LOC > CenterLinePixel
        continue
    end

    % Convert the right edge location to mm
    RHT_EDGE_LOCS(k) = ((CenterLinePixel/PixScale)-
(RHT_EDGE_LOC/PixScale));

    % Binarizing the flame surface from left to right in the row
    FlameSurf(k,LFT_EDGE_LOC:RHT_EDGE_LOC) = 1;

    % Calculating the individual row flame thickness (mm)
    ROW_FLM_THK(k) = 0.5*(LFT_EDGE_LOCS(k)-RHT_EDGE_LOCS(k));

end
% Calculate the mean flame thickness (mm)from the row thicknesses
FlameThk = mean(nonzeros(ROW_FLM_THK));
% Calculate the mean flame area (mm^2) from the binary flame
surface
FlameArea = (bwarea(FlameSurf))/PixelArea;
End

```

Appendix C.4 – Dynamic Pressure Measurement Processing MATLAB code

The “ACOUSTIC_BurnerFace.m” function reads in Burner Face DPT output and conducts frequency and time domain analysis. This function requires the user to input the dynamic pressure transducer sampling frequency, “SampleFreq”. The user must also input a frequency at which the signal will be split into a bandpass filtered signal $1 < f < \text{FiltFreq}$ and a high pass filtered signal $\text{FiltFreq} < f < \text{SampleFreq}$. The user must also enter in a time divider, “TemporalDiv” for the calculation of time-varying signal RMS and kurtosis values. The user is then directed to select the Microsoft Excel file which contains the measured DPT signal. This file should be created from the TDMS output file from National Instruments LabView SignalExpress. This function calls for the specific location of the Burner Face DPT in the output TDMS file after it is converted to an Excel file (e.g. 'E2:E240001' below) in the current GTRC configuration, which could be updated to read in any Excel location, if necessary. The function outputs the DPT signal, total signal RMS and kurtosis value, and time varying RMS and kurtosis values. Full signal, bandpass, and high pass FFT and PSDs are created and plotted. Using a peak-finding algorithm, the dominant frequencies are identified in all FFT and PSD plots, along with their corresponding amplitudes. These are output in descending order from maximum amplitude to minimum amplitude. The dominant frequencies are also plotted on the output FFT and PSD plots. This function also outputs “.WAV” audio files of the full signal, bandpass signal, and high pass signal. The function is setup below for reading in 240000 DPT measurements (or 60 seconds of signal at 4 kHz sampling rate).

For other DPT locations used in this study, “Pilot”, “Exhaust”, and “Plenum”, the MATLAB code is almost identical, but instead refers to a different column location to read in the DPT measurement in the TDMS output/Microsoft Excel input file (e.g. 'B2:B240001' for the “Pilot” DPT, 'C2:C240001' for the “Exhaust” DPT, and 'E2:E240001' for the “Plenum” DPT). Thus, these separate codes have not been replicated here for brevity.

```
function [SampleTime, BurnerFace_DPT, BurnerFaceRMS,
BurnerFaceRMS_Var, BurnerFaceRMS_LP, BurnerFaceRMS_Var_LP,
BurnerFaceRMS_HP, BurnerFaceRMS_Var_HP, ...
BurnerFaceK, BurnerFaceK_Var, BurnerFaceK_LP, BurnerFaceK_Var_LP,
BurnerFaceK_HP, BurnerFaceK_Var_HP, ...
BurnerFaceFFT, BurnerFaceFreq_FFT, BurnerFaceMag_FFT, ...
BurnerFacePSD, BurnerFaceFreq_PSD, BurnerFaceMag_PSD, ...
BurnerFaceFFT_LP, BurnerFaceFreq_FFT_LP, BurnerFaceMag_FFT_LP, ...
BurnerFacePSD_LP, BurnerFaceFreq_PSD_LP, BurnerFaceMag_PSD_LP, ...
BurnerFaceFFT_HP, BurnerFaceFreq_FFT_HP, BurnerFaceMag_FFT_HP, ...
```

```

BurnerFacePSD_HP, BurnerFaceFreq_PSD_HP, BurnerFaceMag_PSD_HP ] =
ACOUSTIC_BurnerFace(SampleFreq, FiltFreq, TemporalDiv)

% Dialogue box opens to select Excel file containing the DPT
measurements
[listOfFiles, folder] = uigetfile ('*.xlsx', 'Select acoustic data');
fullFileName = fullfile(folder, listOfFiles);
%Read in the DPT measurement timestamps
SampleTime = xlsread(fullFileName, 2, 'A2:A240001');
%Read in the Burner Face DPT measurement
BurnerFace_DPT = xlsread(fullFileName, 2, 'E2:E240001');

%Use the nextpow2 function to increase the performance of FFT when the
%length of a signal is not a power of 2.
N = 2^nextpow2(length(SampleTime));

%Calculation of full signal Burner Face DPT FFT
BurnerFaceFFT1 = fft(BurnerFace_DPT, N);
L_BurnerFaceFFT = length(BurnerFaceFFT1);
BurnerFaceFFT2 = abs(BurnerFaceFFT1/L_BurnerFaceFFT);
BurnerFaceFFT = BurnerFaceFFT2(1:L_BurnerFaceFFT/2+1);
BurnerFaceFFT(2:end-1) = 2*BurnerFaceFFT(2:end-1);
f1 = SampleFreq*(0:(L_BurnerFaceFFT/2))/L_BurnerFaceFFT;

%Calculation of Burner Face Dominant Frequencies from full signal FFT
[PKS LOCS] = findpeaks(BurnerFaceFFT, 'MINPEAKDISTANCE', 500);
BurnerFaceFreq_FFT = zeros(1,length(PKS)-1);
BurnerFaceMag_FFT = zeros(1,length(PKS)-1);
freq = 0:SampleFreq/N:SampleFreq/2;

    for n = 1:(length(PKS)-1)
        [BurnerFaceMag_FFT(n) IPK] = max(PKS);
        LOCPK = LOCS(IPK);
        BurnerFaceFreq_FFT(n) = freq(LOCPK);
        PKS(IPK) = min(PKS);
    end

%Plot the full signal FFT and dominant frequencies
figure(1)
plot(f1,BurnerFaceFFT, BurnerFaceFreq_FFT, BurnerFaceMag_FFT, 'o',
'MarkerEdgeColor','k', 'MarkerFaceColor','k')
title('Single-Sided Amplitude Spectrum of Burner Face DPT')
xlabel('f (Hz)')
ylabel('|BurnerFace FFT (f)|')

%Calculation of full signal Burner Face DPT PSD
BurnerFaceFFT_PSD = BurnerFaceFFT(1:L_BurnerFaceFFT/2+1);
BurnerFacePSD_1 = (1/(SampleFreq*L_BurnerFaceFFT)) *
abs(BurnerFaceFFT_PSD).^2;
BurnerFacePSD_1(2:end-1) = 2*BurnerFacePSD_1(2:end-1);
f2 = 0:SampleFreq/L_BurnerFaceFFT:SampleFreq/2;
BurnerFacePSD = 10*log10(BurnerFacePSD_1);

%Calculation of Burner Face Dominant Frequencies from full signal PSD
[PKS LOCS] = findpeaks(BurnerFacePSD, 'MINPEAKDISTANCE', 500);
BurnerFaceFreq_PSD = zeros(1,length(PKS)-1);
BurnerFaceMag_PSD = zeros(1,length(PKS)-1);
freq = 0:SampleFreq/N:SampleFreq/2;

```

```

for n = 1:(length(PKS)-1)
    [BurnerFaceMag_PSD(n) IPK] = max(PKS);
    LOCPK = LOCS(IPK);
    BurnerFaceFreq_PSD(n) = freq(LOCPK);
    PKS(IPK) = min(PKS);
end

%Plot the full signal PSD and dominant frequencies
figure(2)
plot(f2,BurnerFacePSD, BurnerFaceFreq_PSD, BurnerFaceMag_PSD, 'o',
'MarkerEdgeColor','k', 'MarkerFaceColor','k')
grid on
title('Power Spectral Density of Burner Face DPT')
xlabel('Frequency (Hz)')
ylabel('Power/Frequency (dB/Hz)')

% Create the high pass and bandpass Butterworth filters
HP_filt = design(fdesign.highpass('n,f3dB',30, FiltFreq,4000),
'butter');
LP_filt = design(fdesign.bandpass('N,F3dB1,F3dB2', 30, 1, FiltFreq,
4000), 'butter');

% Apply the high pass and bandpass filters to the input DPT signal
BurnerFace_DPT_LP = filter(LP_filt, BurnerFace_DPT);
BurnerFace_DPT_HP = filter(HP_filt, BurnerFace_DPT);

%Calculation of BurnerFace DPT Bandpass FFT
BurnerFaceFFT1_LP = fft(BurnerFace_DPT_LP, N);
L_BurnerFaceFFT_LP = length(BurnerFaceFFT1_LP);
BurnerFaceFFT2_LP = abs(BurnerFaceFFT1_LP/L_BurnerFaceFFT_LP);
BurnerFaceFFT_LP = BurnerFaceFFT2_LP(1:L_BurnerFaceFFT_LP/2+1);
BurnerFaceFFT_LP(2:end-1) = 2*BurnerFaceFFT_LP(2:end-1);
f3 = SampleFreq*(0:(L_BurnerFaceFFT_LP/2))/L_BurnerFaceFFT_LP;

%Calculation of Burner Face Dominant Frequencies from Bandpass FFT
[PKS LOCS] = findpeaks(BurnerFaceFFT_LP, 'MINPEAKDISTANCE', 500);
BurnerFaceFreq_FFT_LP = zeros(1,length(PKS)-1);
BurnerFaceMag_FFT_LP = zeros(1,length(PKS)-1);
freq = 0:SampleFreq/N:SampleFreq/2;

for n = 1:(length(PKS)-1)
    [BurnerFaceMag_FFT_LP(n) IPK] = max(PKS);
    LOCPK = LOCS(IPK);
    BurnerFaceFreq_FFT_LP(n) = freq(LOCPK);
    PKS(IPK) = min(PKS);
end

%Plot the bandpass signal FFT and dominant frequencies
figure(3)
plot(f3,BurnerFaceFFT_LP, BurnerFaceFreq_FFT_LP, BurnerFaceMag_FFT_LP,
'o', 'MarkerEdgeColor','k', 'MarkerFaceColor','k')
title('Single-Sided Amplitude Spectrum of Low Pass Filtered Burner
Face DPT')
xlabel('f (Hz)')
ylabel('|BurnerFace FFT (f)|')
xlim([0 FiltFreq])

```

%Calculation of BurnerFace DPT Bandpass PSD

```

BurnerFaceFFT_PSD_LP = BurnerFaceFFT_LP(1:L_BurnerFaceFFT_LP/2+1);
BurnerFacePSD_1_LP = (1/(SampleFreq*L_BurnerFaceFFT_LP)) *
abs(BurnerFaceFFT_PSD_LP).^2;
BurnerFacePSD_1_LP(2:end-1) = 2*BurnerFacePSD_1_LP(2:end-1);
f4 = 0:SampleFreq/L_BurnerFaceFFT_LP:SampleFreq/2;
BurnerFacePSD_LP = 10*log10(BurnerFacePSD_1_LP);

```

%Calculation of Burner Face Dominant Frequencies from Bandpass PSD

```

[PKS LOCS] = findpeaks(BurnerFacePSD_LP, 'MINPEAKDISTANCE', 500);
BurnerFaceFreq_PSD_LP = zeros(1,length(PKS)-1);
BurnerFaceMag_PSD_LP = zeros(1,length(PKS)-1);
freq = 0:SampleFreq/N:SampleFreq/2;

```

```

for n = 1:(length(PKS)-1)
    [BurnerFaceMag_PSD_LP(n) IPK] = max(PKS);
    LOCPK = LOCS(IPK);
    BurnerFaceFreq_PSD_LP(n) = freq(LOCPK);
    PKS(IPK) = min(PKS);
end

```

%Plot the bandpass signal PSD and dominant frequencies

```

figure(4)
plot(f4,BurnerFacePSD_LP, BurnerFaceFreq_PSD_LP, BurnerFaceMag_PSD_LP,
'o', 'MarkerEdgeColor','k', 'MarkerFaceColor','k')
grid on
title('Power Spectral Density of Low Pass Filtered Burner Face DPT')
xlabel('Frequency (Hz)')
ylabel('Power/Frequency (dB/Hz)')
xlim([0 FiltFreq])

```

%Calculation of Burner Face DPT High Pass FFT

```

BurnerFaceFFT1_HP = fft(BurnerFace_DPT_HP, N);
L_BurnerFaceFFT_HP = length(BurnerFaceFFT1_HP);
BurnerFaceFFT2_HP = abs(BurnerFaceFFT1_HP/L_BurnerFaceFFT_HP);
BurnerFaceFFT_HP = BurnerFaceFFT2_HP(1:L_BurnerFaceFFT_HP/2+1);
BurnerFaceFFT_HP(2:end-1) = 2*BurnerFaceFFT_HP(2:end-1);
f5 = SampleFreq*(0:(L_BurnerFaceFFT_HP/2))/L_BurnerFaceFFT_HP;

```

%Calculation of Burner Face Dominant Frequencies from High Pass FFT

```

[PKS LOCS] = findpeaks(BurnerFaceFFT_HP, 'MINPEAKDISTANCE', 500);
BurnerFaceFreq_FFT_HP = zeros(1,length(PKS)-1);
BurnerFaceMag_FFT_HP = zeros(1,length(PKS)-1);
freq = 0:SampleFreq/N:SampleFreq/2;

```

```

for n = 1:(length(PKS)-1)
    [BurnerFaceMag_FFT_HP(n) IPK] = max(PKS);
    LOCPK = LOCS(IPK);
    BurnerFaceFreq_FFT_HP(n) = freq(LOCPK);
    PKS(IPK) = min(PKS);
end

```

%Plot the high pass signal FFT and dominant frequencies

```

figure(5)
plot(f5,BurnerFaceFFT_HP, BurnerFaceFreq_FFT_HP, BurnerFaceMag_FFT_HP,
'o', 'MarkerEdgeColor','k', 'MarkerFaceColor','k')
title('Single-Sided Amplitude Spectrum of High Pass Filtered Burner
Face DPT')

```

```

xlabel('f (Hz)')
ylabel('|BurnerFace FFT (f)|')
xlim([FiltFreq (SampleFreq/2)])

%Calculation of Burner Face DPT High Pass PSD
BurnerFaceFFT_PSD_HP = BurnerFaceFFT_HP(1:L_BurnerFaceFFT_HP/2+1);
BurnerFacePSD_1_HP = (1/(SampleFreq*L_BurnerFaceFFT_HP)) *
abs(BurnerFaceFFT_PSD_HP).^2;
BurnerFacePSD_1_HP(2:end-1) = 2*BurnerFacePSD_1_HP(2:end-1);
f6 = 0:SampleFreq/L_BurnerFaceFFT_HP:SampleFreq/2;
BurnerFacePSD_HP = 10*log10(BurnerFacePSD_1_HP);

%Calculation of Burner Face Dominant Frequencies from High Pass PSD
[PKS LOCS] = findpeaks(BurnerFacePSD_HP, 'MINPEAKDISTANCE', 1000);
BurnerFaceFreq_PSD_HP = zeros(1,length(PKS)-1);
BurnerFaceMag_PSD_HP = zeros(1,length(PKS)-1);
freq = 0:SampleFreq/N:SampleFreq/2;

    for n = 1:(length(PKS)-1)
        [BurnerFaceMag_PSD_HP(n) IPK] = max(PKS);
        LOCPK = LOCS(IPK);
        BurnerFaceFreq_PSD_HP(n) = freq(LOCPK);
        PKS(IPK) = min(PKS);
    end

%Plot the high pass signal PSD and dominant frequencies
figure(6)
plot(f6,BurnerFacePSD_HP, BurnerFaceFreq_PSD_HP, BurnerFaceMag_PSD_HP,
'o', 'MarkerEdgeColor','k', 'MarkerFaceColor','k')
grid on
title('Power Spectral Density of High Pass Filtered Burner Face DPT')
xlabel('Frequency (Hz)')
ylabel('Power/Frequency (dB/Hz)')
xlim([FiltFreq (SampleFreq/2)])

%Write Burner Face DPT audio files to current working directory
wavwrite(BurnerFace_DPT, 4000, 'BurnerFace_DPT.wav')
wavwrite(BurnerFace_DPT_LP, 4000, 'BurnerFace_DPT_LP.wav')
wavwrite(BurnerFace_DPT_HP, 4000, 'BurnerFace_DPT_HP.wav')

%BurnerFace DPT Temporal Analysis

%Calculation the number of signal divisions using the input
TemporalDiv
divs = length(SampleTime)*(1/SampleFreq)*(TemporalDiv^-1);
BurnerFace_DPT_T = BurnerFace_DPT';
BurnerFace_DPT_Div = reshape(BurnerFace_DPT_T, [], divs);

BurnerFace_DPT_LP_T = BurnerFace_DPT_LP';
BurnerFace_DPT_LP_Div = reshape(BurnerFace_DPT_LP_T, [], divs);

BurnerFace_DPT_HP_T = BurnerFace_DPT_HP';
BurnerFace_DPT_HP_Div = reshape(BurnerFace_DPT_HP_T, [], divs);

%Calculation of full, bandpass, and high pass signal kurtosis
BurnerFaceK = kurtosis(BurnerFace_DPT);
BurnerFaceK_LP = kurtosis(BurnerFace_DPT_LP);
BurnerFaceK_HP = kurtosis(BurnerFace_DPT_HP);

```

```
%Initiate time varying kurtosis variables for full, bandpass, and
%high pass signals
BurnerFaceK_Var = zeros(1, size(BurnerFace_DPT_Div,2));
BurnerFaceK_Var_LP = zeros(1, size(BurnerFace_DPT_LP_Div,2));
BurnerFaceK_Var_HP = zeros(1, size(BurnerFace_DPT_HP_Div,2));

%Calculation of full signal, bandpass, and high pass signal RMS
BurnerFaceRMS = sqrt(mean(BurnerFace_DPT.^2));
BurnerFaceRMS_LP = sqrt(mean(BurnerFace_DPT_LP.^2));
BurnerFaceRMS_HP = sqrt(mean(BurnerFace_DPT_HP.^2));

%Initiate time varying RMS variables for full, bandpass, and
%high pass signals
BurnerFaceRMS_Var = zeros(1, size(BurnerFace_DPT_Div,2));
BurnerFaceRMS_Var_LP = zeros(1, size(BurnerFace_DPT_LP_Div,2));
BurnerFaceRMS_Var_HP = zeros(1, size(BurnerFace_DPT_HP_Div,2));

%Calculate the time varying kurtosis and RMS values for the full,
%bandpass, and high pass signals that have been divided per the
%TemporalDiv.
for k = 1:size(BurnerFace_DPT_Div,2)
    BurnerFaceK_Var(k) = kurtosis(BurnerFace_DPT_Div(:,k));
    BurnerFaceK_Var_LP(k) = kurtosis(BurnerFace_DPT_LP_Div(:,k));
    BurnerFaceK_Var_HP(k) = kurtosis(BurnerFace_DPT_HP_Div(:,k));

    BurnerFaceRMS_Var(k) = sqrt(mean(BurnerFace_DPT_Div(:,k).^2));
    BurnerFaceRMS_Var_LP(k) =
sqrt(mean(BurnerFace_DPT_LP_Div(:,k).^2));
    BurnerFaceRMS_Var_HP(k) =
sqrt(mean(BurnerFace_DPT_HP_Div(:,k).^2));
end
```

Appendix C.5 – PIV Image Processing, Length Scale, and Turbulence Characterization MATLAB code

The “PIV_Length_Scale.m” function reads in numerical instantaneous velocity vector map output as .CSV files from DynamicStudio software and outputs mean velocity, RMS velocity, turbulence, and length scale calculations. All velocity outputs are in both the “u” (radial) and “v” (axial) directions, in both single column vector and contour plots. The functions requires the user to input the number of instantaneous images, “NumImages”, as well as the radial and axial location (“X” and “Y”) that match the location of interest within the flow field for calculating single point values such as the length scale or velocity information (output as “Lset” and “Vset”). The user must also input the mean burner exit nozzle velocity for calculation of the relative turbulence intensity.

The length scale is calculated using the correlation function as described in Chapters 3 and 5. The length scale is output as 4 length scales (longitudinal and transverse in both axial and radial directions), calculated using two methods (1/e method and integration method), for a total of 8 length scales output per “X,Y” input location. For calculation of the length scale at other locations in the flow field than the centerlines in both X and Y (from DynamicStudio output, the image centerlines here are X = 40, Y = 30), the code is currently formatted to explore locations X < 40 (from burner centerline to left edge of the image) and Y < 30 (from field of view axial centerline to burner exit nozzle).

```
function [Xmm, r, Ymm, y, Umean, Vmean, Urms, Vrms, Uturb, Vturb,
Uturb_per, Vturb_per, ...
    Umean_contour, Vmean_contour, Urms_contour, Vrms_contour,
    Uturb_contour, Vturb_contour, ...
    Uturb_per_contour, Vturb_per_contour, Ry_u, Ry_ue, Ry_v, Ry_ve
    Rr_u, Rr_v, Rr_ue, Rr_ve, ...
    Vset, Lset] = PIV_Length_Scale(NumImages, X,Y, BulkVelo)

% Prompt user to select .CSV files for PIV input (.CSV output from
% DynamicStudio software).
[listOfFiles, folder] = uigetfile ('*.csv', 'Select your image',
'MultiSelect', 'on');
fullFileName = fullfile(folder, listOfFiles{1});
% Read in first .CSV file into an array
M = csvread(fullFileName, 6);

% Read in the x and y coordinates (mm) used
Ymm = M(:,6);
Xmm = M(:,5);
% Calculate the width of the contour map (radial direction)
Xlength = 1+ max(M(:,1));
```

```

Xlength1 = Xlength - (41-X);
% Calculate the height of the contour map (axial direction)
Ylength = 1+ max(M(:,2));
Ylength1 = Ylength - (31-Y);
Xmm_contour = zeros(Ylength, Xlength);
Ymm_contour = zeros(Ylength, Xlength);

% Convert Xmm and Ymm columns into matrix
for Yloc = 1:Ylength
    for Xloc = 1:Xlength
        Xmm_contour(Yloc, Xloc) = Xmm(Xlength*(Yloc-1)+Xloc);
        Ymm_contour(Yloc, Xloc) = Ymm(Xlength*(Yloc-1)+Xloc);
    end
end

% Scaling the radial correlation evaluation axis by the input radial
location
r = linspace(-(Xmm(41))-(Xmm(41)-Xmm(X)), (Xmm(41)+(Xmm(41)-
Xmm(X))), Xlength);

% Scaling the axial correlation evaluation axis by the input axial
location
y = linspace(-(Ymm_contour(31, 41))-(Ymm_contour(31, 41)-
Ymm_contour(Y, X))), (Ymm_contour(31, 41)+(Ymm_contour(31, 41)-
Ymm_contour(Y, X))), Ylength);

% Initializing velocity variables
Umean_sum = 0;
Vmean_sum = 0;
Urms_sum = 0;
Vrms_sum = 0;
Uturb_sum = 0;
Vturb_sum = 0;
Umean_contour = zeros(Ylength, Xlength);
Vmean_contour = zeros(Ylength, Xlength);
Urms_contour = zeros(Ylength, Xlength);
Vrms_contour = zeros(Ylength, Xlength);
Uturb_contour = zeros(Ylength, Xlength);
Vturb_contour = zeros(Ylength, Xlength);
Uturb_per_contour = zeros(Ylength, Xlength);
Vturb_per_contour = zeros(Ylength, Xlength);

% Error check that number of files selected equals the input value
if NumImages ~= length(listOfFiles)
    msg = 'Error Occured - File Number Mismatch';
    error(msg);

% Calculate velocity variables
else
    % Calculate mean U and V velocity at each point in vector map
    for j=1:length(listOfFiles)
        fullFileName = fullfile(folder, listOfFiles{j});
        % Open each .CSV file and read into array
        M = csvread(fullFileName, 6);
        U_PIV = M(:,9);
        V_PIV = M(:,10);
        Umean_sum = Umean_sum + U_PIV;
        Vmean_sum = Vmean_sum + V_PIV;
    end
end

```

```

end

Umean = Umean_sum ./ NumImages;
Vmean = Vmean_sum ./ NumImages;

% Calculate the U and V fluctuating velocity component
for k=1:length(listOfFiles)
    fullFileName = fullfile(folder, listOfFiles{k});
    M = csvread(fullFileName, 6);
    U_PIV = M(:,9);
    V_PIV = M(:,10);
    % u' = u - U
    Uturb1 = U_PIV - Umean;
    Vturb1 = V_PIV - Vmean;
    Urms_sum = Urms_sum + Uturb1.^2;
    Vrms_sum = Vrms_sum + Vturb1.^2;
    Uturb_sum = Uturb_sum + Uturb1;
    Vturb_sum = Vturb_sum + Vturb1;
end

% Calculate Urms and Vrms
Urms = sqrt(Urms_sum ./ NumImages);
Vrms = sqrt(Vrms_sum ./ NumImages);

% Calculate mean turbulence value
Uturb = Uturb_sum ./ NumImages;
Vturb = Vturb_sum ./ NumImages;

% Calculate relative turbulence intensity
Uturb_per = 100*abs(Urms ./ (2*BulkVelo));
Vturb_per = 100*abs(Vrms ./ (2*BulkVelo));
% Convert all velocity component columns into contour maps
for Yloc = 1:Ylength
    for Xloc = 1:Xlength
        Umean_contour(Yloc, Xloc) = Umean(Xlength*(Yloc-1)+Xloc);
        Vmean_contour(Yloc, Xloc) = Vmean(Xlength*(Yloc-1)+Xloc);
        Urms_contour(Yloc, Xloc) = Urms(Xlength*(Yloc-1)+Xloc);
        Vrms_contour(Yloc, Xloc) = Vrms(Xlength*(Yloc-1)+Xloc);
        Uturb_contour(Yloc, Xloc) = Uturb(Xlength*(Yloc-1)+Xloc);
        Vturb_contour(Yloc, Xloc) = Vturb(Xlength*(Yloc-1)+Xloc);
        Uturb_per_contour(Yloc, Xloc) = Uturb_per(Xlength*(Yloc-
1)+Xloc);
        Vturb_per_contour(Yloc, Xloc) = Vturb_per(Xlength*(Yloc-
1)+Xloc);
    end
end

% Calculate axial integral length scale, Ly for u' (transverse) and v'
% (longitudinal)

% Initializing R(y) variables
Ry_u1 = zeros(Y-1, 1);
Ry_u2 = zeros(Ylength1-Y+1, 1);
Ry_v1 = zeros(Y-1, 1);
Ry_v2 = zeros(Ylength1-Y+1, 1);
Uturb2_contour = zeros(Ylength, Xlength);
Vturb2_contour = zeros(Ylength, Xlength);
Uturb3_contour = zeros(Ylength, Xlength);

```

```

Vturb3_contour = zeros(Ylength, Xlength);

% Calculate R(y),u and R(y),v correlation function at (X,Y) from
% bottom of image to Y
for z1 = 0:(Y-1)
    Ry_usum1 = 0;
    Ry_vsum1 = 0;
    for n=1:length(listOfFiles)
        fullFileName = fullfile(folder, listOfFiles{n});
        M = csvread(fullFileName, 6);
        U_PIV2 = M(:,9);
        Uturb2 = U_PIV2 - Umean;
        V_PIV2 = M(:,10);
        Vturb2 = V_PIV2 - Vmean;
        for Yloc = 1:Ylength
            for Xloc = 1:Xlength
                Uturb2_contour(Yloc, Xloc) = Uturb2(Xlength*(Yloc-
1)+Xloc);
                Vturb2_contour(Yloc, Xloc) = Vturb2(Xlength*(Yloc-
1)+Xloc);
            end
        end
        Ryu1 = (Uturb2_contour(Y, X)*Uturb2_contour((Y-z1), X));
        Ry_usum1 = Ry_usum1 + Ryu1;

        Ryv1 = (Vturb2_contour(Y, X)*Vturb2_contour((Y-z1), X));
        Ry_vsum1 = Ry_vsum1 + Ryv1;

    end
    Ryu1_mean = Ry_usum1/NumImages;
    Ryv1_mean = Ry_vsum1/NumImages;
    Ry_u1(z1+1) = Ryu1_mean ./ ((Urms_contour(Y, X)*Urms_contour((Y-
z1), X)));
    Ry_v1(z1+1) = Ryv1_mean ./ ((Vrms_contour(Y, X)*Vrms_contour((Y-
z1), X)));
end

% Calculate R(y),u and R(y),v correlation function at (X,Y) from Y to
% top of imagee
for z2 = 0:(Ylength-Y)
    Ry_usum2 = 0;
    Ry_vsum2 = 0;
    for n=1:length(listOfFiles)
        fullFileName = fullfile(folder, listOfFiles{n});
        M = csvread(fullFileName, 6);
        U_PIV3 = M(:,9);
        Uturb3 = U_PIV3 - Umean;
        V_PIV3 = M(:,10);
        Vturb3 = V_PIV3 - Vmean;
        for Yloc = 1:Ylength
            for Xloc = 1:Xlength
                Uturb3_contour(Yloc, Xloc) = Uturb3(Xlength*(Yloc-
1)+Xloc);
                Vturb3_contour(Yloc, Xloc) = Vturb3(Xlength*(Yloc-
1)+Xloc);
            end
        end
        Ryu2 = (Uturb3_contour(Y, X)*Uturb3_contour((Y+z2), X));

```

```

Ry_usum2 = Ry_usum2 + Ryu2;
Ryv2 = (Vturb3_contour(Y, X)*Vturb3_contour((Y+z2), X));
Ry_vsum2 = Ry_vsum2 + Ryv2;

end
Ryu2_mean = Ry_usum2/NumImages;
Ryv2_mean = Ry_vsum2/NumImages;
Ry_u2(z2+1) = Ryu2_mean ./ ((Urms_contour(Y,
X)*Urms_contour((Y+z2), X)));
Ry_v2(z2+1) = Ryv2_mean ./ ((Vrms_contour(Y,
X)*Vrms_contour((Y+z2), X)));
end

% Combine two-sided correlation function R(y),u
Ry_u1 = flipud(Ry_u1);
Ry_u = vertcat(Ry_u1, Ry_u2(2:end));

% Combine two-sided correlation function R(y),v
Ry_v1 = flipud(Ry_v1);
Ry_v = vertcat(Ry_v1, Ry_v2(2:end));

% Calculate Ly,u by R(y) = 1/e method
Ry_ue = Ry_u-(1/exp(1));
PPy_ue = spline(y, Ry_ue);
ZEROy_ue = fnzeros(PPy_ue, [min(y),max(y)]);
dif1 = abs(ZEROy_ue(1,:)-0) ;
Ly_ue = abs(ZEROy_ue(1, (dif1 == min(dif1))));

% Calculate Ly,v by R(y) = 1/e method
Ry_ve = Ry_v-(1/exp(1));
PPy_ve = spline(y, Ry_ve);
ZEROy_ve = fnzeros(PPy_ve, [min(y),max(y)]);
dif2 = abs(ZEROy_ve(1,:)-0) ;
Ly_ve = abs(ZEROy_ve(1, (dif2 == min(dif2))));

% Calculate Ly,u by integration to first zero-crossing method
PPy_uint = spline(y, Ry_u);
ZEROy_uint = fnzeros(PPy_uint, [min(y),max(y)]);
TF1 = isempty(ZEROy_uint);
if TF1 == 0
    dif3 = abs(ZEROy_uint(1,:)-0) ;
    Ly_uint = abs(quad(@ppval,0,ZEROy_uint(1, (dif3 ==
min(dif3))), [], [], PPy_uint));
else Ly_uint = 0;
end

% Calculate Ly,v by integration to first zero-crossing method
PPy_vint = spline(y, Ry_v);
ZEROy_vint = fnzeros(PPy_vint, [min(y),max(y)]);
TF2 = isempty(ZEROy_vint);
if TF2 == 0
    dif4 = abs(ZEROy_vint(1,:)-0) ;
    Ly_vint = abs(quad(@ppval,0,ZEROy_vint(1, (dif4 ==
min(dif4))), [], [], PPy_vint));
else Ly_vint = 0;
end

```

```

% Calculate radial integral length scale, Lr for u' (longitudinal) and
% v' (transverse)

% Initializing R(r) variables
Rr_u1 = zeros(X-1, 1);
Rr_u2 = zeros(Xlength1-X, 1);
Rr_v1 = zeros(X-1, 1);
Rr_v2 = zeros(Xlength1-X, 1);
Uturb4_contour = zeros(Ylength, Xlength);
Vturb4_contour = zeros(Ylength, Xlength);
Uturb5_contour = zeros(Ylength, Xlength);
Vturb5_contour = zeros(Ylength, Xlength);

% Calculate R(r),u and R(r),v correlation function at (X,Y) from left
% side of image to X
for z3 = 0:(X-1)
    Rr_usum1 = 0;
    Rr_vsum1 = 0;
    for n=1:length(listOfFiles)
        fullFileName = fullfile(folder, listOfFiles{n});
        M = csvread(fullFileName, 6);
        U_PIV4 = M(:,9);
        V_PIV4 = M(:,10);
        Uturb4 = U_PIV4 - Umean;
        Vturb4 = V_PIV4 - Vmean;
        for Yloc = 1:Ylength
            for Xloc = 1:Xlength
                Uturb4_contour(Yloc, Xloc) = Uturb4(Xlength*(Yloc-
1)+Xloc);
                Vturb4_contour(Yloc, Xloc) = Vturb4(Xlength*(Yloc-
1)+Xloc);
            end
        end
        Rr_u1 = (Uturb4_contour(Y, X)*Uturb4_contour(Y, (X-z3)));
        Rr_usum1 = Rr_usum1 + Rr_u1;

        Rrv1 = (Vturb4_contour(Y, X)*Vturb4_contour(Y, (X-z3)));
        Rr_vsum1 = Rr_vsum1 + Rrv1;

    end
    Rr_u1_mean = Rr_usum1/NumImages;

    Rr_u1(z3+1) = Rr_u1_mean ./ ((Urms_contour(Y, X)*Urms_contour(Y,
(X-z3))));

    Rrv1_mean = Rr_vsum1/NumImages;

    Rr_v1(z3+1) = Rrv1_mean ./ ((Vrms_contour(Y, X)*Vrms_contour(Y,
(X-z3))));

end

% Calculate R(r),u and R(r),v correlation function at (X,Y) from X to
% right side of image
for z4 = 0:(Xlength-X)
    Rr_usum2 = 0;
    Rr_vsum2 = 0;
    for n=1:length(listOfFiles)

```

```

fullFileName = fullfile(folder, listOfFiles{n});
M = csvread(fullFileName, 6);
U_PIV5 = M(:,9);
V_PIV5 = M(:,10);
Uturb5 = U_PIV5 - Umean;
Vturb5 = V_PIV5 - Vmean;
for Yloc = 1:Ylength
    for Xloc = 1:Xlength
        Uturb5_contour(Yloc, Xloc) = Uturb5(Xlength*(Yloc-
1)+Xloc);
        Vturb5_contour(Yloc, Xloc) = Vturb5(Xlength*(Yloc-
1)+Xloc);
    end
end

Rru2 = (Uturb5_contour(Y, X)*Uturb5_contour(Y, (X+z4)));
Rr_usum2 = Rr_usum2 + Rru2;

Rrv2 = (Vturb5_contour(Y, X)*Vturb5_contour(Y, (X+z4)));
Rr_vsum2 = Rr_vsum2 + Rrv2;
end
Rru2_mean = Rr_usum2/NumImages;

Rr_u2(z4+1) = Rru2_mean ./ ((Urms_contour(Y, X)*Urms_contour(Y,
(X+z4))));

Rrv2_mean = Rr_vsum2/NumImages;

Rr_v2(z4+1) = Rrv2_mean ./ ((Vrms_contour(Y, X)*Vrms_contour(Y,
(X+z4))));
end

% Combine two-sided correlation function R(r),u
Rr_u1 = flipud(Rr_u1);
Rr_u = vertcat(Rr_u1, Rr_u2(2:end));

% Combine two-sided correlation function R(r),v
Rr_v1 = flipud(Rr_v1);
Rr_v = vertcat(Rr_v1, Rr_v2(2:end));

% Calculate Lr,u by R(y) = 1/e method
Rr_ue = Rr_u-(1/exp(1));
PPr_ue = spline(r, Rr_ue);
ZEROr_ue = fnzeros(PPr_ue, [min(r),max(r)]);
dif5 = abs(ZEROr_ue(1,:)-0) ;
Lr_ue = abs(ZEROr_ue(1, (dif5 == min(dif5))));

% Calculate Lr,v by R(y) = 1/e method
Rr_ve = Rr_v-(1/exp(1));
PPr_ve = spline(r, Rr_ve);
ZEROr_ve = fnzeros(PPr_ve, [min(r),max(r)]);
dif6 = abs(ZEROr_ve(1,:)-0) ;
Lr_ve = abs(ZEROr_ve(1, (dif6 == min(dif6))));

% Calculate Lr,u by integration to first zero-crossing method
PPr_uint = spline(r, Rr_u);
ZEROr_uint = fnzeros(PPr_uint, [min(r),max(r)]);
TF3 = isempty(ZEROr_uint);

```

```
if TF3 == 0
    dif7 = abs(ZEROr_uint(1,:)-0) ;
    Lr_uint = abs(quad(@ppval,0,ZEROr_uint(1,(dif7 ==
min(dif7))), [], [], PPr_uint));
else Lr_uint = 0;
end

% Calculate Lr,v by integration to first zero-crossing method
PPr_vint = spline(r, Rr_v);
ZEROr_vint = fnzeros(PPr_vint, [min(r),max(r)]);
TF4 = isempty(ZEROr_vint);
if TF4 == 0
    dif8 = abs(ZEROr_vint(1,:)-0) ;
    Lr_vint = abs(quad(@ppval,0,ZEROr_vint(1,(dif8 ==
min(dif8))), [], [], PPr_vint));
else Lr_vint = 0;
end

%Output integral length scale values at (X,Y)
Lset = [Ly_ue,Ly_uint, Lr_ue,Lr_uint, Ly_ve, Ly_vint, Lr_ve, Lr_vint];

%Output velocity values at (X,Y)
Vset = [Umean_contour(Y,X), Vmean_contour(Y,X), Urms_contour(Y,X),
Vrms_contour(Y,X), Uturb_per_contour(Y,X), Vturb_per_contour(Y,X)];

end
```

APPENDIX D – IMAGE PROCESSING STATISTICAL ANALYSIS

Appendix D.1 – Chemiluminescence Total Image Number Selection

For all stable operating conditions, 200 instantaneous chemiluminescence images are captured and temporally averaged before the Abel deconvolution is applied. This total image number value was selected by statistical analysis of the signal to noise ratio (SNR) of the chemiluminescence integral intensity. For a set of OH* chemiluminescence images, the instantaneous integral image intensity, I'_{OH^*} , is calculated for each image per Equation 4.1. Then, an evaluation of the mean and standard deviation of the instantaneous integral intensity is made as a function of the number of images utilized in the calculation. Finally, using Equation D.1, the SNR is evaluated in the same manner as a function of the number of images in the dataset, N .

$$SNR(N) = \frac{I_{OH^*}(f(N))}{\sigma(f(N))} \quad (D.1)$$

The number of images used in the dataset is selected as the point at which the SNR(N) variation is sufficiently reduced, as shown in Figure D.1. As an example, the mean (Figure D.1.a), standard deviation (Figure D.1.b), and SNR (Figure D.1.c) are plotted as a function of N for a set of instantaneous integral intensity OH* chemiluminescence images for a 55 kW, CH₄-air flame at $\varphi = 1.0$ and atmospheric temperature and pressure in the HPGSB-2.

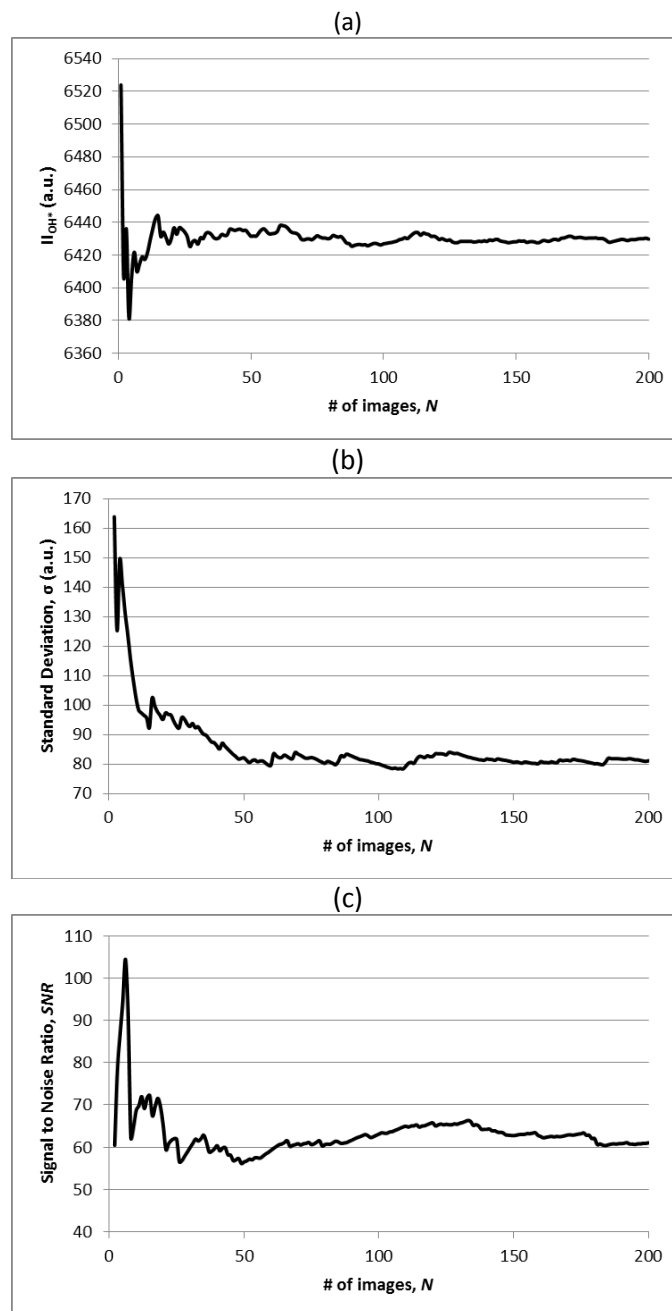


Figure D.1: Mean (a), standard deviation (b), and SNR (c) of I_{OH^*} for a 55 kW atmospheric CH_4 -air flame at $\varphi = 1.0$ as a function of N images used in their calculation

Appendix D.2 – PLIF Total Image Number Selection

For all stable operating conditions, 500 instantaneous OH PLIF images are captured and temporally averaged after the correction processes described in Section 4.2.2 are applied. This total image number was selected by statistical analysis of the SNR of the measured maximum OH PLIF intensity. For a set of OH PLIF images, the maximum OH PLIF intensity, I_{OH} , is calculated for each image. Then, an evaluation of the mean and standard deviation of the maximum OH PLIF intensity is made as a function of the number of images utilized in the

calculation. Finally, using Equation D.2, the SNR is evaluated in the same manner as a function of the number of images in the dataset, N .

$$SNR(N) = \frac{I_{OH}(f(N))}{\sigma(f(N))} \quad (D.2)$$

The number of images used in the dataset is selected as the point at which the SNR(N) variation is sufficiently reduced, as shown in Figure D.2 below. As an example, the mean (Figure D.2.a), standard deviation (Figure D.2.b), and SNR (Figure D.2.c) are plotted as a function of N for a set of OH PLIF images for a 55 kW, premixed CH₄-air flame at $\varphi = 0.7$ and atmospheric temperature and pressure in the HPGSB. For these measurements, a number of different image intensifier gate times, $t_{gate} = 0.1 \mu\text{s}$, $0.75 \mu\text{s}$, and $1.5 \mu\text{s}$ were also utilized while the image intensifier gain was held constant (Gain = 900).

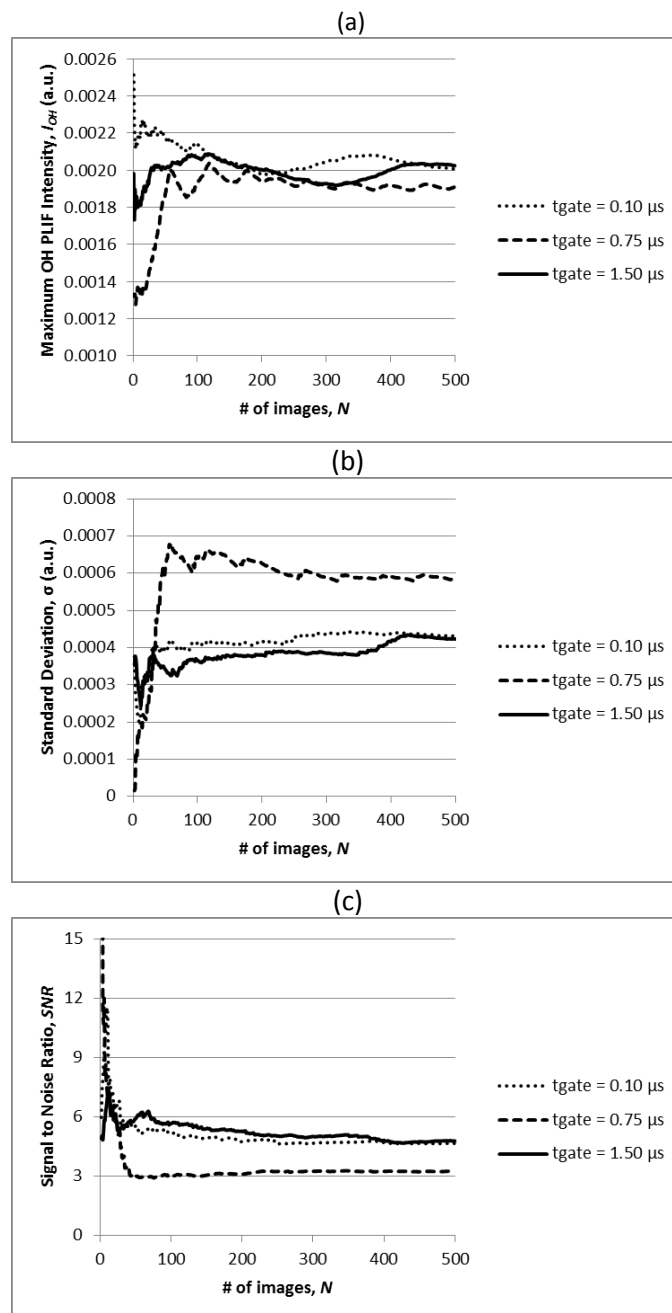


Figure D.2: Mean (a), standard deviation (b), and SNR (c) of maximum OH PLIF intensity, I_{OH} , for a 55 kW atmospheric CH_4 -air flame at $\phi = 0.7$ as a function of N images used in their calculation

Appendix D.3 – PIV Total Image Number Selection

For all stable conditions, 200 PIV images pairs were used in the calculation of flow fields and turbulence characteristics. The number of images utilized for the extraction of key flow field features from PIV measurements is critical, particularly in the case of confined flows using quartz, as these are inevitably coated with the seeding material, introducing noise into the PIV image pairs by representing zero-velocity particles and limiting measurement times. However, a sufficient number of images must also be captured for the extracted values to converge.

This process is shown in Figure D.3 where the integral length scale (Figure D.3.a), mean axial and radial velocities (Figure D.3.b), RMS velocity fluctuations (Figure D.3.c), and relative turbulence intensity (Figure D.3.d) are plotted against the number of images used in their determination with isothermal air flow in the HPGSG-2 with open cylindrical confinement at $T_2 = 573$ K and $P_2 = 0.11$ MPa. All values are calculated along the burner centerline ($r = 0$ mm) at an axial location of $y = 32$ mm above the burner exit nozzle, within the CRZ as evidenced by the negative mean axial velocity component, v , seen in Figure 5.10.b. These critical measures are seen to converge near to their final value after 200 image pairs, thus this value is selected for all further measurements.

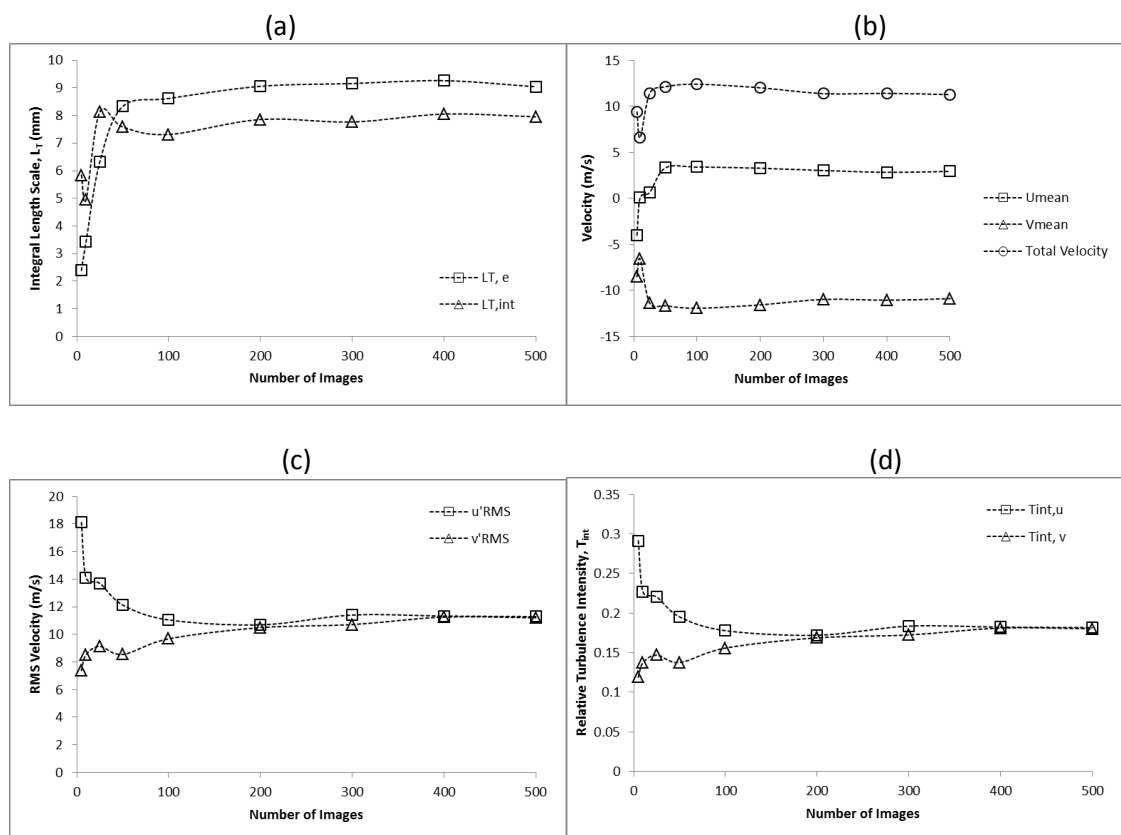


Figure D.3: Influence of the number of PIV image pairs, N , used in the calculation of integral length scale (L_T , a), mean axial and radial velocity (v and u , b), RMS velocity (v'_{RMS} and u'_{RMS} , c), and relative turbulence intensity (T_{int} , d) in the HPGSB-2, open confinement, at $\dot{m}_{air} = 26.25$ g/s, $T_2 = 573$ K, $P_2 = 0.11$ MPa

APPENDIX E – GLOBAL EXPERIMENTAL SWIRL BURNERS**Table E.1: Global experimental confined swirl burners and their operating pressures**

Institute	Designation	D _{dump} (mm)	D _{confine} (mm)	Expansion Ratio	Operating Pressure (MPa)	[Ref]
Cardiff University	HPGSB	40	140	3.50	0.30	[112-121]
Cardiff University	HPGSB-2	40	100	2.50	0.40	[122-126]
Cardiff University	AGSB	28	42 - 56	1.50 - 2.00	0.10	[55-57, 110-112]
Lund	Volvo VT40	54	100	1.85	0.10	[127, 128]
ETH Zurich	Alstom EV5	50	94	1.88	0.10	[69, 129]
PSU		55	110 - 190	2.00 - 3.45	0.10	[130]
MIT		38	76	2.00	0.10	[131, 132]
DLR		40	85	2.13	0.10	[133]
TU-Munich	BRS Burner	40	90	2.25	0.10	[134, 135]
Bucknell		18	45	2.50	0.10	[136]
Cambridge		37	95	2.57	0.10	[89]
NETL	ESS Burner	29.92	82.55	2.76	0.10	[137]
KAIST		38.1	109.2	2.87	0.10	[138]
KIT		---	---	2.90	0.10	[139]
UTM		40	120	3.00	0.10	[140]
Georgia Tech		23	70	3.04	0.10	[74-77]
TU-Berlin		34	105	3.09	0.10	[141]
LBNL	Low Swirl Burner	57	180	3.16	0.10	[142]
EM2C		22	70	3.18	0.10	[143]
INU		40	130	3.25	0.10	[144]
KIT	SBS Burner	25	89	3.56	0.10	[145]
DLR		24	89	3.71	0.10	[146]
Lund / SINTEF	Variable Swirl Burner	15	63	4.20	0.10	[147]
KFUPM		16	70	4.38	0.10	[148]
CNRS		16	80	5.00	0.10	[78]
Sandia	CRF Burner	20	115	5.75	0.10	[149]
EM2C		25	150	6.00	0.10	[150]
BYU	ATS Burner	18	152	8.44	0.10	[151]
EM2C	CESAM-HP	30	70	2.33	0.32	[152]
Georgia Tech		19	51	2.68	0.45	[153]
Georgia Tech		19	76.5	4.03	0.45	[154]
DLR	DS Burner	40	80	2.00	0.50	[64]
CNRS		18	80	4.44	0.50	[79]
DLR	SITL DLE Burner	86	165	1.92	0.60	[95]
PSU		20	45	2.25	0.65	[155]
DLR	TM Burner	27.85	85	3.05	0.70	[62, 90, 156]
NETL	SimVal Burner	65	180	2.77	0.80	[157, 158]
DLR	Twente Burner	30	85	2.83	2.00	[159]